From Spitzer Mid-InfraRed Observations and Measurements of Peculiar Velocities to Constrained Simulations of the Local Universe

J. Sorce

N° d'ordre: 78-2014 Année 2014

THÈSE

délivrée par

L'UNIVERSITÉ CLAUDE BERNARD DE LYON 1, FRANCE

et préparée en cotutelle avec

L'UNIVERSITÉ DE POTSDAM, ALLEMAGNE

ÉCOLE DOCTORALE

Physique et Astrophysique - PHAST

pour l'obtention

DU DIPLÔME DE DOCTORAT

(arrêté du 7 août 2006 / arrêté du 6 janvier 2005)

soutenue publiquement le 12 06 2014

par

Jenny SORCE

From Spitzer Mid-InfraRed Observations and Measurements of Peculiar Velocities to Constrained Simulations of the Local Universe

---

Directeurs de thèse:

Mme COURTOIS Hélène (*Lyon*) et M STEINMETZ Matthias (*Potsdam*)

JURY:

Mme AUGIER Corinne (présidente du jury)

Mme COURTOIS Hélène (directrice de thèse)

M. GOTTLÖBER Stefan (examinateur)

M. PORCIANI Cristiano (rapporteur)

M. STEINMETZ Matthias (directeur de thèse)

M. TULLY Brent (examinateur)

M. YEPES Gustavo (rapporteur)

From Spitzer Mid-InfraRed Observations and Measurements of Peculiar Velocities to Constrained Simulations of the Local Universe

by

Jenny Sorce

2011-2014

University of Lyon
Institut de Physique Nucléaire
4 rue Enrico Fermi
69100 Villeurbanne
FRANCE

University of Potsdam
Leibniz Institut für Astrophysik
An der Sternwarte 16
14482 Potsdam
DEUTSCHLAND

I would like to dedicate this dissertation to my present and hopefully future closest family. There is no doubt that without their continued presence, support, love and encouragements, none of this work would have happened.

Abstract (long version)

Galaxies are observational probes to study the Large Scale Structure of the Universe. In the standard cosmological paradigm, their gravitational motions are *direct* tracers of the total (dark included) matter density and therefore of the Large Scale Structure. In this model, of an isotropic and homogeneous on large enough scales Universe, structure formation is the result of gravitational instabilities driven by primordial density perturbations generated during the early inflationary epoch just after the Big Bang. Analytical treatments of structure formation and galaxy evolution are complex. Thus, their studies rely on numerical cosmological simulations. Still, only one universe observable from a given position, in time and space, is available for comparisons with simulations. The related cosmic variance affects grandly our ability to interpret the results. Simulations constrained by observational data are a perfect remedy to this problem. Achieving such simulations requires the full extent of the international projects Cosmicflows and CLUES.

Cosmicflows aims at cartographying the matter in the Local Universe. In this regard, catalogs of accurate distance measurements to map deviations, due to baryonic and dark matters, from the overall Hubble expansion are built. These measures are mainly obtained with the galaxy luminosity-rotation rate correlation or Tully-Fisher relation. We present the calibration of that relation in the mid-infrared with observational data from Spitzer Space Telescope. The greatest advantage is an all-sky consistency of the measures, removing any systematics, due to the utilization of various observational instruments, which could create spurious cosmic flows. In addition, the mid-infrared band permits to obtain motions of galaxies very close to the obscured, by our galaxy disk, zone where major structures could be. From this calibration combined with the surface photometry of numerous galaxies, accurate distance estimates are derived. They will be included in the third catalog of the project. In the meantime, two catalogs up to 30 and 150 h^{-1} Mpc have been released.

We report improvements and applications of the CLUES' method on these two catalogs. The technique produces simulations, replicas of the Local Universe, constrained by observational data. It is based on the constrained realization algorithm. Beforehand, the cosmic displacement field is computed with the Zel'dovich approximation. This latter is then reversed to relocate reconstructed three-dimensional constraints to their precursors' positions in the initial field. The size, never equalled before, of a peculiar velocity catalogs such as *cosmicflows-2*, with 8000 galaxies within 150 h^{-1} Mpc, highlighted the importance of minimizing the different observational biases. The Local Universe, being neither isotropic nor homogeneous, developing a general corrective solution would be inadequate. By carrying out tests on mock catalogs, built from cosmological simulations, a method to minimize observational bias can be derived. Finally, for the first time in the field, cosmological simulations are constrained *solely* by peculiar velocities. The process is successful as the analysis of the resulting simulations shows that they resemble the Local Universe. The major attractors and voids are simulated at positions approaching observational positions by a few megaparsecs, thus reaching the limit imposed by the linear theory.

keywords: spatial mid-infrared observations, distance estimates, peculiar velocities, constrained cosmological simulations, dark matter, Local Universe

Abstract (short version)

Galaxies are observational probes to study the Large Scale Structure. Their gravitational motions are tracers of the total matter density and therefore of the Large Scale Structure. Besides, studies of structure formation and galaxy evolution rely on numerical cosmological simulations. Still, only one universe observable from a given position, in time and space, is available for comparisons with simulations. The related cosmic variance affects our ability to interpret the results. Simulations constrained by observational data are a perfect remedy to this problem. Achieving such simulations requires the projects Cosmicflows and CLUES. Cosmicflows builds catalogs of accurate distance measurements to map deviations from the expansion. These measures are mainly obtained with the galaxy luminosity-rotation rate correlation. We present the calibration of that relation in the mid-infrared with observational data from Spitzer Space Telescope. Resulting accurate distance estimates will be included in the third catalog of the project. In the meantime, two catalogs up to 30 and 150 h^{-1} Mpc have been released. We report improvements and applications of the CLUES' method on these two catalogs. The technique is based on the constrained realization algorithm. The cosmic displacement field is computed with the Zel'dovich approximation. This latter is then reversed to relocate reconstructed three-dimensional constraints to their precursors' positions in the initial field. The size of the second catalog (8000 galaxies within 150 h^{-1} Mpc) highlighted the importance of minimizing the observational biases. By carrying out tests on mock catalogs, built from cosmological simulations, a method to minimize observational bias can be derived. Finally, for the first time, cosmological simulations are constrained *solely* by peculiar velocities. The process is successful as resulting simulations resemble the Local Universe. The major attractors and voids are simulated at positions approaching observational positions by a few megaparsecs, thus reaching the limit imposed by the linear theory.

Résumé (version longue)

Les galaxies sont des sondes observationnelles pour l'étude des structures de l'Univers. Dans le paradigme standard cosmologique, leur mouvement gravitationnel permet de tracer *directement* la densité totale de matière (noire incluse). Dans ce modèle, d'un univers isotropique et homogène aux grandes échelles, la formation des structures est le fruit d'instabilités gravitationnelles induites par des fluctuations de densité primordiales générées pendant la période d'inflation suivant le Big Bang. Les traitements analytiques de formation des structures et galaxies se révèlent complexes. C'est pourquoi leur étude s'appuie sur les simulations numériques cosmologiques. Cependant, un seul univers observable à partir d'une position donnée, en temps et espace, est disponible pour comparaison avec les simulations. La variance cosmique associée affecte fortement notre capacité à interpréter les résultats. Les simulations contraintes par les données observationnelles constituent une solution optimale au problème. Réaliser de telles simulations requiert toute l'ampleur des projets internationaux Cosmicflows et CLUES.

Cosmicflows a pour objectif de cartographier la matière dans l'Univers Local. Pour cela, des catalogues de mesures de distances précises, afin d'obtenir les déviations de l'expansion globale dues aux matières baryonique et noire, sont construits. Ces mesures sont principalement obtenues avec la corrélation entre la luminosité des galaxies et la vitesse de rotation de leur gaz, aussi appelée relation de Tully-Fisher. La calibration de cette relation est présentée dans le mi-infrarouge avec les observations du télescope spatial Spitzer. L'avantage majeur est une consistance des mesures dans tout le ciel, qui permet d'effacer les systématiques liées à l'utilisation de différents télescopes, pouvant engendrer de faux courants cosmiques. La bande mi-infrarouge permet également de sonder les mouvements des galaxies très proches de la zone obscurée, par le disque de notre galaxie, où d'importantes structures peuvent se trouver. Cette calibration, associée à la photométrie de surface de nombreuses galaxies, fournit des estimations de distances précises qui seront intégrées au troisième catalogue de données du projet. En attendant, deux catalogues de mesures atteignant 30 et 150 h^{-1} Mpc ont été publiés.

Les améliorations et applications de la méthode du projet CLUES sur les deux catalogues sont présentées. La technique permet d'obtenir des simulations, répliques de l'Univers Local, contraintes par les données observationnelles. Elle est basée sur l'algorithme de réalisation contrainte. Au préalable, l'approximation de Zel'dovich permet de calculer le champ de déplacement cosmique. Son inversion repositionne les contraintes tridimensionnelles reconstruites à l'emplacement de leur précurseur dans le champ initial. La taille, jamais égalée auparavant, d'un catalogue de vitesses particulières tel que *cosmiflows-2*, contenant 8000 galaxies jusqu'à une distance de 150 h^{-1} Mpc, a permis de mettre en évidence l'importance de minimiser les différents biais observationnels. L'Univers Local n'étant ni homogène, ni isotropique, le développement d'une solution corrective générale ne serait pas approprié. En réalisant des tests sur des catalogues de similis, issus des simulations cosmologiques, une méthode de minimisation des biais observationnels peut être dérivée. Finalement, pour la première fois dans le domaine, des simulations cosmologiques sont contraintes *uniquement* par des vitesses particulières de galaxies. Le procédé est une réussite car l'analyse des simulations obtenues montre leur grande ressemblance à l'Univers Local. Les principaux attracteurs et vides sont simulés à des positions approchant de quelques mégaparsecs les positions observationnelles, atteignant ainsi la limite fixée par la théorie linéaire.

mots-clefs: observations spatiales dans le mi-infrarouge, estimations de distances, vitesses particulières, simulations cosmologiques contraintes, matière noire, Univers Local

Résumé (version courte)

Les galaxies sont des sondes observationnelles pour l'étude des structures de l'Univers. Leur mouvement gravitationnel permet de tracer la densité totale de matière. Par ailleurs, l'étude de la formation des structures et galaxies s'appuie sur les simulations numériques cosmologiques. Cependant, un seul univers observable à partir d'une position donnée, en temps et espace, est disponible pour comparaison avec les simulations. La variance cosmique associée affecte notre capacité à interpréter les résultats. Les simulations contraintes par les données observationnelles constituent une solution optimale au problème. Réaliser de telles simulations requiert les projets Cosmicflows et CLUES. Cosmicflows construit des catalogues de mesures de distances précises afin d'obtenir les déviations de l'expansion. Ces mesures sont principalement obtenues avec la corrélation entre la luminosité des galaxies et la vitesse de rotation de leur gaz. La calibration de cette relation est présentée dans le mi-infrarouge avec les observations du télescope spatial Spitzer. Les estimations de distances résultantes seront intégrées au troisième catalogue de données du projet. En attendant, deux catalogues de mesures atteignant 30 et 150 h^{-1} Mpc ont été publiés. Les améliorations et applications de la méthode du projet CLUES sur les deux catalogues sont présentées. La technique est basée sur l'algorithme de réalisation contrainte. L'approximation de Zel'dovich permet de calculer le champ de déplacement cosmique. Son inversion repositionne les contraintes tridimensionnelles reconstruites à l'emplacement de leur précurseur dans le champ initial. La taille inégalée, 8000 galaxies jusqu'à une distance de 150 h^{-1} Mpc, du second catalogue a mis en évidence l'importance de minimiser les biais observationnels. En réalisant des tests sur des catalogues de similis, issus des simulations cosmologiques, une méthode de minimisation des biais peut être dérivée. Finalement, pour la première fois, des simulations cosmologiques sont contraintes *uniquement* par des vitesses particulières de galaxies. Le procédé est une réussite car les simulations obtenues ressemblent à l'Univers Local. Les principaux attracteurs et vides sont simulés à des positions approchant de quelques mégaparsecs les positions observationnelles, atteignant ainsi la limite fixée par la théorie linéaire.

Zusammenfassung (lange Version)

Die Verteilung der Galaxien liefert wertvolle Erkenntnisse über die großräumigen Strukturen im Universum. Im kosmologischen Standardmodell ist ihre durch Gravitation verursachte Bewegung ein *direkter* Tracer für die Dichteverteilung der gesamten Materie. In diesem Modell ist die Strukturentstehung die Folge von Gravitationsinstabilitäten, welche ihren Ursprung in primordialen Dichtefluktuationen haben, die in der inflationären Phase der kosmologischen Expansion unmittelbar nach dem Big Bang entstanden sind. Die Strukturentstehung und die Bildung von Galaxien ist außerordentlich komplex und analytisch nicht behandelbar. Daher basiert ihre Erforschung auf kosmologischen numerischen Simulationen. Es gibt jedoch von einem gegebenen Ort aus nur ein einziges beobachtbares Universum, welches mit der Theorie und den Ergebnissen unterschiedlicher Simulationen verglichen werden muß. Die kosmische Varianz erschwert es, beobachtbare großräumige Strukturen mit Simulationen zu reproduzieren. Simulationen, deren Anfangsbedingungen durch Beobachtungsdaten eingegrenzt sind ("Constrained Simulations") stellen eine geeignete Lösung dieses Problems dar. Die Durchführung solcher Simulationen ist das Ziel der internationalen Projekte Cosmicflows und CLUES.

Die Zielsetzung von Cosmicflows ist eine Kartierung der Materieverteilung im lokalen Universum. Zu diesem Zweck werden Kataloge mit akkuraten Entfernungsbestimmungen erstellt, welche die durch das lokale Gravitationsfeld von baryonischer und dunkler Materie verursachte Abweichung von der allgemeinen Hubble-Expansion des Universums abbilden. Diese Messungen werden hauptsächlich aus der Korrelation zwischen Leuchtkraft und Rotationsgeschwindigkeit von Spiralgalaxien, der Tully-Fisher-Beziehung, gewonnen. In dieser Arbeit wird die Kalibrierung dieser Beziehung im mittleren Infrarot mithilfe von Daten vom Spitzer Space Telescope vorgestellt. Der größte Vorteil gegenüber anderen Datensätzen ist die Konsistenz der Messungen über den gesamten Himmel und damit eine wesentliche Verringerung systematischer Fehler durch die Verwendung unterschiedlicher Meßinstrumente. Außerdem ist es im mittleren Infrarot möglich, auch die Bewegung jener Galaxien zu messen, die sehr nah an dem durch die galaktische Scheibe der Milchstraße verdeckten Bereich liegen, in welchem massereiche Strukturen vermutet werden. Wird diese Kalibrierung mit Oberflächenphotometrie vieler Galaxien kombiniert, erhält man sehr genaue Entfernungsbestimmungen. Diese Entfernungsbestimmungen werden im dritten Katalog des Cosmicflows-Projekts enthalten sein. Bisher wurden zwei Kataloge veröffentlicht, mit Entfernungen bis zu 30 beziehungsweise 150 h^{-1} Mpc.

In dieser Arbeit wird die CLUES-Methode auf diese zwei Kataloge angewendet und Verbesserungen werden vorgestellt und diskutiert. Mit der CLUES-Methode kann man auf der Grundlage von Beobachtungsdaten des heutigen lokalen Universums seine Enstehung simulieren. Die Grundlage dafür bildet der Algorithmus der "Constrained Realizations". Zunächst wird das kosmische Verschiebungsfeld mithilfe der Zeldovich-Näherung bestimmt. In umgekehrter Richtung kann man damit die aus heutigen Beobachtungsdaten rekonstruierten dreidimensionalen Constraints an ihren Ursprungsort im frühen Universum zurückzuversetzen. Der *cosmicflows-2* Katalog, welcher die Pekuliargeschwindigkeiten von 8000 Galaxien bis zu einer Entfernung von 150 h^{-1} Mpc enthält, bietet einen bisher unerreichten Datenumfang. Es ist daher eine besondere Herausforderung, den Einfluss verschiedener Beobachtungsfehler (Bias) zu minimieren. Da das lokale Universum weder homogen noch isotrop ist, reicht eine allgemeine Korrektur nicht aus. Eine für das lokale Universum angepasste Korrekturmethode lässt sich durch die Untersuchung von Mock-Katalogen finden, welche aus kosmologischen Simulationen gewonnen werden. Schließlich stellt diese Arbeit erstmals kosmologische Simulationen vor, die *ausschließlich* durch Pekuliargeschwindigkeiten eingegrenzt sind. Der Erfolg dieser Methode wird dadurch bestätigt, dass die daraus resultierenden Simulationen dem beobachteten lokalen Universum sehr ähnlich sind. Die relevanten Attraktoren und Voids liegen in den Simulationen an Positionen, welche bis auf wenige Megaparsec mit den beobachteten Positionen übereinstimmen. Die Simulationen erreichen damit die durch die lineare Theorie gegebene Genauigkeitsgrenze.

Schlüsselwörter: Beobachtungen im mittleren Infrarot, Abstandsmessungen, Pekuliargeschwindigkeiten, kosmologische Simulationen, Dunkle Materie, Lokales Universum

Zusammenfassung (kurze Version)

Die Verteilung der Galaxien liefert wertvolle Erkenntnisse über die großräumigen Strukturen im Universum. Ihre durch Gravitation verursachte Bewegung ist ein *direkter* Tracer für die Dichteverteilung der gesamten Materie. Die Strukturentstehung und die Entwicklung von Galaxien wird mithilfe von numerischen Simulationen untersucht. Es gibt jedoch nur ein einziges beobachtbares Universum, welches mit der Theorie und den Ergebnissen unterschiedlicher Simulationen verglichen werden muß.. Die kosmische Varianz erschwert es, das lokale Universum mit Simulationen zu reproduzieren. Simulationen, deren Anfangsbedingungen durch Beobachtungsdaten eingegrenzt sind ("Constrained Simulations") stellen eine geeignete Lösung dieses Problems dar. Die Durchführung solcher Simulationen ist das Ziel der Projekte Cosmicflows und CLUES. Im Cosmicflows-Projekt werden genaue Entfernungsmessungen von Galaxien erstellt, welche die Abweichung von der allgemeinen Hubble-Expansion abbilden. Diese Messungen werden hauptsächlich aus der Korrelation zwischen Leuchtkraft und Rotationsgeschwindigkeit von Spiralgalaxien gewonnen. In dieser Arbeit wird die Kalibrierung dieser Beziehung im mittleren Infrarot mithilfe von Daten vom Spitzer Space Telescope vorgestellt. Diese neuen Entfernungsbestimmungen werden im dritten Katalog des Cosmicflows-Projekts enthalten sein. Bisher wurden zwei Kataloge veröffentlicht, mit Entfernungen bis zu 30 beziehungsweise 150 h^{-1} Mpc. In dieser Arbeit wird die CLUES-Methode auf diese zwei Kataloge angewendet und Verbesserungen werden vorgestellt und diskutiert. Zunächst wird das kosmische Verschiebungsfeld mithilfe der Zeldovich-Näherung bestimmt. In umgekehrter Richtung kann man damit die aus heutigen Beobachtungsdaten rekonstruierten dreidimensionalen Constraints an ihren Ursprungsort im frühen Universum zurückzuversetzen. Durch den großen Datenumfang des *cosmicflows-2* Katalogs (8000 Galaxien bis zu einer Entfernung von 150 h^{-1} Mpc) ist es besonders wichtig, den Einfluss verschiedener Beobachtungsfehler zu minimieren. Eine für das lokale Universum angepasste Korrekturmethode lässt sich durch die Untersuchung von Mock-Katalogen finden, welche aus kosmologischen Simulationen gewonnen werden. Schließlich stellt diese Arbeit erstmals kosmologische Simulationen vor, die *ausschließlich* durch Pekuliargeschwindigkeiten eingegrenzt sind. Der Erfolg dieser Methode wird dadurch bestätigt, dass die dadurch erzeugten Simulationen dem beobachteten lokalen Universum sehr ähnlich sind. Die relevanten Attraktoren und Voids liegen in den Simulationen an Positionen, welche bis auf wenige Megaparsec mit den beobachteten Positionen übereinstimmen. Die Simulationen erreichen damit die durch die lineare Theorie gegebene Genauigkeitsgrenze.

From Spitzer Mid-InfraRed Observations and Measurements of Peculiar Velocities to Constrained Simulations of the Local Universe

Contents

List of Figures

List of Tables

"Nothing happens
until something moves."
Albert Einstein

Chapter 1

Motivation

With the emergence of modern cosmology came the cosmological principle which relies on the strong assumption that the distribution of matter, in the Universe, is homogeneous and isotropic about all locations when viewed on a large enough scale. This last part of the axiom is essential as observations soon revealed that nearby galaxies are distributed in an inhomogeneous way (e.g. Bahcall, 1984; Longair and Einasto, 1978). As a matter of fact, large scale structures which can extend up to 100 h^{-1} Mpc (Bahcall, 1984; Oort, 1982) can be observed in the whole observable Universe. Galaxies, which constitute themselves local inhomogeneities, have a tendency to gather in groups or even clusters, which can regroup to form superclusters, linked by filaments. The assumption of homogeneity on "small scales" had to be banished (Chincarini, 1981). Current maps of our neighborhood on Figures 1.1 and 1.2 show that indeed superclusters and clusters in the Universe are linked by filaments constituted of galaxies. These filaments delimit nearly empty regions or voids as large as 300 h^{-1} Mpc (e.g. Bahcall, 1984). The presence of such regions devoid of galaxies is striking. Mapping the Universe is essential to determine the limit of the cosmological principle. Besides, observations also revealed that the Universe undergoes an accelerated (Perlmutter et al., 1998; Riess et al., 1998) expansion (Hubble, 1929) suggesting the existence of a dark energy.

Beyond the simple acknowledgement of the existence of the Large Scale Structure, in an homogeneous and isotropic on a large enough scale Universe in accelerated expansion, is implied the study of its formation and evolution. There is no doubt that this dynamics of the Universe is gravitationally related (e.g. Peebles, 1980). Structures are the probable

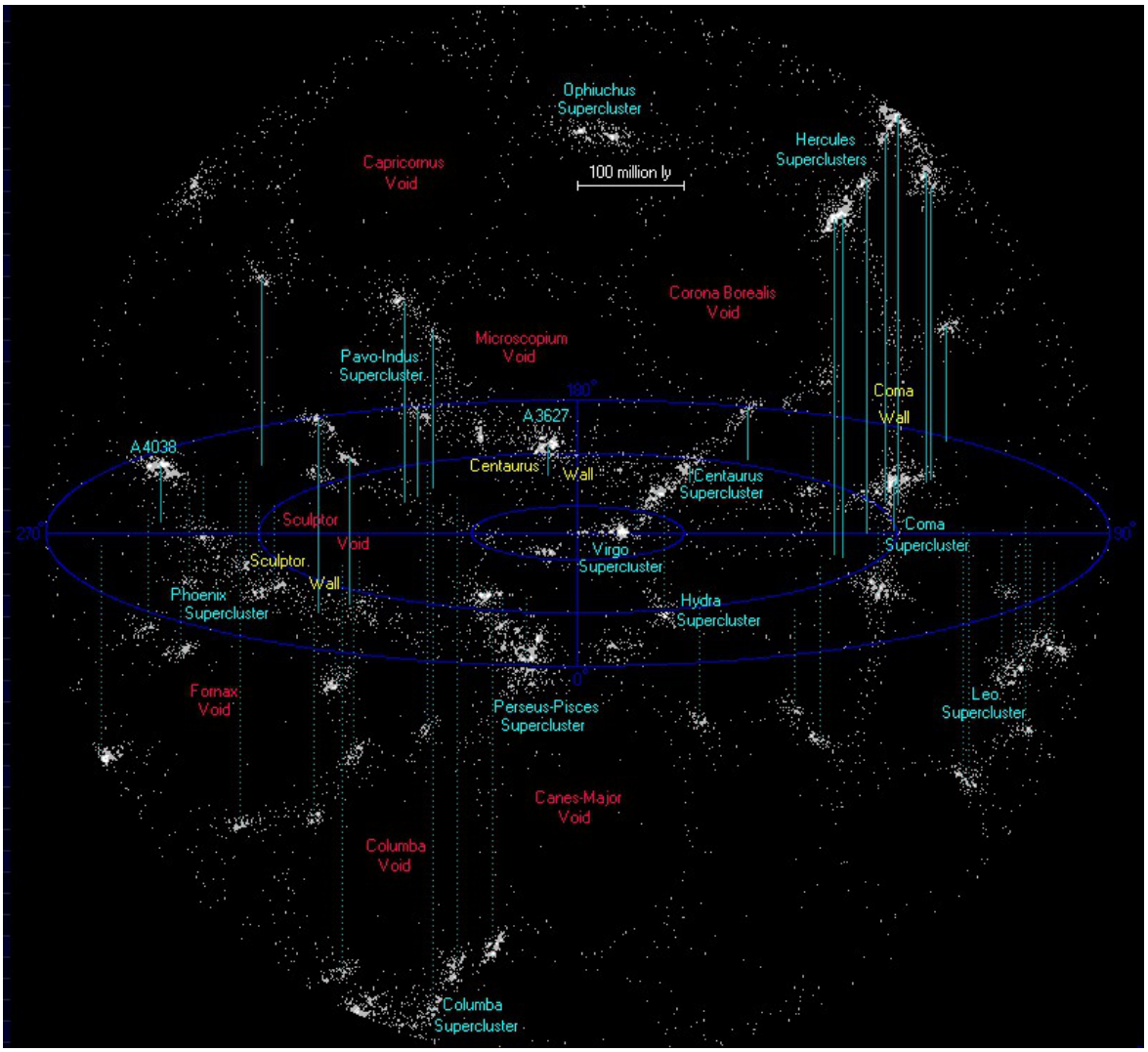

FIGURE 1.1: Schematic map of the nearest Superclusters centered on the Milky Way. Large structures of the Local Universe are visible: wide regions devoid of galaxies or voids (names written in red) are delimited by long filaments formed by galaxies (white dots). Superclusters (pale blue color) are at the nodes of these filaments. Their positions, with respect to the supergalactic plane in dark blue, is defined by pale blue lines either solid if their are above the plane or dotted if they are below it. The yellow color indicates walls (from http://www.atlasoftheuniverse.com).

results of irregularities in the primordial (early after the Big Bang) density field which have grown under the influence of gravity (e.g. Press and Schechter, 1974; Silk et al., 1983). In that sense, the presence of a dipole in the Cosmic Microwave Background temperature map (Fixsen et al., 1996) is a compelling evidence of the motion of our Galaxy at high speed (over 600 km s^{-1}) because of gravity. However, the considerable majority ($\approx 70\%$) of this posited motion is due to the gravitational influence of large scales with origins that have yet to be understood.

Gravitational dynamics is too complex to be analytically studied in details. Thus, studies rely on simulations based on numerical methods. The recent development of large parallel

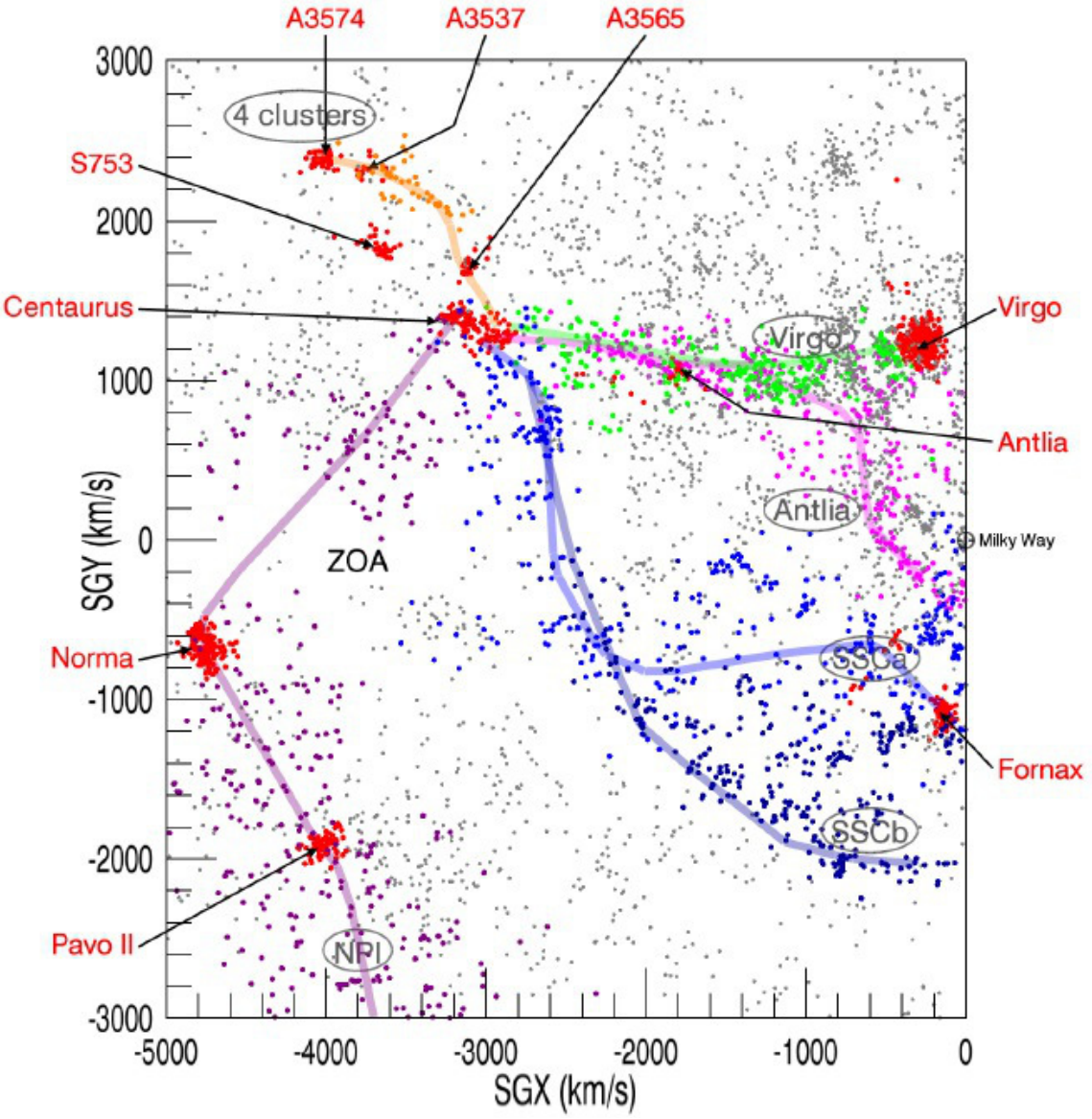

FIGURE 1.2: Supergalactic XY slice of 4000 km s^{-1} thickness in Z showing five filaments joining up in the Centaurus cluster. Red dots stand for the major clusters identified in red and filament names are in grey oval shapes. The five filaments and galaxies belonging to them are depicted with five different colors. Orphan galaxies are in grey (from Courtois et al., 2013).

supercomputers and of highly efficient numerical codes (e.g. Kravtsov et al., 1997; Springel, 2005; Teyssier, 2002), to simulate the gravitational clustering of dark matter, led to a better understanding of structure formation at all scales. Ordinary matter contributes to less than 20% of the total matter in the Universe, thus, accordingly, it can be neglected in simulations in a first approximation. The resulting scheme is 1) cosmic structures grow via the sole gravitational instabilities pre-existing in the initial density field in the form of Gaussian fluctuations (Press and Schechter, 1974) ; 2) in a dissipationless gravitational collapse, dark halos are shaped (Gunn and Gott, 1972) ; 3) and galaxies form with the halos following the

radiative cooling of baryons[1] (e.g. Efstathiou, 2003). Two powerful concepts can describe the formation of galaxies : 1- gasdynamical simulations (e.g. Scannapieco et al., 2005) ; 2- populating dark matter halos with semi-analytical models (e.g. Cole et al., 2000) or abundance matching techniques (e.g. Klypin et al., 2013). To summarize, to study a particular region or object, one can consider extracting a part of the larger box, resimulate it using higher resolution with or without adding baryonic particles. In this latter case, the simulation needs to be populated. This numerical progress has been accompanied by a huge amount of new observational data, which became available over the last decade. As a result, because on short distances tiny dwarf galaxies can be detected as well as big galaxies, structure formation in the nearby Universe can be observed on all possible scales ensuring that observations and simulations can be compared on every scale.

Resulting large simulations (e.g. Alimi et al., 2012; Angulo et al., 2012a; Fosalba et al., 2013; Klypin et al., 2011; Springel et al., 2005) have already widely contributed to establish the standard model of cosmology. Through comparisons with observations, it has become possible to decide between models and numerical algorithms. For instance, Hot Dark Matter was ruled out as the dominant matter component as it implies that large scale structures form first, before fragmenting, recently, into small structures in contradiction with observations of small scale structures at high redshifts (e.g. Petry et al., 1998; Rauch et al., 1999, 2001). Still, while ensuing comparisons between (nearby) observations and simulations have revealed that Large Scale Structure formation can be well described within the Cold Dark Matter (CDM) scenario as a result of an accretion of small structures, there are several open problems related to the formation of these small scale structures. These problems are due to differences in the number of galaxy satellites (Klypin et al., 1999; Moore et al., 1999), the size of voids (Tikhonov and Klypin, 2009) and the number of dwarfs between the observed and simulated local universes (Zavala et al., 2009). To compare more precisely theoretical predictions with observed nearby small scale structures, replicas of the Local Universe needs to be simulated to remove the dependence on the specificity of the environment, namely to avoid the cosmic variance contained in the random realizations. This can be done in the framework of simulations whose Initial Conditions are constrained by nearby observational data. Such constrained simulations are ideal laboratories to study the formation and evolution processes of the Universe in general but also of its constituents such as galaxies. By their constrained nature, they reduce effectively the cosmic variance related to the fact that as fixed observers in the Universe we can observe only one angle of our Universe, at one time.

Accordingly, the CLUES project[2] (Constrained Local UniversE Simulations, Gottlöber et al.,

[1] The goal of this work is to study scales large enough for the influence of baryons to be negligible. Consequently, studies in this work are conducted in a dark matter only context.

[2] http://www.clues-project.org/

2010) developed the concept of constrained simulations. The first constrained Initial Conditions were produced by Ganon and Hoffman (1993), using the Mark III catalog of peculiar velocities (Willick et al., 1996). Kolatt et al. (1996) used these Initial Conditions to perform the first constrained simulations of the nearby Universe, more than ten years after the first standard numerical simulation was run within a Cold Dark Matter cosmological context (Davis et al., 1985). Later, Bistolas and Hoffman (1998) produced Initial Conditions constrained by redshift surveys. They were followed by Mathis et al. (2002) and Lavaux (2010) and very recently by Heß et al. (2013). There exists a real trade-off between the two sets of observational data available: radial peculiar velocities and redshift surveys. While measuring velocities is a tremendous challenge to the observers' community, on the theoretical side these velocities are unbiased tracers of the underlying gravitational field as they account for both baryonic and dark matter. On the other hand, very large and deep surveys of galaxy redshifts are more easily produced but galaxies constitute biased markers of the underlying mass distribution since they account only for the luminous matter. Moreover, the bias is poorly known (e.g. Baugh, 2013). Thus, radial peculiar velocity catalogs have inevitably a great potential and a promising future. The new project Cosmicflows[3] (e.g. Courtois and Tully, 2012a,b; Tully and Courtois, 2012) is an ideal constraints-supplier to perform constrained simulations of the nearby Universe.

Cosmicflows is an international project, with as many arms as an octopus, whose goal is to map the Local Universe. Within this context, the collaboration accumulates accurate distances of thousands of galaxies via observations and distance indicators such as the luminosity-linewidth rotation rate correlation or Tully-Fisher relation (Tully and Fisher, 1977), the Cepheid-period luminosity (Freedman et al., 2001), the Tip of the Red Giant Branch (Lee et al., 1993) , the Surface Brightness Fluctuation (Tonry et al., 2001), the Fundamental Plane (Colless et al., 2001) and the Supernovae of type Ia (Jha et al., 2007) methods. A major part of the program involves exploitation of the Tully-Fisher relation. Activities in this regard began with the gathering of HI profiles for the necessary kinematic information using the Green Bank and Parkes Telescopes (Courtois et al., 2009, 2011b) and the accumulation of optical photometry for the necessary magnitude and inclination information using the University of Hawaii 2.24m telescope (Courtois et al., 2011a) and the available literature. The project has already supplied the community with two catalogs of accurate distances up to 30 h^{-1} Mpc (Tully et al., 2008) and 150 h^{-1} Mpc (Tully et al., 2013) respectively. Both are downloadable at the Extragalactic Distance Database website[4] (Courtois et al., 2009; Tully et al., 2009) of the project. This work presents an extension of the optical part of the project with a shift to the mid-infrared wavelengths already partly published in (Sorce et al., 2012a, 2013b, 2012b). Results from this work will become part of another

[3] http://www.ipnl.in2p3.fr/projet/cosmicflows/
[4] http://edd.ifa.hawaii.edu/

catalog of the project with a greater accuracy. This third catalog will extend the coverage both in distances and close to the Zone of Avoidance (zone which looks devoid of data only because of the extinction of our Galactic disk) where our knowledge is still very limited. The holy grail of Cosmicflows is the use of these resulting distance estimates to determine radial peculiar velocities to be combined with the CLUES project.

First of all, these catalogs can be used with the Wiener-Filter technique (e.g. Zaroubi et al., 1995) to reconstruct the Local Universe. Still, if reconstructions of the velocity and density field of our neighborhood already enable the studies of the Bulk Flow and motions (e.g. Courtois et al., 2012), it presents us only with the linear part of the theory (e.g. Nusser, 2008; Zaroubi et al., 1999) and solely at redshift, z, null (namely the Universe today). Combined with the Constrained Realizations technique (e.g. Hoffman and Ribak, 1991), the catalogs can supply us with constrained Initial Conditions which, once run, can give insights into the evolution and formation of the Large Scale Structure from high redshifts up to today including non-linear events such as mergers. Studying the early history of our Universe will help decide between theoretical models which are all built to reproduce the observed expansion at late times (e.g. Xia et al., 2012). However, the first simulations output from the Constrained Realization method presented a shift in the position of structures of approximately 10 h^{-1} Mpc at $z = 0$ with respect to the observed Universe today. Moreover, additional density constraints were required to form the nearby clusters (Klypin et al., 2003). A new methodology has been developed to improve the simulations by taking into account the cosmic displacement field of data-points from high redshifts to $z = 0$ at first order (Doumler et al., 2013a,b,c). This methodology called the Reverse Zel'dovich Approximation, which works well on simple mocks on Figure 1.3, reveals itself to be insufficient when applied to observational data. This work presents tests on more realistic mocks to refine the process. Re-establishing the 3 directions of peculiar velocities is proved to be a satisfactory refinement for the process to work with observational datasets (work already published in Sorce et al., 2014). The resulting constrained dark matter only simulations are excellent replicas of our Universe, obtained for the first time *solely* with observational radial peculiar velocities from the first catalog of the project Cosmicflows. The uncertainty in positions has been reduced to ~ 3 h^{-1} Mpc (the limit imposed by the linear theory) for the best realizations. This work concludes with the application of the whole process on the second catalog of the project Cosmicflows firstly analyzed to reduce bias effects which become more important with the increasing spatial extent of the catalog. A method is actually proposed in this work to minimize biases. The cosmological model considered in this work is the standard ΛCDM and the simulations have been run with the Lagrangian GADGET code (Springel, 2005).

This work aims at studying several processes both observational and numerical in analytical and quantitative ways in the loop defined by the combination of the Cosmicflows and CLUES

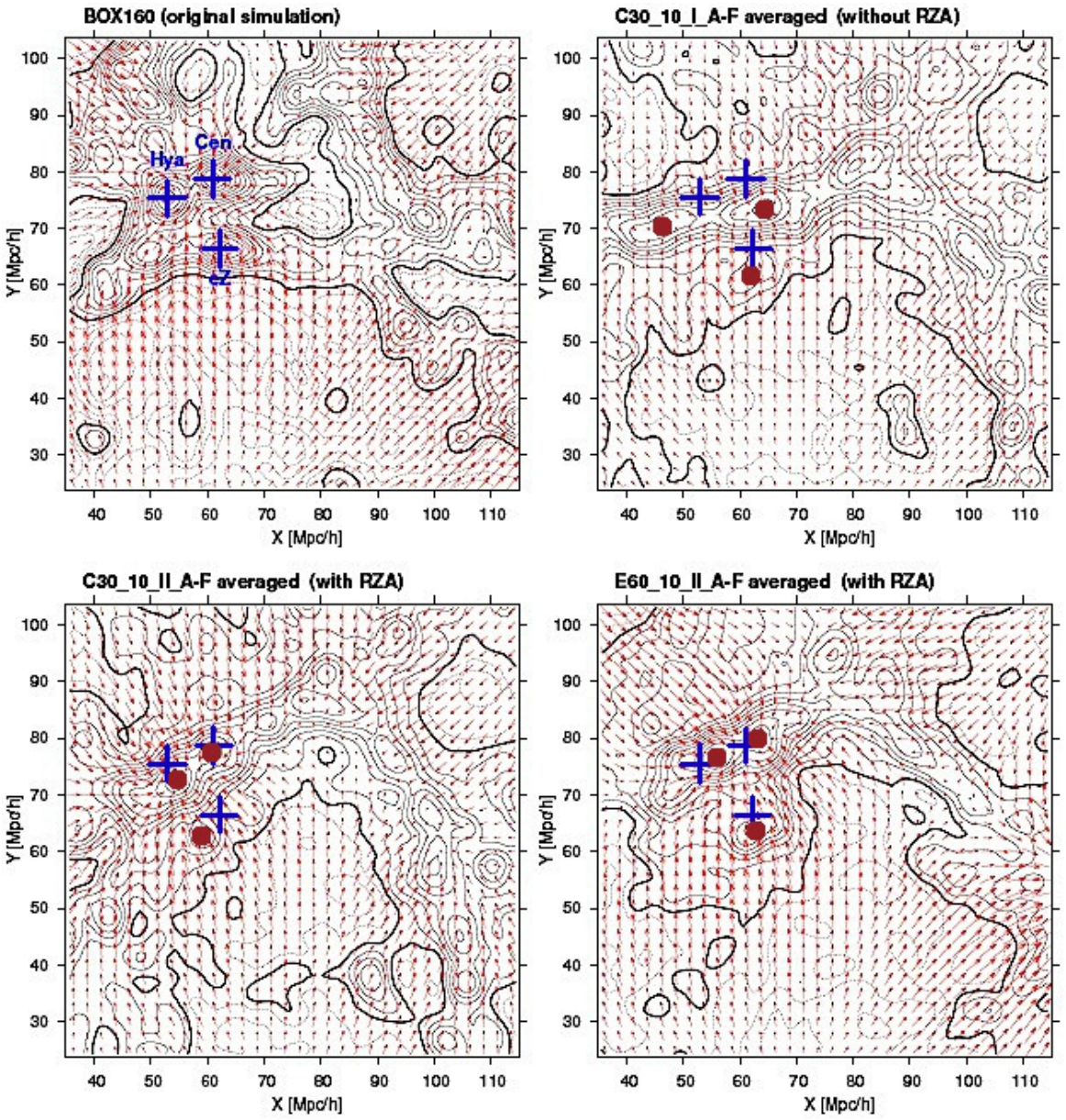

FIGURE 1.3: Density and velocity fields in a 10 h^{-1} Mpc thick slice of the original first constrained simulation, named BOX160, of the CLUES project (*top left quadrant*) and the averages of six constrained simulations obtained with mocks built out of BOX160. The constrained Initial Conditions have been obtained without (*top right*) and with the Reverse Zel'dovich Approximation applied to simple mocks mimicking the size and spatial extent of Cosmicflows' first (*bottom left*) and second catalogs (*bottom right*). Blue crosses show the positions of three clusters in the original simulation while red dots locates the clusters in the constrained simulations on average (adapted from Doumler et al., 2013b).

project. What is the quantitative quality of the observational data, of the measurements of luminosities, of the Tully-Fisher relation in the mid-infrared at 3.6 μm? What is the performance of the newest CLUES technique applied to realistic mock and observational radial peculiar velocity catalogs? How can observations and simulations be intertwined to allow refinements of each other? How well and to which extent the simulations constrained by Cosmicflows' catalogs reproduce the Large Scale Structure of the Universe?

To answer these questions, this thesis manuscript is organized as follows. In Chapter 2, the fundamental knowledge about our Universe and especially our neighborhood is described from models to general methods and tools, through nearby observations, including: the standard ΛCDM cosmological model, the linear theory of density perturbations and the numerical cosmological simulation method. Chapter 3 presents the Observed Universe namely, the contribution of the Cosmicflows project to the global scheme. This Chapter includes the surface photometry of a large sample of galaxies up to the construction of a set of accurate distance measurements (in view of a future catalog for the Cosmicflows project) through the calibration of the Tully-Fisher relation and the determination of an Hubble Constant estimate. In Chapter 4, simulations obtained with Cosmicflows' catalogs in the context of the CLUES project are presented. To this end, the method to build constrained Initial Conditions is described and refined with tests on realistic mocks before being applied on the two first catalogs of the Cosmicflows project. The spatial extent of the second catalog of the Cosmicflows project leads us to analyze more thoroughly this catalog to propose a method to minimize biases before building Initial Conditions constrained with it. The last and fifth Chapter (5) summarizes the observational and numerical work accomplished before opening onto new prospectives for both projects.

Chapter 2

Universe in Motion

Cosmology aims at understanding the formation and evolution of structures in the Universe. For that purpose, galaxies constitute one of the sources of observational probes. However, they are only tips of the iceberg of a larger scheme involving more than 90 % of dark matter and energy. These two exotic components are elegantly accounted for in the widely accepted standard cosmological model, implying an homogeneous and isotropic on large enough scales Universe. Structure formation is the result of gravitational instabilities driven by primordial density perturbations. Their studies rely on numerical tools such as N-body methods. Accordingly, this Chapter presents the standard cosmological model in the context of an observed general expansion yet with visible local deviations from this widening. Then, these local variations are explained within the context of the linear theory of density perturbations. Finally, the numerical models used to simulate our Universe are described.

2.1 The Standard Cosmological Model

The standard cosmological model asserts that during the inflation that followed the big bang, the quantum fluctuations become classical such that particles and eventually nuclei were able to condense. Continuing expanding and cooling, the Universe experienced a transition from radiation-dominated era to a matter-dominated epoch. Baryons decoupled from radiations. This corresponds to the last scattering of photons, in other words to the Cosmic Microwave Background (CMB). Afterwards, structures began to form by collapse of small irregularities in an overall close to a homogeneous density distribution. Stars were born and soon reionized the Universe with their radiations while, larger scale structures, such as galaxies, clusters, etc formed. For a more complete description of the concept, we refer the reader to the wealth of the literature (e.g. Binney and Tremaine, 1987; Peacock, 1999; Peebles, 1993). To summarize, the ΛCDM scenario implies a hierarchical structure formation from small to

large scale structures, the latter forming by accretion of the former. This thesis work focus on this matter-dominated era of the Universe in expansion. The next subsections aims at establishing the theoretical framework of such an universe.

2.1.1 An Universe in Expansion

2.1.1.1 The Hubble Law

In 1929, Hubble observed that local galaxies are receding from us at a velocity proportional to their distance. The Hubble Law was born. In other words, any local galaxy at a distance D from us has a velocity v which follows:

$$v = H_0 D \tag{2.1}$$

where H_0 is the Hubble Constant usually expressed in km s^{-1} Mpc^{-1}.

To appreciate the importance of the adjective "local", let's consider a galaxy at a distance x with spatial coordinates fixed for simplicity. Because, photons travel along null geodesics, it follows from the Friedmann-Lemaître-Roberston-Walker metric (key to a solution of the equations of General Relativity written for an homogeneous isotropic Universe, Friedmann, 1922; Lemaître, 1931a,b; Robertson, 1933, 1935, 1936a,b) that:

$$ds^2 = 0 \Rightarrow cdt - a(t)\frac{dx}{\sqrt{1-kx^2}} = 0 \tag{2.2}$$

where c is the vacuum velocity of light in km s^{-1}, ds is the geodesic followed by the light in a time dt, $a(t)$ is the scale factor due to the expansion and k is the curvature of space. Let's assume that the galaxy emits photons with a period $T = t_1 - t_0$ which propagates up to us (located at the distance x). We observe a period $T' = t'_1 - t'_0$. Integrating over time and space equation 2.2 gives:

$$\int_{t_0}^{t'_0} \frac{c}{a(t)}dt = \int_0^x \frac{dx'}{\sqrt{1-kx'^2}} = \int_{t_1}^{t'_1} \frac{c}{a(t)}dt \tag{2.3}$$

which in turn gives:

$$\int_{t_0}^{t_1} \frac{c}{a(t)}dt + \cancel{\int_{t_1}^{t'_0} \frac{c}{a(t)}dt} = \cancel{\int_{t_1}^{t'_0} \frac{c}{a(t)}dt} + \int_{t'_0}^{t'_1} \frac{c}{a(t)}dt \tag{2.4}$$

If we make the reasonable approximation that T and T' are very small with respect to the expansion time, $a(t)$ varies only slightly during both periods. Thus, from equation 2.4:

$$\frac{T}{a(t_0)} \approx \frac{T'}{a(t'_0)} \tag{2.5}$$

In addition, if the galaxy is close enough to us (namely "local"), the scale factor can be assumed as unchanged between the emission and the reception of the signal and the curvature is negligible[1], then from the two first terms of equation 2.3:

$$t'_0 - t_0 \approx \frac{D}{c} \tag{2.6}$$

where $D \approx xa(t_0)$.

Since $v = c\frac{\lambda'-\lambda}{\lambda} = c\frac{T'-T}{T}$, it results from the relations 2.5 and 2.6 that at first order:

$$v = c\frac{a(t'_0) - a(t'_0 - \frac{D}{c})}{t'_0 - (t'_0 - \frac{D}{c})} \times \frac{\frac{D}{c}}{a(t'_0 - \frac{D}{c})} \approx \frac{\dot{a}(t'_0 - \frac{D}{c})}{a(t'_0 - \frac{D}{c})} D = \frac{d\ln a}{dt}|_0 \, D \tag{2.7}$$

The Hubble Law in equation 2.1, valid solely for local galaxies, derives from 2.7 relation with $H_0 = \frac{d\ln a}{dt}|_0 = \frac{\dot{a}_0}{a_0}$. The subscript 0 stands for "as measured today" and the "$\dot{}$" notation is the common writing for the derivative with respect to time. It results from this calculation that the discrepancies from the Hubble Law for galaxies far away from us enable the study of the scale factor history as a function of time.

In this respect, Edwin Hubble's observations of the Hubble Law consolidate the cosmological principle and the equations derived two years before by Lemaître. Namely, under the assumption that we are not privileged observers, the isotropy and homogeneity of the expanding Universe about all locations is confirmed. The rest of this subsection will generalize the Hubble Law in agreement with the cosmological principle and the observed expansion before giving the equations of evolution of the scale factor with time.

2.1.1.2 Generalization

A generalized version of the Hubble Law can be derived with the consideration that distances $D(t)$ between galaxies are simply resized by the scale factor $a(t)$ (the relative positioning is unchanged because of the cosmological principle). Accordingly:

$$D(t) = a(t)D_0 \qquad v(t) = \dot{D}(t) = \dot{a}(t)D_0 = \frac{\dot{a}(t)}{a(t)} D(t) \tag{2.8}$$

[1] In any case we will see later that our Universe is approximately flat.

One can verify that this general case contains the Hubble Law given in equation 2.1 for times t approximately equal to today time so that the corresponding scale factors $a(t)$ are close to a_0.

2.1.1.3 Evolution of the Scale Factor

As a common consensus, the laws of gravity are described by the theory of General Relativity formulated by Einstein in 1915. This general formalism contains Newton's theory of gravity valid for gravitational fields on small scales solely. The Friedmann-Lemaître-Robertson-Walker metric can be shown to have a solution to Einstein's field equations for an homogeneous and isotropic Universe as a whole. However, such a derivation is beyond the scope of this work[2] and we rely on simple thermodynamical considerations (basically adiabatic processes) under the assumption of (relativistic) fluids to explain the equations governing the evolution of the scale factor with time.

Relativity implies that mass m and energy E are equivalent through the famous equation:

$$E = mc^2 \tag{2.9}$$

where c is the vacuum velocity of light.

A direct consequence of relation 2.9 resides in the fact that matter, in the general sense of the term, is not the sole actor of motions. Radiation fields, like the Cosmic Microwave Background, are also responsible for motions. Radiations are then considered similar to a matter with a density ρ and some pressure P which follow the first law of thermodynamics $dU = -PdV$ where dU and dV are the variations of energy and volume. More precisely, in an expanding context with a scale factor a, the first law of thermodynamics can be written:

$$d\rho + (\rho + \frac{P}{c^2})\frac{dV}{V} = d\rho + 3 \times (\rho + \frac{P}{c^2})\frac{da}{a} = d[\ln(\rho)] + 3 \times (1+\omega)d[\ln(a)] = 0 \tag{2.10}$$

where the fact that $U = \rho c^2 V$ (from relations 2.9 and $m = \rho V$), $V \propto a^3$ (from relations 2.8 left and $V \propto D^3$) and $P = \omega \rho c^2$ (pressure related to thermal motion) have been used. ω is a constant depending on the object of study.

Let's consider three cases:

- in classical matter, the pressure is sufficiently smaller than ρc^2 for ω to be considered as null. Gravitational and inertial masses of classical matter are indistinguishable. As a result and as expected from the conservation of mass, the density of classical matter ρ_m is proportional to a^{-3} from equation 2.10,

[2] For a complete derivation of the equations of gravity, we refer the reader to the extensive literature on the subject (e.g. Binney and Tremaine, 1987; Peacock, 1999; Peebles, 1993).

- radiations are quite different since their pressure effect cannot be neglected. Hence, for massless and highly relativistic particles, ω equals $\frac{1}{3}$ from the relation between kinetic energy E_k and temperature T (typically $E_k = \frac{1}{2}mv^2 = \frac{3}{2}k_BT$ where k_B is the constant of Boltzmann). From equation 2.10, $\rho_r \propto a^{-4}$ which is expected because not only ρ_r decreases because of the Universe expansion but also radiations are subject to a loss of energy inversely proportional to a (increase of wavelength by a),
- considering $\omega = -1$, Carroll et al. (1992) defined the finite vacuum energy density or more generally the dark energy with a negative pressure. As expected, this term gathers the quality of a constant in space and time as it is independent of a from equation 2.10.

In such a defined homogeneous isotropic expanding Universe, the Friedmann-Lemaître-Robertson-Walker model describes the Universe with two equations of the scale factor a:

$$\frac{\ddot{a}}{a} = \frac{-4\Pi G}{3}(\rho + \frac{3P}{c^2}) + \frac{\Lambda}{3} \tag{2.11}$$

$$(\frac{\dot{a}}{a})^2 = \frac{8\Pi G}{3}\rho - \frac{Kc^2}{a^2} + \frac{\Lambda}{3} \tag{2.12}$$

where G is the universal gravitational constant, c the vacuum velocity of light, P the pressure, K the scalar curvature and Λ stands for the cosmological constant which reproduces the expansion effect.

The first one of these two equations (2.11) is analogous to the classical equation of motion (after divisions by the scale factor a and the original coordinate x) which stipulates that the acceleration $\ddot{a}x$ equals the sum of the gravitational forces. In the presently defined Universe, the three types of components described above contribute to the gravitational field. Accordingly the sum of the forces can be written:

$$F_{total} = \frac{-G\frac{4\Pi(xa)^3}{3}\rho_m}{(xa)^2} + \frac{-G\frac{4\Pi(xa)^3}{3}(\rho_r + \frac{3P}{c^2})}{(xa)^2} + \frac{-G\frac{4\Pi(xa)^3}{3}(-\frac{P}{c^2})}{(xa)^2} \tag{2.13}$$

With $\rho = \rho_m + \rho_r$ and $\Lambda = 4\Pi G(-\frac{P}{c^2})$ the analogy is complete.

The second equation 2.12 governing the scale factor evolution is comparable to the conservation of energy. It can be directly retrieved from equation 2.11 by first multiplying this latter by $\dot{a}a$. Then, a few relations have to be noticed:

$$\frac{d\dot{a}^2}{dt} = 2\dot{a}\ddot{a} \quad ; \quad \frac{da^2}{dt} = 2\dot{a}a \quad ; \quad \frac{d(\frac{-1}{a})}{dt} = \frac{\dot{a}}{a^2} \tag{2.14}$$

and completed with

$$\frac{d(\rho a^2)}{dt} = 2\rho a\dot{a} + a^2\dot{\rho} = -a\dot{a}(\rho - 3\rho - \frac{a}{\dot{a}}\dot{\rho}) = -a\dot{a}(\rho + \frac{3P}{c^2}) \tag{2.15}$$

where the last equality derives directly from the first thermodynamical law 2.10. Finally, a division by a^2 and an equalization of the constant of integration to $-Kc^2$ gives 2.12. From the fact that K is the scalar curvature and the second equation of the standard cosmological model is similar to the conservation of energy, one can catch a glimpse at a link between energy density and geometry from the metric.

From relation 2.8, we have seen that $H(t) = \frac{\dot{a}}{a}$. The square of this ratio is given by equation 2.12. Setting today density parameters as follows:

$$\Omega_m = \frac{8\Pi G\rho_{m_0}}{3H_0^2} \quad ; \quad \Omega_\Lambda = \frac{\Lambda}{3H_0^2} \quad ; \quad \Omega_K = \frac{Kc^2}{H_0^2} \quad ; \quad \Omega_r = \frac{8\Pi G\rho_{r_0}}{3H_0^2} \tag{2.16}$$

where the subscript 0 stands for today time, it is possible to give an expression of $H(t)$ as a function of the components in the Universe today:

$$H(t) = H_0\sqrt{\frac{\Omega_r}{a^4} + \frac{\Omega_m}{a^3} - \frac{\Omega_K}{a^2} + \Omega_\Lambda} \tag{2.17}$$

where matter and radiation have once again been separated as the expansion does not affect them in a similar way (density of radiation decreases faster than that of matter since $\rho_r = a^{-4}\rho_{r_0}$ while $\rho_m = a^{-3}\rho_{m_0}$).

Various observational programs over the past few years have contributed to the measurements of the density parameters. Table 2.1 recapitulates the different estimates. In this table, for conveniency, the Hubble Constant H_0 is replaced by the parameter h defined such that:

$$H_0 = 100\ h\ \mathrm{km\,s^{-1}\,Mpc^{-1}} \tag{2.18}$$

This parameter is convenient in the sense that, for example, any distance given in Megarparsec per unit of this parameter h is valid in any cosmological model. One remarkable characteristic of the ensemble of measures given in the table is that the sum of the matter and dark energy density parameters is always close to 1 up to a few hundreds of percents. Since today, $H = H_0$, $\Omega_r \approx 0$ ($\Omega_r << 1$ since z became less than 3000, end of the radiation dominated era, beginning of the matter dominated epoch) and the scale factor is the unity by definition, $\Omega_K = \Omega_m + \Omega_\Lambda - 1 \approx 0$ from equation 2.17. Namely, our Universe is likely to be flat. Accordingly, in the matter dominated era, the equation of evolution of the scale factor can be written:

$$\dot{a} = aH(t) = H_0\sqrt{\Omega_m(\frac{1}{a} - 1) + \Omega_\Lambda(a^2 - 1) + 1} \approx H_0\sqrt{\Omega_m\frac{1}{a} + \Omega_\Lambda a^2} \tag{2.19}$$

Cosmological Parameters	WMAP3	WMAP5	WMAP7	WMAP9	Planck
Ω_m (matter density)	0.24	0.279	0.272	0.279	0.307
Ω_Λ (dark energy density)	0.76	0.721	0.728	0.721	0.693
n_s (spectral index)	0.95	0.960	0.961	0.972	0.962
σ_8 (normalization parameter)	0.75	0.817	0.807	0.821	0.834
h (Hubble Constant / 100)	0.73	0.70	0.702	0.700	0.677

TABLE 2.1: Cosmological Parameters measured with the Wilkinson Microwave Anisotropy Probe and Planck Observations: (1) Denomination of the cosmological parameters, (n_s and σ_8 are properties of the power spectrum, itself defined in section 2.2.3.2. The spectral index n_s is the relative distribution of power on large scales and the normalization parameter σ_8 scales the power spectrum to its today value), (2) Three-year WMAP measurements from Spergel et al. (2007), (3) Five-year WMAP measurements from Komatsu et al. (2009), (4) Seven-year WMAP measurements from Komatsu et al. (2011), (5) Nine-year WMAP measurements from Hinshaw et al. (2013), (6) First results obtained with Planck from Planck Collaboration (2013).

To summarize this subsection, the equations governing the evolution of the scale factor underlines the fact that space itself is in expansion. The apparent motion of galaxies receding from each other is solely a consequence of this dilatation of space. Yet, conserving the analogy with a Doppler effect is appropriate.

2.1.2 Variations from the Hubble Expansion

The cosmological principle implies that the Universe is homogeneous and isotropic about all locations. In addition, the expansion implies that the proper physical distance between two galaxies is bound to increase with time and does so at a velocity proportional to the distance. Yet a various set of small scale structures from single galaxies to structures extending over approximately 100 h^{-1} Mpc can be observed in our neighborhood. Gravitationally bound structures exist. Merging processes happen everywhere. These observations are corroborated by the presence of significative outliers in local Hubble diagrams.

2.1.2.1 Bound Structures and Merging Processes

The terminology "universal expansion" refers to the global motion of the cosmic matter, "global" in the sense when analyzing a large volume. However, galaxies close to each others tend to gather in structures possibly bound. Bound as they will not fall apart with increasing time because of the expansion. The local gravity wins over the global expansion effect preventing clusters of galaxies and even galaxies themselves to grow because of the universal expansion. Figures 1.1 and 1.2 in Chapter 1 reflect the existence of such bound structures

in the Local Universe. An extensive list of structures in the sole neighborhood of the Milky Way can be established. Only a few of them of different typical extents are mentioned here as examples: Virgo is the closest cluster of galaxies ; Coma, further away, is another bigger one. Coma is actually part of a larger structure called the Great Wall which extends over 100 h^{-1} Mpc. Our Galaxy, the Milky Way, is itself part of a small structure called the Local Group. The Shapley supercluster which extends at least over 30 h^{-1} Mpc is considered currently as the biggest bound structure in the Local Universe (Reisenegger et al., 2002). In definitive, the presence of an incommensurable number of structures on various scales confirms the role played by gravity.

Gravitational pulls inside and around structures shape motions. For instance, Karachentsev et al. (2009) observe the modification of the Hubble flow around the Local Group because of its mass. Galaxies of Coma I cloud move at large speed. Their motions are probably the result of an infall onto an attractor (Karachentsev et al., 2011). Models of the dynamics inside the Local Group show close passages between the Milky Way and M31 (Andromeda) suggesting a future merging event (e.g. Peebles and Tully, 2013). Actually numerous simulations have already found that the collision between our galaxy and M31 is likely to happen in a few billion years (e.g. Cox and Loeb, 2008; Hoffman et al., 2007). Remnants of galaxy collisions and actual collisions are observed continuously (e.g. Meyerdierks, 1991; Schweizer, 1996). Although this short subsection did not aim at explaining in details such processes, these latter are a proof of concept that the expansion is not the sole actor of observed motions in the Universe. Galaxies have also peculiar motions due to gravitational effects.

2.1.2.2 Voids and Local Flows

Reference frames and systems of coordinates:
To study more thoroughly local motions in our neighborhood it is essential to define a reference frame. Several reference frames exist such as heliocentric, galactocentric, Local Group, Local Sheet, Local Supercluster and CMB reference frames. Conversions from one reference frame to another are summarized in Tully et al. (2008). Their names are in general quite explicit. Usually we place ourselves in the CMB reference frame which consists in correcting for the dipole anisotropy in the Cosmic Microwave Background temperature map. Since this paragraph is prone to study local motions, it is quite appropriate to point out that the observed dipole anisotropy is a compelling evidence that our Galaxy has a peculiar motion with respect to the overall cosmic expansion. The Milky Way is moving in a well specified direction at approximately 630 km s^{-1}. Still, to study local motions, in particular our Galaxy's motion, the Local Sheet reference frame (a slight variant of the Local Group frame) can be more relevant.

In addition, the most used coordinate system is called supergalactic. It is defined by the supergalactic plane (e.g. Lahav et al., 2000), located at the null supergalactic latitude (SGB). The null supergalactic longitude (SGL) is at the intersection of the SGB=0-plane with the galactic plane. Assuming D the distance of an object from us, the object is located in cartesian coordinates at:

$$\begin{aligned} SGX &= D\cos(SGB)\cos(SGL) \\ SGY &= D\cos(SGB)\sin(SGL) \\ SGZ &= D\sin(SGB) \end{aligned} \tag{2.20}$$

where SGX, SGY and SGZ are in the same unit as D.

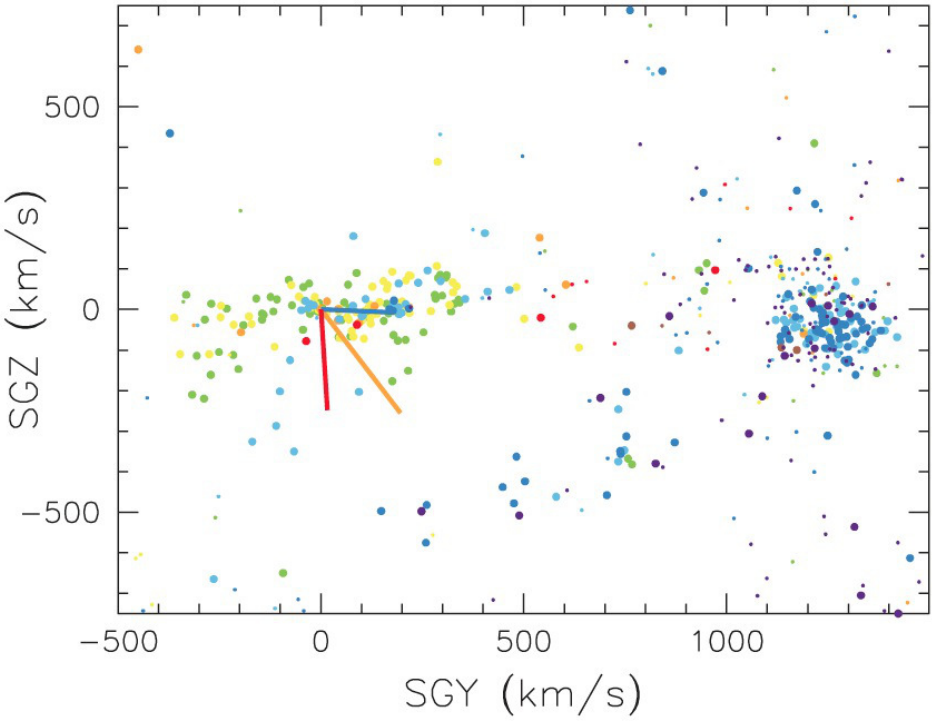

FIGURE 2.1: Motions around and within the Local Sheet. After accounting for a cosmic expansion of 74 km s^{-1} Mpc^{-1}, yellow-orange-red dots indicate peculiar motions away from us while green-blue-purple dots stand for peculiar motion towards us. The orange vector is a motion with respect to the Local Supercluster reference frame at 320 km s^{-1}. The blue and red vectors are motions at 185 km s^{-1} towards Virgo (cluster of blue dots on the right) and at 260 km s^{-1} away from the Local Void in the Local Sheet reference frame (from Tully et al., 2008).

Observed peculiar motions:

Lynden-Bell et al. (1988a) were the first to discover that galaxies have peculiar motions pointing in a very specified direction near Centaurus cluster. They evoke the existence of a Great Attractor with probably an unusual large mass. This Great Attractor pull was confirmed later on by da Costa et al. (1996). These latter also observed a large infall towards the Perseus Pisces Supercluster located approximately across from us with respect to the

Great Attractor region. Furthermore, they noticed that galaxies are organized in filaments which delimit voids. Progress has been made over the past few years to better understand the motion of our Galaxy in this context. Figures 2.1 to 2.3 are a summary of our current knowledge. Our motion is the vector sum of gravitational pulls from many sources. The current understanding is that there are four to six dominant components on well separated spatial scales. The nearest of which are reasonably well understood probably because motion vectors are almost orthogonal (Tully, 2007, 2008a; Tully et al., 2008):

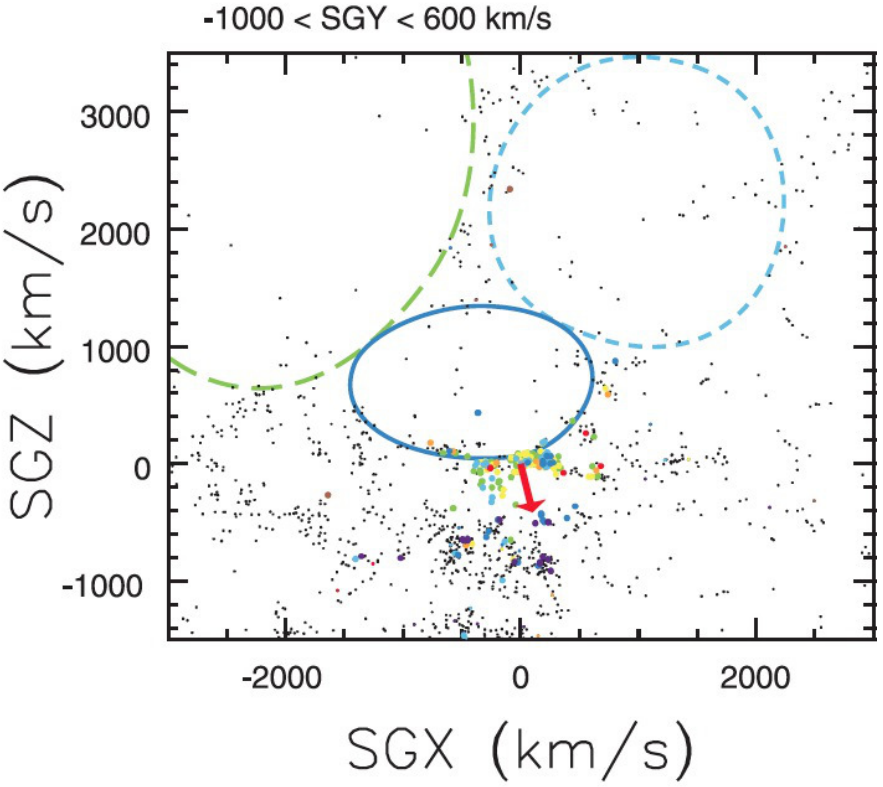

FIGURE 2.2: Region of the Local Void. The solid blue ellipse shows the Inner Local Void, bounded on one edge by the Local Sheet. North and South extensions are identified by blue and green dashed ellipses respectively. The red vector indicates the direction and amplitude of our motion away from the void. A galaxy, ESO 461-36 (blue dot in the Inner Local Void), is escaping from the void with a huge velocity of at least 350 km s^{-1}(approximately the sum of our motion away from the void and its motion towards us) (from Tully, 2008b; Tully et al., 2008).

- at the smallest scale, the Milky Way is falling at 135 km s^{-1} towards the galaxy M31,
- at slightly larger scales ($\approx$ 7 Mpc), the Local Sheet, that contains our Galaxy, is part of the wall delimitating a very large void (Local Void) which appears to expand at 260 km s^{-1} (see Figure 2.2),
- a bit farther ($\approx$ 17 Mpc), the Virgo Cluster, at the heart of the Local Supercluster, is found to pull the Local Sheet at 185 km s^{-1},
- after subtracting all these pulls individually from the CMB dipole vector, it remains to explain a motion of 445 km s^{-1}.

One could argue that the counterintuitive observed motions (galaxies drawing closer instead of receding) visible on Figures 2.1 and 2.3 left are due to the Hubble constant choice when decomposing total observed motions into cosmic expansion and peculiar motions. Selecting a larger value for H_0 would enhance a pattern of overall infalls after accounting for the expansion. On the opposite selecting a smaller value would create a trend towards outflows. Still, Figure 2.3 right confirms that overall patterns in peculiar motions are similar whatever reasonable H_0 value is considered.

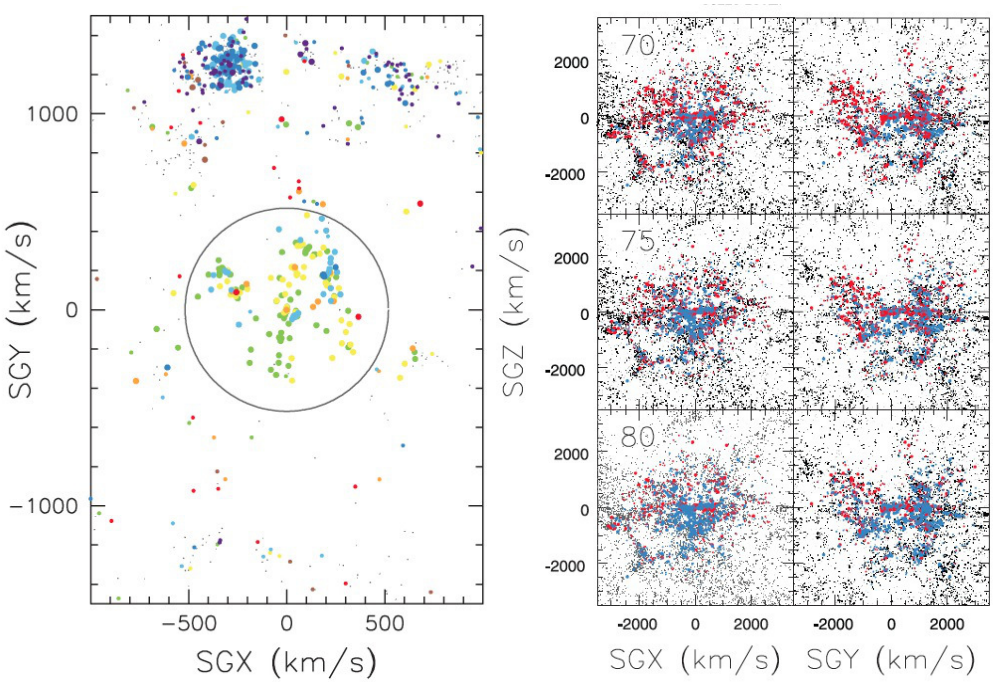

FIGURE 2.3: Local motion patterns. *Left*: The circle gives the outer projection of a 7 Mpc sphere centered at our position. After accounting for a cosmic expansion of 74 km s^{-1} Mpc^{-1}, yellow-orange-red dots indicate peculiar velocities away from us, green-blue-purple dots indicate peculiar motion towards us. Virgo is the cluster of blue dots at the upper left. The local region has an overall peculiar velocity towards Virgo of approximatively 200 km s^{-1}. *Right*: Red dots represents galaxies going away from us. Blue dots are galaxies coming towards us. Whatever value is adopted for H_0 (*top panel* 70, *middle panel* 75 and *bottom panel* 80 km s^{-1} Mpc^{-1}), the counterintuitive pattern of motions with respect to the knowledge of cosmic expansion still appears (from Tully et al., 2008).

Figure 2.4 shows supergalactic XY and YZ planes of the repartition of masses and motions in the Local Universe confirming the overall explanation for the motion of our Galaxy (Courtois et al., 2013). Courtois et al. (2012) also established the predominance of the role played by the Local Void over the Virgo cluster on the Local Flow.

Yet, in an era of "precision cosmology", only 30% of the motion of the Milky Way is understood exactly. In addition, peculiar motion estimates are not yet numerous or accurate enough to demonstrate whether other filaments have similar bulk motions with respect to voids. Moreover, bulk flow measurements are in apparent contradiction with each other. Two schools actually confront their ideas on the end of the bulk flow.

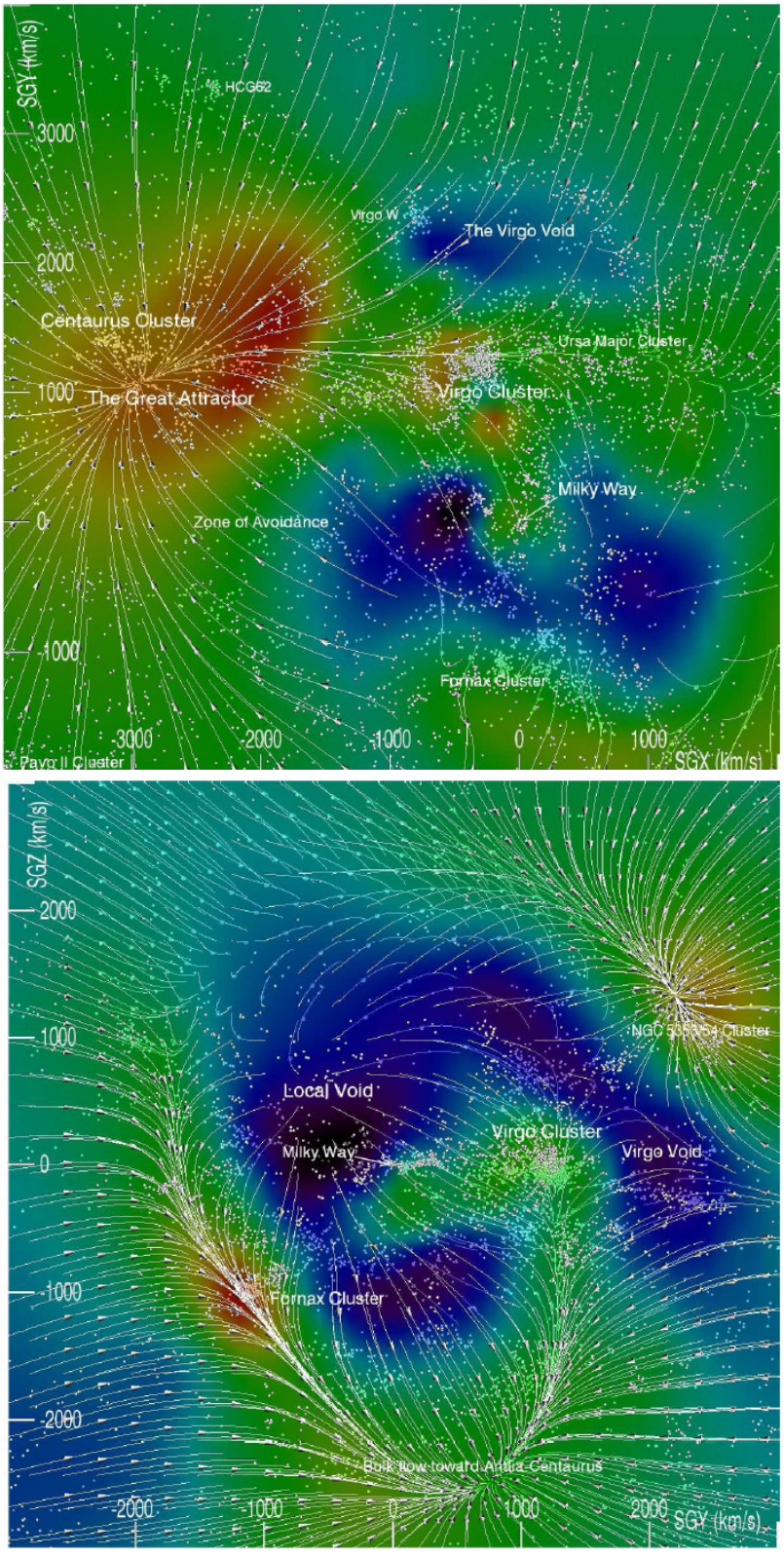

FIGURE 2.4: Supergalactic XY and YZ planes of the reconstruction of the mass distribution and motions in the Local Universe within 30 h^{-1} Mpc. Warm colors show high mass densities while cold colors stand for nearly empty regions or voids. White arrows represent motions. White dots stand for galaxies from a redshift survey called V8k and available at the Extragalactic Distance Database (http://edd.ifa.hawaii.edu) of the Cosmicflows project. A few structures are identified. In the *top panel*, the motion of the Milky Way towards Virgo itself falling onto the Great Attractor region is visible. In the *bottom panel*, the expulsion from the Local Void is visible (from Courtois et al., 2013).

The first school assumes the existence of a large bulk flow which extends up to distances greater than 500 h^{-1} Mpc, they call it the dark flow (Kashlinsky et al., 2012, 2010). Their work relies on the measurement of the bulk flow of X-rays luminous clusters via the Sunyaev Zel'dovich effect (e.g. Sunyaev and Zeldovich, 1980, 1970). On the opposite, the second school does not envisioned the end of the bulk flow as far as 500 h^{-1} Mpc. With supernovae of type Ia studies (e.g. Feindt et al., 2013; Turnbull et al., 2012), they assert that, although the Shapley supercluster is apparently not the end of the bulk flow, there is no such things as a dark flow. This assertion seems confirmed by recent other measurements based on the Sunyaev Zel'dovich effect (Lavaux et al., 2013). Regardless, these multiple facts highlight a fundamental deficiency in our understanding of the Local Universe (composition) and explains the wealth of the Cosmicflows project.

2.1.2.3 Effect on the Redshift

Observations prove that galaxies have deviating motions from the Hubble expansion. Thus, their total velocities v_{tot} can be written as the sum of two terms, one due to the expansion HD, from equation 2.8 right, with D their distances and the other one due to gravitational effects, because of local variations of matter, called peculiar velocity v_{pec}. Accordingly, deriving peculiar velocities of galaxies supposes distances and total velocities to be known. Both can be estimated from observations. We will come back to the estimation of distances in Chapter 3, the observational part of this thesis work. Concerning total velocities, as we name them, close estimates can be obtained with the observational redshift. This redshift is derived from the shift of emitted wavelengths towards higher value because of the expansion or, more generally, because of the total motion (sum of the expansion and peculiar motion) of the emitting galaxy. It can be expressed in terms of wavelengths emitted λ_e and received λ_r:

$$z_{obs} = \frac{\lambda_r - \lambda_e}{\lambda_e} \tag{2.21}$$

Observers measure the redshifts of galaxies by identifying well defined series of lines in their emission or absorption spectra. The advantage of these ensemble of lines is that their values at rest are well known. Since these sequence of lines are unchanged but just shifted, redshifts can be computed from their shifts. An example of such a series of line is the Balmer series. This series consists in a set of spectral line emissions of the hydrogen atom due to transitions from level n (principal quantum number of the electron) greater or equal to 3 to the second level. These lines called H_α, H_β, H_γ, H_δ and H_ϵ are normally part of the visible spectrum. Their wavelength values can be computed with the formula $\lambda = \frac{1}{R_H}(\frac{1}{4} - \frac{1}{n^2})$ where R_H is the Rydberg constant associated with the hydrogen. Hydrogen can be pointed out as a useful element in various fields of Astronomy because it is highly abundant in the Universe.

Such redshift estimates account for the expansion and the peculiar motions of the galaxies. To disentangle all these effects on the redshift, it is useful to introduce a cosmological redshift z_{cos} defined by the hypothetical shift in wavelength if expansion really bears sole responsibility for the shift:

$$z_{cos} = \frac{\lambda_{r_h} - \lambda_e}{\lambda_e} = \frac{1}{a} - 1 \tag{2.22}$$

where we have used $\lambda_{r_h} = a\lambda_e$ obtained with equation 2.8 left. λ_{r_h} is the hypothetical wavelength which would have been received by the observer in the case of pure expansion.

From the definitions of the observational and cosmological redshifts 2.21 and 2.22, an "extra redshift" z_{extra} can be defined:

$$1 + z_{obs} = \frac{\lambda_r}{\lambda_e} = \frac{\lambda_{r_h}}{\lambda_e}\frac{\lambda_r}{\lambda_{r_h}} = (1 + z_{cos})(1 + z_{extra}) \tag{2.23}$$

Then:

$$z_{extra} = \frac{z_{obs} - z_{cos}}{1 + z_{cos}} \tag{2.24}$$

This "extra redshift" is due to peculiar motions.Thus, non-relativistic peculiar velocity estimates v_{pec} are directly obtained with:

$$v_{pec} = cz_{pec} = c\frac{z_{obs} - z_{cos}}{1 + z_{cos}} \tag{2.25}$$

where c is the vacuum speed of light and $z_{pec} = z_{extra}$ is the "peculiar redshift". We will come back to the estimation of the cosmological redshift in Chapter 3 as distance definitions and estimates are required primarily.

It is pertinent to add that, as observers, only the line-of-sight of the coordinates is affected by peculiar motions or, in other words, only the radial component of the distant galaxies' peculiar velocities is accessible through redshift observations. This leads to distortions visible in maps of redshift surveys. Namely, galaxies positioned with redshift measurements on a map form "Fingers-of-God", as shown on Figure 2.5, resulting from the fact that while they are at the same distance from us, because of their different (random) peculiar motions, they appear to be located at different distances. The Kaiser effect (Kaiser, 1987) can also be mentioned although this effect can be detected only on large scales. It differs from the Fingers-of-God in the sense that it affects coordinates of galaxies which are coherently infalling onto a central mass to which they are bound.

In any case, the observations of such patterns are a proof of concept that deviations from the universal expansion, namely peculiar motions exist. These motions are due to local

gravitational fields which are generated by local density fluctuations. The study of primordial cosmological density inhomogeneities is required to understand the process that cause departure from a uniform density.

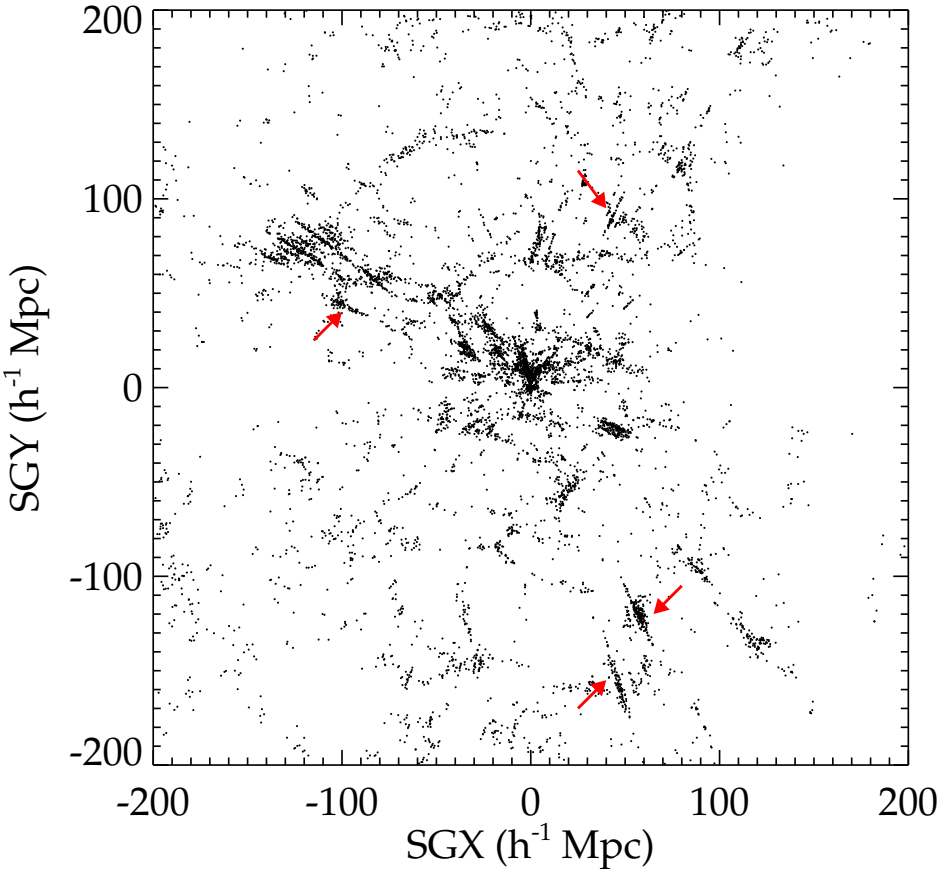

FIGURE 2.5: Supergalactic XY plane representing galaxies (black dots) of the Two-Micron All Sky Survey (2MASS) redshift catalog (Huchra et al., 2012) in a 5 Mpc thick slice. Numerous Fingers-of-God are visible, a few of them are pointed by red arrows.

2.2 The Linear Theory of Density Perturbations

The anisotropies observed in the Cosmic Microwave Background Temperature maps are witnesses of primordial density inhomogeneities. Our interest lies in the effect of these fluctuations which generate weak gravitational fields in addition to the overall gravitational potential. In this context, the overdensity δ defined as:

$$\delta = \frac{\rho - \bar{\rho}}{\bar{\rho}} \tag{2.26}$$

where $\bar{\rho}$ is the mean density and ρ the local density, is useful. Because the relation between matter density and gravitational potential is linear (Poisson equation), homogeneous matter distribution and density fluctuations can be considered separately. Thus, the total gravitational field can be seen as the sum of the average matter distribution and density

fluctuation effects. A simple explanation for the growth of structures because of these small initial perturbations can be presented as follows (e.g. Einasto et al., 2011): in overdense regions, meaning in regions where the overdensity is positive (density greater than the mean density), the density decreases more slowly than on average because the expansion effect is dimmed by the higher gravitational effect. Accordingly, the density contrast between these regions and mean density regions increases. This increased overdensity in turn produces an even stronger gravitational field and the process repeats itself. An opposite phenomenon happens in underdense regions. The expansion is less affected in these regions than in mean density regions by gravity, thus the density decreases faster. The gravitational effect is even weaker and the process continues. Hence, the evolution of structures can be described by the model of gravitational instability corresponding to an increase of density fluctuations.

2.2.1 Continuity, Euler and Poisson Equations

Because the growth of density perturbation length scales is substantially smaller than the Hubble radius ($\frac{c}{H_0} \approx 3000$ h^{-1} Mpc), working in the framework of Newtonian theory of gravity is acceptable. Matter is assumed to be solely in the form of dust which is described as a fluid. The equations of motions are then:

- the continuity or energy equation which states that the matter is conserved. The density decreases only if the fluid has a divergent velocity field meaning that the particles are moving away from each other, namely the total derivative of the density with respect to time t is null:
$$(\frac{\partial \rho(\mathbf{r},t)}{\partial t})_r + (\nabla)_r.(\rho(\mathbf{r},t)\mathbf{v}(\mathbf{r},t)) = 0 \tag{2.27}$$
where ρ is the density and v the velocity. The r subscript signifies that derivatives are with respect to the coordinate $\mathbf{r}$ fixed,

- the Euler equation which describes the conservation of momentum and the behavior of the fluid under the influence of forces (pressure P and gravitational potential Φ), analogous to Newton's first law:
$$(\frac{\partial \mathbf{v}}{\partial t})_r + (\mathbf{v}.\nabla_r)\mathbf{v} = -\frac{\nabla_r P(\mathbf{r},t)}{\rho(\mathbf{r},t)} - \nabla_r \Phi(\mathbf{r},t) \tag{2.28}$$
where the gravitational potential follows the Poisson equation:
$$\nabla_r^2 \Phi = 4\Pi G\rho \tag{2.29}$$
Since we consider only dust the pressure term P is null in the rest of this work.

Equations 2.27 and 2.28 are in general not solvable analytically. It is necessary to linearize these self-gravitating fluid equations for $|\delta| << 1$ (valid at very high redshifts, such as $z \approx 1000$ corresponding to the last time photons and matters interacted, it is the observed Cosmic Microwave Background) to find approximate solutions. One can note that the generalized Hubble law is a special exact solution of these equations for the homogeneous density field ρ. Thus, we can expect that physically relevant solutions are slight deviations from the homogeneous case comforting the prescribed linearization.

2.2.2 Comoving Equations

2.2.2.1 Comoving Coordinates: Definition

At this point, it is useful to introduce the comoving coordinates. These coordinates are a perfect compromise between the Eulerian and Lagrangian coordinates. While an Eulerian observer takes snapshots of the field at different times t, in other words he is more interested in the global variation of the field (grid) in time than in particular objects, a Lagrangian observer follows the chosen objects on the grid. Consequently, while the Eulerian observer can give the velocity in any point of the grid, the Lagrangian observer can locate the particles on the grid but not in time (the lagrangian coordinate is independent of time), thus, to him, it seems particle are immobile (no velocity). A comoving observer is in between. While he proceeds as the Eulerian observer, he forgets about the motion due to expansion. Namely, assimilating the Universe to a growing grid, the comoving observer resizes constantly the grid to its original size. As a result, he has (only) the *peculiar* velocity field in any point of the resized grid. Figure 2.6 schematizes the concept.

However, the Universe is homogeneous and isotropic only when smoothing out small irregularities. As a consequence, depending on the position of the observers, they are not necessarily comoving. That is one of the difficulty of being part of the system under study. A set of fundamental observers is considered comoving if observers are at rest with respect to the matter surrounding them. Since random velocities of galaxies and stars composing them are small (only a few hundreds of km s^{-1}) in comparison with receding velocities between galaxies separated by large distances (many thousands of km s^{-1}), on large scales (typically enough for the assumption of homogeneity to be accurate) any observer who moves with a typical star in a galaxy is considered at rest with respect to his environment and, as a result, is a fundamental observer. A cosmic time also needs to be defined (Gunn, 1978).

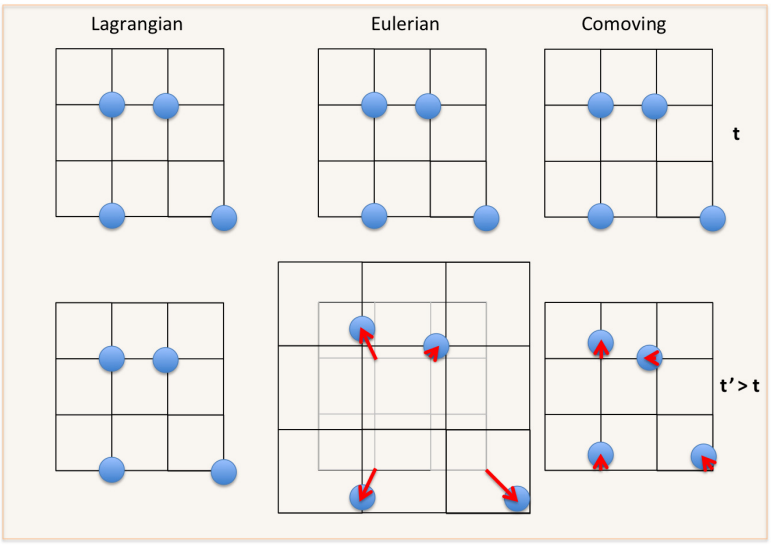

FIGURE 2.6: Schematization of the Lagrangian, Eulerian and Comoving coordinate principles: the Lagrangian observer follows the particles (blue filled circles) on the grid but not in time. Consequently, to him it looks like particles have no velocity. They do not move in time; the Eulerian observer, interested in the global value of the grid at different times, takes the snapshot of the global field at times t and t', he can trace the velocity field (red arrows) ; the comoving observer resizes the grid to remove the dependence on the expansion thus, he can give (only) the *peculiar* velocity field (red arrows).

2.2.2.2 Comoving Coordinates: Equations

Before any linearization of the continuity and Euler equations, changing to comoving coordinates is convenient. Let's define the proper coordinate r at time t by:

$$\mathbf{r} = a(t)\mathbf{x} \tag{2.30}$$

where a is the scale factor and x the comoving coordinate. From this definition, a velocity field v can be derived:

$$\mathbf{v} = \frac{\dot{a}}{a}\mathbf{r} + \mathbf{u}(\frac{\mathbf{r}}{a}, t) \tag{2.31}$$

where u is the deviation from the Hubble expansion, itself given by the first term of the formula by analogy with relation 2.8 right ; u is also called the peculiar velocity field since it would be null in absence of peculiar motion (x would stay unchanged with time in which case $u = a\frac{dx}{dt} = 0$).

Thus, in comoving coordinates using 2.30:

$$(\frac{\partial}{\partial t})_r = (\frac{\partial}{\partial t})_x + (\frac{\partial \frac{\mathbf{r}}{a}}{\partial t})_x.\nabla_x = (\frac{\partial}{\partial t})_x - \frac{\dot{a}}{a}\mathbf{x}.\nabla_x \quad ; \quad \nabla_r = \frac{\partial \mathbf{x}}{\partial \mathbf{r}}\nabla_x = \frac{1}{a}\nabla_x \tag{2.32}$$

where the subscript x stands for derivative with respect to the comoving coordinate x fixed.

From relations 2.30 to 2.32, the continuity and Euler equations 2.27 and 2.28 become:

$$\frac{\partial \rho}{\partial t} + \frac{3\dot{a}}{a}\rho + \frac{1}{a}\nabla.(\rho \mathbf{u}) = 0 \tag{2.33}$$

$$\frac{\partial \mathbf{u}}{\partial t} + \frac{1}{a}(\mathbf{u}.\nabla)\mathbf{u} + \frac{\dot{a}}{a}\mathbf{u} = -\frac{1}{a}\nabla\phi \tag{2.34}$$

where the pressure term has vanished, since we consider solely dust, and $\nabla_x \mathbf{x} = 3$ was used. For simplicity the x subscript is not written. In addition, both the definition 2.26 of the density δ and the equation of motion 2.11 in the Newtonian framework considering dust (namely P and Λ are null) were used. ϕ is now defined has $\Phi - \frac{2\Pi}{3}G\bar{\rho}|\mathbf{r}|^2$. Since it is the variation between the full gravitational potential Φ and the Newtonian gravitational potential $\frac{2\Pi}{3}G\bar{\rho}|\mathbf{r}|^2$, it corresponds to the gravitational potential of the density inhomogeneities. It satisfies the Poisson equation for the density inhomogeneities:

$$\nabla^2\phi(\mathbf{x}, t) = 4\Pi G a^2(t)\bar{\rho}(t)\delta(\mathbf{x}, t) \tag{2.35}$$

From equation 2.26 and $\bar{\rho}(t) \propto a^{-3}$ (namely, $\frac{\partial \bar{\rho}}{\partial t} = -3\frac{\dot{a}}{a}\bar{\rho}$), equation 2.33 can be written:

$$\frac{\partial \delta}{\partial t} + \frac{1}{a}\nabla.[(1+\delta)\mathbf{u}] = 0 \tag{2.36}$$

2.2.3 Density Perturbation Field

2.2.3.1 Linearization

The linearization of equations 2.34 and 2.36 consists in rejecting all terms other than the first order in δ and u. Accordingly, these equations become:

$$\frac{\partial \delta}{\partial t} + \frac{1}{a}\nabla.\mathbf{u} = 0 \quad ; \quad \frac{\partial \mathbf{u}}{\partial t} + \frac{\dot{a}}{a}\mathbf{u} = -\frac{1}{a}\nabla\phi \tag{2.37}$$

Derivating the first of one of the two equations 2.37 with respect to the time and the second one with respect to x, subtracting them after division of the second by a, using the Schwarz theorem, the Poisson equation 2.35 and the left equation in 2.37, we obtain the second-order differential equation for the density perturbation field δ:

$$\frac{\partial^2 \delta}{\partial t^2} + \frac{2\dot{a}}{a}\frac{\partial \delta}{\partial t} = 4\Pi G\bar{\rho}\delta \tag{2.38}$$

Since only δ depends on x in this second-order differential equation, it is possible to find a solution of the form $\delta(\mathbf{x}, t) = D_{\pm}(t)\tilde{\delta}(\mathbf{x})$. From equation 2.38, after division by $\tilde{\delta}(\mathbf{x})$, $D_{\pm}$ is solution of a second order differential equation with two linearly independent solutions.

While one of this solution decreases with time, the other one increases. It is logical to assume that at some later time, the increasing solution will dominate while the other one will have become irrelevant. Considering solely the increasing solution, hereafter D_+, and normalizing it to unity today, $\delta(\mathbf{x},t) = D_+(t)\delta_0(\mathbf{x})$ where δ_0 would be the distribution of density fluctuations at present if the evolution was linear until today. This is the linearly extrapolated density fluctuation field which approximation breaks down as soon as $|\delta|$ is not a lot smaller than the unity anymore. In comoving coordinates, this approximation implies that the spatial shape of the density fluctuations is frozen, only its amplitude can vary (e.g. Heath, 1977). The (linear) growth factor D_+ can be shown to be equal to:

$$D_+(a) = \frac{1}{D_{+0}} \frac{\dot{a}}{a} \int_0^a \frac{da}{\dot{a}^3} \tag{2.39}$$

where $D_{+0} = \frac{1}{H_0} \int_0^1 \frac{da}{\dot{a}^3}$.

This linear theory of density perturbations explain the observed structures in the Universe. Galaxies, clusters, etc result from the gravitational collapse of high peaks in the primordial density field. Current galaxy peculiar motions are proofs of concept that structures are continuously forming and evolving in the Universe. Studying analytically, in details, these motions via the perturbation density field appears to be a complex task. Statistical and numerical methods become resourceful.

2.2.3.2 Fourier Analyses

Before any comment on how to perform statistical measurements on the perturbation field, let's define its Fourier expansions:

$$\delta(\mathbf{k}) = \int \delta(\mathbf{x}) e^{-i\mathbf{k}.\mathbf{x}} d\mathbf{x} \quad ; \quad \delta(\mathbf{x}) = \frac{1}{(2\Pi)^3} \int \delta(\mathbf{k}) e^{-i\mathbf{k}.\mathbf{x}} d\mathbf{x} \tag{2.40}$$

where k is the Fourier mode or wavevector.

Because in an homogeneous and isotropic universe the variance of the perturbation density field has to be the same from about all locations, statistical measurements can be performed. Namely, the gravitational instability yields patterns of inhomogeneities depending on the scale and on the precise matter content of the Universe. To define more precisely the scale-pattern or the variance in amplitude of the perturbation field at all scales, called the power spectrum, it is necessary to go back to the theory of inflation which predicts that the primordial fluctuations can be described by a Gaussian random field (Kolb et al., 1990). Because this field is not only Gaussian but also homogeneous from the cosmological principle, Fourier modes of the perturbation field are uncorrelated (Bardeen et al., 1986). Consequently, it is possible to define the variance in amplitude of the perturbation field at all scales, or power

spectrum P, as a function of the Fourier modes, or wavevectors, k such that the power spectrum is the ensemble of $P(\mathbf{k}) = \langle|\delta_k|^2\rangle = |\delta_k|^2$ where the angle brackets stand for the average over the volume. From this definition, it appears that the amplitude of the power spectrum increases with time t. At t, the power spectrum is $D_+^2(t)P_0$ (from $\delta(\mathbf{x},t) = D_+(t)\delta_0(\mathbf{x})$) where P_0 is the power spectrum today, normalized by σ_8 as given in Table 2.1. Figure 2.7 shows the three power spectra, i.e. cosmological models, which are used in Chapter 4 of this work.

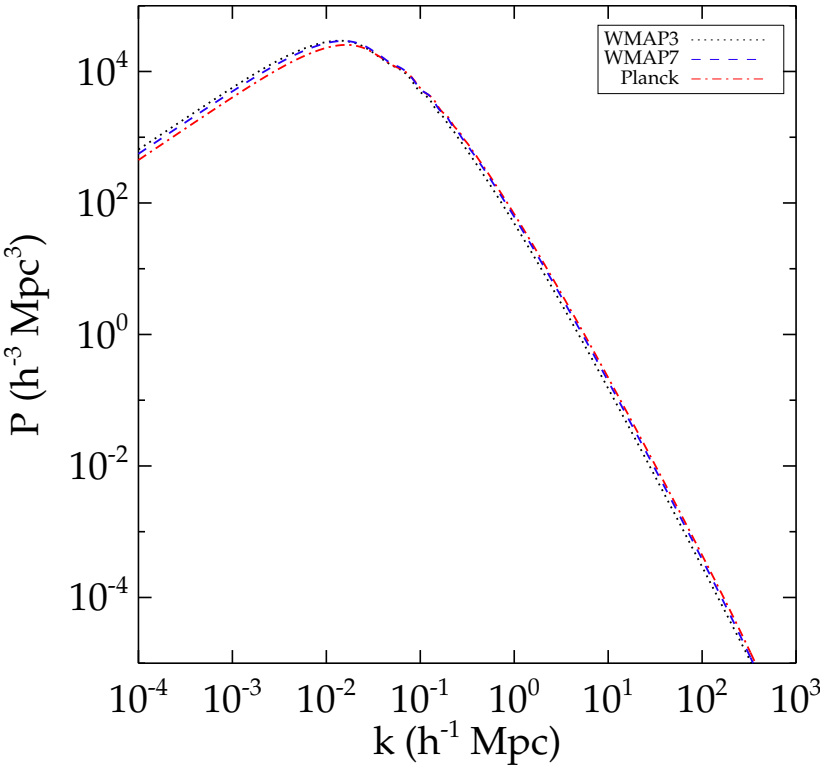

FIGURE 2.7: WMAP3, WMAP7 and Planck Power Spectra (linear part) in logarithmic scales.

Because of all the properties of homogeneity and isotropy from which is also derived the ergodicity (averages over several different random realizations and over a large volume of one realization are equivalent, Adler, 1981) and randomness of the perturbation field, the statistical properties of this latter are fully determined by the power spectrum. For instance, the autocorrelation function of the perturbation density field is defined by:

$$\xi(\mathbf{r}) = \langle\delta(\mathbf{x})\delta(\mathbf{x}+\mathbf{x}')\rangle = \frac{1}{(2\Pi)^3}\int_0^\infty P(\mathbf{k})e^{-i\mathbf{k}.\mathbf{r}}d\mathbf{k} \tag{2.41}$$

The remarkable fact that the perturbation density field is fully determined by the power spectrum, in other words by the Universe content, is at the basis of every simulation.

2.3 N-Body Simulations

All the equations of motions presented in the two first sections of this Chapter are non linear. A solution is given only in the limit of linear perturbations with the linearization. The evolution of the non linear density field can be obtained with N-body simulations of the density field represented by a set of particles.

2.3.1 Dark Matter

Zwicky (1933) noticed that the mass of the Coma cluster obtained with velocity dispersions is a lot greater than the total visible mass (light-emitting mass). Even the addition of the mass of X-ray emissive gases could not account for more than 20% of the total mass of the cluster obtained with gravitation. Most of the mass in the Universe is invisible. Fundamental laws of physics are affected when this invisible mass is not accounted for. For instance, rotation curve of galaxies fail to follow the Newtonian law of gravitation which predicts a decrease in rotational velocity beyond the disk of matter. As a matter of fact, observations at 21 cm (emission line due to the transition between the two hyperfine levels of the ground state of hydrogen, with different energies because of parallel and antiparallel spins) of the hydrogen disk reveal that galaxy masses are not concentrated within regions extending up to the hydrogen disk. If it was the case, from the first law of gravitation (here, $\frac{v^2}{r} = \frac{Gm}{r^2}$), the rotational velocity v of a galaxy beyond the hydrogen disk would decreased as $\frac{1}{\sqrt{r}}$ where r is the distance from the galaxy center. However, the rotational velocity beyond the hydrogen disk is a constant up to large galactocentric distances. The fact that the rotational velocity is a constant implies that the gravitational potential has to be inversely proportional to the distance. Namely, in a sphere of radius r, the mass m is proportional to r and the density is inversely proportional to r^2. As a result, the invisible component of the Universe, called dark matter, is not a uniform mass in which ordinary matter is embedded. Its density is largely function of the galactocentric distance.

Still, the question of what englobes the terminology "dark matter" is not totally answered. The nature of the dark matter is only partly known. Going back to the linear theory of density perturbations, the relativistic hot dark matter particles can be ruled out at least if considered alone[3]. These relativistic particles are not gravitationally bound in the potential wells of density concentrations. Consequently, small scale density perturbations cannot form. This implies that large scale structures have to form first before fragmenting into smaller scale structures. This scenario contradicts observations of small scale structures at high redshifts (e.g. Petry et al., 1998; Rauch et al., 1999, 2001). Still, with the hot characteristic

[3]For more details on an extra hot dark matter component in addition to the dominant cold/warm dark matter component see e.g. Hamann and Hasenkamp (2013); Jeong et al. (2014) for the most recent progress.

dismissed, distinguishing warm from cold dark matter is yet to be done. While the adjective "warm" implies that particles decoupled while relativistic so that today velocities, densities and temperature relative to photons are reduced, the adjective "cold" suggests particle relics which decoupled while classical. The number density can be suppressed and the mass can be as large as desired, the thermal velocities being effectively zero. If decoupling happened at sufficiently high redshifts then the horizon scale was small at that time and free streaming had a negligible impact. As a result, structure formation is a hierarchical process in which large structures grow via the merging of smaller scale structures. In a warm dark matter dominated Universe, if particles decoupled at sufficiently early time (sufficient mass), small scale structures at high redshifts can also be found. The critical mass is around 1-10 keV. Regarding the baryonic characteristic of dark matter particles, from the primordial nucleosynthesis, the baryonic density parameter cannot exceed 0.07 for reasonable Hubble Constant value (e.g. Krauss, 1995). However, the estimate of the total matter density parameter Ω_m is at least 0.2 in Table 2.1. There is a necessity for dark matter to be (mostly) a non baryonic gravitationally dominant component of the Universe (e.g. Hattori, 1994). This work relies on the standard ΛCDM model, thus, cold dark matter is assumed to be the gravitationally dominant component of the Universe without any precision as to the nature of such particles. They could be Weakly Interacting Massive Particles (WIMPs, e.g. Bertone, 2010; Iocco, 2010) to give an example of current theories about dark matter particle nature. In any case, particles composing this dark matter dynamics can be studied with simulations.

2.3.2 N-Body Codes

2.3.2.1 The Modeling

The first problem encountered in the numerical cosmological field of research arises just by the complexity of simulating the entire Universe (probably infinite). We are constrained to simulate only a part of it. For the simulation to be statistically fair, the length L of the chosen cube, which will have to be resized permanently (comoving cube) because of the expansion particularity of the Universe, has to be large enough for the effect of the Large Scale Structure not to be neglected (e.g. Power and Knebe, 2006). The larger the box, the better it probably is, but, with it, comes the implication of a decrease in the mass and length scale resolutions. Because the total mass in the numerical volume is proportional to the cube of the length L times the matter density parameter, the minimum mass resolution which can be obtained for a number of particles n can be derived and a compromise can be achieved.

Still, a particle at the edge of the box has to feel gravitational forces beyond this edge. The box cannot be assumed to be embedded in nothing. From the assumption of the homogeneity of the Universe at scales larger than L, the cube is extended periodically. Thus, a particle

leaving from a boundary will re-enter the box from the opposite side and feel the gravitational effect of particles on the other side. Therefore, the mass distribution has a periodicity of L and quantitative analysis of the results have to be confined to approximately $\frac{L}{2}$.

Regarding matter modeling, since dark matter dominates the matter in the Universe, it is often sufficient to compute the behavior of this dark matter and to consider solely gravitational interactions at least as a first approximation. Baryonic physics can eventually intervene (e.g. Scannapieco et al., 2005) or dark matter only simulations can directly be galaxy populated (e.g. Cole et al., 2000; Klypin et al., 2013). The complete scheme is 1) structures grow via the sole gravitational instabilities pre-existing in the initial density field in the form of Gaussian fluctuations (Press and Schechter, 1974) ; 2) in a dissipationless gravitational collapse, dark halos are shaped (Gunn and Gott, 1972) ; 3) galaxies form with the halos following the radiative cooling of baryons. In this work, dark matter only simulations will be presented, namely, the third step is neglected which is a reasonable assumption on the scales of interests for the conducted studies (baryons have a negligible impact on such scales). Then dark matter halos will be assumed to represent galaxies or at least ensembles of galaxies such as clusters or groups. With this context established, particles of dark matter are represented by bodies of mass m. These macroscopic bodies are assumed to behave like microscopic dark matter particles in a volume $\frac{m}{\rho}$ where ρ is the density of bodies. N-body codes follow the motion of this large number of bodies of mass m under their mutual gravitational attraction. However, equations 2.33 to 2.35 are insufficient to solve properly the behavior of dark matter particles which is multi-streamed in any fixed discretization of the three-dimensional Euclidean space. To obtain a complete description of the behavior of dark matter, the whole phase space has to be considered. Usually, these systems are described with collisionless equations since the time coverage of simulations is much shorter than the relaxation time of these systems.

2.3.2.2 Colisionless Boltzmann and Poisson Equations

In an attempt to mimic the evolution of these systems with an infinite number of particles, the distribution can be seen as a continuum. Then, the gravitational field is not the result of a collection of mass points but that of a smooth mass distribution. Interactions between individual particles are indeed negligible in this large spatial extent context. This smooth mass distribution of non-interacting dark matter particles can be described by the colisionless Boltzmann and Poisson equations in an expanding Universe. The collisionless Boltzmann equation can be applied to the probability distribution function f of a particle to be at a given position. The conservation of this function in phase space implies $\frac{\partial f}{\partial t} + \frac{\partial f \dot{\mathbf{w}}}{\partial \mathbf{w}} = 0$ where $\mathbf{w} = (\mathbf{x}, \mathbf{v})$ with $\mathbf{x}$ the position and $\mathbf{v}$ the velocity. Using Hamilton's equations ($\dot{\mathbf{x}} = \frac{\partial H}{\partial \mathbf{v}}$ and

$\dot{\mathbf{v}} = -\frac{\partial H}{\partial \mathbf{x}}$) and Schwarz's theorem, the Boltzmann equation can be written:

$$\frac{\partial f}{\partial t} + \dot{\mathbf{x}}\frac{\partial f}{\partial \mathbf{x}} + \dot{\mathbf{v}}\frac{\partial f}{\partial \mathbf{v}} = 0 = \frac{\partial f}{\partial t} + [f, H] = \frac{df}{dt} \tag{2.42}$$

where the bracket notation denotes the Poisson Bracket (formulation from Leeuwin et al., 1993) and H is the Hamiltonian. In words, the flow of the probability fluid through phase space is incompressible which means that at any time even if the spatial extent increases (expansion) the probability distribution in phase space stays the same. An analogy would be an ideal set of runners who travel at different but constant speeds. Because of the variety of speeds some would recede faster than others from the departure point and the ensemble of runners will cover a larger area. Still because each one of the runners conserves it original speed, the spatial distribution of velocities and comoving positions stays unchanged. This means that sampling the density and velocity field at a time t, the resulting set of discrete particles will always be a uniform sample of the probability distribution function f. As a result, it is enough to solve the equations of motions for each one of these discrete particles.

The N-body method is based on this principle. In Cartesian comoving coordinates, the Hamiltonian H can be written:

$$H = \sum_{\alpha} \frac{{\mathbf{v}_\alpha}^2}{2a(t)} + \sum_{\alpha \neq \beta} \frac{\phi(\mathbf{x}_\alpha - \mathbf{x}_\beta)}{a(t)} \tag{2.43}$$

where x_i and v_i (i stands for α or β) are the position and velocity of the particle i. Thus, for a discretized system, according to Hamilton's equations and because the gravitational field is conservative (this is usually written in the form of the Poisson equation):

$$\frac{dx_\alpha}{dt} = \frac{1}{a}v_\alpha \quad ; \quad \frac{dv_\alpha}{dt} = -\frac{1}{a}\nabla\phi(\mathbf{x}_\alpha) \quad \text{where} \quad -\nabla\phi(\mathbf{x}_\alpha) = \frac{F_\alpha}{m_\alpha} \tag{2.44}$$

where G is the universal gravitational constant and F_α is the force applied to the α particle by all the other particles of mass m_β defined by:

$$\text{For } \alpha = 1 \text{ to n}, \quad F_\alpha = \sum_{\beta \neq \alpha} G m_\beta m_\alpha \frac{\mathbf{x}_\beta - \mathbf{x}_\alpha}{|\mathbf{x}_\beta - \mathbf{x}_\alpha|^3} \tag{2.45}$$

As a result, the only major requirement is the derivation of the gravitational force exerted on each body α at their current positions by all the other bodies β. Bodies are moved accordingly to the application of the force after a short time and they are assigned the corresponding velocities (e.g. Zemp et al., 2007). To compute efficiently all these forces, Poisson solvers are used. The principle is to used the fact that each computed distance can be used twice in the set of forces 2.45. Thus, for n bodies, instead of n^2 operations, only $\frac{1}{2}n(n-1)$ are required. This number of operations can be reduced some more.

2.3.2.3 GADGET: a TreeSPH Code

Heitmann et al. (2008, 2005) studied the differences between various N-body codes such as RAMSES (Teyssier, 2002), ART (Kravtsov et al., 1997) and GADGET (Springel, 2005). They did not find any substantial variations between the Large Scale Structure obtained from the various codes down to the resolution limit. Because the CLUES collaboration uses widely the GADGET code, this work relies on the same code to facilitate comparisons with, and interactions between, present and future work. GADGET is capable of following a collissionless fluid with the N-body method and an ideal gas with smoothed particle hydrodynamics. For dark matter only simulations, only the N-body part of the code is of interest. GADGET combines different methods depending on the scale of computations to maximize the efficiency of the code. Hence, following Xu (1995), the "Tree method" is used at short range while Fourier techniques ("particle-mesh") are used at long-range.

The tree code method (e.g. Appel, 1985; Barnes and Hut, 1986; Dehnen, 2000) consists in dividing the cube in eight equal subcubes and each subcube containing more than one particle is in turn divided in eight. The process is repeated until each little cube hosts at most one particle. Then, the center of mass of the particles in each size cube is computed. Eventually, multipoles are evaluated so that forces acting on each one of the particles can be easily obtained. With only $n \ln n$ operations against $\frac{1}{2}n(n-1)$, this method effectively increases the performance of the code. Without any intrinsic resolution limit, the technique seems ideal but it is considerably slower than the particle-mesh technique. On the opposite, the particle-mesh relies on fastest computational schemes to obtain the gravitational field (e.g. Klypin and Shandarin, 1983; White et al., 1983). However, because forces at small scales are largely suppressed, the resolution is limited, hence the importance of combining the two techniques. The particle-mesh process consists in estimating the density for a set of points regularly spaced on the grid. The "mass assignment" method is used to allocate the mass of a particle to one or more grid nodes close to it. Several mass assignment schemes exist: 1) the NGP, for "nearest grid point", technique gives the mass of the particle to its closest node. This scheme is rarely used because assigned nodes changed discontinuously as particles move through the grid. 2) the CIC or "cloud-in-cell" method splits each mass into a homogeneous cube with side length equal to the grid spacing. 3) the TSC or "triangular shaped cloud" process splits the mass over more nodes than the CIC technique. CIC is usually a good compromise between the smoother TSC results and the noisier NGP results.

2.3.3 Building Initial Conditions

2.3.3.1 The Zel'dovich Approximation

With a large number of fundamental theoretical and numerical tools in hand to model our Universe, it is worth recalling and reminding the goal of this work: the production of simulations of our Universe. Initial Conditions for the GADGET code are required. These Initial Conditions are constituted of an ensemble of particles with given positions and velocities representing the primordial fields (discretization scheme, e.g. Efstathiou et al., 1985). Primordial and today fields are linked by the Zel'dovich approximation (Zel'dovich, 1970) which stays qualitatively valid even when the perturbations are large. Let's consider a particle at Lagrangian coordinates $\mathbf{x}_L$ and the coordinates of the grid point occupied by the particle at a time $t = 0$, $\mathbf{x}_E$ or Eulerian coordinates. At a later time t, the particle is located on the grid at $\mathbf{x}_E(t) = \mathbf{x}_L(\mathbf{x}_E) + \psi(\mathbf{x}_E, t)$ where $\psi(\mathbf{x}_E, t)$ is the displacement field from the initial position. The Zel'dovich approximation stipulates that this displacement field can be approximated by:

$$\psi(\mathbf{x}_E, t) = D_+(t)\psi_0(\mathbf{x}_E) \tag{2.46}$$

where $\psi_0(\mathbf{x}_E)$ is the initial displacement field. In other words, the displacement field behaves similarly to the perturbation density field. Its direction is frozen and it grows with time. This approximation is the first-order solution of the Lagrangian perturbation theory often referred to as LPT. Positions of particles at a time t can then be derived. This ensemble of particles approximates the primordial density perturbation field provided that the chosen time is small enough (or equivalently z is high enough).

Because the peculiar velocity field u is the time derivative of the Eulerian coordinates minus expansion:

$$\mathbf{u}(\mathbf{x}, t) = a \times \frac{\psi(\mathbf{x}, t)}{D_+(t)} \frac{dD_+}{dt} \times \frac{dt}{da}\dot{a} = \dot{a} f \psi(\mathbf{x}, t) \tag{2.47}$$

where $f = \frac{d(\ln D_+)}{d(\ln a)}$ is the growth rate, the displacement field can be reached through the peculiar velocity field.

Continuing our quest, the peculiar velocity field needs to be determined. From the continuity equation 2.37 left, the (linear) peculiar velocity field $\mathbf{u}$ is directly available from the perturbation density field $\delta = \tilde{\delta} D_+$ provided that this latter is known:

$$\nabla.\mathbf{u} = -a\frac{\partial(\tilde{\delta} D_+)}{\partial t} = -a\frac{\delta}{D_+}\frac{\partial D_+}{\partial t}\frac{\partial t}{\partial a}\dot{a} = -\dot{a} f \delta \tag{2.48}$$

where f is still the growth rate.

Both redshift surveys and peculiar velocity estimates can give access to the perturbation density field with reconstruction techniques such as the Wiener-Filter method (e.g. Zaroubi et al., 1999, 1995). This technique of reconstruction based on correlation functions will be described in more details in Chapter 4. Regardless, to measure the perturbation density field, there are thus two solutions. Either redshift surveys are directly used or they are combined with direct distance measurements to produce radial peculiar velocity measurements.

2.3.3.2 Redshift Surveys or Direct Distance Estimates?

Obtaining radial peculiar velocity measurements is clearly more demanding and one could argue that although it works it is not worth the effort. Still, since galaxies account only for the luminous matter while radial peculiar velocities from direct distance measurements account for both baryonic and dark matter, the trade-off between the two possible sets of observational data to produce constrained simulations is undeniable. Surely, the density field obtained from redshift surveys may be corrected for the bias. Comparisons between density perturbation fields obtained from large deep redshifts surveys and from independent peculiar velocities measurements have resulted in an estimate of this bias (e.g. da Costa et al., 1998) and methods based on redshift surveys flourished to produce constrained Initial Conditions (Heß et al., 2013; Lavaux, 2010; Mathis et al., 2002). However the bias is still poorly known (e.g. Baugh, 2013). Then, relying on *direct, unbiased* tracers of the underlying gravitational field (peculiar velocities) to derive the perturbation density field is highly relevant. The wealth of the Cosmicflows project is based on this last affirmation.

Chapter 3

Observed Universe

Peculiar velocities are departures from the cosmic mean Hubble expansion due to primordial density inhomogeneities. The overarching goal of the Cosmicflows project is to measure distances, to estimate such variations from the expansion, out to redshift $z \sim 0.05$ *(*$\sim$ *150* h^{-1} Mpc*). Distance measurements are gathered from a multitude of methods. Of particular importance to the project are distances accrued from the correlation between the rotation rate of a galaxy and its luminosity or the Tully-Fisher Relation. There are methodologies that provide distance estimates that are individually more accurate but an abiding advantage of this relation is applicability to a large fraction of all galaxies over a wide range of environments and distances. Distances measured on a coherent scale around the sky are required to address properly the cosmological problems of the Hubble Constant and of departures from the mean cosmic flow. Mid-infrared (3.6* μm*) photometry with the Spitzer Space Telescope is particularly valuable as the source of luminosities because it provides products of uniform quality across the sky. Accordingly, this Chapter presents observational data of the Cosmicflows projects, in particular surface photometry of Spitzer mid-infrared data. Subsequently, these data are used to calibrate the Tully-Fisher relation at 3.6* μm *and to give an estimate of the Hubble constant. Finally, the accurate distance measurement catalogs of the project are presented.*

3.1 Distances

Distances in the Universe are not accessible with everyday tools. Indicators like luminosity or size in the sky are required to estimate distances. Because distances are obtained through variables and methodological tools affected by the dynamics, geometry and compositions of the Universe, several definitions and explanations regarding fundamental bases of the tools are requested.

3.1.1 Luminosity Distance

Comoving Radial Distance:
From the definitions of the comoving coordinates 2.30 and cosmological redshift 2.22, the comoving radial distance x of a source with a cosmological redshift z_{cos} in our most likely flat Universe, today is:

$$x = \int \frac{1}{a} dr = \int \frac{-cdt}{a} = \int \frac{-cda}{a^2 H} = \int_0^{z_{cos}} \frac{cdz}{H} = \int_0^{z_{cos}} \frac{cdz}{H_0 \sqrt{(1+z)^3 \Omega_m + \Omega_\Lambda}} \tag{3.1}$$

where equation 2.19 and the metric 2.2 were used.

Luminosity Distance:
Among the variety of distances which can be measured, this work relies on the luminosity distance D_L. This latter is obtained measuring the flux F of celestial objects with the relation:

$$D_L = \sqrt{\frac{L}{4\Pi F}} \tag{3.2}$$

assuming the total intrinsic luminosity L of the object is known.

The flux received from a galaxy at a comoving distance x today ($a = a_0$=1) is proportional to its luminosity distributed on a sphere of radius x. However, emitted particles such as photons are not received as such. They are affected by a double diminution of their frequency due to both the expansion and a loss of energy. Then the flux measured is:

$$F = \frac{L}{(1+z_{cos})^2} \frac{1}{4\Pi x^2} \tag{3.3}$$

From relations 3.2 and 3.3, the luminosity distance D_L can be expressed very simply in function of the comoving distance x as:

$$D_L = (1+z_{cos})x \tag{3.4}$$

It is remarkable that because our Universe is most likely flat, the Friedmann-Lemaître-Robertson-Walker metric 2.2 is considerably simplified. When the relation between the measured and comoving distances could have involved (hyperbolic) sinus functions for a (negative) positive curvature of space, they are simply proportional in the case of a flat Universe.

Our final interest is in the estimation of peculiar velocities. In Chapter 2, the formula 2.25 enables the computation of non-relativistic radial peculiar velocities. However, equations to derive estimates of the cosmological redshift have yet to be discussed.

Relation 3.4 implies that the cosmological redshift can be estimated provided that the integral 3.1 can be calculated. Unfortunately, because of the presence of the cosmological constant, there is no simple solution. An approximation of the generalized Hubble constant is required. For small redshift, the development of H to the second-order in z is satisfactory. After a calculation, that we do not report here, Chiba and Nakamura (1998) give:

$$\frac{H(z)}{H_0} \approx [1 + (1 + q_0)z + \frac{1}{2}[(j_0 + 3q_0 + 2) - (2 + 3q_0 + q_0^2)]z^2] \tag{3.5}$$

$$D_L(z) \approx \frac{cz}{H_0}[1 + 0.5(1 - q_0)z - \frac{1}{6}(1 - q_0 - 3q_0^2 + j_0)z^2] \tag{3.6}$$

where $j_0 = \frac{\dddot{a}a^2}{\dot{a}^3}|_0$ is the jerk parameter and $q_0 = -\frac{\ddot{a}a}{\dot{a}^2}|_0 = 0.5(\Omega_m - 2\Omega_\Lambda)$ is the deceleration parameter obtained with equations 2.11, 2.12 and 2.16. Usually, we take the jerk parameter to be the unity.

Eventually, the cosmological redshift is solution of equation 3.6 where $D_L(z)$ is the measured luminosity distance. It leads to an estimate of the peculiar velocity with 2.25.

Very often, observers work with velocities from the start rather than redshifts. However, one has to be careful when working with velocities as the commonly seen relation $v_{tot} = cz_{obs}$ is inaccurate. From equations 2.23, 2.25, the generalized Hubble Law modified by peculiar motion 2.31 and the relation between cosmological redshift and distance luminosity 3.6, neglecting supplementary relativistic effects, if any, affecting the observational redshift, one finds:

$$\begin{aligned} v_{tot} = H_0 D_L + v_{pec} &\approx cz_{cos}[1 + 0.5(1 - q_0)z_{cos} - \frac{1}{6}(1 - q_0 - 3q_0^2 + j_0)z_{cos}^2] + cz_{pec} \\ &\neq cz_{obs} = c(z_{pec} + z_{cos} + z_{pec}z_{cos}) \end{aligned} \tag{3.7}$$

With these definitions settled, in the rest of this Chapter, distance stands for luminosity distance.

3.1.2 Magnitudes

Observations of brightnesses of stars and galaxies go back as far as the ancient world when lists of celestial objects and their magnitudes were compiled. Since the human eye relates magnitude and flux roughly logarithmically in base ten (denoted log in this whole work), the logarithm scale has been kept over the years although, the relation is now much better defined. The apparent magnitude m of an object is given by:

$$m = -2.5\log F + cst \tag{3.8}$$

where F is the flux and cst is a constant which depends on the chosen system. Multiple systems exist, two are used in this work:

- the *Vega system* which is built for the Vega star to have a zero magnitude in all filters. At only $\sim$ 7-8 parsecs from Earth, Vega, also called Alpha Lyrae, is the brightest star in the constellation Lyra. From the fifth brightest star in the night sky, it comes only second in the sole northern hemisphere after the Arcturus star. From the definition 3.8 of the apparent magnitude, the constant is $2.5\log(F_{Vega})$ plus an additional term depending on the observing telescope,
- the *AB system* which relies on the principle that an object with a constant flux (flat energy distribution) has the same magnitude in all bands. In that case, the constant in equation 3.8 is -48.6 to which the value corresponding to the response of the observational instrument has to be added.

Because objects are all at different distances (the desired variable), comparing their intrinsic luminosities with apparent magnitudes is not direct. Thus, the absolute magnitude M of an object is defined as the apparent magnitude which would be measured for the object if this latter was at 10 parsecs from us without any source of obscuration:

$$M = -2.5\log L + cst' \tag{3.9}$$

where L is the luminosity of the object and cst' a constant.

From the definitions 3.8 and 3.9 of the magnitudes and $F = \frac{L}{4\Pi D^2}$ of the flux, apparent m and absolute M magnitudes of an object can be related to its distance D:

$$\mu = m - M = -2.5\log(\frac{4\Pi \times 10^2}{4\Pi \times [D(pc)]^2}) = 5\log[D(pc)] - 5 = 5\log[D(Mpc)] + 25 \tag{3.10}$$

where μ is called the distance modulus and (pc) and (Mpc) mean that the distance has to be converted either in parsecs or megaparsecs.

In 1934, relation 3.8 between the flux $F = \frac{L}{4\Pi D^2}$ and the apparent magnitude m enabled Hubble to confirm the homogeneity of the Universe. For a homogeneous Universe, the number of galaxies with a flux greater than F in a steradian of the sky should follow the relation:

$$N(>F) = nV = \frac{nr^3}{3} = \frac{n}{3}(\frac{L}{4\Pi F})^{3/2} \propto F^{-3/2} \propto (10^{-0.4m})^{-3/2} = 10^{-0.6m} \tag{3.11}$$

Hubble counted and retrieved the proper relation. Note that in reality the homogeneity is confirmed only for the younger Universe as light received today has been emitted some time in the earlier history of the Universe. In addition, this relation is valid only nearby unless

some correction for the selection bias which affects it farther away is made (see section 4.4 in Chapter 4 for an explanation of the bias).

From this subsection, we learnt that measuring distances relies on obtaining distance modulus estimates, more precisely apparent and absolute magnitudes. The next subsection enlightens us on some of the methodological tools available to obtain such distance modulus measurements.

3.1.3 Distance Indicators

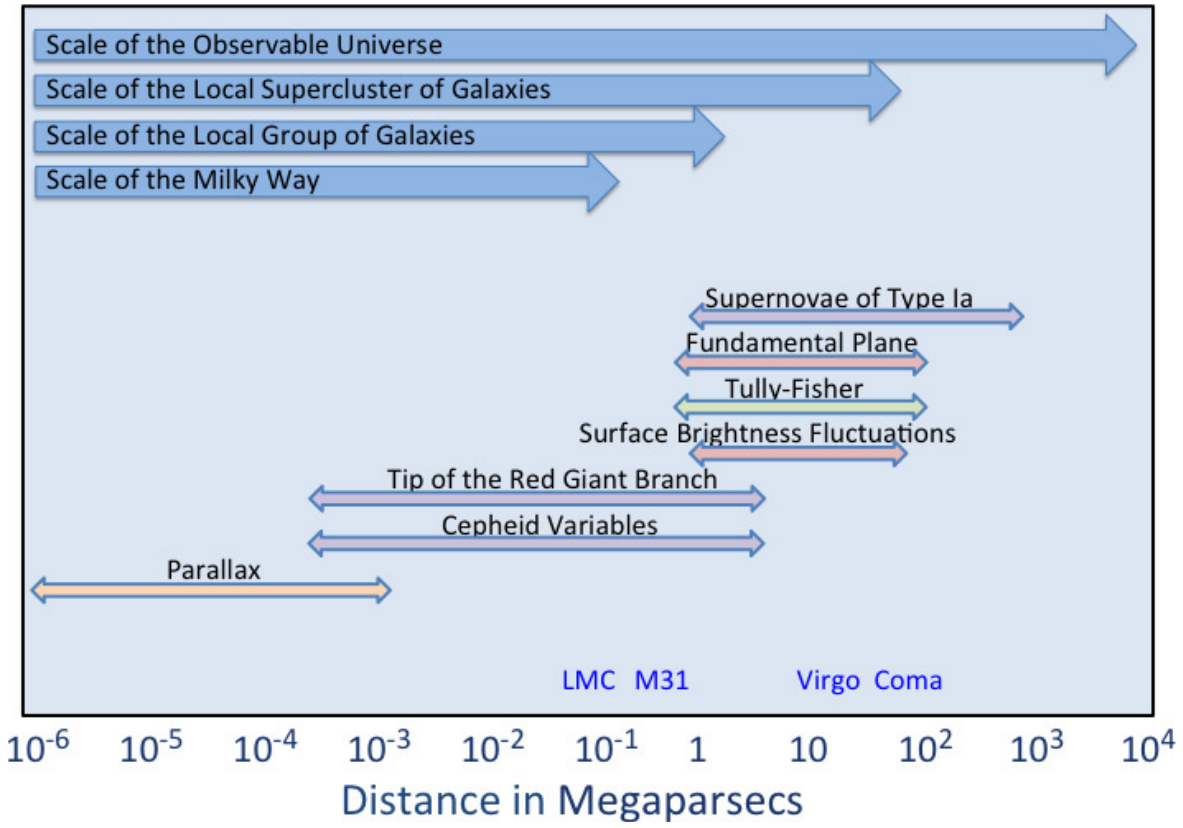

FIGURE 3.1: The cosmic distance ladder or extragalactic distance scale principle is presented here. Each technique from parallax to Supernovae of Type Ia through Cepheids, Tully-Fisher relation, etc is relevant to determine distances on varied scales. The most accurate ones, which can be used close to us, serves as scaler for the other ones. They are called primary distance indicators while the others are named secondary. The double head arrows underlying techniques' names show the range of distances on which methods are relevant. Their colors (except for the orange one) indicate the objects of study: purple for the stars, red for elliptical galaxies, green for spiral galaxies. The parallax is a geometrical method which applies to various but very close objects. A few object are identified in blue: the Large Magellanic Cloud (LMC), the galaxy M31 or Andromeda, the Virgo and Coma clusters. Their horizontal position in the diagram specifies their approximate distance. (This figure heavily borrows from one of Pr. Whittle's lessons, www.astro.virginia.edu).

The cosmic distance ladder or extragalactic distance scale is the ensemble of methods used by observers to determine distances in the Universe. The notion of ladder arises because none

of the techniques used to estimate distances can cover by itself the whole range of values. Distance indicators, as are called these methods, are separated into two groups: the primary distance estimators which are very accurate but can be used only locally and the secondary distance estimators which are less accurate but can provide distances much farther away. Figure 3.1 gives a non extensive list of distance estimators which are briefly described in the next paragraphs (see Jacoby et al., 1992; Rowan-Robinson, 1985, for a more complete review).

3.1.3.1 Primary Distance Estimators

Two primary distance estimators are of particular interests to the Cosmicflows project:

- the Cepheid Period Luminosity relation which is a very accurate method based on the relation between the distance modulus μ of the variable stars or Cepheids and their period P (amount of time necessary for their magnitude to be back to the initial value before repeating the same flux variation pattern again):

$$\mu = a[\log(P) - 1] \tag{3.12}$$

  where a is a constant. Freedman et al. (2001) improved the calibration of this relation by taking into account the Cepheid-metallicity dependence of the relation. Distances are directly obtained from this relation and equation 3.10,

- the Tip of the Red Giant Branch (TRGB) method which relies on the fact that the red giant branch is well developed in stellar populations older than two gigayears. Stars at the tip of the branch are easily resolved if their distance is less than 10 Mpc. This method uses equation 3.13, a correlation between TRGB magnitudes and distance moduli:

$$\mu = m_{TRGB} + BC - M_{Bol,TRGB} \tag{3.13}$$

  where BC is the bolometric correction (conversion from apparent to bolometric magnitudes where the bolometric magnitude is the magnitude that would be measured if all the wavelengths were observed simultaneously), $M_{Bol,TRGB}$ the bolometric luminosity function of metallicity and color and, m_{TRGB} the magnitude for which there is a discontinuity in the Color-Magnitude Diagram of the observed star population. At the core of low-mass star helium flashes, $M_{Bol,TRGB}$ varies only by approximately 0.1 magnitude. Thus, in a Color-Magnitude Diagram, which preserves a record of star formation history rich in details, low-mass stars accumulate along the red giant branch up to the tip as they evolve. The sudden discontinuity in the diagram indicates that

the tip is reached. Relation 3.13 and equation 3.10 enable a direct derivation of the distance.

These two primary distance indicators enable to set the zeropoint of the secondary distance estimators.

3.1.3.2 Secondary Distance Estimators

After observations revealed that kinematic properties and luminosities of galaxies are closely linked, relations have developed. A relation often applies to a particular type of galaxies. Let's first distinguish between the different galaxy types:

- the elliptical galaxies are smooth, featureless stellar systems containing little or no cool interstellar gas or dust and small or no stellar disk. Ten percents of these galaxies can be found in low density regions to over forty percent in dense clusters' centers. In the Hubble sequence, they are named $E0$ to $E7$ where the number 0 to 7 are related to a measure of the axial ratio at the effective radius or radius of the isophote (line of constant luminosity) delimiting half the total luminosity,
- the spiral galaxies, like the Milky-Way or M31, have prominent disks containing stars, gas and dust. Disks have spiral arms which are star forming filaments. These spiral arms are also visible in the old stars in disks. Arms are very variable in shape from one spiral galaxy to the other. About sixty percent of these galaxies can be found in low density regions while their number drops to ten percent in dense regions such as the core of clusters. Most spiral galaxies, like the Milky-Way, have also a bulge or central smooth and amorphous concentration of stars. In the Hubble sequence, spirals are called Sa to Sd. From a to d, the luminosity of their bulge decreases, their arms are less wound and show more individual clumps of young stars, their gas content increases. Spiral galaxies can also be barred like the Milky-Way. The bar is a long smooth stellar structure relic of a rigid system at the center of the disk. To distinguish normal from barred spirals, a "B" is added after the S (SBa,b,c,d),
- the lenticular galaxies (SO, SO^+, SO^-) are galaxies in between ellipticals and spirals. Like ellipticals they do not have arms (so gas and young stars) and, they have a smooth appearance yet they have all the other characteristics of spirals. Found mostly at the center of clusters, they could be old spiral galaxies which interstellar gas has been streamed through different processes (e.g. Rawle et al., 2013),
- the irregular galaxies (Sm, Im), such as the two Magellanic clouds, are kind of spirals but with less sharply defined arms. They are rich in gas and could be the results of merging processes or could have been deformed by close encountering.

An old relic of the Hubble sequence, which was primarily assumed to be an evolutionary sequence of galaxies, left the denomination of early types for elliptical and lenticular galaxies and late types for spirals and irregular galaxies. These two different types of galaxies, mainly ellipticals and spirals, follow different relationships.

Relations for Elliptical Galaxies:

• Relations for elliptical galaxies are usually refinements of the Faber-Jackson relation (Faber and Jackson, 1976) which relies on the fact that on average the velocity dispersion σ_0 measured in the center of ellipticals is proportional to their luminosity L but with a large scatter. The Fundamental plane (Colless et al., 2001) is one of these refinements which supports the fact that not only luminosity and velocity dispersion are related but also the effective radius is proportional to the luminosity. As a result, the effective radius r_e is also proportional to the average effective surface brightness $\langle\mu_e\rangle$ defined as the brightness in magnitude per square arcsecond measured for the surface within the isophote of effective radius. As a matter of fact $L \propto r_e^2\langle\mu_e\rangle \propto \langle\mu_e\rangle^{-cst}$, namely the more luminous the galaxy is, the smaller the effective surface brightness. Then, in a (r_e,$\langle\mu_e\rangle$,σ_0) plane, hence the Fundamental Plane name, ellipticals are close to forming a plane:

$$\log\, r_e = a\langle\mu_e\rangle + b\, \log\, \sigma_0 + c \tag{3.14}$$

where a, b and c are constants. The radial stellar velocity dispersion is determined with spectroscopy measurements where absorption lines are broadened by internal motions of stars. Thus, the velocity dispersion is related to the Gaussian function necessary to match an assumed galaxy spectrum, with all stars at rest with respect to each other, to the observational galaxy spectrum.

The Fundamental Plane can be explained with the virial theorem which states:

$$2E_k + E_p = 0 \text{ (with } E_k = \frac{mv^2}{2} \text{ and } E_p = -\frac{Gm^2}{r}) \iff v^2 = \frac{Gm}{r} \tag{3.15}$$

Setting $r_e = k_r r$, $\sigma_0^2 = k_v v^2$ and $L = k_L\langle\mu_e\rangle r_e^2$, where k_x ($x = r, v$ and L) parameters reflect density, kinematic and luminosity structures of a given galaxy, the virial theorem 3.15 gives:

$$r_e = k_s(\frac{m}{L})^{-1}\sigma_0^2\langle\mu_e\rangle^{-1} \tag{3.16}$$

where $k_s = (Gk_Lk_rk_v)^{-1}$. This relation is analogous to the relation 3.14, if the mass-to-light ratio is assumed to be constant (we will come back to this assumption at the end of this subsection).

• $D_n - \sigma$ (Dressler, 1987) is another variant of the Faber-Jackson relation which considering D_n as a function of $\langle \mu_e \rangle$ and r_e finds a relation with σ_0. D_n is the diameter of the isophote encompassing 20.75 magnitude per square arcsecond.

• A quite different method is the Surface Brightness Fluctuations (Tonry et al., 2001) which measures the fluctuation of the number of bright stars per area element in a galaxy. This fluctuation can be described by a Poisson noise. Accordingly the farther away is the galaxy, the more stars there is in the observed areas, the smaller the relative fluctuation is. This measurement enables the definition of the fluctuation star counts $\bar{N} = \bar{m} - m$ with m the apparent magnitude and $\bar{m}$ the fluctuation magnitude obtained with the flux of the fluctuation signal. Combining the correlation between absolute magnitude M and color (difference between magnitudes of two different Bands, or observational wavelength ranges, for a given galaxy) and the relation between that same color and the fluctuation star counts $\bar{N}$ obtained with the observations of a larger number of galaxies, it is possible to write:

$$M = a + b\bar{N} \tag{3.17}$$

where a and b are again constants.

Relations for Spiral Galaxies:

• This work mainly relies on the Tully-Fisher relation (TFR, Tully and Fisher, 1977). In 1977, the virial theorem 3.15 had been the distance estimator up to the early 70s with what was usually called the "indicative mass" method. It was written, assuming a relation between mass and light, $L \propto v^2 r$ where v is the rotational velocity of the galaxy. Tully and Fisher (1977) suggested two alternatives: $L \propto v^\alpha$ (α ranges from 3 to 4) and $L \propto r^\beta$. They reduced the number of variables from 3 to 2 and departed from the virial theorem. Equation 3.18 is the resulting TFR as written nowadays:

$$M = a + b[\log(W) - 2.5] \tag{3.18}$$

with a and b constants, W is the linewidth of the 21-cm line which corresponds to twice the rotation rate of the galaxy.

This relation implies that more massive galaxies are both more luminous and rotate faster. It holds for galaxies with disks stabilized by rotation basically, spiral galaxies. There is no proper mathematical derivation for this relation, but an explanation can help make it plausible even to the cautious reader which remembers that flat ends of galaxy rotation curves imply the most probable existence of a dark matter. Because of this flat end, at a distance r sufficiently large from the center of the galaxy, the mass m can be written $m = v_{max}^2 \frac{r}{G}$. Since the mean surface brightness $\langle \mu \rangle$ is $\frac{L}{r^2}$, the luminosity becomes $L = (\frac{L}{m})^2 \frac{1}{G^2 \langle \mu \rangle} v_{max}^4$. This last equation is analogous to 3.18 assuming the mass-to-light ratio (the same assumption

was made for ellipticals) and the mean surface brightness to be identical for every spiral. Because of the existence of dark matter, this also implies that the ratio of luminous to dark matter is quite similar among spirals. The similarity between different rotational curves and the fact that the mass-to-light ratio of a stellar population should not depend strongly on its age (at least in the red and infrared wavelength) seem in agreement with this last implication. Another variation called the baryonic Tully-Fisher relation (McGaugh et al., 2000) exists which, instead of accounting only for the luminous mass, takes into account the total baryonic (stellar and gas) mass. We will come back to it in the prospectives (Chapter 5).

We close this section with the supernovae of type Ia (SNIa) which have remarkable properties such as their high luminosities ($10^9\, L_\odot$) and their apparent homogeneous nature (Riess et al., 1995). Kowal (1968) established the first Hubble diagram that suggested SNIa could be used as extragalactic distance indicators. Two decades later, Phillips (1993) demonstrated the existence of a decline rate-absolute magnitude dependence for SNIa, validating that type Ia supernovae can act as standard candles. Namely the luminosity or absolute magnitude of these objects is always nearly the same. Work in subsequent years (Amanullah et al., 2010; Hamuy et al., 1995; Hicken et al., 2009; Jha et al., 2007) has produced alternate descriptions of the correlations between the intrinsic luminosities of SNIa and the shapes of their light curves. The properties of SNIa can be used to determine distances to galaxies at many hundreds of Megaparsecs. At such distances, objects are expected to have recessional velocities that individually differ from the mean by at most a few percent and collectively should define the cosmic expansion. Thanks to the great precision of SNIa distance estimates, high redshift SNIa revealed that the expansion of the universe is currently accelerating (Perlmutter et al., 1999; Riess et al., 1998). The SNIa method can provide the best estimate of the Hubble parameter once the zeropoint scale is set. Independent distances are needed to the hosts of low redshift SNIa (Folatelli et al., 2010; Riess et al., 2011, 2009) to establish the absolute scale. Then, measuring the apparent magnitude m and using the definition of the distance modulus 3.10, a distance estimate can be provided.

Actually, except for the Fundamental plane which provides the angular distance, all the above mentioned relations are based on this principle. They supply the absolute magnitude M which when combined with the measured apparent magnitude m enable the determination of the distance modulus μ, an estimate of the distance D with equation 3.10 closely follows. Still, measurements of apparent magnitudes are required and above all constants in all these relations need to be determined for each observational bands as they vary with it. Namely relations need to be calibrated. The constant which gives the zeropoint can only be obtained with primary distance indicators, hence the name of secondary distance indicators given to the estimators in this subsection. Because the interest of the Cosmicflows project goes mainly to the Tully-Fisher relation, the next two sections focus on the two types of observations and

on the surface photometry, performed to acquire apparent magnitudes, required to calibrate the Tully-Fisher relation and to compile an extensive list of accurate distances.

3.2 Observations

As theories can only be tested when directly confronted with observations or indirectly via simulations which are in turn compared with observations, these latter are essential to understand our Universe. To acquire optimal observational datasets, instruments need to be designed with care. Instruments are selected on their sensitivity which determines how dim a source can be and still be observable. This sensitivity depends on intrinsic properties of the telescope (aperture, sensitivity of the detectors, efficiency) but also on extrinsic parameters such as light or radio (depending on the wavelength of observations) pollution and atmospheric turbulences which decrease the angular resolution (minimal angular separation that can have two sources in the sky to be separately detected). The spectral resolution (capabilities to separate the different wavelengths) and the efficiency in terms of number of observations requested to observe a region (the larger the field-of-view, the less observations are required) are also of interests to the observers. For the Tully-Fisher relation, two kind of observations are needed: optical or infrared photometry and radio, precisely HI, observations. As a result two types of instruments are requested and described below along with observations.

3.2.1 RadioAstronomy: HI Observations

With the large number of radiotelescopes available (to date, Arecibo is the largest single dish and has the highest sensitivity, Greenbank is the largest fully steerable radio-instrument, Parkes has the advantage of being in the southern hemisphere unlike the two first mentioned telescopes), the Cosmicflows project has now analyzed HI profiles for over 14,000 galaxies in a consistent way, deriving a linewidth parameter W_{m50} with suitable precision (error estimate $\leq$ 20 km s^{-1}) for over 11,000 galaxies (Courtois et al., 2009, 2011b). These observations are mainly part of the Cosmicflows Large Program on the 100m Green Bank Telescope and complementary southern observations on the Parkes Telescope and the merging of various previous observations re-measured for consistency (Courtois et al., 2009, 2011b). The parameter W_{m50} is a measure of the HI profile width at 50% of the mean flux within the velocity range encompassing 90% of the total HI flux. It gives measures: 1) at a level low enough to capture the range of rotation motions while high enough to be above the noise, 2) with wings in profiles adequately observed, and 3) not sensitive to details of the profile shape (single or double peaked profiles, asymmetric peaks). All these new measurements are available for public use at the Extragalactic Distance Database (EDD, Tully et al., 2009)

website[1] of the Cosmicflows project alongside HI profiles. This observed parameter W_{m50} is transformed into the more physically motivated parameter W^i_{mx} through three steps that are justified in Courtois et al. (2009, 2011b); Tully and Fouque (1985). These transformations remove a slight relativistic broadening and a broadening due to finite spectral resolution, adjust to twice the projected maximum rotation velocity and de-project to edge-on orientation. Appropriate formulations of the adjustments of W_{m50} are given by:

$$\begin{aligned} W^c_{m50} &= \frac{W_{m50}}{1+z} - 2\Delta\nu\lambda \\ W^2_{mx} &= W^{c\ 2}_{m50} + W^2_{t,m50}(1 - 2e^{-(\frac{W_{m50^c}}{W_{c,m50}})^2}) - 2W_{m50^c}W_{t,m50}(1 - e^{-(\frac{W_{m50^c}}{W_{c,m50}})^2}) \\ W^i_{mx} &= \frac{W_{mx}}{\sin i} \end{aligned} \tag{3.19}$$

with z the redshift, $\Delta\nu$ the spectral resolution after smoothing, λ determined empirically (broadening is statistically described for $\lambda = 0.25$), $W_{t,m50}$ the turbulent broadening, $W_{c,m50}$ the transition from boxcar to Gaussian intrinsic profiles ($W_{c,m50} = 100$ km s^{-1} and $W_{t,m50} = 9$ km s^{-1}give the best fit), i the inclination from face-on. The final W^i_{mx} parameter statistically approximates twice the maximum rotation velocity of a galaxy. The inclination from face-on is defined by (Holmberg, 1958):

$$\cos i = \sqrt{\frac{(\frac{b}{a})^2 - q_0^2}{1 - q_0^2}} \tag{3.20}$$

where $\frac{b}{a}$ is the axial ratio and q_0, chosen to be 0.20, is the statistical axial ratio of a galaxy viewed edge-on. Arguments can be made for a more complex dependence of q_0. Fortunately, the choice of q_0 has a negligible effect on distance measurements if one is consistent between calibrators (galaxies used to calibrate the relation) and targets (galaxies to which the relation is applied) (Tully and Pierce, 2000). A q_0 value of 0.13 (0.20) yields an inclination of 81° (90°) for $\frac{b}{a} = 0.20$. This gives a $\frac{1}{\sin i}$ difference on the corrected linewidth of only 1.2%. As one progresses toward larger axial ratio, the difference in assigned inclination is reduced but the $\frac{1}{\sin i}$ correction is growing. The product of the two is a roughly constant shift of 1.2% in the corrected linewidth at all inclination $i > 45°$. Still, the problem of de-projection is recurrent in observations. Accordingly within the Cosmicflows project, we have initiated a Citizen Science Project which should be opened soon to the public. It consists in sorting galaxies by their orientation from face-on to determine statistically and more precisely their inclination.

Linewidth error estimates are based on the level of the signal, S, at 50% of mean flux divided by the noise, N, measured beyond the extremities of the signal. Profiles with error estimates smaller than 20 km s^{-1} are retained. These profiles meet a minimum flux per channel

[1] http://edd.ifa.hawaii.edu; catalog 'All Digital HI'

requirement of signal-to-noise $S/N \geq 2$ and acceptance after visual inspection. Figure 3.2 shows two of such profiles. Errors in the logarithmic linewidth parameter tend to be larger for slow rotators since a typical measurement uncertainty of $10 - 20$ km s^{-1} causes a larger fractional uncertainty with a narrow profile. The largest uncertainties are associated with more face-on galaxies, those toward the 45° cutoff. At this limit, a 5° error in inclination results in an 8% error in linewidth.

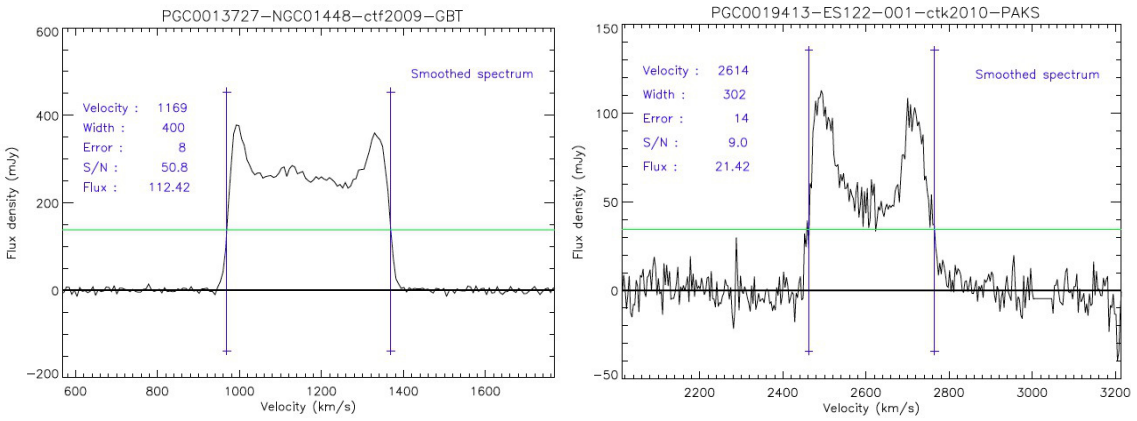

FIGURE 3.2: Suitable HI profiles of two galaxies obtained with the Green Bank (*left*) and Parkes (*right*) telescopes. The rotational velocities of these galaxies are half the given "Width" once corrected. "Width" corresponds to the linewidth parameter W_{m50}: a measure of the HI profile width at 50% of the mean flux within the velocity range encompassing 90% of the total HI flux (from Courtois et al., 2011b).

3.2.2 Photometry: Observational Band

Photometry raises the issue not only of the instrument choice but also of the wavelength of observation. Table 3.1 recapitulates the photometric letters usually attributed to each observational wavelength from the ultraviolet up to the limit with the mid-infrared. Numerous observations are already available in several bands from blue to red (B to R Bands) in the optical up to the near-infrared (e.g. I Band) through various observational surveys (e.g. the Sloan Digital Sky Survey, SDSS, Abazajian et al., 2003). The near-infrared up to its limit with the mid-infrared has even been explored with, for example, the J, H, K Bands of the Two Micron All Sky Survey (2MASS, Huchra et al., 2012). Yet, until recently, although it has long been appreciated that photometry in the infrared may offer advantages because of reduced extinctions, mid-infrared observations were mostly on hold. The difficulty arises from the fact that observations in the infrared from the ground are affected by high and variable sky foreground and by thermal radiations. As a result, much of the flux from galaxies, which lies in extended components with surface brightnesses that are well below the ground based sky level, is lost and very low surface brightness galaxies are not even seen. Observations from space remove the problem of the high contamination by Earth atmosphere. From a perch above the atmosphere, essentially the total magnitude of targets

can be recorded in exposures of a few minutes. Accordingly, the optimal instrument for our work is a spatial telescope observing in the mid-infrared. In addition, and a very important point, the photometry from such a telescope has consistent properties in all directions on the sky. Thus, acquisition of mid-infrared data from a spatial telescope contributes to great advances in photometry which were lacking to the Cosmicflows project to match the large progress achieved with HI observations.

Ultraviolet			**Near-infrared**		
U	~ 300	u	I	~ 800	I_C, i
			Z	~ 900	z
Visible			Y	~ 1020	
B (blue)	~ 400		J	~ 1200	
V (violet)	~ 500		H	~ 1600	
G (green)	~ 600	g	K	~ 2200	K_s, K'
R (red)	~ 700	R_C, r	**beyond: Mid-infrared**		

TABLE 3.1: Photometric observational bands: (1) and (4) photometric letter, (2) and (5) approximate observational wavelength (depends on the filter), nm, (3) and (6) examples of specific filter-bands mentioned throughout this work.

3.3 Surface Photometry

Obscurations within the galaxies and due to the Milky Way which are minimized in the mid-infrared are not the sole advantage of infrared observations. Infrared flux arises in large measure from old stars that should optimally represent the baryonic mass that presumably couples to the rotation rate to give the TFR. Accordingly, it was suggested (Aaronson et al., 1979) that the TF methodology might be improved by moving to infrared bands, particularly when it is used to measure distances. Thus, although progress with infrared observations of galaxies was difficult because of the high and variable sky foreground at near-infrared wavelengths and overwhelming thermal emission at mid-infrared wavelengths with ground-based observations, several attempts to derive the TFR in the close to the mid-infrared band were made. The most modern serious attempt has drawn on the K_s magnitudes of 2MASS (Karachentsev et al., 2002). However, this shallow survey, like with the earlier work in the infrared, only registers the high surface brightness components of light from galaxies and can actually miss low surface brightness galaxies entirely.

3.3.1 Spitzer: an Instrument of Choice

The situation dramatically changed with the launch of *Spitzer Space Telescope* (Werner et al., 2004). With observations using the InfraRed Array Camera (IRAC, Fazio et al.,

2004) onboard *Spitzer Space Telescope*, the "sky" is far reduced from observations on the ground, now dominated by diffuse zodiacal light and the stochastic distribution of background high redshift galaxies. For example, integrating about four minutes in IRAC channel 1 permits area photometry at levels that can compete with ground-based optical imaging with comparable exposures, i.e. to levels that include all but a few percent of the total light of a galaxy.

3.3.1.1 The InfraRed Array Camera Channel 1

The Cosmicflows with Spitzer program concentrates on IRAC channel 1 observations in the 3.6 μm window that give magnitudes [3.6] in the AB system. This window provides observations with minimal dust extinction (Draine and Lee, 1984). It lies at a minimum of the zodiacal background radiation (Ootsubo et al., 1998).

Figure 3.3 provides examples of the spectral energy distribution of spiral galaxies (Silva et al., 1998). The Spitzer [3.6] band lies on the Rayleigh-Jeans tail of the spectral energy distribution of normal populations of stars, not yet strongly affected by flux from warm dust that starts to become a factor at longer wavelengths than 4 μm. The discrete spectral features seen in the spectral energy distribution arise from Polycyclic Aromatic Hydrocarbon molecules (Tielens, 2008). The highest frequency Polycyclic Aromatic Hydrocarbon, at 3.3 μm is contained within the [3.6] bandpass. Meidt et al. (2012) have investigated the impact of various contributors to flux in the 3.6 μm window with six representative spiral galaxies observed with the Spitzer Survey of Stellar Structure in Galaxies (S^4G, Sheth et al., 2010) program. They find contributions from 1) hot dust and Polycyclic Aromatic Hydrocarbons together at the level of $9 \pm 4\%$ of the global flux in the 3.6 μm band, 2) intermediate age asymptotic giant branch and red supergiant branch stars at the level of $3 \pm 2\%$ of the global flux, and 3) old stars, predominantly K and M giants for the rest, i.e. the great majority. These non-stellar and young stellar contributions should only slightly degrade the correlation between old stars and mass in normal spirals.

Using Spitzer IRAC channel 1, a point spread function with mean FWHM $1.66''$ is sampled with $1.2''$ pixels. The field of view is $5.2'$, adequate to encompass most galaxies to beyond twice d_{25}, the diameter at a B isophote of 25 magnitude per square arcsecond. Larger galaxies require mosaics. Integrations with the Cosmicflows with Spitzer (CFS) program involve the combination of 8 x 30 seconds slightly dithered exposures for a total of four minutes per field. As will be discussed, these integrations provide images that probe somewhat fainter limits than most ground-based optical photometry programs and much fainter limits than ground-based infrared photometry programs. Spitzer surface brightness levels reach ten magnitudes below typical ground-based infrared sky levels. No existing near-infrared ground survey

achieves the accuracy obtained with *Spitzer Space Telescope*. The outstanding advantages of space observations are background stability and all-sky consistency (Fazio et al., 2004).

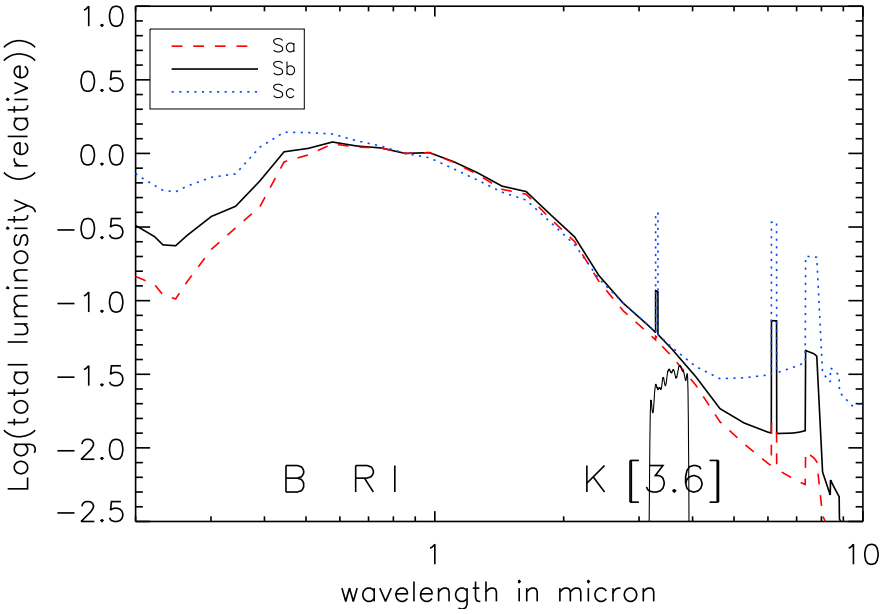

FIGURE 3.3: Comparative SED for spirals of types Sa (red, dashed), Sb (black, solid), and Sc (blue, dotted). The Spitzer [3.6] passband is illustrated along with the wavelengths associated with B, R, I, K bands. The relative scales of the SED are offset to match at 0.8 μm. Features at 3.3 μm arise from Polycyclic Aromatic Hydrocarbon molecules.

3.3.1.2 The Observational Sample

The cycle 8 post-cryogenic program Cosmicflows with Spitzer avoids repetition of earlier Spitzer observations. Archival information is used where available. Major contributions from earlier programs come from SINGS, the Spitzer Infrared Nearby Galaxies Survey (Dale et al., 2005, 2007) and LVL, the Local Volume Legacy survey (Dale et al., 2009) carried out during the cryogenic phase, then S^4G, the Spitzer Survey of Stellar Structure in Galaxies (Sheth et al., 2010), and CHP, the Carnegie Hubble Program (Freedman et al., 2011), subsequently carried out during the post cryogenic phase. Smaller programs supply us with a few more fields. These data are available for public use at the Spitzer Heritage Archive website[2]. The variety of source programs introduces variations in the details of the acquisition, particularly affecting total integrations, dithering procedures, and the extent of fields referenced to d_{25}. However, with all the data that will be considered the fields are large enough and the exposure times are long enough that at most only a few percent of the light from a target is lost.

In subsection 3.3.5, a comparison between 241 magnitudes from S^{4}G-pipeline (Muños-Mateos et al. in prep.) and from the Spitzer-adapted version of ARCHANGEL used in this work reveals the very good agreement between both magnitudes. As a result, S^{4}G-magnitudes are directly

[2]http://irsa.ipac.caltech.edu/data/SPITZER/docs/spitzerdataarchives/

used to derive distances for all the other, relevant to the Cosmicflows project, galaxies of the large S^{4}G program.

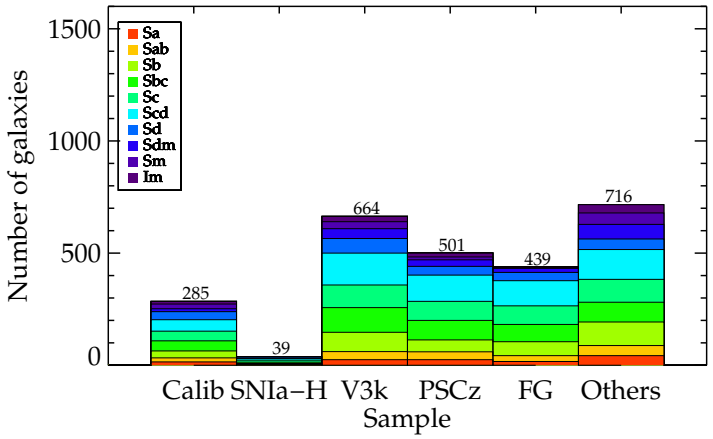

FIGURE 3.4: Histogram of the number of galaxies per subsamples in CFS and diverse programs, mostly S^{4}G (65%). Calib is constituted of Tully-Fisher calibrators, SNIa-H contains hosts of Supernovae of Type Ia, V3k is built of galaxies with $v_{hel} < 3000$ km s^{-1} , PSCz is derived from the Infrared Astronomical Satellite point-source Redshift Survey and FG is a catalog of flat galaxies. "Others" stands for galaxies of interests which do not fall into one of the previously cited categories. The gradient of colors shows the proportion of each morphological type from the HyperLeda Database in each sample.

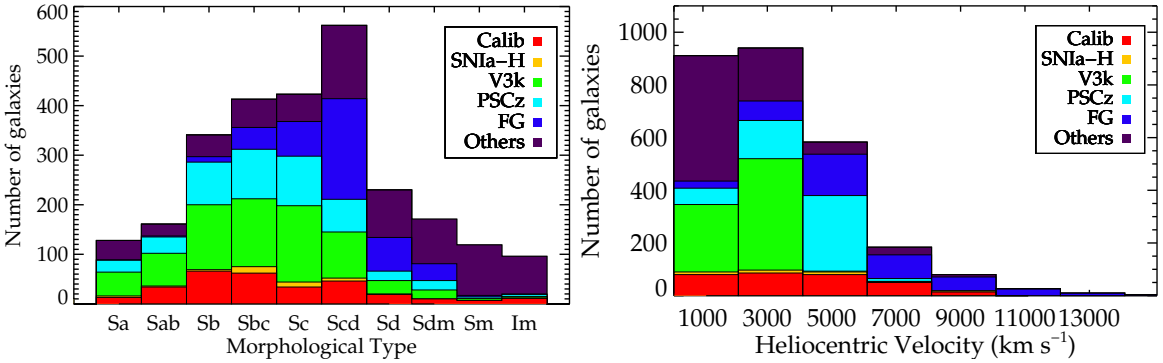

FIGURE 3.5: Histograms of the morphological type (*left*) from HyperLeda and of the heliocentric velocity (*right*) from EDD for the whole compilation of galaxies. The gradient of colors gives in which proportion each subsample contribute to a given type (*left*) and range of heliocentric velocities (*right*).

In Figure 3.4, galaxies which surface photometry has either been measured for the Cosmicflows project or that comes from S^{4}G are distinguished by their occurrence in five subsamples: 1. the Tully-Fisher calibrators (Calib), 2. the hosts of Supernovae of Type Ia (SNIa-H), 3. the V3k, 3000 km s^{-1} sample (V3k), 4. the Infrared Astronomical Satellite point source Redshift Survey sample (PSCz) and 5. the flat galaxy sample (FG). These subsamples are completed with galaxies from various surveys. If a galaxy lies within multiple samples, in the following the galaxy is assigned to the sample that includes it that is discussed first. Galaxies of interest of to the project but which do not fall into one of the previous categories constitute the sixth subsample. All these supplementary galaxies are mostly from

S^4G (65%). Among the galaxies left, the majority has been observed by SINGS (2%), LVL (3%) and CHP (16%) programs.

- The first two of these subsamples have been already widely described (Courtois and Tully, 2012b; Tully and Courtois, 2012; Tully and Pierce, 2000). The first subsample constitutes a template for the calibration of the Tully-Fisher relation: galaxies in 13 clusters for the slope and galaxies with cepheids or Tip of the Red Giant Branch distances for the zeropoint. The second subsample is constituted of galaxies to set the zeropoint scale of the Supernovae of Type Ia method. The two subsamples will be discussed more precisely in subsections 3.4.1 and 3.4.3 when used at 3.6 microns. Approximately one third of the first subsample is constituted of galaxies observed for CFS with Spitzer. Others have been observed by previous Spitzer programs, mostly CHP and S^4G. Half of the SNIa-H subsample is made of CFS observations while the other half contains mostly CHP observations.

- The third subsample is a catalog developed over the years called V3k (Tully et al., 2008) with the magnitude cutoff M_K < -21 mag. It extends up to the velocity limit, 3000 km s^{-1} , imposed by the capabilities of early-generation radio telescopes to obtain useable HI profiles and gives coverage of the traditional Local Supercluster (de Vaucouleurs, 1953). Figures 3.4 and 3.5 left shows that these galaxies are in majority of type later than Sa. Types come from the HyperLeda database (Paturel et al., 2003). Figure 3.5 right confirms that the heliocentric velocities, v_{hel} from EDD, of these galaxies are mostly less than 3300 km s^{-1}. Among the 683 galaxies available for this third subsample about a quarter comes from the CFS survey. This sample provides a high density and precision map of the Local Supercluster centered on Virgo.

- The next subsample is based on the redshift survey PSCz (Saunders et al., 2000) of sources drawn from a flux-limited sample at 100 μm obtained with the InfraRed Astronomical Satellite. This point source-redshift sample is constituted of galaxies with far infrared - 60-100 μm - colors such that their flux arises predominantly from cirrus. The sample is dominated by normal spirals distributed around the Sc type as Figures 3.4 and 3.5 show. The heliocentric velocity limit is 6000 km s^{-1} to obtain reasonable HI lines with current radio telescopes. This subsample includes the Norma-Hydra-Centaurus and the Perseus-Pisces superclusters in opposite directions and many low latitude galaxies b - offering good coverage above $|b| = 5°$. The bifurcation between our flow direction and a motion towards Perseus-Pisces, highlighted by Erdoğdu et al. (2006), will be located thanks to this subsample. The PSCz sample will also strongly constrain the CMB dipole component within 6000 km s^{-1}. CFS contains the majority (445) of these galaxies.

- The last subsample is constituted of flat galaxies from the catalog of Karachentsev et al. (1999). These edge-on systems have a major to minor axis ratio greater than 7 implying minimal de-projection of their HI linewidths. The flat galaxies are principally of type Scd, as shown in Figures 3.4 and 3.5 left. They constitute a homogeneous class of HI rich systems but they have a low space density because of the strong inclination constraint. Extinction problems existing at optical bands and for ground-based telescopes are practically removed with IRAC channel 1. The whole flat galaxy subsample comes from CFS observations.

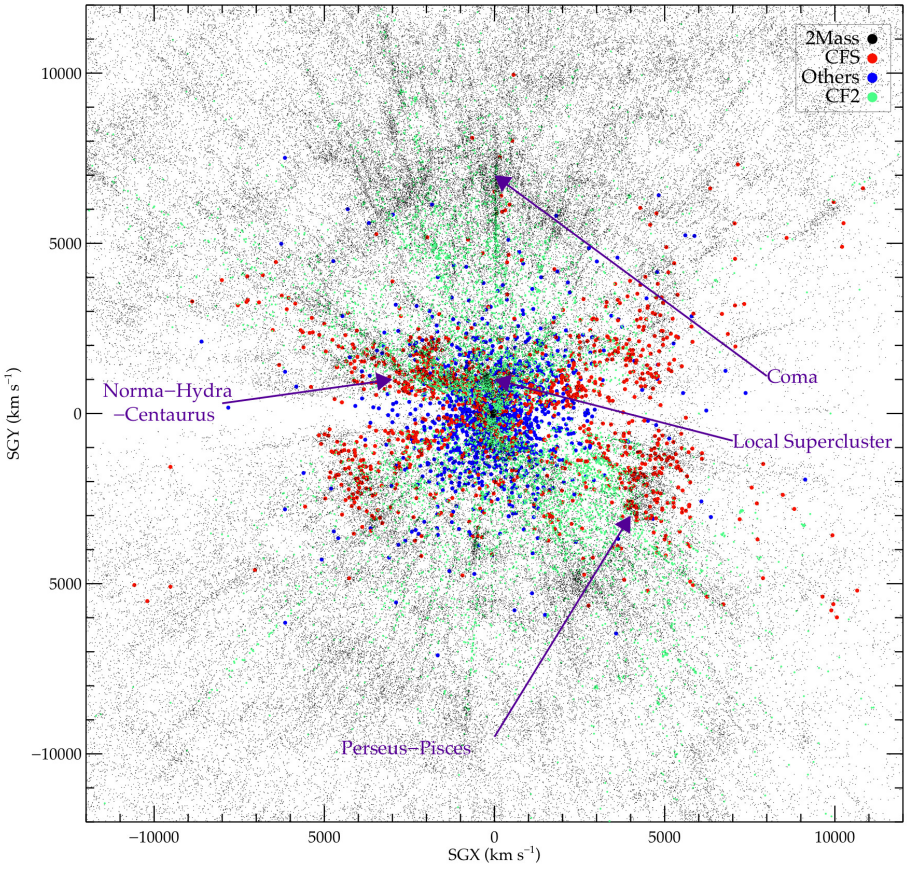

FIGURE 3.6: In the XY supergalactic plane (no restriction on Z), galaxies of the CFS survey (red dots) are superimposed to the 2MASS redshift catalog (tiny black dots) available at EDD. Blue dots stand for galaxies of interests to the Cosmic Flows project but observed by different programs, mostly S^4G. A few superclusters are identified by violet arrows. CFS gives special attention to galaxies at low galactic latitudes. Green dots represent the second catalog of the Cosmicflows project. Future catalogs of the Cosmicflows project will have a better coverage near the Zone Of Avoidance, reconstructions of the Local Universe will be more accurate in that region.

Figure 3.6 illustrates the combined coverage of CFS and other relevant surveys with *Spitzer Space Telescope*. CFS complements previous surveys with galaxies at low galactic latitudes

for two reasons. First, CFS complements the important S^4G survey that has a $|b| = 30°$ lower limit. Second, we recognize that photometry from WISE, the Wide-Field Infrared Survey Explorer (Wright, 2008), will be useful but be at a competitive disadvantage to Spitzer in the crowded star fields at lower galactic latitudes because of resolution issues. With Spitzer observations, future catalogs of the Cosmicflows project will contain more data close to the Zone Of Avoidance than the second catalog of the project. This catalog will be discussed at the end of this Chapter but is already superimposed on the same figure.

3.3.2 Spitzer-Adapted ARCHANGEL: a Tool for Surface Photometry

3.3.2.1 Surface Photometry: Definition

Large numbers of pixels complicate simple parameter extractions. A galaxy is spread over a large area of the sky. At some point outer pixels have more sky luminosity (zodiacal light and background contaminants) than galaxy luminosity. Then determining the "sky" level dominates the total magnitude error budget. An analysis of a large galaxy (extending across many pixels) requires surface photometry involving fits of isophotes, lines of constant luminosity. Isophotes are often set to be ellipses (Milvang-Jensen and Jørgensen, 1999). Our interest is with spiral galaxies with types typically between Sa and Scd. A well behaved spiral is approximated by an oblate spheroid that appears circular when viewed face-on and projects to an ellipse when viewed toward edge-on. Galaxy 2D images described by elliptical isophotes can be summed in annuli to reduce to a 1D description. Then, the 1D profiles are fitted by various functions in order to extract the radial surface brightness (SB) distribution, global structure or geometrical characteristics, spatial orientation, stellar populations, characteristics of dust, etc. To obtain apparent magnitudes, de Vaucouleurs (1977) introduced the growth curve, a plot of magnitude within a radius as a function of radius. With an adequate signal to noise ratio, it could be enough to place large apertures around galaxies and sum the total amount of light, minus the sky contribution. In practice, a galaxy luminosity distribution decreases towards larger radii so larger apertures catch more galaxy light but also introduce more sky noise. Some light is inevitably lost below the sky level. Isophotal intensities associated with the galaxy light at large radii are sensitive to the sky setting. Restriction to a smaller radius leads to underestimates of total light. The problem is that galaxies do not have discrete edges.

It is never possible to measure 100% of the light of a galaxy. Measurements are made to an isophotal level dictated by telescope optics, detector, exposure times, and sky brightness. Different authors measure magnitudes to different isophotal levels then often extrapolate to total magnitudes. Our interest is with spiral galaxies for TF use. These galaxies characteristically decay exponentially in luminosity with radius. In an ideal case, light contained within

a specified isophotal level is a simple function of the disk central surface brightness and of the exponential decay scale length. To extrapolate in such a case one can assume that the light at large radii falls off like an exponential disk with a central surface brightness and scale length characterized by a fit to the main body of the galaxy. The estimated contribution lost below the sky level can be added to what is observed to give an extrapolated magnitude (Tully et al., 1996).

The total luminosity in some passband λ is given by:

$$L_T^\lambda = L_{lim}^\lambda + 2\Pi\frac{b}{a}\mu_0\int_{r_{lim}}^{\infty} re^{-\frac{r}{\alpha}}dr \tag{3.21}$$

where L_{lim} is the observed luminosity within a limiting isophote, $\frac{b}{a}$ is the isophote axial ratio, μ_0 is the exponential disk central surface brightness, α is the disk scale length, and r is the radius from the center. Performing the integration by parts gives:

$$L_T^\lambda = L_{lim}^\lambda - 2\Pi\frac{b}{a}\mu_0\alpha^2[(1+\frac{r}{\alpha})e^{-\frac{r}{\alpha}}]_{r_{lim}}^{\infty} \tag{3.22}$$

Relation 3.22 can be transformed to logarithmic units. From definition 3.8, the total magnitude m_T (no limit) is:

$$m_T^\lambda = \mu_0^\lambda - 2.5\log 2\Pi\frac{b}{a} - 5\log\alpha \tag{3.23}$$

where $\mu_0^\lambda = -2.5\log\mu_0$. Then, the magnitude within an isophote corresponding to the radius r is:

$$m_r^\lambda = m_T^\lambda - 2.5\log[1-(1+\frac{r}{\alpha})e^{-\frac{r}{\alpha}}] \tag{3.24}$$

At n scale lengths, $\frac{r}{\alpha} = n$, the surface brightness drops by $-2.5\log(e^{-n}) = 1.086\ n$. The number of scale lengths observed between μ_0 and $\mu_{r_{lim}}$ is $\Delta n = \frac{\mu_{r_{lim}}-\mu_0}{1.086}$. This gives the extrapolation Δm_{ext} beyond the observed m_r^λ that has to be added to the measured magnitude m_r^λ:

$$\Delta m_{ext} = 2.5\log[1-(1+\Delta n)e^{-\Delta n}] \tag{3.25}$$

The fraction of the total light above or below a given isophote depends only on Δn. There is no dependency on α or $\frac{b}{a}$. This exponential fitting model might give an overestimate because: 1) of an additional bulge component so additions to the disk contribute fractionally less to the total light, in that case, profiles deviate at small radii and 2) the disk may truncate at large radii, in that case growth curves deviate from the exponential relation at large radii. These situations are well known (e.g. De Vaucouleurs 1959, Kent 1985). Fortunately, given that Spitzer photometry is already fairly deep, profile extrapolations add only a few percent of the total light. The only extrapolations significant are either for galaxies that extend beyond the field of the instrument or for extremely low surface brightness galaxies which is overall not the case in this work.

3.3.2.2 ARCHANGEL

Schombert (2007); Schombert and Smith (2012) developed ARCHANGEL, a flexible tool for galaxy surface photometry built of a combination of FORTRAN and Python routines. ARCHANGEL performs procedures such as: 1) masking of stars and flaws, 2) ellipse fitting at expanding radii from the galaxy center, 3) compression of 2D information into 1D surface brightness and magnitude growth curves as a function of radius, and 4) extrapolation via fits to the magnitude growth curve at large radii involving rational functions. Position angles and ellipticities are freely determined at each radial step in the development of the growth curve. At large radii noise dominates and position angle and ellipticity are frozen for the remaining outward steps in radius. An interesting feature was implemented in ARCHANGEL in this work concerning the flexibility in where these parameters become frozen so that they may be frozen at all radii. Total magnitudes, the most important product of this analysis, are found to be negligibly affected by position angle and ellipticity details at intermediate radii. Still, an added feature enables to give, directly from the start of the process, position angle and/or ellipticity, would ARCHANGEL not succeed in fitting the galaxy properly otherwise. Comparisons with alternative photometry are discussed in subsection 3.3.5. Figure 3.7 provides an example of masking and ellipse fitting with the Spitzer-adapted ARCHANGEL. Not to underestimate the total luminosity, masked pixels are then filled with the isophote mean luminosity to which they belong.

A significant source of uncertainty arises from the setting of the sky level and will be discussed thoroughly in subsection 3.3.4. In ARCHANGEL the sky is taken as the median of sky boxes placed around the galaxy. This method gives realistic initial sky background estimates (Hall et al., 2012). If targets are modest in size there is reasonable control of the sky level. If the sky is set properly then the magnitude growth curve should go asymptotically flat at large radii. One can also evaluate the sky setting by looking at the Surface Brightness as a function of radius. Surface Brightnesses are not expected to flare or drop precipitously at the sky level, although such occurrences are not phenomenologically excluded (Erwin et al., 2008; MacArthur et al., 2003). Visual inspections of the magnitude growth curve and Surface Brightness dependence with radius ensure an optimal sky setting. Fortunately, sky values are low in Spitzer data, even if we will show in the last section that this problem remains our major source of uncertainty.

An issue related to the sky problem is the matter of the terminal radius of an analysis. A limit to the fitting process can be imposed by signal-to-noise considerations. Integration times permit us to reliably reach a radius $a_{26.5}$ at the isophotal level 26.5 mag arcsec^{-2} in the [3.6] band. We try to extend the ellipse fitting to 1.5 $a_{26.5}$ in the [3.6] band. A goal of the program is to assure that the ellipse fitting extends to at least 1.5 $a_{26.5}$, with mosaics if necessary. This [3.6] band dimension is not available before the observation so we rely on a

substitution found to be comparable based on the B band diameter d_{25}, requiring that the observed area extend to a radius 1.5 d_{25} (Sheth et al., 2010). ARCHANGEL is then run twice on each galaxy, at first with 1.5 d_{25} to obtain a first estimate of $a_{26.5}$ and then again but with the first estimate of $a_{26.5}$. We found the process to be robust as first and second estimates of $a_{26.5}$ are very similar (so are other parameters) except in a few cases (mostly low surface brightness galaxies).

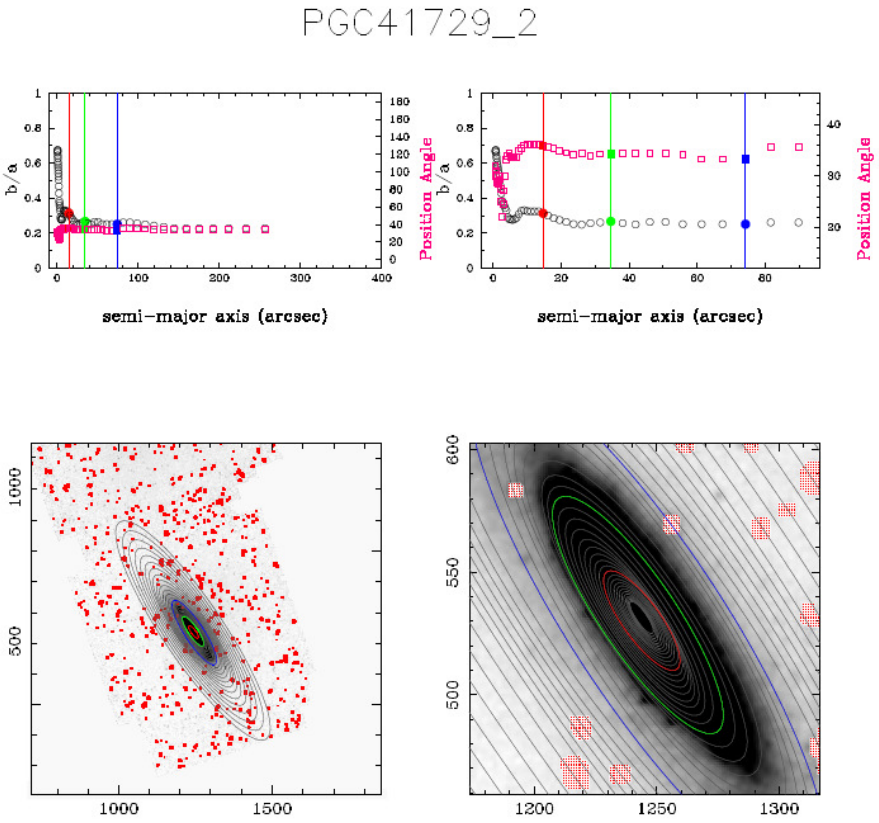

FIGURE 3.7: Output of the ARCHANGEL software showing the axial ratio $\frac{b}{a}$ and the position angle in the two *top* panels and the fitted ellipses and the masking in the two *bottom* panels for PGC41729 or NGC4522.

The mean Surface Brightness in magnitudes per square arcsecond in an annulus at radius r depends on the mean flux in a pixel at that radius $F(r)$ and the mean sky flux in a pixel S:

$$\mu(r) = -2.5\log(\frac{F(r) - S}{0.6}) + 21.585 \tag{3.26}$$

where the constant in the denominator provides a conversion from pixels to arcseconds. The other constant 21.585 comes from the fact that pixel size and zeropoint ($F_0 = 280.9$ Jy) for Spitzer Post Basic Calibrated data are constant. The conversion factor C for the flux, from MJy sr^{-1} to Jy per pixel, is equal to 8.461595×10^{-6} for Channel 1 and a pixel size of 0.6". As a result, the constant (or zeropoint for the AB system in that precise case) value

is $2.5 \log(\frac{F_0}{C}) = 18.8$ (value for 0.6" per pixel) $+2.785$ (conversion Vega to AB system from the IRAC Instrument handbook[3] and Caputi et al., 2006). At optical bands it is common practice to quote magnitudes in the Vega photometric system but working in the mid-infrared it is more useful to use the AB system. Where comparisons are made between optical and mid-infrared, we use the following transformations (Frei and Gunn, 1994):

$$\begin{aligned} B(Vega) &= B(AB) + 0.163 \\ R_C(Vega) &= R_C(AB) - 0.117 \\ I_C(Vega) &= I_C(AB) - 0.342 \end{aligned} \tag{3.27}$$

ARCHANGEL allows to describe the Surface Brightness as the sum of disk and bulge components. Instead, we choose to restrict to disk fits only. With multiple component fits there are frequently trade-offs such that the overall fit may be satisfactory but the physical meanings of parameters are ambiguous. Usually the dominant radial Surface Brightness characteristic of spiral galaxies is an exponential decay of projected luminosity with radius. Deviations are most frequently seen toward the center where a bulge may become dominant. It is beyond the scope of this program to dissect galaxy images into detailed morphological components because such dissection has negligible effect on the product that most interests us: total magnitudes. We restrict fitting to a rough characterization of the exponential fall-off. Accordingly, surface brightness profiles as a function of radius are fitted by simple straight lines between a_e (radius of the isophote encompassing half of the total light in the [3.6] band) and $a_{26.5}$ (radius of the 26.5 mag arcsec^{-2} isophote in the [3.6] band). In rare cases, fits are adjusted by eye, if they are clearly inappropriate between a_e and $a_{26.5}$ after checking that the background brightness variation is not causing any unexpected surface brightness profile changes. Figure 3.8 displays an example of surface brightness fit obtained with ARCHANGEL. μ_0 is obtained by extrapolation as shown by the following relationship:

$$\mu^{[3.6]}(r) = \mu_0^{[3.6]} + 1.0857\frac{r}{\alpha} \tag{3.28}$$

This corresponds to an exponential profile $L^{[3.6]}(r) = L_0^{[3.6]} e^{-r/\alpha}$. $L_0^{[3.6]}$ and $\mu_0^{[3.6]}$ are the disk central surface brightnesses in intensity and magnitude units respectively. α is the disk scale length and r is the distance from the galactic center. Some concerns may arise about the disk-only fitting technique for bulge galaxies. However, de Jong (1996a) showed that disk-only fits gave unbiased disk parameters relative to a 2D fit decomposition parameters within only 0.5 mag arcsec^{-2}.

Surface brightness values between two isophotes are then added up to constitute the growth curve. An example of a magnitude growth curve as a function of semi-major axis is shown in

[3] http://irsa.ipac.caltech.edu/data/SPITZER/docs/irac/ iracinstrumenthandbook/

Figure 3.8. The light from each succeeding annulus contributes to the (negatively) increasing magnitude with increasing radius. If the sky value is properly set then the growth curve will asymptotically flatten. Should the curve turn over it would be inferred that the sky level is set too high - flux from the galaxy is being attributed to the sky and being removed. Conversely, the sky set too low causes flux from the sky to be attributed to the galaxy and the growth curve will fail to flatten. Given a growth curve as seen in Figure 3.8 it is straightforward to define the useful parameters a_{20}, a_e, and a_{80} enclosing 20%, 50%, and 80% of the light respectively. The associated surface brightnesses, magnitudes and semi-major radii are illustrated in Figures 3.7 and 3.8.

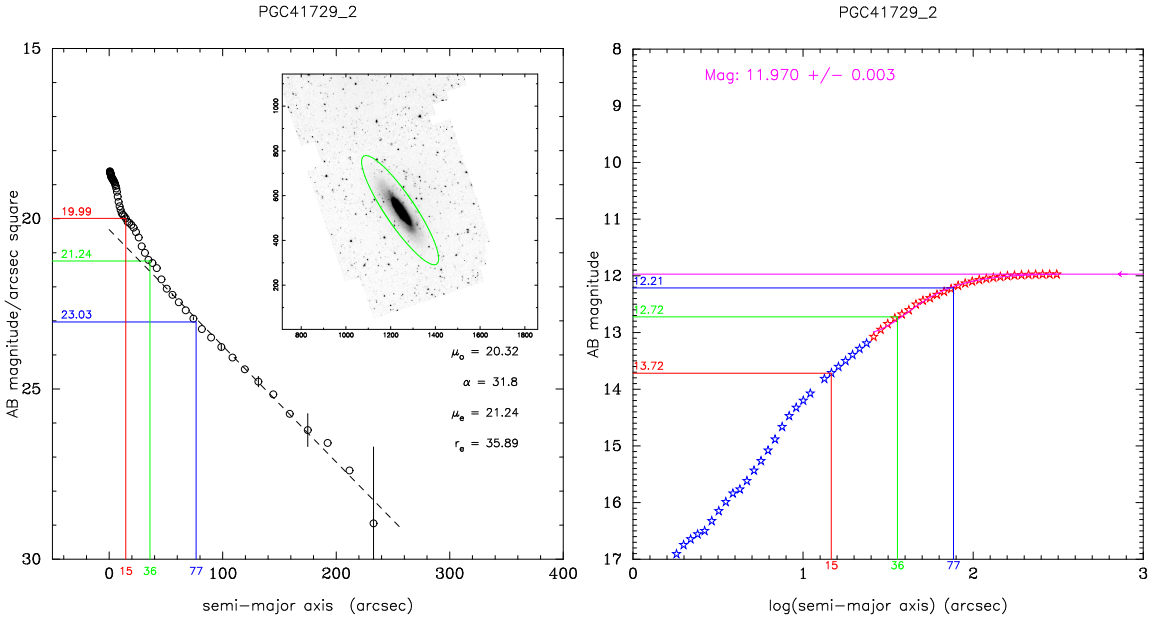

FIGURE 3.8: Example of an ARCHANGEL output surface brightness profile and its disk-only fit between a_e and $a_{26.5}$ at 3.6 microns (*left*) and growth curve (*right*) for PGC41729 or NGC4522. *Left*: parameters of the fit, disk central surface brightness (μ_0) and scale length (α) are listed on the figure. Two more parameters also listed are the effective surface brightness (μ_e) and radius ($r_e = a_e$). No correction has been applied yet to the data. The green ellipse on the inset image represents the 26.5 mag arcsec^{-2} isophote at 3.6 microns. *Right*: the incremental growth of the apparent magnitude of the galaxy with radius is shown by the progression of stars. The fit providing an extrapolation to a total magnitude is generated over the domain of the red stars. The level of the total magnitude is shown in magenta. In both panels, red, green and blue lines show the radii enclosing 20%, 50% and 80 % of the total light.

The Spitzer photometry is sufficiently deep that magnitudes in the growth curve approach the total magnitude of the galaxy. One way to extend to the total magnitude uses the procedure built into ARCHANGEL based on interpolations and extrapolations with rational functions. Such functions have a wide range in shape and have better interpolating properties than polynomial functions. They suit data where an asymptotic behavior is expected. The quadratic form/quadratic form, meaning a degree of two in both numerator and denominator is the simplest choice. The asymptotic magnitude is the ratio of the second order coefficients of the

numerator and denominator. However, rational functions are non-linear. They can produce vertical asymptotes due to roots in the denominator that are to be ignored. Fit uncertainties are given by the standard error of the estimate $SEE = \sqrt{\frac{1}{n}\sum_{i=1}^{n}(m(r_i)_{fit} - m(r_i)_{measured})^2}$. Because of the convergence problem that can occur with rational functions, we provide in total three magnitudes that approximate the global magnitude of the galaxy: $[3.6]_{26.5}$, an isophotal magnitude that directly measures the light within a reliably attained radius, $[3.6]_{tot}$, a "total" magnitude given by the asymptote of the ARCHANGEL rational function extrapolation, and $[3.6]_{ext}$, an "extrapolated" magnitude assuming a continuation of the exponential disk beyond the radius of the isophote 26.5 mag arcsec^{-2} obtained with equation 3.25. The relative merits of these magnitudes will be discussed in subsection 3.3.4. Other products are the average Surface Brightness within a_e and a_{20} and a concentration index $C_{82} = a_{80}/a_{20}$. Table 3.2 gives the parameters that are extracted for the galaxy used as an example in Figures 3.7 and 3.8 and illustrates what is seen in a single row in the catalog "*Spitzer [3.6] Band Photometry*" at EDD and in Appendix A (although restricted to twenty entries and simplified: common name, date and exposure time are absent). Capabilities within EDD allow a user to link to other catalogs, thereby accessing all manner of information about each target.

Figure 3.9 gathers as examples the three outputs obtained with ARCHANGEL for five galaxies, each one of them belonging to at least one of the five subsamples of the CFS program.

1	2	3	4	5	6	7	8	9	10
PGC	Name	Date	Exp	$a_{26.5}$	$[3.6]_{26.5}$	$[3.6]_{tot}$	σ_m	$[3.6]_{ext}$	μ_0
41729	NGC4522	2007.02.14T14:46:36.378	240	181	11.98	11.970	0.003	11.957	20.32

11	12	13	14	15	16	17	18	19	20	21	22	23	24
α	b/a	$\sigma_{b/a}$	PA	a_{80}	μ_{80}	a_e	μ_e	$<\mu_e>$	a_{20}	μ_{20}	$<\mu_{20}>$	C_{82}	RefLink
31.8	0.26	0.01	34	77	23.04	36	21.24	20.31	15	19.99	19.53	5.2	SSOV

TABLE 3.2: Extracted photometry parameters. (1) Principal Galaxies Catalog number, (2) common name, (3) date of Spitzer observation, (4) nominal total integration, seconds (actual time collecting photons somewhat less), (5) $a_{26.5}$: major axis radius at isophote 26.5 mag arcsec^{-2}, (6) $[3.6]_{26.5}$: AB magnitude within $a_{26.5}$, (7) $[3.6]_{tot}$: total AB magnitude from rational function asymptote, (8) σ_m: root mean square deviations, rational function fit, (9) $[3.6]_{ext}$: total AB magnitude by extrapolating flux beyond $a_{26.5}$ assuming continuance of exponential disk, (10) μ_0: central disk surface brightness from inward extrapolation of disk fit, mag arcsec^{-2}, (11) α: exponential disk scale length, arcsec, (12) b/a: ratio of minor to major axes, (13) $\sigma_{b/a}$: uncertainty in axial ratio, (14) PA: position angle of major axis, deg. (15) a_{80}: major axis radius of annulus enclosing 80% of total light, arcsec, (16) μ_{80}: surface brightness at a_{80}, mag arcsec^{-2}, (17) a_e: 'effective radius', major axis radius of annulus enclosing 50% of total light, arcsec, (18) μ_e: surface brightness at a_e, mag arcsec^{-2}, (19) $<\mu_e>$: average surface brightness within a_e, mag arcsec^{-2}, (20) a_{20}: major axis radius of annulus enclosing 20% of total light, arcsec, (21) μ_{20}: surface brightness at a_{20}, mag arcsec^{-2}, (22) $<\mu_{20}>$: average surface brightness within a_{20}, mag arcsec^{-2}, (23) C_{82}: concentration index, a_{80}/a_{20}, (24) Spitzer program link.

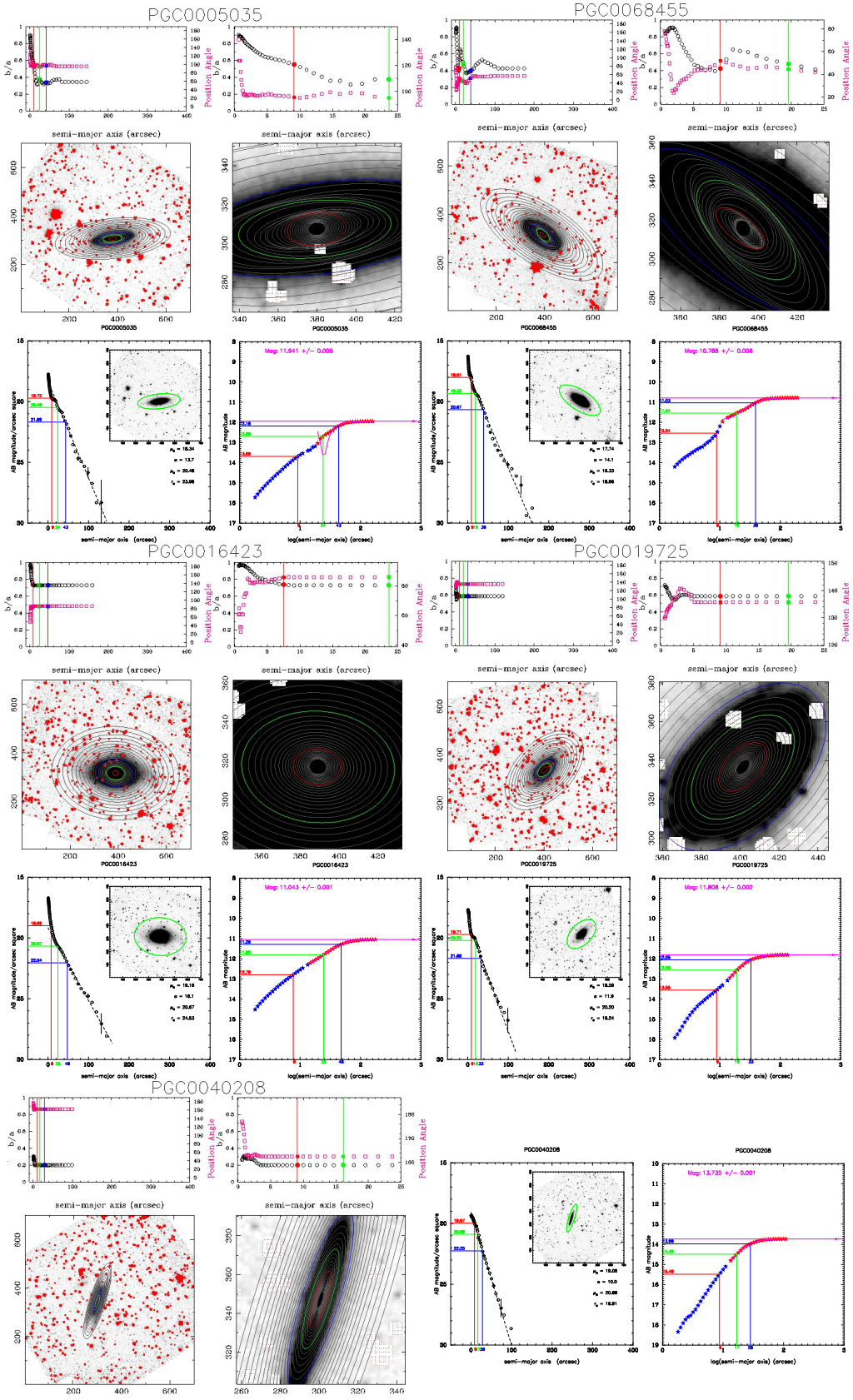

FIGURE 3.9: Surface photometry outputs from the ARCHANGEL software. PGC0005035 is from the Calib subsample. PGC0016423 has hosted at least one supernovae of Type Ia. PGC0068455 and PGC0019725 are in the V3k and PSCz catalogs respectively. PGC0040208 is a flat galaxy. For each galaxy, the variations of the position angle and of the b/a ratio are given as a function of the radius in arcsec. The masks is shown in red on top of the galaxy images and the fitted ellipses are in black. Surface brightness profiles, growth curves and their fits are represented. In every plot, except for the insert in the growth curve plot, red, green and blue colors show the annuli encompassing 20, 50 and 80% of the light. On the insert, the green ellipse is the isophote at 26.5 mag arcsec $^{-2}$ in the [3.6] band.

3.3.2.3 Some Analyses

In this subsection, we focus mostly on the Cosmicflows with Spitzer sample although the additional Spitzer archival galaxies minus S^{4}G's are processed equally. We present the different parameters derived with the software ARCHANGEL for each one of the CFS galaxies. We claim at the beginning of subsection 3.3.1.2 that we choose to observe each galaxy to within at least twice d_{25} to capture most of galaxy lights and to minimize magnitude measurement uncertainties. Then, we force ellipse fitting up to 1.5 $\times$ $a_{26.5}$. Figure 3.10 confirms that d_{25} from the third reference catalog (RC3) in EDD, used to set observations, and $a_{26.5}$ obtained after reduction are comparable representatives of size. The scatter is only 41 arcseconds around a 1:1 linear relation. The observational sensitivity is sufficient for our ultimate goal since at 26.5 mag arcsec^{-2} the isophotal magnitude is already very close to extrapolated ones on Figure 3.11. We will show this in more details in subsection 3.3.4.

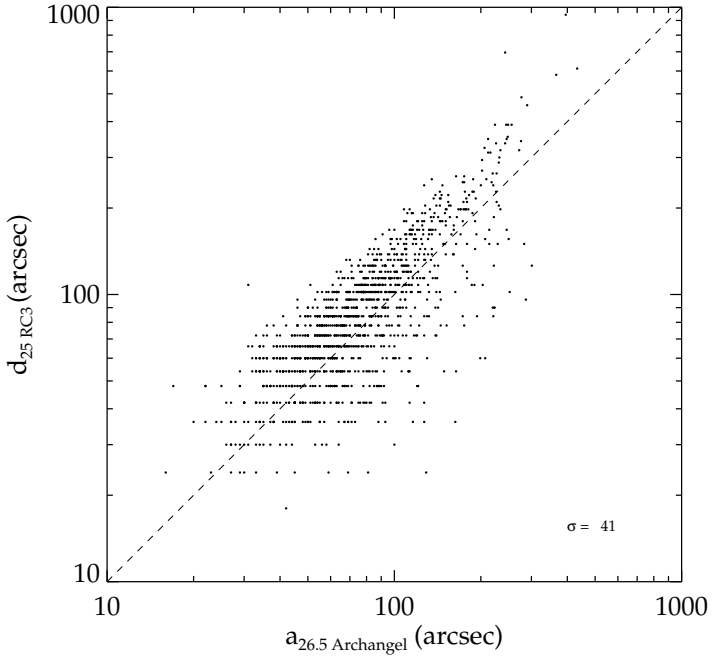

FIGURE 3.10: Comparison between the radius in arcsecond of the isophote at 26.5 mag arcsec^{-2} in the [3.6] band, obtained after reduction with ARCHANGEL, and the radius at 25 mag arcsec^{-2} at B band used beforehand to set observational parameters. These parameters are proportional to each other. In the case of an optimal 1:1 linear relation, the scatter is only 41 arcseconds.

Histograms of the other parameters are given in Figure 3.12 in mag arcsec^{-2} for surface brightnesses and in arcseconds for corresponding radii. For all these parameters there is no outliers.

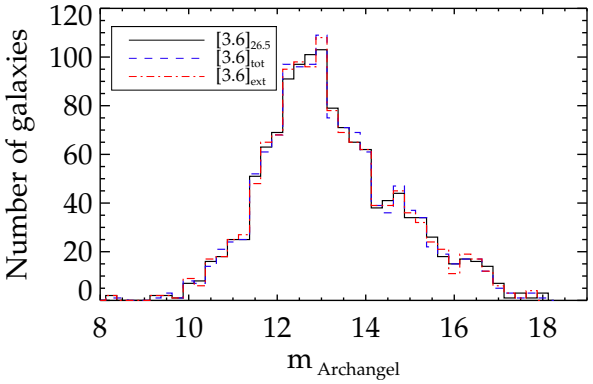

FIGURE 3.11: Histograms of the three magnitudes derived with ARCHANGEL. The magnitude at the 26.5 mag arcsec^{-2} isophote at 3.6 μm, $[3.6]_{26.5}$ (black straight line), the magnitude obtained by the extrapolation of the growth curve, $[3.6]_{tot}$ (blue dashed line) and the magnitude assuming a continuous exponential disk, $[3.6]_{ext}$ (red dotted-dashed line).

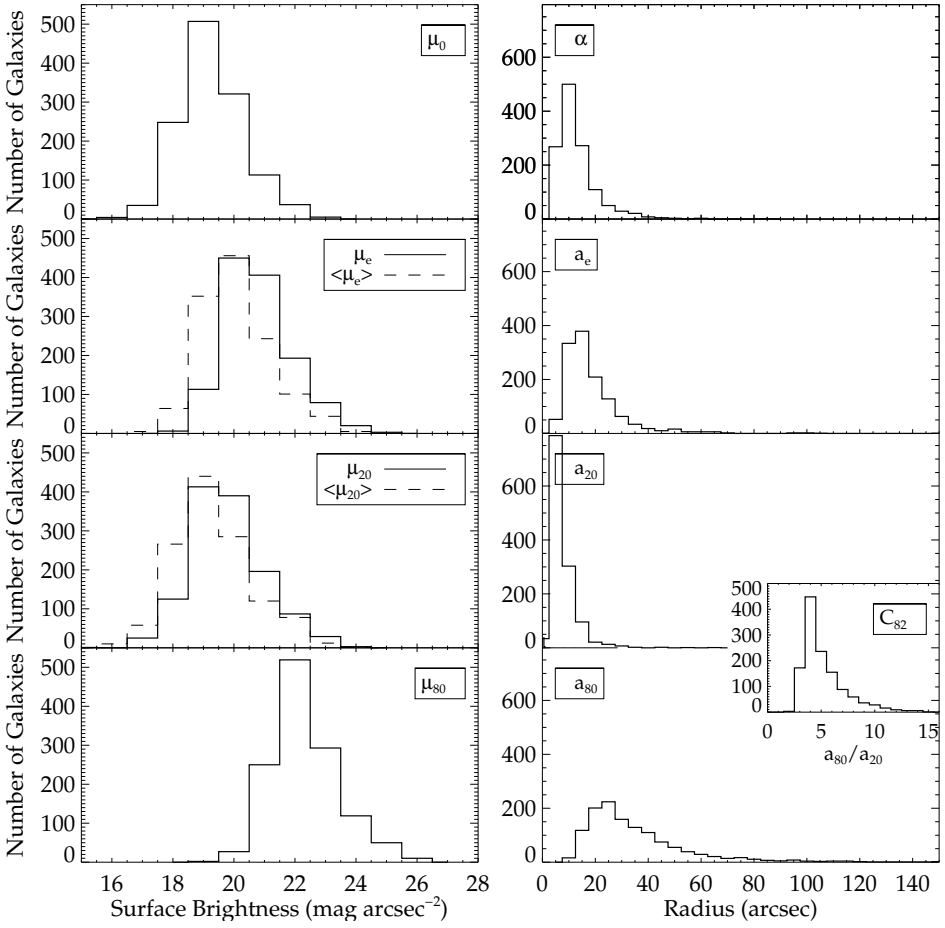

FIGURE 3.12: Histograms of some of the parameters computed with the ARCHANGEL software. *Left, from top to bottom*, histograms in solid lines of the central disk surface brightness μ_0 and of the surface brightnesses at 50, 20 and 80% of the total light μ_e, μ_{20} and μ_{80} (mag arcsec^{-2}). Histograms of the average of the surface brightnesses between 0 and 50 and 20% of the light, $< \mu_e >$ and $< \mu_{20} >$ respectively, are overplotted in dashed lines. *Right, from top to bottom*, disk scale length α and annuli encompassing 50, 20 and 80% of the light a_e, a_{20} and a_{80}, in arcseconds. The histogram of the concentration index, $C_{82} = a_{80} / a_{20}$ is overplotted in a small panel on the right side of the a_{20} and a_{80} histograms.

One specificity of the adapted version of ARCHANGEL is the computation of the minor to major axis, b/a, ratio which is defined as the mean of the b/a ratios between 50% and 80% of the light. Measuring b/a ratios is not an easy task and a comparison with the ratios from the HyperLeda Database in B-band on Figure 3.13 left shows that at least one b/a source cannot be trusted. Each value needs to be checked before any usage. The initiated Citizen Science Project to order galaxies by inclinations to which we contribute will be most useful. Position angles on the other hand are in good agreements on the right of the same Figure.

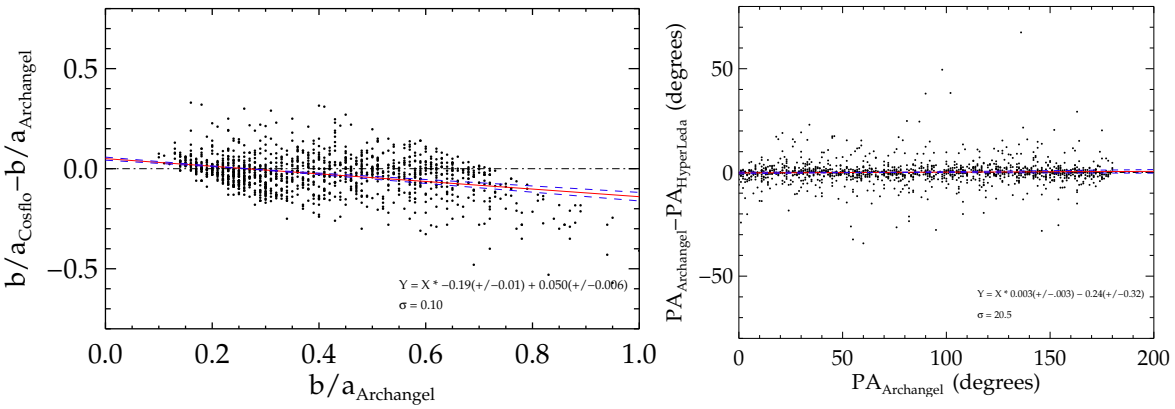

FIGURE 3.13: *Left*: Residual between Cosmicflows program b/a ratios and the b/a ratios obtained with ARCHANGEL versus ARCHANGEL's b/a ratios. *Right*: Differences between ARCHANGEL-derived position angles and HyperLeda's versus ARCHANGEL's. The black dotted-dashed lines show the perfect case y=0, the red straight lines are linear fits to the data (with a 3 σ clipping (20 galaxies) in the right panel), the blue dashed lines are the 1 σ uncertainties.

3.3.3 Corrected Magnitudes and Surface Brightnesses

Several effects affect light as it travels towards us. Apparent magnitude measurements [3.6] need to be corrected for these effects. Corrected apparent magnitudes $[3.6]^{b,k,i,a}$ for Spitzer IRAC channel 1 data are given by:

$$[3.6]^{b,i,k,a} = [3.6] - A_b^{[3.6]} - A_i^{[3.6]} - A_k^{[3.6]} + A_a^{[3.6]} \tag{3.29}$$

with $A_b^{[3.6]}$ galactic extinction correction, $A_i^{[3.6]}$ internal extinction correction, $A_k^{[3.6]}$ k-correction, and $A_a^{[3.6]}$ aperture correction. All these terms are described in details hereafter in different subsections. Briefly, extinction is due to the reduction in a source apparent brightness by absorption, scattering or radiation as light travels towards us. Only in extreme cases, light is totally extinguished. Attenuation would be a more appropriate term. There are several potential sources of extinction such as Earth atmosphere, Milky-Way and target galaxy dust. Spitzer is in space which prevents any atmospheric extinction. The k-correction is a term to correct for the reddening of light due to the universe expansion and the aperture correction is a particularity of the instrument.

Disk central surface brightnesses will be the object of study in subsection 3.3.6 and its measurements also need to be corrected. Inclination effects are quite confusing at optical band because the path length of observed surface brightnesses, varying with the line-of-sight, and extinction, work in opposite way on measured μ_0 values. At 3.6 microns we can assume the obscuration to be negligible and therefore only the geometric effect of the inclination on surface brightnesses needs to be taken into account. We measure the face-on $\mu_0^{[3.6],a,i}$ as follows:

$$\mu_0^{[3.6],a,i} = \mu_0^{[3.6],a} - 2.5C^{[3.6]}\log(\frac{b}{a}) \tag{3.30}$$

with $C^{[3.6]}$=1 accordingly (intrinsic extinction negligible), $\frac{b}{a}$ the axial ratio and $\mu_0^{[3.6],a}$ the disk central surface brightness corrected for aperture as described in the following subsections.

3.3.3.1 Galactic Extinction Correction

The InterStellar Medium consists of small dust particles with diameters between 0.01 and 1 μm. They scatter, absorb and re-emit light. Blue light is more strongly scattered and absorbed than red light. Sources appear dimmer and redder. Schlegel et al. (1998) mapped this effect. The resulting galactic extinction and reddening map is an exquisite tool to compute extinction correction. To obtain this map, they combine the far-infrared emission (100 μm) of InfraRed Astronomical Satellite, the Diffuse InfraRed Background Experiment on COsmic Background Explorer satellite and the colors of background galaxies from Automated Plate Measurement Galaxy Survey. The colors allow dust normalization to E(B-V) reddening in magnitudes. Diffuse InfraRed Background Experiment provides absolute calibration across several passbands. It maps the dust color temperature and converts the 100 μm emission to dust column density. The relationship between ultraviolet/optical extinction and far-infrared emission depends on the grain size distribution. Then, assuming that the dust grain size distribution is everywhere the same and using the mean value in the diffuse InterStellar Medium given by Cardelli et al. (1989), galactic extinction depends only on object coordinates and observational wavelengths λ. The InfraRed Science Archive provides an online tool at http://irsa.ipac.caltech.edu/applications/DUST/ with these 100 μm cirrus maps that supply us with the differential reddenings $E(B-V)$. We use the correction term given by Cardelli et al. (1989) accounting for a small shift to the centroid of the Spitzer passband:

$$A_b^{[3.6]} = R_{[3.6]}E(B-V) \tag{3.31}$$

with $R_{[3.6]} = 0.20$. Galactic extinction magnitude corrections at [3.6] are only 9% compared to those at I_C and 4% of the corrections at B. Corrections at latitudes above 15° are almost always 0.05 magnitude or less, with uncertainties around 0.01 magnitude.

3.3.3.2 Internal Extinction Correction

Internal extinction is usually the greatest concern. Galaxies of the same intrinsic size and luminosity appear dimmer when seen edge-on because path lengths through their own absorbing dust increase. Fortunately, in the infrared such extinction is very small. Giovanelli et al. (1997b, 1995) showed that there is a luminosity dependence to galaxy internal obscurations (high-luminosity cases are more reddened). Tully et al. (1998) confirmed and provided an alternative description of the effect. There is a subtle problem because absolute magnitudes (luminosities) are not known a priori. They are a product of the analysis. Tully et al. (1998) framed magnitude corrections in term of a distance-independent surrogate, the linewidth parameter, W^i_{mx}. Accordingly, the internal extinction correction can be written:

$$A_i^{[3.6]} = \gamma_{[3.6]} \log(a/b) \tag{3.32}$$

where $\gamma_{[3.6]}$ is:

$$\gamma_{[3.6]} = 0.10 + 0.19(\log\, W^i_{mx} - 2.5) \tag{3.33}$$

if $W^i_{mx} > 94$ km s^{-1} and $\gamma_{[3.6]} = 0$ otherwise. W^i_{mx} is defined by equations 3.19.

There is an advantage to this formulation of the internal extinction. If the inclination is underestimated, $\log(a/b)$ is underestimated driving $A_i^{[3.6]}$ low but then W^i_{mx} is overestimated which drives $\gamma_{[3.6]}$, hence $A_i^{[3.6]}$ up. The two terms in $A_i^{[3.6]}$ are affected in opposite directions. Regardless, internal absorption corrections are always small, rarely reaching 0.1 magnitude at 3.6 μm. Uncertainties in these corrections are less than 0.02 magnitude.

3.3.3.3 K-Correction

A wavelength emitted at a redshift z increases by a factor $(1+z)$ by the time it reaches us. As galaxy emissions depend on the wavelength (confer non-flat spectral energy distributions), the received amount of light in a given finite band might be incorrect. It is over/underestimated unless some k-correction is applied (e.g. Oke and Sandage, 1968). k-correction depends on spectral energy distribution, redshift and observing passband. The derivation of k-corrections are generally based on the template fitting of observed spectral energy distributions. They require redshift and color photometry (at least one) or morphological type to build a template (e.g. Blanton and Roweis, 2007; Chilingarian et al., 2010; Cowie et al., 1994; Han, 1992a). Our interest lies with spiral galaxies, a k-correction based on morphological type is ideal. Huang et al. (2007) happened to develop eleven model Spectral Energy Distributions ranging from a pure early template, i.e. an old "early-type" stellar population as might be found in an elliptical galaxy or spiral bulge, to a pure late template, i.e. a mix of stars and interstellar emission as might be found in "late-type" spiral galaxy disk. Convolving each one of the

spectral energy distributions with IRAC filter functions, they show a linear dependence of the k-correction with redshift at 3.6 μm. In addition, this linear dependence is independent of the galaxy type at small redshifts, at this position on the Rayleigh-Jeans tail of the spectral energy distribution of star light. We use the low-z formulation by Huang et al. (2007):

$$A_k^{[3.6]} = -2.27\ z \tag{3.34}$$

with z the galaxy redshift. Uncertainties are at the level of 0.01 magnitude or less.

3.3.3.4 Aperture Correction

The fourth and last adjustment is the aperture correction. Aperture corrections are required for extended source photometry with Spitzer (e.g. galaxies) because their absolute calibrations are tied to point sources with IRAC observations. There is extended emission from the Point Spread Function outer wings, and the scattering of the diffuse emission across the focal plane that is captured by the extended source photometry but not by the calibrations on point sources. Since the photometry is normalized to 12" apertures, a correction must be applied for large apertures (Reach et al., 2005, and IRAC Instrument Handbook)[4]. For an effective aperture radius r in arcseconds, the channel 1 IRAC extended source aperture correction recommended is:

$$F_{IRAC\,true} = F_{IRAC\,measured} \times (ae^{-r^b} + c) \tag{3.35}$$

where $a = 0.82$, $b = 0.37$ and $c = 0.91$. Then the extended source aperture correction in magnitudes is:

$$A_a^{[3.6]} = -2.5\log(ae^{-r^b} + c). \tag{3.36}$$

The average correction for galaxies of interest to our program is 0.10. The variations on this correction from source to source for our galaxies, which are typically larger than 1′, is 0.01 magnitudes and 10% relative uncertainties in the adjustment are negligible.

Regarding surface brightnesses, fluxes need to be corrected directly with equation 3.35 before using relations 3.26, 3.28 and 3.30. The correction is very small for IRAC channel 1. For example, the disk central surface brightness of PGC7544 shown in Figure 3.14 becomes 18.10 after correction against 18.06 before. This is largely within the retained uncertainty (0.5 mag arcsec^{-2}) on disk central surface brightness measurements for the project developed in subsection 3.3.6.

[4]http://irsa.ipac.caltech.edu/data/SPITZER/docs/irac/ iracinstrumenthandbook/

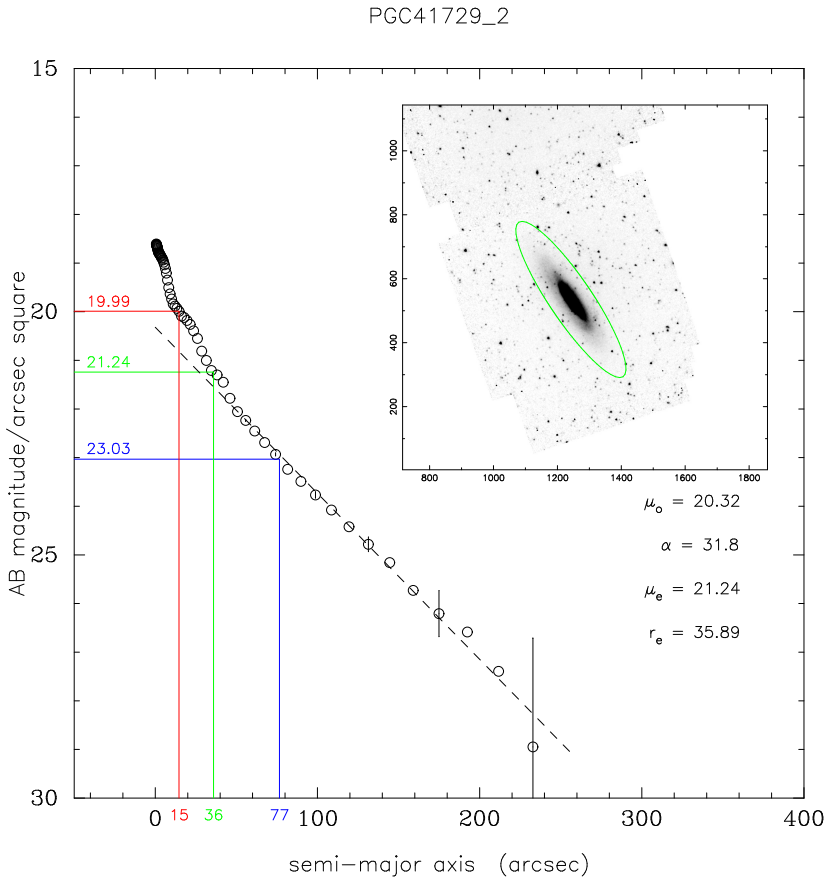

FIGURE 3.14: Example of an ARCHANGEL output surface brightness profile and its disk-only fit between a_e and $a_{26.5}$ at 3.6 microns for PGC7554. Parameters of the fit, disk central surface brightness (μ_0) and scale length (α) are listed on the figure. Two more parameters also listed are the effective surface brightness (μ_e) and radius ($r_e = a_e$). No correction has been applied yet to the data. Radii enclosing 20%, 50% and 80 % of the total light are given by red, green and blue lines. The green ellipse on the inset image represents the 26.5 mag arcsec^{-2} isophote at 3.6 microns.

3.3.4 Uncertainties

An extremely important virtue of the Spitzer [3.6] band photometry is the robustness of the luminosity measurements (a) with uniformity across the sky, (b) with inclusiveness of target light because of the sensitivity, and (c) because adjustments are small. There was a discussion of uncertainties associated with the different corrections in the previous subsections and it can be summarized that as long as sources are not in extremely obscured regions of our Galaxy ($A_b^{[3.6]} < 1$) then the global *uncertainty* in adjustments is at the level of 0.03 magnitude or less, with internal absorption within sources dominant in the error budget. The IRAC handbook gives a $2-3\%$ error on the absolute flux calibration (excluding the aperture correction), but more importantly for this program, it claims photometry is repeatable across the sky at the 1% level.

Among our parameters we determine isophotal, "total", and "extrapolated" magnitudes. The latter two both approximate the global magnitude, the "total" from the rational function asymptote of the growth curve and the "extrapolated" from the extension of the exponential disk fit beyond the radius of the isophotal magnitude. By construction, $[3.6]_{26.5}$ is fainter than $[3.6]_{ext}$ and should be fainter than $[3.6]_{tot}$. The average difference $\langle [3.6]_{26.5} - [3.6]_{ext} \rangle = 0.016$ magnitude corresponds to a typical disk fit of 6.2 exponential scalelengths at the 26.5 mag arcsec^{-2} isophote. The typical *uncertainty* in this extrapolation is below 0.01 magnitude except if the target is extremely low surface brightness. Surface Brightness profiles of spirals can depart from a pure exponential at large radii, either with flares or truncations and because of the interplay between bulges and disks (Kent, 1985). Yet because such a large fraction of the flux is captured by the deep Spitzer integrations the differences between measured isophotal and extrapolated magnitudes are so small as to leave little room for uncertainty in the extrapolation.

By comparison, $\langle [3.6]_{26.5} - [3.6]_{tot} \rangle = 0.007$ magnitude, that is, $[3.6]_{tot}$ is fainter than $[3.6]_{ext}$ by 0.009 magnitude on average. The root mean square scatter is 0.018 magnitude between these alternative measures. The differences are primarily due to a slight instability in the rational function fits. We give preference to the *exponential disk extrapolations*.

We turn to what is probably the largest source of error, the determination of the "sky" level. With observations in space at [3.6] band this noise level is dominated by diffuse zodiacal light and discrete high redshift galaxies. The discrete contaminants can be easily seen to very faint levels in regions beyond the galaxy. They are less easy to see and exclude if they are superimposed on the target galaxy. A major task before running a surface photometry analysis is the removal of contaminants like foreground stars and background galaxies. Our approach is to not be too aggressive with the removal of contaminants. We remove contaminants as best we can on the target and remove contaminants in the adjacent sky to the same level, leaving in place fainter sources since such sources must also be hidden within the galaxy.

It was described in the section on ARCHANGEL photometry that sky settings were established from the median of pixel fluxes in boxes placed around the galaxy and validated by the nature of the magnitude growth curve (it should go asymptotically flat) and the surface brightness profiles (flares or cutoffs as noise dominance are approached as suspicious but not considered a conclusive sign of bad sky setting). In order to generate a quantitative test of the effects of sky variance we have run Spitzer-adapted ARCHANGEL on 235 galaxies, part of the Tully-Fisher calibrator sample defined in Tully and Courtois (2012). This sample contains only a few low surface brightness and irregular galaxies.

A first run gives us the sky value S and its uncertainty σ_{sky}. We run ARCHANGEL two more times with sky values of $S \pm \sigma_{sky}$ respectively for each one of our selected galaxies. This

gives us three extrapolated magnitudes that we call $[3.6]_0$, $[3.6]_+$, and $[3.6]_-$. Figures 3.15 and 3.16 show the variation of $(|[3.6]_0 - [3.6]_-| + |[3.6]_0 - [3.6]_+|)/2$ as functions of type and apparent magnitude. These plots show the sensitivity to the choice of sky value and that this sensitivity becomes particularly acute for low surface brightness systems. The galaxies of type Sd, identified in the plots as low surface brightness galaxies, and the Magellanic irregular galaxies are clear outliers. There are also three galaxies with very bright objects nearby that could influence the sky level with stray light and might explain their position in Figure 3.16. These three are retained in the calculations of the offset and scatter since they are typical spiral galaxies but the low surface brightness and irregular galaxies are excluded. Magnitude uncertainties due to the sky error are of the order 0.04 ± 0.02. Uncertainties with low surface brightness and irregular galaxy magnitudes tend to be more important which is understandable. Low surface brigthness galaxies have by definition surface brightness values closer to that of the sky and irregular galaxies not only tend to be low surface brightnesses but in addition might not be well described by elliptical isophotes. Changing the sky value a little might change the measured flux considerably toward the external part of such galaxies. Low surface brightness and irregular galaxies apart, Figure 3.16 indicates that uncertainties do not strongly increase at fainter magnitudes.

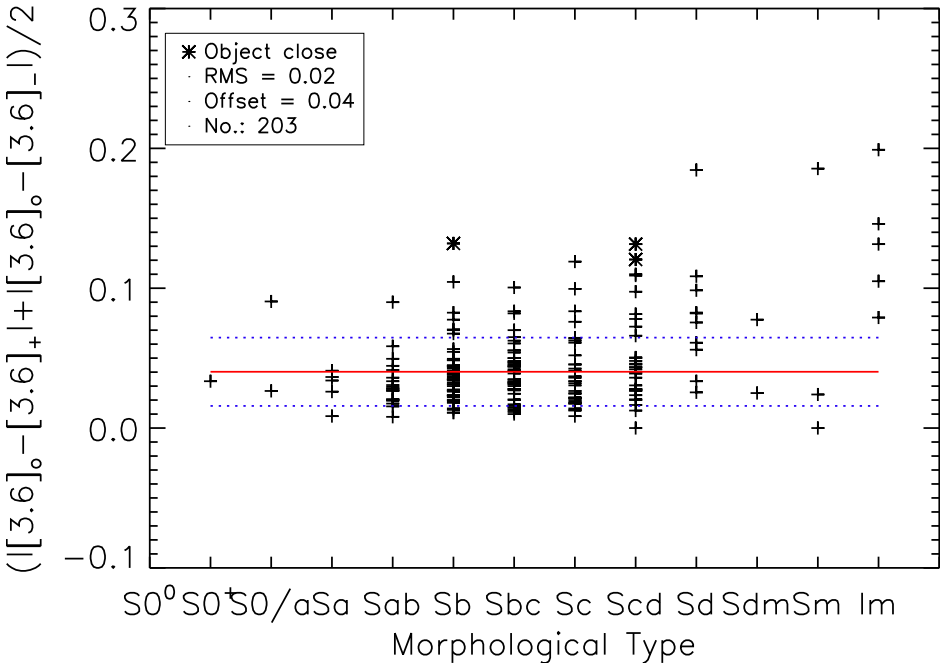

FIGURE 3.15: Variation of magnitude uncertainty as a function of morphological type. The mean offset of 0.04 magnitude and root mean square scatter of 0.02 magnitude indicated by the solid red and dotted blue lines respectively excludes types Sd and later. Three cases with contamination from nearby bright objects are indicated by asterisks. The scatter is asymmetric about the mean since an absolute value difference from the fiducial value cannot be less than zero.

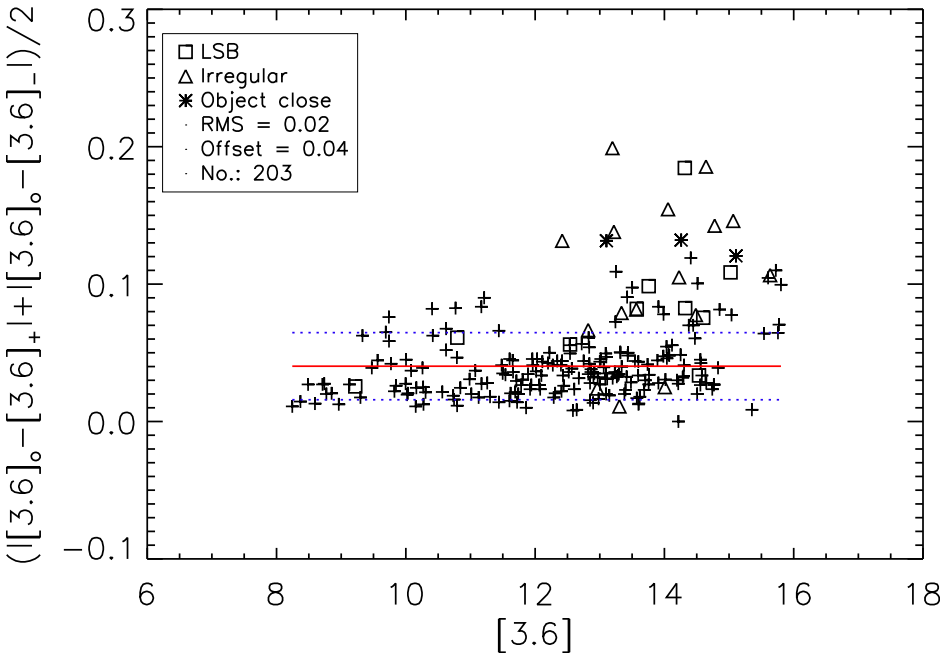

FIGURE 3.16: Variation of magnitude uncertainty as a function of magnitude. Type Sd systems, here referred to as low surface brightness galaxies, are represented by squares and types Sdm-Sm-Im irregular galaxies are represented by triangles. Asterisks locate galaxies with a very bright object close to them. The mean offset and scatter lines have the same meaning as in the previous figure.

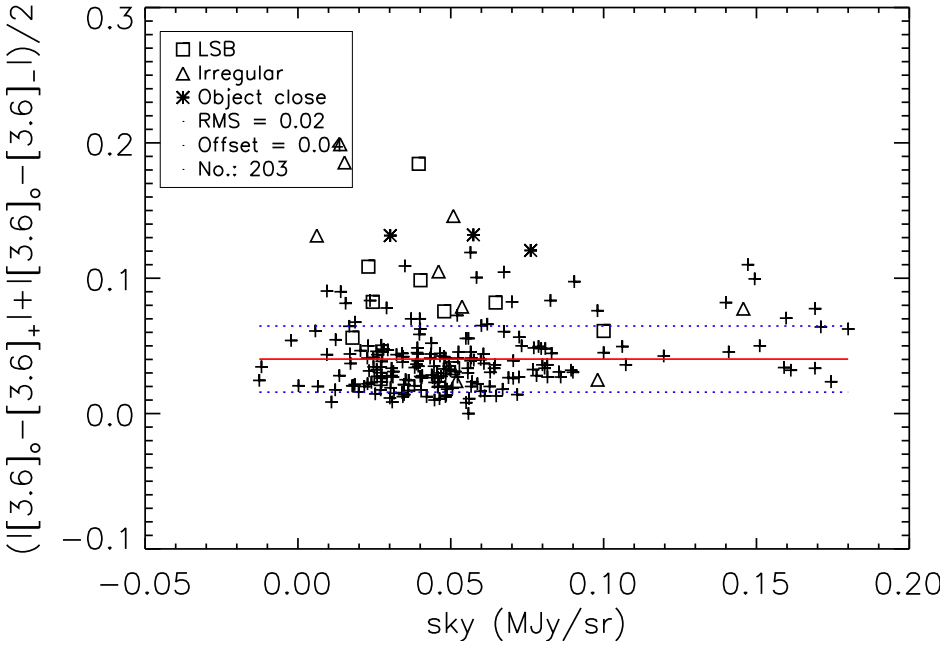

FIGURE 3.17: Variation of magnitude uncertainty as a function of the sky value in MJy sr^{-1}. Squares represent low surface brightness galaxies while triangles stand for irregular ones. Galaxies represented by asterisks are galaxies with a very bright object close to them. Sky values can be four times higher than on average without resulting in abnormally high uncertainty in magnitudes.

Next we test for uncertainties in magnitude due to the sky against the sky value itself, as well as against the isophotal semi-major axis in the [3.6] band $a_{26.5}$, inclination from face-on, and apparent area defined as the area of the ellipse at $a_{26.5}$ to see if any trends exist. The results in Figures 3.17 and 3.18 show no correlation. In Figure 3.17, we can see that the uncertainty in magnitude does not depend on the sky value. We checked for a dependence on sky uncertainty and find no correlation. These results suggest that the total and extrapolated disk apparent magnitudes are adequate (we do not show the plots for both magnitudes here as they are very similar). In any case, the highest sky values are relatively moderate (< 0.20 MJy sr^{-1}). One can also notice that sky values and sky uncertainties are not correlated, evidently a reflection of the relative uniformity of background across dimensions of $5 - 10$ arcminutes. Structure in the background could be a worse problem when the sky setting is very low. Perhaps it is a surprise that the uncertainty is not proportional on the galaxy apparent area (Figure 3.18, bottom). The more pixels that are affected by changing the sky value, the more the magnitude might change. In any case, these tests indicate that magnitude uncertainties can be taken to be approximately constant for all normal spiral galaxies.

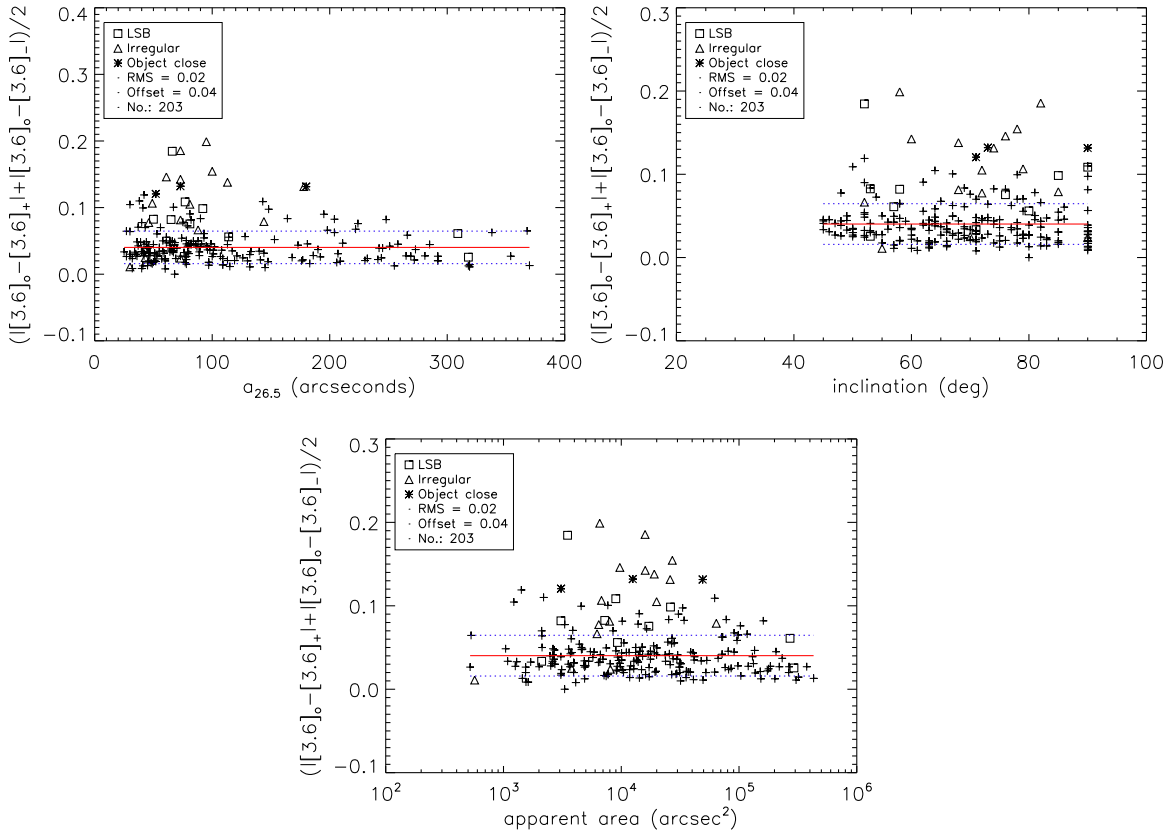

FIGURE 3.18: Variation of magnitude uncertainty as a function of three galaxy characteristics: (*top left*) semi-major axis, *(top right)* inclination, and *(bottom)* apparent area. Squares, triangles and asterisks represent low surface brightness, irregular, and possibly contaminated galaxies respectively. There is no apparent correlation between the magnitude uncertainty and the radius, inclination, or apparent area of a galaxy.

Regarding surface brightness uncertainties, we have seen that concerns, which might have arise about the disk-only fitting technique, are not very relevant. Since de Jong (1996a) showed that disk-only fits gave unbiased disk parameters relative to a 2D fit decomposition parameters within 0.5 mag arcsec^{-2} and because the background (distant galaxies and zodiacal light) uncertainties lead to a small magnitude uncertainty even for IRAC channel 1, we retain an uncertainty budget of 0.5 mag arcsec^{-2} for $\mu_0^{[3.6]}$ measurements.

3.3.5 Comparisons with Other Pipelines

Our ARCHANGEL analysis procedures can be compared with other reductions of Spitzer observations. Comparisons with magnitudes found by the projects SINGS (Muñoz-Mateos et al., 2009), CHP (Freedman et al., 2011, private communication) and S^{4}G (Muñoz-Mateos, in prep.) show that the Cosmicflows project is on the same magnitude scale as all these projects. In the case of CHP we give special attention to a comparison because CHP and CFS, have the common ambition of measuring galaxy distances. We do the same with S^{4}G as we take directly magnitudes derived from their pipeline. As we go forward, we want to understand to what degree the alternative photometry analyses are interchangeable. A comparison is given between the sources in Figure 3.19. There is a slight tendency for CHP values to be brighter for the largest galaxies, with essentially no difference faintward of $[3.6] = 12$. The most likely explanation for a difference with the bright and large galaxies is small differences in the way sky values are set. The root mean square scatter in the differences (6 deviant points rejected) is ± 0.052 which, if attributed equally, implies an uncertainty in an individual measurement of ± 0.037 magnitude for each source. S^{4}G values tend to be dimmer for the smallest galaxies. Again probably because of the way sky values are set which is in this case quite different from us. Instead of using sky boxes, they compute sky values out of annuli located just at the extremity of what they estimate to contain the totality of the galaxy light. This different sky setting might also explain the slight increase in the root mean square scatter (4 galaxies rejected) which reaches ± 0.1 giving an uncertainty about ± 0.07 magnitude for each source. Regardless, it is reassuring that our magnitudes are in agreements with these two alternative computations.

Comparisons with other projects give comparable results. Typical zeropoint differences are ± 0.015 and root mean square uncertainties are $\pm 0.05 - 0.07$ magnitude. A summary of comparisons are given in Table 3.3. These results provide an estimate of the internal errors of alternate fitting procedures with the same data. We recall that our two measures of magnitude agree at the level of 0.01 with scatter ± 0.02. In summary of errors, the dominant contributions are sky settings (0.04 magnitude), flux calibration (0.02 magnitude), and extinction (0.02 magnitude), leading to total uncertainties in magnitudes of ~ 0.05 mag. The great interest with the CFS program is to use TFR to measure distances to galaxies and

the typical scatter in TFR is 0.4 magnitude, 20% in distance. With errors on photometry after corrections held to 0.05 magnitude the contribution to the distance error budget from photometry is minor.

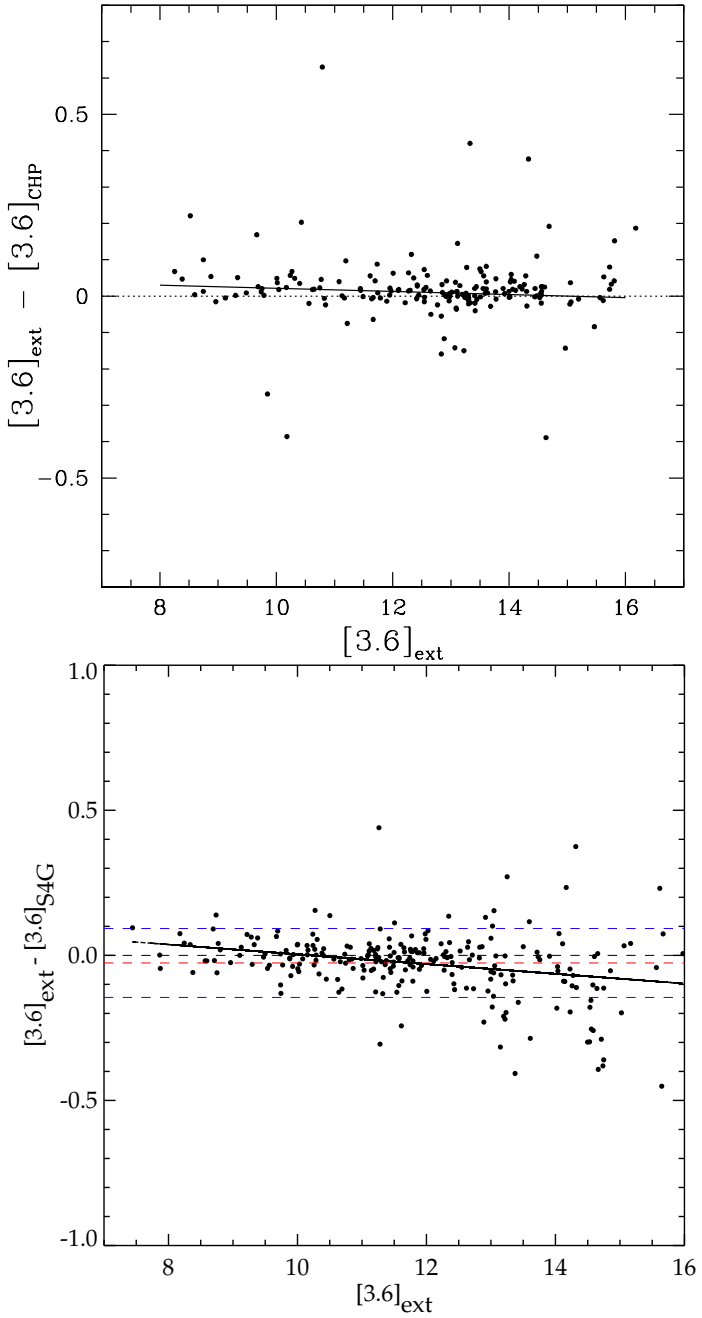

FIGURE 3.19: Comparisons between exponential disk extrapolated magnitudes $[3.6]_{ext}$ of ARCHANGEL and asymptotic total magnitudes from CHP (*top*) and S^{4}G (*bottom*) programs. *Top*: the slight tilt of the thick line best fit, and the offset of $\langle [3.6]_{ext} - [3.6]_{CHP} \rangle = 0.01$ from the dotted line null value, have only $2 - 2.5\ \sigma$ significance. Both the tilt and the offset have been computed rejecting 6 deviant points. *Bottom*: the fit at 3 σ clipping (4 galaxies rejected) has a slope of -0.02 ± 0.004 and a zeropoint of 0.17 ±0.04. The red dashed thick line stands for the offset at -0.02 magnitude and the blue dashed lines represent the scatter at 0.1 magnitude. Deviant cases except for 2 are low surface brightness galaxies and we find no reason to reject ARCHANGEL values.

Program	N	Range	$m_{other} - m_{Archangel}$	scatter
S4G	241	7-16	-0.02	0.10
CHP	171	8-16	-0.01	0.05
SINGS	12	8-10	0.02	0.07
Various*	5	9-11	0.01	0.03

TABLE 3.3: Comparisons between ARCHANGEL magnitudes and other magnitudes: (1) program name (* measurements from a small number of programs focused on large galaxies, Jarrett, private communication) (2) number of galaxies compared, (3) range of magnitudes over which the comparison is made, mag, (4) difference ARCHANGEL magnitude − other magnitude, mag, and (5) scatter, mag.

Finally, from the comparisons we consider that CHP, S^{4}G and ARCHANGEL magnitudes can be used indifferently. For a better precision they are averaged when more than one of them is available in section 3.4.

3.3.6 Bimodality in Disk Central Surface Brightness: a Study Example Based on Photometry Parameters

In this subsection, we report on measurements of the disk central surface brightnesses (μ_0) at 3.6 microns for 438 galaxies selected by distance and absolute magnitude cutoffs from the more than 2350 galaxies in the Spitzer Survey of Stellar Structure in Galaxies *(S^{4}G), one of the largest and deepest homogeneous mid-infrared datasets of nearby galaxies. Our sample contains nearly three times more galaxies than the most recent study of the μ_0 distribution. We demonstrate that there is a bimodality in the distribution of μ_0. Between the low and high surface brightness galaxy regimes there is a lack of intermediate surface brightness galaxies. Caveats invoked in the literature from small number statistics to the knowledge of the environmental influences, and possible biases from low signal to noise data or corrections for galaxy inclination are investigated. Analyses show that the bimodal distribution of μ_0 cannot be due to any of these biases or statistical fluctuations. It is highly probable that galaxies settle in two stable modes: a dark matter dominated mode where the dark matter dominates at all radii - this gives birth to low surface brightness galaxies - and a baryonic matter dominated mode where the baryons dominate the dark matter in the central parts - this gives rise to the high surface brightness disks. The lack of intermediate surface brightness objects suggests that galaxy evolution does not favor a mode where dark matter and baryons are equally present in the central parts of galaxies.*

3.3.6.1 Introduction

Observational surveys of the distribution of galaxy parameters in diverse environments provide essential constraints for theoretical models of galaxy formation and evolution (e.g. Thompson, 2003). The sample selection in these surveys needs to be as bias-free as possible to conduct an appropriate analysis. Recently a number of large surveys (e.g. Dale et al., 2009; Sheth et al., 2010; Stoughton et al., 2002) have been conducted with various telescopes that have led to multiple findings of bimodal distributions of galaxies in terms of color (Baldry et al., 2004; Brammer et al., 2009; Martínez et al., 2006; Whitaker et al., 2011), star formation (Wetzel et al., 2012) and disk central surface brightnesses (μ_0, e.g. McDonald et al., 2009a,b). Bailin and Harris (2008) have even suggested a trimodal distribution for galaxy concentrations.

Surface brightness profiles were first studied in 1948 by De Vaucouleurs and later on by Sersic (1959) and Freeman (1970). However, the first convincing evidence of a μ_0 bimodal distribution was published only a long time after by Tully and Verheijen (1997). This study revealed that the μ_0 distribution in Ursa Major was discontinuous with a lack of galaxies of intermediate surface brightness, or alternatively that there was an excess of low and high surface brightness (L/HSB) galaxies. The authors suggested two stable modes for galaxy formation: a dominant dark matter component at all radii giving birth to LSB galaxies and a dominant baryonic matter in the center giving rise to HSB galaxies. They suggested that the low number of Intermediate Surface Brightness (ISB) galaxies could be the result of galaxies avoiding the situation where baryonic and dark matters are co-dominant in the center. The very few ISB galaxies could also indicate that there is a small probability for LSB galaxies to turn into HSB galaxies at some point. However, the authors expressed concerns because of possible large errors in fitting galaxy disks due to shallow K'-band observations which could lead to premature truncation of disks. As a result bulges could be partially included in fits leading to a bias in μ_0. Later Bell and de Blok (2000) argued that the bimodality could also be an artifact due to incorrect inclination-corrections applied to the μ_0 values. They noted that the bimodality could also result from small number statistics. McDonald et al. (2009b) studied a larger number of galaxies in the Virgo cluster to overcome the problem of small number statistics and found a bimodal distribution too. However, they were hesitant to claim that bimodality is inherent to all environments because they had studied only one cluster and felt that different environments could show different behavior of μ_0.

The goal of this section is to address all of these issues with a study of 438 galaxies selected from the *Spitzer Survey of Stellar Structure in Galaxies* (S^4G, Sheth et al., 2010). We study the μ_0 distribution to confirm the evidence of the gap found in the Ursa Major and Virgo clusters. The confirmation of a gap can place constraints on present day galaxy distributions

which are essential to the comprehension of galaxy formation and evolution. Post-Basic Calibrated Data used for measurements are publicly available at the Spitzer Heritage Archive website. We show that the 438 galaxies constitute a representative sample to an absolute magnitude of -15 in the 3.6 μm band of the *Spitzer Space Telescope* (Fazio et al., 2004; Werner et al., 2004). The sample extends up to 20 Mpc and includes all morphological types later than SO^-. The key attributes of the sample are that it is a homogeneous dataset with a large number of galaxies from the field and cluster environments imaged with excellent photometry (Reach et al., 2005). The mid-infrared wavelengths also offer a view of galaxies at very low extinction (Draine and Lee, 1984) and with 4 minutes of integration time per pixel, the data are significantly deeper than anything that can be obtained from the ground for a large sample of galaxies. In the rest of this section, after testing ARCHANGEL measurements of μ_0 at 3.6 μm, we discuss the sample selection, the bimodal distribution of $\mu_0^{[3.6]}$ and the likelihood of obtaining a dip at ISBs from statistical fluctuations of a flat μ_0 distribution selection.

3.3.6.2 Ursa Major: Testing Measurements of μ_0 at 3.6 μm

To test ARCHANGEL measurements of μ_0 at 3.6 μm to that obtained in previous papers, we retrieve the available 43 of 78 previously used Ursa Major galaxies (Tully and Verheijen, 1997) from the Spitzer archive. Sixteen of these galaxies are from the Carnegie Hubble Program (Freedman et al., 2011) and 27 are from the S^4G survey. Disk central surface brightness values obtained with our procedure at 3.6 microns in the AB system are compared to values obtained in the K' band in the Vega system from the 1997 paper in the top panel of Figure 3.20. We find a good agreement between K' and [3.6] band values. Bottom panels of the same figure show μ_0 distributions for the 43 galaxies in common with the previous studies. The bottom right panel also shades the galaxies according to their type - one immediately sees that the early type galaxies have a higher μ_0 (ie, are usually HSBs) compared to the usually lower surface brightness late type galaxies demonstrating the known strong correlation between morphological type and the disk central surface brightness. The previous studies found values for LSB and HSB peaks in the K'-band at about 19.7–20.0 for LSBs and 17.3–17.5 for HSBs (mag arcsec^{-2} in the Vega system). We find values of 22.5 and 19.5 for LSBs and HSBs at 3.6 μm but in the AB system as shown in Figure 3.20. A conversion between the Vega and AB systems re-establishes the proper relative positions between peaks in the K' and [3.6] bands. Namely, at 3.6 microns, peaks are located at smaller values in the Vega system ($[3.6](Vega) = [3.6](AB) - 2.785$) than in the K' band in the same system. A single Gaussian model of the μ_0 distribution can be rejected at more than the 99% confidence level while the significance of a double Gaussian modeling is quite high (54%). However these 43 galaxies do not constitute a complete sample and cannot lead to a universal conclusion

about the bimodality we seek to test. Still the comparisons show that our procedure gives results similar to the previous studies and does not introduce any particular bias.

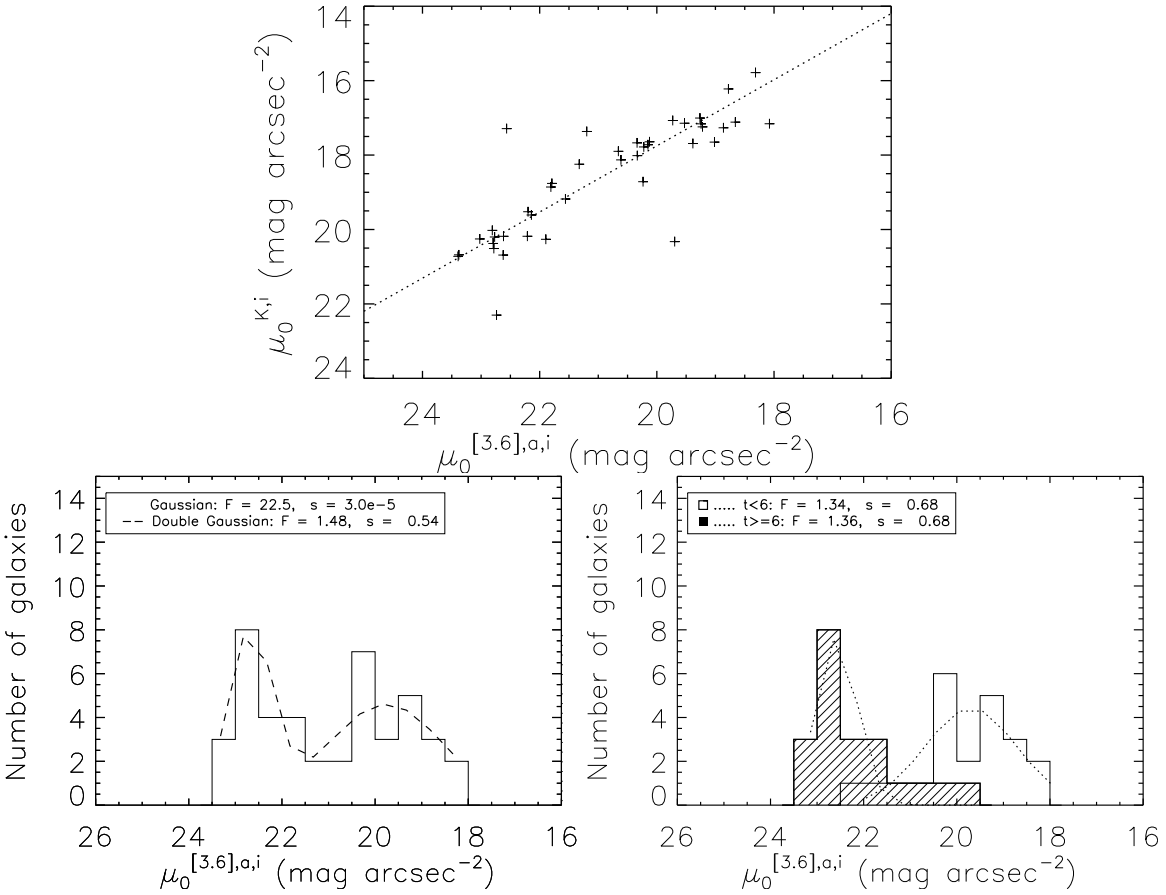

FIGURE 3.20: *Top*: Comparison between disk central surface brightnesses from Tully & Verheijen 1997 in the K'-band, Vega system and this work, AB system. The dotted line is the 1:1 relation shifted by the average K'(Vega)-[3.6](AB) value of the sample. *Bottom left*: Histogram of the disk central surface brightnesses corrected for inclination and aperture of 43 Ursa Major galaxies. The dashed line represents the sum of two Gaussian fits from LSB and HSB subsample modelings. While the significance level (s) of the F-Test (F) for the double Gaussian is high, the single Gaussian modeling can be rejected at more than the 99% confidence level. *Bottom right*: Distributions of type greater than 6 galaxy disk central surface brightnesses (dashed histogram) and type smaller than 6 galaxy disk central surface brightnesses (plain histogram) for the available galaxies of the Ursa Major cluster.

As stipulated in subsection 3.3.2.2, surface brightnesses are fitted with disk-only. Tully and Verheijen (1997) and McDonald et al. (2009a) were concerned about the disk-only fitting technique for bulge galaxies. However, they respectively showed that neither dropping bulge galaxies nor making a bulge-disk decomposition removed the bimodality. They also asserted that their results were not significantly affected by alternative decompositions. We have retained in subsection 3.3.4 an uncertainty budget of 0.5 mag arcsec^{-2} for $\mu_0^{[3.6]}$ measurements. This leads to a choice of bin sizes of 0.5 mag arcsec^{-2} for histograms of $\mu_0^{[3.6]}$ distributions.

3.3.6.3 Sample Selection

The S^4G survey is a volume-, magnitude-, and diameter-limited ($d < 40\ Mpc$, $|b| > 30^o$, $m_{Bcorr} < 15.5$ and $D_{25} > 1'$) survey of over 2,350 galaxies observed with channels 1 and 2 (3.6 and 4.5 μm respectively) of the IRAC instrument (Fazio et al., 2004) aboard the Spitzer Space Telescope (Werner et al., 2004). It is a very large extremely deep, representative and homogeneous sample of nearby galaxies containing all Hubble types. We use only the 3.6 μm band data that we preferred for the Cosmicflows project based on the knowledge that 4.5 μm fluxes have a higher contribution from hot dust than fluxes at 3.6 μm (Meidt et al., 2012). We extracted from the S^4G survey every galaxy of type later than SO^- up to a distance of roughly 20 Mpc according to the Extragalactic Distance Database. At low redshift, surface brightnesses are independent from distances. Thus, distances used here are simple estimates derived from redshifts tethered to a Virgo infall model constrained by distance measurements. The resulting sample goes down to an absolute magnitude limit of -16 in the B band in the Vega magnitude system. This faint magnitude limit prevents the loss of low surface brightness galaxies (LSB, Zhong et al., 2008) from the volume surveyed and guarantees the presence of galaxies of intermediate surface brightnesses.

Figure 3.21 shows histograms of the sample as function of 1) numerical morphological type, which increases with the "lateness" of the literal type (E to Im through S), 2) absolute 3.6 μm magnitude and 3) distance. The left panel in Figure 3.21 shows a deficit of Type-7/8 galaxies and a small excess of Type-5/6 galaxies but this is not a bias from the selection – the distribution of the full S^4G sample shown with the dashed line also displays the same behavior. Moreover, the morphological T-type assignments from HyperLeda (Paturel et al., 2003) are qualitative with an uncertainty of δT=1. There is also no a priori expectation of similar numbers of galaxies in each category in a given volume.

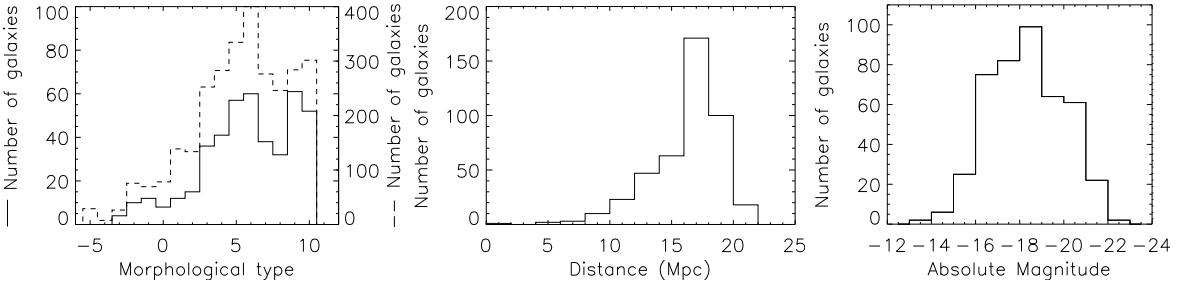

FIGURE 3.21: Histograms showing the distributions of the 438 galaxies extracted from the S^4G sample. *From left to right*: Morphological type from HyperLeda database (we chose all galaxies with T > -3 or later than SO^-). The dashed histogram is the distribution of HyperLeda types for the whole S^4G sample ; Distance to the galaxies from the Extragalactic Distance Database ; Absolute Magnitude ($M_{[3.6]} < -16$ in the AB system).

Figure 3.22 shows the angular distribution across the sky of the 438 galaxies; point sizes are set according to their distances from us. We perform aperture photometry for the 438 Post

Basic Calibrated Data of the galaxy sample using the adapted for this work ARCHANGEL software following the process detailed in subsection 3.3.2.2.

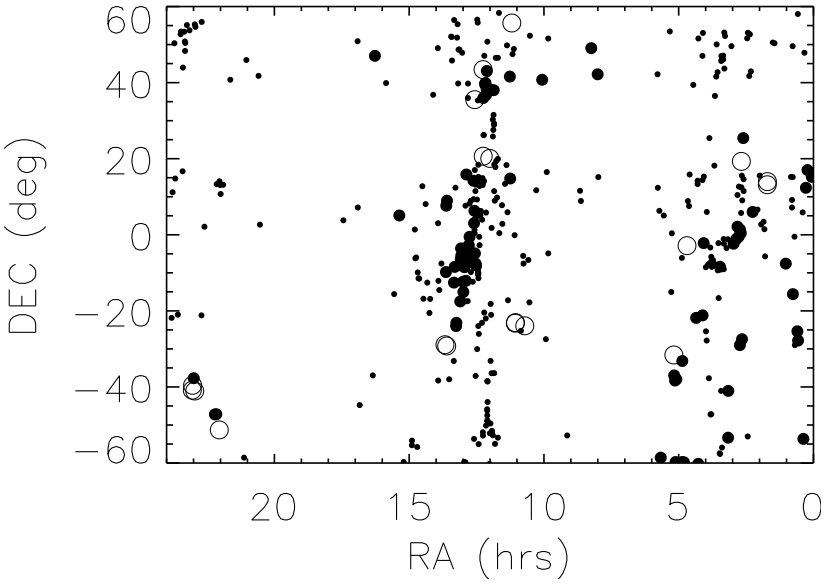

FIGURE 3.22: Angular distribution on the sky of the 438 S^4G galaxies. Size of the symbols represents the distance to the galaxy. The largest symbols show galaxies closer than 10 Mpc, the medium sized symbols stand for galaxies between 10 and 15 Mpc, and the smallest symbols show galaxies farther than 15 Mpc.

3.3.6.4 A Lack of Intermediate Surface Brightness Galaxies

The entire $\mu_0^{[3.6],a,i}$ distribution for the 438 galaxy sample from S^{4}G is shown in Figure 3.23. It reveals a hint of bimodality – There is a lack of galaxies between 21 mag arcsec^{-2} and 22 mag arcsec^{-2} (less than 45 galaxies versus more than 60 galaxies at the peaks). We fit this distribution with a double Gaussian assuming a population with μ_0 greater than 21.5 mag arcsec^{-2} and a population with μ_0 less than 21.5 mag arcsec^{-2} - roughly reflecting a LSB and HSB population respectively (see top panel in Figure 3.24) . This model has a much higher significance (can only be rejected at a 21% confidence level) compared to a simple Gaussian model which can be rejected at a 55% confidence level.

As shown in the top panel of Figure 3.24, the ad-hoc limit of 21.5 mag arcsec^{-2} matches well with the well known fact that LSB galaxies are in general of late Hubble type while HSB galaxies are in general of early Hubble type (e.g. de Jong, 1996b). In this figure, the LSB galaxies appear only for types later than the Scd type. The bottom panel of Figure 3.24 shows the $\mu_0^{[3.6],a,i}$ distribution for each morphological type in the 438 galaxy sample. The histogram peak shifts to the left (higher $\mu_0^{[3.6],a,i}$) with increasing morphological types, supporting the correlation between types and the disk central surface brightnesses.

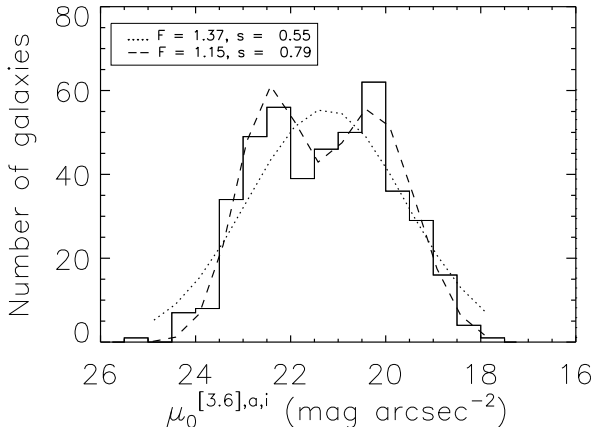

FIGURE 3.23: Histogram of the aperture-inclination corrected disk central surface brightnesses. A Gaussian fit (dotted line) to the distribution can be rejected at the 55 % confidence level (F=F-Test, s=significance level) while a sum of two Gaussians respectively from the modelings of LSB and HSB disk central surface brightness subsample distributions can be rejected only at the 21% confidence level (dashed line) supporting the bimodality seen previously.

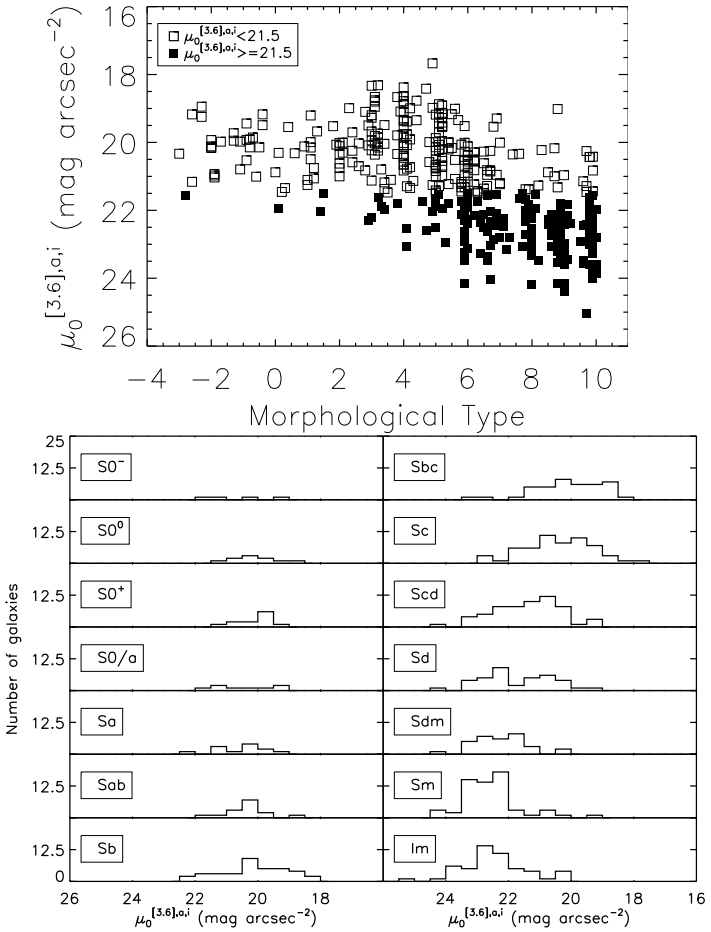

FIGURE 3.24: *Top*: disk central surface brightness versus morphological type. An ad-hoc limit set at $\mu_0^{[3.6],a,i} = 21.5$ mag arcsec^{-2} shows that galaxies with $\mu_0^{[3.6],a,i} > 21.5$ mag arcsec^{-2} appear for types greater than ~ 6 (later than Scd). *Bottom*: Peaks of the $\mu_0^{[3.6],a,i}$ distributions shift to the left with increasing morphological type.

Since the double Gaussian modeling can be rejected as a model for the total sample at the 21% (against 55% for the single Gaussian modeling) confidence level, we next define selection criteria to understand better which galaxies are in the gap and what might be causing a bimodality.

Close neighbor: galaxies with a close neighbor ($D < 80\ kpc$) can undergo interactions which can potentially modify their μ_0 values. If there are only two parent populations (HSB and LSB types), then mergers / interactions could move galaxies into the gap separating the HSB and LSB galaxies (Tully and Verheijen, 1997). We remove galaxies with close neighbors to test the postulate that this will increase the bimodal nature of the μ_0 distribution. We assume that a galaxy with a velocity, v, has a "close neighbor" whenever there is another galaxy within 80 kpc with a velocity equal to $v\pm$ 200 km s^{-1} . We find only a few galaxies with close neighbors as shown on Figure 3.25. The remaining "isolated" sample consists of 411 galaxies. The distribution of the 27 galaxies with close neighbors looks quite flat - although the numbers are too small to investigate the nature of the distribution. Quite a few of the 27 galaxies are in the gap. This agrees with the hypothetical scenario proposed by Tully and Verheijen (1997) in which LSB galaxies tend to turn into HSB galaxies progressively going through a stage as intermediate surface brightness galaxies due to an interaction with a neighbor.

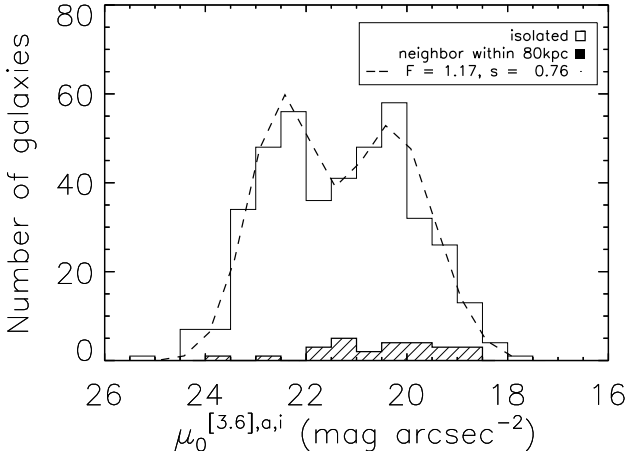

FIGURE 3.25: Separation between galaxies with at least one neighbor closer than 80 kpc (dashed histogram) and without a neighbor within 80 kpc (plain histogram). The velocity of the neighbor has to be within ± 200 km s^{-1} of the galaxy velocity. The dashed line is the sum of two Gaussians. It cannot be rejected at more than the 24 % confidence level (1 σ significance level (s)) with a F-Test (F).

Inclination: next we explore the effect of inclination corrections as noted by Bell and de Blok (2000). According to them, the effects of dust and projection geometry may not be negligible, even in the mid-infrared: 1) averaging ellipse surfaces at high inclinations to obtain μ_0 may result in a systematically smaller value (Huizinga, 1994), 2) assuming a thin, uniform, slab disk at high inclinations may lead to incorrect conclusions because three

dimensionality of stellar structures affects the inclination correction in non-trivial ways. It is difficult to characterize the surface brightnesses of edge-on galaxies because integrating along the line of sight may hide the effects of sub-structures like bars and spiral arms (e.g. Mosenkov et al., 2010). No precise method exists for correcting such effects and the coefficient $C^{[3.6]}$ in equation 3.30 itself may vary with galactic radius. In absence of a proper (or even better) method to correct for inclination and because numerically obtained inclinations are quite uncertain (see for example, Figure 3.13), we decided to remove every galaxy with an inclination greater than $\sim 73^o$ ($\frac{b}{a}$=0.35)[5] leaving us with 292 galaxies. Figure 3.26 displays the bimodal distribution of this refined sample along with the distribution for the "edge-on" galaxies. The inclined galaxies are well-described by a single Gaussian that peaks in the previously observed gap between the HSB and LSB galaxies. The remainder of the sample is well-fitted with a double Gaussian model which cannot be rejected at more than the 16 % confidence level with the F-Test (based on the ratio of model and data variances).

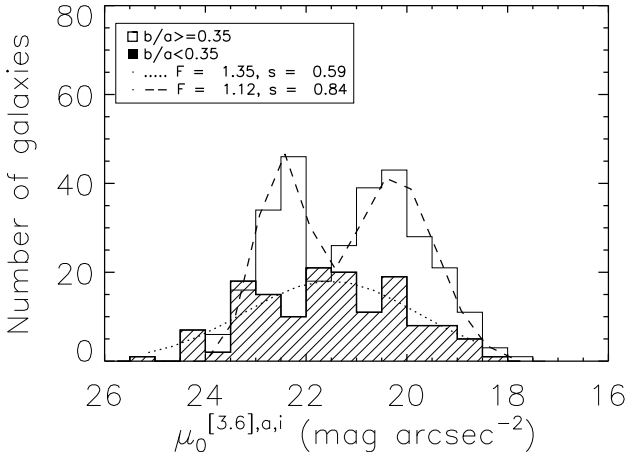

FIGURE 3.26: Distribution of disk central surface brightnesses of highly inclined galaxies ($i > 73^o$, dashed histogram) against the others ($i < 73^o$, plain histogram). The $\mu_0^{[3.6],a,i}$ distribution of highly inclined galaxies is fitted by a Gaussian (dotted line) whereas the less inclined galaxy $\mu_0^{[3.6],a,i}$ distribution is fitted by a double Gaussian (dashed line) (F=F-Test, s=significance level).

Axial Ratio: an error in the axial ratio is another source of error in the inclination correction we apply to get the face-on $\mu_0^{[3.6],a}$ value. An error of 0.2 in the axial ratio leads to an error of about 0.5 mag arcsec^{-2} (namely a change of bin in our histograms). We remove every galaxy whose ARCHANGEL derived ratios differ from that found in HyperLeda database (Paturel et al., 2003) by more than 0.2. The resulting distribution of $\mu_0^{[3.6],a,i}$ is shown in Figure 3.27. Where the axial ratio between the HyperLeda values and that measured by ARCHANGEL in the S^{4}G data are similar (408 galaxies), the bimodal distribution is still visible. There are fewer LSB galaxies in this plot compared to the original because LSB galaxies are the

[5] 0.4 instead of 0.35 was the choice of Bell and de Blok (2000). Because of the uncertainties on inclinations ($\sim 4-5^0$), choosing 0.35 (73^0) over 0.4 (69^0) does not change the conclusions.

ones most affected by a change in observations (optical versus mid-infrared). The double Gaussian modeling cannot be rejected at more than the 19% confidence level.

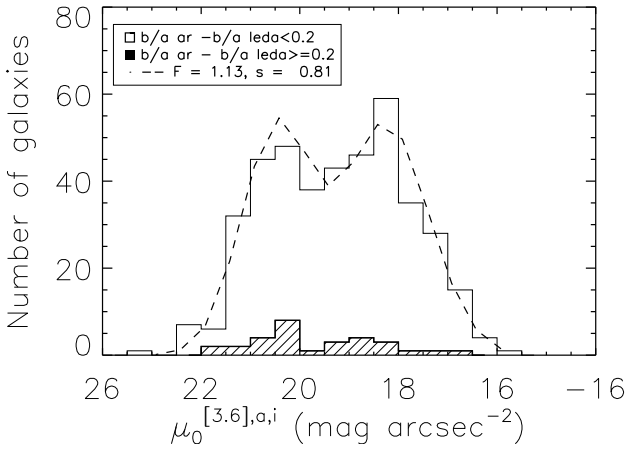

FIGURE 3.27: Distribution of $\mu_0^{[3.6],a,i}$ separating galaxies which "ARCHANGEL axial ratios" differ by more than 0.2 from "HyperLeda axial ratios" (dashed histogram) from which that do not (plain histogram). The total sample is modeled by a sum of two Gaussians (dashed line) (F=F-Test, s=significance level).

Combination of selection criteria: if we now combine the three selection criteria (isolated, non-inclined galaxies, with similar axial ratios in the optical and mid-infrared) we get a sample of 249 galaxies. On Figure 3.28, the $\mu_0^{[3.6],a,i}$ distribution for this highly refined sample clearly shows the bimodality. The double Gaussian modeling now cannot be rejected at more than the 19% confidence level according to the F-Test. On the contrary, the single Gaussian modeling can be rejected at a 81% confidence level with the same test. Thus we conclude that the $\mu_0^{[3.6],a,i}$ distribution of the sample is bimodal and that there is a lack of intermediate surface brightness galaxies.

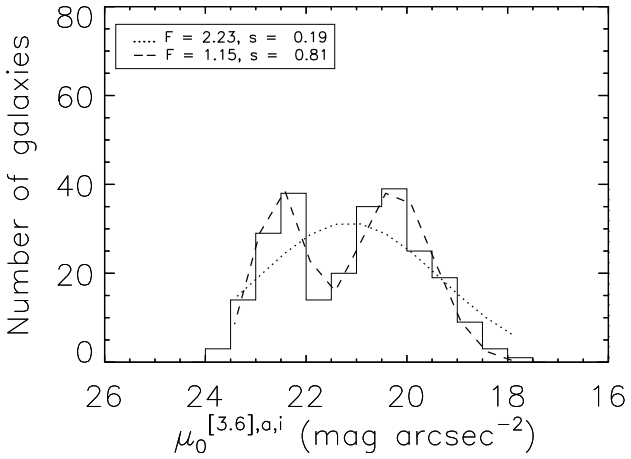

FIGURE 3.28: $\mu_0^{[3.6],a,i}$ histogram after dropping galaxies inclined by more than 73^o, with a neighbor closer than 80 kpc and with an axial ratio different by more than 0.2 between HyperLeda and S^{4}G data. A double Gaussian (dashed line) clearly fits the distribution far better than a single Gaussian (dotted line) (F=F-Test, s=significance level).

3.3.6.5 Why a Dip at Intermediate Surface Brightness?

The different results of previous sections demonstrate strongly that the $\mu_0^{[3.6],a,i}$ distribution is bimodal. Is it possible that the bimodality is from statistical fluctuations? To obtain the likelihood of getting a dip at intermediate surface brightness from a statistical fluctuation, we simulated a flat $\mu_0^{[3.6],a,i}$ distribution of 700 galaxies with μ_0 between 19 and 24 mag arcsec^{-2}. We chose a flat distribution in agreement with the current description of disk central surface brightness distribution (McGaugh, 1996; McGaugh et al., 1995). This flat distribution has an upper brightness limit to disk central surface brightnesses that must have a physical origin (Freeman, 1970) and a lower brightness limit due to observational limitations in the simulations. Each 1 mag arcsec^{-2} size bin contained the same number of galaxies. We randomly selected 249 galaxies from that distribution and looked at the likelihood of obtaining a gap between two peaks. We repeated the selection 10,000 times and retained only simulations with a gap between two peaks and a number of galaxies in the gap no greater than 50 % the number of galaxies in the peaks. This is approximately what we observe in Figure 3.28. Table 3.4 lists the histogram parameters of the 9 simulations out of the 10,000 simulations which showed a distribution similar to the observed bimodality we observed in the 249 galaxy sample. The last line corresponds to the mean values for the 9 simulations. Thus the likelihood of randomly obtaining the observed bimodality is only $\sim$ 0.1 %.

Simulations	peak$_1$	pos. peak$_1$	peak$_2$	pos. peak$_2$	gap	position gap	%$_1$	%$_2$
431	71	24.0	62	22.0	31	23.0	44	50
870	63	23.0	61	21.0	27	22.0	43	44
2603	64	24.0	63	21.0	30	22.0	47	48
3923	65	20.0	59	23.0	28	22.0	43	48
4852	66	24.0	61	22.0	23	23.0	35	38
4887	64	23.0	63	20.0	28	21.0	44	44
8330	66	22.0	62	24.0	30	23.0	46	48
8421	67	23.0	60	20.0	30	22.0	45	50
9233	63	23.0	62	21.0	30	22.0	48	48
Mean	65	23	61	21	28	22	44	46

TABLE 3.4: Kept simulations: (1) Number characterizing the simulation out of 10,000. Only simulations with two peaks and a gap in between are selected. The number of galaxies in the gap has to be at most 50 % the galaxy number in peaks. Only 9 out of 10,000 simulations are similar to the observed bimodality. In other words, there is only a $\sim$ 0.09 % probability that the bimodality is due to a statistical fluctuation. (1) - (2) Value (number of galaxies) and Position (mag arcsec^{-2}) of the first peak, (3) - (4) Value (number of galaxies) and Position (mag arcsec^{-2}) of the second peak, (5) - (6) Value (number of galaxies) and Position (mag arcsec^{-2}) of the gap, (7) - (8) Percentage of galaxies in the gap with respect to the number of galaxies in the first and second peaks respectively.

In the Vega system, peaks have been found at 17.5-18 and 20 mag arcsec^{-2} for both Virgo and Ursa Major Clusters in the K' band and in the H band respectively (McDonald et al., 2009a,b; Tully and Verheijen, 1997). The gap found in between has a width of one unit in magnitude per square arcsecond and is located at ∼19 mag arcsec^{-2}. In this study, at 3.6 μm in the AB system, the observed bimodal distribution shows two peaks at 20.5 and 22.5 mag arcsec^{-2} and a gap of width 1 mag arcsec^{-2} at 21.5 mag arcsec^{-2} in between. This excellent agreement between the studies, including the shift to smaller values when moving towards longer wavelengths (visible after applying the AB-Vega system conversion) already shown in Figure 4 of the 1997 paper, is a strong evidence for an inherent bimodality in the local galaxy population.

The results reveal a clear separation between $\mu_0^{[3.6]}$ of HSB and LSB galaxies. The former are probably dominated by baryonic matter at their centers whereas the latter are likely dark matter dominated at all radii (Tully and Verheijen, 1997). Along with a lack of intermediate surface brightness galaxies, the data suggest that the two (L/HSB) peaks signify two stable configurations of galaxy formation (Mestel, 1963). Systems that retain large angular momentum from their formation may prevent the baryonic matter from collapsing to form a stellar disk that could dominate the dark halo at the galaxy center. These systems may reach a rotational equilibrium at densities where the dark matter halo remains dominant and the galaxies appear as LSB galaxies. On the other hand, galaxies with low angular momentum, either because of their formation or because they transferred their angular momentum away from much of their gas, allow baryonic matter to collapse and form disks that can dominate the dark matter halo at the center. This hypothesis is supported by the differences between typical LSB and HSB rotation curves. LSB galaxies reach flat rotation at very large radii from their centers (Swaters et al., 2010) whereas HSB galaxies reach their maximal rotation speed at, or within, r=2.15 α where α is the disk scale length (Courteau, 1997).

The gap between the two peaks suggests that galaxy formation does not favor a situation where the dark matter and the baryonic matter have equal weight in the center. The few galaxies present in this gap may be transitioning from LSB to the HSB galaxies as suggested by the experiment with the close neighbor pairs. Eventually all galaxies that undergo interactions may end up as HSB galaxies so that the peak of HSB systems should be higher than the LSB peak in environments where interactions are common.

Our 438 galaxy sample is representative of all galaxies later than SO^- in the half of the sky at the Galactic poles within the volume extending to 20 Mpc and brighter than $M_B = -16$. The galaxies lie in clusters, groups, and the field. The bimodality in disk central surface brightnesses first found in moderate and high density regions is found to be pervasive. Galaxies are mostly HSB or LSB but rarely ISB. This phenomenon must have a physical explanation, one that probably will give an important clue regarding the process of galaxy

formation. Seeking for such a bimodality to be present in disk central surface brightness distributions of simulated galaxies could unravel some mystery about the process of galaxy formation.

3.4 Tully-Fisher Relation

This section expounds the calibration of the Tully-Fisher relation in the mid-infrared. It results from a commonality of interests between the overall Cosmicflows project (subprogram Cosmicflows with Spitzer, initiated in cycle 8) and the Carnegie Hubble Program (CHP, initiated in Spitzer proposal cycle 6). The intent of CHP is to reduce systematics arising in the determination of the Hubble Constant by giving attention to a mid-infrared calibration of the Cepheid Period-Luminosity relation and a second part addresses the properties of the rotation rate–luminosity correlation of galaxies or Tully-Fisher Relation (TFR). Cosmicflows seeks to obtain accurate distance measurements for thousands of galaxies using the mid-infrared TFR in order to map deviations from Hubble flow. Since the TFR zeropoint is established by the Cepheid distance measurements, the Cepheid Period-Luminosity relation calibration is required. Freedman et al. (2011) describe the goals of CHP and Freedman et al. (2012) report on the results of the Cepheid calibration that gives a distance modulus for the Large Magellanic Cloud of 18.48 ± 0.03 magnitudes.

3.4.1 Calibration at 3.6 μm

The ensuing discussion about the Tully-Fisher calibration borrows on the recent re-calibration of the I band correlation by Tully and Courtois (2012) (hereafter TC12). The strategy consists in forming a template relation using samples from 13 galaxy clusters and the establishment of a zeropoint using nearby galaxies with independent Cepheid period-luminosity or Tip of the Red Giant Branch (TRGB) distances. [3.6] magnitudes are obtained mostly with ARCHANGEL and are eventually combined with CHP measurements. HI profile and inclination information are the same as in TC12. The significant difference is the replacement of mid-infrared for optical luminosities. It turns out that although the new photometry has high fidelity and the photometry correction terms are small there is an intrinsic color term in the [3.6] band TFR. Scatter in the relation will be reduced upon application of a color correction. We will conclude the section with an estimate of the Hubble Constant.

3.4.1.1 Calibrators

The slope and zeropoint calibrator samples are described in detail in TC12. The correlation slope is established from a template built from galaxies in 13 clusters from the closest Virgo cluster up to Abell clusters, the farthest being Abell 2634. As a matter of fact, the only departure in terms of an extension from the I band calibration occurs precisely in the case of Abell 2634. The CHP program included observations of a larger region including Abell 2666. The two clusters are close in projection and, evidently, in distance. We find no discernible difference in distance between galaxies closest on the sky to Abell 2634 versus those closest to Abell 2666. We propose to average over the entire complex.

Each cluster sample is comprised of galaxies likely to be at similar distances. There was an attempt to include all galaxies with suitable properties down to a defined faint luminosity level to have an unbiased sampling of the cluster volume to a magnitude limit. Candidates are chosen out of a projection-velocity window. We care about minimizing relative distance effects in the TFR so it is more important to minimize interlopers than maximize true members. Cluster members that are "window outsiders" would not be expected to lie in any preferred part of the TF diagram. The selection criteria are:

- morphological types earlier than Sa are excluded (SO types are similar to spirals but have been shown not to lie on the same Tully-Fisher relation, e.g. Bedregal et al., 2006; Williams et al., 2010),
- HI profiles with adequate signal-to-noise are required,
- HI profiles should present no evidence of confusion or tidal disruption,
- inclinations less than 45° are rejected to limit large linewidth de-projection errors. Tests with samples that satisfy this limit have not revealed that this selection gives rise to a distance bias (TC12).

Criteria for inclusion of zeropoint calibrators are similar, with the additional requirement that they have very well known distances from either Cepheid or TRGB measurements. In TC12, the Cepheid scale had been set by a distance modulus for the Large Magellanic Cloud of 18.50 magnitude (Freedman et al., 2001). Here we adopt the slightly modified modulus $18.48 \pm [0.03 - 0.06]$ magnitude based on mid-infrared photometry of Cepheids in the Large Magellanic Cloud and in our Galaxy, the latter anchored with trigonometric parallaxes (Monson et al., 2012). The TRGB distances are based on a Population II calibration but have been demonstrated to be on a consistent scale (Rizzi et al., 2007; Tully et al., 2008).

At the time of this calibration work, Cosmicflows with Spitzer observations were incomplete, still already 230 of 314 galaxies (73%) used in the I band calibration (plus 9 other galaxies

introduced with the extension of the Abell 2634 sample to include Abell 2666) had Spitzer [3.6] photometry, including 26 of 36 (72%) that set the zeropoint. The completion was greater than 60% with each of 12 of the 13 template clusters (the Pisces filament is the exception). Consequently, we proceeded with the TFR calibration with the available material. The data that are used in the following discussion are collected into Table B.1 of Appendix B. This table includes CFS and CHP total magnitudes, each including the four corrections described in subsection 3.3.3, and averages of the two methods. The table also gives inclination and linewidth information drawn from TC12 and color terms for color corrections described in subsection 3.4.1.3. The galaxies in Table B.1 of Appendix B are either part of the zeropoint calibration sample (ZP) or a member of a cluster contributing to the slope template.

3.4.1.2 Slope and Zeropoint

The TFR calibration requires the definition of a slope and the establishment of an absolute scale. The slope is the trickiest item because there is a correlation between its value and a form of Malmquist bias. Given two galaxies at the same distance with the same linewidth, the brighter galaxy might be chosen but not the fainter one. The potential bias depends on the slope of the correlation because with a relatively flat slope most intrinsically luminous galaxies lie above the correlation while with a very steep slope these same galaxies tend to lie below the correlation. Consider a target for a distance measurement in the field that intrinsically lies above the assumed mean relation, the trend for distant galaxies if the relation is flat. With the distance measurement the target is assigned the mean luminosity of the correlation at the target's linewidth so given a distance that is too small. This bias has repeatedly been discussed at length, most recently by TC12. The salient point is that the so-called "inverse" relation (ITFR), the least squares regression where errors are taken to be in linewidth only, gives results that are close to bias free. Willick (1994) pointed out that, while in his experiments the ITFR bias was reduced by a factor 6 from that incurred using the direct relation, yet a small bias remained because the sample selection was not made in the band he considered. We have the same problem. Our strategy is to use the ITFR and then evaluate the bias with simulations anticipating that, like with the I band calibration, the effects will be small. The bias tests are discussed in a later subsection 3.4.1.4. The calibration process has been described in detail by Tully and Pierce (2000) and TC12. With the I band relation there was no clear evidence for scatter due to a third parameter but the situation at [3.6] is different. A color term is found and that matter will be discussed in subsection 3.4.1.3.

The measurement of distances requires the hypothesis of a universal correlation. To begin, we make inverse fits to each one of the clusters separately. We use the least square fitting mathematical procedure which consists in finding the best-fitting curve to a set of point by

minimizing the sum of the residual squares (given points minus model). Squares are used as they can be assimilated to a continuous differentiable quantity contrary to absolute values. The condition for the sum of the residual squares to be an extremum (minimum in our case) for a linear fit of n points (x, y) is given by:

$$\frac{\partial \sum_{i=1}^{n}[y_i - (a + bx_i)]^2}{\partial a} = 0 \qquad \text{and} \qquad \frac{\partial \sum_{i=1}^{n}[y_i - (a + bx_i)]^2}{\partial b} = 0 \tag{3.37}$$

where y_i are the variables to fit as a function of the x_i variables and a, b are constants. Because we want inverse fits, y_i are to be assimilated to logarithms of linewidths, more precisely to $\log W^i_{mx} - 2.5$ and x_i to magnitudes m.

In matrix form, equations 3.37 can be written:

$$\begin{bmatrix} n & \sum_{i=1}^{n} x_i \\ \sum_{i=1}^{n} x_i & \sum_{i=1}^{n} x_i^2 \end{bmatrix} \begin{bmatrix} a \\ b \end{bmatrix} = \begin{bmatrix} \sum_{i=1}^{n} y_i \\ \sum_{i=1}^{n} x_i y_i \end{bmatrix} \tag{3.38}$$

which gives:

$$\begin{bmatrix} a \\ b \end{bmatrix} = \frac{1}{n\sum_{i=1}^{n} x_i^2 - (\sum_{i=1}^{n} x_i)^2} \begin{bmatrix} \sum_{i=1}^{n} y_i \sum_{i=1}^{n} x_i^2 - \sum_{i=1}^{n} x_i \sum_{i=1}^{n} x_i y_i \\ n\sum_{i=1}^{n} x_i y_i - \sum_{i=1}^{n} x_i \sum_{i=1}^{n} y_i \end{bmatrix} \tag{3.39}$$

where we have used the relation between a 2x2 matrix and its inverse:

$$\begin{bmatrix} a_1 & a_2 \\ a_3 & a_4 \end{bmatrix}^{-1} = \frac{1}{a_1 a_4 - a_3 a_2} \begin{bmatrix} a_4 & -a_2 \\ -a_3 & a_1 \end{bmatrix} \tag{3.40}$$

The correlation coefficient *corr* is the ratio of the covariance *cov* over the product of variances σ_x, σ_y:

$$corr = \frac{cov}{\sigma_x \sigma_y} = \frac{\sum_{i=1}^{n}(x_i - \bar{x})(y_i - \bar{y})/n}{\sum_{i=1}^{n}(y_i - \bar{y})^2/n \sum_{i=1}^{n}(x_i - \bar{x})^2/n} \tag{3.41}$$

where barred quantities stand for the means. With the definitions of variances and covariance, $b = \frac{cov}{\sigma_x^2}$ and $a = \bar{y} - b\bar{x}$.

Standard errors on b and a can be derived with:

$$err_a = \sqrt{\frac{n\sigma_y^2 - n\, b\, cov}{n-2}\left(\frac{1}{n} + \frac{\bar{x}^2}{n\sigma_x^2}\right)} \qquad \text{and} \qquad err_b = \sqrt{\frac{n\sigma_y^2 - n\, b\, cov}{n-2}\frac{1}{n\sigma_x^2}} \tag{3.42}$$

However, once a and b are computed, the relation needs to be inverted to find the Tully-Fisher relation: $[x_i(= m)] = -\frac{b}{a} + \frac{1}{b}[y_i(= \log W^i_{mx} - 2.5)]$. We define the errors on such an "inverse" slope $(\frac{1}{b})$ as the product of the standard error on the "direct" slope by the "inverse" slope divided by the "direct" slope. The standard error on the "direct" slope is obtained with the

relation 3.42 but this time with y_i assimilated to magnitudes m and x_i to $\log W^i_{mx} - 2.5$ in the procedure.

Dotted lines in Figures 3.29 and 3.30 illustrate the inverse fits of the TFR for each cluster. Slopes are quite similar between clusters. Slopes and their uncertainties are given for each cluster in Table 3.5. The individual fits are consistent with the soon to be derived best fit and hence with the universal correlation hypothesis[6]. As cluster distances increase, the faint luminosity limits decrease in magnitudes. However, no dependence of the slope with distance is seen, as would be a marker of Malmquist bias (we still make a tiny correction for bias to cluster moduli as described in subsection 3.4.1.4).

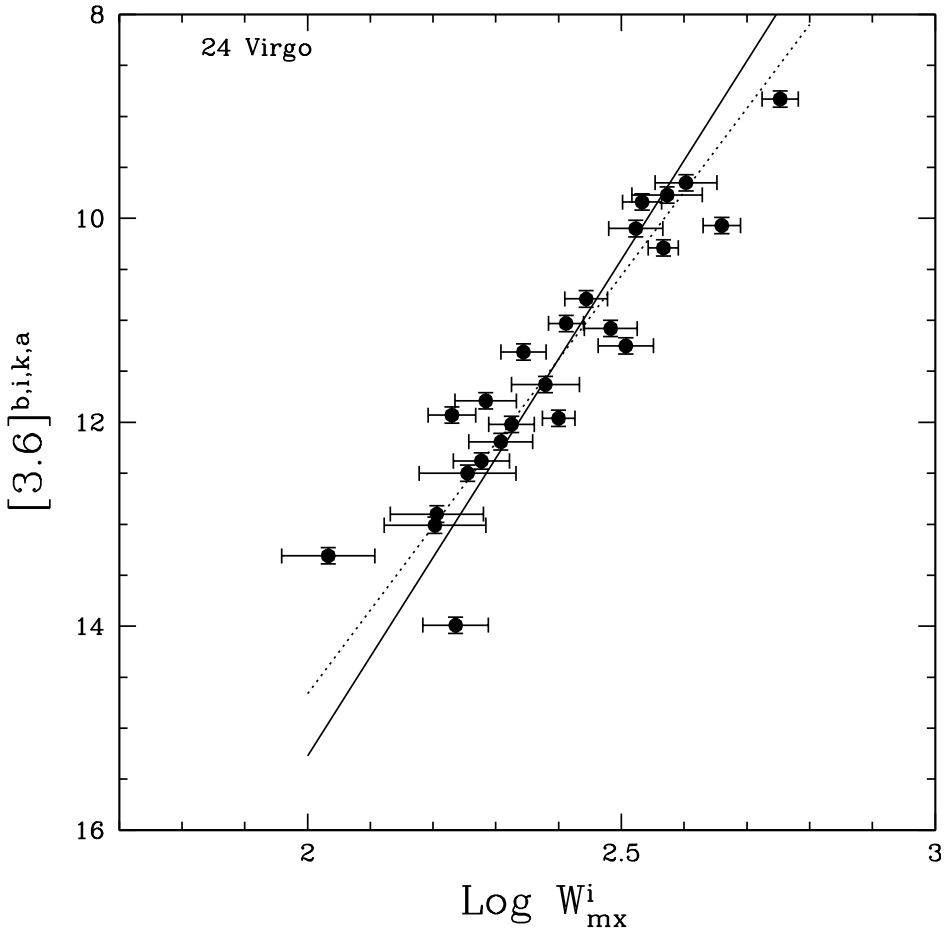

FIGURE 3.29: Tully-Fisher relation at 3.6 μm for the Virgo Cluster. The solid line gives the inverse fit of the universal template correlation. The dotted line is the inverse fit of the correlation for the Virgo Cluster alone.

[6]Note that Mocz et al. (2012) calibrated the TFR in u, g, r, i, z bands of SDSS for over 25,000 galaxies and found no dependence on the environment. If there is one it would be only at the 3% level. This comforts our assumption.

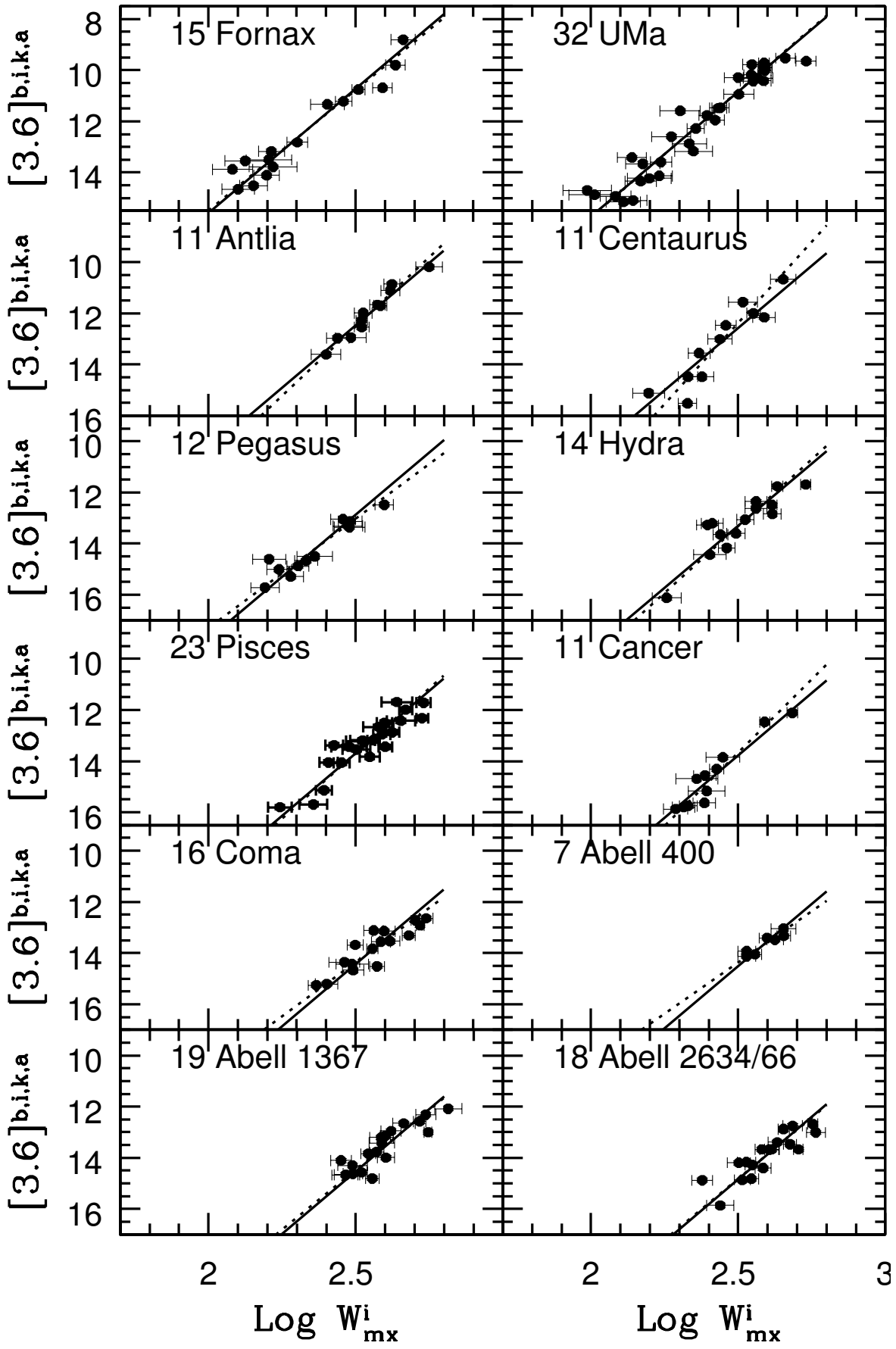

FIGURE 3.30: Tully-Fisher relation at 3.6 μm for the Fornax, Ursa Major, Antlia, Centaurus, Pegasus, Hydra, Pisces, Cancer, Coma, Abell 400, Abell 1367 and Abell 2634/66 clusters. Solid lines give the inverse fit of the universal template correlation. Dotted lines are the inverse fits of the TF correlation for each cluster.

The next step is to combine the 13 individual cluster correlations by vertical translations. The Virgo Cluster is used as a reference. Each preliminary zeropoint from the individual fits ($-\frac{b}{a}$) provides us with a first estimate of the relative distance between the Virgo Cluster and the cluster in question. Apparent magnitude zeropoints confirm that Virgo, Fornax and Ursa Major are the closest clusters. Then come Antlia-Centaurus-Pegasus, then Hydra-Pisces-Cancer, and finally Coma and the three Abell clusters A1367, A400 and A2634/66. To establish the best universal slope and the best relative distances between clusters, we follow an iterative procedure. We initially consider the nearest three clusters because they are observed to comparable depths in intrinsic magnitude. The Fornax and Ursa Major magnitudes are shifted according to the difference in zeropoint with respect to Virgo. A least squares fit of the ITFR is made to this ensemble. The slope obtained from this fit is then assumed in a fit to the three clusters separately with only the zeropoint as a free parameter in each case. The first assumed offset for a cluster is corrected for the deviation of the mean zeropoint $\bar{zpt} = \frac{1}{n}\sum_{i=1}^{n}(x_i - slope \times y_i)$ of that cluster from Virgo's zeropoint. Given the new zeropoint offsets the cycle is repeated, leading to rapid convergence. This procedure is repeated with the addition of each distance group in turn. Again, convergence is rapid. It is to be stressed that this procedure works because, following expectations, the slope of the ITFR is not affected by the magnitude level of truncation. This procedure would manifestly *not* work with the direct or bi-variate relations where the slopes vary with the level of truncation. In the end we obtain a slope of -9.74 ± 0.22 for the template ITFR. Zeropoint offsets with this "universal" slope are shown in Figure 3.31 and give relative distance moduli of clusters referenced to the Virgo Cluster. The universal slope of the ITFR is displayed in Figure 3.31 as well as by the solid lines in Figures 3.29 and 3.30. The error on each cluster zeropoint (offset + Virgo's zeropoint) is obtained by the standard deviation, *stddev* (scatter), of the galaxy zeropoints, $zpt = x_i - slope \times y_i$, divided by the square root of the number n of galaxies in the cluster:

$$err_{zpt} = stddev\sqrt{\frac{1}{n}} = \sqrt{\sum_{i=1}^{n}\frac{(zpt - \bar{zpt})^2}{n-1}\frac{1}{n}} \tag{3.43}$$

At the time of this calibration work, [3.6] photometry was available for 26 nearby galaxies with suitable morphologies, inclinations, and linewidths that also have well measured distances from either the Cepheid period-luminosity or TRGB methodologies. These 26 are a subset of the 36 absolute calibrator galaxies used in the I band calibration (TC12). Their luminosity-linewidth correlation is seen in Figure 3.32 where now the ordinate is absolute magnitude from the established distances. The line is a least squares fit with the slope -9.74 prescribed by the template. The zeropoint is -20.34 ± 0.10 where the error is the sum in quadrature of the standard deviations (scatters) of all the calibrators together and of the zeropoint calibrators divided by their respective number. The most deviant point is the fastest rotator, NGC

2841, with a deviation of 2.7 σ with respect to the template dispersion. This galaxy was a 2.3 σ deviant in the I band calibration. There is nothing unusual about this galaxy other than its extreme rotation rate so we see no reason to disregard it as a calibrator.

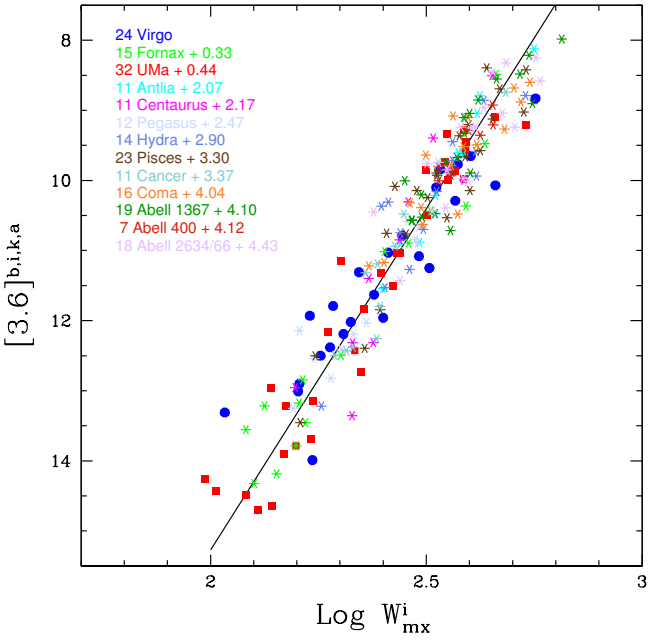

FIGURE 3.31: Template Tully-Fisher relation in the [3.6] band obtained with data from 213 galaxies in 13 clusters. Offsets given with respect to the Virgo Cluster represent distance modulus differences between each cluster and Virgo. The solid line is a least squares fit to all the galaxies with errors entirely in linewidths, the ITFR.

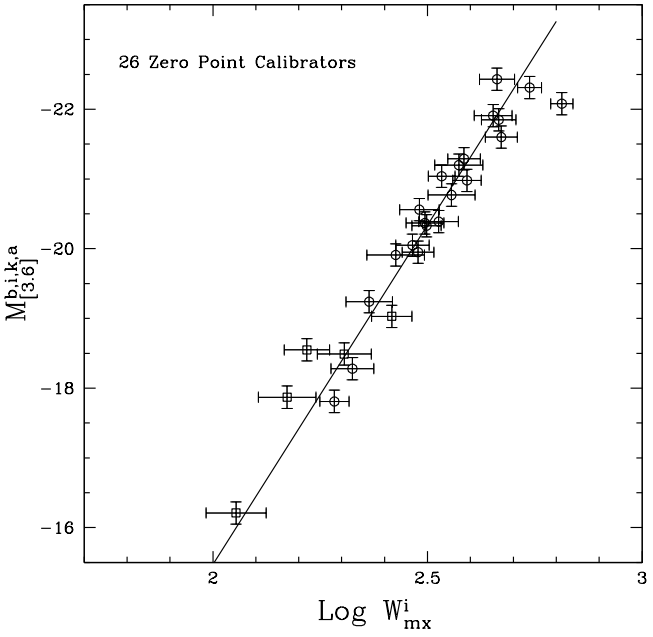

FIGURE 3.32: TFR for the 26 galaxies with distances established by observations of Cepheid stars (circles) or Tip of the Red Giant Branches (squares). The solid line is the least squares fit with the slope established by the 13 cluster template. The zeropoint of the TFR is set at the value of this fit at $\log W^i_{mx} = 2.5$.

The distance to the Virgo Cluster is given by the zeropoint of the constrained slope shown in Figure 3.31 minus the zeropoint of the absolute calibration shown in Figure 3.32. Application of this shift allows both cluster template and zeropoint calibrator galaxies to be plotted together as seen in Figure 3.33. The ITFR expression in the [3.6]-band is given by:

$$M^{b,i,k,a}_{[3.6]} = -(20.34 \pm 0.10) - (9.74 \pm 0.22)(\log W^{i}_{mx} - 2.5) \tag{3.44}$$

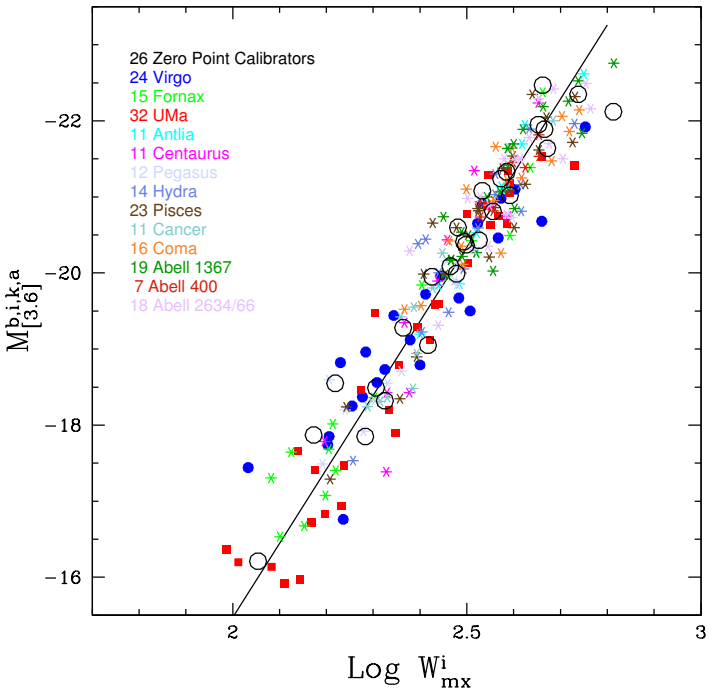

FIGURE 3.33: The template of the [3.6] band - HI linewidth correlation is built with 213 galaxies in 13 clusters extending in range from 1000 to 10,000 km s^{-1} with the absolute magnitude scale set by 26 zeropoint calibrators.

The TFR scatter in magnitudes (relevant for distance measurements) for the entire cluster template sample is ±0.49 magnitude from the universal ITFR, corresponding to a scatter in distance of 25%. The scatter for the 26 zeropoint calibrators is a similar 0.44 magnitude. Dispersion increases toward fainter magnitudes as well documented at I band by Giovanelli et al. (1997a). The sample presented here is still limited but the dispersion is consistent with a Gaussian distribution. With large samples (Tully et al., 2008) one finds that about 3% of candidates are more deviant than anticipated by Gaussian statistics. The causes are not always evident.

Scatter may arise from:

- measurement uncertainties affecting magnitudes, inclinations, and linewidths but observational errors are not likely to account for the whole scatter (e.g. Bothun and Mould, 1987),

- correction uncertainties applied to measured parameters,
- "cosmic" scatter, e.g. cluster depth effects or interlopers, deviations from disk planarity, other gravitational and photometric asymmetries, variations in the stellar population make-up, variations in disk-to-bulge ratios, etc.

Whatever the sources, we have a standard to meet set by the I band analysis. The sample used in the current analysis involve more than 70% of the sample used in the I-band calibration (TC12). Inclinations and linewidths are the same, the factors mentioned associated with cosmic scatter are the same, corrections to photometric parameters are reduced in the mid-infrared, and the integrity of the magnitude measurements must be at least as good or better with the Spitzer observations since observations are made all-sky with the same instrumental configuration. Error bars on magnitudes are reduced compared with those in I band to the degree that observational errors in magnitudes are a minimal component of uncertainties. Yet the scatter found at I band is less: $\pm$0.41 magnitude for the cluster template sample, lower with a significance of 2 σ, and 0.36 magnitude for the zeropoint calibrators. As much as half of the increase in magnitude scatter will occur because the slope of the correlation is steeper in the mid-infrared. However there could be an additional explanation for the increased scatter found at [3.6].

	v_{CMB}	N	Slope	ZP	scatter	ZP_{color}	scatter	bias	DM	Dist	V/D
V	1410	24	-8.21±0.71	10.40±0.14	0.67	10.49±0.11	0.56	0.00	30.83±0.14	14.7±0.9	96.2±6.9
F	1484	15	-9.39±0.66	10.73±0.13	0.49	10.86±0.12	0.47	0.00	31.20±0.14	17.4±1.2	85.4±6.4
U	1101	32	-9.83±0.52	10.84±0.10	0.55	10.94±0.08	0.44	0.00	31.28±0.11	18.0±0.9	61.1±4.2
An	3119	11	-10.79±0.79	12.47±0.07	0.23	12.44±0.06	0.21	0.04	32.82±0.10	36.6±1.7	85.1±4.2
Ce	3679	11	-12.69±1.76	12.57 ±0.19	0.62	12.58±0.18	0.59	0.01	32.93±0.20	38.5±3.5	95.4±8.8
Pe	3518	12	-8.55±0.94	12.87±0.13	0.44	12.89±0.12	0.42	0.01	33.24±0.14	44.5±3.0	79.1±5.4
H	4121	14	-10.48±1.49	13.30±0.14	0.53	13.35±0.14	0.52	0.05	33.74±0.16	56.0±4.2	73.6±5.5
Pi	4779	23	-10.15±0.82	13.70±0.10	0.47	13.69±0.08	0.40	0.02	34.05±0.11	64.6±3.4	74.0±3.9
Ca	4940	11	-11.46±1.17	13.77±0.12	0.39	13.78±0.10	0.34	0.02	34.14±0.13	67.3±4.0	73.4±4.4
Co	7194	16	-8.49±1.10	14.44±0.12	0.49	14.50±0.10	0.39	0.06	34.90±0.13	95.4±5.6	75.3±4.5
A4	7108	7	-8.03±1.40	14.52±0.08	0.21	14.50±0.08	0.21	0.10	34.94±0.11	97.3±5.1	73.1±3.8
A1	6923	19	-9.38±1.16	14.50±0.11	0.47	14.50±0.11	0.42	0.08	34.92±0.14	96.4±6.0	71.8±4.5
A2	8381	18	-9.55±1.38	14.83±0.12	0.51	14.85±0.10	0.44	0.05	35.24±0.13	111.7±6.6	75.0±4.4

TABLE 3.5: Properties of the Cluster Fits: (1) Cluster name (V Virgo, F Fornax, U Ursa Major, An Antlia, Ce Centaurus30, Pe Pegasus, H Hydra, Pi Pisces, Ca Cancer, Co Coma, A4 Abell 400, A1 Abell 1367 and A2 Abell 2634 and 2666, (2) Mean velocity of the cluster with respect to the CMB, km s^{-1}, (3) Number of studied galaxy per cluster, (4) Slope of the inverse fit, (5) Zero point relative to Virgo's zeropoint, no color adjustment, mag, (6) Scatter, no color adjustment, (7) Zero point relative to Virgo's zeropoint after color adjustment, mag, (8) Scatter after color adjustment, mag, (9) Bias, mag, (10) Bias corrected Distance Modulus, mag, (11) Cluster Distance, Mpc, (12) Hubble parameter, km s^{-1} Mpc^{-1}

3.4.1.3 A Color Dependence

It has long been known that the TFR steepens toward longer wavelengths (e.g. Courteau et al., 2007; Tully et al., 1982). The effect is seen in Figure 3.34 (Note: in the discussions in this section all optical photometry values have been transferred from Vega system to AB system according to relations 3.27). There is a strong color correlation with linewidth, more rapidly rotating galaxies tend to be redder, so at longer wavelengths the high rotation end of the TFR rises with respect to the low rotation end. Within a small linewidth interval, redder galaxies will rise more than bluer galaxies. It follows that red and blue galaxies cannot be well mixed in the TFR at all wavelengths. The trends that could be anticipated are shown in Figure 3.36 (only a portion of the sample have photometric measurements at B band). The comparison of fluxes at four bands from B to [3.6] for individual sources given in Figure 3.35 confirms the well known linkage between galaxy type and color. Early type galaxies have relatively more infrared flux relative to late type galaxies. This point was also illustrated with the representative spectral energy distribution plots in Figure 3.3. Galaxies that are more luminous and earlier in type are dominated by older, more metal enriched red giant stars emitting more in the infrared.

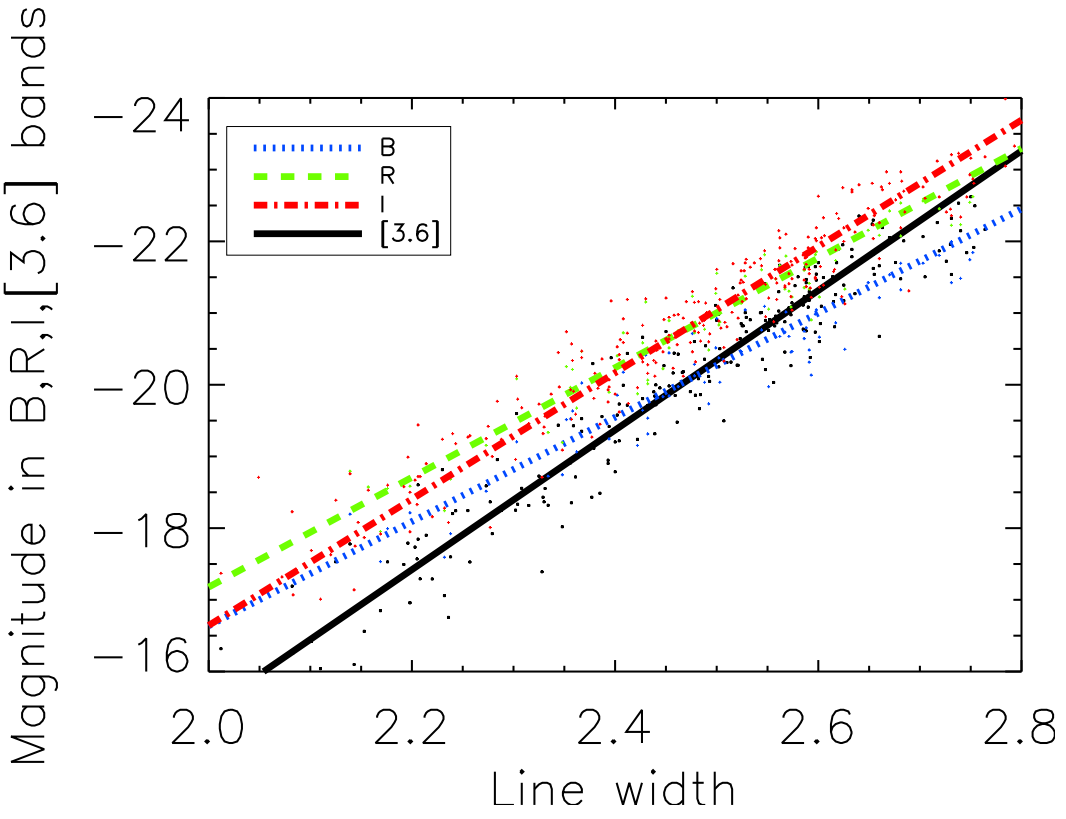

FIGURE 3.34: TFR in B, R, I and [3.6] bands. B and R bands data are from Tully and Pierce (2000) , I band data are from TC12 and [3.6] band data are from section 3.3. Linewidths are the same as used by TC12. The slopes steepen from blue to red, with values -7.27 at B, -7.65 at R, -8.81 at I, and -9.74 at [3.6].

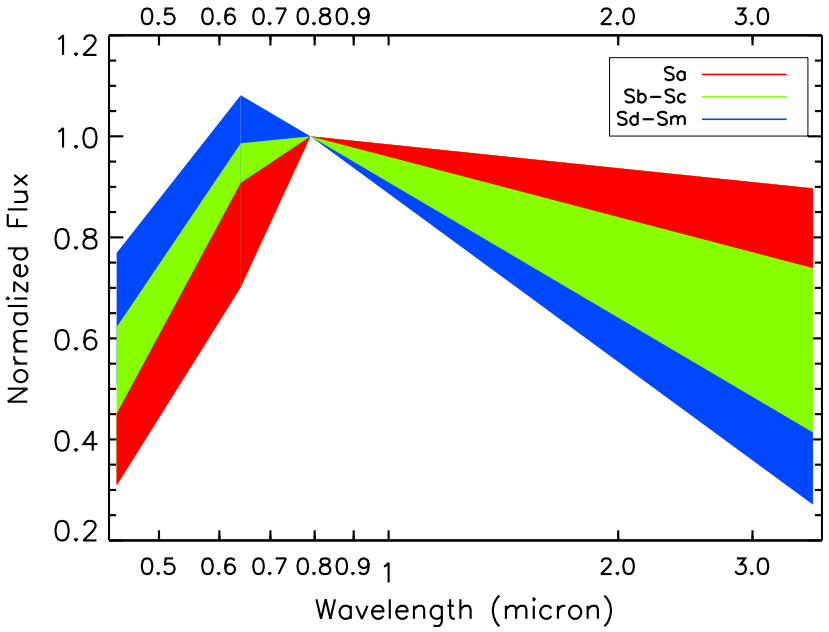

FIGURE 3.35: Representation of fluxes at B, R, I,[3.6] bands normalized to unity at I band. Type Sa: red; types Sb-Sc: green; types Sd-Sm: blue. The extrema are defined by members of our sample and color swaths indicate the domains dominated by the different types.

There have been long standing suggestions that the dispersion in the TFR might be reduced by inclusion of additional parameters. In an early instance (Rubin et al., 1985), when only photographic or photoelectric magnitudes were available, the case was framed in terms of galaxy types which are strongly correlated with color. Masters et al. (2006) have maintained the use of a type separation with I band work. Tully and Pierce (2000) acknowledged the hint of a type dependence in the I band relation but concluded that the evidence remained too weak to warrant adding complexity to the TFR analysis. The situation changes with the mid-infrared information. In spite of superior photometry the scatter in the TFR is increased and there is a significant color signature. The variations in spectral energy distribution implicit in the range of representative colors shown in Figure 3.35 provide a natural explanation given the extended lever arm from the optical to the [3.6] band.

There is also the possibility that some flux in the [3.6] band may come from other than old stars. Meidt et al. (2012) determined that 12±5% of [3.6] flux arises from hot dust, Polycyclic Aromatic Hydrocarbon emission, or young to intermediate age stars in six representative spiral galaxies observed with *Spitzer Space Telescope*. However the variance of 0.05 mag is small compared with the ITFR scatter. Moreover, it can be anticipated that the galaxies most affected by manifestations of star formation are later, bluer types, whence augmented flux will tend to diminish a color term arising from old stars. Whatever the cause, it can be anticipated that the scatter can be decreased with the introduction of a color correction. To address this issue we consider the straight line fits included in the top and bottom left panels of Figure 3.36. The fits are least squares minimizations on the ordinate parameter;

the difference in magnitude of a target from the mean TFR. The bottom right panel shows the concordant variation of color with linewidth. Faster rotators tend to be redder.

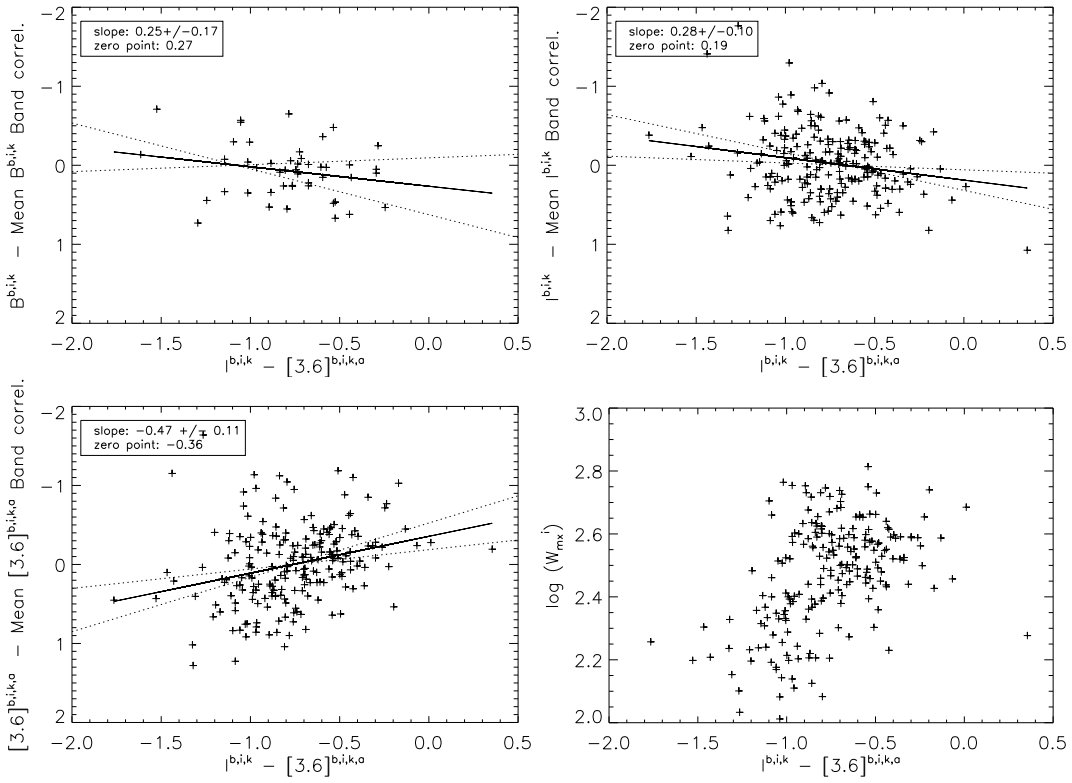

FIGURE 3.36: *Top and left bottom panels*: Deviations from the mean ITFR relation as a function of $I - [3.6]$ color. Solid and dotted lines are best fits and 95% probability limits. *Top left*: At B band red galaxies tend to lie below the mean relationship. *Top right*: At I band there is a hint that red galaxies lie low although the correlation fit is dominated by a few extreme cases. *Bottom left*: At [3.6] band the sense of the correlation has flipped and red galaxies tend to lie above the mean relation. *Bottom right*: The correlation between linewidth and color.

In the mid-infrared case, the offset for an individual galaxy from the mean fit in Figure 3.36 is:

$$\Delta M_{[3.6]}^{color} = M_{[3.6]}^{b,i,k,a} + 20.34 + 9.74(\log W_{mx}^{i} - 2.5). \tag{3.45}$$

An equivalent correction can be constructed with apparent magnitudes rather than absolute magnitudes, $\Delta[3.6]^{color} = \Delta M_{[3.6]}^{color}$, with an appropriate replacement of the zeropoint constant in equation 3.45. The correction term commensurate with the fit in the third panel of Figure 3.36 is:

$$\Delta[3.6]^{color} = \Delta M_{[3.6]}^{color} = -(0.47 \pm 0.11)[(I^{b,i,k} - [3.6]^{b,i,k,a}) + 0.77]. \tag{3.46}$$

where both $I^{b,i,k}$ and $[3.6]^{b,i,k,a}$ band magnitudes are in the AB system. $I^{b,i,k,a}$ is the corrected I-band apparent magnitude. We introduce a new color adjusted magnitude parameter $C_{[3.6]} = [3.6]^{b,i,k,a} - \Delta[3.6]^{color}$ where the distinct nomenclature emphasizes the composite

nature of this pseudo-magnitude. Next, the analysis discussed in subsection 3.4.1.2 leading to the construction of Figure 3.31 is repeated. Likewise, the adjustments are applied to the calibrators with independently established distances and the procedures that lead to Figure 3.33 are repeated. The adjusted relations are shown in Figure 3.37. The new correlation is described by the formula:

$$M_{C_{[3.6]}} = -(20.34 \pm 0.08) - (9.13 \pm 0.22)(\log W^i_{mx} - 2.5) \tag{3.47}$$

The flattening of the adjusted relation comes about since redder systems move downward and redder galaxies tend to have larger linewidths. The overall magnitude scatter in the new relation is ±0.44 magnitude (corresponding to a scatter in distance of 22%), down from 0.49 magnitude before adjustment, and comparable with 0.41 found at I band with an otherwise comparable analysis (TC12). The comparable numbers for the zeropoint calibrators alone are a scatter of 0.37 with the adjusted parameter $C_{[3.6]}$, 0.44 before the adjustment, and 0.36 at I band. The comparisons between [3.6] and I have some imprecision because the sample sizes for the latter are 25% greater. The TFR parameters derived from alternative samples and bandpasses are summarized in Table 3.7.

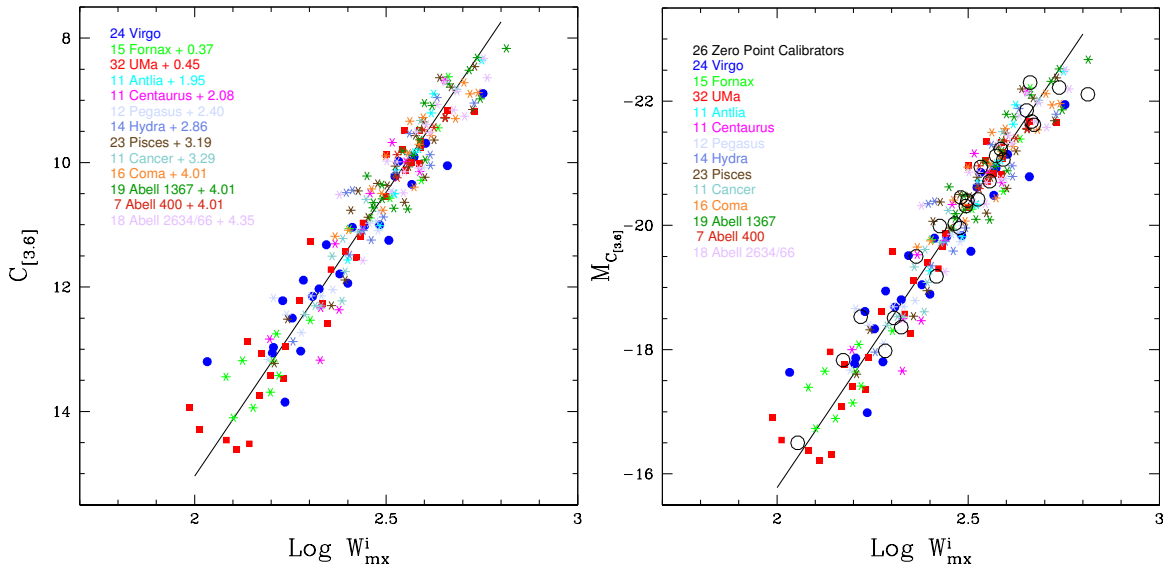

FIGURE 3.37: The ITFR after adjustments for the color term. *Left*: Color adjusted apparent magnitudes translated to the relative distance of the Virgo Cluster. *Right*: Color adjusted absolute magnitudes with the absolute distance scale established by the galaxies with independent distances represented by large open circles.

3.4.1.4 Bias and an Hubble Constant Estimate

Willick (1994) showed that a small Malmquist bias exists in the use of the ITFR, although reduced from the direct TFR by a factor of 6 in the situation he explored (Willick et al.,

1995). Reducing the bias reflects on the Hubble Constant (e.g. Bottinelli et al., 1986). The bias arises from two effects:

- sample selection departs from an idealized case of a flat magnitude limit because samples have been selected in blue bands and color terms translate to a slope in the limiting magnitude in the infrared: slower rotators which tend to be bluer are favored for inclusion over faster rotators which tend to be redder (see Figure 3.38, left). It is the so-called Gould's effect (Gould, 1993),
- the shape of the galaxy luminosity function contributes to the bias because there are more intrinsically fainter galaxies that scatter bright-ward through errors than intrinsically brighter galaxies that scatter faint-ward (Eddington, 1913). The bias increases with distance as the effect of the exponential cutoff of the luminosity function plays an increasing role while for the direct fit it is a constant whatever the completeness of the cluster considered is (e.g. Teerikorpi, 1990, 1993).

The Schechter luminosity function is written:

$$\Phi(L) = (\frac{\Phi^*}{L^*})(\frac{L}{L^*})^{\alpha}\exp(\frac{-L}{L^*}) \tag{3.48}$$

where L^* is a characteristic luminosity above which the distribution decreases exponentially, α is the slope for "small" luminosity L, and Φ^* specifies the normalization. Since $\frac{dL}{L} = -0.4\ \ln 10\ dM$ from the definition of the absolute magnitude 3.9, it can be rewritten as a function of magnitude:

$$\Phi(M) = \Phi(L)|\frac{dL}{dM}| = \Phi(L)0.4\ln 10L = (0.4\ln 10)\Phi^* 10^{0.4(\alpha+1)(M-M^*)}\exp(-10^{0.4(M^*-M)}) \tag{3.49}$$

where $M^* \propto -2.5\log L^*$. This equation depends both on galaxy type and environment.

The amplitude of the bias from the two effects was explored with the calibration at I band (TC12). The situation now with the [3.6] band sample is slightly worse than at I because the wavelength interval from selection at B is larger. The bias analysis carried out in the case of the I band calibration is repeated here, tailored to the current situation. We first combine the Virgo, Fornax, and Ursa Major samples to improve statistics and include contributions from a range of environments. This ensemble is described by a Schechter (1976) function with faint end slope $\alpha = -0.9$ and a bright end cutoff at $M^{\star}_{[3.6]} = -22$. Then we randomly populate an artificial TFR to match the observed [3.6] band relation in terms of slope and zeropoint, drawing from the Schechter luminosity function. We fake a scatter of 0.4 magnitude. The faint limit or cutoff is determined empirically to roughly obey the relation $M^{lim}_{[3.6]} = C_\ell - 2.70(\log W^i_{mx} - 1.8)$ where C_ℓ couples with distance. The artificial TFR and the cutoff for

the nearest clusters is shown in the left panel of Figure 3.38. The dashed blue line indicates the cutoff experienced at a distance modulus of 31. The cutoff, characterized by C_ℓ, slides to brighter (more negative) magnitudes linearly with increasing distance modulus. The bias $\langle \Delta M \rangle_{measured}$ is determined at intervals of C_ℓ corresponding to increasing distance. More precisely, for each successive sample with a different cutoff C_ℓ, the inverse slope is determined and compared to the expected slope without any bias (namely, slope given to the artificial TFR). Then $\langle \Delta M \rangle_{measured}$ is the average deviation in magnitudes obtained with the inverse slope from the fiducial relation with the expected slope where $\langle \Delta M \rangle_{true} = 0$ by construction. The growth of the bias as a function of cutoff magnitude is seen in the right panel of Figure 3.38. The solid curve, normalized to zero at a distance modulus $\mu = 31$ where even the faintest of useful candidates are included, is described by the formula between bias, b, and distance modulus, μ:

$$b = -0.0065(\mu - 31)^2 \tag{3.50}$$

By comparison, the coefficient in the case of the I band analysis is -0.005. The letters at the bottom of the figure are codes for the 13 calibrating clusters (see Table 3.5 to decipher codes) and their horizontal placements indicate the respective sample limits and projection upward gives the corresponding biases. These biases are recorded in Table 3.5 and are reflected in the adjusted cluster moduli and distances. For a galaxy in the field, the corrected distance modulus μ^c can be expressed as

$$\mu^c = (C_{[3.6]} - M_{C_{[3.6]}}) + 0.0065[(C_{[3.6]} - M_{C_{[3.6]}}) - 31]^2 \tag{3.51}$$

The last column in Table 3.5 records the "Hubble parameter" for each cluster: the velocity of the cluster in the CMB frame divided by the measured distance. These quantities are plotted against distance in Figure 3.39. A similar figure was presented as a summary of results from the I band calibration with the same 13 clusters (TC12: distances compared in Table 3.7). Here, as there, we see a large scatter in the Hubble parameter for the nearer clusters and small scatter for the more distant clusters. It can be anticipated that the measures for the nearer clusters are strongly affected by peculiar motions. The five clusters within 40 Mpc are all part of our extended supercluster complex: either within the historic Local Supercluster or the so-called Great Attractor region. The low scatter among the seven clusters more distant than 50 Mpc ($v_{CMB} > 4000$ km s^{-1}) suggests that the relative contributions of peculiar velocities have a modest effect on redshifts at such large distances.

In the case of the I band calibration, the mean value of the Hubble parameter for the seven most distant clusters was 75.1 ± 2.7 km s^{-1} Mpc^{-1} where the error is just the root mean square scatter of the seven contributions. That value would increase to 75.8 with the revised Large Magellanic Cloud distance from Monson et al. (2012). With the present calibration, including the new Large Magellanic Cloud distance, the fit shown in Figure 3.39 gives a value

of $H_0 = 73.8$ with a root mean square scatter of 1.1 and a standard deviation of 0.4 km s^{-1} Mpc^{-1} for the same seven clusters considered previously. If the fit is extended to include the Pegasus Cluster at 44.5 Mpc then $H_0 = 74.4$ and the scatter is 2.0 km s^{-1} Mpc^{-1}. The effect of a deviant radial motion of 200 km s^{-1} is illustrated in the figure as a function of distance.

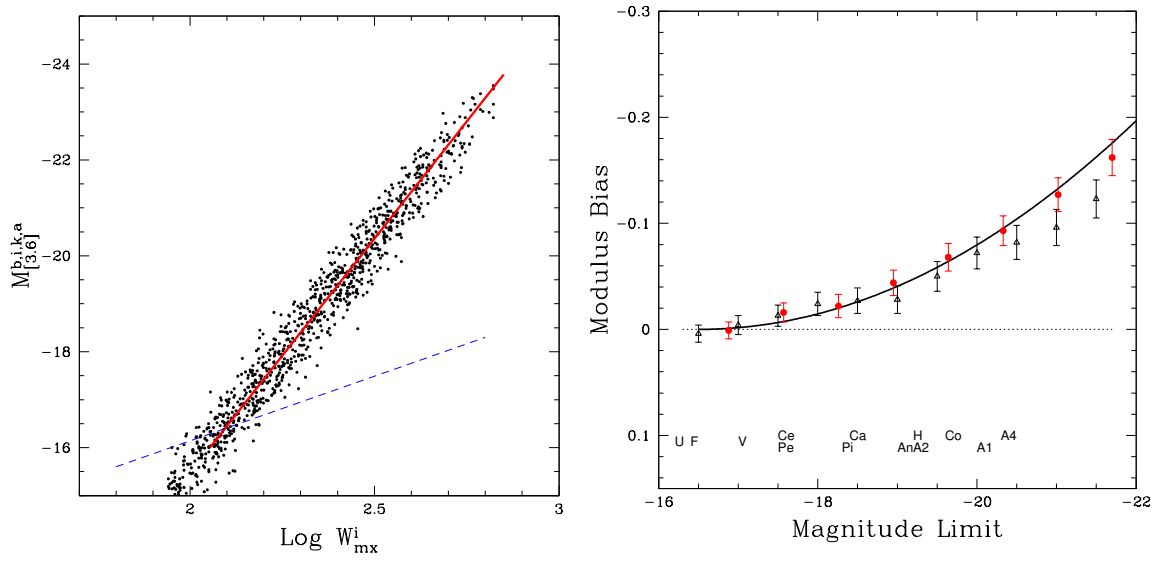

FIGURE 3.38: *Left*: Simulated TFR drawing randomly from a Schechter luminosity function with slope $\alpha = -0.9$ and cutoff $M^\star = -22$. The ITFR has slope -9.13 and scatter 0.4 magnitude. The dashed blue slanting line illustrates the color dependence at the faint limit resulting from sample selection in the blue. *Right*: Bias $\langle \Delta M \rangle_{measured}$ as a function of absolute magnitude limit which increases with distance. Black triangles: flat faint limit; red circles: faint limit increasing with increasing linewidth in accordance with the blue line in the left panel. Solid curve: the empirical bias fit $b = -0.0065(\mu - 31)^2$. Letters at the bottom are codes for the 13 calibrating cluster (see Table 3.5 for translation of codes). Their horizontal positions indicate sample limits and vertical intercepts with the solid curve give the corresponding biases.

The uncertainty from the fit in Figure 3.39 is given by the statistics of the deviations of the seven contributions. It is unrealistically low. This error is what is expected if there is perfect Hubble expansion. If peculiar motions of 200 km s^{-1} are the norm, and given the expected statistical errors on the distance D of each cluster (4-5 % according to Table 3.5), the anticipated scatter around the mean Hubble value is ± 2.6 km s^{-1} Mpc^{-1}. We have used the propagation of error formula giving in this case:

$$err_{H=\frac{v}{D}} = \sqrt{(\frac{\partial H}{\partial v} err_v)^2 + (\frac{\partial H}{\partial D} err_D)^2} = \frac{1}{D}\sqrt{200^2 + (v \times 0.045)^2} \qquad (3.52)$$

where the error on the velocity v was assimilated to the peculiar motions and $0.045 = \frac{err_D}{D}$ is a compromise between the 4-5 % statistical error on distances. The scatter is half this value. We consider this to be our 1 σ random error. We have several sources of systematic error. The dominant component, creating almost 4% uncertainty in H_0, comes from the

uncertainty in the TFR zeropoint with just 26 calibrators. Combined with a small uncertainty from the finite population of the template, the uncertainty in H_0 associated with the TFR calibration (assuming the zeropoint calibrator distances are perfect) is typically ± 2.9 km s^{-1} Mpc^{-1}. We have used 1) the error on the zeropoint (and distance modulus μ) 0.08 mag, 2) $err_D = err_\mu \frac{\ln(10)}{5} D$ from the definition of the distance modulus 3.10 and 3) formula 3.52 reduced to errors on distances D solely. However, the zeropoint calibrator distances are not perfect. Freedman et al. (2012) and Riess et al. (2011) report that with new Milky Way parallaxes for Cepheid stars and mid-infrared Spitzer photometry the uncertainty in the Cepheid scale is in the range $\pm[1.9 - 2.5]$ km s^{-1} Mpc^{-1}. The TRGB zeropoint calibration which concerns 4 of the 26 calibrators, has similar or smaller systematics. The cumulative systematic error (sum in quadrature) in H_0 is $\pm[3.5-3.8]$ km s^{-1} Mpc^{-1}. Combining random and systematic components we find $H_0 = 73.8 \pm 2.6(\text{ran}) \pm [3.5 - 3.8](\text{sys})$ km s^{-1} Mpc^{-1}.

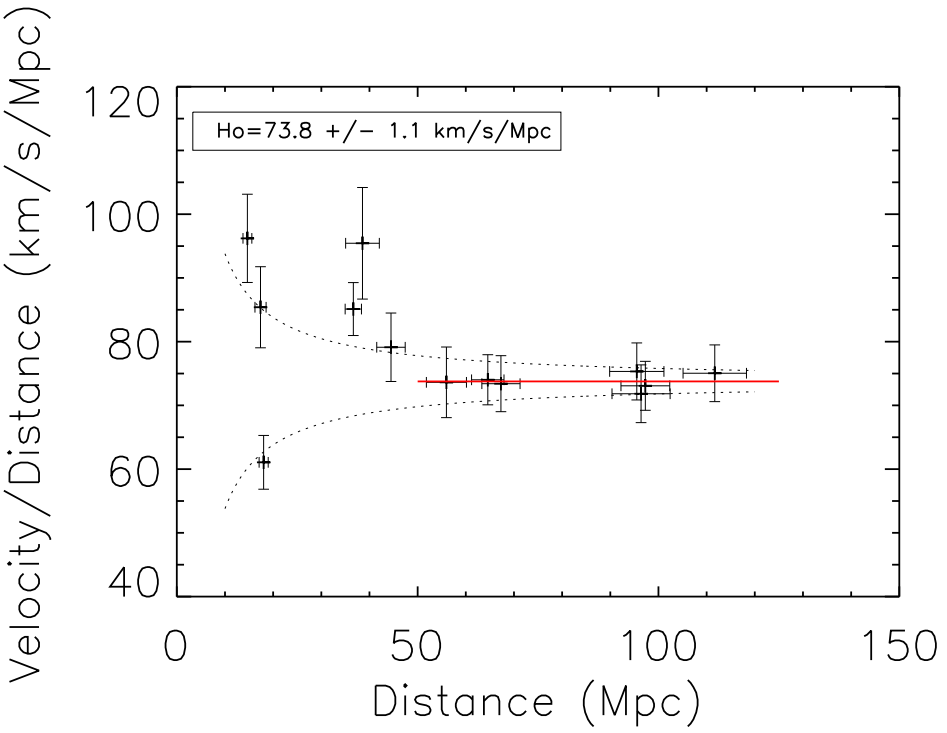

FIGURE 3.39: Hubble parameter as a function of distance. The red solid line is a fit to cluster points at distances greater than 50 Mpc ($v_{CMB} > 4000$ km s^{-1}). The fit gives $H_0 = 73.8 \pm 1.1$ km s^{-1} Mpc^{-1}. Curved dotted lines illustrate deviations in velocity of 200 km s^{-1} from the fit.

3.4.2 Robustness of the Calibration

In this section, the robustness of both the calibration method and the mid-infrared TFR presented in the previous subsections is shown. The previously expounded calibration was indeed presented at the time of its release as preliminary, especially because of the lack of completeness of the calibrator sample. Still, this subsection confirms this first calibration.

Magnitudes used in this subsection come from ARCHANGEL (Cosmicflows with Spitzer survey completed in the mean time). They are combined with this time S^4G-pipeline (magnitudes publicly released in the mean time) or CHP-pipeline magnitudes (as earlier) or both when they are available.

3.4.2.1 Increasing the Calibrator Sample and Changing the Selection Band

The previously derived template TFR made use of 213 galaxies in 13 clusters. The zero point calibration was given by 26 additional galaxies. The inverse fit was used to calculate the slope of the relation and a very small correction was computed to remove a bias. The same analysis is done here but using an updated sample of template and zeropoint calibrators. This sample is improved with respect to the previous one by two aspects:

- the number of calibrators is increased from 213+26 to 287+32. The list of these calibrators and characteristics are given in the second table (Table B.2) of Appendix B,
- galaxies are now selected in K Band which decreases the selection bias. The selection of calibrators is extended to be complete to K=11.75 magnitude, the limit of the 11.75-2MASS Redshift Survey (Huchra et al., 2012)

This new set of calibrators follows the same rules as the previous one. Typically, candidates are chosen out of a projection-velocity window, morphological types earlier than Sa are excluded, profiles with visible confusion or tidal disruption are disregarded and inclinations must be greater than 45°. Zeropoint calibrators also need to have a very well known distance from Cepheid or Tip of the Red Giant Branch measurements.

Then, we proceed exactly as described in subsection 3.4.1:

- an inverse TFR is fitted to each one of the clusters separately. Figure 3.40 left shows the example of the Virgo cluster. Parameters for every cluster are given in Table 3.6. The inverse fit assumes errors only in linewidth to obtain results close to free of Malmquist magnitude selection bias. Yet, there will be a tiny bias residual because of the bright end cutoff of the luminosity Schechter function although it should be somewhat smaller than for the previous calibration where, in addition, the selection was made in the B band. We investigate this bias relic at the end of this subsection,

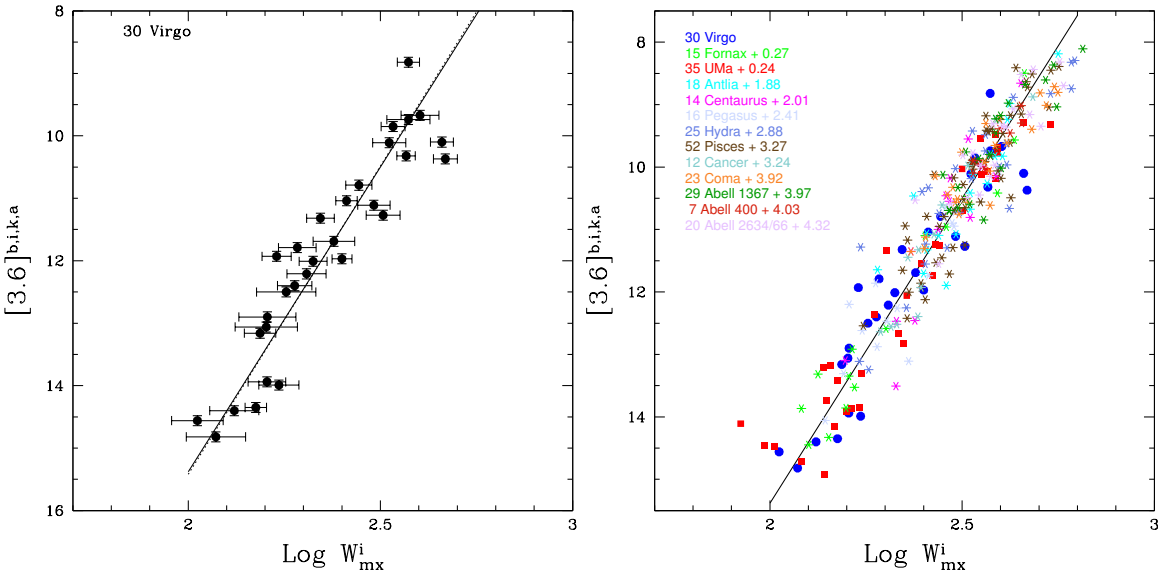

FIGURE 3.40: *Left*: Inverse Tully-fisher relation at 3.6 microns for the Virgo cluster in dotted line. The solid line stands for the inverse Tully-Fisher of the template cluster. *Right*: Universal inverse TFR at 3.6 microns obtained with 287 galaxies in 13 clusters. Numbers of galaxies selected for the calibration per clusters are given in front of clusters' names while distance modulus differences between each cluster and Virgo are visible after clusters' names.

- because slopes are quite similar between clusters in Table 3.6, individual fits are consistent with the postulate of a universal TFR. Thus the 13 clusters are combined into one template cluster. Virgo is taken as the reference cluster and each one of the 12 other clusters is shifted to be on the same scale. Three by three, clusters are inserted into the template and offsets between them and Virgo are found by an iterative process which relies on least squares fits of the inverse TFR. Convergence is quick. We obtain a slope of -9.77 ± 0.19, insignificantly different from the previous slope -9.74 confirming the robustness of the previous calibration and of the method. The universal slope and the offsets with respect to Virgo are shown on Figure 3.40 right,

- the zeropoint scale is set by the distance modulus of the Large Magellanic Cloud, 18.48 ± [0.04-0.07] magnitude (Monson et al., 2012; Riess et al., 2011). Then, the 32 zeropoint calibrators give the zeropoint of the universal TFR assuming the slope of the cluster template. Their correlation is visible on Figure 3.41 left where now absolute magnitudes replace apparent magnitudes. The zeropoint of the TFR is the difference between the zeropoint given by zeropoint calibrators on Figure 3.41 left and by Virgo in Figure 3.40 right: -20.31 ± 0.09. The zeropoint is once again insignificantly larger than that of the previous calibration, -20.34,

- the universal relation at 3.6 microns is visible on Figure 3.41 right and is given by a slightly updated version of the previous calibration 3.44:

$$M^{b,i,k,a}_{[3.6]} = -(20.31 \pm 0.09) - (9.77 \pm 0.19)(\log W^i_{mx} - 2.5) \tag{3.53}$$

with a scatter of 0.54 for the 13 clusters and 0.45 for the 32 zeropoint calibrators. The causes of such a scatter have already been discussed. We will again apply a color correction in the next subsection to confirm the color corrected TF relation derived before and the robustness of such a process.

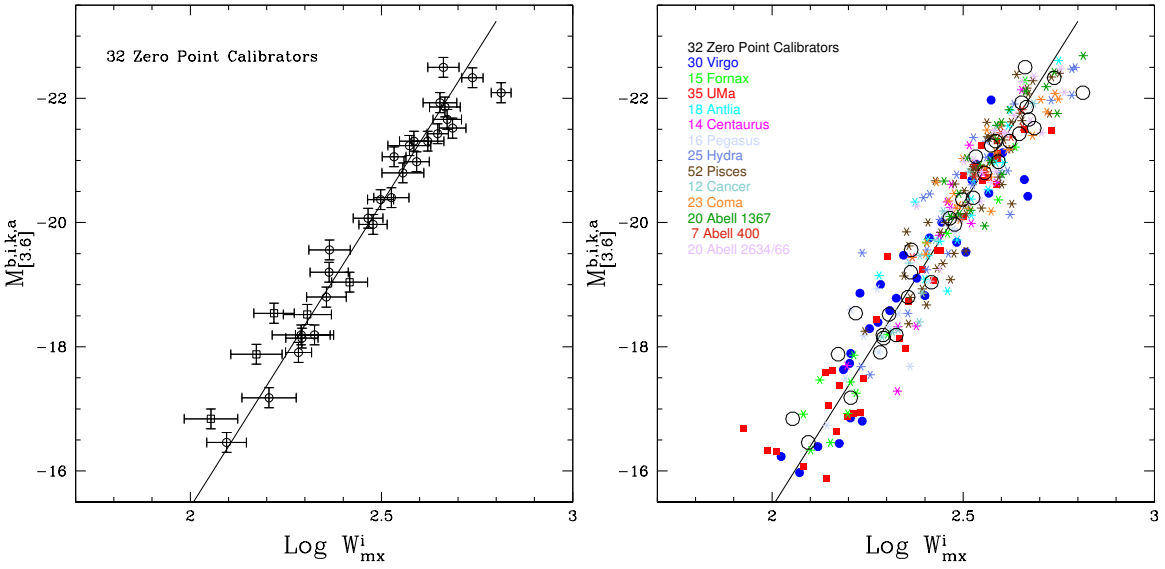

FIGURE 3.41: *Left*: Inverse TFR for the 32 zeropoint calibrators with distances obtained with Cepheids (circles) or Tip of the Red Giant Branch (squares). The slope of the solid line is given by the luminosity-linewidth correlation of the template cluster while the zeropoint is obtained with the least squares fit to the 32 galaxies. The zeropoint is set at $\log W^i_{mx} = 2.5$. *Right*: Inverse Tully-Fisher relation at 3.6 microns with the slope built out of 287 galaxies in 13 clusters and the zeropoint set by 32 galaxies with very accurate distances.

3.4.2.2 Again a Color Term

Because of the increased number of data, we double check the color term deriving a new estimate. The straight line fit given in Figure 3.42 left is again a least squares minimization with respect to the difference in magnitude of a galaxy from the derived TFR. In the [3.6] band, a galaxy is offset from the TFR by:

$$\begin{aligned} \Delta M^{color}_{[3.6]} &= M^{b,i,k,a} + 20.31 + 9.77(\log W^i_{mx} - 2.5) \\ &= -(0.52 \pm 0.10)[(I^{b,i,k} - [3.6]^{b,i,k,a}) + 0.73] \end{aligned} \tag{3.54}$$

Note that I Band magnitudes have been shifted from the Vega to the AB system by 0.342 magnitude. Slope and zeropoint are slightly smaller than those obtained before (-0.47 and -0.36) but within the uncertainty. Still, for completeness, we use this new estimate. Color

adjusted parameters, $C_{[3.6]} = [3.6]^{b,i,k,a}$ - $\Delta[3.6]^{color}$, are derived accordingly and then, considered as pseudo-magnitudes to produce the "control" color corrected calibration. The procedure described in the previous subsection is reiterated with a number of galaxies slightly decreased due to a lack of I Band measurements (273+31).

This color corrected calibration is visible on Figure 3.42 right and given by:

$$M_{C_{[3.6]}} = -(20.31 \pm 0.07) - (9.10 \pm 0.21)(\log W^i_{mx} - 2.5) \tag{3.55}$$

with 0.45 and 0.37 as new scatters. A summary of the derived parameters for this TFR are given in Table 3.7 as well as in Table 3.8 along those of the previous calibration and those of TC12 for the I Band. Although a direct comparison has some imprecision because of the different galaxy samples, the agreement is excellent. The robustness of the procedure and of the derived TF relations is confirmed. Namely, no major bias affects the relation as it is almost independent of the calibrator sample in terms of completeness and band selection.

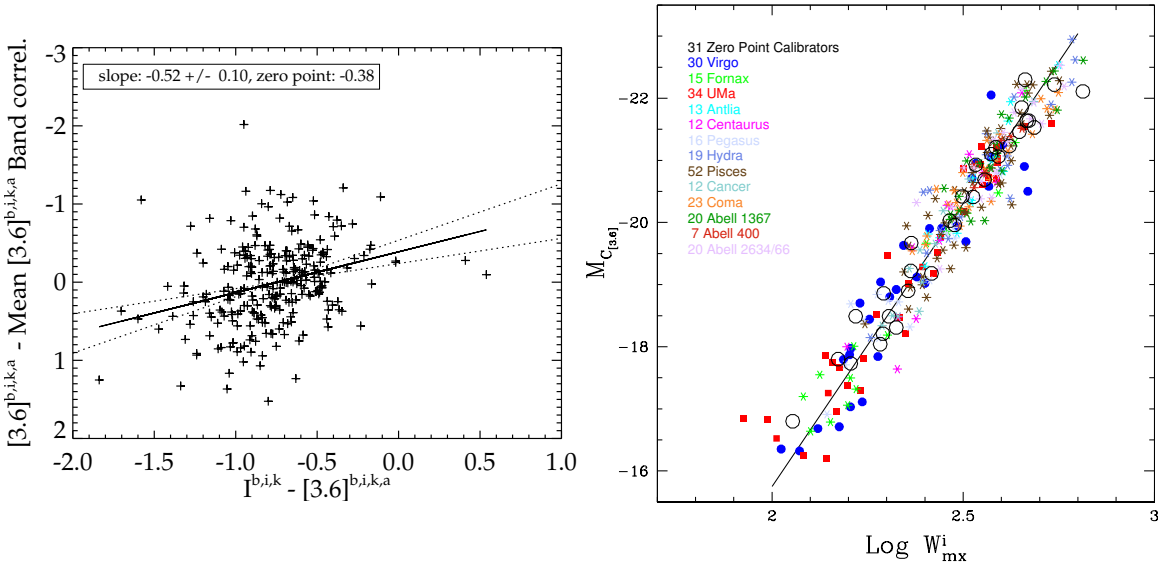

FIGURE 3.42: *Left*: Deviation from the universal inverse TFR as a function of $I^{b,i,k}$ - $[3.6]^{b,i,k,a}$ color. The solid line stands for the best fit while the dotted lines represent the 95% probability limits. Red galaxies tend to lie above the relation while blue galaxies are preferentially below the relation. *Right*: Relation for pseudo-absolute magnitudes with the zeropoint set by galaxies with independent very accurate distance estimates (open circles).

3.4.2.3 Re-derivation of the Bias

Although all TFRs derived are again inverse fits (errors solely in linewidths), a small Malmquist selection bias residual still remains. The situation is improved in this case because galaxies are selected in K (instead of B) band. This change in wavelength selection reduces the interval between sample selection and photometry bands. However, because of the morphology

of the luminosity function, the amplitude of the bias still increases with distance as the selection limit approaches the exponential cutoff of the luminosity function. Consequently, the bias analysis is reiterated but without consideration of a faint end cutoff color dependence. Virgo, Fornax and Ursa Major are this time modeled with a Schechter (1976) function with a faint end slope of -1.0 and a bright end cutoff at -22. Then, a random population is built out of this Schechter function to match the TFR at 3.6 microns in terms of slope, zeropoint and scatter. The bias is estimated as the average deviation of sampled distances from the input TFR for successive brighter cutoffs but we take the opposite convention with respect to before for conveniency. The corresponding curve normalized to zero at a distance modulus of 31 is shown in Figure 3.43 and can be written:

$$bias = 0.004(\mu - 31)^{2.3} \tag{3.56}$$

where μ is the distance modulus. The coefficient 0.004 is smaller than before (0.0065) because of the previous color dependence. However, the 2.3 exponent is larger than before because of a larger assumed scatter (0.45 against 0.4) which confirms that the scatter dominates the bias relic (Giovanelli et al., 1997a). At the bottom of Figure 3.43, letters standing for the 13 clusters are positioned at their cutoffs while the corresponding biases are given by projection onto the curve. Bias corrections for each cluster are given in Table 3.7 alongside the letters to match them with the names of clusters. Corrections are already included in moduli and distances given in this same table. As for an individual galaxy, the bias corrected distance modulus μ is obtained by adding $0.004(\mu - 31)^{2.3}$. For completeness, the bias correction for the *non* color adjusted relation, obtained similarly, is given by $bias = 0.006(\mu - 31)^{2.3}$.

Distances obtained for the 13 clusters are compared with previous estimates in Table 3.8. Overall distances are in good agreement with each other and within uncertainties. Combining these distances with velocities with respect to the cosmic microwave background, but this time corrected for a cosmological model assuming $\Omega_m = 0.27$ and $\Omega_\Lambda = 0.73$ with the approximative formula in Tully et al. (2013) (to account for the fact that the real total velocity is given by formula 3.7), it is possible to derive a "Hubble parameter" for each cluster. These values are given in Table 3.7 and plotted in Figure 3.44. A straight line fit to the logarithms of these parameters for clusters at a distance greater than 50 Mpc gives a Hubble value of 75.0 $\pm$ 3.9 km s^{-1} Mpc^{-1} where 3.9 correspond to twice the statistical scatter. Proceeding with equation 3.52 as before, we found 2.0 km s^{-1} Mpc^{-1}. Then 2.0 stands for the 1 σ random error and the cumulative systematic error is the same as before (the only change is the error on the zeropoint that is insignificantly decreased from 0.08 to 0.07). Then, combining all the uncertainties $H_0 = 75.0 \pm 2.0$ (ran) $\pm$ [3.5-3.8] (sys) km s^{-1} Mpc^{-1}. This value is somewhat different to that obtained before principally because of the use of better estimates of total velocities. Still, first and second estimates are within uncertainties and differ only at the level of 1.2 km s^{-1} Mpc^{-1}. The change in total velocities

brings the Hubble Constant estimate close to the value found in the I Band (75.1) and to the value found including the sample of supernovae (75.2, that we derived using the previous calibration and which is presented in the next subsection, 3.4.3).

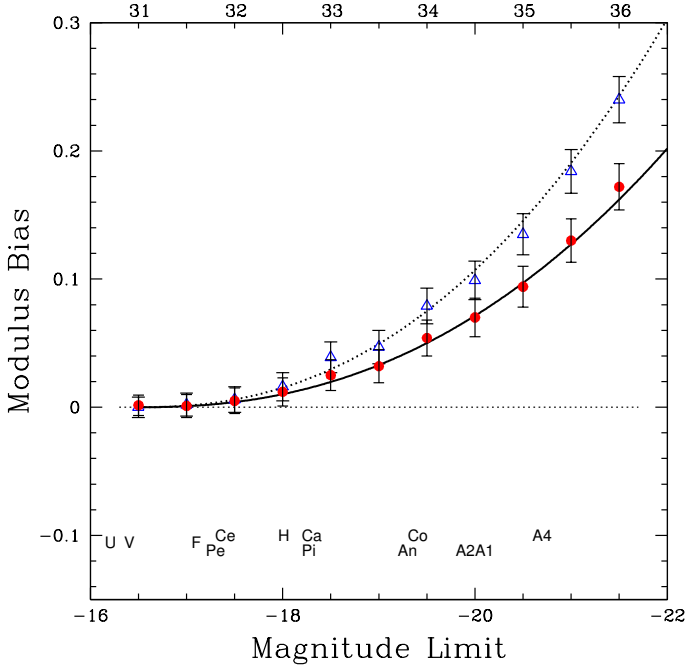

FIGURE 3.43: Bias measured as a function of absolute magnitude cutoff. The dotted and solid black curves are fits to the blue triangles and red filled circles which are bias estimates at successive cutoffs for the [3.6] TF calibration and for the color adjusted TF relation. The formulas are $0.004(\mu - 31)^{2.3}$ for the red curve and $0.006(\mu - 31)^{2.3}$ for the blue curve. Letters at the bottom stand for the 13 clusters given in Table 3.7. They are positioned at the magnitude limits of clusters and their vertical projections onto the curve give the corresponding biases. The bias for an individual galaxy with a measured modulus is given by projection onto the curves from the top axis.

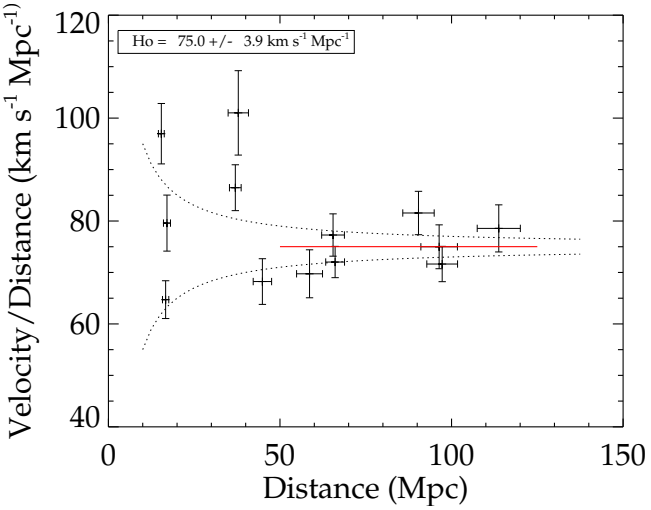

FIGURE 3.44: Hubble parameter as a function of distance. The solid red line at 75.0 ± 3.9 km s^{-1} $Mpc^{-1}$is a fit to the logarithms of cluster "Hubble parameters" at distances greater than 50 Mpc. Dotted lines show the expected values for a deviation of ± 200 km s^{-1} from the mean Hubble flow.

	v_{mod}	eV	N	Slope	ZP	scatter	ZP_{color}	scatter	bias	DM	Dist	V/D
V	1495	37	30-30	-9.88±0.73	10.50±0.12	0.64	10.63±0.10	0.55	0.00	30.94±0.12	15.4±0.9	97.0±5.9
F	1358	45	15-15	-9.56±0.63	10.77±0.12	0.46	10.85±0.11	0.42	0.00	31.16±0.13	17.1±1.0	79.6±5.4
U	1079	14	35-34	-9.32±0.52	10.74±0.11	0.64	10.80±0.10	0.57	0.00	31.11±0.12	16.7±0.9	64.7±3.7
An	3198	74	18-13	-10.07±1.33	12.37±0.12	0.52	12.48±0.07	0.27	0.05	32.84±0.10	37.0±1.7	86.5±4.5
Ce	3823	82	14-12	-12.92±1.74	12.51±0.16	0.60	12.58±0.16	0.55	0.00	32.89±0.17	37.8±3.0	101±8.2
Pe	3062	78	16-16	-9.84±1.03	12.91±0.14	0.55	12.94±0.11	0.44	0.01	33.26±0.13	44.9±2.7	68.2±4.4
H	4088	72	25-19	-9.12±0.94	13.38±0.14	0.71	13.52±0.13	0.55	0.01	33.84±0.14	58.6±3.8	69.7±4.7
Pi	4759	39	52-52	-11.02±0.75	13.77±0.07	0.50	13.76±0.06	0.45	0.03	34.10±0.09	66.1±2.7	72.0±3.0
Ca	5059	82	12-12	-11.65±1.02	13.74±0.11	0.39	13.75±0.10	0.31	0.02	34.08±0.11	65.5±3.3	77.3±4.1
Co	7370	76	23-23	-7.97±0.67	14.42±0.10	0.49	14.40±0.09	0.42	0.07	34.78±0.11	90.4±4.6	81.6±4.2
A4	7228	97	7-7	-8.00±1.38	14.47±0.11	0.48	14.46±0.09	0.42	0.15	34.92±0.12	96.4±5.3	75.0±4.3
A1	6969	93	20-20	-9.32±0.92	14.53±0.08	0.21	14.53±0.07	0.19	0.10	34.94±0.10	97.3±4.5	71.6±3.4
A2	8938	164	20-20	-9.55±0.97	14.82±0.11	0.50	14.88±0.10	0.43	0.09	35.28±0.12	113.8±6.3	78.6±4.6

TABLE 3.6: Properties of the Cluster Fits (Robustness): (1) Cluster name (V Virgo, F Fornax, U Ursa Major, An Antlia, Ce Centaurus30, Pe Pegasus, H Hydra, Pi Pisces, Ca Cancer, Co Coma, A4 Abell 400, A1 Abell 1367 and A2 Abell 2634 and 2666, (2) Mean velocity of the cluster with respect to the CMB corrected for the cosmological model, km s^{-1}, (3) Error on the velocity, km s^{-1}, (4) Number of studied galaxy per cluster for the original TFR and for the color-corrected TFR, (5) Slope of the inverse fit, (6) Zero point relative to Virgo's zeropoint, no color adjustment, mag, (7) Scatter, no color adjustment, (8) Zero point relative to Virgo's zeropoint after color adjustment, mag, (9) Scatter after color adjustment, mag, (10) Bias, mag, (11) Bias corrected Distance Modulus, mag, (12) Cluster Distance, Mpc, (13) Hubble parameter, km s^{-1} Mpc^{-1}.

Sample	Ngal	Slope	Scatter	Zero Point
I template	267	-8.81±0.16	0.41	–
I zeropoint	36	–	0.36	-21.39±0.07 (Vega)
[3.6] template	213	-9.74±0.22	0.49	–
[3.6] zeropoint	26	–	0.44	-20.34±0.10 (AB)
M_C template	213	-9.13±0.22	0.44	–
M_C zeropoint	26	–	0.37	-20.34±0.08 (AB)
Control [3.6] template	287	-9.77±0.19	0.54	–
Control [3.6] zeropoint	32	–	0.45	-20.31±0.09 (AB)
Control M_C template	273	-9.10±0.21	0.45	–
Control M_C zeropoint	31	–	0.37	-20.31±0.07 (AB)

TABLE 3.7: TFR parameters in TC12 for the I Band obtained with the B band selected calibrator sample, in subsection 3.4.1 for the [3.6] calibration derived with part of the B band selected calibrator sample and in subsection 3.4.2 for the calibration computed with K band selected calibrators.

Cluster	Control	Calib.	TC12	Cluster	Control	Calib.	TC12
Virgo	15.4±0.9	14.7±0.9	15.9±0.8	Pisces	66±3	65±3	64±2
Fornax	17.1±1.0	17.4±1.2	17.3±1.0	Cancer	66±3	67±4	65±3
Ursa Major	16.7±0.9	18.0±0.9	17.4±0.9	Coma	90±5	95±6	90±4
Antlia	37±2	37±2	37±2	Abell 400	96±5	97±5	94±5
Centaurus	38±3	39±4	38±3	Abell 1367	97±5	96±6	94±5
Pegasus	45±3	45±3	43±3	A 2634/66	114±6	112±7	/
Hydra	59±4	56±4	59±4	Abell 2634	/	/	121±7

TABLE 3.8: Comparisons between cluster distances from subsections 3.4.2, 3.4.1 and TC12: (1)-(4) Cluster name, (2)-(5) control calibration distance, Mpc, (3) calibration distance, Mpc (4) TC12 distance, Mpc

3.4.3 Hubble Constant & Supernovae of Type Ia

This subsection builds on a calibration of the SNIa absolute distance scale begun with a core of distances based on the correlation between galaxy rotation rates and optical I_C band photometry. This work extends the calibration to the use of mid-infrared photometry acquired at 3.6 *μm with* Spitzer Space Telescope. *The great virtue of the satellite observations is constancy of the photometry at a level better than 1% across the sky. This calibration is based on 39 individual galaxies and 8 clusters that have hosted well observed SNIa. The* 3.6 *μm calibration at time of this work was not yet as extensively based as the I_C band calibration but was already sufficient to justify a report. Regardless, it has been shown to be robust in the previous subsection. Distances based on the mid-infrared photometry are insignificantly different than reported at I_C band. The I_C band result is confirmed with only a small adjustment. Incorporating a 1% decrease in the Large Magellanic Cloud distance, the study indicates $H_0 = [75.2 - 75.9] \pm 3.3$ km s^{-1} Mpc^{-1}.*

In subsection 3.1.3, the SNIa method was expounded as the potential supplier of the best Hubble parameter estimate once the zeropoint scale is set. Independent distances are needed to the hosts of low redshift SNIa (Folatelli et al., 2010; Riess et al., 2011, 2009) to establish that absolute scale. The Cosmicflows project had already contributed to the establishment of the SNIa scale (Courtois and Tully, 2012b) primarily using constraints imposed by distances acquired with the correlation between the luminosities and rotation rates of galaxies (Tully and Fisher, 1977), the Tully-Fisher relation (TFR). Optical I_C band luminosities were used in that study. Now there is the opportunity to refine the calibration with the use of photometry at 3.6 μm obtained with *Spitzer Space Telescope* (Werner et al., 2004). The great advantage with Spitzer observations is photometric integrity to better than 1% across the sky. Additional advantages are minimal obscuration either within hosts or from our Galaxy,

magnitude measures approximating total magnitudes because of low backgrounds, and fluxes dominated by light from old stars which presumptively correlates with galaxy mass. Roughly 4000 galaxies have been observed with *Spitzer* and at the time of this work already, 39 galaxies had been observed that have hosted SNIa and are appropriate for an application of the TFR methodology. The present discussion parallels the paper by Courtois and Tully (2012b) with the important difference being the use of mid-infrared [3.6] photometry in place of optical I_C photometry.

Three parameters are needed to obtain distances with the TFR: a luminosity, a measure of rotation, and an inclination to account for projection effects. Our sample in this study is a subset of the sample used for the same purpose of a determination of SNIa host absolute luminosities by Courtois and Tully (2012b). Consequently, we use the same information on rotation rates, from HI profile information, and inclinations, from optical band imaging. The difference in this work is the replacement of I_C luminosities with [3.6] luminosities from observations using *Spitzer Space Telescope* IRAC channel 1. At the time of this work we had 39 galaxies (close to our current number of 45) that have hosted SNIa from the list of 56 galaxies given by Courtois and Tully (2012b). Their parameters are accumulated in Table 3.11. Using the TFR, we obtain their distance estimates.

Distance measurements obtained via the TFR are individually uncertain. Averaging over a cluster provides a more robust distance so we include clusters in our analysis. Thirteen clusters were used to form the calibration template for the [3.6] band TFR so there is a good distance determination for each of these clusters. Suitably observed SNIa have been observed in eight of these clusters. Pertinent information is provided in Table 3.9. With the two nearest clusters (Virgo and Fornax) high quality distance measures are available from Cepheid and Surface Brightness Fluctuation observations and these measures contribute to (indeed, dominate) the values of the moduli in column 3 of the table. The averaging over multiple contributions follows Courtois and Tully (2012b). When there were more than one SNIa observed per galaxy or cluster, or more than one observation per SNIa, we take averaged SNIa modulus estimates.

Distances determined with the TFR enable us to set a zeropoint for the SNIa distance scale. Consideration of a large sample of SNIa in the redshift range $0.03 < z < 0.5$ leads us to an estimate of the Hubble Constant. Courtois and Tully (2012b) discuss the accumulation of a sample of SNIa from five sources (Amanullah et al., 2010; Folatelli et al., 2010; Hicken et al., 2009; Jha et al., 2007; Prieto et al., 2006) with scale shifts as appropriate to match the scale of the last of these sources, a compilation referred to as UNION2. Relevant distance moduli are gathered from these five sources and recorded in Tables 3.9 and 3.11 with averaging in the case of clusters with multiple recorded SNIa events. Moduli drawn from the tables are compared in Figure 3.45.

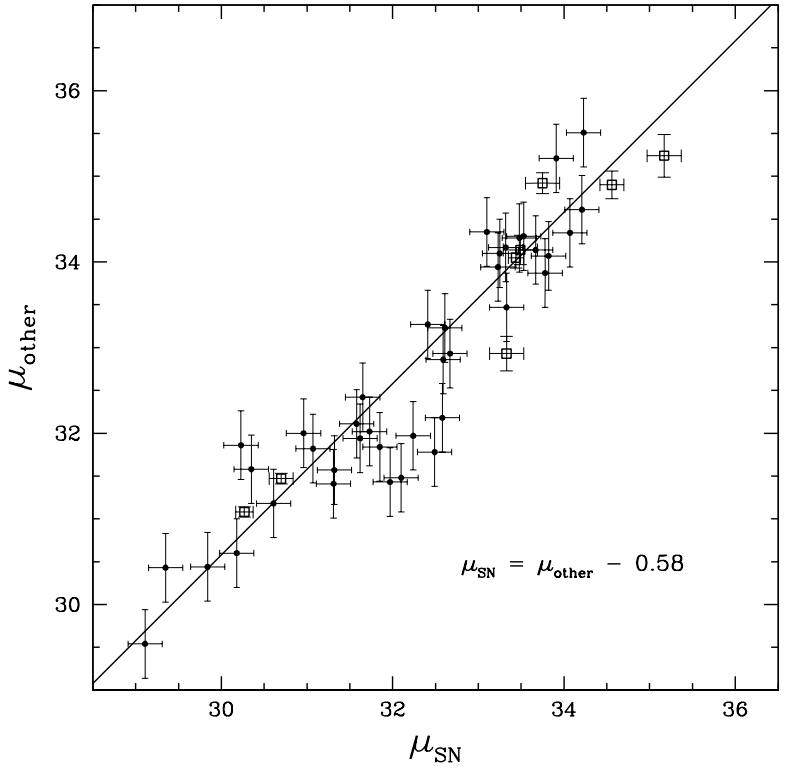

FIGURE 3.45: Comparison between moduli derived with SNIa and with "other" methods: the TFR, with Cepheid and Surface Brightness Fluctuation supplements. The comparisons include 39 individual galaxies with TFR measurements (filled points) and eight clusters (open squares). The straight line is a weighted fit to the 39 galaxies with TFR distances and six of the eight clusters.

The straight line in this figure is a fit, assuming slope unity, to the 39 individual galaxies each with weight 1 and six clusters each with weight 9. The locations of two clusters are deviant (Centaurus at 5 σ under the fit in Figure 3.45 and A1367 at 3 σ over the fit). These two clusters were deviant and rejected from the optical SNIa calibration (Courtois and Tully, 2012b) and for consistency in the comparison are again rejected from the fit. The offset between the newly determined distance moduli (other) and the SNIa moduli on the UNION2 scale is $\mu_{other} - \mu_{SN} = 0.58$. The comparable fit with I_C band material was shown in Figure 5 of Courtois and Tully (2012b). The offset in that earlier case was 0.56. It is instructive to compare results using only identical galaxies and clusters rather than using the ensemble. Figure 3.46 compares distance moduli measured alternatively with mid-infrared [3.6] photometry and optical I_C photometry observed from the ground, using the same line width and inclination parameters. The comparison involves the 13 clusters used to establish the TFR template at I_C (Tully and Courtois, 2012) and [3.6] (this work) and the 39 individual galaxies that have hosted SNIa (Courtois and Tully (2012b) and this work). With the individual SNIa hosts there is a hint of an increase in the difference between moduli for the more distant cases but the trend is not statistically significant. No such trend is seen

with the clusters. Overall the [3.6] moduli are greater than the I_C moduli by 0.02 ± 0.02 mag. The difference of 1% in distance is not statistically significant. The [3.6] calibration increases distances by 1% so reduces H_0 by 1%. It is to be noted, though, that the new mid-infrared calibration is tied to a distance to the Large Magellanic Cloud that is 1% closer than assumed in I Band. With a common choice of Large Magellanic Cloud distance, the [3.6] band distances are 2% greater than those at I_C band.

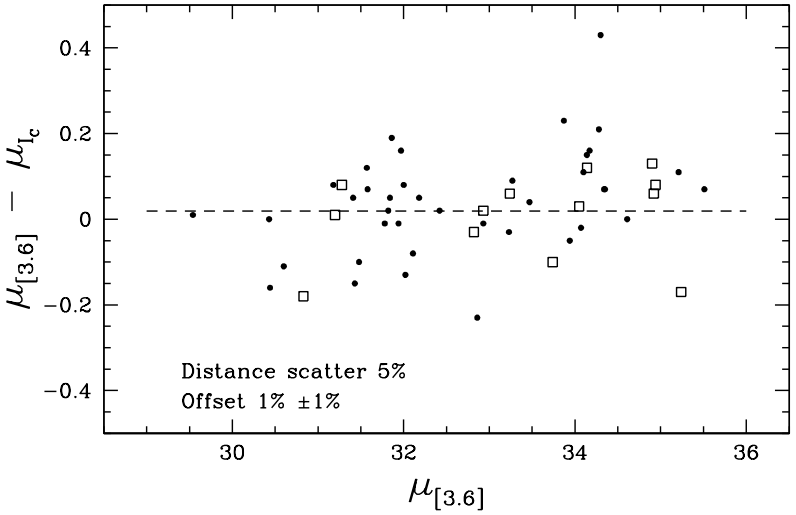

FIGURE 3.46: Differences in TFR distance moduli measured at [3.6] and at I_C plotted against the [3.6] moduli. Filled points: the 39 galaxies that have hosted SNIa ; Open squares: the 13 TFR template calibrator clusters.

The final calibration of the SNIa distance scale in the I_C band analysis of Courtois and Tully (2012b) leads to the determination of the Hubble Constant shown in their Figure 8. It is based on a fit over the redshift range $0.03 < z < 0.5$ to the UNION2 sample (Amanullah et al., 2010), with cosmological parameters $\Omega_m = 0.27$, and $\Omega_\Lambda = 0.73$. The result obtained in that paper was $H_0 = 75.9 \pm 3.8$ km s^{-1} Mpc^{-1}. In the present work, distances are decreased by 1% due to a revised Large Magellanic Cloud modulus and increased 2% with the switch from optical I_C to mid-infrared [3.6] magnitudes. The present calibration is in statistical agreement with the earlier work though formally gives a result 1% lower. An error budget was discussed by Courtois and Tully (2012b). Their 5% uncertainty is a combination of the 3% error budget discussed at length by Freedman and Madore (2010); Freedman et al. (2011); Riess et al. (2011) and 4-4.5% due to some concerns regarding 1) the scatter in SNIa measurements, 2) the effect of peculiar velocities which are not null although peculiar velocities are low with respect to the mean expansion at such distances and, 3) the absence of all-sky consistency. Uncertainties are reduced with this new work in two respects. First, there is increased confidence in the absolute scale set by the distance to the Large Magellanic Cloud (Freedman and Madore, 2010). Second, the mid-infrared calibration of the TFR removes latent concerns about possible photometric differences in different parts of the sky.

These two improvements warrant a decrease in our total error estimate to reach 4.3-4.5%, the major part of the decrease is due to the all-sky consistency. As a result, our best estimate for the Hubble Constant was at that time $H_0 = 75.2 \pm [3.2 - 3.4]$ km s^{-1} Mpc^{-1}.

However, as mentioned before, at the time of this work only 39 hosts of SNIa had been observed with Spitzer. Now, 45 host galaxies have all the required parameters to be compared with SNIa measurements. The new information extends the previous work by only six galaxies and we do not expect much change with regard to the offsets between SNIa and TF distance moduli estimates, neither do we between I and [3.6] band measurements especially because the calibration at 3.6 μm has been shown to be very robust. Still, for the sake of completeness, Figure 3.47 shows the results when the six additional galaxies are included in the sample and the newest TFR is used to derive moduli. Characteristics of these galaxies are in Table 3.12 in red, exactly like the color they have been attributed in the Figure, alongside the slightly different magnitudes and moduli for all the other host galaxies with the last calibration. For the clusters, new parameters are alongside the first parameters in Table 3.9.

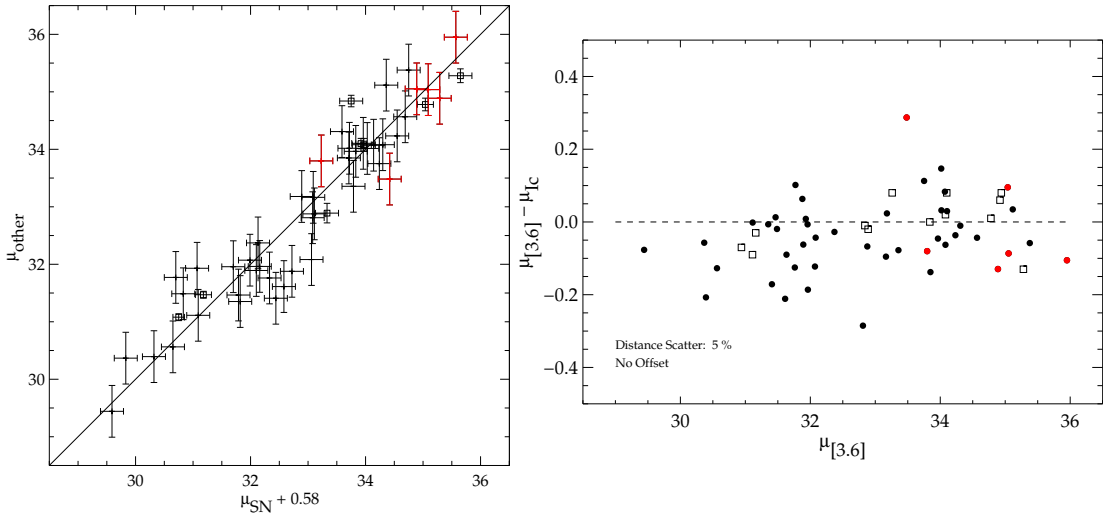

FIGURE 3.47: *Left*: Comparison between moduli derived with SNIa and with "other" methods (TFR, with Cepheid and Surface Brightness Fluctuation supplements). The solid line is the weighted fit to the 45 galaxies (filled points) with TFR distances and six of the eight clusters (open squares). *Right*: Differences in TFR distance moduli measured at [3.6] and at I_C in function of the [3.6] moduli. The 45 galaxies that have hosted SNIa are represented by filled points while the open squares stand for the 13 TFR template calibrator clusters. In both panels, red points stand for the late obtained photometric data.

Overall, the offset between SNIa distance moduli and other distance moduli is unchanged while the offset between TF distance moduli from the [3.6] and I band is slightly decreased to zero but that is within the uncertainty of the previously derived offset (1%±1%). The trend of increase in the difference between the two band moduli is more pronounced than before. This is probably due to the fact that, in the latest calibration, the bias correction (with a higher exponent but a smaller multiplicative coefficient) increases first more slowly

than the first derived bias correction with the distance but then, around 32.6-32.7 mag, roles are reversed. Because clusters as their are less affected by the change of sign observed in the difference between the two bias corrections due to their sole exponents, the offset was computed giving a higher weight to these latter. The [3.6] band distances are greater than the I band distances but only by 1% due to the Large Magellanic Cloud distance estimate change. Regardless, the Hubble Constant estimate about 75-76 km s^{-1} Mpc^{-1} we gave before is still correct. Table 3.10 recapitulates Hubble Constant estimates of this section.

Cluster	v_{CMB}	v_{mod}	$\mu_{other\,1}$	$\mu_{other\,2}$	μ_{SN}	SNIa names
Virgo	1410	1495	31.08*±0.06	31.08*±0.06	30.27±0.10	1991bg, 1994D, 1999cl, 2006X
Fornax	1484	1358	31.47*±0.06	31.47*±0.06	30.70±0.14	1980N, 1992A
Cen30	3679	3823	32.93±0.20	32.89±0.17	33.33±0.20	2001cz
Pisces	4779	4759	34.05±0.11	34.07±0.09	33.44±0.09	1998ef, 1999ej, 2000dk, 2001en, 2006td
Cancer	4940	5059	34.14±0.13	34.06±0.11	33.49±0.20	1999aa
Coma	7194	7370	34.90±0.13	34.71±0.11	34.56±0.14	2006cg, 2007bz
A1367	6923	6969	34.92±0.14	34.84±0.10	33.75±0.20	2007ci
A2634/66	8381	8938	35.24±0.13	35.19±0.17	35.17±0.20	1997dg

TABLE 3.9: Properties of clusters with SNIa: (1) Cluster name, (2) Mean velocity of the cluster with respect to the CMB, km s^{-1}, (3) Mean velocity of the cluster with respect to the CMB corrected for the cosmological model, km s^{-1}, (4) TFR distance modulus corrected for bias, mag, (5) Latest TFR distance modulus corrected for bias, mag, (6) SNIa distance modulus, mag, (7) SNIa identifications. *Virgo and Fornax are special cases discussed in the text.

	Computation from	H_0 (km s^{-1} Mpc^{-1})
1.	I Calib.	75.1 ± 2.7 (ran) (75.8*)
2.	[3.6] Calib.	73.8 ± 2.6 (ran) ± [3.5-3.8] (sys)
3.	[3.6] Control Calib.	75.0†± 2.0 (ran) ± [3.5-3.8] (sys)
4.	I Calib. + SNIa	75.9 ± 3.8
5.	[3.6] Calib. + SNIa	75.2 ± [3.2-3.4]
6.	[3.6] Control Calib. + SNIa	75.9 ± [3.2-3.4]

TABLE 3.10: Hubble Constant Estimates: 1.,2.,3. obtained with distance measurements derived from the TFRs in I band (Tully and Courtois, 2012) and at 3.6 μm (subsections 3.4.1, 3.4.2), 4. obtained with scaling the type Ia supernovae method (Courtois and Tully, 2012b) using distance moduli derived from the TFR in I band among others, 5.,6. obtained with comparisons between distance moduli derived from the I and [3.6] band TFRs and the scaling of the type Ia supernovae method (subsection 3.4.3). * adopting a closer (by 0.02 mag) distance modulus for the Large Magellanic Cloud, † using velocities with respect to the cosmic microwave background corrected for the cosmology.

Name	PGC	SNIa	v_{CMB}	W^i_{mx}	$[3.6]^{b,i,k,a}$	$C_{[3.6]}$	$M_{C_{[3.6]}}$	μ_{TF}	μ_{SN}
UGC00646	3773	1998ef	5011	389	12.89	12.88	-21.16	34.10	33.25
PGC005341	5341	1998dm	1663	236	12.91	12.79	-19.18	31.97	32.24
NGC0673	6624	1996bo	4898	445	12.04	12.19	-21.69	33.94	33.23
NGC0958	9560	2005A	5501	584	11.09	11.24	-22.77	34.07	33.82
ESO300-9	11606	1992bc	5918	323	14.69	14.67	-20.42	35.21	33.91
NGC1148	13727	2001el	1092	386	10.05	10.05	-21.13	31.18	30.61
UGC03329	17509	1999ek	5277	525	12.13	11.89	-22.35	34.30	33.53
UGC03375	18089	2011gc	5792	535	11.82	11.78	-22.42	34.28	33.48
PGC018373	18373	2003kf	2295	234	12.72	12.69	-19.15	31.84	31.85
UGC03432	18747	1996bv	5015	289	14.20	14.12	-19.98	34.17	33.32
UGC03576	19788	1998ec	6013	393	13.03	13.07	-21.20	34.34	34.07
UGC03370	20513	2000fa	6525	371	13.48	13.56	-20.97	34.61	34.21
UGC03845	21020	1997do	3136	257	13.35	13.39	-19.52	32.93	32.67
NGC2841	26512	1999by	804	650	8.68	8.66	-23.20	31.86	30.23
NGC3021	28357	1995al	1797	303	11.68	11.84	-20.17	32.02	31.73
NGC3294	31428	1992G	1831	431	10.77	10.84	-21.57	32.42	31.65
NGC3368	32192	1998bu	1231	428	8.80	8.89	-21.54	30.43	29.35
NGC3370	32207	1994ae	1609	312	11.68	11.81	-20.29	32.11	31.58
NGC3627	34695	1989b	1061	385	8.33	8.40	-21.12	29.54	29.11
NGC3663	35006	2006ax	5396	443	12.44	12.41	-21.68	34.14	33.67
NGC3672	35088	2007bm	2223	399	10.59	10.68	-21.26	31.94	31.62
NGC4501	41517	1999cl	2601	570	8.84	8.90	-22.68	31.58	30.35
NGC4527	41789	1991T	2072	362	9.34	9.56	-20.88	30.44	29.84
NGC4536	41823	1981B	2144	341	9.81	9.96	-20.64	30.60	30.18
NGC4639	42741	1990N	1308	336	11.18	11.23	-20.58	31.82	31.07
NGC4680	43118	1997bp	2824	237	12.09	12.23	-19.20	31.43	31.97
NGC4679	43170	2001cz	4935	427	11.83	11.90	-21.53	33.47	33.33
NGC5005	45749	1996ai	1178	601	9.05	9.11	-22.89	32.00	30.96
ESO576-040	46574	1997br	2385	170	13.82	13.69	-17.88	31.57	31.32
PGC47514	47514	2007ca	4517	285	14.03	13.89	-19.93	33.87	33.78
NGC5584	51344	2007af	1890	267	11.75	11.74	-19.67	31.41	31.31
IC1151	56537	1991M	2274	242	12.91	12.88	-19.28	32.18	32.58
NGC6063	57205	1999ac	2950	308	13.06	13.01	-20.24	33.27	32.41
UGC10738	59769	2001cp	6726	585	12.52	12.61	-22.78	35.51	34.23
UGC10743	59782	2002er	2574	206	12.74	12.83	-18.64	31.48	32.10
NGC6962	65375	2002ha	3936	633	11.11	11.19	-23.09	34.35	33.10
IC5179	68455	1999ee	3158	444	10.86	11.15	-21.69	32.86	32.59
NGC7329	69453	2006bh	3143	461	11.24	11.36	-21.83	33.23	32.61
NGC7448	70213	1997dt	1838	316	11.37	11.44	-20.34	31.78	32.49

TABLE 3.11: Properties of individual SNIa-host galaxies: (1) Common name, (2) PGC name, (3) SNIa identification, (4) Mean velocity of host galaxy with respect to the CMB, km s^{-1}, (5) Corrected rotation rate parameter corresponding to twice the maximum velocity, km s^{-1}, (6) Corrected 3.6 μm magnitude in the AB system, mag, (7) Color adjusted magnitude, mag, (8) Absolute color adjusted magnitude, mag, (9) TFR distance modulus corrected for bias, mag, (10) SNIa distance modulus, mag.

Name	PGC	v_{CMB}	v_{mod}	W^i_{mx}	$[3.6]^{b,i,k,a}$	$C_{[3.6]}$	$M_{C_{[3.6]}}$	μ_{TF}	μ_{SN}
UGC00139	963	3975	3626	311	13.43	13.51	-20.25	33.80	33.33
UGC00646	3773	5348	4898	389	12.85	12.84	-21.13	34.02	33.82
PGC005341	5341	1964	1601	236	12.84	12.72	-19.15	31.88	32.82
NGC0673	6624	5241	5051	444	11.96	12.15	-21.66	33.85	33.81
NGC0958	9560	5732	5623	592	11.09	11.23	-22.79	34.08	34.40
UGC01993	9618	8005	7967	485	12.97	12.94	-22.00	35.04	35.19
IC1844	10448	6846	6693	309	13.55	13.23	-20.22	33.48	34.52
ESO300-009	11606	6045	6017	321	14.67	14.64	-20.37	35.12	34.46
PGC011767	11767	8701	8671	422	13.16	13.35	-21.46	34.89	35.39
NGC1448	13727	1194	1062	388	9.97	9.99	-21.12	31.11	31.19
UGC03329	17509	5253	5668	524	11.74	11.65	-22.31	34.01	34.13
UGC03375	18089	5783	5879	534	11.63	11.67	-22.38	34.10	34.06
PGC018373	18373	2168	2281	239	12.45	12.54	-19.22	31.76	32.43
UGC03432	18747	4996	5080	289	13.93	13.96	-19.96	33.96	33.93
UGC03576	19788	5966	6009	392	12.94	13.01	-21.17	34.23	34.65
UGC03770	20513	6378	6646	371	13.48	13.55	-20.95	34.57	34.79
UGC03845	21020	3034	3166	257	13.33	13.36	-19.50	32.88	33.21
NGC2841	26512	637	810	650	8.63	8.61	-23.16	31.77	30.80
NGC3021	28357	1515	1781	302	11.64	11.82	-20.14	31.96	32.26
NGC3294	31428	1567	1838	431	10.76	10.82	-21.54	32.37	32.23
NGC3368	32192	906	1332	427	8.77	8.86	-21.50	30.37	29.93
NGC3370	32207	1367	1622	311	11.69	11.81	-20.26	32.07	32.09
NGC3627	34695	723	1454	384	8.26	8.36	-21.08	29.44	29.69
NGC3663	35006	5040	5389	443	12.42	12.37	-21.65	34.07	34.24
NGC3672	35088	1860	2210	399	10.57	10.66	-21.23	31.89	32.20
NGC4501	41517	2268	1740	570	8.75	8.85	-22.64	31.49	30.93
NGC4527	41789	1736	2090	361	9.32	9.56	-20.84	30.39	30.42
NGC4536	41823	1808	2162	341	9.81	9.95	-20.61	30.56	30.75
NGC4639	42741	1003	1740	348	11.25	11.26	-20.69	31.96	31.80
NGC4680	43118	2491	2811	237	12.10	12.24	-19.17	31.41	32.54
NGC4679	43170	4665	3824	426	11.72	11.84	-21.49	33.36	33.89
NGC5005	45749	1011	1177	601	9.01	9.08	-22.85	31.93	31.17
ESO576-040	46574	2095	2407	169	13.72	13.61	-17.85	31.47	31.89
PGC047514	47514	4217	4577	284	13.96	13.82	-19.89	33.75	34.34
NGC5584	51344	1655	191	266	11.74	11.72	-19.64	31.35	31.92
IC4423	51549	9115	9691	470	13.73	13.92	-21.88	35.95	35.67
IC1151	56537	2176	2287	241	12.83	12.83	-19.25	32.08	33.16
NGC6063	57205	2841	2958	308	12.98	12.95	-20.21	33.18	32.99
UGC10738	59769	6716	6850	584	12.37	12.53	-22.74	35.38	34.85
UGC10743	59782	2744	2581	218	12.59	12.76	-18.85	31.61	32.68
NGC6962	65375	4200	3695	639	11.05	11.15	-23.09	34.31	33.69
IC5179	68455	3400	3108	444	10.80	11.14	-21.66	32.81	33.18
UGC12133	69428	7391	7213	442	13.17	13.32	-21.64	35.05	34.99
NGC7329	69453	3245	3150	461	11.19	11.34	-21.80	33.16	33.19
NGC7448	70213	2170	1752	309	11.32	11.40	-20.23	31.63	32.72

TABLE 3.12: Properties of individual SNIa galaxies (latest results): (1) Common name, (2) PGC name, (3) Mean velocity of host galaxy with respect to the CMB, km s^{-1}, (4) Mean velocity of host galaxy with respect to the CMB corrected for the cosmological model, km s^{-1}, (5) Corrected rotation rate parameter corresponding to twice the maximum velocity, km s^{-1}, (6) Corrected 3.6 μm magnitude in the AB system, mag, (7) Color adjusted magnitude, mag, (8) Absolute color adjusted magnitude, mag, (9) TFR distance modulus corrected for bias, mag, (10) SNIa distance modulus, mag. Supplementary galaxies with respect to the first work are in red.

3.5 Catalogs of Accurate Distance Estimates

Near, intermediate, and far TFR samples in the Cosmicflows program were described by Courtois et al. (2011b) and in subsection 3.3.1.2. To summarize:

- the "near" sample is intended to achieve dense coverage of a volume extending to 3300 km s^{-1} with inclusion of all galaxies later than Sa that are brighter than $M_K = -21$, inclined greater than 45°, and not obscured, disrupted, or confused,
- the "intermediate" sample is drawn from flux and color limits applied to an Infrared Astronomical Satellite Redshift Survey (Saunders et al., 2000). The flux limit at 60 μm is 0.6 Jy, the color criterion to separate normal spirals from active nuclei is a ratio of 100 μm to 60 μm flux greater than one, there is a velocity cutoff at 6000 km s^{-1}, and there is the same inclination restriction as with the near sample,
- the "far" sample is restricted to extreme edge-on systems drawn from Flat Galaxy catalogues (Karachentsev et al., 1999; Mitronova et al., 2004). Candidates in the sample that lie at declinations accessible to Arecibo Telescope have velocities extending to 15,000 km s^{-1}.

These are the well defined samples. In addition distances are derived to all other suitably observed galaxies. A quite separate and active component of Cosmicflows is a program with *Hubble Space Telescope* to obtain Tip of the Red Giant Branch distances to nearby, spatially resolved galaxies (Jacobs et al., 2009; Makarov et al., 2006; Rizzi et al., 2007). Exquisite distances (5% accuracy) are available for approaching 300 galaxies within $\sim$ 10 Mpc. Still, generally the information for the additional systems comes from archives. Thus, distances for Cosmicflows encompass measures by other methodologies discussed in the literature. Foremost among these are Cepheid Period-Luminosity Relation (e.g. Freedman et al., 2001, 2012), Surface Brightness Fluctuation (e.g. Blakeslee et al., 2010; Tonry et al., 2001), Fundamental Plane (e.g. Colless et al., 2001), and Supernova Ia (Amanullah et al., 2010; Folatelli et al., 2010) procedures. The diverse material is drawn together in the Extragalactic Distance Database (Tully et al., 2009). EDD goes beyond the compilation of catalogs relevant to extragalactic distances to include redshift catalogs, that with various levels of completion describe the distribution of galaxies in the Local Universe, and group catalogs, that help identify entities where averaging over velocities or distances is reasonable. The first assembly of distances in this program (Tully et al., 2008) has now been given the name *cosmicflows-1*. A core team was involved in the assembly of *cosmicflows-2* (Courtois and Tully, 2012b; Tully and Courtois, 2012; Tully et al., 2013). This work increases the size of this second catalog by 20% in spatial regions not necessarily accessible from the ground (like very close to the Zone Of Avoidance). It will help constitute the third catalog of the project, *cosmicflows-3*.

In the three subsequent subsections, the two first catalogs are described and an insight into the third one is given.

3.5.1 Cosmicflows-1

Cosmicflows-1 is the first catalog of the Cosmicflows project. Publicly released by Tully et al. (2008), it is available at the Extragalactic Distance Database. This catalog contains accurate distance measurements of 1797 galaxies up to 3000 km s^{-1}. These distances are given on the Cepheid reference scale from the Hubble Space Telescope Key Project (Freedman et al., 2001) with which Tip of the Red Giant Branch (TRGB) and Surface Brightness Fluctuation (SBF) measurements from the literature are in agreement. Distance estimates obtained with the SBF indicator come in majority from Tonry et al. (2001). These three methods Cepheid Period-Luminosity (PL), TRGB and SBF claim comparable accuracies. Consequently, an uncertainty about 10% is assigned to distance measurements obtained with these estimators. Tully-Fisher (TF) distance estimates from Tully and Pierce (2000) and Karachentsev et al. (2002) are added to this ensemble after a small adjustment to be on the same reference scale. A 20% uncertainty is allocated to these last measures.

Some of these 1797 galaxies have two or three (even four for PGC2557) distances estimates but the majority of them has solely TF estimates (1199), giving the reason for keeping distance estimates from this method although it is less accurate than other distance indicators: the Tully-Fisher relation gives access to a large number of galaxy distance measurements. The double-entry Table 3.13 gives the number of galaxies which have estimates from SBF, TRGB, PL, TF methods or a combination of them. These galaxies are part of clusters such as Virgo (142 galaxies), Fornax (34), Centaurus (13), Antlia (11) and Ursa Major (51, often mentioned as a cluster, it is more probably a cloud, see for example Karachentsev et al., 2013), while some belong to groups like ComaI (12), Maffei (13) and VirgoW (11). A total of 437 galaxies are lonely at this point, either because they are in the field or because of the restricted number of measures available in the group/cluster to which they belong. We denote 152 pairs of galaxies, again some are the pure result of the limited number of data points. Other galaxies can be gathered by 3 or more, the maximum is reached for Virgo.

	SBF	TRGB	PL	TF	PL-TF	TRGB-TF	TRGB-PL-TF
SBF	334	9	1	8	5	1	1
TRGB	-	184	11	13	2	-	-
PL	-	-	10	19	-	-	-
TF	-	-	-	1199	-	-	-

TABLE 3.13: Number of Measurements per Method in *cosmicflows-1*, double-entry table: (*Line*) Number of galaxies with First Distance Estimates obtained with the SBF, TRGB, PL or TF methods and (*Column*) Potential Second, Third and Fourth Distance Estimates obtained with a combination of SBF, TRGB, PL and TF relations. Only PGC2557 has four distance estimates.

3.5.2 Cosmicflows-2

The second catalog of the Cosmicflows project was publicly released by Tully et al. (2013). It gathers over 8000 accurate distance measurements obtained from various methods from the Cepheid Period Luminosity (PL) to the Tully-Fisher (TF) relations going through the Surface Brightness Fluctuation (SBF), the type Ia Supernovae (SNIa), the Tip of the Red Giant Branch (TRGB), the Fundamental Plane (FP) and other miscellaneous methods such as RR Lyrae, Horizontal Branch, Eclipsing Binary. This catalog extends up to 30,000 km s^{-1}, ten times the extent of the first catalog, and it enhances the density of measurements within the first catalog spatial coverage. The scale is still given by Cepheids but from a slightly refined version (Freedman et al., 2012; Riess et al., 2011). TRGB measurements are on the same scale (e.g. Rizzi et al., 2007). With its all-sky consistency, the work presented in this Chapter contributed to slightly re-evaluate the I-band TFR scale (Tully and Courtois, 2012) in agreement with the tiny difference found between I and [3.6] distance estimates at the time of the second catalog release. Regardless, above all, the Spitzer work confirms the results found in I band which were lacking an all-sky consistency as the I band work is a gathering of several telescope data.

Among the galaxies constituting the catalogs approximately half of them are isolated galaxies. The others are mostly in clusters such as Virgo (160), Coma (132), Abell 2151 or Hercules (87), Pisces (74), Hydra (71), Abell 2196/99 (66), Abell 400 (63), Fornax (54), Abell 2634 (54), Centaurus (49), Abell 0426 or Perseus (47), Klemola44 (46), Ursa Major (45), Cancer (42), Abell 0548 (42), Pegasus (41) etc. In total, they can be gathered in approximately 500 groups and clusters. Again the TFR supplies most of the measurements (5856 of the galaxies have a unique TF distance estimate, see Table 3.14) then comes Fundamental plane (FP), SBF (S) closely followed by SNIa (SN), TRGB (T), PL (P) and finally a few miscellaneous (M) methods. It is to be noted that galaxy distances obtained with different methods are not necessarily compared and averaged over each galaxies. In the case of measurements from both SBF and TF methods, distances are averaged after grouping. It is also frequently the case for distances obtained with both SNIa and TF methods.

With this variety of different distance estimates, the remarkable property of *cosmicflows-2* is the distribution of uncertainties which is strongly bimodal with peaks at around 8-10% and 20% uncertainties on distances. A higher uncertainty is attributed to galaxies with solely FP estimates (25%) producing another small peak. In the grouped version of the catalog, the distribution of uncertainties has an additional feature: groups and clusters with several distance measurements from the TF / FP relations produce another peak at around 15% but also contribute to the 8-10% peak.

	P	T	M	S	SN	TF	FP	T-TF	S-TF	SN-TF	T-S	T-M.	T-M-S-TF	S-FP	SN-FP
P	3	14	-	-	4	11	-	9	4	5	3	6	1	-	-
T	-	192	10	12	-	20	-	-	2	-	-	-	-	1	-
M	-	-	3	-	-	-	-	-	-	-	-	-	-	-	-
S	-	-	-	270	1	10	75	-	-	-	-	-	-	-	3
SN	-	-	-	-	216	50	7	-	-	-	-	-	-	-	-
TF	-	-	-	-	-	5856	3	-	-	-	-	-	-	-	-
FP	-	-	-	-	-	-	1370	-	-	-	-	-	-	-	-

TABLE 3.14: Number of Measurements per Method in *cosmicflows-2*, double-entry table: (Line) Number of galaxies with First Distance Estimates obtained with the PL (P), TRGB (T), SBF (S), SNIa (SN), TF and FP methods and various distance indicators (M) ; (Column) Second, Third, Fourth and Fifth Distance Estimates potentially obtained with a combination of all the distance estimators at hand. Only PGC39600 has five distance estimates.

3.5.3 Cosmicflows-3: an Insight

This Chapter has been the occasion to expound the observational campaign Cosmicflows with Spitzer (CFS), a photometric component of the Cosmicflows project. The primarily goal of this observational survey is to increase the number of distance estimates close to the Zone Of Avoidance using the Tully-Fisher relation. The first channel (3.6 μm) of the InfraRed Array Camera onboard the Spitzer Space Telescope is indeed the instrument of choice to obtain the required excellent photometry. At this wavelength the Zone of Avoidance and uncertainties on measurements are considerably reduced. Surface photometry of 1270 galaxies constituting the CFS sample observed in cycle 8 with IRAC channel 1 and over 400 additional galaxies observed in various other surveys have been presented in section 3.3. The Spitzer Survey of Stellar Structure in Galaxies supplies many more galaxies of interests to the Cosmicflows project. The final set is constituted of about 2,000 galaxies with required parameters (heliocentric velocity or redshift, W_{mx}, b/a, E(B-V), R_λ at [3.6] (and I), γ_λ at [3.6] (and I), [3.6] and if available I), to derive an estimate of their distance with the mid-infrared (color adjusted) TFR, all available. Axial ratios come either from previous estimates of the Cosmicflows program or from HyperLeda if they are from Paturel et al. (2003). Galaxies without estimates of their axial ratios will be added later on thanks to the Citizen Science project. Inclination have been obtained with formula 3.20 to correct linewidths and magnitudes. The compilation of I band magnitudes is described in Tully et al. (2013). It gathers magnitudes used in Tully and Pierce (2000); Tully et al. (2008), themselves borrowing from Giovanelli et al. (1997b); Mathewson et al. (1992); Pierce and Tully (1988); Tully et al. (1996), but also recent derivations from Courtois et al. (2011a); Springob et al. (2007) and Hall et al. (2012). Tully et al. (2013) showed that these I-band magnitudes are on a consistent scale after small adjustments with the exception of those of Hall et al. (2012) because they use a significantly different filter. Accordingly these latter are

adjusted with the formulas prescribed by Smith et al. (2002) and Tully et al. (2013). These corrections involve a translation from Sloan g, r, i band (Gunn i band) to Cousins I band:

$$I = i - 0.14(g - r) - 0.35 \tag{3.57}$$

where cases with r-i≥0.95 are excluded, and account for a slight tilt between I and I_c, from the Cosmicflows project, magnitudes.

$$I_c = 1.017\, I - 0.221 \tag{3.58}$$

I-band magnitudes are corrected with the following formula (Chilingarian et al., 2010; Schlafly and Finkbeiner, 2011; Tully and Pierce, 2000):

$$\begin{aligned} I^{b,i,k} &= I - A_i^I - A_k^I - A_b^I \qquad \text{where :} \\ A_i^I &= (0.92 + 1.63(\log \mathrm{W}^{\mathrm{i}}_{\mathrm{mx}} - 2.5))\log(\mathrm{b/a}) \quad (\text{if } \mathrm{A}^{\mathrm{I}}_{\mathrm{i}} < 0 \text{ then } \mathrm{A}^{\mathrm{I}}_{\mathrm{i}} = 0) \\ A_b^I &= 1.94 \times E(B-V) \\ A_k^I &= 0.302z + 8.768z^2 - 68.680z^3 + 181.904z^4 \end{aligned} \tag{3.59}$$

where the terms have the same signification as those in the relation 3.29 for [3.6] magnitudes. Besides, these latter are corrected with that relation.

When available, I-band magnitudes are converted to the AB system with equation 3.27 and pseudo-magnitudes are derived with formula 3.54. Combined with the (color corrected) Tully-Fisher relation 3.55 applied to linewidths, they enable the derivation of distance moduli with relation 3.10. These latter are corrected for the selection bias with equation 3.56 before deriving distance estimates with formula 3.10 used in reverse. Eventually distance estimates given in the table of Appendix C will be incorporated into a new data release of the Cosmicflows project, increasing the size of the previous catalog by 20%, including in spatial regions close to the Zone Of Avoidance.

In addition, EDD contains a bit more than 10,000 linewidths (with an error below 20 km s^{-1}) of galaxies which inclinations are greater than 45°. Acquiring the photometry for the galaxies without any photometric measurement to be matched with their linewidth is accordingly the next top priority of the Cosmicflows project. This photometry supplied by all sky surveys such as the Wide-field Infrared Survey (WISE, Wright, 2008) combined with the ongoing TF calibration (Neil et al. in prep. for WISE) will result in the compilation of *cosmicflows-3* which will gather all the distance material available. At present, we estimate that this third catalog of accurate distance estimates could contain in total (including distance estimates from Cepheids, TRGB, etc) around 14,000 measures, almost twice the size of the latest *cosmicflows-2* catalog. It will have approximately the same coverage as the second catalog

but with an enhanced density, especially next to the Zone Of Avoidance thanks to Spitzer observations. Figures 3.48 and 3.49 give an overview of the provisional *cosmicflows-3*.

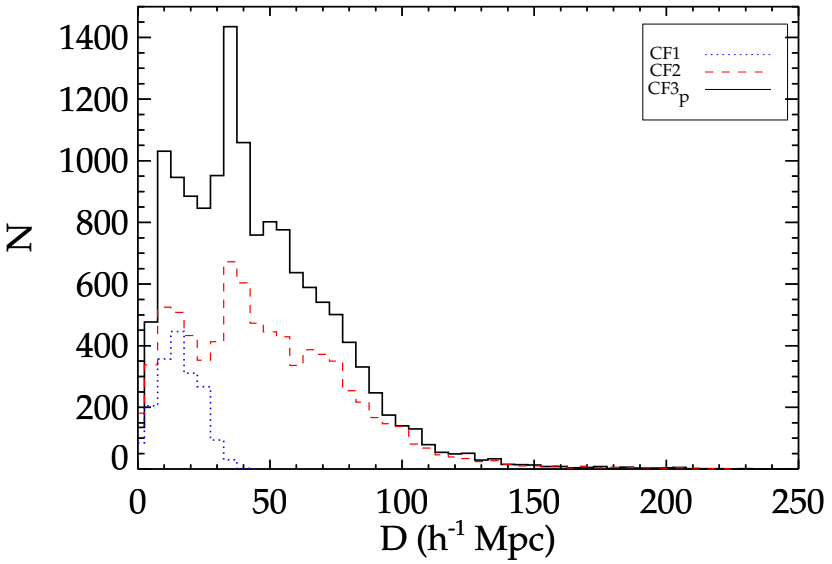

FIGURE 3.48: Histograms of distances in cosmicflows-1 (blue dotted line),-2 (red dashed line) and provisional *cosmicflows-3* (black solid line).

We have closed this Chapter with catalogs of Cosmicflows which gather peculiar motions of galaxies in the Local Universe. These peculiar velocities are departures from the cosmic mean expansion and it is assumed that they arise due to density irregularities. Two regimes require separate attention. The high density environments in and around collapsed halos are at the extreme of non-linear dynamics. Within the collaboration, a Numerical Action Method was developed that provide an optimal description of the distribution of mass affecting galaxies on curved orbits on first approach to an attractor (Peebles et al., 2001; Peebles and Tully, 2013; Shaya et al., 1995). The other extreme is the regime of linear dynamics. A procedure used that is appropriate with redshift data sets of 10^5 or more objects is based on the action principle (Lavaux et al., 2010). However the methodology that most interests us starts with Wiener filtering of the peculiar velocity field resulting in descriptions of the density and velocity fields independent of information provided by redshift surveys (Courtois et al., 2012; Zaroubi et al., 1995). The fields can then be mapped back to initial conditions that are then the starting point for constrained simulations that attempt to approximate the observed universe with a computer model (Courtois and Tully, 2012a; Doumler et al., 2013b; Gottlöber et al., 2010; Klypin et al., 2003). Such constrained simulations constitute the second course of this work in the framework of the CLUES collaboration.

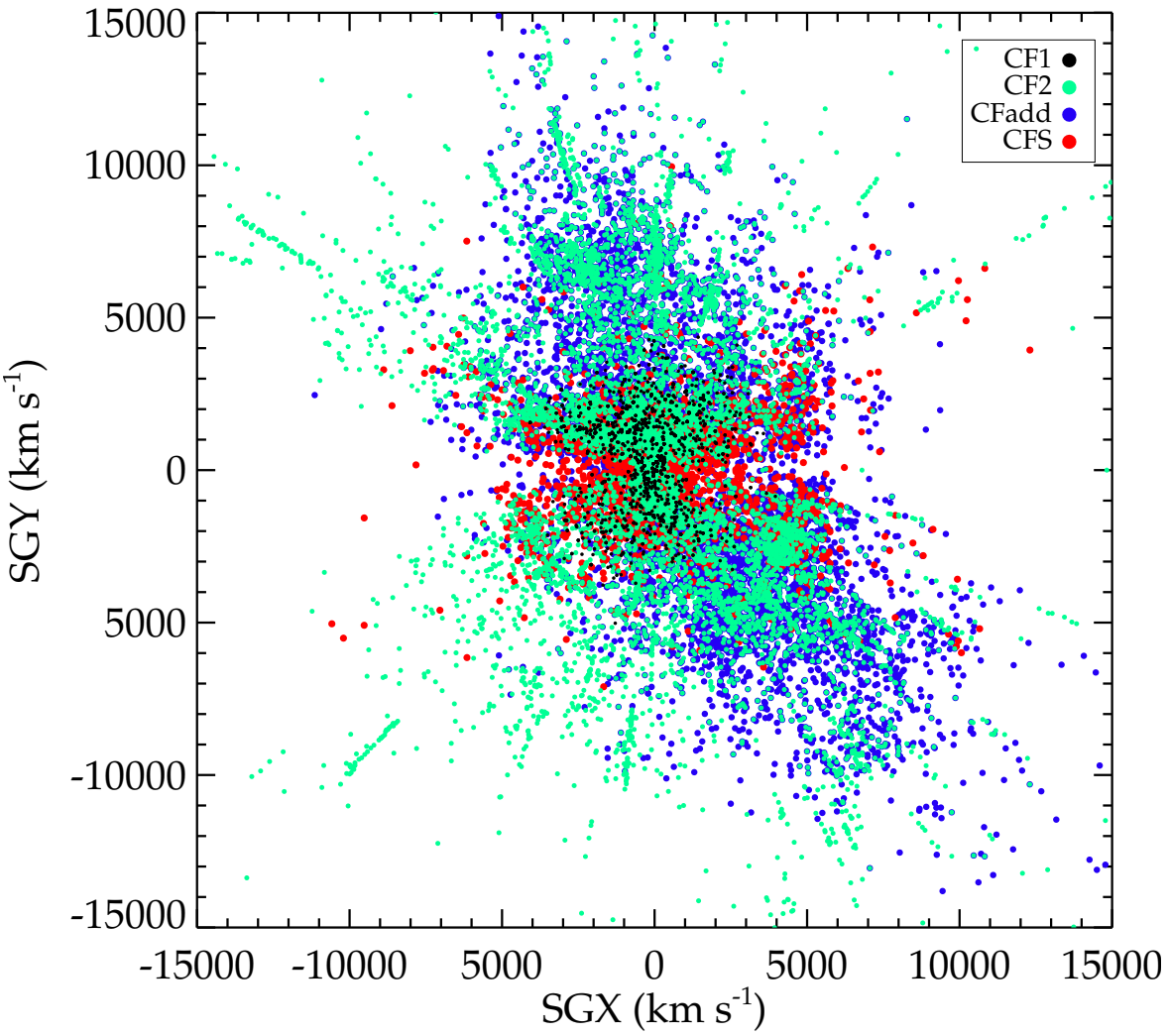

FIGURE 3.49: XY supergalactic plane showing the provisional *cosmicflows-3* catalog. Black dots stand for the contribution of *cosmicflows-1* (available since 2008), green dots represent *cosmicflows-2* (available since the end of 2013), red dots are galaxies analyzed in this work with Spitzer and blue dots are galaxies which will be studied with all sky surveys such as WISE. The ensemble of all these dots (galaxies) constitutes the provisional *cosmicflows-3* catalog with over 14,000 accurate distance estimates. Spitzer observations contribute to *cosmicflows-3* by considerably increasing the number of distance estimates near the Zone Of Avoidance.

Chapter 4

Simulated Universe

Numerical simulations provide the opportunity to develop studies of the formation and evolution of structures. The overarching goal of the CLUES project is to produce constrained simulations *which best approximate the observed nearby Universe by reducing the so-called cosmic variance. Such constrained simulations stem from initial conditions obeying a set of observational constraints in addition to the random component. Constraints can either be peculiar velocities or galaxy distributions. Peculiar velocities, obtained from direct distance measurements, are data of choice to achieve constrained simulations of the Local Universe reliable down to a scale of a few Megaparsecs. Unlike redshift surveys, peculiar velocities are direct tracers of the underlying gravitational field as they trace both baryonic and dark matter. Yet, the method, designed over the past few years to produce initial conditions constrained by peculiar velocities, necessitated additional density constraints to result in simulations that resemble the Local-Universe. Accordingly, this Chapter presents the first attempt to use* solely *observational peculiar velocities to constrain cosmological simulations of the nearby universe. First the general method to produce constrained initial conditions is reviewed. Then, the process, as it was at the beginning of this work, is augmented and tested on realistic mocks before being applied to the first catalog of the Cosmicflows project. Finally the process is reiterated with the second catalog of the Cosmicflows project after minimizing observational biases in this latter. The second generation of constrained simulations of the Local Universe is unveiled.*[1]

[1]This Chapter makes use of the ICeCoRe code and we refer the reader to "TH2012_Doumler_Timur.pdf " downloadable at "http://phd-physics.universite-lyon.fr" for more details on this code.

4.1 Constrained Simulations

Under the assumption of a dark-matter only Universe, even the simplest problem of the emergence of structures defies a proper and detailed analytical treatment. As a result, the study of the formation of the Large Scale Structure of the Universe relies heavily on numerical simulations. Actually, large scale dark matter simulations (e.g., Alimi et al., 2012; Angulo et al., 2012b; Klypin et al., 2011; Prada et al., 2012; Watson et al., 2013) constitute the backbone of the study of structure formation in the Universe. The standard model of cosmology asserts that the primordial fluctuations are constituted by a Gaussian random field whose statistical properties are determined by its power spectrum. An accurate determination of the power spectrum is enabled by the cosmological parameters. These latter are obtained from observations of the fluctuations in the cosmic microwave background radiation combined with Baryonic Acoustic Oscillations and supernova measurements (Komatsu et al., 2011; Larson et al., 2011; Planck Collaboration, 2013). Standard cosmological computations use then Initial Conditions drawn from random realizations of the primordial Gaussian perturbation field which properties correspond to a given power spectrum. By contrast, *constrained simulations* stem from Initial Conditions obeying a set of observational constraints in addition to the random component. They provide a different approach to cosmological simulations to better approximate the observed nearby Universe to study it more thoroughly. Namely, they aim at reducing the so-called cosmic variance due to our fixed position in the Universe combined with the fact that we can only observed one realization (one universe) of the theoretical model at one time. This cosmic variance affects greatly the results. For example, Garrison-Kimmel et al. (2014) reveal the importance of the surrounding environment (in particular the approaching M31) to derive a proper stellar halo mass relation in the Local Group.

4.1.1 Constrained Initial Conditions

Initial conditions can either be constrained by peculiar velocities or galaxy distributions:

- the first constrained initial conditions were produced by Ganon and Hoffman (1993), using the Mark III catalog of peculiar velocities (Willick et al., 1996). These initial conditions were then used to perform the first constrained simulation of the nearby universe by Kolatt et al. (1996). The CLUES (Constrained Local UniversE Simulations) project has been ever since running a variety of pure dark matter and hydrodynamical constrained simulations of the Local Universe, aiming mostly at studying a variety of issues concerning the Local Group (for a general review Gottlöber et al., 2010, and references therein),

- galaxy redshift surveys provide a different source of constraints. This was first pioneered by Bistolas and Hoffman (1998) and followed later on by Mathis et al. (2002) and Lavaux (2010) and very recently by Heß et al. (2013).

There is a considerable tradeoff between using peculiar velocities and spatial distributions of galaxies from redshift surveys. Galaxy redshifts are quite easy to measure accurately. Very large and deep surveys are now routinely produced. However, galaxy distributions constitute biased tracers of the underlying density field. The mass-to-light bias has yet to be completely modeled and corrected for. On the other hand, measuring peculiar velocities poses formidable challenges to observational cosmologists. The observations are susceptible to systematic biases, and the resulting catalogs are noisy, sparse and with an incomplete sky coverage. Still, on the theoretical side, peculiar velocities are unbiased tracers of the underlying mass distribution. As long as virial motions inside clusters can be suppressed, the construction of the underlying density and velocity fields can be easily performed. The procedure to reconstruct underlying density and velocity field (and eventually to build initial conditions) with peculiar velocities is based on the linear Wiener-Filter and Constrained Realization of Gaussian fields algorithms (Hoffman, 2009; Hoffman and Ribak, 1991; Zaroubi et al., 1995). These techniques are described more thoroughly in the next section.

4.1.2 Constrained Realizations

4.1.2.1 The Wiener-Filter Technique

The Wiener-Filter (WF) technique is a very efficient and straightforward method to recover from sparse and noisy data the Gaussian underlying fields assuming a prior model. Developed in 1949 by Wiener for the field of signal processing, it consists in reducing the amount of noise in a dataset to generate an estimate of the underlying true signal. Introduced in 1992 by Rybicki and Press, in the astrophysical and cosmological fields of research, it was soon after used to reconstruct fields from observational datasets (e.g. Zaroubi et al., 1995). This technique requires only the computation of a correlation matrix and its inverse. More precisely, the Wiener-Filter corresponds to the minimal variance estimator of the data with respect to the assumed prior model. This function is obtained by minimizing the square of the residuals R_i between the underlying field $f_i = \sum_{i=1}^{n} F_{ij} C_j$ and the model $f'_i = \sum_{i=1}^{n} F'_{ij} C_j$ where F' is the Wiener-Filter of the data (best fit to the data) after the minimization process and C_j are the n constraints, either galaxy redshift surveys, i.e densities (Erdoğdu et al., 2006; Fisher et al., 1995; Kitaura et al., 2009), or peculiar velocities like for the Cosmicflows project (Courtois et al., 2012; Zaroubi et al., 1999). Namely, $\langle R_i R_j \rangle = \langle (f_i - f'_i)(f_j - f'_j) \rangle$ needs to be minimized. Processing in a similar way to the derivation of the least square

fitting method explain in Chapter 3, subsection 3.4.1.2, but with higher order matrixes, it is then possible to write:

$$f_i = \sum_{j=1}^{n}\sum_{i=1}^{n}\langle f_i C_i\rangle\langle C_i C_j\rangle^{-1} C_j \tag{4.1}$$

where $\langle AB\rangle$ notations stand for the correlation functions involving the assumed prior model.

In subsection 2.2.3.2 of Chapter 2, we have seen that from their statistical properties, the underlying fields are fully determined by the power spectrum. Assuming the power spectrum as the prior model, replacing f_i by either $\delta(\mathbf{r})$ or $v_{x,\,y,\,or\,z}(\mathbf{r})$, equation 4.1 seems sufficient to obtain both the full underlying density δ and velocity $\mathbf{v}$ fields from a dataset constituted of n constraints $\{C_0, C_1, ..., C_n\}$ (the Wiener-Filter can inter/extrapolate in absence of data). On the practical side, observational data contain uncertainties. Data points can thus be re-written $C_i = c_i + \epsilon_i$ where ϵ_i is the error on the data. Two approximations can be made regarding these errors:

- they constitute a purely statistical noise which results in an absence of correlation with the data. Then, $\langle f_i C_j\rangle = \langle f_i c_j\rangle$ and $\langle C_i C_j\rangle = \langle c_i c_j\rangle + \langle \epsilon_i \epsilon_j\rangle$,
- they have a Gaussian distribution[2]. Then, $\langle \epsilon_i \epsilon_j\rangle = \delta_{ij}^K \epsilon_j$ where δ_{ij}^K is the Kronecker function which can take only two values, 1 if $i = j$ and 0 otherwise.

From these two approximations and equation 4.1, the perturbation density and velocity fields can be estimated with:

$$\delta^{WF}(\mathbf{r}) = \sum_{i=1}^{n}\langle \delta(\mathbf{r}) c_i\rangle \eta_i \tag{4.2}$$

$$v_\alpha^{WF} = \sum_{i=1}^{n}\langle v_\alpha(\mathbf{r}) c_i\rangle \eta_i \quad \text{with} \quad \alpha = x, y, z \tag{4.3}$$

where $\eta_i = \sum_{j=1}^{n}\langle C_i C_j\rangle^{-1} C_j$ are the components of the correlation vector η with $C_i = c_i + \epsilon_i$ and $\langle C_i C_j\rangle = \langle c_i c_j\rangle + \langle \epsilon_i \epsilon_j\rangle$.

Regarding the associated correlation functions, they are given by:

$$\begin{aligned}\langle \delta(\mathbf{r}')\, v_\alpha(\mathbf{r}'+\mathbf{r})\rangle &= \frac{\dot{a}f}{(2\Pi)^3}\int_0^\infty \frac{ik_\alpha}{k^2} P(\mathbf{k}) e^{-i\mathbf{k}.\mathbf{r}} d\mathbf{k} \\ &= -\dot{a}f\hat{r}_\alpha \zeta(r)\end{aligned} \tag{4.4}$$

$$\begin{aligned}\langle v_\alpha(\mathbf{r}')\, v_\beta(\mathbf{r}'+\mathbf{r})\rangle &= \frac{(\dot{a}f)^2}{(2\Pi)^3}\int_0^\infty \frac{k_\alpha k_\beta}{k^4} P(\mathbf{k}) e^{-i\mathbf{k}.\mathbf{r}} d\mathbf{k} \\ &= (\dot{a}f)^2 \Psi_{\alpha\beta}\end{aligned} \tag{4.5}$$

[2]Note that this hypothesis is not actually fully valid because distances are logarithmically linked to distance moduli by equation 3.10. Consequently, errors have a lognormal distribution. We will more thoroughly explain and investigate this matter when confronted with the extended *cosmicflows-2* dataset in section 4.4.2.

where

- P is the assumed prior power spectrum, $\hat{\mathbf{r}} = \frac{\mathbf{r}}{r}$, the superscript WF specifies that these are Wiener-Filter estimates of the true fields,
- $\zeta = \frac{1}{2\Pi^2} \int_0^\infty k^2 j_0(\mathbf{kr}) P(\mathbf{k}) d\mathbf{k}$,
- $\Psi_{\alpha\beta} = [\Psi_T \delta^K_{\alpha\beta} + (\Psi_R - \Psi_T)\hat{r}_\alpha \hat{r}_\beta]$,
  with $\Psi_T = \frac{1}{2\Pi^2} \int_0^\infty \frac{j_1(\mathbf{kr})}{\mathbf{kr}} P(\mathbf{k}) d\mathbf{k}$ and $\Psi_R = \frac{1}{2\Pi^2} \int_0^\infty [j_0(\mathbf{kr}) - \frac{2j_1(\mathbf{kr})}{\mathbf{kr}}] P(\mathbf{k}) d\mathbf{k}$.
  The "j_is" denote the common Bessel functions.

To summarize, in the Wiener-Filter technique, data dominate the reconstruction in region where they are dense and accurate. On the opposite when they are noisy and sparse, the reconstruction is a prediction based on the assumed prior model. Schematically data are multiplied by $\frac{P}{P+\epsilon^2}$ and the reconstruction tends to the null overdensity field when data degrade. Consequently, the Wiener-Filter field estimates are non-power preserved. They cannot be used to build initial conditions as these latter need to be Gaussian fields with statistical properties given by the power spectrum. In cause is the variance of the residual which is minimized but not negligible. As a result, the true field is the sum of the mean field (or Wiener-Filter estimate) and of the residual. Unfortunately, this residual is not known but it can be approximated to produce initial conditions with the proper statistical properties. This technique relies on the Constrained Realization (CR) of Gaussian fields.

4.1.2.2 The Constrained Realization of Gaussian Fields

Evaluating the residual, required to complete the Wiener-Filter obtained mean field to produce proper initial conditions, needed some ingenuity. Bertshinger (1987) suggested first the utilization of constrained realizations to derive initial conditions, yet the algorithm used at that time revealed to be unpractical due to a slow convergence. Hoffman and Ribak (1991, 1992) were the first one to present the exact optimal algorithm to evaluate the residual. Their procedure relies on the fact that the variance of the residual is independent of the constraints. Basically, $\langle RR' \rangle = \langle ff' \rangle$ is fully determined by the assumed prior model. Thus, considering a set of mock constraints $\tilde{C}_i$ of a random generated field $\tilde{f}^{RR}$, which statistics are characterized by the same assumed prior model as the observational constraints, the Wiener-Filter of the random field can be written:

$$\tilde{f}^{WF} = \sum_{j=1}^{n} \sum_{i=1}^{n} \langle f_i \tilde{C}_i \rangle \langle \tilde{C}_i \tilde{C}_j \rangle^{-1} \tilde{C}_j = \sum_{j=1}^{n} \sum_{i=1}^{n} \langle f_i C_i \rangle \langle C_i C_j \rangle^{-1} \tilde{C}_j \tag{4.6}$$

since the correlation functions are independent of the values of the constraints, they depend solely on the assumed prior model. This gives by definition of the residual:

$$\tilde{R} = \tilde{f}^{RR} - \tilde{f}^{WF} = \tilde{f}^{RR} - \sum_{j=1}^{n}\sum_{i=1}^{n}\langle f_i C_i\rangle\langle C_i C_j\rangle^{-1}\tilde{C}_j \tag{4.7}$$

Finally, from equations 4.1 and 4.7 the constrained realization field is:

$$f^{CR} = f^{WF} + \tilde{R} = \tilde{f}^{RR} + \sum_{j=1}^{n}\sum_{i=1}^{n}\langle f_i C_i\rangle\langle C_i C_j\rangle^{-1}(C_j - \tilde{C}_j) \tag{4.8}$$

Applying relation 4.8 to the perturbation fields and keeping the same approximations as before for the errors:

$$\delta^{CR}(\mathbf{r}) = \delta^{RR}(\mathbf{r}) + \sum_{i=1}^{n}\langle\delta(\mathbf{r})c_i\rangle\eta_i \tag{4.9}$$

$$v_\alpha^{CR} = v_\alpha^{RR}(\mathbf{r}) + \sum_{i=1}^{n}\langle v_\alpha(\mathbf{r})c_i\rangle\eta_i \quad \text{with} \quad \alpha = x, y, z \tag{4.10}$$

where the components of the correlation vector are now $\eta_i = \sum_{j=1}^{n}\langle C_i C_j\rangle^{-1}(C_j - \overline{C_j})$. Here again, the constraints can be either densities or velocities. The combination of the projects Cosmicsflows and CLUES, namely this work, uses *solely* peculiar velocities obtained from direct distance measurements. The similarity between the Wiener-Filter equations (4.2 and 4.3) and the Constrained Realization equations (4.9 and 4.10) can be summarized by pointing that "without the random field, the results of the computation are the Wiener-Filter or mean fields ; with the random field, the resulting fields are precursors to build constrained initial conditions as they have the characteristics of the assumed prior model". Figure 4.1 gives another summary.

A small detail is left to be taken care of. At redshift zero, namely today, radial peculiar velocities are not all linear as assumed in the technique. Assimilating non-linearities with a statistical scatter, it is in principle possible to account for non-linear effects. On the basis that data sample a typical realization of the prior model, i.e. the power spectrum, $\frac{\chi^2}{d.o.f}$, where $\chi^2 = \sum_{i=1}^{n}\sum_{j=1}^{n} C_i\langle C_i C_j\rangle^{-1} C_j$ and d.o.f is the degree of freedom, should be close to 1. Then, adding a "sigma non-linear" σ_{NL} in the model to drive $\frac{\chi^2}{d.o.f}$ close to 1 is sufficient to compensate for the non-linearities. The σ_{NL} is inserted in the data such that $\langle C_i C_j\rangle = \langle c_i c_j\rangle + \delta_{ij}^k\epsilon_j^2 + \delta_{ij}^k\sigma_{NL}^2$.

Ultimately, assuming that the observed peculiar velocities are not strongly affected by non-linear dynamics (curl free field above the scale of virial motions), and assuming a prior cosmological model (here growth rate constant with time), the initial conditions are readily

calculated from the constrained realization fields with the procedure described in subsection 2.3.3 of Chapter 2.

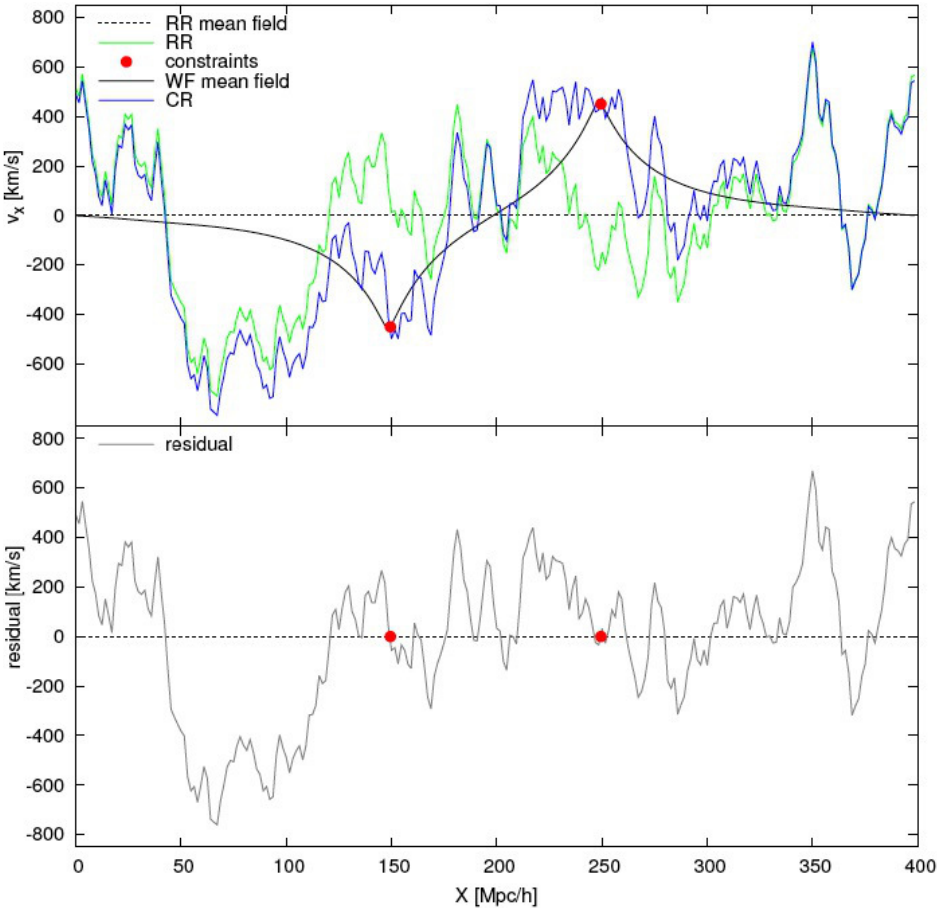

FIGURE 4.1: Principle of the Constrained Realization of Gaussian fields in one dimension. *Top*: the constrained realization field (blue solid line) equals the Wiener-Filter mean field (black solid curve) at the location of the constraints (red dots). The constraints have been put atop a random realization (green solid line). *Bottom*: the residual $\tilde{R}$ is zero at the positions of constraints (red dots). Anywhere else, it is close to the random realization (from Doumler's thesis).

4.1.3 First CLUES Generation (2003 - 2009)

Following the development of the methodology, the first constrained initial conditions were produced by Ganon and Hoffman (1993), using the Mark III catalog of peculiar velocities (Willick et al., 1996). Later on, Kolatt et al. (1996) used these initial conditions to perform the first constrained simulations of the nearby Universe, more than ten years after the first standard numerical simulation was run within a Cold Dark Matter cosmological context (Davis et al., 1985). However, the first simulations output from this method, shown on the left top panel of Figure 1.3 of Chapter 1, did not meet the standards required to fulfill the aims of the CLUES project on two aspects :

- these simulations presented a shift in the position of structures of approximately 10 h^{-1} Mpc at z=0 with respect to the today observed Universe. In other words, constrained simulated halos were, at z=0, located 10 h^{-1} Mpc away from the reference objects' original positions,
- additional density constraints were required to form nearby clusters (Klypin et al., 2003).

4.2 Reverse Zel'dovich Approximation

The major drawback of the Constrained Realization method is the fact that it is formulated in an Eulerian way at a precise time. As a result the cosmic displacement field is neglected, although galaxies observed today are at different comoving positions from their progenitors at higher redshifts. A first attempt to improve this shortcoming has been recently suggested by Doumler et al. (2013a,b,c) who tested the remedy against simple mock catalogs. They recover positions up to a few Megaparsecs, typically approximately $5 - 6$ h^{-1} Mpc. The technique, described in the following subsection, was yet to be tested on realistic mocks and on observational dataset. Accordingly this work takes three additional steps:

- the whole process to produce initial conditions from peculiar velocities is tested on more realistic mocks which include a zone of galactic extinction and errors on distances,
- the technique is refined, tested against the same realistic mocks and compared with results from the previous chain of processes,
- in a subsequent section, the refined technique is applied to the *cosmicflows-1* catalog of observational peculiar velocities (Tully et al., 2008, and subsection 3.5.1).

Throughout this section, distances are in h^{-1} Mpc. All figures are presented after a Gaussian smoothing of the fields at 2 h^{-1} Mpc, which is the intrinsic floor value validity of the linear theory, as it will be re-measured.

4.2.1 Method

4.2.1.1 RZA-radial (2009 - 2012)

Evaluating exactly the cosmic displacement field is not feasible because of the numerous non-linear events on small scales which have occurred over time, yet in subsection 2.3.3, we presented the Zel'dovich approximation (equation 2.46) which stays valid even when

perturbations are large. Then, evaluating the Zel'dovich linear displacement field from the Wiener-Filter reconstructed overdensity field (using equations 2.48 and 2.47) gives a solution to the problem: reversing this displacement in time to move the constraints from $z = 0$ backwards to their progenitors' approximated positions at higher redshifts enable to account for the cosmic displacement field. Called the Reverse Zel'dovich Approximation (RZA) by its designers (Doumler et al., 2013a,b,c), in the framework of Lagrangian perturbation theory, it can be written directly from the Zel'dovich approximation 2.46, equation 2.47 and the fact that today $\dot{a}|_0 = \frac{\dot{a}_0}{[a_0=1]} = H_0$:

$$\mathbf{x}_{L\,init}(\mathbf{x}_E) = \mathbf{x}_E(t) - \mathbf{\Psi}(\mathbf{x}_E, t) = \mathbf{x}_E(t) - \frac{\mathbf{u}(\mathbf{x}_E, t)}{H_0 f} \tag{4.11}$$

where $\mathbf{x}_E$ is the (Eulerian) position of a data point at time t, $\mathbf{x}_{L\,init}$ is the initial (Lagrangian) position, $\mathbf{\Psi}$ is the displacement field, $\mathbf{u}$ is the perturbation or peculiar velocity field and f is the growth rate.

Once re-located at their precursors' approximated positions, the constraints are inserted into the Constrained Realization method to set initial conditions. Tested against simple mocks, positions are recovered up to a few Megaparsecs, typically $\approx 5 - 6\,\mathrm{h}^{-1}\,\mathrm{Mpc}$ (Doumler et al., 2013a,b,c). Still, the first application of the process to the first observational catalog of the Cosmicflows project reveals that the method can be refined.

4.2.1.2 RZA3D, CLUES Second Generation (2013 -)

Because observed constraints have uncertainties (and are probably also affected by biases), the peculiar velocity field is not accurately described by solely one (radial) component (unique component accessible from direct observations). An additional step can thus be added to the initial technique called RZA-radial from now on. In the refined technique (RZA3D) constraints are not only moved to their progenitors' positions but, also, the *observed uncertain* peculiar velocities are replaced by fully WF-reconstructed three component vectors. Such resulting constraints have already been given by the Wiener-Filter a weight according to their precision. Typically, the Wiener-Filter field goes to the null value when there is no coherent signal or when data points have too large errors. Thus, no error should be allocated to RZA3D derived constraints when input in the Constrained Realization algorithm[3]. Initial conditions are then produced in the standard way.

In other words, RZA3D differs from the initial RZA-radial on two points:

- instead of observed radial peculiar velocities, the constraints are now the Wiener-Filter estimated peculiar velocities,

[3]This is in a sense similar to an unbiased minimal variance estimator (Zaroubi, 2002)

- initial conditions are constructed under the assumption of null statistical errors to prevent the double signal suppression resulting from the successive application of the Wiener-Filter (to obtain 3D velocities) and of the Constrained Realization (to produce initial conditions).

Figure 4.2 provides a schematic presentation of the WF/RZA method which prepares the constraints to be input into the Constrained Realization algorithm.

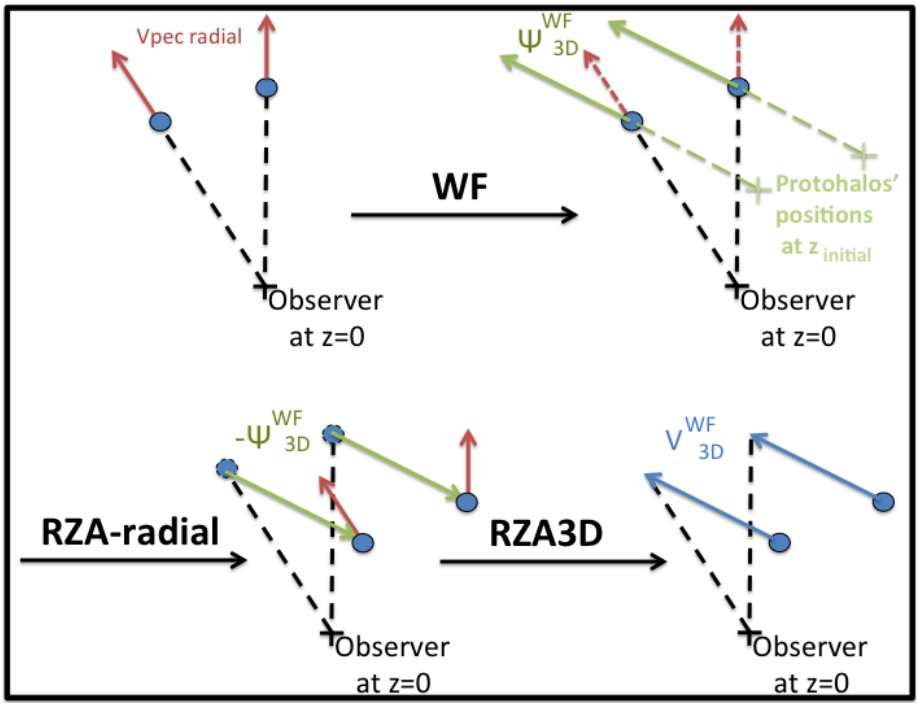

FIGURE 4.2: The refinement of the WF/RZA technique. The Wiener-Filter applied to observed radial peculiar velocities provides full 3D reconstructed peculiar velocity field v_{3D}^{WF} which allows to derive the cosmic displacement field Ψ_{3D}^{WF} (see equation 2.47). In the initial RZA-radial technique the observational (radial) constraints at $z = 0$ are re-located by -Ψ_{3D}^{WF} to their progenitors' positions at higher redshifts. Since the peculiar velocity field is curl free (above the scale of virial motions) it is supposed to be fully defined by only one component. However, because observed peculiar velocities have uncertainties (and are probably affected by biases), RZA-radial is insufficient. The proposed refinement in RZA3D takes care of this flaw by using the full 3D Wiener-Filter reconstructed peculiar velocities v_{3D}^{WF} as constraints.

4.2.2 Building Mocks

When working on scales of a few tens of Megaparsecs (enclosing a volume we call the Local Universe), the cosmic variance is a major concern because these scales are far smaller than the scale of homogeneity of the Universe. As a matter of fact, the observational dataset used in this section only reaches once to twice the size of our filament (from Ursa-Major to Centaurus clusters, the distance is roughly $40\,\mathrm{h}^{-1}\,\mathrm{Mpc}$). This leads to a bias:

- our position (as observers) is unique (peculiar) and impacts highly the data collections. In other words since we are living in a supercluster bounding a very large void, the observed peculiar velocities are very much dominated by a specific local structure dynamics,

Thus we must:

- test the methodology against a replica of the actual nearby Universe to be in the same particular dynamical conditions (including the presence of a nearby very large void),
- run several constrained numerical simulations to estimate the confidence level at which the observed large scale structures are recovered with a given methodology whatever the random component.

Accordingly, mock catalogs are drawn from a previous constrained simulation of the Local Universe (Klypin et al., 2003). This particular simulation, hereafter BOX160, is a dark matter only simulation of 1024^3 particles in a computational box of side length $L = 160\,\mathrm{h}^{-1}\,\mathrm{Mpc}$ constrained by peculiar velocity catalogs and a sample of positions and masses of X-ray selected nearby clusters. Since this simulation was computed in the WMAP3 framework, tests on the mock are also conducted in the WMAP3 framework. WMAP3, described in Table 2.1, is a flat universe with a matter density of $\Omega_m = 0.24$, a $\sigma_8 = 0.75$ normalization and $H_0 = 73$ km s^{-1} Mpc^{-1}.

BOX160 reproduces many of the key structures of the nearby universe, such as Virgo, Coma and Centaurus clusters, Perseus-Pisces supercluster and the Great Attractor region. A Local Group-like structure has been identified in the simulation and a mock observer is attached to that object. The catalog is built with respect to this observer. We assume that galaxies follow the peculiar velocities of dark matter halos in which they reside. Consequently, a mock catalog of dark matter halos has been extracted from BOX160 with the Amiga halo finder (Knollmann and Knebe, 2009). A comparison between the various halo-finders by Knebe et al. (2013) did not reveal any substantial difference between the resulting list of halos and their characteristics. Consequently, the halo finder choice should not impact our work. The output list of parameters contains halo coordinates in h^{-1} Mpc, peculiar velocities in km s^{-1} and masses in $\mathrm{h}^{-1}\,\mathrm{M}_\odot$. Halos are selected in a sphere of 30 h^{-1} Mpc radius around the mock observer to mimic as much as possible the extent of the Cosmicflows project's first catalog to be used later on. Two novelties with respect to the mocks of Doumler et al. (2013a,b,c) are introduced. To simulate a zone without data similar to that produced by the extinction of our galaxy's disk (Zone of Avoidance), every halo with a latitude in between $\pm 10°$ is removed. Major players in the local dynamics, such as the mock Great Attractor, are thus (partly) masked by this extinction zone. The mock catalog is also designed to reproduce

the current observational limits: a 20% uncertainty on galaxy distances, and thereby on derived radial peculiar velocities. For simplicity the relative errors are assumed to follow a normal distribution around the true distances D. Resulting distances D' correspond to the observational measured distances with their uncertainties. The mock radial peculiar velocities are then computed as the difference between the total velocity (expansion+peculiar motion) and the modified distances D' multiplied by 100 (Hubble Constant $\times$ h^{-1} as distances are in h^{-1} Mpc). This procedure takes place in the Cosmic Microwave Background frame of reference, namely in the framework of the computational box.

The reconstruction of the Large Scale Structure, and of its initial conditions, from peculiar velocities is hampered by virial motions of galaxies in clusters. Such motions cannot be accounted for in the present proposed WF/RZA/CR framework. Grouping distance measurements of galaxies at the same distance (belonging to a same cluster) into a single data point with a reduced error could provide a partial remedy to the problem. However, the issue of grouping a given catalog constitutes a formidable challenge that has not been adequately solved yet. Fortunately late-type galaxies constitute roughly 80% of *cosmicflows-1* data (Tully et al., 2008). Such galaxies reside mostly in the field where virial motions do not dominate cosmic flows, thus they are less affected by this problem. The mock catalog is quite similar on this matter. The halo selection procedure described earlier give 1467 halos. Still, 95% of these halos that serve as mock data points are isolated. As a result, virial motions do not dominate cosmic flows in the mock either. Such a mock catalog is a reasonable proxy to the first catalog of the project Cosmicflows.

4.2.3 Application on Mocks

In this subsection, the full machinery to obtain constrained simulations is tested on the mock built in subsection 4.2.2. The WF/RZA/CR algorithm is first applied using both variants of the RZA to obtain precursors of initial conditions. A σ_{NL} term is used to account for the non-linear contributions of the radial peculiar velocities, which are not included in the model. From these precursors, initial conditions are set and input in GADGET-2 (Springel, 2005) N-body code to perform dark matter only simulations. The boxsize, 160 h^{-1} Mpc long on each side, is almost three times the extent of the mock. Periodic boundary conditions can be assumed without any risk of spurious phenomena in the central 60 h^{-1} Mpc region to be analyzed. In addition, the distribution of the peculiar velocity field values at high redshifts (in the initial conditions) is quite Gaussian in Figure 4.3. This implies that there are enough modes to define large scale flows (and velocities through large scale correlations). As a result, the 160 h^{-1} Mpc box has a large enough size for computations. The grid size is $N = 256^3$. Knebe et al. (2009) showed that the choice of the initial redshift value has no

substantial impact on the resulting dark matter halo properties at $z = 0$. Thus, we only seek to avoid shell-crossing. Hence, simulations are started at z= 60.

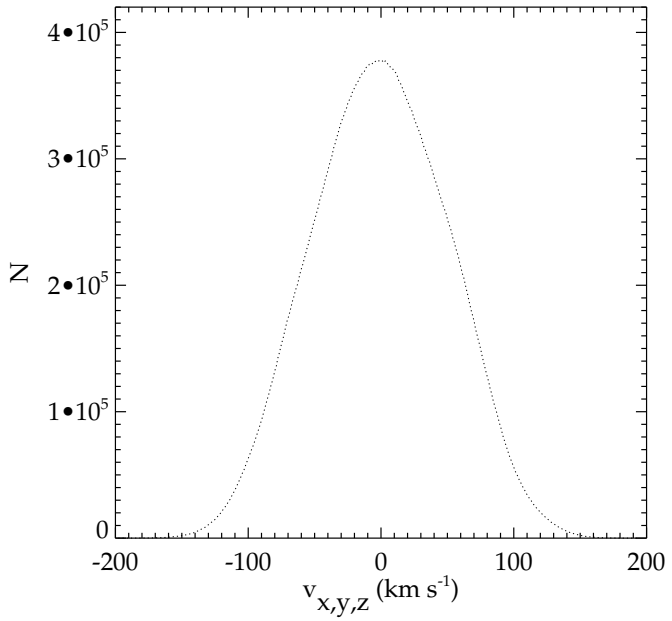

FIGURE 4.3: Distribution of the velocity field components, at $z = 60$, in the initial conditions. The distribution is quite Gaussian implying that there are enough modes to define large scale flows (and velocities through large scale correlations) within a boxsize of 160 h^{-1} Mpc long on each side.

4.2.3.1 Wiener-Filter Reconstruction of the Mock Universe

To facilitate the comparisons between the initial BOX160 and its Wiener-Filter reconstruction from a mock, the BOX160 velocity field is interpolated on a 256^3 grid using a Cloud-In-Cell interpolation scheme. Figure 4.4 displays the confidence level zones of the reconstruction with respect to the original BOX160. The zones result from a cell-to-cell comparison, within the central 60 h^{-1} Mpc region, between the velocity grids of the Wiener-Filter reconstruction and of the reference simulation. The total scatter around the 1:1 relation is 201 km s^{-1} or 1.7 σ. The Wiener-Filter velocity field is thus a good reconstruction of the BOX160 source.

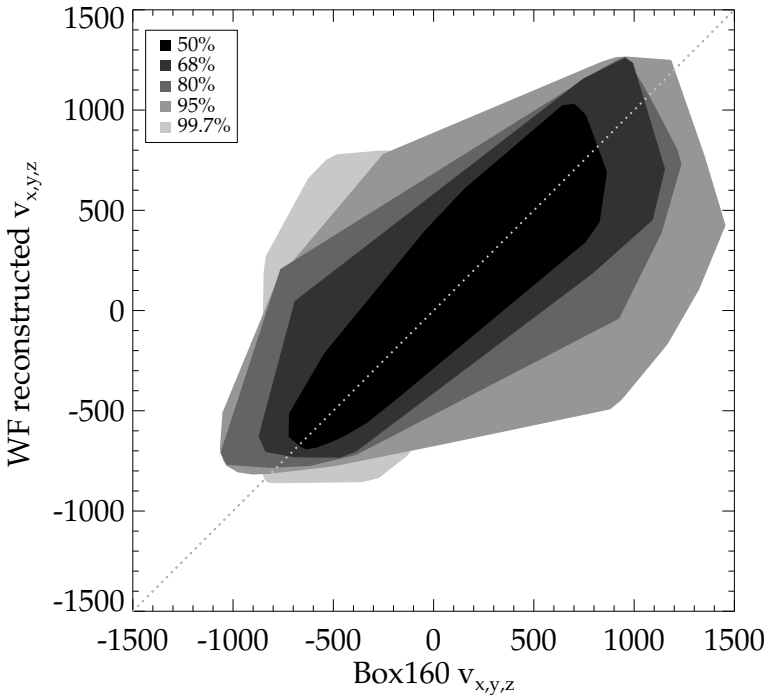

FIGURE 4.4: Confidence level zones obtained with a cell-to-cell comparison between the velocity grids of the reference simulation BOX160 and its Wiener-Filter reconstruction within a 30 h^{-1} Mpc radius sphere. For example, 50 % of the peculiar velocity pairs, ($value_{cell\ xyz\ BOX160}$; $value_{cell\ xyz\ WF}$) can be found in the darker zone. This zone, slightly scattered around a 1:1 relation, shows the good agreement between the velocity values in a cell from the reference simulation and in the very same cell from the reconstruction. 68 % of the pairs are in the sum of the two internal zones and so on. 68, 95 and 99.7 % correspond to 1, 2 and 3 σ uncertainties.

Figure 4.5 shows two planes centered on the look-alike of the Milky-Way of the reference simulation and of its reconstruction obtained with the Wiener-Filter technique applied to the mock. Velocity (black arrows) and density (contours) fields are plotted. The green contour displays the mean density level. The main features - direction of the cosmic flows and attractors' positions - are properly reconstructed. The feature, in the XY plane, is the Great Attractor region look-alike with three density peaks from the reference simulation marked by red crosses in both quadrants. In YZ, the red cross locates the density peak of the mock Virgo halo in the reference simulation. These qualitative analyses illustrate the claim that, with a sparse and noisy mock similar to *cosmicflows-1* (in terms of number of constraints, zone of extinction without data and large errors on peculiar velocities), the Wiener-Filter is an optimal reconstruction tool in the linear regime of the gravitational instability. Structures are not necessarily reconstructed at their exact positions since the intrinsic accuracy is about 2 h^{-1} Mpc. Still, overall, the density field is recovered when considering only the linear theory on all scales.

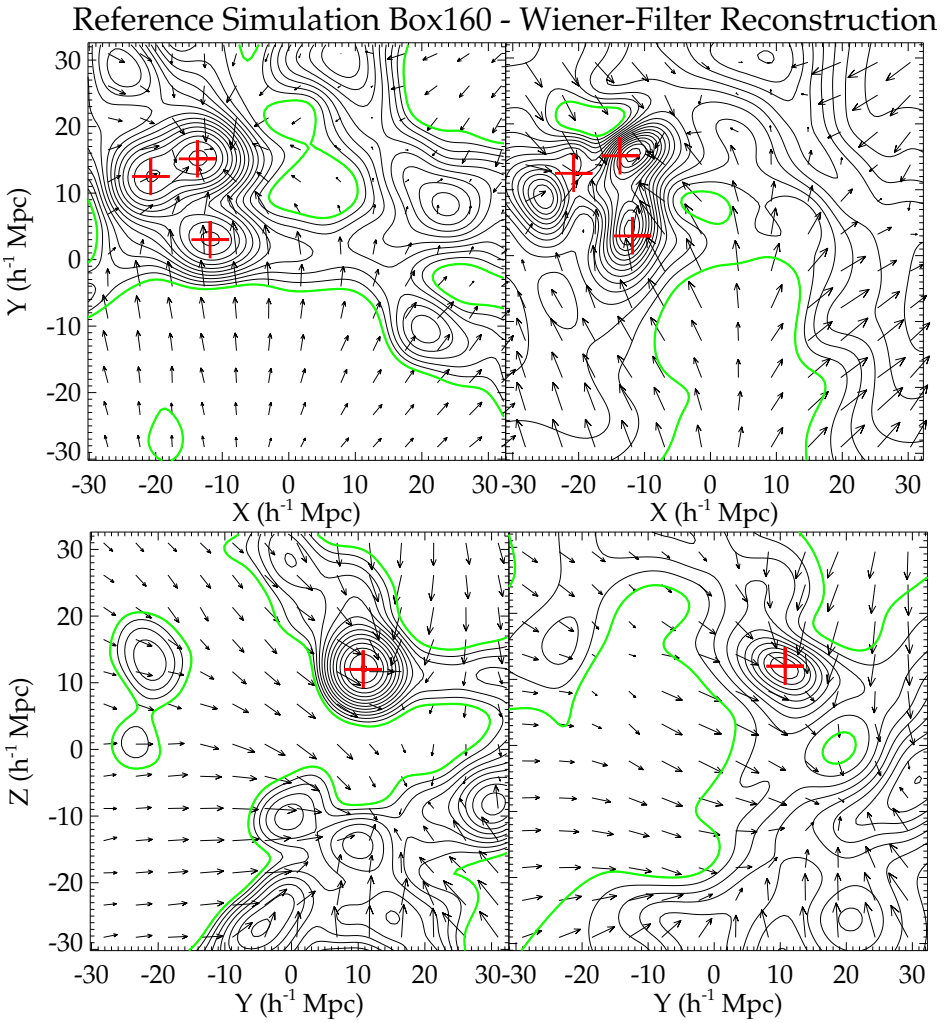

FIGURE 4.5: XY and YZ views of the reference simulation BOX160 (*left*) and its Wiener-Filter reconstruction (*right*) restricted to the central 60 h^{-1} Mpc zone. The reconstruction has been obtained using only radial peculiar velocity data from a realistic mock catalog containing about the same errors and same number of data-points as the observational *cosmicflows-1* catalog. The cosmic flows are represented by black arrows. Overdensity iso-contours are delimited by solid black lines. The green contour delimitates the mean density. Red crosses show the positions of the major density peaks in the reference simulation. Even with this sparse and noisy realistic mock, the Wiener-Filter has enough signal to properly recover the original cosmic flows and density peaks with a precision of about 2-3 h^{-1} Mpc in position.

4.2.3.2 Constrained Simulations: RZA-radial versus RZA3D

Once the continuous fields obtained with the Wiener-Filter technique have been extrapolated at the data points' positions, constraints are displaced from their $z = 0$ location to their progenitors' position at higher redshifts. In addition, constraints are replaced by their full Wiener-Filter reconstruction in the RZA3D technique. Since simulations are run with periodic boundary conditions, only the divergent part of the velocity field (velocities due to

densities inside the box solely) is used to generate initial conditions. Hence, any tidal motion due to densities outside of the box is removed.

A major objective of this subsection is to compare RZA-radial and RZA3D algorithms. However, cosmic variance can affect the comparison between methods. To take care of this effect:

- each RZA-radial derived Initial Condition shares the same random component with one of the RZA3D obtained Initial Condition. Hence, the simulations resulting from the same random seed initial conditions are expected to reproduce the same Large Scale Structure,
- ten constrained initial conditions are built to estimate the confidence level on structure positions for each procedure.

Resulting simulations are also compared with the reference BOX160 to estimate the average misplacement of simulated structures at $z = 0$ with respect to original locations. The comparison between the constrained simulations and BOX160 is done on a 256^3 Cloud-In-Cell interpolated grid after smoothing the density and velocity fields with a Gaussian kernel of 2.0 h^{-1} Mpc. When averaging over an increasing number of constrained simulations, the standard deviation with respect to BOX160 starts at 0.47 in logarithmic unit of density for one simulation and decrease to a plateau value of 0.37 when considering eight or more simulations. Adding more than ten simulations would not produce, on average, other high and deep density zones that could be compared between the two methods and with BOX160 (or the 0.37 value would have continued to decrease). The standard deviation of RZA3D simulations around their average is smaller than that of RZA-radial both in terms of velocity and density (0.34 against 0.35 in logarithmic unit of density and 246 against 258 km s^{-1}). Although there is a random component, constrained simulations of BOX160 obtained with RZA3D method have stronger features, reproduced at very similar positions, than RZA-radial constrained simulations. The cosmic variance is reduced with RZA3D because constraints are stronger than in the RZA-radial case as seen on Figure 4.6. The η_i components of the data-data correlation vector η have higher absolute values with RZA3D than with RZA-radial.

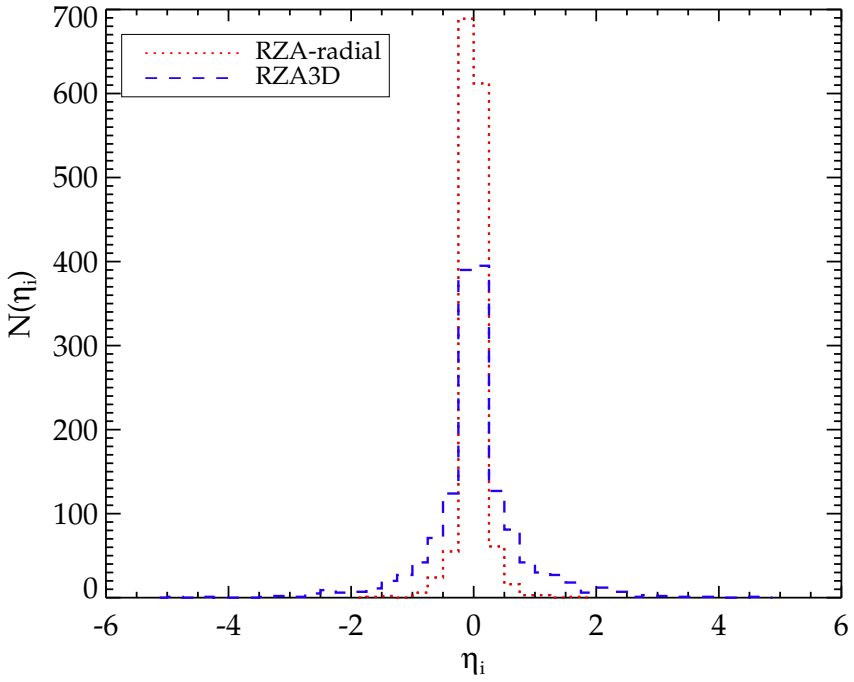

FIGURE 4.6: Distribution functions of the component values η_i of the data-data correlation vector η computed with RZA-radial (dotted red line) and RZA3D (dashed blue line) constraints. The higher the absolute value of η_i, the more the corresponding constraint contributes in the constrained Initial Condition. Since the distribution obtained with RZA3D is wider than that resulting from RZA-radial, RZA3D constraints are stronger than RZA-radial ones.

BOX160 contains some replicas of prominent nearby structures such as Virgo, Hydra and Centaurus. These halos are named hereafter s-Virgo, s-Hydra and s-Centaurus to distinguish them from the observed ones. BOX160 contains also a halo called s-Cz (in accord with Doumler et al., 2013b). These target objects are used to monitor the quality of the simulations. Figure 4.7 shows the density field in the planes containing these objects of the actual simulation BOX160 (top panel), of RZA-radial (middle panel), and RZA3D (bottom panel) with simulations averaged on ten different realizations. The main dark matter halos from BOX160 used as tracers are marked by red crosses in the six panels. There is a recurrent overdensity at the expected location of s-Virgo (high density peak in the YZ plot) only in the RZA3D simulations.

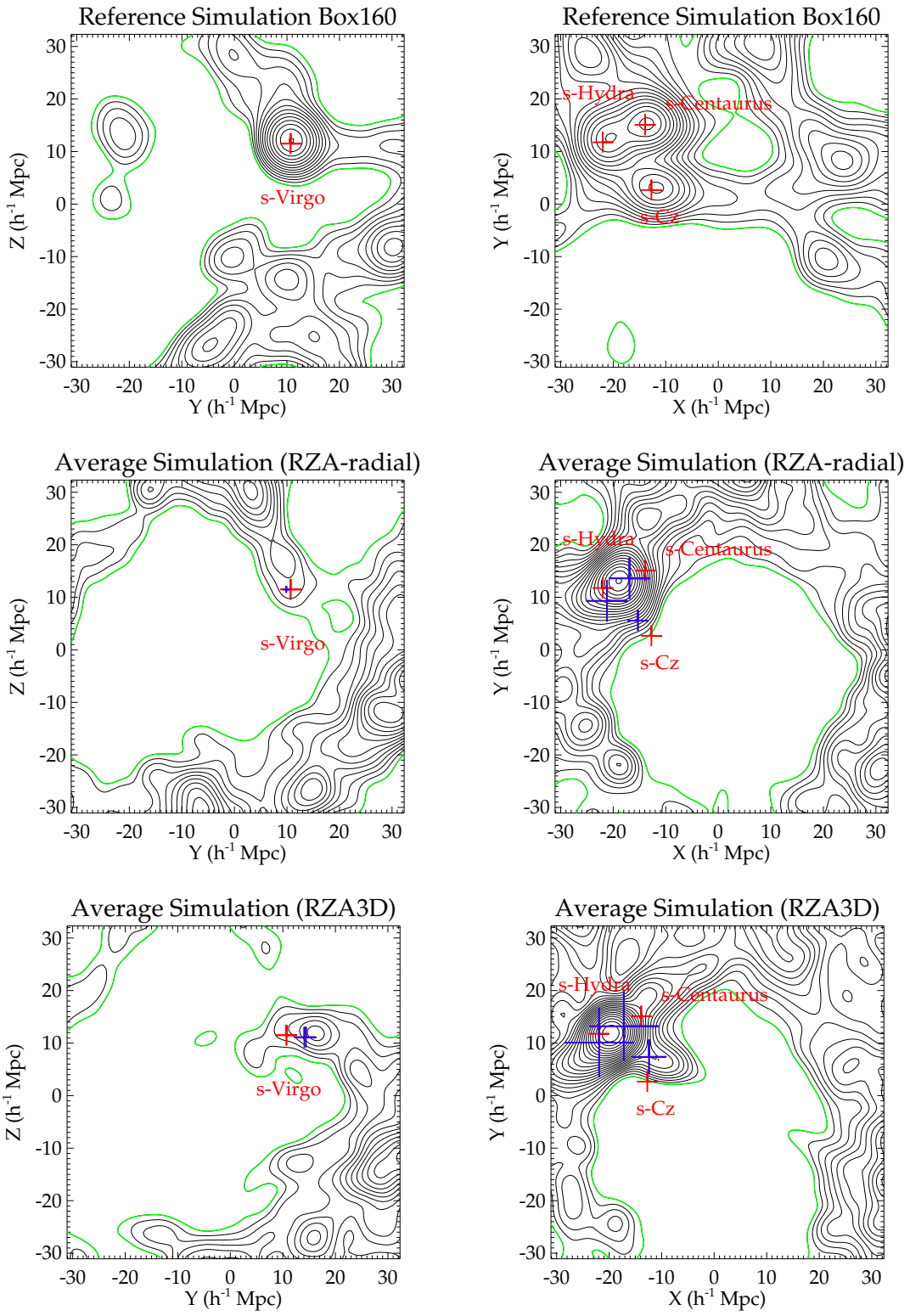

FIGURE 4.7: Visualization of planes containing main simulated attractors (positioned at X=7 and at Z=-6 h^{-1} Mpc). Solid black iso-contours delimit overdensities. The green color stands for the mean density in the box. *Top*: Reference simulation. *Middle*: Average over ten constrained simulations using RZA-radial on the mock. *Bottom*: Average over ten constrained simulations applying RZA3D on the mock. Red crosses show original positions of s-Virgo, s-Hydra, s-Centaurus and s-Cz in the reference simulation. Positions of the averaged replicas in the constrained simulations are shown in blue. Crosses' sizes are proportional to the number of replicas found out of ten simulations.

For a more quantitative analysis, dark matter halos are obtained with the Amiga halo finder for each one of the simulations and the s-halos are identified when recovered. A halo in a constrained simulation is considered to be a replica of a BOX160 halo when the difference in position is smaller than approximately 6 h^{-1} Mpc and when masses are of the same order. The search is restricted to a sphere of 6 h^{-1} Mpc since the scope of this work is to find a method resulting in an error below 6 h^{-1} Mpc (3 σ). Blue crosses on Figure 4.7 are located at the average position of the look-alikes of s-Virgo, s-Hydra, s-Centaurus and s-Cz halos in the constrained simulations. The cross sizes are proportional to the number of simulations (out of ten) in which a replica has been found. Table 4.1 recapitulates the characteristics of the targeted halos and of their look-alikes: virial masses, positions and standard deviations. RZA-radial fails to recover s-Hydra and s-Centaurus as separate individual objects in five out of ten simulations, thus they are not reported in the table. In these five out of ten simulations, they are collapsed into a single object. The table also records the average of each replicas distance to the genuine halo. The typical difference is about 5 h^{-1} Mpc for the RZA3D technique against 6 h^{-1} Mpc for RZA-radial. However, because with RZA-radial more halos are not found in the 6 h^{-1} Mpc sphere (they are outside of the sphere so farther away) than with RZA3D, the value for RZA-radial is more biased (lowered) by the restricted search than that of RZA3D. Still, studying the standard deviations of the position errors shows that it is possible to reach the floor value imposed by the linear regime, 2-3 h^{-1} Mpc with some random seeds for RZA3D while it is always impossible with RZA-radial. The table proves an enhanced accuracy of the RZA3D method in terms of position errors (when compared with BOX160). The gain is also clear in term of reliability-robustness of the results since more replicas (out of ten different random seed simulations) are found at a similar location (smaller standard deviations in positions) with RZA3D than with RZA-radial.

We can also consider a comparison between high density peaks in the Wiener-Filter and in the constrained simulations. The density peak reconstructed by the Wiener-Filter in the bottom right quadrant of Figure 4.5 is also present in six RZA3D simulations out of ten when looking within a ~ 6 h^{-1} Mpc sphere centered on the Wiener-Filter peak. By contrast, there is a peak in only three RZA-radial simulations out of ten within the same sphere. In both cases, the typical misplacement is 4-5 h^{-1} Mpc with a standard deviation about 1 h^{-1} Mpc.

RZA3D applied to a mock *cosmicflows-1* catalog outperforms RZA-radial applied to the same mock. The stronger the constraints, the more the cosmic variance that exists over ten constrained simulations because of a different random component is reduced. The number and accuracy of constraints in a *cosmicflows-1*-like catalog are adequate to simulate properly a look-alike of the Local Universe, within a 30 h^{-1} Mpc radius sphere, with a precision reaching the intrinsic limitation of the technique.

Simulation case	Mass	Average Position X, Y, Z	Average Distance to reference halo	Nb of occurrences
Box160 s-Virgo	3.3	7.12, 10.7, 11.5		
RZA-radial s-Vir.	0.25	3.40, 9.88, 17.2	6.9	1/10
RZA3D s-Vir.	0.34 ; $\sigma = 0.05$	7.78, 14.4, 11.1 ; σ= 2.4	5.4 ; σ=1.6	5/10
Box160 s-Centaurus	6.07	-13.9, 15.1, -8.81		
RZA-radial s-Cent.	3.1 ; $\sigma = 2.8$	-16.9, 13.6, -9.62 ; σ= 3.0	6.0 ; $\sigma = 0.4$	5/10
RZA3D s-Cent.	7.9 ; $\sigma = 4.0$	-17.2, 13.2, -10.5 ; σ= 1.9	5.0 ; $\sigma = 1.5$	10/10
Box160 s-Hydra	5.18	-22.0, 11.8, -3.35		
RZA-radial s-Hyd.	4.7 ; $\sigma = 2.3$	-21.2, 9.32, -4.87 ; σ= 1.9	3.1 ; $\sigma = 1.5$	5/10
RZA3D s-Hyd.	4.7; $\sigma = 2.0$	-21.9, 10.1, -4.58 ; σ= 1.3	3.0 ; $\sigma = 1.2$	10/10
Box160 s-Cz	0.96	-12.7, 2.68, -6.36		
RZA-radial s-Cz	0.80 ; $\sigma = 0.44$	-15.3, 5.56, -10.1 ; σ= 2.3	6.3 ; $\sigma = 0.57$	3/10
RZA3D s-Cz	0.40 ; $\sigma = 0.19$	-12.4, 7.37, -7.20 ; σ= 2.3	6.0 ; $\sigma = 1.9$	5/10

TABLE 4.1: Average parameters and standard deviations σ for target halos looked for in a 6 h^{-1} Mpc sphere centered on their original positions in the reference simulation. (1) simulation in which the halos are looked for, (2) dark matter mass in 10^{14} h^{-1} $M_\odot$, (3) average coordinates X, Y and Z and standard deviations, h^{-1} Mpc, (4) average distance to the genuine halo and standard deviation, h^{-1} Mpc, (5) number of simulations (out of ten with a different random seed) which contain a replica.

4.3 Constrained Simulations with Cosmicflows-1

Cosmicflows-1, catalog of peculiar velocities (Tully et al., 2008, and subsection 3.5.1), is used to perform constrained simulations of the Local Universe. For every simulation, we assume a ΛCDM model in the 7-year Wilkinson and Microwave Anisotropy Probe (WMAP7) framework (Komatsu et al., 2011). The cosmological parameters are $H_0 = 70$ km s^{-1} Mpc^{-1}, Ω_m=0.272 and Ω_Λ=0.728 (see Table 2.1). Figure 4.10 recapitulates the main results of this section:

- the left column is the first step of the WF/RZA/CR technique, namely the Wiener-Filter,
- the middle column represents the outcomes of one single simulation,
- the last (right) column shows the average over ten different realizations.

These results are described in the subsequent subsections. Note that we perform in parallel the same work within the WMAP3 framework to evaluate the impact of a change in cosmology. Finding no substantial difference, we decided to present only fields obtained within the WMAP7 framework to match previous work conducted with *cosmicflows-1*.

4.3.1 Wiener-Filter Reconstruction of the Local Universe

Reconstructions of the Local Universe obtained with the Wiener-Filter applied to *cosmicflows-1* have already been presented at length in Courtois et al. (2012, 2013) (see Figure 2.4 for some of the results). This work only uses the Wiener-Filter as a step in the process to reach the ultimate goal, namely the constrained simulations. Regardless, in absence of access to the full fields of the Local Universe to compare our final products with, the Wiener-Filter maps of *cosmicflows-1* are taken as proxies to the actual Universe and, thus, are worth presenting. In the reconstruction, supergalactic cartesian coordinates are centered on the Milky-Way and the XY supergalactic plane contains the Local Structure. The three main planes are shown at the supergalactic Z=0, Y=12.5 and X=−2.5 h^{-1} Mpc coordinates to fit the location of the Virgo cluster. For a direct comparisons between the real Universe and the Wiener-Filter reconstructed large scale structure the V8k galaxy redshifts catalog is overplotted as grey dots. This catalog contains 30,124 galaxies with distances modified by a numerical action model of the Virgo infall for $v < 3000$ km s^{-1}. It is available at the Extragalactic Distance Database website. Qualitatively, the real Virgo cluster and the void behind are reconstructed in the supergalactic XY plane. Virgo is also visible next to the Local Void in the YZ supergalactic plane. It can also be found in the XZ supergalactic slice.

4.3.2 Constrained Simulations of the Local Universe

The Wiener-Filter reconstructed velocity field is then extrapolated at the location of the data points. Next, RZA-radial and RZA3D methods are applied to *cosmicflows-1* constraints in order to construct initial conditions with the constrained realization algorithm. Ten random seeds are used to build initial conditions with periodic boundary conditions for both methods. It is to be noted that observational radial peculiar velocities are measurements of motions related to the whole gravitational potential. However, simulations are here run in a relatively small box, with periodic boundary conditions, where not all the attractors responsible for the entire motions are present. Thus, replacing velocities that result from the entire gravitational potential by velocities related to the gravitational potential in the box (namely RZA3D instead of RZA-radial) is more accurate and constitutes another advantage of the RZA3D method. Resulting initial conditions are then run from redshifts 60 to 0. The cosmic variance in terms of standard deviations of ten simulations with respect to their average is 1.45 against

1.40 in logarithmic unit of density and 303 against 291 km s^{-1} for RZA-radial and RZA3D respectively. Values are in agreement with results found previously in subsection 4.2.3 for mock constrained simulations. RZA3D constraints are stronger than RZA-radial ones.

4.3.2.1 Constrained Simulations and WMAP7/ΛCDM Cosmology

In order to check the compatibility of *cosmicflows-1* constrained simulations with the standard model of cosmology, random simulations are run with the same seeds used to set up the constrained initial conditions. Figure 4.8 compares the final power spectra and mass functions at $z = 0$ of ten RZA3D constrained simulations and corresponding random ones (RZA-radial results in very similar, if not identical, plots which are thus not shown). A clear overlap is seen, which leads to conclude that the methodology preserves the cosmology. As the method does not modify the cosmology, its validity is not altered.

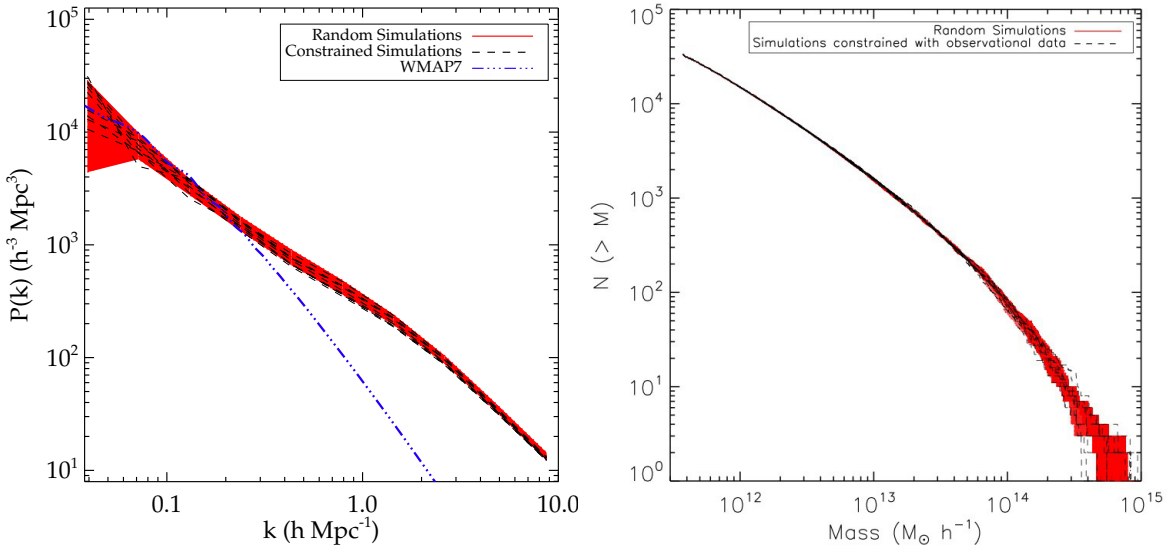

FIGURE 4.8: Power spectra (*left*) and mass functions (*right*) of the ten constrained simulations of the Local Universe obtained with RZA3D applied to *cosmicflows-1* (black dashed lines). The red shaded areas correspond to the range within which the ten random simulations, with the same cosmology as constrained simulations (same assumed prior model), are contained. The dashed-dotted blue line in the left panel stands for the linear part of WMAP7. Both constrained and random power spectra and mass functions overlap each other.

4.3.2.2 Constrained Simulations and Local Cosmography

In the simulations, the supergalactic coordinates are parallel to the box coordinates with the origin at the center of the box where ideally there is a Milky-Way-like. Table 4.2 and Figure 4.9 are proofs that no Virgo cluster is simulated at the expected location out of ten RZA-radial simulations constrained by the observational peculiar velocity catalog assuming

either WMAP7 or WMAP3 (choice which results in negligible differences). Accordingly and in agreement with the theoretical study which advocate the utilization of RZA3D, the rest of the section focuses only on the analysis of RZA3D constrained simulations. The compatibility of the constrained simulations with the observed local cosmography is presented.

Case	Mass	Average supergalactic X,Y,Z position	Average distance to the observed Virgo cluster	Nb of occurences
Observed Virgo cluster	4*	-2.74, 12.0, -0.518		
RZA3D (WMAP7)	0.7 ; $\sigma = 0.3$	1.23, 13.8, 2.2 ; $\sigma = 1.2$	5.4; $\sigma = 1.2$	8/10
RZA3D (WMAP3)	0.5 ; $\sigma = 0.2$	1.30, 13.8, 0.70 ; $\sigma = 1.0$	4.7; $\sigma = 0.8$	8/10
RZA-radial (WMAP7)				0/10
RZA-radial (WMAP3)				0/10

TABLE 4.2: Average parameters and standard deviations σ for the halos representative of Virgo. (1) simulations in which the halos are looked for, 2) mass in 10^{14} h^{-1} $M_{\odot}$. *Estimation of the total (baryonic + dark matter) mass (e.g. Ekholm et al., 2000; Karachentsev and Nasonova, 2010). (3) average supergalactic coordinates X, Y and Z and their standard deviations, h^{-1} Mpc, (4) distance from the simulation halo to the observed Virgo location and standard deviation σ, h^{-1} Mpc, (5) number of occurrences in ten different simulations (if a halo similar to Virgo was found in a $6\,h^{-1}$ Mpc sphere).

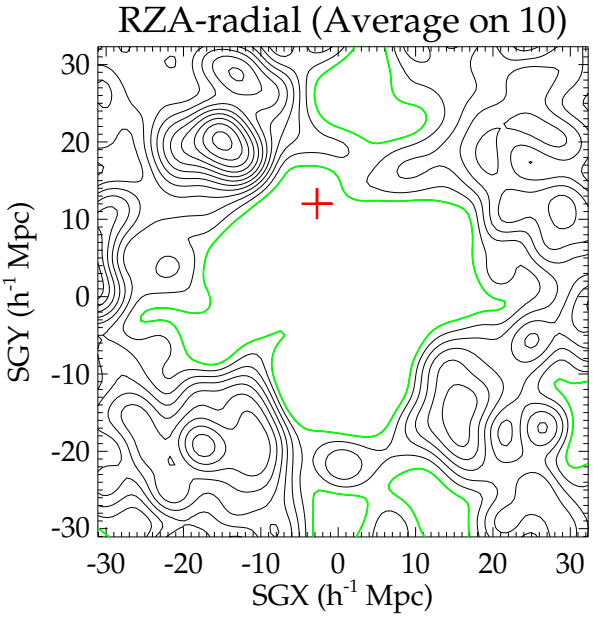

FIGURE 4.9: Average of ten constrained simulations obtained with RZA-radial applied to the observational catalog of peculiar velocities *cosmicflows-1*. Virgo is never simulated at the expected location, a void stands at its position.

Figure 4.10 displays the Wiener-Filter reconstruction of the *cosmicflows-1* catalog (left), one single RZA3D simulation (middle column) and an average of ten RZA3D constrained

simulations (right). Fields are smoothed by a Gaussian kernel of 2 h^{-1} Mpc. Red crosses mark the position of the Virgo cluster in the observed Universe (see Table 4.2 for the exact position). The Local Void and Virgo Void are also indicated. The Wiener-Filter serve as targets for the constrained simulations, with the caveat that the Wiener-Filter provides only the linear overdensity field. The inner $R = 30$ h^{-1} Mpc volume is dominated by the Local Supercluster. The general structure of the Local Universe including positions of the voids are quite well reproduced by a constrained simulation. The average over ten different realizations shows that in general the Virgo cluster region is well simulated at a similar location whatever random component is used.

To quantify the reliability of the RZA3D technique in simulating the Virgo cluster and the area surrounding it:

- the high density peak of the Wiener-Filter reconstruction is identified in each RZA3D simulation,
- the Amiga halo finder is used to identify replicas of the cluster in the constrained simulations.

To proceed, we use the same process as with the mock catalog. There is a density peak at a similar location to the Wiener-Filter peak in the ten RZA3D constrained simulations. The typical misplacement with respect to the Wiener-Filter peak is about 8-9 h^{-1} Mpc with a standard deviation about 2 h^{-1} Mpc. Although the supergalactic Y and Z components are very similar in the Wiener-Filter ($\sim$ 13 and 1 h^{-1} Mpc) and in the simulations ($\sim$ 13 $\pm$ 1 and 3 $\pm$ 2 h^{-1} Mpc), the error in position is quite high because in the supergalactic X direction the shift in position, with respect to *cosmicflows-1* Virgo cluster, is negative in the Wiener-Filter ($\sim$ -3 h^{-1} Mpc) while it is positive in the simulations ($\sim$ 4 h^{-1} Mpc). Still, there is absolutely no density peak in the RZA-radial constrained simulations even when looking in a 10 h^{-1} Mpc sphere centered on the Wiener-Filter density peak. The blue crosses in Figure 4.10 stand for the positions (average positions, in the right column) of the Virgo-like halos. Table 4.2 provides details about masses, positions, errors in position and standard deviations. For completeness, the table presents the results obtained in both WMAP7 and WMAP3 frameworks although differences are negligible. A Virgo-like halo is present in eight out of ten simulations. By comparison, with RZA-radial, no replica of Virgo in 6 h^{-1} Mpc spheres centered on the observational position was found.

A synthetic Local Universe with a Virgo cluster using *only observational peculiar velocities* is produced for the first time thanks to the WF/RZA/CR technique described in this work. This is a proof of concept that the WF/RZA/CR method can be applied to observational peculiar velocities to successfully build constrained Initial Conditions.

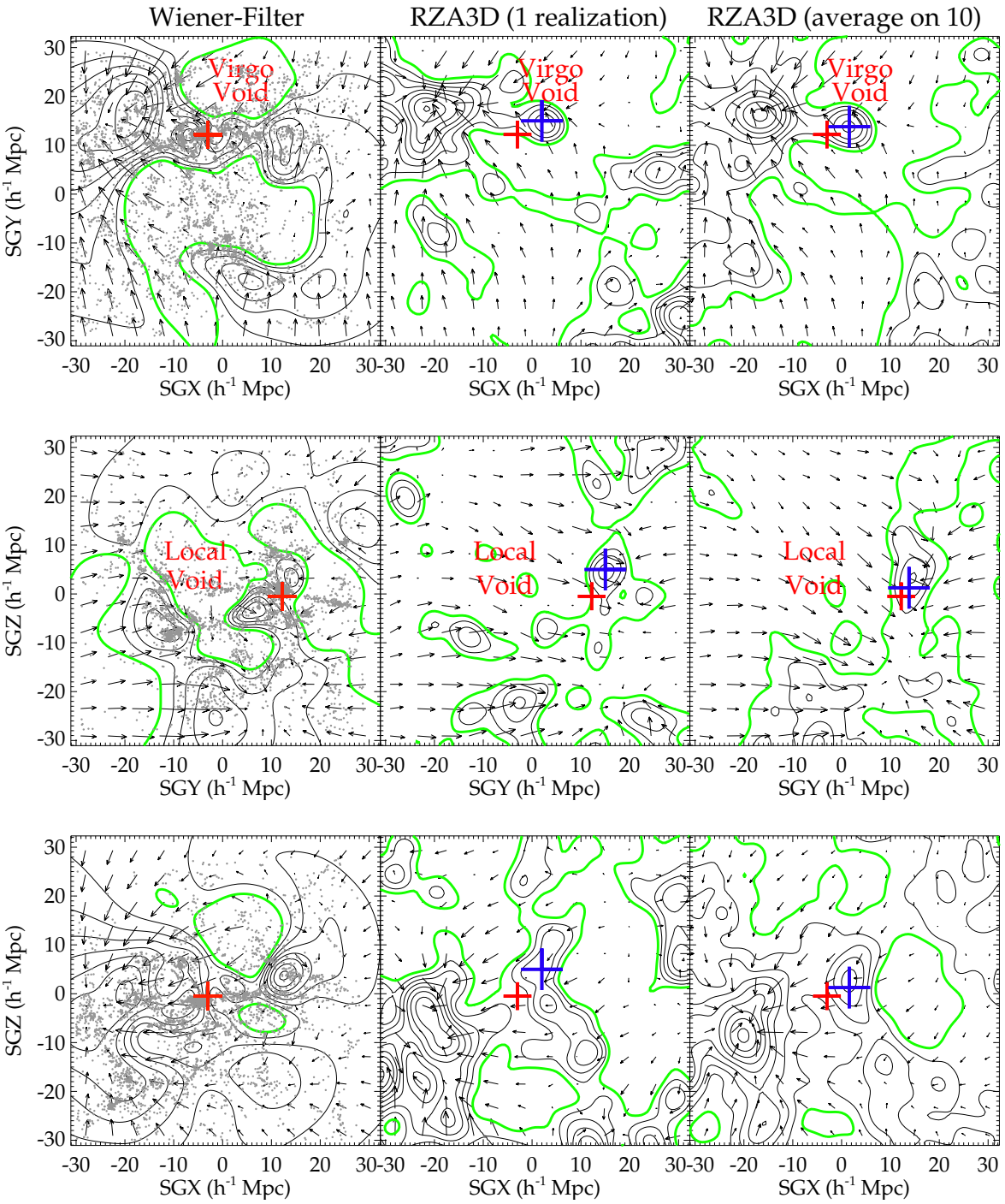

FIGURE 4.10: XY, YZ and XZ supergalactic slices of the Wiener-Filter reconstruction (*left*), of one constrained simulation (*middle*) and of the average of ten constrained simulations (*right*) of the Local Universe within a 30 h^{-1} Mpc radius sphere. The supergalactic slices are located at Z = 0, X = -2.5 and Y=12.5 h^{-1} Mpc to fit the location of the Virgo cluster. The overdensity, at 2 h^{-1} Mpc Gaussian smoothing, is represented with black isocontours. The green contour stands for the mean density. The flows are shown with black arrows. In the XY supergalactic plane, the Virgo cluster and the Virgo Void are both reconstructed (*left column*) and simulated (*middle column*). Virgo is also visible next to the Local Void in the YZ supergalactic slice. In general Virgo is well simulated, at a similar location, whatever random component is used (*right column*). V8k (catalog of redshifts) galaxies are shown for reference as grey dots in a $\pm$ 10 h^{-1} Mpc thick slice on the Wiener-Filter reconstruction. The red crosses locate Virgo in *cosmicflows-1*. The bigger blue crosses represents the (average) location of the Virgo-like halos.

4.4 Biases

A preliminary study of the second catalog of the Cosmicflows project (Tully et al., 2013, and subsection 3.5.2) revealed that although superior in size (number of constraints and spatial coverage) than *cosmicflows-1*, some bias effects cannot be ignored anymore at this level. This section aims at presenting the different biases that can affect observational catalogs like *cosmicflows-2*. This section and the subsequent one do not have the pretension to correct for the whole lot of biases but try to minimize their effects proposing some recipes to be applied to the observational catalog.

4.4.1 Malmquist Biases

Distance estimates are subject to severe systematic biases which affect the derived radial peculiar velocities. Almost always all gathered under the term "Malmquist Bias", in reality three types of Malmquist Bias can be distinguished:

- the most often mentioned Malmquist Bias, successively called Problem I, Selection Effect/Bias, "r against V", Distance-dependent, Frequentist, Calibration problem, M-bias of the second kind (Kaptney, 1914; Malmquist, 1922; Han, 1992b; Hendry and Simmons, 1994; Sandage, 1994; Teerikorpi, 1990, 1993, 1995, 1997; Willick, 1994), is analogous to a selection effect in magnitude resulting in underestimated distances. A magnitude limit in a selected sample result in a mean apparent magnitude smaller than it should be. As the limit decreases, in unit of magnitudes with the distance, the bias increases. Namely, dwarfs and other dimmer galaxies are more and more under-represented in the sample with respect to brighter galaxies as the observer looks farther and farther. Consequently, their contribution to the mean apparent magnitude is increasingly reduced. Thus, the mean increases slower than it would have, with the distance or redshift, would all the galaxies have really been included. This explains why equation 3.11 is not valid at higher redshift unless some corrections are made. In this work, this bias affects principally the calibration of the Tully-Fisher relation: as some faint galaxies are "missing" in the sample, the absolute slope of the relation is underestimated so are distances (data points are lacking in the Tully-Fisher diagram below the fitted relation. Where they to be present, the absolute slope would have been higher). In this work, this selection effect was minimized with two successive processes: 1) inverse fits were used to calibrate the Tully-Fisher relation and 2) a correction to be applied on distance modulus estimates was derived to minimize the bias relic (Tully and Courtois, 2012, and section 3.4). This relic is due principally to the fact that galaxies are more likely to be scattered towards brighter "regions" in the diagram than the opposite because of the shape of the Schechter luminosity function,

- the second bias is called the Homogeneous Malmquist Bias and gathers terminology such as Problem II, General Malmquist Bias, Geometry Bias, "V against r", Classical, Bayesian, Inferred-distance problem, M-bias of the first kind (Kaptney, 1914; Malmquist, 1920; Han, 1992b; Hendry and Simmons, 1994; Lynden-Bell et al., 1988b; Sandage, 1994; Strauss and Willick, 1995; Teerikorpi, 1990, 1993, 1995, 1997). Because our observations are restricted to a sphere centered on us, from the homogeneity of the Universe, the number of observable galaxies increases with the distance. Then considering a true distance $\langle r \rangle$, there is a higher probability to observe a galaxy at $\langle r \rangle + dr$ than at $\langle r \rangle - dr$. Consequently, the probability for a galaxy which distance estimate is r to have been put closer is higher than the opposite. Namely, we are more likely to underestimate the distance. In practice, it is even more complicated than that because of the presence of small scale structures. The bias is a function of the direction of observation. This leads us to the third Malmquist Bias,

- the last of the Malmquist Bias is called the Inhomogeneous Malmquist Bias (e.g. Dekel, 1994; Hudson, 1994; Landy and Szalay, 1992). It is the result of the small scale structures, namely of the fluctuations of the number of galaxies. To apprehend this bias, let's consider a group of galaxies at $\langle r \rangle$ with null radial peculiar velocities for simplicity. Because of observational uncertainties, these galaxies are randomly scattered to the foreground and background of $\langle r \rangle$. For all galaxies at the same redshift, their estimated radial peculiar velocities obtained on either side of $\langle r \rangle$ result in an inaccurate infall towards $\langle r \rangle$ giving birth to spurious structures and flows. In other words, galaxies are more likely to be scattered from high density regions towards low density regions than the opposite. Reducing this bias and the previous one (which are highly related) is a complicated task and we suggest that grouping galaxies in groups and clusters might reduce this bias as recommended by e.g. Burstein et al. (1990) and Nusser and Davis (2011): because galaxies in a same cluster or group are approximately at the same distance, averaging over galaxy distance estimates (to keep only distance estimates of groups and clusters) reduces errors on distances, thus on radial peculiar velocities, of clusters and groups by the square root of the number of estimates. Retracing the footsteps of the methods proposed for instance by Dekel et al. (1999) for the POTENT technique or by Hudson (1994), in addition to grouping, we can envisage to correct the distances or more appropriately, we can minimize their uncertainties. We will propose a method to reduce uncertainties on distances devised during this work in the next section. However, unlike the above mentioned methods, ours is based on correcting peculiar velocities. Before explaining the proposed method, we define another bias.

4.4.2 Error Bias

This last bias results from the assumption that fractional errors on distances, hence errors on radial peculiar velocities, have a Gaussian distribution (see subsection 4.1.2). In reality, because distances are obtained via a logarithmic function applied to distance moduli (equation 3.10), a Gaussian (symmetric) distribution of errors on distance moduli results in a lognormal (asymmetric) distribution of fractional errors on distances and as a result of errors on peculiar velocities. This asymmetric bias associated with the Gaussian weight distribution, by assumption, in the bayesian Wiener-Filter technique, results in a spurious overall velocity infall onto the Local Volume. After assessing the existence of this bias, a method is proposed to minimize it. This technique based on probabilities and Gaussian distributions is similar to bayesian methods. It is developed and tested with very realistic mock catalogs, look-alikes of the second data release of the Cosmicflows project. To control the cosmic variance, mocks are built out of ten different realizations of constrained cosmological simulations of the Local Universe. The method is then applied to cosmicflows-2 *in the last section.*

Errors on observed peculiar velocities grow linearly with the distance. Although these errors can soon be larger than the peculiar velocities themselves, the bayesian Wiener-Filter technique applied to radial peculiar velocities reconstruct overall the overdensity and velocity fields (e.g. Courtois et al., 2012, and subsection 4.3.1). More importantly this distribution of errors is not symmetric when considering two constraints one located closer to the observer than it should be and the other one positioned farther away. This asymmetry introduces a strong bias in the final recovered velocity field. As a matter of fact, observed distances D of galaxies are derived from the distance modulus μ. Thus even if distance errors in magnitudes are distributed evenly around the modulus value, since a logarithmic function is used to derive the distance in Megaparsecs from the modulus μ in magnitudes, the error in megaparsecs is not anymore distributed symmetrically around the distance value D, as shown by the following set of equations derived from the definition of the distance modulus 3.10:

$$\begin{aligned} \Delta\mu &= \sqrt{\Delta m^2 + \Delta M^2} \approx \Delta M \quad \text{symmetric around } \mu \\ \Delta D &= (\Delta\mu \times ln(10) \times D)/5 \quad \text{asymmetric around } D \end{aligned} \tag{4.12}$$

where Δ notations stand for the uncertainties.

Since radial peculiar velocities and their uncertainties are derived from distances by the classical equation 3.7, the asymmetric distribution propagates onto peculiar velocity errors via $\Delta v_{pec} = H_0 \times \Delta D$. This asymmetrical error distribution results in a bias in peculiar velocities. Large negative peculiar velocities have an abnormal large error which cannot be properly propagated in the Wiener-Filter because the sign of the error on a particular

distance modulus is unknown. As an example, let's consider a galaxy at 100 Mpc, with v_{pec}=0 km s^{-1}, H_0=75 km s^{-1} Mpc^{-1}. A 2 σ error on the distance modulus gives either 34.2 or 35.8 mag instead of $\mu = 35$. The derived distance is either 69 or 145 Mpc, giving a radial peculiar velocity of 2311 or -3338 km s^{-1}. As a result, a larger error is made by allocating a radial peculiar velocity of -3338 km s^{-1} to this galaxy than when assuming 2311 km s^{-1}. However, the sign of the error on the distance moduli is unknown, hence, although -3338 km s^{-1} is assigned to this galaxy, proportionally the same uncertainty is attributed to that peculiar velocity as it would have been if the value 2311 km s^{-1} was given. Since, the Wiener-Filter technique uses the errors on peculiar velocities as an indication of the strength of the signal in the correlation matrixes, it results in giving the same weight to both values although the absolute negative value is more incorrect than the positive value. This asymmetrical bias results in a spurious overall large infall seen in the velocity field. Figure 4.11 reveals a skewness towards negative peculiar velocities in *cosmicflows-2* confirming the presence of the asymmetry which impacts the reconstruction.

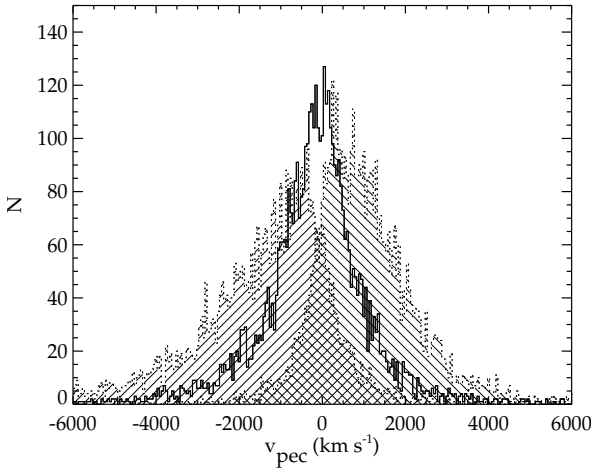

FIGURE 4.11: Histogram (solid line) of radial peculiar velocities in *cosmicflows-2* dataset. The dashed histograms stand for the possible variations of the histogram shape because of uncertainties on radial peculiar velocities. A larger tail is visible in the negative side of this diagram due to the error bias.

Yet, before continuing, it is legitimate to question the relationship between all the above mentioned biases. If they are intertwined, then we can assume that minimizing one we will also drive the others closer to their minimum. Surely, minimizing all of them is better but in absence of such a possibility, it is interesting to define the relations between the biases. As a matter of fact, Homogeneous and Inhomogeneous Malmquist Biases are related. If the first one is due to a larger probability of scatter from farther distances to closer distances, the second one is the result of a larger probability of scatter from high density regions towards low density regions. In addition, Sandage (1994) highlighted the connection between Selection Bias (also a higher probability of scatter from fainter to brighter "regions" than the opposite) and the Homogeneous Malmquist Bias. As for Landy and Szalay (1992), they proved that the error lognormal distribution influences the Inhomogeneous Malmquist Bias affecting grandly

the conclusion on the backside infall onto an attractor. Figure 4.12 recapitulates the bias effects in the form of a diagram. Minimizing a bias, thus decreasing distance uncertainties, we potentially decrease all the others as they all have effects proportional to distance errors. The selection effect has already been minimized, we choose to approach the last presented bias and we propose a method to minimize it too.

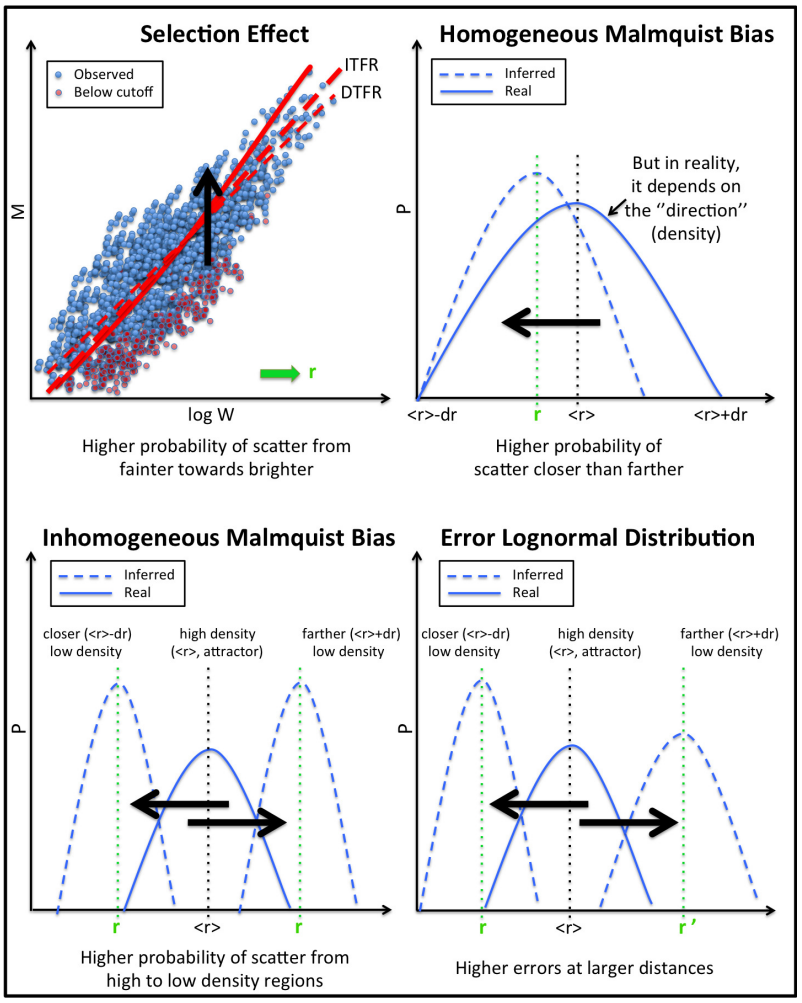

FIGURE 4.12: Schematization of the different bias effects on individual distance estimates, hence on individual inferred radial peculiar velocities. *From left to right, top to bottom*: selection effect, galaxies are more likely to be scattered towards brighter "regions", as a result without appropriate correction distance estimates are too small; homogeneous Malmquist bias, the probability to find a galaxy at $\langle r \rangle + dr$ is higher than at $\langle r \rangle - dr$, consequently without correction distances are again underestimated; inhomogeneous Malmquist bias, it is even more complicated than that because the distribution of galaxies is not homogeneous on small scales, thus galaxies are more likely to be scattered from high to low density regions resulting in spurious flow patterns; another complication comes from the lognormal distribution of errors on distance measurements which results on larger errors at larger distances. The big black arrows in each panel show the "direction" in which galaxies are more likely to be scattered. The dashed red and blue lines give an example of what we could measure and infer for an individual galaxy with a given uncertainty, while the red and blue solid lines mimic the distance range of where the galaxy is more likely to be. Biases are highly related. Minimizing one potentially helps minimizing another. Above all, reducing errors on distances probably drives all of them down.

4.4.3 Minimizing Bias(es)

We can advocate that the effects of all the above mentioned biases were reduced (thus negligible) in *cosmicflows-1* for at least two reasons:

- the coverage of *cosmicflows-1* was smaller than that of *cosmicflows-2* and we know that bias effects increase with the distance (errors are proportional to distances),
- *cosmicflows-1* was in majority constituted of spiral galaxies which are mostly in the field. On the opposite, *cosmicflows-2* contains a large fraction of elliptical galaxies because it uses, in particular, distance estimates from the Fundamental Plane relation (see section 3.5). Ellipticals populate in majority dense regions unlike spirals. *Cosmicflows-2* is then more likely to suffer from non-linear motions and from the Inhomogeneous Malmquist Bias due to high concentrations of single measurements in dense regions.

It is important to note that these biases are by definition highly dependent on the studied sample (e.g. Landy and Szalay, 1992). Thus, mocks built to test correction methods have to be very realistic especially since these correction methods rely only on the information at hand.

4.4.3.1 A Gaussian Distribution of Radial Peculiar Velocities

Instead of correcting distances as widely proposed in previous methods (e.g. Dekel et al., 1999; Hudson, 1994), we propose to adjust first peculiar velocities and then go back to distances to correct them. Our process is then based on the distribution of radial peculiar velocities rather than on the radial distribution of galaxies (e.g. Hudson, 1994; Landy and Szalay, 1992). Sheth and Diaferio (2001) proved that the distribution of radial peculiar velocities considering groups and clusters (namely removing virial motions) should be a Gaussian. Consequently, unless we are located at a particular position in the Universe, which is highly improbable, the distribution of radial peculiar velocities obtained from our position should be close to a Gaussian too. As a matter of fact, Gaussianity is found in mock peculiar velocity catalogs drawn from N-body simulations described in subsection 4.4.3.2. Namely, dark matter halos (what we can actually have access to with dark matter only simulations and which are themselves well described by the linear theory) are equivalent to groups, clusters or isolated galaxies. To derive a method to minimize the error bias in observational datasets, this Gaussianity will be the initial assumption. Yet, if studying simulations, Bhattacharya (2008) confirmed the overall Gaussian distribution of radial peculiar velocities, he also warns us that:

- the cosmic variance due to the particularity of our neighborhood,
- Poisson noise due the restricted size of the sample of peculiar velocities,

both affect the distribution. Still, a major advantage of our study comes from the fact that:

- we use constrained simulations of the Local Universe to produce a set of mocks on which we test our method,
- our mocks mimic as much as possible the characteristics of the observational catalog under study.

As a result, both cosmic variance and Poisson noise are reduced.

4.4.3.2 Very Realistic Mocks

To test our method to be discussed in the next subsection, we need to build even more realistic mocks than whose built to test the augmented Reverse Zel'dovich Approximation (RZA3D). These mocks need to match *cosmicflows-2* on several aspects which are:

- the repartition of the data points (number, spatial coverage and distribution including the Zone Of Avoidance),
- the distribution of errors which is highly bimodal in *cosmicflows-2* (see Tully et al., 2013, and subsection 3.5.2),
- the asymmetry bias (namely the errors need to be inserted at the level of the distance moduli not directly on distances anymore),
- the exact error on a distance is unknown, only its 1 σ uncertainty is available.

Several realizations are tested to measure the robustness and the accuracy of the method discussed in the next subsection. Because results are similar, if not identical, for every mock tested, only one mock built out of one of the ten simulations is discussed in full length and breadth in this work. The simulation has 512^3 particles and is 320 h^{-1} Mpc wide. It was computed within the framework of the CLUES project (Constrained Local Universe Simulations, Gottlöber et al., 2010) using the method described in section 4.2. A look alike for all the major structures of the Local Universe can be found in this chosen simulation. Figure 4.13 allows to identify in the XY plane: the Shapley supercluster in the top left corner, Coma in the top middle, Virgo is close to the center and the Centaurus-Great Attractor region is on Virgo's left side. Using Amiga halo finder (Knollmann and Knebe, 2009), a list of halos is

drawn from this simulation. Halos are then selected to match *cosmicflows-2* grouped catalog in terms of size (number of constraints), distance extent and spatial distribution (including a Zone Of Avoidance). On Figure 4.13, this compiled list of halos is visible as blue dots in a 10 h^{-1} Mpc thick slice in the XY plane.

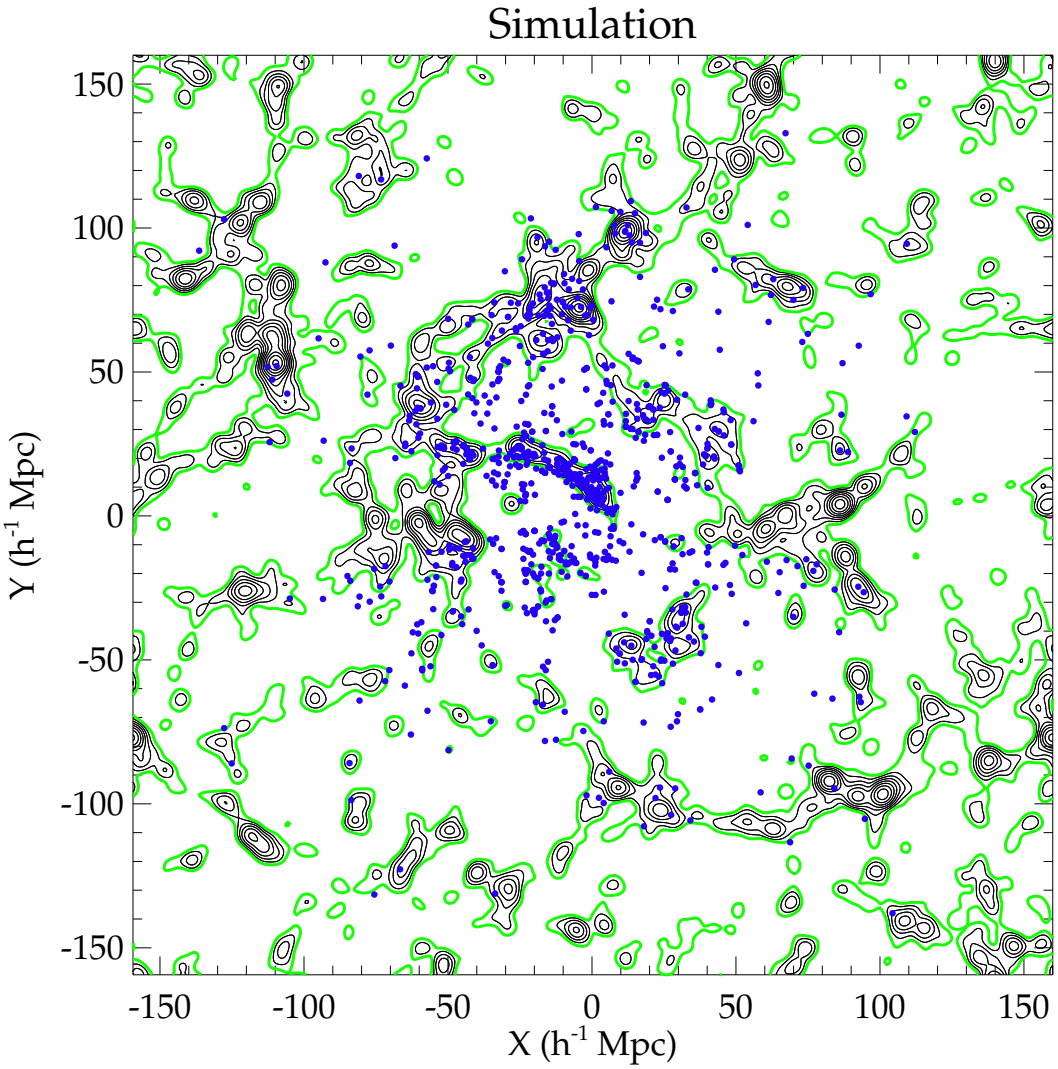

FIGURE 4.13: Distribution of selected halos (blue dots) in the XY plane (± 5 h^{-1} Mpc slice in Z) of a cosmological simulation which is similar to the Local Universe. Halos are selected to build a mock similar to the second catalog of the Cosmicflows project. Black and green contours show the density field and the mean density.

As predicted by Sheth and Diaferio (2001), the distribution of halo radial peculiar velocities (computed with respect to the center of the box, where the Milky-Way like is assumed to be) of this mock catalog can be modeled by a Gaussian visible in Figure 4.14 in blue. This mock is called original in the sense that it has no error on galaxy distances yet. To match *cosmicflows-2* observed catalog as closely as possible, errors need to be inserted into the mock. To preserve the asymmetry problem, a Gaussian distribution of errors with 0.2 magnitude scatter (as on average in the observational catalog) is added to distance moduli. Then to

preserve the strongly bimodal distribution of errors visible in *cosmicflows-2*, constraints at large distances from the center of the box which were attributed a (close to) zero error are reassigned to have a 1 σ (0.42 magnitude) error on distance moduli. Disrupted distances and corresponding radial peculiar velocities are then computed. Figure 4.14 displays the distribution of radial peculiar velocities for this "biased mock" by a dotted black line. This distribution is flatter than a theoretical Gaussian with a larger tail on the negative side and, in that sense, is very similar to *cosmicflows-2* distribution on Figures 4.11 and 4.21. Figure 4.15 also presents the histograms of fractional errors on distances (left) and of errors on radial peculiar velocities (right) in black. Then, because in the observed universe, the exact error made on a particular measurement is unknown, distances are attributed either a 9%, 15%, 20% or 25% uncertainty in accordance with their real inserted errors to match the distribution of uncertainties in *cosmicflows-2*.

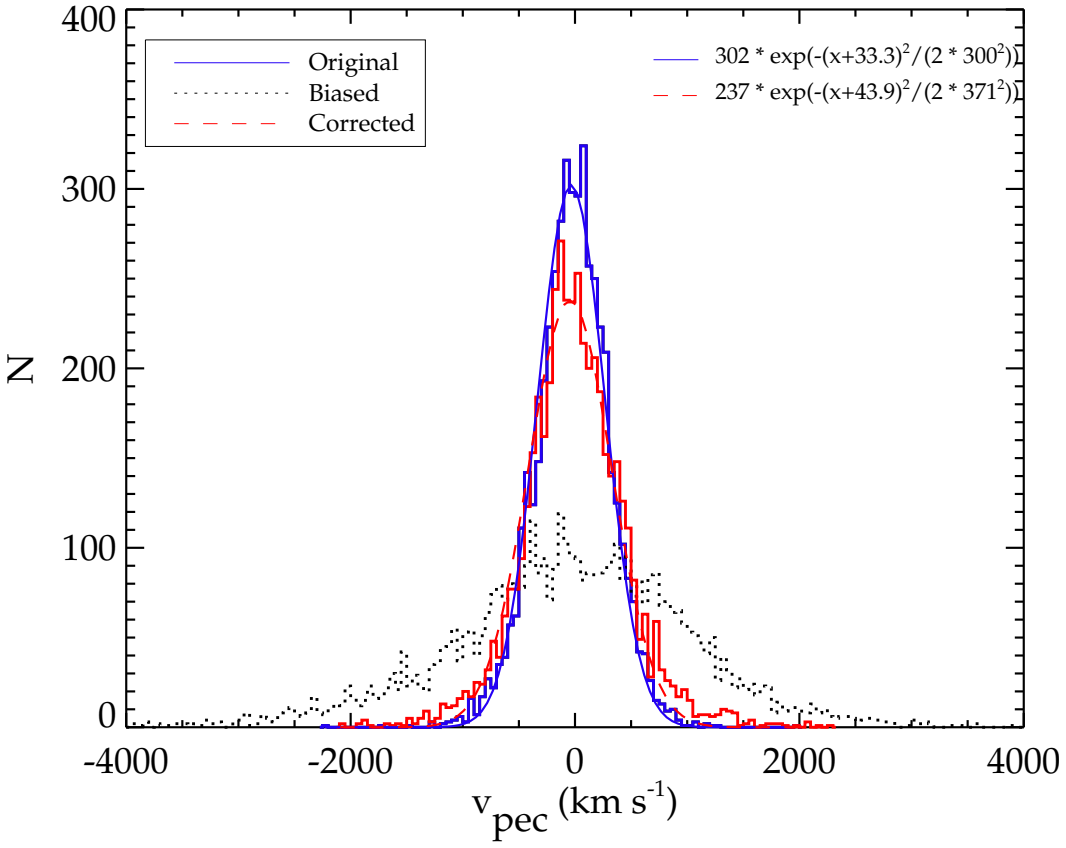

FIGURE 4.14: Distribution of radial peculiar velocities in the original mock catalog (blue solid histogram) and in the mock containing the asymmetry bias (black dotted histogram). The original distribution of radial peculiar velocities can be modeled by a normal distribution (blue solid curve). The distribution of corrected radial peculiar velocities (red solid line) is shown by the red histogram. A Gaussian can also fit this distribution (red dashed line).

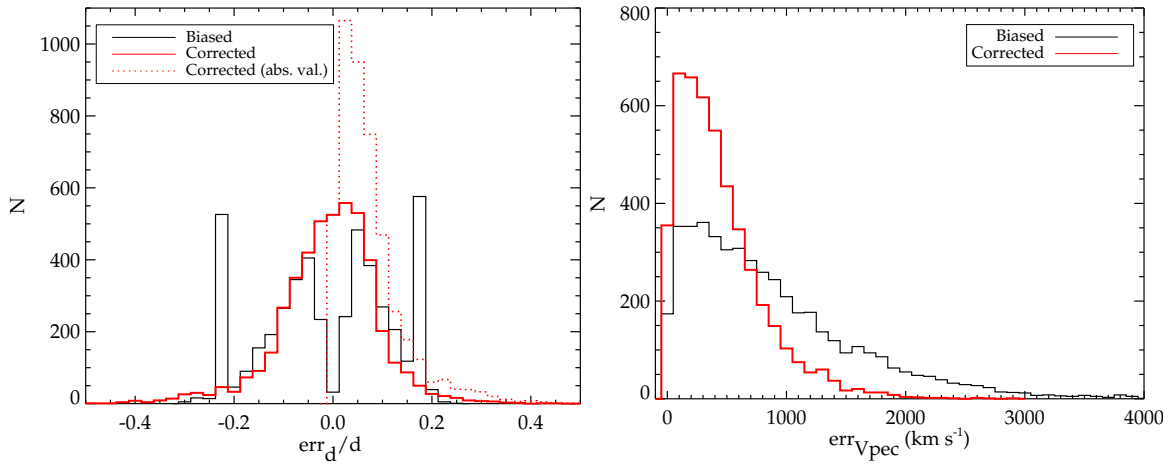

FIGURE 4.15: Histograms of fractional errors on distances (*left*) and on radial peculiar velocities (*right*) in the biased mock (solid black lines) and in the corrected mock (solid red lines). The bimodal distribution of fractional errors on distances with two peaks at 8-10% and 20% errors (absolute values) similar to *cosmicflows-2* is visible. The dotted red histogram shows the distribution of absolute fractional errors on distances after minimization of the bias with a median at 0.06.

4.4.3.3 The Method

To minimize the bias in the mock catalog, an approach similar to a bayesian way is taken. After application of the process, the mock should have a Gaussian radial peculiar velocity distribution with variance and location peak similar to the original ones. In the mock case, variance and peak are determined by the mock with the original positions, hence velocities. Regardless, in the ten different realizations, the standard deviation of the Gaussian fitted to the radial peculiar velocity distributions for mocks similar to *cosmicflows-2* is always around 300 ± 50 km s^{-1}. As a result, a peculiar velocity is modified according to its probability of belonging to the theoretical Gaussian (with a typical standard deviation of 300 km s^{-1}) and according to its uncertainty. Two cases can be distinguished, either the radial peculiar velocity is positive or it is negative. Then corrected radial peculiar velocities are derived with equations 4.13 and 4.14 devised in this work:

if $v_{pec} > 0$,

$$v_{pec\,c} = f[p(v_{pec} - \Delta) + (1-p)(v_{pec} + \Delta)] + (1-f)v_{pec} \tag{4.13}$$

if $v_{pec} < 0$,

$$v_{pec\,c} = f[p(v_{pec} + \Delta) + (1-p)(v_{pec} - \Delta)] + (1-f)v_{pec} \tag{4.14}$$

where Δ is the radial peculiar velocity uncertainty (Δv_{pec}) ; p is the probability that a radial peculiar velocity does not belong to the theoretical Gaussian (thus it needs to be corrected and it should either be reduced if it is highly positive or increased it is highly negative) ; f is the probability that the radial peculiar velocity estimate is wrong. Namely, f is proportional

to the fractional uncertainty on distances (peculiar velocities) normalized to the maximum fractional uncertainty plus 0.05 (best parameter in our different realizations to retrieve a distribution close to the theoretical Gaussian) to keep a minimum of trust towards the initial measurements.

These corrected radial peculiar velocities enable us to compute distances for constraints using the classical formula 3.7 in reverse order. After corrections, the distributions of radial peculiar velocities, fractional errors on distances, and errors on radial peculiar velocities are all shown on Figures 4.14 and 4.15 in red. The distribution of absolute fractional errors on distances shown by the red dotted line reveals that, after correction, the distribution of errors is poissonian with a median at 0.06. These distributions and median values are typical for all the mocks built out of the ten different realizations. The distribution of radial peculiar velocities can now be approximated by a Gaussian with variance and peak similar to the original one. Fractional errors on distances are distributed on an approximate Gaussian and the distribution of uncertainties on radial peculiar velocities is less flat and contained in a smaller interval of values.

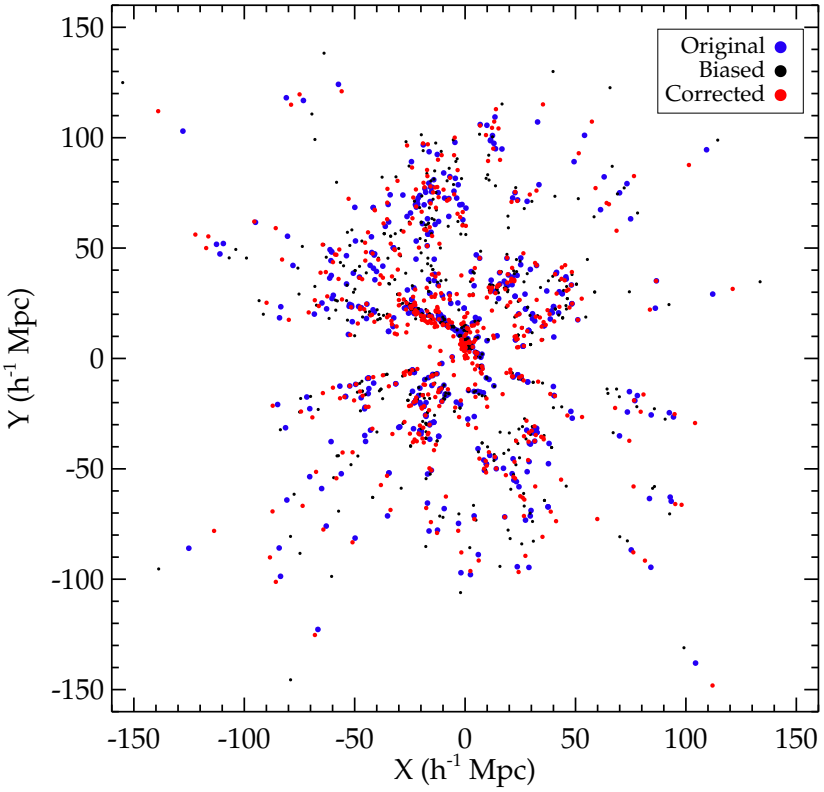

FIGURE 4.16: Distribution of constraints in the XY plane in a $\pm$ 5 h^{-1} Mpc thick slice. Blue dots stand for constraints at their true positions. Black dots are constraints from the biased mock. Constraints located at corrected positions are shown as red dots. These latter are overall closer to blue dots than black ones. Namely, after correction, positions (hence distances and radial peculiar velocities) are more accurate than previous ones.

Figure 4.16 is a proof of concept that, after correction, positions (hence distances and corrected radial peculiar velocities) are overall closer to the true positions than biased ones. On this figure, blue dots stand for the true positions in the XY plane of halos in a $\pm$ 5 h^{-1} Mpc thick slice. Red dots represent constraints at corrected positions while black dots show halos at their location before correction. Red dots are overall closer to blue dots than dark ones. Namely, in the corrected mock, positions (distances and velocities) attributed to constraints are closer to true ones than biased positions are. Other slices have been looked at resulting in the same conclusion. Moreover, no additional bias is created since, after correction, positions are not always closer to / farther from the center of the box than original ones. Namely, distances are not all under/over-estimated. The reconstruction technique is put into practice in the next subsection on this minimized biased mock. Fractional errors of 6% on distances are assumed in agreement with the upper limit of fractional error medians found in the various corrected mocks.

4.4.3.4 Tests

For purposes of completeness, the Wiener-Filter technique is applied to three mock catalogs: biased, corrected and, as a mean of control, original with positions and 3D peculiar velocities, to remove any bias due to an increasing smoothing with distance. The reconstruction obtained with the original mock represents the best overdensity and velocity fields we can expect from the Wiener-Filter method would the data be perfect. As the goal of this subsection is not to test the accuracy of the Wiener-Filter technique already widely tested (e.g. Courtois et al., 2012; Zaroubi, 2000; Zaroubi et al., 1999, 1995, and subsection 4.3.1), it is in a sense easier to compare the reconstruction obtained with biased and corrected mocks to that former reconstruction to determine to which extent the bias is properly minimized. The three reconstructions are on Figure 4.17. The reconstruction obtained with the biased mock (middle column) present what is expected from the asymmetry problem, namely a large infall in contradiction with the simulation. In addition, structures are extended and very round. On the opposite, the strict infall has disappeared from the reconstruction resulting from the corrected mock (last column). Structures are more sharply defined in good agreement with the best result we can obtain using the Wiener-Filter technique on a catalog similar to *cosmicflows-2* but ideal (first column). After this qualitative analysis, a quantitative one can be derived from cell-to-cell comparisons between reconstructions obtained with the original and the two other mocks. Such comparisons are visible on Figure 4.18 between cells within 200 h^{-1} Mpc.

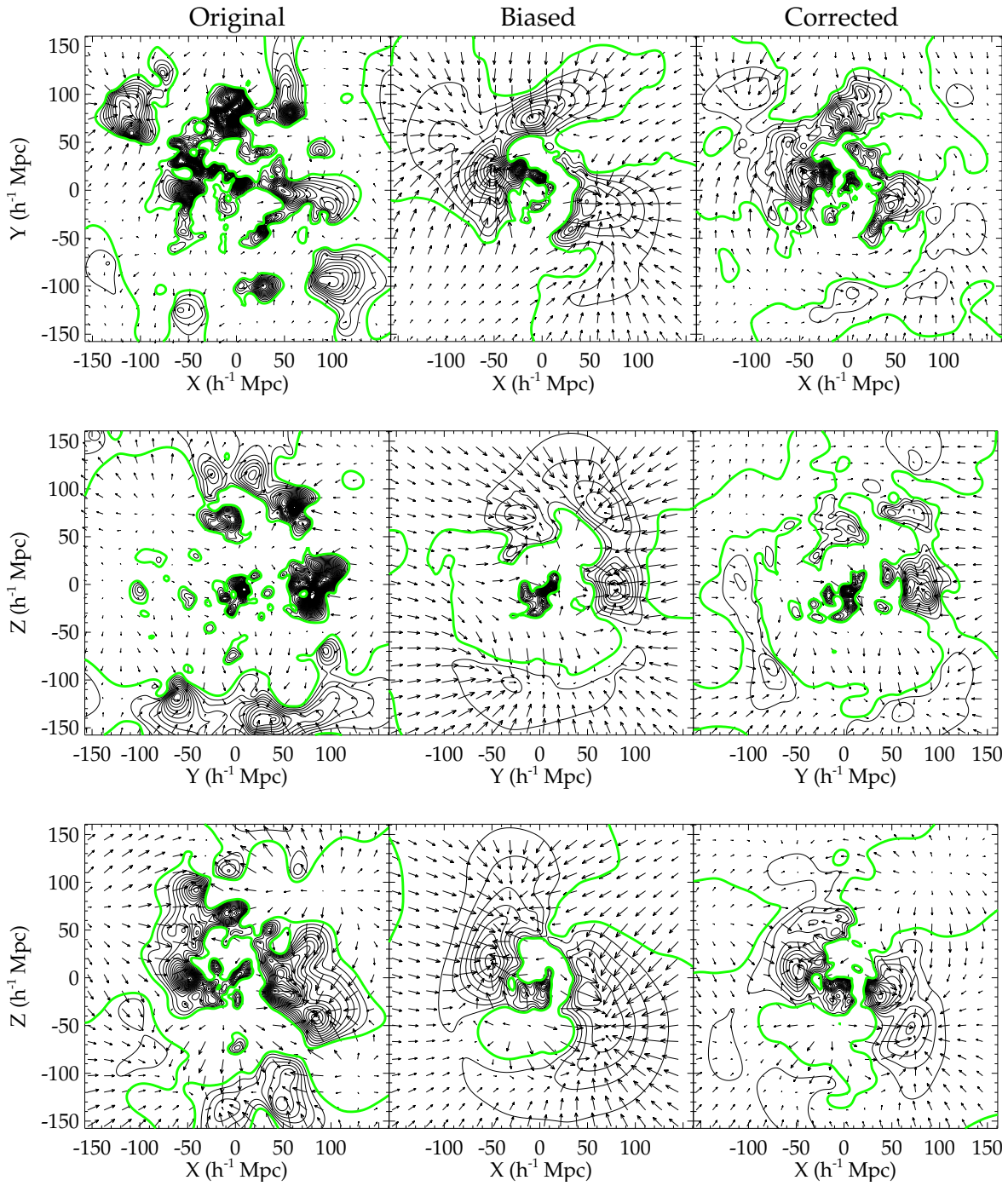

FIGURE 4.17: XY (*top*), YZ (*middle*) and XZ (*bottom*) slices of the overdensity (black contours) and velocity (black arrows) fields reconstructed with the Wiener-Filter technique applied to the original (*left*), biased (*middle*) and corrected (*right*) mocks. The green contours show the mean density. The net spurious infall onto the volume is clearly visible in the velocity field reconstructed from the biased mock and structures are round. On the opposite, structures are more sharply defined (for instance, the look-alike of Shapley in the top left corner of the XY plane) in the reconstruction obtained with the corrected mock and the strong infall has disappeared (for instance, the expulsion from the void in the top right corner of the XZ plane).

The scatter around the 1:1 linear relation is smaller when comparing all but 0.3% of the cells within 200 h^{-1} Mpc between reconstructions obtained with original and corrected mocks than between those obtained with original and biased mocks. Even when considering the whole box, standard deviations are 378 km s^{-1} (2.1 σ) for the reconstruction obtained with the corrected mock against 433 km s^{-1} (2.4 σ) for that obtained with the biased mock. This is probably the results of the flatter radial peculiar velocity distribution in the biased mock rather than a close to a Gaussian distribution in the corrected mock. The slight tilt, observed in the comparisons, is due to the fact that the Wiener-Filter smooths according to given errors. Since no error was attributed to constraints in the original mock while some were given to velocities in the biased and corrected mocks, the reconstructed velocity fields resulting from the Wiener-Filter applied to these two last mocks are smoother than the velocity field obtained with the original mock. A point which is important to notice as a large lack of power will lead to simulations (the final goal) lacking some power on all scales. Namely, the random field added by the Constrained Realization technique would not suffice to re-establish the proper power. Thus, once a process is applied to an observational catalog, checking the power left in the data is required.

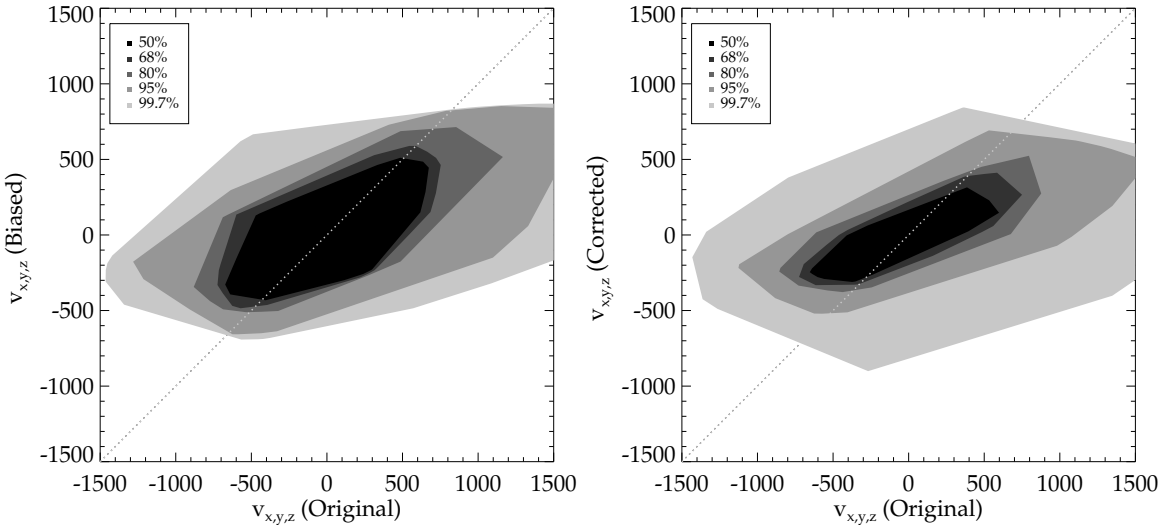

FIGURE 4.18: Cell-to-cell comparisons within 200 h^{-1} Mpc between reconstructions obtained with original and biased mocks (*left*) and between those obtained with original and corrected mocks (*right*). The gradient of grey delimits the 50, 68, 80, 95 and 99.7 % confidence zones. Apart from the 0.3% cells which cannot be find in the 95% confidence zone, all the other cells are less scattered around the 1:1 ideal relation when comparing original and corrected mocks than when comparing original and biased mocks.

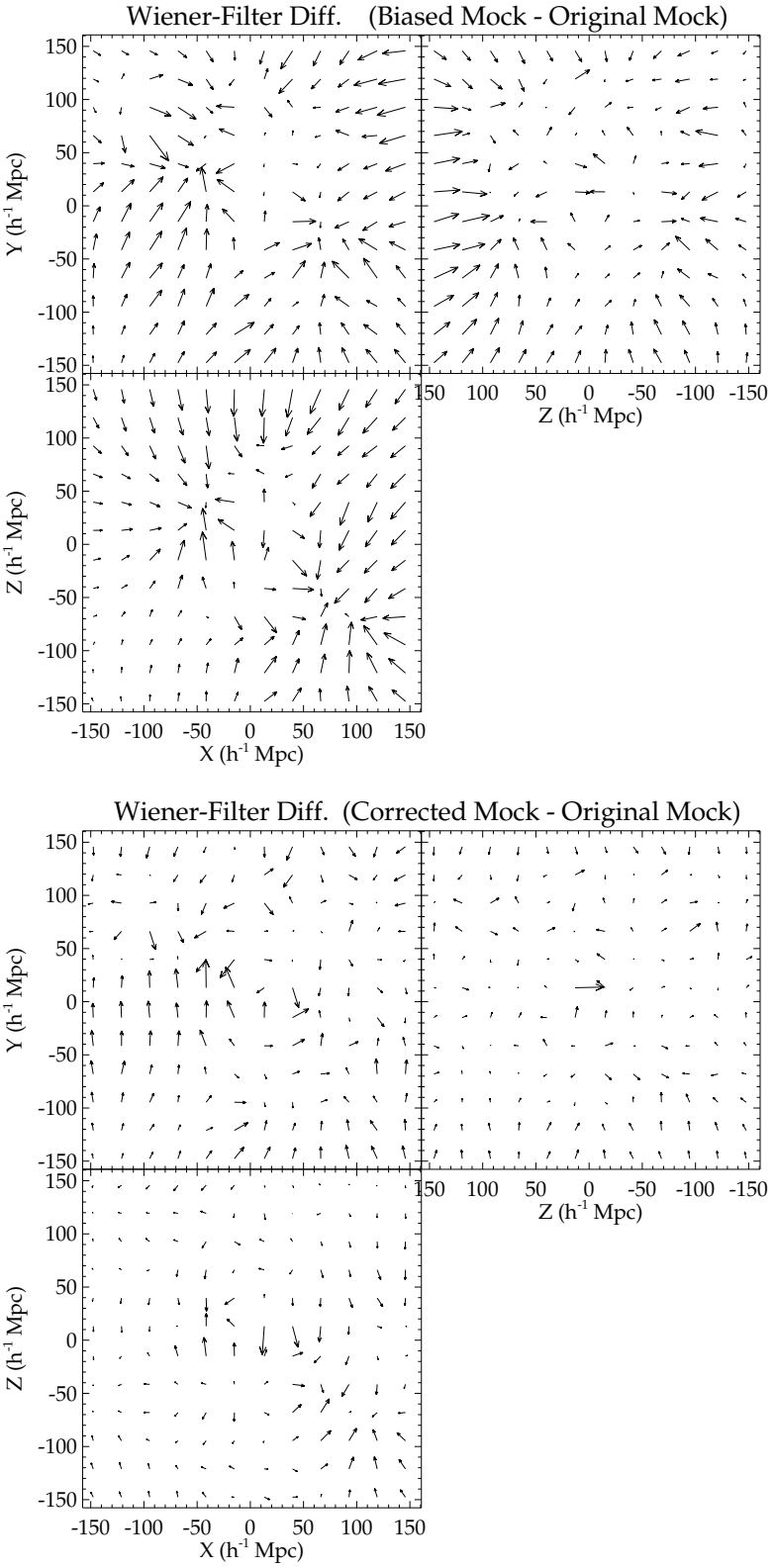

FIGURE 4.19: Residual velocity fields in the XY, YZ and XZ planes when subtracting the Wiener-Filter reconstructed fields obtained with the original mock to those obtained with biased (*top*) and corrected (*bottom*) mocks. Velocity fields have been first normalized by their maximal value. While the spurious infall due to the bias is clearly visible in the residual between reconstructions obtained with biased and original mocks, the effect is minimized when looking at the difference between the fields obtained with corrected and original mocks. As no major pattern in the *bottom* panel is missing in the *top* panel, the correction process does not lead to additional false patterns in the velocity field.

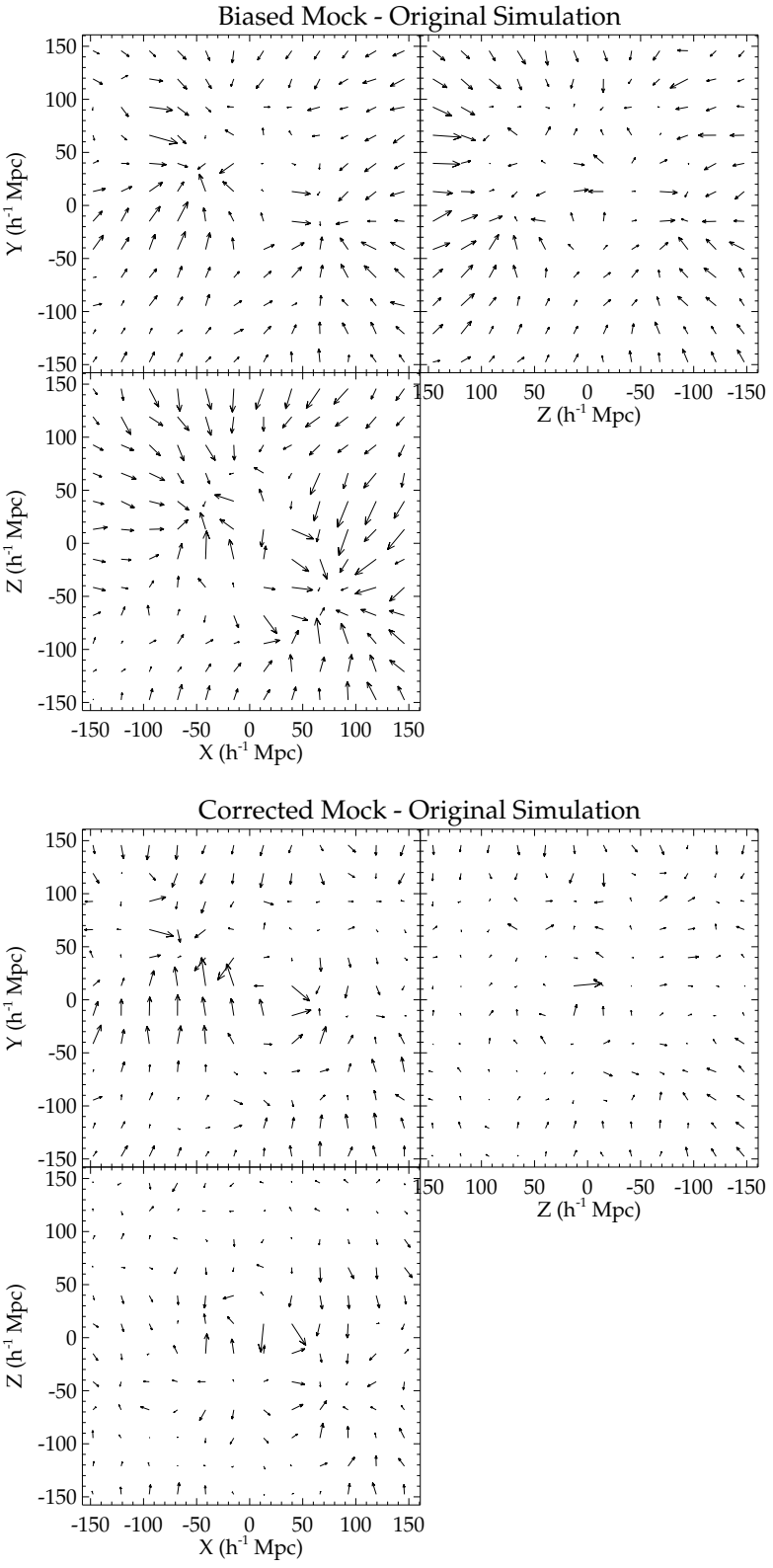

FIGURE 4.20: Same as the previous figure except for the reconstructed velocity field obtained with the original mock. It is replaced by the velocity field from the original simulation. Conclusions are unchanged.

To check that the infall bias into the box is indeed minimized without creating additional spurious patterns in the velocity field, Figure 4.19 shows the residual between velocity fields normalized by their maximal value obtained with biased, corrected and original mocks. On this figure, the spurious infall present in the reconstruction derived with the biased mock is visible while it is largely minimized in the field reconstructed from the corrected mock. No flow which was not in the biased reconstruction appears in the velocity field obtained after application of the correction process. Residual flows are dimmed or in another word minimized. For completeness, Figure 4.20 represents the residual between reconstructions and the original simulation. Standard deviations between original simulated and reconstructed velocity fields are 191 km s^{-1} and 225 km s^{-1} when corrected and biased mocks are used respectively. The exact same conclusions can be drawn. The process devised in this work contributes to decrease the bias in the mock catalog.

Because our procedure also decreases errors on distances, in addition to the latent relationship between the biases, we can suggest that it also contributes to some extent to the minimization of the Malmquist Biases. Regardless, our main concern is with the constrained simulations which are not affected as much as the reconstruction by the bias (since the precursory simulation used to test the proposed correction is itself based on a preliminary version of *cosmicflows-2*), probably because RZA3D, through the Wiener-Filter, is capable of removing itself most of the biases by replacing noisy radial peculiar velocities with noise-filtered 3D peculiar velocities. Argumentations can be made in favor of more mathematical derivations but, because of the cosmic variance, biases, and thus the required correction, highly depend on the catalog at hand. Thus, we found the method we propose here to be satisfactory to reach our ultimate goal.

4.5 CLUES with Cosmicflows-2

In this last section, we apply the whole process to the observational catalog *cosmicflows-2* within the framework of Planck cosmology but with a slightly modified normalization, than that given in Table 2.1, in agreement with the value chosen in other works of the CLUES project ($\sigma_8 = 0.829$). From the bias minimization up to the RZA3D method, *cosmicflows-2* is adjusted before being input in the Constrained Realization of Gaussian Fields algorithm to produce initial conditions which are run with GADGET.

4.5.1 Minimization of the Bias(es)

For comparison purposes, the Wiener-Filter is first applied to three versions of *cosmicflows-2* (CF2). The primary or biased version which can be compared with the biased mock, the

corrected version to be linked with the corrected mock and the version released in Tully et al. (2013). This *cosmicflows-2* version, hereafter CF2-catalog, contains a small correction made at that time to reduce the asymmetry bias. That correction consists in shrinking large negative radial peculiar velocities to make the radial peculiar velocity distribution more symmetric as it is visible on Figure 4.21. However, both distances and uncertainties are kept in the process.

4.5.2 Reconstruction of the Local Universe Within 160 h^{-1} Mpc

Figure 4.22 shows the reconstruction obtained out of CF2-biased, CF2-catalog and CF2-corrected. This figure shows that the small correction previously made goes in the proper direction. The spurious infall is less pronounced although the correction is not quite strong enough to minimize the effect of the asymmetry bias. The correction proposed in this work on the other hand reveals that the reconstructed velocity field resulting from the Wiener-Filter applied to CF2-corrected does not suffer from the spurious infall anymore. For instance in the top left corner of the supergalactic YZ plane on Figure 4.22, there is an eviction from the void.

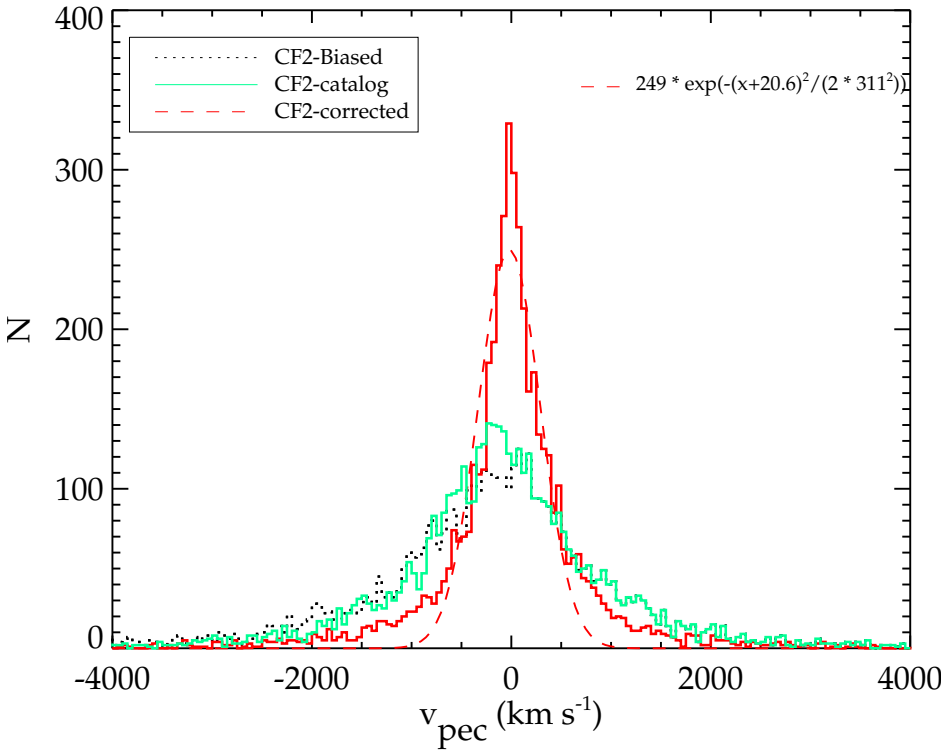

FIGURE 4.21: Radial peculiar velocity distributions in CF2-biased (dotted black line), CF2-catalog (solid green line) and CF2-corrected (solid red line). After correction, the distribution of radial peculiar velocities in CF2-corrected can be fitted by a Gaussian (dashed red line) with variance and peak close to the original ones (obtained with mocks).

Moreover, it appears that the χ^2/d.o.f (with d.o.f the degree of freedom) value of the CF2-catalog is below 1. As this value measures the adequacy between the data and the power spectrum, a value less than 1 reveals than the dataset is missing some power probably because the allocated error budget is too large when applying the Wiener-Filter. For instance, considering TF distance estimates, since they do not all have a 20 % error (this is the TFR scatter or 1 σ uncertainty), assigning to each one of them such an error does not constitute the optimal solution. Still, in absence of another solution, these large uncertainties are allocated to every TF distance measurements of isolated galaxies in CF2-biased and CF2-catalog. The signal is oversmoothed by the Wiener-Filter. On the opposite, a value greater than 1 is due to the non-linear part of the dataset which is not taken into account a priori in the linear bayesian Wiener-Filter technique. As explained before in subsection 4.1.2, a sigma non-linear added in quadrature to the radial peculiar velocity errors can re-establish a value close to 1. As Initial Conditions can be derived solely from catalogs with value close to 1 or resulting simulations will lack some power at all scales, the χ^2/d.o.f value should be controlled. Namely the power spectrum of the resulting simulations will not match a measured power spectrum, such as Planck power spectrum, if χ^2/d.o.f is not close to 1.

To estimate the quality of the reconstruction of the Local Universe obtained with the Wiener-Filter applied to CF2-corrected, Figure 4.23[4] shows the reconstructed overdensity field to which is superimposed the 2MASS redshift catalog as white dots. The gradient of colors gives an estimate of the overdensity in the reconstruction with an increase from blue to red. Typically, voids are in blue and overdensities are in red/orange. Structures of the Local Universe are reconstructed.

[4]This figure was made with the SDvision software (e.g. Pomarède et al., 2013).

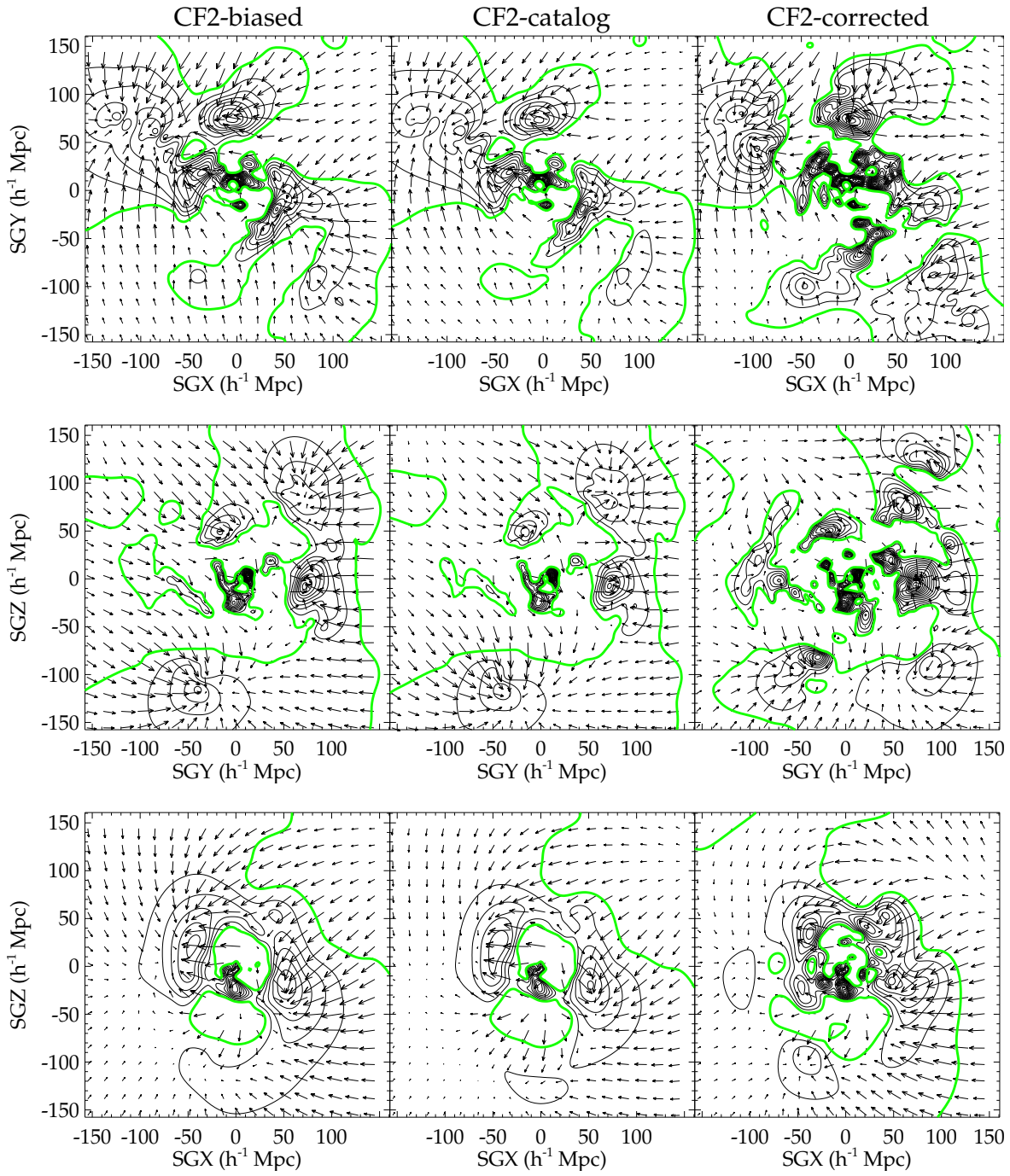

FIGURE 4.22: Supergalactic XY (*top*), YZ (*middle*) and XZ (*bottom*) slices of the overdensity (black contours) and velocity (black arrows) fields reconstructed with the Wiener-Filter technique applied to CF2-biased (*left*), CF2-catalog (*middle*) and CF2-corrected (*right*). The green contours show the mean density. The net spurious infall onto the volume is clearly visible in the velocity field reconstructed from CF2-biased and structures are quite extended. On the opposite, structures are more sharply defined in the reconstruction obtained with the corrected mock (for instance, the great wall on the left of the supergalactic YZ plane) and the strong infall has disappeared (for instance, evictions from regions at the top left and right corners of the supergalactic YZ and XZ planes are clearer).

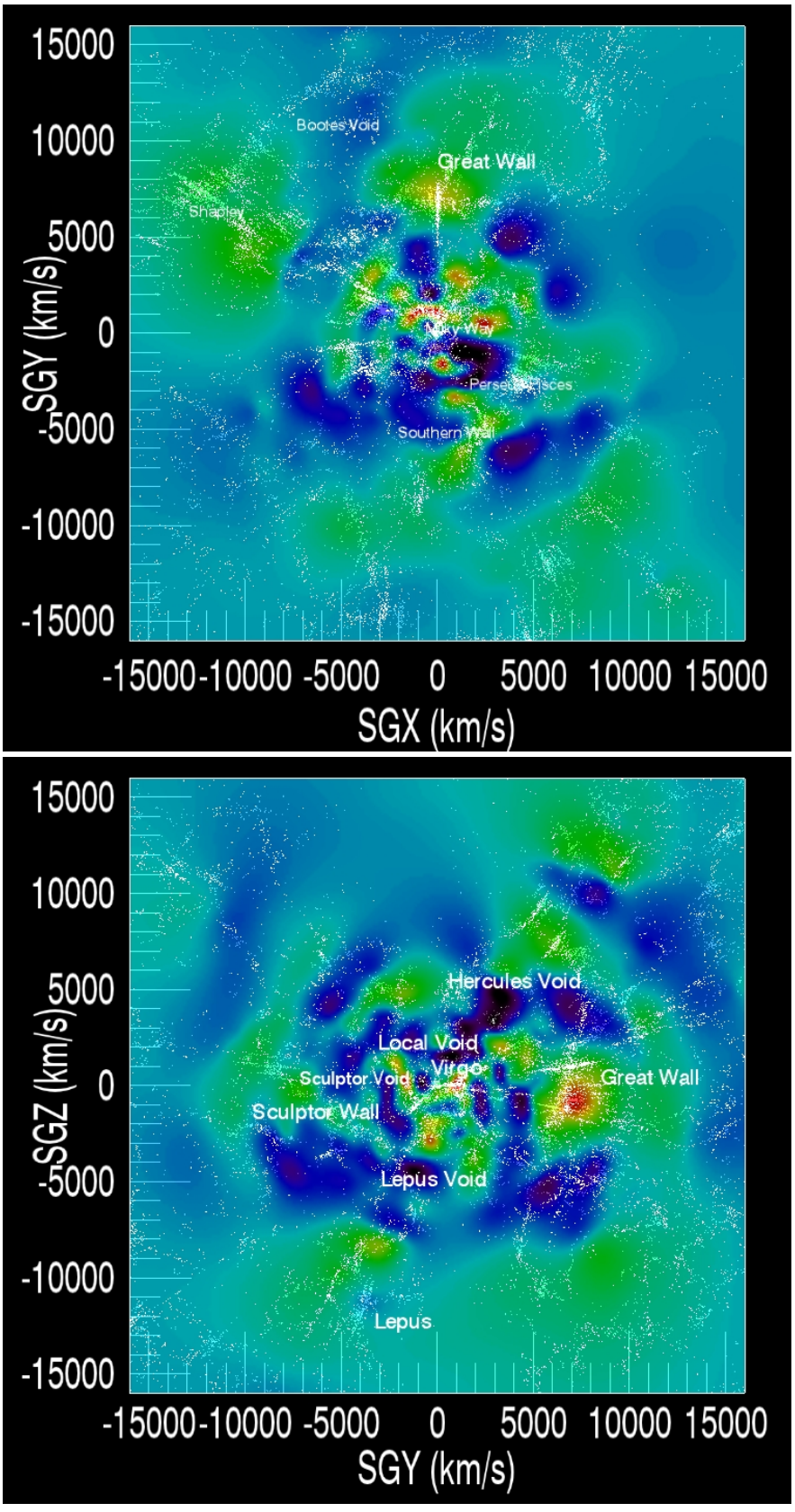

FIGURE 4.23: XY and YZ supergalactic planes of the reconstructed overdensity field smoothed at 2 h^{-1} Mpc of the Local Universe obtained with the Wiener-Filter applied to CF2-corrected. The color gradient represents the overdensity field: from blue to red, the overdensity increases. Typically blue regions stand for voids while red/orange zones are overdensities. Galaxies from the 2MASS redshift survey are superimposed as white dots for comparison purposes only. Structures of the Local Universe are well recovered. The "finger-of-Gods" mentioned in subsection 2.1.2.3 of Chapter 2 are clearly visible in 2MASS, thus the comparison has its limitation.

4.5.3 Constrained Simulations of the Local Universe: Main Attractors and Voids

4.5.3.1 Increasing the Resolution

The spatial coverage of the *cosmicflows-2* catalog has required an extent in boxsize that would drastically reduce the resolution of any simulation based on a 256^3 grid. Consequently, constrained realization fields cannot be transformed in initial conditions for GADGET as such. To increase the number of particles from 256^3 to 512^3, we use the software GINNUNGAGAP, developed within the CLUES project by Steffen Knollmann. This package requires the white noise of the constrained realization fields, the power spectrum and the assumed cosmology. With all these parameters, it is capable of increasing the size of the grid to then produce primordial fields to build initial conditions for GADGET.

The white noise field $\omega(\mathbf{x})$ is generated with the density perturbation field $\delta(\mathbf{x})$ and the power spectrum $P(\mathbf{x})$ which follow the relation in Fourier space:

$$\delta(\mathbf{k}) = \sqrt{P(\mathbf{k})}.\omega(\mathbf{k}) \tag{4.15}$$

Note that this method applied in reverse enable the production of a random field with the statistics of the power spectrum for the constrained realization technique: it is enough to generate a Gaussian white noise field with zero-mean and unity-variance and to combine it with the power spectrum according to formula 4.15 (Bertschinger, 2001; Prunet et al., 2008).

4.5.3.2 Local Cosmography, an Insight in the Zone of Avoidance

With a series of ten constrained simulations, containing 512^3 particles, produced with the observational data, *cosmicflows-2*, within the framework of Planck cosmology, following the whole process described in this Chapter, we can study in more details the Local Universe. We choose to present the result for the best realization we have for a boxsize of 500 h^{-1} Mpc and a grid of 512^3. Regardless, the ten realizations are very similar. They have all variances about 0.44 in unit of density around their average. This latter is visible in Figure 4.24 alongside the chosen realization.

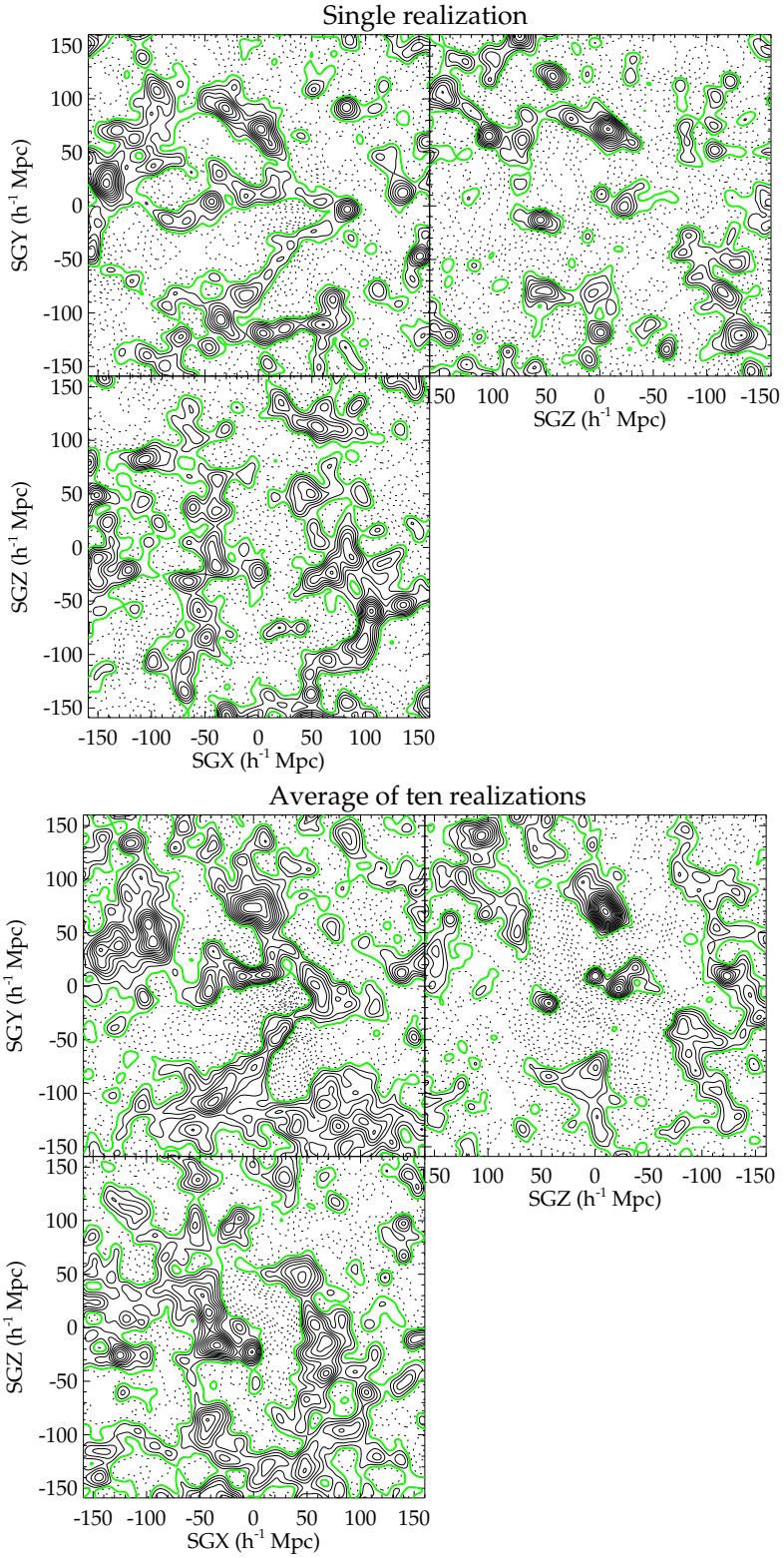

FIGURE 4.24: Supergalactic XY, YZ and XZ planes of one realization (*top*) and of the average of ten constrained simulations (*bottom*) of the Local Universe obtained with *cosmicflows-2*. Solid black contours show overdensities while dashed black contours are underdensities. The mean density is in green. Underdensities in the average have to be present in most of the simulations. In other words, there cannot be in any simulation a major peak at their locations (if there is any overdensity it cannot be higher than half the value of the highest peaks). The most underdense regions have to be underdense in all the simulations. Regarding the highest peaks, they have to be present at least in approximately half the simulations to show up as high as they are. The highest peaks and the largest voids in the unique realization are present in the average revealing they are stable in the different realizations. These peaks and large voids correspond to large overdensities (superclusters) and underdensities (major voids) in the Local Universe.

This average shows the voids and the peaks with the highest probability. In other words, large voids and high density peaks are visible in the average only if they are formed in the majority of the ten realizations. For instance, the highest peaks in the different realizations have values around 16-20 in unit of density. Since the highest peak values in the average are approximately 8-10 in unit of density, the highest peaks have to be present at least in approximately half of the ten realizations (0.5×[16-20]) at the exact same location. As for underdense regions (including voids), their value in unit of density is necessarily below 1, thus underdensities need to be present in approximately all the simulations. If there is any exception, the overdensity at this location cannot be higher than approximately half the value of the highest peak ([8-10] in unit of density). This value quickly decreases with the number of peaks to reach underdensity values. In other words, in this average of ten realizations, the major overdensities are representative at 2 σ and voids at more than 3 σ. Back to the 500 h^{-1} Mpc boxsize, it is a compromise between a better resolution but a greatly reduced zone of possible study due to boundary conditions and, a decreased resolution but a zone of study which extends just at the limit of the Shapley supercluster where no spurious effect should appear because of boundary conditions.

In the chosen realization, on Figure 4.25, a look alike for most superclusters and voids in the Local Universe can be found. Maps of superclusters and voids to assess the quality of the constrained simulation are given in Figures 4.26 and 1.1 (Chapter 1). Little is known about structures in the Zone of Avoidance but, from what can be found in the literature, the simulation reproduces quite well the observations also in this zone:

- a connection between the Perseus-Pisces supercluster below the the Zone of Avoidance to a Abell cluster (Abell 569) above the zone of obscuration around SGX≈6000 km s^{-1} (Chamaraux et al., 1990; Focardi et al., 1984) is recovered,
- the Perseus-Pisces chain folding back into the zone of obscuration around SGX≈7500 km s^{-1} (Marzke et al., 1996; Pantoja et al., 1997) phenomenon is also visible,
- a filament extends from Hydra and Antlia *clusters* across the Zone Of Avoidance around -3000 km s^{-1} to reach the region of the Great Attractor (∼Centaurus Supercluster, Kraan-Korteweg et al., 1994). A potential supercluster is on an extension of the filament around -6000 km s^{-1} in the zone of obscuration (Kraan-Korteweg et al., 1994),
- and last but not least, Kraan-Korteweg et al. (1994) noted a clustering around -15,000 km s^{-1} in the zone hidden by our galaxy dust, a potential connection between the Horologium and Shapley Superclusters. The simulation contains this high density zone. Actually more than half of our ten constrained simulations has a high density zone at this position. Consequently, although it is slightly beyond the maximum zone of study we established (L/2 where L is the boxsize, or [-L/4,L/4]), it looks like it is a robust structure not an artifact of periodic boundary conditions.

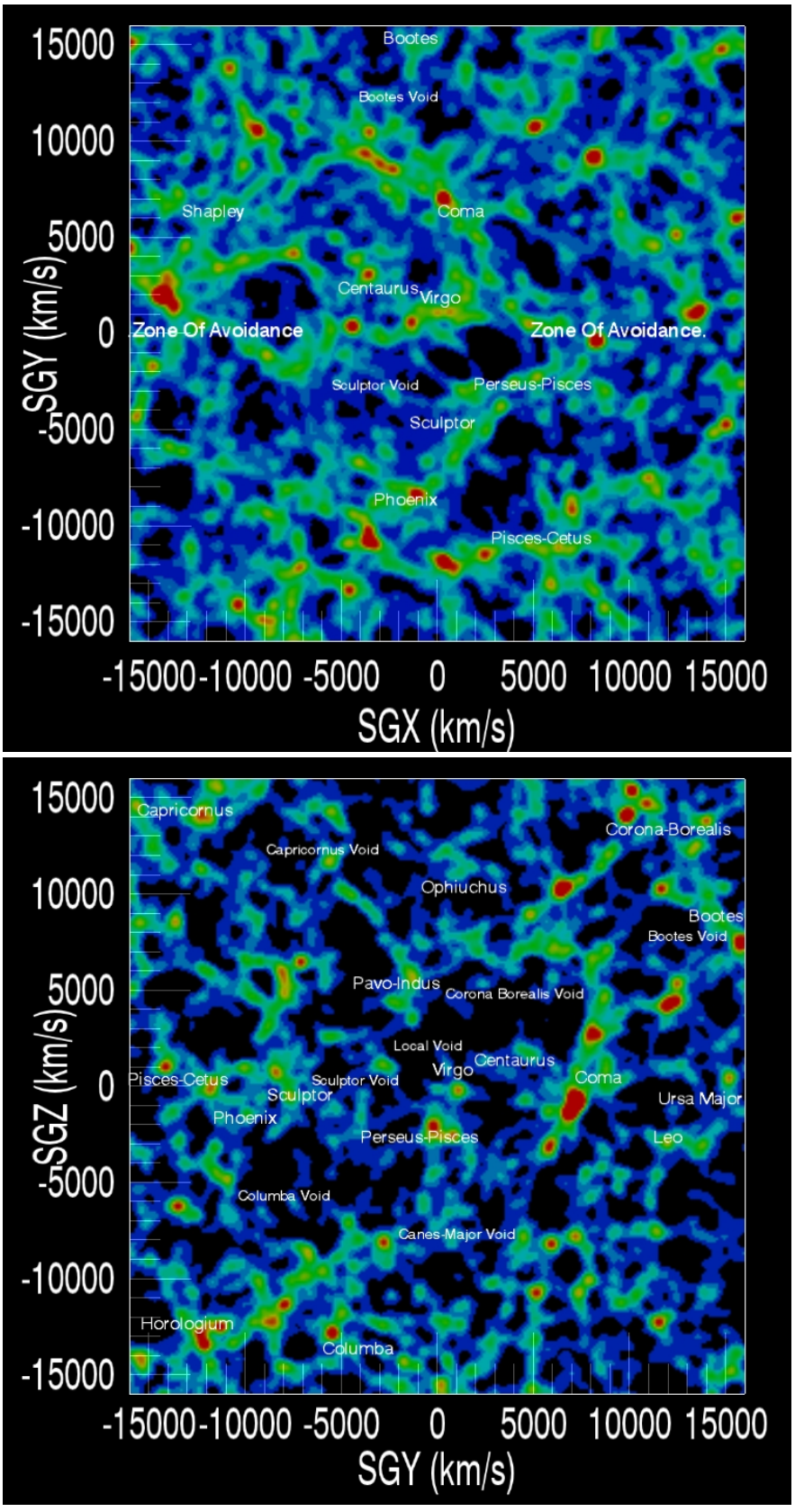

FIGURE 4.25: XY and YZ supergalactic planes of the smoothed at 2 h^{-1} Mpc simulated density field of the Local Universe for the best realization obtained with *cosmicflows-2* catalog. The color gradient represents the density field: from blue to red, the overdensity increases. Typically the darkest regions stand for voids while red/orange zones are large overdensities and green are filaments. Major overdensities and voids in the simulation can be paired with a major supercluster or void in the Local Universe (white color names). Note that in the XY plane Sextans and Bootes superclusters are not in the plane.

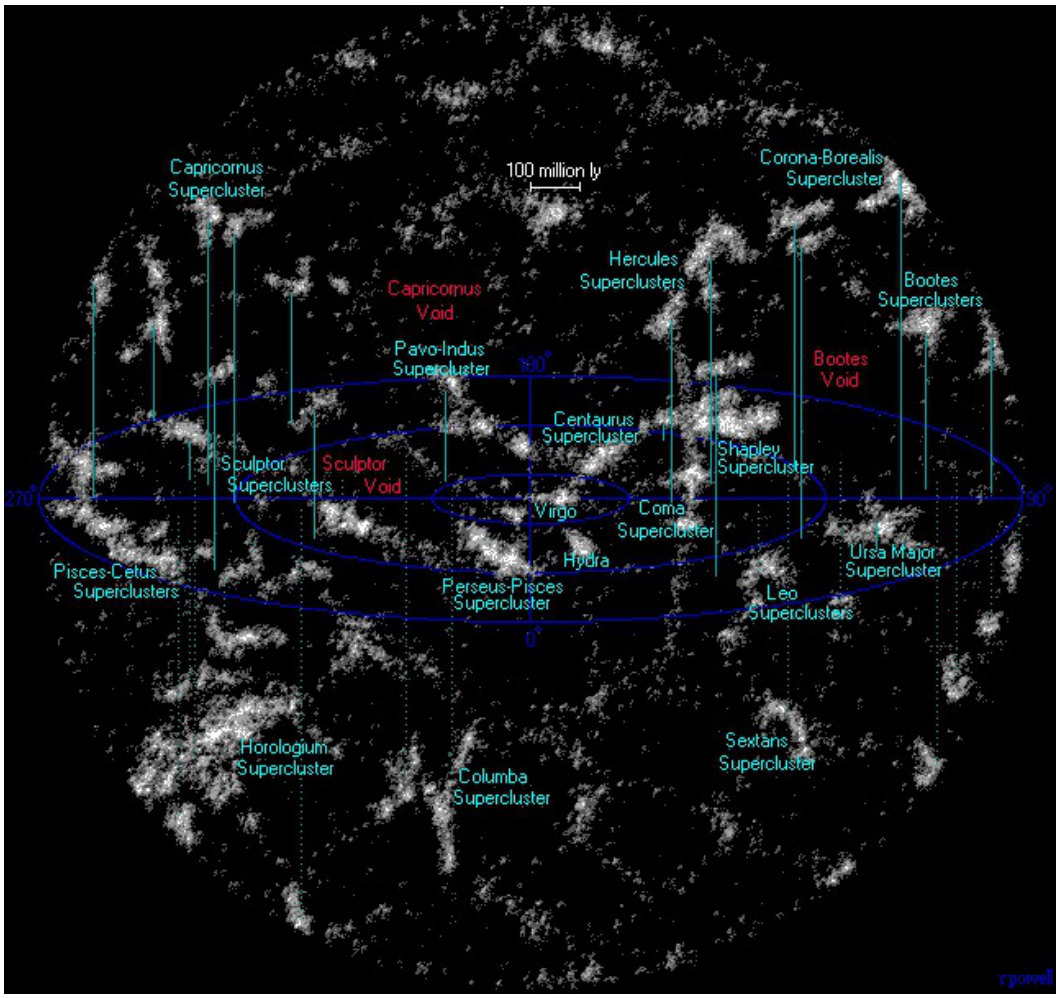

FIGURE 4.26: Representation of the superclusters and major voids in the Local Universe (from www.atlasoftheuniverse.com).

Before going into a more quantitative analysis, Figure 4.27 shows side by side reconstruction and simulation. On that figure, the simulation has been smoothed at 5 h^{-1} Mpc to facilitate the comparison with the smoothed at 2 h^{-1} Mpc Wiener-Filter field computed on half the grid size. Although the Wiener-Filter shows only the linear field, reconstruction and simulation agree very well. The reconstruction presents more feature in the center but the increasing smoothing with the distance to the center of the box is probably the cause for such an observation. The simulation allows to go deeper into the Zone of Avoidance and to extend further the study of the Large Scale Structure and, more importantly, it supplies the whole density field (including non-linearities).

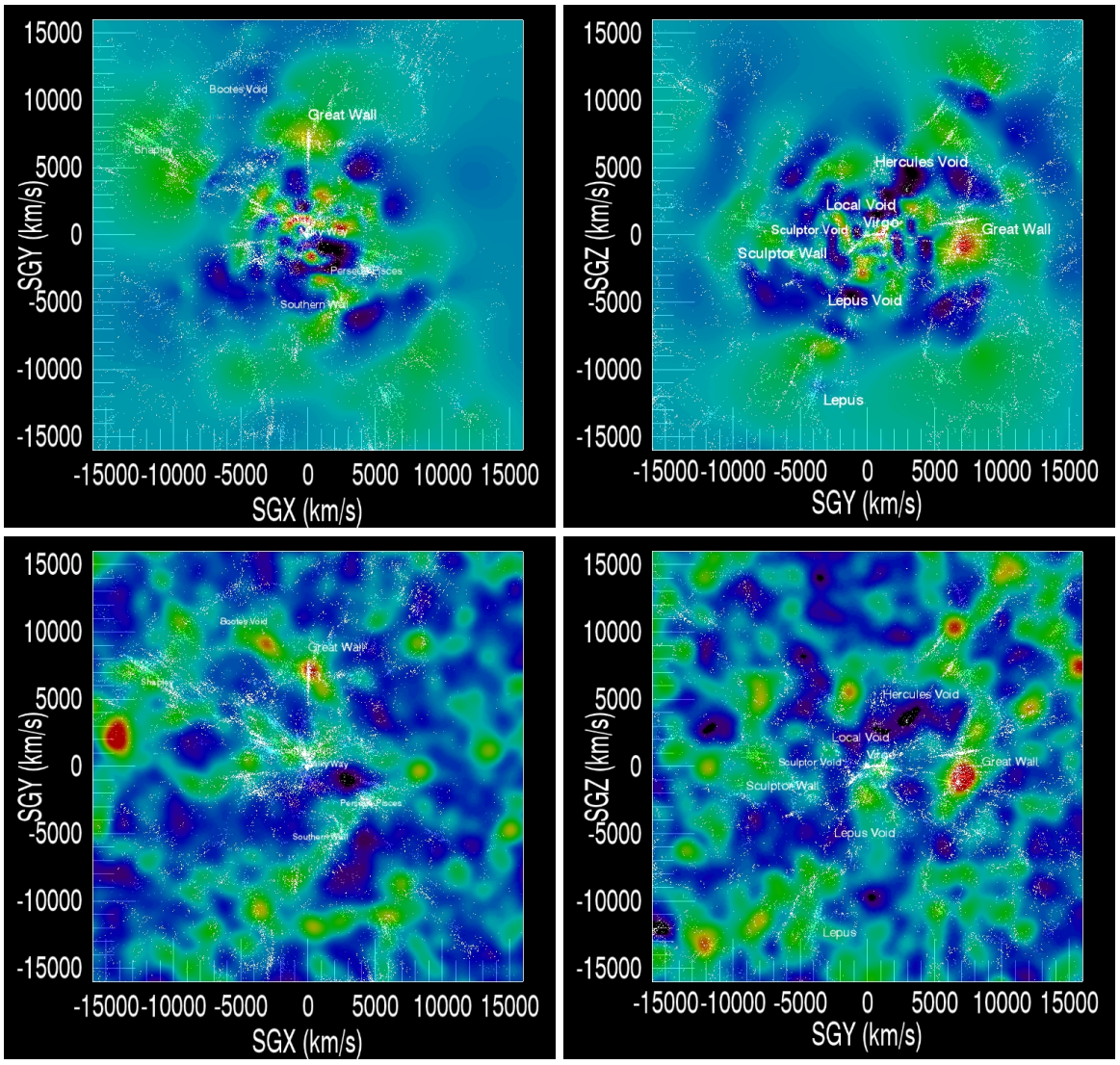

FIGURE 4.27: Comparisons between reconstruction and constrained simulation of the Local Universe obtained both with *cosmicflows-2* modified by the process explained in this work. To facilitate the comparison, the simulation has been smoothed at 5 h^{-1} Mpc and the reconstruction at 2 h^{-1} Mpc. Galaxies from the 2MASS redshift survey, in a $\pm$ 10 h^{-1} Mpc thick slice, are superimposed as white dots for comparison purposes only. Structures of the Local Universe are well recovered in both cases. A few of them are identified (white names). While the Wiener-Filter reconstructs fairly well the Local Universe in the center of the box, the simulation allows to go farther in distances and deeper into the Zone of Avoidance and, more importantly, it supplies the whole density field (including non-linearities).

4.5.3.3 Recovering Clusters

Finally, we turn our attention to the study of halos. To match halos in the simulation with clusters in the Local Universe, we use first Amiga halo finder to compile the list of halos in the simulation. Then, we look for look-alikes of known Abell clusters (Tully et al. private communication) and we add to the list Virgo and, as another example, Ursa Major. We did not look especially for the Coma Supercluster because it is surely fragmented and regardless

it is composed of Abell clusters. Thirteen Abell clusters in addition to Virgo, Ursa Major and their paired halos alongside their distance, their supergalactic coordinate, their mass and their shift in position are given in Table 4.3. The ability to found dark matter halos at so close positions (about 3-4 h^{-1} Mpc for a search restricted to a 6 h^{-1} Mpc sphere) to that of observed clusters is remarkable. Masses are not always satisfactory but two parameters can be in cause, first simulations are run with dark matter only; second and probably with the most effect, the mass resolution of the simulation is not exceptionally high. The process is repeated for Virgo and Ursa Major in the nine other realizations. Including the tenth chosen realization, we found nine Virgo-like and ten Ursa Major-like dark halos in a 6 h^{-1} Mpc radius sphere. The look-alikes of Virgo have masses ranging between 1.04 and 4.29 10^{13} h^{-1} $M_\odot$ with a median at 2.23 10^{13} h^{-1} $M_\odot$. As for the Ursa Major-like halos, their masses are about 1.39 (median) and varies between 1.05 and 3.74 10^{13} h^{-1} $M_\odot$. More remarkable than masses, are the small shifts in positions in intervals like [3.03-5.58] (median 3.53) and [1.39-4.2] (median 2.5) in h^{-1} Mpc for replicas of Virgo and Ursa Major respectively.

In any case, Figure 4.28 is a proof of concept that densities are overall recovered at the positions of Abell clusters. We can conclude with the remarkable agreement between reconstructions, simulations and observations of the Local Universe. This is the first time that such simulations are produced using *solely* peculiar velocities to reproduce all the major attractors and voids in the Local Universe at positions shifted by a few megaparsecs. Even the assumptions and observations regarding the content of the Zone of Avoidance seem to be recovered. The next step is inevitable: increasing the resolution to 1) better recover halos and pursue with more detailed studies of the Local Universe and 2) run gas simulations.

Name	Mass	D	SGX	SGY	SGZ	δ_{SGX}	δ_{SGY}	δ_{SGZ}	δ_{SG}
Virgo	4e+14*	12.26	-2.79	11.93	-0.56				
19219	2.23e+13	12.15	0.74	12.08	-1.04	3.54	0.16	-0.48	3.57
Ursa Major	3.4e+13*	12.27	5.06	11.16	0.58				
15991	2.60e+13	13.85	7.38	11.64	1.34	2.32	0.48	0.76	2.49
100005	4.58e+14*	69.8	-2.45	68.59	-12.71				
580	2.16e+14	70.82	-0.75	69.59	-13.17	1.68	1.00	-0.45	2.00
200046	2.92e+14*	96.8	70.18	-54.65	-38.19				
6499	5.11e+13	92.13	67.39	-51.68	-35.73	-2.79	2.97	2.47	4.76
100041	2.49e+14*	94.3	10.34	59.96	72.05				
4935	6.16e+13	92.92	5.30	59.16	71.46	-5.04	-0.80	-0.58	5.13
100018	2.36e+14*	74.7	-4.27	74.18	-7.67				
25	7.60e+14†	73.33	0.24	73.00	-6.96	4.51	-1.19	0.72	4.72
100083	1.55e+14*	99.7	-45.52	31.60	82.88				
4425	6.67e+13	98.60	-45.87	29.18	82.26	-0.35	-2.42	-0.63	2.53
120005	1.35e+14*	72.1	-2.42	71.25	-10.75				
6052	5.35e+13	74.20	-3.11	73.70	-8.01	-0.70	2.44	2.74	3.74
200022	1.12e+14*	48	-36.84	-27.28	14.23				
1095	1.56e+14	43.68	-33.54	-22.99	15.94	3.31	4.29	1.72	5.68
100175	1.10e+14*	99.7	-91.89	34.42	-17.65				
936	1.70e+14	97.86	-91.28	30.88	-17.02	0.61	-3.54	0.63	3.65
200252	1.07e+14*	85.8	48.88	-55.70	-43.24				
4161	6.94e+13	85.72	49.74	-53.71	-44.60	0.86	1.99	-1.36	2.56
200052	9.88e+13*	64.5	34.57	-47.57	-26.50				
5462	5.74e+13	69.25	39.50	-49.45	-28.10	4.93	-1.88	-1.59	5.51
200032	9.61e+13*	58.1	-36.00	-32.27	32.22				
608	2.09e+14	54.15	-35.02	-29.10	29.31	0.98	3.17	-2.91	4.41
100337	7.58e+13*	95.4	15.48	42.12	-84.18				
5762	5.55e+13	101.13	17.46	44.55	-89.10	1.97	2.43	-4.91	5.83
100061	6.97e+13*	71.2	1.30	71.06	-4.28				
436	2.49e+14	71.52	4.01	71.35	-2.77	2.72	0.29	1.51	3.13

TABLE 4.3: Virgo, Ursa Major and 13 Abell cluster look-alikes in the best realization: (1) name of the cluster/halo, (2) mass, h^{-1} $M_{\odot}$ within Planck cosmology. *Estimation of the total (baryonic + dark matter) mass (e.g. Ekholm et al., 2000; Karachentsev and Nasonova, 2010; Karachentsev et al., 2013; Tully, 2010) and Tully et al. private communication. † is likely to be a component of the Coma supercluster (this halo accounts for approximately half the total mass of Coma), (3) distance from the center of the box, h^{-1} Mpc, (4) to (6) supergalactic coordinates, h^{-1} Mpc, (7) to (9) shift in position on the supergalactic coordinates, h^{-1} Mpc and (10) total shift in position (sum in quadrature), h^{-1} Mpc.

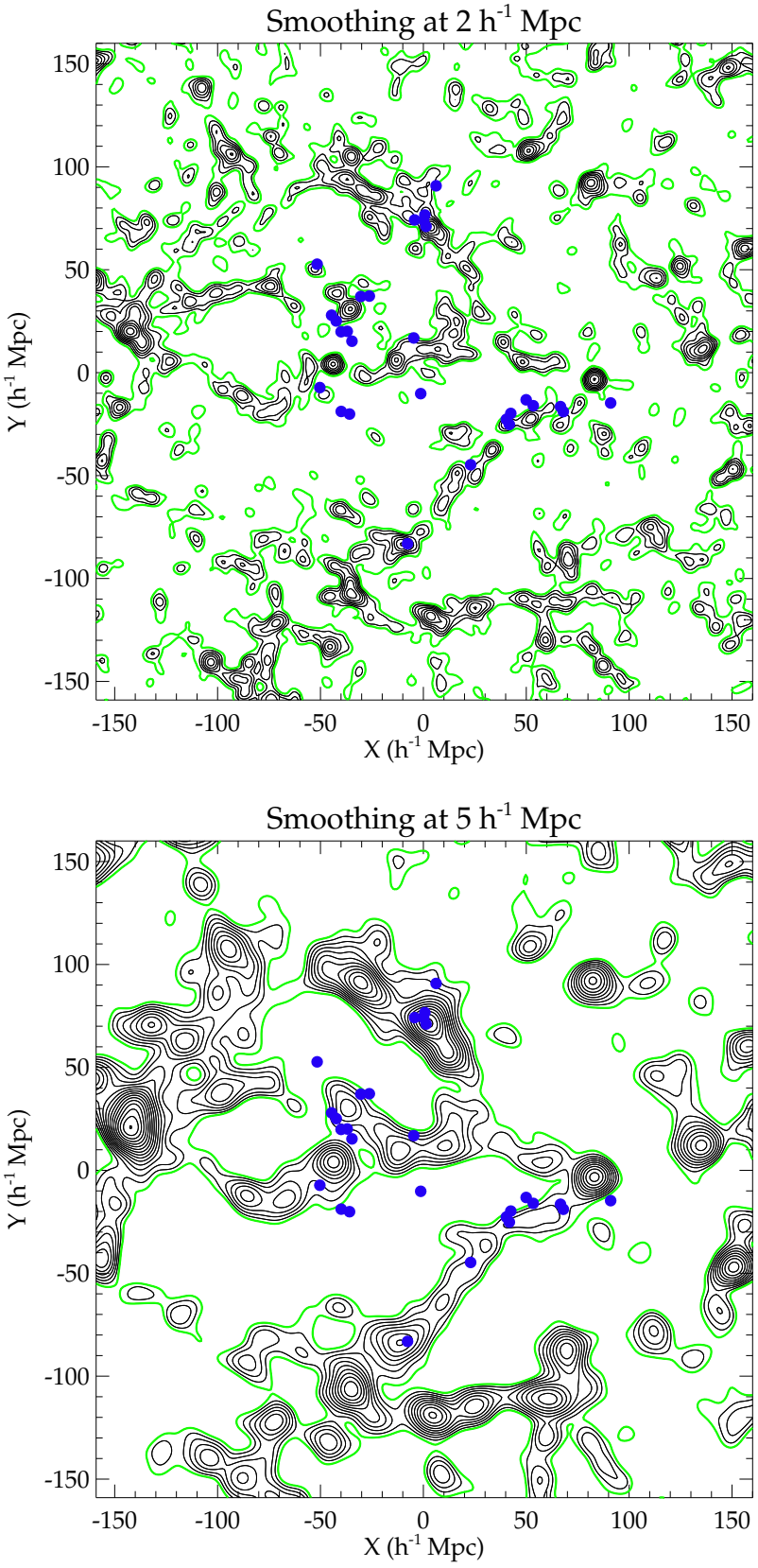

FIGURE 4.28: Superposition of Abell clusters (blue dots, Tully et al. private communication), located in a $\pm$ 10 h^{-1} Mpc thick slice in Z in the XY supergalactic plane, on top of a constrained simulation of the Local Universe. Black and green contours stand for the overdensities and mean density. The simulation has been obtained with the process described in this work applied to *cosmicflows-2* catalog. *Top*: simulation smoothed at 2 h^{-1} Mpc, *bottom*: smoothing at 5 h^{-1} Mpc. Overdensities are overall simulated at the positions of Abell clusters. No Abell cluster lie at the center of a major void.

Chapter 5

Summary & Prospectives

The work presented in this manuscript results from the combination of two international projects: The observational project Cosmicflows which goal is to cartography the Local Universe. In this regard, this project's accomplishment consists in catalogs of accurate distance measurements to map local deviations from the Hubble expansion. These distance estimates are mainly obtained with the Tully-Fisher distance indicator ; The CLUES project which produces constrained simulations of the Local Universe with, in this case, the observational catalogs of peculiar velocities built by the first project. These velocities are ideal tracers of the underlying gravitational field at the origin of the formation of structures as they account for both baryonic and dark matter. Resulting constrained simulations of the Local Universe enable to apprehend our environment with exquisite tools to better understand the formation and evolution of our neighborhood. In this closing Chapter, we summarize the work accomplished within these two projects and propose some perspectives.

5.1 Summary

5.1.1 Observed Universe

A great concern with studies of motions on large scales with the correlation between galaxy luminosities and their rotation rates or Tully-Fisher relation (TFR, Tully and Fisher, 1977) has been the possibility that systematic errors in photometry could create spurious flows. Small offsets between different observers, instruments, conditions, hemispheres, or seasons could be sky-sector dependent. With the new generation of telescopes both in the radio field and in the photometric domain, cosmic flow studies have received an impetus. The space-base Spitzer telescope (Werner et al., 2004) is an example of such a telescope with

enhanced capacities. Probably the single most important advantage of the use of space-based photometry such as offered by the Spitzer mission comes from the confidence that measurements are on the same scale at better than 1% in all parts of the sky. There are other advantages. Obscuration is minimal both within targets and from our Galaxy and backgrounds are very low. This latter point is especially significant because studies of galaxy flow patterns can now reach high levels of completion across the sky. Then it is a considerable advantage that the great majority of flux at [3.6] band arises from old stars that are good representatives of the baryonic mass, mainly those on the red giant branch. It can be surmised from the modest scatter in the Tully-Fisher relation that there is a close coupling between the mass in stars and the dynamical mass. There is also an advantage, at least vis à vis ground infrared observations, with the sensitivity achieved because of very low sky noise. All but a few percent of the total flux is measured within isophotes resolved from the noise.

Our photometric procedures for the semi-automated analysis of Spitzer IRAC (Fazio et al., 2004) channel 1 data at 3.6 μm have been described. The galaxy surface photometry was carried out with the ARCHANGEL software (Schombert, 2007; Schombert and Smith, 2012) adapted for Spitzer data input. Material of interests for the project was available for about 2000 galaxies from the Spitzer Heritage Archive including the subprogram Cosmicflows with Spitzer. We have demonstrated the ability to use *Spitzer Space Telescope* mid-infrared data to perform surface photometry with a relatively high accuracy. No correlation was found between magnitude uncertainties and other important galaxy parameters such as inclination, apparent area, or semi-major axis. We concluded that, after all corrections, uncertainties on magnitudes are of the order ± 0.05 for the regular spiral galaxies at the heart of the project. These uncertainties are small compared with the typical overall scatter in the Tully-Fisher relation. Low surface brightness galaxies or very irregular ones require special attention but these classes of galaxies are not of principal interest to us.

The current goal of the project is to measure distances, hence map peculiar velocities, across the local universe within $10,000$ km s^{-1} using mainly the Tully-Fisher relation. The Extragalactic Distance Database (EDD, Tully et al., 2009) contains HI profile information (Courtois et al., 2009) that provides useful linewidths for over 11,000 galaxies. Spitzer observations provided the complementary photometric information required for a dense, detailed map of structure and motions in the near part of the Universe especially close to the Zone of Avoidance due to the obscuration by our galactic disk dust.

First, galaxies selected as part of the calibrator sample were used to calibrate the mid-infrared Tully-Fisher relation. Then, using the calibrated relation, distance estimates have been derived for the rest of the galaxies with acceptable inclinations and available linewidths that either we have reduced or that come from the S^{4}G analysis. A small disadvantage with the mid-infrared TFR calibration has been revealed with the documentation of a color term.

This color term is understood as the natural consequence of the correlation between galaxy rotation rate or luminosity and color (Tully et al., 1982). At a given linewidth, red galaxies progressively become brighter relative to blue galaxies as one considers the TFR at longer wavelengths. Evidence is accumulating that intrinsic scatter in the simple two parameter-TFR is minimal with photometry at about 1 μm. A consequence of the color dependence is a steepening of the TFR toward the infrared. At the expense of the requirement of extra knowledge in the form of a color, the TFR in the [3.6] band was reformulated in a form with scatter that matches the best optical formulations. The correction is small and not acutely dependent on the color measurement. The appropriate inverse TFR equation for the measurement of distances is, after checking the robustness deriving two relations with two different calibrator samples (selection in B and K bands):

$$M_{C_{[3.6]}} = -(20.31 \pm 0.07) - (9.10 \pm 0.21)(\log W^i_{mx} - 2.5) \tag{5.1}$$

where $M_{C_{[3.6]}}$ is derived from the corrected apparent magnitude $[3.6]^{b,i,k,a}$ of a source minus the color term $\Delta[3.6]^{color} = -(0.52 \pm 0.10)[(I^{b,i,k} - [3.6]^{b,i,k,a}) + 0.73]$ with I Band magnitude shifted to the AB system. The slope of this formulation has been derived from a sample of 273 galaxies distributed in 13 clusters, while the zeropoint is established from 31 calibrators with Cepheid or tip of the red giant branch distances. The root mean square scatter in distances found with these galaxies (cluster template and zeropoint calibrators combined) of 0.43 mag, 22% in distance, is close to the accuracy found with the overlapping I band study (Tully and Courtois, 2012).

Distance measures derived with this calibration are subject to a small Malmquist bias or selection effect (Willick, 1994), requiring the distance modulus correction $\mu^c = \mu + 0.004(\mu - 31)^{2.3}$. After application of bias and color corrections, a preliminary estimate of the Hubble Constant can be made from the velocities and distances to seven clusters at $V_{CMB} > 4000$ km s^{-1}. Accounting for all error sources (sum in quadrature), the determination is $H_0 = 75.0 \pm 5.5$ km s^{-1} Mpc^{-1}. The difference between the value determined with this mid-infrared analysis compared with the I band value found with the same procedures and an overlapping sample is $\Delta H_0 < 1$ km s^{-1} Mpc^{-1}, not a formally significant difference. We reiterate that the great strength of the present calibration is the high confidence in uniformity over the entire sky. Nevertheless the present sample of only seven clusters beyond the domain of known extreme peculiar velocities was unsatisfactorily small. Subsequently, the [3.6] band calibration was extended to a calibration of the Type Ia supernova (SNIa) scale, analogous to what has been done at I band (Courtois and Tully, 2012b), permitting a determination of H_0 at $z \sim 0.1$.

The mid-infrared TFR calibration of the SNIa distance scale led to a result for the Hubble Constant that is not significantly different from the earlier optical TFR calibration. The

earlier calibration made use of a considerably larger collection of material. Besides using over 50% more individual TFR galaxies, it gave consideration to 61 groups or clusters hosting SNIa with distances not only from the TFR but also with Cepheid, surface brightness fluctuation, and fundamental plane measurements (Courtois and Tully, 2012b). Nevertheless we contend that the present confirming work has value because it puts to rest a concern with the optical study. The optical photometry was acquired by a diverse community of observers on several telescopes with a variety of detectors and filters and subject to the vagaries associated with ground-based observations. This mid-infrared photometry has been acquired with a single observing configuration in space advertising photometric consistency across the sky to better than 1%. The study has extended the calibration to distances where peculiar velocities should have negligible impact and we found $H_0 = 75.5 \pm 3.3$ km s^{-1} Mpc^{-1}.

Distances for Cosmicflows encompass measures by other methodologies than the TFR either from the literature or from other subprograms of the project. Foremost among these are Cepheid Period-Luminosity Relation (Freedman et al., 2001, 2012), Tip of the Red Giant Branch (Lee et al., 1993; Makarov et al., 2006; Rizzi et al., 2007), Surface Brightness Fluctuation (Blakeslee et al., 2010; Tonry et al., 2001), Fundamental Plane (Colless et al., 2001), and Supernova Ia (Jha et al., 2007; Riess et al., 2011) procedures. The diverse material is drawn together in EDD which goes beyond the compilation of catalogs relevant to extragalactic distances to include redshift catalogs, that with various levels of completion describe the distribution of galaxies in the Local Universe, and group catalogs, that help identify entities where averaging over velocities or distances is reasonable. The first assembly of distances in this program (Tully et al., 2008) has now been given the name *cosmicflows-1*. This work has contributed to build the second catalog of the Cosmicflows project (*cosmicflows*-2, Tully et al., 2013) and has initiated the development of a third one with Spitzer observations which will be completed with other measurements in the mid-infrared (WISE, Wright, 2008, Neil et al. in prep.). With two catalogs ready *cosmicflows-1* and *cosmicflows-2* and a third one in preparation, a collaboration with the CLUES project has been established to pursue reconstructions (e.g. Courtois et al., 2012) and constrained simulations (e.g. Gottlöber et al., 2010) of the Local Universe.

5.1.2 Simulated Universe

A great concern with numerical simulations to be compared with observations to study the Local Universe is cosmic variance. This cosmic variance is due to the fact that there is only one universe that we can observe only, at one time, from our "particular" position within the Large Scale Structure environment. Namely, the surrounding environment of the object of study is as important as the object (e.g. Garrison-Kimmel et al., 2014). To minimize the cosmic variance effect, the CLUES collaboration works within the framework

of numerical cosmological constrained simulations of the Local Universe. The first CLUES simulations based on the Mark III catalog of peculiar velocities (Klypin et al., 2003) were not very precise: 1) structures in the simulation at z=0 were shifted by 10 h^{-1} Mpc from their observed positions and 2) density constraints were used to simulate nearby clusters. The main deficiency of the Constrained Realization of Gaussian fields algorithm (Hoffman and Ribak, 1991, 1992) used to produce the initial conditions was not to account for the cosmic displacement field whereas galaxies observed today are at different locations from their precursors at higher redshifts. A partial remedy to the problem, called the Reverse Zel'dovich Approximation, was suggested and tested by Doumler et al. (RZA, 2013a,b,c). This approximation consists in shifting constraints back in time from their positions at redshift z=0 to the locations of their precursors at higher redshifts. The technique was yet to be tested on more realistic mocks and on an actual observational catalog of the Cosmicflows project. The work presented in this manuscript is thus the first attempt to produce simulations constrained *solely* by an observational catalog of peculiar velocities from the Cosmicflows project.

Since *cosmicflows-1* (peculiar velocity catalog) extends only out to about 30 h^{-1} Mpc (radius), derived constrained simulations are subject to the cosmic variance inherent to the particularities of our neighborhood. Accordingly to test either a reconstruction or a generator of initial conditions method, mock catalogs have to be drawn from a previous constrained simulation which looks like the Local Universe and an ensemble of initial conditions has to be produced. The mock catalogs used in this work have been designed to mimic the observational catalog by including distance measurement errors and a large continuous zone without data (Zone of Avoidance due to our Galaxy extinction). Tests on these mocks and on *cosmicflows-1* revealed that the original RZA, from now-on called RZA-radial, method could be refined. We suggested that *observational* radial peculiar velocities are subject to uncertainties and probably also biases which prevent them from completely defining the curl free velocity field. Thus, the RZA algorithm with its additional feature, which replaces original observed radial peculiar velocity vectors by their full 3D reconstructions provided by the Wiener-Filter estimator (Zaroubi et al., 1999, 1995), should be a remedy to this flaw. The augmented RZA method (called RZA3D) has been tested against the same mocks and resulting simulations have been compared with RZA-radial and original simulations. The enhanced precision and reliability of RZA3D has been validated. The RZA3D methodology has been subsequently applied to the actual *cosmicflows-1* catalog. Only after such a process of the observational dataset, the Constrained Realization of Gaussian fields technique was applied to build various realizations of the initial conditions. The different ensuing simulations recover the observed Large Scale Structure with a typical accuracy of 5 h^{-1} Mpc in position, the best realizations reaching a 2-3 h^{-1} Mpc precision, i.e. the limit imposed

by the linear theory. The methodology succeeded in performing robust constrained simulations using *only observational peculiar velocities* as constraints. However, *cosmicflows-1* was too shallow to enable constrained simulations that could reproduce all the main attractors and voids of the local dynamics. *Cosmicflows-2* catalog which contains more than 8,000 galaxy distances (1,800 in *cosmicflows-1*) and extends out to about 150 h^{-1} Mpc was more appropriate.

Yet, reiterating the process with the second catalog of the Cosmicflows project revealed that this greater spatial extent catalog suffered from biases (Kaptney 1914 ; Malmquist, 1920 and e.g. Dekel, 1994; Han, 1992b; Hendry and Simmons, 1994; Hudson, 1994; Landy and Szalay, 1992; Sandage, 1994; Teerikorpi, 1990, 1993, 1995, 1997) that needed to be minimized before pursuing with the work. First, *cosmicflows-2* was grouped. Second, a correction devised in this work to minimize in particular the asymmetry bias observed in the second catalog of the international Cosmicflows project was proposed. This bias is due to the fact that distance errors have a lognormal distribution rather than a Gaussian one resulting in an asymmetric radial peculiar velocity distribution. This asymmetric distribution inserted in the bayesian Wiener-Filter technique results in a spurious infall onto the Local Volume as, by assumption, a Gaussian weight distribution is assigned to radial peculiar velocities. The correction was developed and tested on mocks closely matching *cosmicflows-2* in terms of size (coverage, number, spatial distribution including the Zone of Avoidance), lognormal errors, uncertainties (quasi bimodal distribution) and absence of exact knowledge of errors. The method to minimize the bias, similar to bayesian ways as it relies on probabilities and Gaussian distributions, corrects velocities according to the following formula proposed in this work:

if $v_{pec} > 0$,

$$v_{pec\,c} = f[p(v_{pec} - \Delta) + (1-p)(v_{pec} + \Delta)] + (1-f)v_{pec} \tag{5.2}$$

if $v_{pec} < 0$,

$$v_{pec\,c} = f[p(v_{pec} + \Delta) + (1-p)(v_{pec} - \Delta)] + (1-f)v_{pec} \tag{5.3}$$

where Δ is the radial peculiar velocity uncertainty (Δv_{pec}) ; p is the probability that a radial peculiar velocity does not belong to the theoretical Gaussian (thus it needs to be corrected and it should either be reduced if it is highly positive or increased it is highly negative) ; f is the probability that the radial peculiar velocity estimate is wrong. Namely, f is proportional to the fractional uncertainty on distances (peculiar velocities) normalized to the maximum fractional uncertainty plus 0.05 (best parameter in our different realization to retrieve a distribution close to the theoretical Gaussian) to keep a minimum of trust towards the initial measurements. After correction, distances are computed accordingly and a 6% fractional error on distances is assumed in agreement with the upper limit of the fractional error medians measured for the corrected mocks. As this method reduces the error on distances,

we can expect that it also minimizes other Malmquist Biases to some extent especially since biases are all related to distance errors (Landy and Szalay, 1992; Sandage, 1994).

The whole process has then been applied to the second catalog of the Cosmicflows project from the minimization of the asymmetry bias up to RZA augmented, both devised in this work. Then the resulting dataset was input in the Constrained Realization of Gaussian fields algorithm to produce constrained simulations of the Local Universe. The second generation of constrained simulations of the Local Universe performed in this work, *solely from observational peculiar velocities*, has finally been presented and shown to reproduce the Large Scale Structure of the Local Universe. The majority of the superclusters of the Local Universe within 200 h^{-1} Mpc are recovered so are the filaments interconnecting them, even across the Zone Of Avoidance. Major voids are also simulated. Looking for specific clusters like the Abell clusters a handful of them are found with appropriate masses. Regardless, these halo-replicas are found at locations approaching by a few megaparsecs, typically 3-4 h^{-1} Mpc, the observational positions of Abell clusters.

5.1.3 Conclusion

Galaxies are sources of observations. Still, they are only tips of the iceberg of a larger scheme which involves a mysterious dark component: the dark matter and energy. The standard cosmological model is currently accepted as an elegant theory in which are included these two necessary exotic dark components. Subsequently, although it can be far from the truth, this cosmological model enables to simulate the formation and evolution of the Universe in a remarkable agreement with observations. From initial perturbations to growth of structures, the Universe seems to be understood to a great extent. Comparisons and synergies between observations from the Cosmicflows project and constrained simulations from the CLUES project presented in this work confirm the largely accepted scheme at least on large scales. The only missing component to perfect comparisons between observations and simulations are baryons. They still need to be analyzed and studied in thorough details in simulations to reconcile entirely observations with theories. Yet, before taking this step, 1) observational catalogs are improvable especially in terms of coverage, *cosmicflows-3* is an example, and potentially reduction of uncertainties and biases, 2) resulting dark matter constrained simulations have yet to be studied more thoroughly to deliver some aspects of the Local History before adding any gas material. The constant back-and-forth between observations and simulations provides us with a way to refine our numerical methods but also to better exploit our observational data (e.g. removing biases, Lavaux et al., 2008, and section 4.4.3).

5.2 Prospectives

The main goal of the combined "CosmicCLUES"[1] project is to study the Local Universe formation and evolution to better understand the cosmology of our Universe and as a result the nature of dark matter. To this end, carrying on developing the synergy between the theoretical, observational and numerical fields of research is essential. The direct comparisons between the observed and the simulated universes will enable to confirm, to refine and to develop the current theoretical understanding of structure formation.

5.2.1 Observations

In the observational field, there are two main points which might be worth looking into:

- first and foremost, there is the increase in size of the future catalogs both in coverage and in density (spatial extent and number of measurements),
- second, the improvement in distance estimate accuracies.

Actually, the collaboration has already begun to work on both points. The first point has begun with the collection of data to build cosmicflows-3. Spitzer has already supplied part of it and, for instance, WISE (Wright, 2008) will provide the rest of it. The calibration of the Tully-Fisher relation for WISE bands is already in progress (Neil et al. in prep). Gathering even more data from archives regarding HI profiles and re-measurements in a consistent way are also ongoing (Courtois et al. in prep). Photometric data will then be collected from other all-sky surveys like PanStarrs (Kaiser et al., 2002). *Cosmicflows-4* can be envisaged with 100,000 observations, up to 500 h^{-1} Mpc, from the Australian Square Kilometre Array Pathfinder and Apertif (Johnston and Deboer, 2008; Verheijen et al., 2008). Regarding the second point, the collaboration has taken three paths, 1) one which tries to improve grouping of galaxies (Tully et al. private communication). As a reminder, grouping improves group distance estimate accuracies as the square root of the number of grouped galaxies, 2) one which aims at reducing the uncertainty on galaxy inclinations with the soon to be launched Citizen Science project (alternatively, a recent paper by Obreschkow and Meyer (2013) proposes a method to derive the Tully-Fisher relation without galaxy inclinations. This process can indirectly be used to constrain inclinations of galaxies with unknown inclinations, this matter could be look into more thoroughly) and 3) the last one which concentrates on reducing the scatter in the Tully-Fisher relation (Zaritsky et al., 2014) using the Baryonic Tully-Fisher relation. That is now deemed appropriate to explain in more detail this Baryonic Tully-Fisher relation (BTFR) and the results found. This

[1] Note that this name is not official and is just given here for conveniency.

relation relies on the observations that the scatter in the TFRs varies with the use of another parameter (color, half light radius, concentration index, size, morphology, see e.g. Pizagno et al., 2007) which probably means that the ratio of dark-luminous matter varies within the disk populations. Perhaps so, but what about the relation baryonic-dark mass? As the baryonic mass is the sum of the stellar and gas mass (formula 5.4), a tighter correlation between the baryonic mass and the rotation rate of galaxies would imply that the classic TF is valid because luminosity approximates quite well the stellar mass and the gas mass is negligible in most galaxies. Deviant galaxies from the classic TF are indeed gas dominated galaxies and special galaxies in the sense that they are not classic disk dominated spirals. The BTFR is able to reconcile disagreements which can be found between such different systems, namely they do lie on the same BTFR but have their own classic TFR (e.g for massive disk galaxies and for Hickson compact group galaxies, Noordermeer and Verheijen, 2007; Torres-Flores et al., 2013). The Faber-Jackson relation (FJR) has also its equivalent the BFJR (Catinella et al., 2012).

$$M_{gas} = \underbrace{1.4}_{\substack{\text{accounts for} \\ \text{H}_e \text{ \& metals}}} \times [\underbrace{(3.7 - 0.8T + 0.043T^2)}_{\substack{\text{corrects for} \\ \text{M}_{H_2}}} + 1] \times \underbrace{(2.36 \times 100000 \times D_L^2 \times F_{HI})}_{\substack{\text{gives} \\ \text{M}_{HI}}} \tag{5.4}$$

$$M_* = 10^{5.65}\ F_{[3.6]}^{2.85}\ F_{[4.5]}^{-1.85}\ (\frac{D_L}{0.05})^2\ M_\odot$$

$$M_{baryonic} = M_* + M_{gas}$$

from McGaugh and de Blok (1997); Zaritsky et al. (2014) with T the numerical morphological type, between approximately 0 and 10 for late type galaxies, and from Eskew et al. (2012). M_{gas} is in units of 10^5 $M_\odot$, F_X are fluxes (integrated within the HI profile in units of Jy km s^{-1} or in [3.6] and [4.5] Spitzer bands in Jy) and D_L the luminosity distance. Zaritsky et al. (2014) noted that the baryonic content of the galaxy considered, $M_{baryonic}$ as above defined, accounts only for the condensed fraction of baryons onto the central region of spiral galaxies (both extremely cold and hot material and far from the center baryons are not considered). A fraction found to be a constant 40% (Zaritsky et al., 2014).

In any case, the BTFR relation is found to have a reduced scatter with respect to the classic TF in various bands (e.g. Zaritsky et al., 2014, at 3.6 μm). However, stellar masses are still to be better determined. For instance, some tensions between BTFR slopes found by McGaugh (2012) and Zaritsky et al. (2014) might be due partially to stellar normalizations. As a matter of fact, gas-dominated galaxies and stellar-dominated galaxies if fitted separately share the same BTFR slope but when fitted together result in a higher BTFR slope. The

slope can be driven up more or less depending on the different stellar-normalizations affecting the stellar-dominated galaxy zeropoint. A reconciliation is absolutely necessary because the slope value influence the derived distance estimates. On another matter, a higher slope (≈4) privileges the MOdified Newtonian Dynamics model (Milgrom, 1983a,b,c) over the standard ΛCDM model.

Although the BTFR has a quite reduced scatter with respect to the classic TFR in the dwarfs regime, it is not null or small enough to be yet accounted for by the sole observational errors. Among the possible effects, we note the concentration of dark matter that may vary differently from the center to the edge (Dutton, 2012) or some interaction between baryonic and dark matter that may come into play (Desmond, 2012). These are even more reasons to test the relations with simulations, to compare simulated and observed galaxies to better understand galaxy formation.

5.2.2 Simulations

Large scales are well reproduced by dark matter only simulations but on small scales because of the complexity of star and galaxy formation, the baryonic physics cannot be neglected. Accordingly, for the CLUES project, the next step after reproducing the local Large Scale Structure is to dig into the matter of galaxy formation and evolution in the Local Universe. However, running a full hydrodynamical simulation including star formation within the Large Scale volume with the necessary resolution is currently unconceivable. Then, the CLUES project can follow different paths:

- running gasdynamical simulations in a smaller volume with higher resolution. Such simulations can be envisaged within the framework of zoomed simulations. To this end, the method presented and refined in this work to build constrained initial conditions could be used to produce constrained density fields. These density fields could then be converted into white noise fields which would ultimately be input in GINNUNGAGAP to produce multi-scale initial conditions or, alternatively, into the publicly available MUSIC (Multi-Scale initial conditions) code developed by Hahn and Abel (2011) which, to date, has been more tested. These codes both use the popular "zoom-in" technique (see Bertschinger, 2001, for the precursor of the technique) which consists in increasing the resolution in region of interests (clusters of galaxies, specific objects) selected in the simulation at $z = 0$. To this end, the corresponding peak patch in the initial white noise field from which the region of interest is going to emerge has to be identified. Then, the resolution is increased in the white noise field in this particular patch while the large scale is left at low resolution. Large scale modes have to be kept to preserve their tidal influences on the particular region of interests. Assuming that the baryon

distribution at the initial redshift follows that of dark matter, a Boltzmann solver (e.g. Birrell and Rafelski, 2014) allows then to compute velocity and density fields. Resulting multi-scale hydrodynamical initial conditions could then be input in GADGET,

- running high resolution dark matter only simulations of the full box so that halos of 10^9 h^{-1} $M_\odot$ could be resolved. At this point, parameters of the simulations could be tuned by first testing intermediate resolutions (for instance a simulation box of approximately 320 h^{-1} Mpc side length with 2048^3 particles, in a Planck cosmology, results in a particle mass around 3.3×10^8 h^{-1} $M_\odot$. Thus, dark matter halos of 10^{10} h^{-1} $M_\odot$ are resolved with 30 particles). Regardless, the same pre-required white noise as before could be input in GINNUNGAGAP to increase the resolution but homogeneously (not locally anymore). Objects in these resulting simulations could then be identified with a spherical overdensity halo finder (Amiga Halo finder, Knollmann and Knebe, 2009) as well as friends-of-friends algorithms. Outputs from these algorithms would enable to populate these simulations with galaxies using the abundance matching techniques which consist in attributing observed galaxies to simulated dark matter halos. The more massive the host halo, the more massive the galaxy is assumed to be. Then, a stellar-to-halo mass relation could be derived from this observation/simulation combination (e.g. Behroozi et al., 2010; Moster et al., 2010). However, the derived stellar-to-halo mass relation depends widely on the observational limits of the galaxy survey used to pair dark matter halos with galaxies (e.g. Garrison-Kimmel et al., 2013). In addition, even if these different stellar-to-halo mass relations could be reconciled and could be extended at low mass ends, they might depend on the environment. Therefore, the development of a stellar-to-halo mass relation in each one of the specific region of the Local Universe to study would have to be privileged to, eventually, conclude on the (non)-universality of such a relation. For example, within the CLUES project, the stellar-to-halo mass relation was derived for Local Group galaxies (Brook et al., 2013). Thus, it could be first checked that the same relation for Local Group-like galaxies is found. Since running, a full gasdynamical simulation with the same resolution and the same boxsize is currently impossible, thorough comparisons with the full box would not be possible but chosen specific regions could be compared. For instance, the stellar-to-mass halo relation could be derived for the Local Group-like galaxies in the gas simulation in order to be compared with the result obtained in the dark matter simulations combined with the abundance matching technique,

- running a series of lower resolution simulations (for instance 1024^3 particles with the same typical boxsize as used for the high resolution simulation, results in a mass particle about 2 10^9 h^{-1} $M_\odot$). These dark matter only constrained simulations could then be used to study the cosmic variance in terms of scatter in positions of structures and in merging histories of the replicas of local clusters. The merging history with the higher

statistical probability could give clues as to where to look for radio relics produced during merger events or, at least, provide an estimate of the number of radio relics which could be observed by future surveys obtained with LOw-Frequency ARray and Westerbork Synthesis Radio telescopes (Nuza et al., 2012). Studying the mass accretion history (defined by formation, assembly and last major merging times) of several nearby groups-like, mass accretion history which has been find to be quiet in the Local Group case (Forero-Romero et al., 2011), might solve the question of how large and mid scale environments around groups induce different mass accretion history. Currently, it is clear that low density environment and isolation criteria are both not adapted to end up, after selection, with only quiet mass accretion history groups-like (Forero-Romero et al., 2011). This work would answer the question "how unique is the Local Group in a given cosmological context?" to better distinguish between models. For instance, Libeskind et al. (2013) has shown that within Warm Dark Matter, the Local Group is more likely to be more diffuse than observed today than within cold dark matter. This leads to an increased trust towards the cold nature of the dark matter although it is not impossible to find the proper Local Group in a warm context, excluding the eviction of the Warm Dark Matter from theories.

In parallel, the theoretical approach might also be improved. For instance, the first order linear approximation used to compute the cosmic displacement field in the RZA could be refined up to the second order using the second order Lagrangian Perturbation Theory (e.g. Kitaura, 2013; Kitaura et al., 2012) or even the Augmented Lagrangian Perturbation Theory proposed by Kitaura and Heß (2013). This method builds on the difference between the long and short range components of the displacement. Namely, at small scales the second order fails because of shell crossing, it is then replaced by a spherical collapse model. Finally, a comparison between simulations constrained with different types of constraints, peculiar velocities and distribution of galaxies (Heß et al., 2013) could also give the advantages and the limitations of each method. Regardless, the variety of simulations expounded above would need to be performed in between.

We conclude this manuscript with an overview, Figure 5.1, of this work, realized within the context of the global "CosmicCLUES" project scheme, and we extend it to the future work which can be envisaged.

Figure 5.1 ⇒

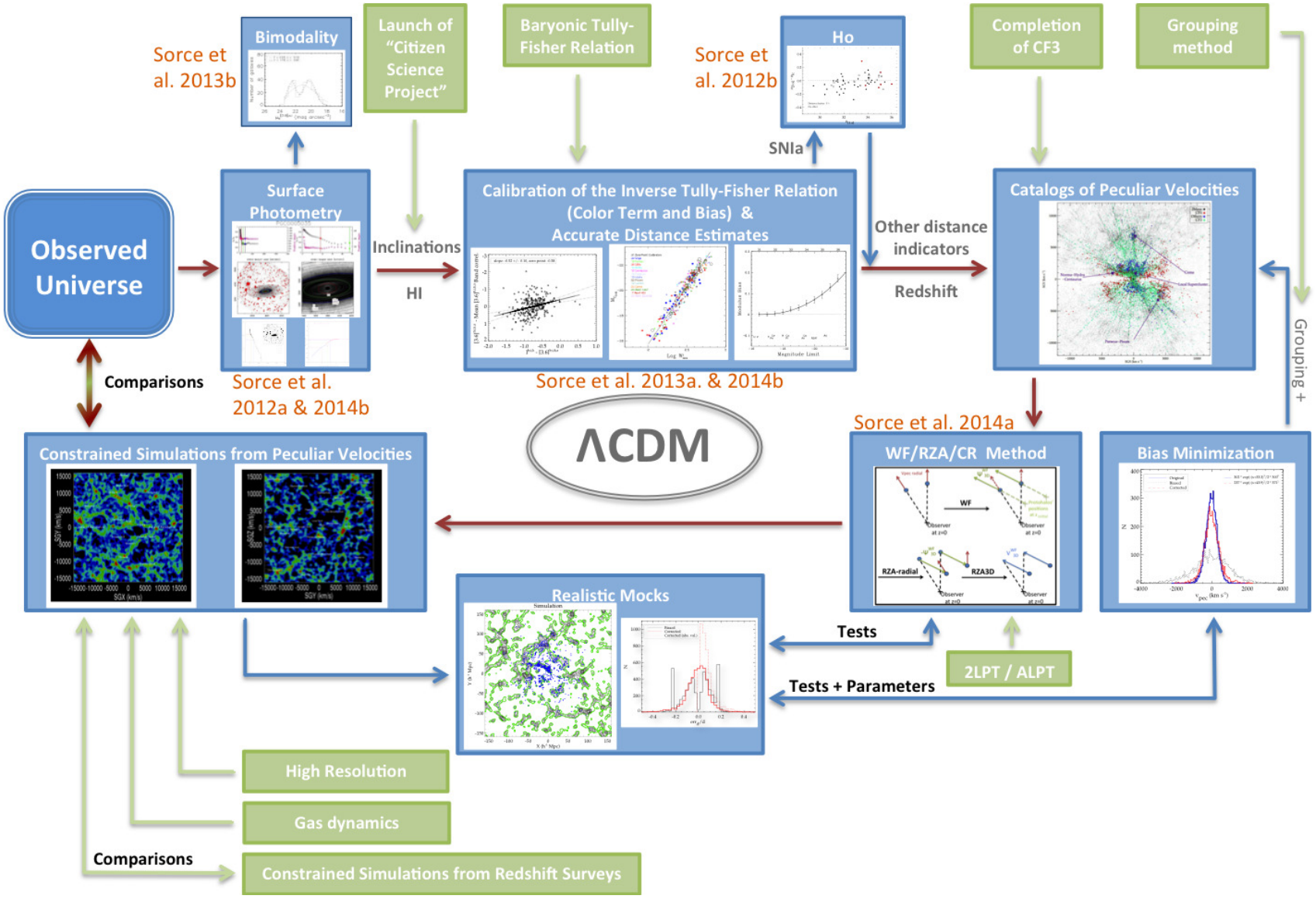
Observed Universe
Comparisons
Surface Photometry
Sorce et al. 2012a & 2014b
Bimodality
Sorce et al. 2013b
Launch of "Citizen Science Project"
Inclinations
HI
Baryonic Tully-Fisher Relation
Calibration of the Inverse Tully-Fisher Relation (Color Term and Bias) & Accurate Distance Estimates
Sorce et al. 2013a. & 2014b
Ho
Sorce et al. 2012b
SNIa
Other distance indicators
Redshift
Completion of CF3
Grouping method
Catalogs of Peculiar Velocities
Grouping +
ΛCDM
Sorce et al. 2014a
WF/RZA/CR Method
WF
RZA-radial
RZA3D
Bias Minimization
Constrained Simulations from Peculiar Velocities
Realistic Mocks
Tests
Tests + Parameters
2LPT / ALPT
High Resolution
Gas dynamics
Comparisons
Constrained Simulations from Redshift Surveys

FIGURE 5.1: Outlines of current and envisaged additional future work are presented. The blue color shows this work (outputs from outside are in grey) from the observations to the constrained simulations through, the calibration of the Tully-Fisher relation and the refinement of the process to build constrained initial conditions (red path) with, parallel work to estimate the Hubble constant, to confirm bimodality in disk central surface brightnesses of galaxies, to build realistic mock to tests methods and to devise a correction to minimize the bias(es) (blue path). This work results from, and, enables a synergy between, simulated and observed universes. Namely, the back-and-forth between observations and simulations provides a way to refine the methods but also to better exploit the observational data to, finally, study the Local Universe, the formation and evolution of structures. In green are the envisaged extensions to this work which will enable a thorough study of the Local Universe thanks to detailed comparisons between observed and simulated universes to better understand the nature of dark matter via its influence on structure formation and galaxy evolution. The proposed future work goes from the baryonic Tully-Fisher relation - to obtain even more accurate distance estimates - up to the addition of gas in simulations through, the launch of the Citizen Science project - to obtain better inclination estimates - the refinement of the grouping technique, the production of higher resolution constrained simulations, a higher order development in the computation of the cosmic displacement field and the completion of the cosmicflows-3 catalog in addition to, comparisons with simulations constrained with redshift surveys. Basically, the prospective work proposes to augment the quality of the now fully functional red path.

Appendix A

Extragalactic Distance Database: Spitzer [3.6] Band Photometry

1	2	3	4	5	6	7	8	9	10	11	12	13	14	15	16	17	18	19	20	21
PGC	$a_{26.5}$	$[3.6]_{26.5}$	$[3.6]_{tot}$	σ_m	$[3.6]_{ext}$	μ_0	α	b/a	$\sigma_{b/a}$	PA	a_{80}	μ_{80}	a_e	μ_e	$\langle\mu_e\rangle$	a_{20}	μ_{20}	$\langle\mu_{20}\rangle$	C_{82}	Prog.
94	49	15.93	15.932	0.004	15.913	19.73	7.9	0.20	0.00	53	30	23.70	17	22.39	22.37	8	22.15	21.79	3.9	CFS
143	405	11.72	11.467	0.001	11.437	23.45	144.4	0.44	0.00	3	430	27.87	230	25.09	24.38	107	24.12	23.91	4.0	CHP
527	48	16.11	16.001	0.002	15.962	22.59	13.2	0.29	0.00	33	34	25.46	17	24.01	22.87	8	22.41	22.09	4.4	CFS
698	124	11.24	11.209	0.003	11.201	20.71	23.2	0.63	0.00	171	30	21.67	11	19.45	17.90	4	16.77	16.36	8.4	CHP
701	223	11.38	11.329	0.075	11.360	19.74	35.9	0.26	0.00	44	113	23.14	58	21.45	20.70	29	20.43	20.15	3.8	SINGS
767	68	12.78	12.769	0.024	12.776	18.96	9.9	0.51	0.06	149	29	21.92	14	20.60	19.93	6	19.67	19.00	5.1	CFS
963	77	13.47	13.453	0.007	13.438	20.66	14.2	0.44	0.02	80	33	23.51	16	21.36	20.54	7	20.27	19.83	4.9	CFS
1315	50	13.09	13.082	0.003	13.088	18.68	7.0	0.69	0.05	154	23	22.25	15	20.96	20.37	7	20.34	20.00	3.5	CFS
1592	121	11.78	11.771	2.410	11.778	18.64	16.8	0.21	0.01	3	62	22.80	22	19.78	18.82	9	18.38	18.04	6.9	CFS
1658	105	12.71	12.713	0.009	12.705	18.15	13.7	0.13	0.03	170	35	21.25	13	18.99	18.62	5	18.48	18.06	6.5	CFS
1713	57	14.68	14.667	0.003	14.650	20.61	10.4	0.36	0.00	126	35	23.93	21	22.74	22.14	10	21.99	21.49	3.6	CHP
2098	40	15.97	15.928	0.002	15.962	19.36	6.1	0.23	0.00	84	23	23.21	14	22.39	22.06	8	21.87	21.68	2.9	CFS
2578	77	14.73	14.650	0.001	14.655	21.77	17.7	0.41	0.00	1	64	25.59	42	24.31	23.77	30	23.65	23.36	2.2	LVL
2747	102	13.18	13.200	0.002	13.177	17.98	13.0	0.11	0.00	178	46	21.69	28	20.42	19.98	15	19.75	19.66	3.0	CFS
2781	47	13.09	13.091	0.002	13.086	18.91	6.7	0.65	0.09	8	20	22.14	13	20.96	19.96	5	19.32	18.84	3.9	CFS
2865	190	13.07	12.844	0.237	13.056	19.68	30.2	0.14	0.03	108	115	23.95	24	20.37	20.10	8	20.08	19.15	14.4	CFS
2899	45	15.20	15.169	0.003	15.167	20.78	8.5	0.43	0.01	41	28	24.17	16	22.89	22.24	6	22.17	21.70	4.3	CFS
2928	50	14.76	14.730	0.003	14.738	20.37	8.9	0.38	0.00	104	25	23.38	14	22.04	21.44	6	21.26	20.88	4.3	CFS
2964	41	14.83	14.826	0.010	14.817	19.39	6.2	0.27	0.01	139	18	22.43	10	21.28	20.54	4	20.22	19.91	4.6	CFS
2992	29	15.52	15.500	0.020	15.468	21.16	6.0	0.81	0.04	49	18	24.41	9	22.91	22.21	5	22.15	21.65	3.3	LVL
...																				

TABLE A.1: Extracted photometry parameters. (1) Principal Galaxies Catalog number, (2) $a_{26.5}$: major axis radius at isophote 26.5 mag arcsec^{-2}, (3) $[3.6]_{26.5}$: AB magnitude within $a_{26.5}$, (4) $[3.6]_{tot}$: total AB magnitude from rational function asymptote, (5) σ_m: rms deviations, rational function fit, (6) $[3.6]_{ext}$: total AB magnitude by extrapolating flux beyond $a_{26.5}$ assuming continuance of exponential disk, (7) μ_0: central disk surface brightness from inward extrapolation of disk fit, mag arcsec^{-2}, (8) α: exponential disk scale length, arcsec, (9) b/a: ratio of minor to major axes, (10) $\sigma_{b/a}$: uncertainty in axial ratio, (11) PA: position angle of major axis, deg. (12) a_{80}: major axis radius of annulus enclosing 80% of total light, arcsec, (13) μ_{80}: surface brightness at a_{80}, mag arcsec^{-2}, (14) a_e: 'effective radius', major axis radius of annulus enclosing 50% of total light, arcsec, (15) μ_e: surface brightness at a_e, mag arcsec^{-2}, (16) $\langle\mu_e\rangle$: average surface brightness within a_e, mag arcsec^{-2}, (17) a_{20}: major axis radius of annulus enclosing 20% of total light, arcsec, (18) μ_{20}: surface brightness at a_{20}, mag arcsec^{-2}, (19) $\langle\mu_{20}\rangle$: average surface brightness within a_{20}, mag arcsec^{-2}, (20) C_{82}: concentration index, a_{80}/a_{20}, (21) Spitzer program.

Appendix B

Calibrator Parameters

Table B.1

PGC	Name	$[3.6]^{b,i,k,a}_{ext}$	$[3.6]^{b,i,k,a}_{CHP}$	$[3.6]^{b,i,k,a}_{ave}$	Diff	b/a	Inc	W_{mx}	W^i_{mx}	W^i_{mxl}	S
9332	NGC0925	10.866	10.231	10.549	-1.589	0.57	57.	194	231.	2.364	ZP
13179	NGC1365	8.818	8.812	8.815	-0.725	0.61	54.	371	459.	2.662	ZP
13602	NGC1425	10.693	10.700	10.697	-1.197	0.46	65.	354	391.	2.592	ZP
17819	NGC2090	10.477	10.287	10.382	-1.052	0.43	67.	277	301.	2.478	ZP
21396	NGC2403	8.558	8.370	8.464	-1.354	0.53	60.	226	261.	2.417	ZP
23110	NGC2541	/	11.949	11.949	-1.189	0.49	63.	188	211.	2.325	ZP
26512	NGC2841	8.644	8.644	8.644	-1.114	0.45	66.	592	650.	2.813	ZP
28120	NGC2976	9.904	/	9.904	-0.924	0.53	60.	129	149.	2.173	ZP
28357	NGC3021	11.693	/	11.693	-0.773	0.57	57.	254	303.	2.481	ZP
30197	NGC3198	10.368	10.326	10.347	-1.177	0.39	70.	296	315.	2.498	ZP
30819	IC2574	11.750	/	11.750	-1.630	0.40	69.	106	113.	2.054	ZP
32007	NGC3351	9.208	9.210	9.209	-0.879	0.70	47.	262	359.	2.556	ZP
32207	NGC3370	11.739	/	11.739	-0.889	0.56	58.	264	312.	2.494	ZP
34554	NGC3621	8.989	9.035	9.012	-1.002	0.45	66.	266	292.	2.465	ZP
34695	NGC3627	8.314	8.254	8.284	-0.894	0.53	60.	333	385.	2.585	ZP
39422	NGC4244	10.333	/	10.333	-1.413	0.20	90.	192	192.	2.283	ZP
40692	NGC4414	9.368	9.367	9.368	-0.638	0.60	55.	378	463.	2.666	ZP
41812	NGC4535	9.783	9.751	9.767	-0.817	0.72	45.	265	374.	2.573	ZP
41823	NGC4536	9.840	9.856	9.848	-0.818	0.38	71.	322	341.	2.533	ZP
42408	NGC4605	10.161	/	10.161	-0.971	0.41	69.	154	165.	2.219	ZP
42510	NGC4603	10.682	10.663	10.673	-0.913	0.64	52.	353	450.	2.653	ZP
42741	NGC4639	11.250	11.255	11.253	-1.073	0.60	55.	274	336.	2.526	ZP
43451	NGC4725	8.922	8.893	8.908	-1.068	0.56	58.	397	470.	2.672	ZP
51344	NGC5584	11.763	11.819	11.791	-1.171	0.73	44.	186	267.	2.426	ZP
69327	NGC7331	8.409	8.377	8.393	-0.873	0.44	66.	501	547.	2.738	ZP
73049	NGC7793	9.298	/	9.298	-1.048	0.62	53.	162	202.	2.306	ZP
40095	NGC4312	11.307	/	11.307	-1.087	0.27	79.	217	221.	2.344	V
40105	NGC4313	11.029	/	11.029	-1.079	0.22	85.	257	258.	2.412	V
40201	NGC4330	11.956	/	11.956	-1.156	0.17	90.	251	251.	2.400	V
40507	NGC4380	11.084	/	11.084	-1.274	0.52	61.	265	304.	2.483	V
40516	NGC4383	11.628	/	11.628	-0.768	0.58	56.	199	239.	2.379	V
40581	NGC4388	10.294	/	10.294	-0.984	0.26	80.	364	369.	2.567	V
40622	NGC4396	12.381	/	12.381	0.279	0.35	73.	181	189.	2.277	V
40644	NGC4402	10.816	10.772	10.794	-0.634	0.34	74.	267	278.	2.444	V
40644	NGC4402	10.816	10.772	10.794	-0.634	0.34	74.	267	278.	2.444	V

PGC	Name	$[3.6]^{b,i,k,a}_{ext}$	$[3.6]^{b,i,k,a}_{CHP}$	$[3.6]^{b,i,k,a}_{ave}$	Diff	b/a	Inc	W_{mx}	W^{i}_{mx}	W^{i}_{mxl}	S
41024	NGC4450	9.648	/	9.648	-1.028	0.67	49.	304	401.	2.603	V
41061	IC3392	11.789	/	11.789	-0.889	0.42	68.	178	192.	2.284	V
41472	NGC4498	12.193	/	12.193	-1.203	0.48	64.	182	203.	2.308	V
41504	IC0797	13.010	/	13.010	-1.010	0.69	48.	118	160.	2.203	V
41517	NGC4501	8.827	/	8.827	-0.967	0.48	64.	507	566.	2.753	V
41608	IC3476	12.901	/	12.901	-0.951	0.64	52.	126	161.	2.206	V
41729	NGC4522	12.022	/	12.022	-1.082	0.25	81.	209	211.	2.325	V
41812	NGC4535	9.785	9.753	9.769	-0.819	0.72	45.	265	374.	2.573	V
41823	NGC4536	9.828	9.844	9.836	-0.806	0.38	71.	322	341.	2.533	V
42081	IC3583	13.311	/	13.311	-1.341	0.42	68.	100	108.	2.033	V
42396	NGC4595	12.495	/	12.495	-1.095	0.70	47.	131	180.	2.255	V
42544	NGC4607	11.929	/	11.929	-0.499	0.20	90.	170	170.	2.230	V
42741	NGC4639	11.243	11.247	11.245	-1.095	0.55	58.	274	321.	2.507	V
42857	NGC4654	10.103	10.097	10.100	-0.850	0.56	58.	282	334.	2.523	V
43001	IC3742	13.985	/	13.985	-1.395	0.40	69.	161	172.	2.236	V
43254	NGC4698	10.069	/	10.069	-1.159	0.44	66.	419	457.	2.660	V
11856	ESO357-007	14.728	14.580	14.654	-1.494	0.24	82.	125	126.	2.101	F
12181	ESO357-012	13.471	13.519	13.495	-0.975	0.66	50.	123	160.	2.205	F
12404	IC1913	14.106	14.115	14.111	-1.211	0.22	85.	157	158.	2.198	F
12952	NGC1351A	12.808	12.839	12.823	-0.933	0.21	86.	200	200.	2.302	F
13059	NGC1350	9.804	9.797	9.801	-1.081	0.47	64.	390	433.	2.636	F
13089	ESO418-008	13.770	13.796	13.783	-1.093	0.70	47.	121	166.	2.220	F
13179	NGC1365	8.814	8.808	8.811	-0.721	0.61	54.	371	459.	2.662	F
13458	NGC1406	10.774	10.753	10.763	-0.723	0.22	85.	322	323.	2.510	F
13571	ESO358-051	13.522	13.555	13.539	-1.079	0.50	62.	118	134.	2.125	F
13602	NGC1425	10.686	10.693	10.690	-1.190	0.46	65.	354	391.	2.592	F
13687	NGC1436	11.301	11.382	11.341	-0.911	0.63	52.	201	254.	2.404	F
13809	ESO358-063	11.245	11.198	11.222	-1.032	0.24	82.	285	288.	2.459	F
13854	ESO302-009	/	14.513	14.513	-1.533	0.21	86.	142	142.	2.153	F
13998	ESO359-003	13.901	13.861	13.881	-1.261	0.42	68.	112	121.	2.082	F
14071	NGC1484	/	13.172	13.172	-1.222	0.24	82.	162	164.	2.214	F
34971	UGC06399	14.126	/	14.126	-1.546	0.28	78.	167	170.	2.232	U
35202	UGC06446	14.406	14.047	14.227	-1.867	0.63	52.	125	158.	2.198	U
35676	NGC3726	10.318	10.259	10.288	-1.038	0.58	56.	263	316.	2.500	U
36343	UGC06667	13.553	13.563	13.558	-1.468	0.14	90.	173	173.	2.238	U
36699	NGC3877	10.187	10.172	10.180	-0.980	0.24	82.	347	350.	2.544	U
36825	UGC06773	14.704	/	14.704	-1.784	0.44	66.	89	97.	1.987	U
36875	NGC3893	10.348	10.281	10.314	-0.834	0.66	50.	283	369.	2.567	U
37036	NGC3917	11.477	11.461	11.469	-1.219	0.24	82.	273	276.	2.440	U
37038	UGC06818	14.340	/	14.340	-1.400	0.35	73.	141	147.	2.169	U
37290	NGC3949	10.921	10.949	10.935	-0.965	0.63	52.	252	318.	2.502	U
37306	NGC3953	9.531	9.531	9.531	-0.931	0.50	62.	404	457.	2.660	U
37418	UGC06894	14.934	/	14.934	-1.144	0.16	90.	121	121.	2.083	U
37466	NGC3972	11.940	11.961	11.950	-1.050	0.29	78.	258	264.	2.422	U
37525	UGC06917	12.959	12.781	12.870	-1.450	0.59	55.	178	216.	2.334	U
37542	NGC3985	12.604	/	12.604	-0.994	0.62	53.	150	187.	2.273	U
37553	UGC06923	13.650	13.665	13.657	-1.397	0.42	68.	139	150.	2.176	U
37617	NGC3992	9.749	9.555	9.652	-1.152	0.55	58.	459	538.	2.731	U
37691	NGC4013	10.017	9.993	10.005	-0.695	0.22	85.	388	390.	2.591	U
37697	NGC4010	/	11.781	11.781	-0.891	0.17	90.	248	248.	2.394	U
37700	UGC06969	15.150	/	15.150	-1.300	0.31	76.	125	129.	2.110	U
37735	UGC06983	13.338	12.996	13.167	-1.397	0.66	50.	171	223.	2.348	U
38283	NGC4085	11.478	11.472	11.475	-0.775	0.24	82.	268	270.	2.432	U
38302	NGC4088	9.788	9.779	9.783	-0.793	0.39	70.	331	352.	2.547	U
38356	UGC07089	13.413	/	13.413	-1.313	0.22	85.	137	138.	2.139	U

PGC	Name	$[3.6]^{b,i,k,a}_{ext}$	$[3.6]^{b,i,k,a}_{CHP}$	$[3.6]^{b,i,k,a}_{ave}$	Diff	b/a	Inc	W_{mx}	W^{i}_{mx}	W^{i}_{mxl}	S
38370	NGC4100	10.441	10.402	10.421	-1.021	0.31	76.	374	385.	2.586	U
38392	NGC4102	10.224	10.640	10.432	-0.782	0.57	57.	298	355.	2.551	U
38795	NGC4157	9.723	9.726	9.724	-0.644	0.19	90.	387	387.	2.588	U
38951	UGC07218	14.874	/	14.874	-1.384	0.53	60.	89	103.	2.012	U
38988	NGC4183	12.317	12.246	12.281	-1.351	0.17	90.	227	227.	2.356	U
39241	NGC4217	/	9.889	9.889	-0.639	0.27	79.	383	390.	2.591	U
39344	UGC07301	15.093	15.087	15.090	-1.370	0.16	90.	139	139.	2.143	U
40537	NGC4389	11.587	/	11.587	-0.847	0.66	50.	154	201.	2.303	U
29727	IC2556	13.642	13.577	13.610	-1.330	0.55	58.	214	251.	2.400	An
29898	IC2559	12.885	13.057	12.971	-1.001	0.41	69.	256	275.	2.439	An
30308	NGC3223	10.180	10.190	10.185	-0.875	0.69	48.	415	562.	2.750	An
30716	ESO375-026	12.335	12.230	12.283	-0.743	0.20	90.	332	332.	2.521	An
31493	ESO437-014	11.660	11.685	11.673	-0.873	0.31	76.	364	375.	2.574	An
31761	NGC3347A	11.996	11.980	11.988	-0.948	0.34	74.	322	335.	2.526	An
31995	ESO318-004	11.715	11.678	11.697	-1.037	0.23	83.	382	385.	2.585	An
29993	IC2560	11.129	11.093	11.111	-1.031	0.46	65.	376	415.	2.618	An
31875	NGC3347B	12.579	12.508	12.543	-1.323	0.26	80.	327	332.	2.521	An
31926	NGC3347	10.838	10.879	10.858	-1.138	0.36	72.	401	421.	2.624	An
32039	ESO437-056	12.921	12.975	12.948	-1.088	0.64	52.	239	305.	2.484	An
41010	ESO322-017	15.041	15.198	15.119	-1.539	0.40	69.	147	157.	2.196	Ce
42181	NGC4575	11.555	11.565	11.560	-0.680	0.62	53.	263	328.	2.516	Ce
42271	ESO322-042	/	13.357	13.357	-1.257	0.31	76.	226	233.	2.367	Ce
42369	NGC4603A	12.485	12.450	12.468	-0.868	0.39	70.	270	287.	2.458	Ce
42510	NGC4603	10.679	10.660	10.669	-0.909	0.64	52.	353	450.	2.653	Ce
42880	ESO381-014	14.529	14.423	14.476	-1.226	0.21	86.	213	213.	2.329	Ce
43073	NGC4672	12.034	11.962	11.998	-0.958	0.24	82.	353	356.	2.552	Ce
43282	ESO268-044	12.938	13.074	13.006	-0.776	0.47	64.	247	274.	2.438	Ce
43717	ESO323-027	12.167	12.148	12.158	-0.958	0.53	60.	335	387.	2.588	Ce
44695	ESO269-028	14.444	14.510	14.477	-1.177	0.38	71.	225	238.	2.377	Ce
45573	ESO269-052	15.456	15.581	15.519	-1.659	0.17	90.	213	213.	2.328	Ce
70702	IC1474	13.054	13.053	13.053	-0.433	0.49	63.	255	287.	2.457	Pe
70803	UGC12451	/	15.007	15.007	-1.477	0.24	82.	172	174.	2.240	Pe
70880	NGC7562A	14.667	15.082	14.875	-1.825	0.25	81.	199	201.	2.304	Pe
70927	PGC070927	14.497	16.548	14.497	-1.237	0.64	52.	180	230.	2.361	Pe
70981	NGC7593	13.365	13.352	13.359	-0.829	0.63	52.	239	302.	2.479	Pe
71034	UGC12494	14.670	14.655	14.662	-1.372	0.31	76.	208	214.	2.331	Pe
71051	IC5309	13.142	13.120	13.131	-1.011	0.49	63.	270	303.	2.482	Pe
71087	NGC7610	13.337	13.287	13.312	-1.052	0.61	54.	241	298.	2.474	Pe
71159	PGC071159	14.605	14.621	14.613	-1.203	0.43	67.	148	161.	2.206	Pe
71181	NGC7631	12.470	12.479	12.475	-1.105	0.42	68.	366	395.	2.597	Pe
71260	UGC12562	15.723	15.715	15.719	-1.449	0.27	79.	153	156.	2.192	Pe
71262	UGC12561	15.287	15.285	15.286	-1.436	0.32	75.	184	190.	2.279	Pe
31154	ESO436-034	11.730	11.653	11.692	-0.662	0.23	83.	533	537.	2.730	H
31242	ESO436-039	12.499	12.487	12.493	-0.593	0.20	90.	412	412.	2.615	H
31360	ESO437-004	12.606	12.629	12.617	-0.867	0.50	62.	322	364.	2.561	H
31590	ESO437-018	13.602	13.591	13.596	-0.826	0.33	74.	300	311.	2.493	H
31626	ESO437-022	14.177	14.156	14.166	-1.246	0.27	79.	284	289.	2.461	H
31642	ESO437-025	13.218	13.193	13.205	-0.915	0.37	71.	245	258.	2.412	H
31677	ESO437-030	11.759	11.755	11.757	-0.997	0.22	85.	428	430.	2.633	H
31683	ESO501-068	13.065	13.051	13.058	-1.168	0.32	75.	323	334.	2.524	H
31690	ESO437-031	14.422	14.431	14.427	-1.297	0.62	53.	203	254.	2.404	H
31732	ESO437-034	16.163	16.081	16.122	-1.932	0.39	70.	170	181.	2.257	H
31738	ESO437-035	13.270	13.262	13.266	-0.956	0.37	71.	236	249.	2.396	H

PGC	Name	$[3.6]^{b,i,k,a}_{ext}$	$[3.6]^{b,i,k,a}_{CHP}$	$[3.6]^{b,i,k,a}_{ave}$	Diff	b/a	Inc	W_{mx}	W^i_{mx}	W^i_{mxl}	S
31805	ESO501-075	12.361	12.345	12.353	-1.023	0.50	62.	322	364.	2.561	H
31951	ESO501-082	12.819	12.861	12.840	-0.970	0.42	68.	383	414.	2.616	H
31981	ESO437-054	13.674	13.620	13.647	-0.477	0.21	86.	275	276.	2.440	H
3664	UGC00633	13.448	13.437	13.443	-1.133	0.27	79.	392	399.	2.601	Pi
3773	UGC00646	12.970	12.951	12.961	-1.201	0.38	71.	367	389.	2.590	Pi
3866	UGC00669	13.385	13.381	13.383	-0.543	0.25	81.	264	267.	2.427	Pi
3950	UGC00679	15.810	15.793	15.802	-1.312	0.23	83.	174	175.	2.243	Pi
4110	UGC00714	13.430	13.454	13.442	-0.922	0.71	46.	216	301.	2.478	Pi
4210	UGC00732	13.540	13.558	13.549	-1.069	0.60	55.	260	318.	2.503	Pi
4561	NGC0444	14.052	14.051	14.051	-1.301	0.25	81.	253	256.	2.408	Pi
4596	NGC0452	11.984	11.988	11.986	-1.126	0.29	78.	457	468.	2.670	Pi
4735	UGC00841	14.045	14.066	14.056	-1.076	0.23	83.	282	284.	2.453	Pi
5061	NGC0496	13.200	13.187	13.194	-0.984	0.55	58.	285	334.	2.524	Pi
5132	NGC0512	12.321	12.316	12.318	-1.058	0.28	78.	521	532.	2.726	Pi
5284	UGC00987	12.497	12.499	12.498	-1.018	0.32	75.	383	396.	2.598	Pi
5344	NGC0536	11.708	11.722	11.715	-1.255	0.36	72.	513	539.	2.731	Pi
5563	UGC01066	16.788	16.712	16.750	-1.800	0.28	78.	158	161.	2.208	Pi
6502	NGC0668	12.669	12.650	12.660	-0.890	0.69	48.	279	378.	2.577	Pi
6607	UGC01257	13.819	13.835	13.827	-1.107	0.44	66.	324	354.	2.548	Pi
6799	NGC0688	12.437	12.405	12.421	-0.981	0.68	48.	337	450.	2.654	Pi
6851	UGC01316	15.702	15.673	15.687	-1.537	0.47	64.	205	228.	2.357	Pi
6865	UGC01319	13.222	13.223	13.222	-0.712	0.71	46.	241	335.	2.525	Pi
7066	UGC01366	12.885	12.861	12.873	-1.203	0.29	78.	412	422.	2.625	Pi
7254	UGC01405	15.148	15.130	15.139	-1.229	0.16	90.	247	247.	2.393	Pi
7387	NGC0753	11.703	11.653	11.678	-0.798	0.71	46.	314	437.	2.640	Pi
7504	UGC01459	13.122	13.228	13.175	-0.925	0.16	90.	362	362.	2.559	Pi
23146	PGC023146	14.336	14.282	14.309	-0.919	0.19	90.	267	267.	2.427	Ca
23169	UGC04299	12.460	12.480	12.470	-0.820	0.18	90.	389	389.	2.590	Ca
23338	PGC023338	15.151	15.180	15.165	-1.385	0.68	48.	185	247.	2.393	Ca
23347	PGC023347	14.693	14.685	14.689	-0.889	0.72	45.	162	229.	2.359	Ca
23374	PGC023374	15.620	15.647	15.633	-1.373	0.35	73.	232	243.	2.385	Ca
23420	PGC023420	13.863	13.828	13.845	-1.045	0.66	50.	215	280.	2.448	Ca
23567	UGC04386	12.106	12.115	12.110	-1.100	0.23	83.	480	483.	2.684	Ca
23661	UGC04400	15.790	15.715	15.753	-1.453	0.20	90.	214	214.	2.330	Ca
23662	UGC04399	14.570	14.558	14.564	-1.214	0.36	72.	232	244.	2.387	Ca
23748	UGC04424	15.854	15.742	15.798	-1.548	0.27	79.	203	207.	2.315	Ca
142820	PGC142820	15.892	15.852	15.872	-1.402	0.28	78.	190	194.	2.288	Ca
42765	UGC07890	14.429	14.422	14.425	-0.945	0.67	49.	233	308.	2.488	Co
43142	UGC07955	13.809	13.849	13.829	-1.059	0.18	90.	361	361.	2.558	Co
43278	PGC043278	13.685	13.669	13.677	-0.637	0.26	80.	311	316.	2.499	Co
43686	UGC08013	14.531	14.511	14.521	-1.371	0.29	78.	365	374.	2.573	Co
43726	UGC08017	12.664	12.618	12.641	-0.601	0.37	71.	521	549.	2.740	Co
43840	PGC043840	14.672	14.658	14.665	-0.885	0.43	67.	286	310.	2.492	Co
43863	UGC08025	12.705	12.735	12.720	-1.100	0.19	90.	505	505.	2.703	Co
44795	IC0842	13.524	13.540	13.532	-1.032	0.49	63.	368	414.	2.617	Co
44921	IC4088	13.302	13.311	13.306	-1.116	0.30	77.	467	480.	2.681	Co
45097	UGC08161	13.581	13.547	13.564	-0.794	0.43	67.	355	385.	2.586	Co
45366	UGC08195	15.258	15.266	15.262	-1.262	0.17	90.	233	233.	2.367	Co
45549	IC4202	12.925	12.918	12.922	-1.162	0.18	90.	524	524.	2.719	Co
45580	UGC08229	13.203	13.075	13.139	-0.799	0.53	60.	342	395.	2.597	Co
45366	UGC08195	15.258	15.266	15.262	-1.262	0.17	90.	233	233.	2.367	Co
45549	IC4202	12.925	12.918	12.922	-1.162	0.18	90.	524	524.	2.719	Co
45580	UGC08229	13.203	13.075	13.139	-0.799	0.53	60.	342	395.	2.597	Co

PGC	Name	$[3.6]^{b,i,k,a}_{ext}$	$[3.6]^{b,i,k,a}_{CHP}$	$[3.6]^{b,i,k,a}_{ave}$	Diff	b/a	Inc	W_{mx}	W^i_{mx}	W^i_{mxl}	S
45668	UGC08244	15.219	15.193	15.206	-1.356	0.38	71.	238	252.	2.402	Co
45742	IC4210	14.375	14.352	14.363	-0.963	0.64	52.	227	289.	2.462	Co
45757	NGC5004A	13.196	13.228	13.212	-0.742	0.43	67.	336	365.	2.562	Co
10913	UGC02364	13.933	13.917	13.925	-1.205	0.35	73.	323	338.	2.529	A4
10943	UGC02375	13.320	13.339	13.329	-1.219	0.30	77.	440	452.	2.655	A4
11074	UGC02405	13.494	13.472	13.483	-1.203	0.37	71.	400	422.	2.625	A4
11102	UGC02415	14.145	14.118	14.131	-0.861	0.35	73.	323	338.	2.529	A4
11136	UGC02423	13.399	13.411	13.405	-0.945	0.33	74.	382	396.	2.598	A4
11255	UGC02444	13.050	13.049	13.050	-0.620	0.62	53.	361	451.	2.654	A4
11306	UGC02454	14.048	14.048	14.048	-1.188	0.22	85.	359	361.	2.557	A4
35347	NGC3697	12.581	12.577	12.579	-1.239	0.32	75.	504	521.	2.717	A1
35622	PGC035622	14.679	14.667	14.673	-0.983	0.58	56.	243	292.	2.466	A1
35942	UGC06583	13.415	13.434	13.424	-0.644	0.59	55.	319	387.	2.588	A1
35978	PGC035978	14.669	14.658	14.664	-1.134	0.49	63.	261	293.	2.467	A1
36132	PGC036132	14.317	14.284	14.300	-0.980	0.62	53.	247	308.	2.489	A1
36349	PGC036349	13.205	13.199	13.202	-0.512	0.56	58.	327	387.	2.587	A1
36431	UGC06686	13.118	13.165	13.142	-1.312	0.16	90.	398	398.	2.600	A1
36466	UGC06697	12.989	13.011	13.000	-1.160	0.20	90.	557	557.	2.746	A1
36604	NGC3861	12.290	12.323	12.307	-1.077	0.57	57.	459	547.	2.738	A1
36683	PGC036683	14.112	14.088	14.100	-0.850	0.39	70.	265	282.	2.450	A1
36706	NGC3884	12.084	12.081	12.083	-0.923	0.72	45.	462	652.	2.814	A1
36778	PGC036778	14.798	14.815	14.806	-1.226	0.23	83.	357	359.	2.556	A1
36779	PGC036779	13.987	13.994	13.991	-1.181	0.37	71.	379	400.	2.602	A1
36856	PGC036856	13.757	13.779	13.768	-0.858	0.27	79.	366	372.	2.571	A1
37143	UGC06837	14.555	14.580	14.567	-0.737	0.18	90.	331	331.	2.520	A1
37264	NGC3947	12.642	12.649	12.645	-0.905	0.57	57.	386	460.	2.663	A1
37288	NGC3951	12.949	12.944	12.947	-0.807	0.49	63.	371	417.	2.620	A1
37409	UGC06891	13.822	13.849	13.835	-1.135	0.26	80.	344	349.	2.543	A1
37463	PGC037463	14.625	14.624	14.624	-1.174	0.37	71.	293	309.	2.490	A1
71597	UGC12631	13.460	13.487	13.473	-1.023	0.32	75.	459	475.	2.676	A2
71795	UGC12678	13.669	13.668	13.668	-1.238	0.22	85.	505	507.	2.705	A2
71880	UGC12701	14.286	14.275	14.281	-0.651	0.26	80.	348	353.	2.548	A2
72024	UGC12721	13.384	13.391	13.387	-1.047	0.44	66.	394	430.	2.633	A2
72115	PGC072115	12.759	12.749	12.754	-0.134	0.51	61.	425	484.	2.685	A2
72169	PGC072169	13.654	13.679	13.666	-0.696	0.24	82.	377	381.	2.580	A2
72188	UGC12746	12.883	12.884	12.883	-0.733	0.19	90.	451	451.	2.654	A2
72233	UGC12755	13.011	13.016	13.014	-1.164	0.53	60.	503	581.	2.764	A2
72328	NGC7747	12.677	12.681	12.679	-1.109	0.40	69.	531	568.	2.754	A2
72411	PGC072411	13.700	13.631	13.665	-0.965	0.45	66.	367	403.	2.605	A2
72438	PGC072438	13.688	13.658	13.673	-0.683	0.32	75.	398	412.	2.614	A2
72665	PGC072665	14.178	14.155	14.167	-0.747	0.48	64.	302	337.	2.528	A2
72751	PGC072751	14.199	14.186	14.193	-0.803	0.59	55.	262	318.	2.502	A2
72784	PGC072784	14.413	14.388	14.401	-1.021	0.48	64.	344	384.	2.585	A2
72968	PGC072968	14.850	14.854	14.859	-1.189	0.27	79.	321	327.	2.514	A2
85512	PGC085512	15.880	15.848	15.864	-0.954	0.55	58.	234	275.	2.439	A2
91814	PGC091814	14.898	14.859	14.878	-1.118	0.20	90.	239	239.	2.378	A2
169662	PGC169662	14.842	14.794	14.818	-1.058	0.26	80.	346	351.	2.545	A2

TABLE B.1: Calibrator parameters for the Tully-Fisher relation: (1) PGC number, (2) Common Name, (3) CFS corrected magnitude, mag, (4) CHP corrected magnitude, mag, (5)CFS and CHP averaged corrected magnitude, mag, (6) Color term ($I^{b,i,k} - [3.6]^{b,i,k,a}_{ave}$), mag, (7) Axial Ratio, (8) Inclination, degrees, (9) linewidth not corrected for inclination, km s^{-1}, (10) linewidth corrected for inclination, km s^{-1}, (11) Logarithm of the inclination corrected linewidth, (12) Sample ZP Zeropoint Calibrators, V Virgo, F Fornax, U Ursa Major, An Antlia, Ce Centaurus30, Pe Pegasus, H Hydra, Pi Pisces, Ca Cancer, Co Coma, A4 Abell 400, A1 Abell 1367 and A2 Abell 2634 and 2666

Table B.2

PGC	Name	$I_{ext}^{b,i,k}$	$[3.6]_{ave}^{b,i,k,a}$	$C_{[3.6]_{ave}}^{b,i,k,a}$	b/a	Inc	W_{mx}	W_{mx}^{i}	W_{mxl}^{i}	S
2758	NGC0247	7.79	9.10	8.98	0.31	76.	190	196	2.292	ZP
3238	NGC0300	7.28	8.40	8.38	0.71	46.	140	195	2.290	ZP
9332	NGC0925	8.96	10.25	10.14	0.57	57.	194	231.	2.364	ZP
13179	NGC1365	8.09	8.77	8.97	0.61	54.	371	459.	2.662	ZP
13602	NGC1425	9.50	10.72	10.64	0.46	65.	354	391.	2.592	ZP
17819	NGC2090	9.33	10.38	10.39	0.43	67.	277	301.	2.478	ZP
21396	NGC2403	7.11	8.46	8.32	0.53	60.	226	261.	2.417	ZP
23110	NGC2541	10.76	12.06	11.94	0.49	63.	188	211.	2.325	ZP
26512	NGC2841	7.53	8.65	8.63	0.45	66.	592	650.	2.813	ZP
28120	NGC2976	8.98	9.89	9.97	0.53	60.	129	149.	2.173	ZP
28630	NGC3031	5.20	6.29	6.28	0.54	59.	416	485	2.686	ZP
30197	NGC3198	9.17	10.33	10.28	0.39	70.	296	315.	2.498	ZP
30819	IC2574	10.12	11.12	11.16	0.40	69.	106	113	2.054	ZP
31671	NGC3319	10.55	11.82	11.72	0.54	59.	195	227.	2.356	ZP
32007	NGC3351	8.33	9.20	9.31	0.70	47.	262	312.	2.556	ZP
32192	NGC3368	7.88	8.80	8.88	0.64	52.	329	418.	2.621	ZP
34554	NGC3621	8.01	9.01	9.05	0.45	66.	266	292.	2.465	ZP
34695	NGC3627	7.39	8.28	8.38	0.53	60.	333	385	2.585	ZP
39422	NGC4244	8.92	10.25	10.12	0.20	90.	192	192.	2.283	ZP
39600	NGC4258	6.84	7.98	7.95	0.40	69.	414	444.	2.647	ZP
40596	NGC4395	9.08	11.21	10.66	0.73	44.	112	161	2.206	ZP
40692	NGC4414	8.73	9.38	9.60	0.60	55.	378	463.	2.666	ZP
41812	NGC4535	8.95	9.75	9.89	0.72	45.	265	374	2.573	ZP
41823	NGC4536	9.03	9.85	9.98	0.38	71.	322	341.	2.533	ZP
42408	NGC4605	9.19	10.17	10.22	0.41	69.	154	165.	2.219	ZP
42510	NGC4603	9.76	10.67	10.75	0.64	52.	353	450.	2.653	ZP
42741	NGC4639	10.18	11.27	11.26	0.60	55.	274	336.	2.526	ZP
43451	NGC4725	7.84	8.87	8.89	0.56	58.	397	470.	2.672	ZP
47368	NGC5204	/	11.93	/	0.50	62.	186	267.	2.095	ZP
60921	NGC6503	8.67	9.78	9.76	0.32	75.	223	231.	2.363	ZP
69327	NGC7331	7.52	8.39	8.50	0.44	66.	501	547.	2.738	ZP
73049	NGC7793	8.25	9.27	9.30	0.62	53.	162	202.	2.306	ZP
40095	NGC4312	10.23	11.32	11.31	0.27	79.	217	221.	2.344	V
40105	NGC4313	9.97	11.04	11.04	0.22	85.	257	258.	2.412	V
40201	NGC4330	10.81	11.97	11.92	0.17	90.	251	251.	2.400	V
40507	NGC4380	9.82	11.11	11.00	0.52	61.	265	304.	2.483	V
40516	NGC4383	10.87	11.69	11.82	0.58	56.	199	239.	2.379	V
40530	IC3311	12.81	13.94	13.91	0.21	86.	160	160.	2.205	V
40581	NGC4388	9.32	10.32	10.36	0.26	80.	364	369.	2.567	V
40622	NGC4396	12.67	12.40	13.10	0.35	73.	181	189.	2.277	V
40644	NGC4402	10.17	10.79	11.03	0.34	74.	267	278.	2.444	V
40811	IC3365	13.06	14.40	14.26	0.42	68.	122	132.	2.120	V
41024	NGC4450	8.63	9.67	9.69	0.67	49.	304	401.	2.603	V
41061	IC3392	10.92	11.79	11.90	0.42	68.	178	192.	2.284	V
41472	NGC4498	11.00	12.21	12.14	0.48	64.	182	203.	2.308	V
41504	IC0797	12.01	13.06	13.07	0.69	48.	118	160.	2.203	V
41517	NGC4501	7.88	8.82	8.89	0.48	64.	507	566.	2.573	V
41608	IC3476	11.97	12.90	12.97	0.64	52.	126	161.	2.206	V
41729	NGC4522	10.95	12.01	12.02	0.25	81.	209	211.	2.325	V
41763	IC0800	12.07	13.16	13.15	0.68	48.	115	154.	2.187	V
41812	NGC4535	8.96	9.74	9.89	0.72	45.	265	374.	2.573	V

PGC	Name	$I_{ext}^{b,i,k}$	$[3.6]_{ave}^{b,i,k,a}$	$C_{[3.6]_{ave}}^{b,i,k,a}$	b/a	Inc	W_{mx}	W_{mx}^{i}	W_{mxl}^{i}	S
41823	NGC4536	9.04	9.85	9.99	0.38	71.	322	341.	2.533	V
42160	PGC042160	13.55	14.56	14.59	0.62	53.	85	106.	2.024	V
42230	UGC07802	13.05	14.35	14.23	0.18	90.	150	150.	2.176	V
42348	IC3617	13.36	14.82	14.62	0.52	61.	103	118.	2.072	V
42396	NGC4595	11.42	12.50	12.50	0.70	47.	131	180.	2.255	V
42544	NGC4607	11.45	11.93	12.24	0.20	90.	170	170.	2.230	V
42741	NGC4639	10.16	11.27	11.25	0.55	58.	274	321.	2.507	V
42833	NGC4651	9.43	10.37	10.44	0.64	52.	364	466.	2.669	V
42857	NGC4654	9.26	10.11	10.23	0.56	58.	282	334.	2.523	V
43001	IC3742	12.61	13.99	13.83	0.40	69.	161	172.	2.236	V
43254	NGC4698	8.92	10.10	10.04	0.44	66.	419	457.	2.660	V
11856	ESO357-007	13.17	14.72	14.47	0.24	82.	125	126.	2.101	F
12181	ESO357-012	12.53	13.62	13.61	0.66	50.	123	160.	2.205	F
12404	IC1913	12.91	14.13	14.05	0.22	85.	157	158.	2.198	F
12952	NGC1351A	11.90	12.86	12.92	0.21	86.	200	200.	2.302	F
13059	NGC1350	8.72	9.84	9.82	0.47	64.	390	433.	2.636	F
13089	ESO418-008	12.70	13.80	13.79	0.70	47.	121	166.	2.220	F
13179	NGC1365	8.10	8.77	8.98	0.61	54.	371	459.	2.662	F
13458	NGC1406	10.05	10.78	10.96	0.22	85.	322	323.	2.510	F
13571	ESO358-051	12.46	13.59	13.56	0.50	62.	118	134.	2.125	F
13602	NGC1425	9.51	10.69	10.63	0.46	65.	354	391.	2.592	F
13687	NGC1436	10.44	11.37	11.44	0.63	52.	201	254.	2.404	F
13809	ESO358-063	10.19	11.23	11.25	0.24	82.	285	288.	2.459	F
13854	ESO302-009	12.98	14.60	14.32	0.21	86.	142	142.	2.153	F
13998	ESO359-003	12.63	14.14	13.91	0.42	68.	112	121.	2.082	F
14071	NGC1484	11.95	13.19	13.10	0.24	82.	162	164.	2.214	F
34971	UGC06399	12.59	14.09	13.87	0.28	78.	167	170.	2.232	U
35202	UGC06446	12.37	14.16	13.79	0.63	52.	125	158.	2.198	U
35676	NGC3726	9.26	10.27	10.30	0.58	56.	263	316.	2.500	U
36343	UGC06667	12.10	13.55	13.35	0.14	90.	173	173.	2.238	U
36699	NGC3877	9.21	10.17	10.23	0.24	82.	347	350.	2.544	U
36825	UGC06773	12.93	14.70	14.34	0.44	66.	89	97.	1.987	U
36875	NGC3893	9.49	10.31	10.44	0.66	50.	283	369.	2.567	U
36930	UGC06792	/	14.10	/	0.21	86.	163	163.	2.213	U
37036	NGC3917	10.26	11.49	11.41	0.24	82.	273	276.	2.440	U
37038	UGC06818	12.95	14.40	14.20	0.35	73.	141	147.	2.169	U
37290	NGC3949	9.98	10.93	10.99	0.63	52.	252	318.	2.502	U
37306	NGC3953	8.61	9.53	9.61	0.50	62.	404	457.	2.660	U
37418	UGC06894	13.80	14.96	14.91	0.16	90.	121	121.	2.083	U
37466	NGC3972	10.91	11.97	11.98	0.29	78.	258	264.	2.422	U
37525	UGC06917	11.43	12.90	12.69	0.59	55.	178	216.	2.334	U
37542	NGC3985	11.62	12.60	12.65	0.62	53.	150	187.	2.273	U
37553	UGC06923	12.27	13.66	13.50	0.42	68.	139	150.	2.176	U
37617	NGC3992	8.51	9.55	9.57	0.55	58.	459	538.	2.731	U
37691	NGC4013	9.32	10.00	10.20	0.22	85.	388	390.	2.591	U
37697	NGC4010	10.90	11.78	11.88	0.17	90.	248	248.	2.394	U
37735	UGC06983	11.78	13.06	12.95	0.66	50.	171	223.	2.348	U
37832	UGC06992	12.79	13.97	13.91	0.45	66.	128	140.	2.147	U
38283	NGC4085	10.71	11.48	11.64	0.24	82.	268	270.	2.432	U
38302	NGC4088	9.00	9.79	9.94	0.39	70.	331	352.	2.547	U
38356	UGC07089	12.10	13.45	13.31	0.22	85.	137	138.	2.139	U
38370	NGC4100	9.41	10.42	10.45	0.31	76.	374	385.	2.586	U
38375	UGC07094	13.21	14.35	14.32	0.36	72.	80	84.	1.924	U

PGC	Name	$I_{ext}^{b,i,k}$	$[3.6]_{ave}^{b,i,k,a}$	$C_{[3.6]_{ave}}^{b,i,k,a}$	b/a	Inc	W_{mx}	W_{mx}^{i}	W_{mxl}^{i}	S
38392	NGC4102	9.66	10.36	10.55	0.57	57.	298	355.	2.551	U
38795	NGC4157	9.09	9.72	9.95	0.19	90.	387	387.	2.588	U
38951	UGC07218	13.50	14.72	14.64	0.53	60.	89	103.	2.012	U
38988	NGC4183	10.93	12.30	12.15	0.17	90.	227	227.	2.356	U
39237	NGC4218	12.34	13.41	13.41	0.61	54.	116	143.	2.157	U
39241	NGC4217	9.26	9.92	10.13	0.27	79.	383	390.	2.591	U
39344	UGC07301	13.73	15.16	14.97	0.16	90.	139	139.	2.143	U
40537	NGC4389	10.74	11.58	11.70	0.66	50.	154	201.	2.303	U
29727	IC2556	12.33	13.58	13.49	0.55	58.	214	251.	2.400	An
29895	IC2558	/	13.52	/	0.61	54.	154	190.	2.280	An
29898	IC2559	12.01	12.97	13.03	0.41	69.	256	275.	2.439	An
29993	IC2560	10.12	11.11	11.15	0.46	65.	376	415.	2.618	An
30308	NGC3223	9.36	10.06	10.25	0.69	48.	415	562.	2.750	An
30534	ESO317-023	11.12	11.70	11.96	0.47	64.	363	403.	2.605	An
30716	ESO375-026	11.57	12.29	12.47	0.20	90.	332	332.	2.521	An
30774	NGC3250C	/	12.14	/	0.37	71.	348	367.	2.565	An
31053	NGC3258C	/	13.20	/	0.67	49.	194	256.	2.408	An
31058	ESO436-032	/	13.77	/	0.51	61.	253	288.	2.459	An
31094	NGC3258D	/	12.34	/	0.42	68.	219	236.	2.374	An
31273	NGC3281D	11.92	12.94	12.97	0.22	85.	255	256.	2.408	An
31493	ESO437-014	10.83	11.67	11.79	0.31	76.	364	375.	2.574	An
31761	NGC3347A	11.07	11.99	12.07	0.34	74.	322	335.	2.526	An
31875	NGC3347B	11.25	12.55	12.43	0.26	80.	327	332.	2.521	An
31926	NGC3347	9.74	10.86	10.84	0.36	72.	401	421.	2.624	An
31995	ESO318-004	10.69	11.70	11.73	0.23	83.	382	385.	2.585	An
32039	ESO437-056	11.89	12.95	12.96	0.64	52.	239	305.	2.484	An
41010	ESO322-017	13.62	15.11	14.89	0.40	69.	147	157.	2.196	Ce
42181	NGC4575	10.93	11.56	11.79	0.62	53.	263	328.	2.516	Ce
42245	ESO322-040	/	12.82	/	0.68	48.	248	332.	2.521	Ce
42271	ESO322-042	12.15	13.36	13.29	0.31	76.	226	233.	2.367	Ce
42369	NGC4603A	11.66	12.47	12.61	0.39	70.	270	287.	2.458	Ce
42510	NGC4603	9.84	10.67	10.80	0.64	52.	353	450.	2.653	Ce
42640	NGC4603D	11.62	12.56	12.63	0.62	53.	235	293.	2.467	Ce
42880	ESO381-014	13.28	14.48	14.41	0.21	86.	213	213.	2.329	Ce
43073	NGC4672	11.10	12.00	12.09	0.24	82.	353	356.	2.552	Ce
43282	ESO268-044	12.27	13.01	13.18	0.47	64.	247	274.	2.438	Ce
43717	ESO323-027	11.25	12.16	12.24	0.53	60.	335	387.	2.588	Ce
43893	ESO323-038	/	12.19	/	0.49	63.	263	295.	2.469	Ce
44695	ESO269-028	13.34	14.47	14.44	0.38	71.	225	238.	2.377	Ce
45573	ESO269-052	13.93	15.52	15.25	0.17	90.	213	213.	2.328	Ce
70702	IC1474	12.67	13.06	13.42	0.49	63.	255	287.	2.457	Pe
70803	UGC12451	13.57	15.03	14.83	0.24	82.	172	174.	2.240	Pe
70880	NGC7562A	13.09	14.88	14.51	0.25	81.	199	201.	2.304	Pe
70927	PGC070927	13.31	15.52	14.93	0.64	52.	180	230.	2.361	Pe
70981	NGC7593	12.55	13.36	13.50	0.63	52.	239	302.	2.479	Pe
71034	UGC12494	13.33	14.67	14.53	0.31	76.	208	214.	2.331	Pe
71049	UGC12501	13.13	14.15	14.18	0.21	86.	258	259.	2.413	Pe
71051	IC5309	12.16	13.13	13.18	0.49	63.	270	303.	2.482	Pe
71055	NGC7608	12.24	13.22	13.27	0.27	79.	279	284.	2.453	Pe
71087	NGC7610	12.28	13.31	13.33	0.61	54.	241	298.	2.474	Pe
71155	UGC12535	13.47	14.27	14.41	0.23	83.	187	188.	2.275	Pe
71159	PGC071159	13.45	14.61	14.56	0.43	67.	148	161.	2.206	Pe
71181	NGC7631	11.40	12.48	12.48	0.42	68.	366	395.	2.597	Pe

PGC	Name	$I_{ext}^{b,i,k}$	$[3.6]_{ave}^{b,i,k,a}$	$C_{[3.6]_{ave}}^{b,i,k,a}$	b/a	Inc	W_{mx}	W_{mx}^{i}	W_{mxl}^{i}	S
71260	UGC12562	14.30	15.72	15.54	0.27	79.	153	156.	2.192	Pe
71262	UGC12561	13.87	15.29	15.11	0.32	75.	184	190.	2.279	Pe
93031	PGC093031	15.15	16.47	16.34	0.21	86.	139	139.	2.144	Pe
31001	ESO501-002	12.28	13.54	13.44	0.20	90.	420	420.	2.623	H
31154	ESO436-034	11.06	11.70	11.93	0.23	83.	533	537.	2.730	H
31217	NGC3285	10.18	11.17	11.21	0.51	61.	545	621.	2.793	H
31238	ESO436-038	/	15.13	/	0.57	57.	190	227.	2.355	H
31242	ESO436-039	11.92	12.50	12.76	0.20	90.	412	412.	2.615	H
31293	NGC3285B	/	12.90	/	0.63	52.	241	304.	2.483	H
31355	ESO501-022	/	15.99	/	0.23	83.	170	171.	2.233	H
31360	ESO437-004	11.78	12.62	12.74	0.50	62.	322	364.	2.561	H
31513	NGC3312	9.52	11.20	10.88	0.34	74.	584	608.	2.784	H
31557	ESO501-051	10.46	11.62	11.57	0.59	55.	501	608.	2.784	H
31590	ESO437-018	12.80	13.60	13.74	0.33	74.	300	311.	2.493	H
31593	ESO437-019	12.00	12.87	12.98	0.70	47.	288	395.	2.597	H
31626	ESO437-022	12.94	14.17	14.09	0.27	79.	284	289.	2.461	H
31642	ESO437-025	12.32	13.21	13.31	0.37	71.	245	258.	2.412	H
31677	ESO437-030	10.79	11.76	11.81	0.22	85.	428	430.	2.633	H
31683	ESO501-068	11.92	13.06	13.03	0.32	75.	323	334.	2.524	H
31690	ESO437-031	13.15	14.43	14.32	0.62	53.	203	254.	2.404	H
31730	ESO437-033	/	12.30	/	0.68	48.	252	337.	2.527	H
31732	ESO437-034	14.21	16.12	15.68	0.39	70.	170	181.	2.257	H
31738	ESO437-035	12.34	13.27	13.34	0.37	71.	236	249.	2.396	H
31805	ESO501-075	11.36	12.36	12.40	0.50	62.	322	364.	2.561	H
31822	ESO437-040	/	14.16	/	0.19	90.	172	172.	2.236	H
31829	ESO501-078	/	14.11	/	0.22	85.	253	254.	2.405	H
31951	ESO501-082	11.90	12.84	12.91	0.42	68.	383	414.	2.616	H
31981	ESO437-054	13.20	13.62	13.96	0.21	86.	275	276.	2.440	H
2747	UGC00485	12.00	13.20	13.13	0.11	90.	344	344.	2.537	Pi
2865	UGC00501	12.21	13.09	13.19	0.17	90.	375	375.	2.574	Pi
2899	UGC00509	13.88	15.27	15.11	0.45	66.	210	230.	2.362	Pi
2928	UGC00511	13.42	14.80	14.64	0.22	85.	269	270.	2.432	Pi
3020	UGC00525	12.96	14.21	14.12	0.50	62.	199	225.	2.352	Pi
3081	UGC00536	13.63	15.20	14.94	0.50	62.	219	248.	2.394	Pi
3133	UGC00542	11.60	12.70	12.69	0.24	82.	366	369.	2.568	Pi
3184	PGC003184	13.24	14.56	14.43	0.39	70.	281	299.	2.476	Pi
3222	UGC00557	13.24	14.72	14.51	0.43	67.	258	280.	2.447	Pi
3235	UGC00556	12.57	12.44	13.07	0.53	60.	366	423.	2.626	Pi
3274	UGC00565	13.36	14.44	14.44	0.30	77.	222	228.	2.358	Pi
3285	PGC003285	14.08	15.39	15.27	0.54	59.	218	254.	2.404	Pi
3332	UGC00575	13.22	14.22	14.26	0.20	90.	276	276.	2.441	Pi
3466	PGC003466	13.73	14.92	14.86	0.61	54.	179	221.	2.345	Pi
3606	IC0066	12.48	13.33	13.45	0.44	66.	359	392.	2.593	Pi
3611	NGC0338	10.82	11.66	11.78	0.40	69.	529	566.	2.752	Pi
3664	UGC00633	12.34	13.45	13.43	0.27	79.	392	399.	2.601	Pi
3773	UGC00646	11.79	12.97	12.91	0.38	71.	367	389.	2.590	Pi
3866	UGC00669	12.87	13.39	13.68	0.25	81.	264	267.	2.427	Pi
3903	UGC00673	13.58	14.98	14.81	0.36	72.	279	293.	2.467	Pi
3950	UGC00679	14.52	15.81	15.70	0.23	83.	174	175.	2.243	Pi
4110	UGC00714	12.55	13.44	13.54	0.71	46.	216	301.	2.478	Pi
4210	UGC00732	12.50	13.55	13.56	0.60	55.	260	318.	2.503	Pi
4561	NGC0444	12.78	14.06	13.95	0.25	81.	253	256.	2.408	Pi
4563	UGC00809	12.95	13.96	13.99	0.21	86.	300	301.	2.478	Pi

PGC	Name	$I_{ext}^{b,i,k}$	$[3.6]_{ave}^{b,i,k,a}$	$C_{[3.6]_{ave}}^{b,i,k,a}$	b/a	Inc	W_{mx}	W_{mx}^{i}	W_{mxl}^{i}	S
4596	NGC0452	10.89	11.99	11.98	0.29	78.	457	468.	2.670	Pi
4735	UGC00841	13.01	14.06	14.07	0.23	83.	282	284.	2.453	Pi
4971	UGC00909	12.82	13.92	13.91	0.69	48.	238	322.	2.508	Pi
5061	NGC0496	12.24	13.20	13.26	0.55	58.	285	334.	2.524	Pi
5132	NGC0512	11.29	12.31	12.34	0.28	78.	521	532.	2.726	Pi
5284	UGC00987	11.51	12.51	12.55	0.32	75.	383	396.	2.598	Pi
5344	NGC0536	10.48	11.72	11.63	0.36	72.	513	539.	2.731	Pi
5440	UGC01033	11.99	13.30	13.18	0.19	90.	337	337.	2.528	Pi
5450	NGC0551	11.62	12.73	12.71	0.43	67.	372	404.	2.606	Pi
5702	NGC0582	11.23	12.30	12.30	0.27	79.	438	446.	2.649	Pi
6045	UGC01160	12.90	13.79	13.89	0.17	90.	319	319.	2.504	Pi
6189	UGC01178	12.10	12.68	12.94	0.20	90.	366	366.	2.563	Pi
6473	UGC01234	13.36	14.52	14.47	0.59	55.	265	322.	2.507	Pi
6502	NGC0668	11.79	12.66	12.77	0.69	48.	279	378.	2.577	Pi
6607	UGC01257	12.74	13.83	13.82	0.44	66.	324	354.	2.548	Pi
6799	NGC0688	11.46	12.42	12.48	0.68	48.	337	450.	2.654	Pi
6851	UGC01316	14.17	15.69	15.46	0.47	64.	205	228.	2.357	Pi
6865	UGC01319	12.54	13.22	13.42	0.71	46.	241	335.	2.525	Pi
7066	UGC01366	11.71	12.88	12.83	0.29	78.	412	422.	2.625	Pi
7097	NGC0721	12.10	13.16	13.17	0.60	55.	275	337.	2.527	Pi
7254	UGC01405	13.94	15.13	15.07	0.16	90.	247	247.	2.393	Pi
7300	UGC01416	12.72	13.76	13.78	0.52	61.	368	423.	2.627	Pi
7387	NGC0753	10.92	11.68	11.84	0.71	46.	314	437.	2.640	Pi
7504	UGC01459	12.29	13.18	13.28	0.16	90.	362	362.	2.559	Pi
7646	UGC01493	11.64	12.45	12.59	0.37	71.	346	365.	2.562	Pi
7847	NGC0801	10.72	11.90	11.84	0.25	81.	459	464.	2.667	Pi
8185	NGC0818	10.85	11.78	11.85	0.41	69.	448	481.	2.682	Pi
23146	PGC023146	13.40	14.32	14.40	0.19	90.	267	267.	2.427	Ca
23169	UGC04299	11.67	12.48	12.62	0.18	90.	389	389.	2.590	Ca
23289	UGC04324	12.41	13.22	13.36	0.39	70.	308	328.	2.515	Ca
23338	PGC023338	13.80	15.17	15.02	0.68	48.	185	247.	2.393	Ca
23347	PGC023347	13.82	14.69	14.80	0.72	45.	162	229.	2.359	Ca
23374	PGC023374	14.28	15.64	15.49	0.35	73.	232	243.	2.385	Ca
23420	PGC023420	12.82	13.85	13.87	0.66	50.	215	280.	2.448	Ca
23567	UGC04386	11.03	12.12	12.11	0.23	83.	480	483.	2.684	Ca
23661	UGC04400	14.32	15.76	15.57	0.20	90.	214	214.	2.330	Ca
23662	UGC04399	13.37	14.57	14.50	0.36	72.	232	244.	2.387	Ca
23748	UGC04424	14.27	15.80	15.56	0.27	79.	203	207.	2.315	Ca
42820	ESO574-023	14.49	15.88	15.72	0.28	78.	190	194.	2.288	Ca
42726	UGC07877	13.37	14.48	14.46	0.28	78.	321	328.	2.515	Co
42765	UGC07890	13.49	14.43	14.50	0.67	49.	233	308.	2.488	Co
43142	UGC07955	12.78	13.84	13.85	0.18	90.	361	361.	2.558	Co
43278	PGC043278	13.05	13.68	13.91	0.26	80.	311	316.	2.499	Co
43359	UGC07978	12.98	13.98	14.02	0.63	52.	295	372.	2.571	Co
43575	UGC08004	13.23	14.48	14.39	0.39	70.	285	303.	2.482	Co
43686	UGC08013	13.15	14.53	14.37	0.29	78.	365	374.	2.573	Co
43726	UGC08017	12.05	12.63	12.89	0.37	71.	521	549.	2.740	Co
43840	PGC043840	13.78	14.67	14.77	0.43	67.	286	310.	2.492	Co
43863	UGC08025	11.63	12.73	12.72	0.19	90.	505	505.	2.703	Co
44416	PGC044416	13.19	14.06	14.17	0.32	75.	260	269.	2.430	Co
44795	IC0842	12.51	13.53	13.56	0.49	63.	368	414.	2.617	Co
44921	IC4088	12.19	13.31	13.29	0.30	77.	467	480.	2.681	Co
45097	UGC08161	12.77	13.57	13.71	0.43	67.	355	385.	2.586	Co

PGC	Name	$I_{ext}^{b,i,k}$	$[3.6]_{ave}^{b,i,k,a}$	$C_{[3.6]_{ave}}^{b,i,k,a}$	b/a	Inc	W_{mx}	W_{mx}^{i}	W_{mxl}^{i}	S
45366	UGC08195	14.00	15.27	15.17	0.17	90.	233	233.	2.367	Co
45549	IC4202	11.77	12.93	12.88	0.18	90.	524	524.	2.719	Co
45580	UGC08229	12.35	13.14	13.29	0.53	60.	342	395.	2.597	Co
45668	UGC08244	13.86	15.22	15.07	0.38	71.	238	252.	2.402	Co
45742	IC4210	13.40	14.36	14.42	0.64	52.	227	289.	2.462	Co
45757	NGC5004A	12.48	13.22	13.39	0.43	67.	336	365.	2.562	Co
45905	UGC08294	13.75	15.04	14.93	0.66	50.	195	254.	2.405	Co
46028	UGC08317	13.09	14.24	14.20	0.43	67.	276	300.	2.476	Co
46427	NGC5081	11.46	12.72	12.62	0.38	71.	530	561.	2.749	Co
10913	UGC02364	12.82	13.93	13.91	0.35	73.	323	338.	2.529	A4
10943	UGC02375	12.20	13.33	13.30	0.30	77.	440	452.	2.655	A4
11074	UGC02405	12.36	13.49	13.46	0.37	71.	400	422.	2.625	A4
11102	UGC02415	13.34	14.13	14.28	0.35	73.	323	338.	2.529	A4
11136	UGC02423	12.53	13.42	13.52	0.33	74.	382	396.	2.598	A4
11255	UGC02444	12.51	13.05	13.33	0.62	53.	361	451.	2.654	A4
11306	UGC02454	12.95	14.05	14.04	0.22	85.	359	361.	2.557	A4
35347	NGC3697	11.36	12.58	12.50	0.32	75.	504	521.	2.717	A1
35622	PGC035622	13.70	14.67	14.72	0.58	56.	243	292.	2.466	A1
35942	UGC06583	12.79	13.43	13.66	0.59	55.	319	387.	2.588	A1
35978	PGC035978	13.54	14.67	14.64	0.49	63.	261	293.	2.467	A1
36132	PGC036132	13.33	14.30	14.35	0.62	53.	247	308.	2.489	A1
36349	PGC036349	12.70	13.20	13.50	0.56	58.	327	387.	2.587	A1
36371	PGC036371	12.75	13.73	13.78	0.46	65.	292	323.	2.509	A1
36431	UGC06686	11.85	13.15	13.03	0.16	90.	398	398.	2.600	A1
36466	UGC06697	11.85	13.01	12.96	0.20	90.	557	557.	2.746	A1
36604	NGC3861	11.24	12.34	12.33	0.57	57.	459	547.	2.738	A1
36683	PGC036683	13.26	14.10	14.22	0.39	70.	265	282.	2.450	A1
36706	NGC3884	11.17	12.08	12.16	0.72	45.	462	652.	2.814	A1
36778	PGC036778	13.59	14.82	14.74	0.23	83.	357	359.	2.556	A1
36779	PGC036779	12.83	13.99	13.94	0.37	71.	379	400.	2.602	A1
36856	PGC036856	12.93	13.77	13.89	0.27	79.	366	372.	2.571	A1
37143	UGC06837	13.84	14.57	14.75	0.18	90.	331	331.	2.520	A1
37264	NGC3947	11.76	12.65	12.75	0.57	57.	386	460.	2.663	A1
37288	NGC3951	12.15	12.95	13.09	0.49	63.	371	417.	2.620	A1
37409	UGC06891	12.73	13.84	13.82	0.26	80.	344	349.	2.543	A1
37463	PGC037463	13.47	14.63	14.58	0.37	71.	293	309.	2.490	A1
71597	UGC12631	12.48	13.48	13.52	0.32	75.	459	475.	2.676	A2
71795	UGC12678	12.46	13.67	13.60	0.22	85.	505	507.	2.705	A2
71880	UGC12701	13.67	14.29	14.53	0.26	80.	348	353.	2.548	A2
72024	UGC12721	12.38	13.39	13.42	0.44	66.	394	430.	2.633	A2
72115	PGC072115	12.64	12.76	13.26	0.51	61.	425	484.	2.685	A2
72169	PGC072169	13.00	13.63	13.86	0.24	82.	377	381.	2.580	A2
72188	UGC12746	12.18	12.84	13.05	0.19	90.	451	451.	2.654	A2
72233	UGC12755	11.90	13.02	13.00	0.53	60.	503	581.	2.764	A2
72328	NGC7747	11.61	12.64	12.66	0.40	69.	531	568.	2.754	A2
72411	PGC072411	12.73	13.67	13.74	0.45	66.	367	403.	2.605	A2
72438	PGC072438	13.01	13.68	13.89	0.32	75.	398	412.	2.614	A2
72665	PGC072665	13.44	14.10	14.31	0.48	64.	302	337.	2.528	A2
72751	PGC072751	13.41	14.13	14.31	0.59	55.	262	318.	2.502	A2
72784	PGC072784	13.40	14.29	14.39	0.48	64.	344	384.	2.585	A2
72968	PGC072968	13.69	14.81	14.79	0.27	79.	321	327.	2.514	A2
85512	PGC085512	14.93	15.87	15.94	0.55	58.	234	275.	2.439	A2
85551	PGC085551	14.02	14.47	14.79	0.47	64.	338	375.	2.574	A2

PGC	Name	$I_{ext}^{b,i,k}$	$[3.6]_{ave}^{b,i,k,a}$	$C_{[3.6]_{ave}}^{b,i,k,a}$	b/a	Inc	W_{mx}	W_{mx}^{i}	W_{mxl}^{i}	S
91814	PGC091814	13.81	14.85	14.87	0.20	90.	239	239.	2.378	A2
169662	PGC169662	13.78	14.77	14.81	0.26	80.	346	351.	2.545	A2
1809186	PGC1809186	13.90	14.91	14.94	0.36	72.	281	295.	2.470	A2

TABLE B.2: Calibrator parameters for the control Tully-Fisher relation: (1) PGC number, (2) Common Name, (3) I band corrected magnitude, mag, (4) [3.6] averaged corrected magnitude, mag, (5) Pseudo [3.6] magnitude, mag, (6) Axial Ratio, (7) Inclination, degrees, (8) linewidth not corrected for inclination, km s^{-1}, (9) linewidth corrected for inclination, km s^{-1}, (10) Logarithm of the inclination corrected linewidth, (11) Sample ZP Zeropoint Calibrators, V Virgo, F Fornax, U Ursa Major, An Antlia, Ce Centaurus30, Pe Pegasus, H Hydra, Pi Pisces, Ca Cancer, Co Coma, A4 Abell 400, A1 Abell 1367 and A2 Abell 2634 and 2666

Appendix C

Distance Estimates

PGC	Name	l	b	sgl	sgb	v_{hel}	v_{mod}	t	b/a	w_{mx}	$logw^{i}_{mx}$	I	$I^{b,i,k}$	[3.6]	[3.6]*	$C_{[3.6]}$	M_C	$M_{[3.6]}$	μ_C	d_C	$\mu_{[3.6]}$	$d_{[3.6]}$
218	NGC07814	106.4089	-45.1745	309.0614	16.4026	1051	695	2.0	0.20	455	2.658	9.18	8.63	9.61	9.57	9.46	-21.75	-21.85	31.20	17.4	31.42	19.2
255	UGC00017	106.2149	-46.0989	308.1422	16.0958	878	521	9.1	0.63	98	2.092	13.85	14.07	14.78	14.87	14.83	-16.60	-16.33	31.43	19.3	31.20	17.4
279	NGC007817	108.2283	-40.7605	313.8141	17.1420	2311	1970	4.1	0.26	411	2.620	10.62	10.22	10.84	10.87	10.91	-21.40	-21.48	32.31	29.0	32.36	29.7
527	UGC000054	114.0896	-20.3652	335.8192	19.2667	4249	3993	6.0	0.20	192	2.283	/	/	15.96	16.04	/	/	-18.19	/	/	34.32	73.1
627	AGC020097	13.9928	-80.1378	264.5900	1.9316	1497	1214	4.8	0.21	158	2.200	12.91	12.94	13.92	14.00	13.82	-17.58	-17.37	31.40	19.0	31.38	18.8
698	NGC00023	111.3675	-36.0132	319.3855	16.7229	4568	4275	1.2	0.68	367	2.692	10.83	10.90	11.20	11.31	11.47	-22.06	-22.19	33.56	51.6	33.54	51.1
701	AGC020114	43.6860	-80.4343	269.3872	3.2262	554	250	5.1	0.30	202	2.317	10.40	10.38	11.43	11.44	11.27	-18.64	-18.52	29.91	9.6	29.96	9.8
767	NGC00021	113.2524	-28.7536	327.1050	17.6437	4770	4500	4.0	0.47	382	2.627	12.27	12.17	12.78	12.86	12.88	-21.47	-21.55	34.41	76.3	34.52	80.2
924	UGC00132	108.9883	-48.8920	306.4453	13.1609	1696	1345	7.9	0.32	140	2.161	/	/	14.48	14.56	/	/	-17.00	/	/	31.56	20.5
963	UGC00139	102.8519	-62.1619	292.9641	9.5361	3971	3652	5.1	0.43	287	2.493	12.89	12.83	13.44	13.52	13.54	-20.25	-20.25	33.83	58.3	33.83	58.4
1315	UGC00196	117.5333	-15.1136	341.9918	17.2721	5150	4942	5.3	0.65	256	2.519	/	/	13.09	13.19	/	/	-20.49	/	/	33.74	56.0
1525	UGC00231	113.4792	-45.8820	310.5250	11.6066	843	495	5.9	0.20	204	2.310	12.19	12.02	12.90	12.95	12.84	-18.58	-18.45	31.42	19.2	31.40	19.1
1651	AGC020302	340.4905	-81.5678	262.2390	-2.9613	1831	1572	3.9	0.35	207	2.335	12.58	12.60	13.65	13.73	13.52	-18.81	-18.70	32.34	29.4	32.45	30.9
1658	UGC000256	118.9045	-12.6493	344.7872	16.4431	5173	4978	4.0	0.20	331	2.520	13.02	12.45	12.70	12.74	12.96	-20.49	-20.50	33.49	49.8	33.28	45.3
1665	UGC00260	113.4479	-50.8383	305.8528	9.7393	2134	1792	5.8	0.23	254	2.408	12.35	12.09	12.67	12.71	12.76	-19.47	-19.41	32.24	28.0	32.13	26.7
1713	UGC00272	109.6294	-63.4603	293.4407	6.2135	3917	3604	6.4	0.40	236	2.402	13.58	13.58	14.65	14.74	14.51	-19.42	-19.35	33.98	62.5	34.17	68.4
1851	NGC000134	338.3093	-82.3778	262.8701	-3.5542	1583	1322	4.0	0.28	455	2.666	9.20	8.85	9.29	9.32	9.45	-21.82	-21.93	31.27	18.0	31.26	17.9
1921	UGC00312	114.4661	-54.0753	303.0705	7.9214	4371	4065	8.0	0.42	285	2.488	12.71	12.65	13.44	13.53	13.45	-20.20	-20.19	33.69	54.6	33.78	57.1
1970	UGC00320	113.4616	-59.9491	297.4139	6.1096	2394	2058	6.1	0.20	149	2.173	14.77	14.81	15.85	15.94	15.72	-17.34	-17.12	33.08	41.3	33.08	41.4
1977	IC0001553	51.7638	-85.5297	270.3423	-1.8628	2929	2655	7.0	0.22	256	2.410	12.82	12.63	12.87	12.93	13.15	-19.49	-19.43	32.65	33.9	32.38	29.9
2052	AGC020385	21.8940	-86.1300	268.3344	-2.8241	1580	1301	3.4	0.47	317	2.548	10.43	10.42	10.82	10.89	11.02	-20.74	-20.78	31.77	22.6	31.67	21.6
2071	IC0001555	354.0143	-85.2990	266.2225	-3.5025	1530	1258	7.0	0.57	115	2.137	13.16	13.40	14.34	14.44	14.27	-17.01	-16.76	31.28	18.0	31.20	17.4
2142	IC0001558	58.6007	-86.0752	270.7645	-2.4699	1551	1264	9.0	0.52	110	2.103	12.01	12.25	13.24	13.34	13.15	-16.69	-16.43	29.84	9.3	29.77	9.0
2437	AGC400333	111.5732	-76.5046	282.1291	-0.3496	1638	1322	3.1	0.61	273	2.528	9.99	10.09	10.69	10.78	10.79	-20.57	-20.59	31.36	18.7	31.37	18.8
2445	ES079-005	304.9496	-53.6455	233.6427	-12.4376	1712	1607	7.0	0.41	148	2.202	12.72	12.86	13.77	13.86	13.71	-17.60	-17.40	31.32	18.3	31.26	17.9
2479	UGC00438	120.1021	-37.3172	320.3882	9.6661	4555	4276	5.0	0.70	346	2.675	11.13	11.23	11.63	11.74	11.85	-21.90	-22.02	33.79	57.4	33.82	58.1
2492	PG0002492	110.1297	-79.4921	279.3344	-1.4478	1552	1243	2.0	0.68	134	2.253	/	/	14.05	14.15	/	/	-17.90	/	/	32.06	25.8
2526	AGC020471	109.1648	-80.7868	278.1159	-1.9168	1554	1249	6.0	0.20	187	2.272	13.06	12.99	14.45	14.52	14.09	-18.23	-18.08	32.34	29.3	32.62	33.4
2699	UGC00477	121.2400	-43.3647	314.7419	7.1900	2650	2331	7.9	0.20	223	2.348	13.20	13.01	14.23	14.29	14.00	-18.93	-18.83	32.95	38.9	33.15	42.7
2747	UGC00485	121.8318	-32.5215	325.4576	9.5158	5248	4999	6.1	0.20	344	2.537	13.04	12.59	13.18	13.23	13.27	-20.64	-20.67	33.96	62.0	33.96	62.1
2805	PG0002805	119.9027	-72.7498	286.4339	-0.9546	1342	1021	6.7	0.20	135	2.130	13.30	13.37	14.52	14.61	14.34	-16.95	-16.70	31.28	18.1	31.31	18.2
2865	UGC00501	122.2883	-34.6508	323.4566	8.6359	5103	4846	5.8	0.20	375	2.574	13.10	12.62	13.06	13.10	13.23	-20.98	-21.03	34.27	71.4	34.22	69.8
2899	UGC00509	122.5147	-31.2692	326.8292	9.2455	5157	4910	5.9	0.46	210	2.366	14.23	14.24	15.17	15.27	15.11	-19.09	-19.00	34.25	70.9	34.36	74.4
2928	UGC00511	122.6152	-31.1398	326.9768	9.1915	4602	4342	5.9	0.22	269	2.432	14.05	13.76	14.74	14.80	14.64	-19.69	-19.64	34.39	75.4	34.55	81.3
2964	P0002964	122.7750	-34.1707	324.0245	8.3598	4992	4735	2.8	0.35	186	2.289	/	/	14.82	14.91	/	/	-18.25	/	/	33.20	43.6
2992	UGC00521	122.8400	-50.8471	307.7917	4.1335	682	346	9.9	0.68	109	2.163	/	/	15.47	15.55	/	/	-17.02	/	/	32.59	33.0

PGC	Name	l	b	sgl	sgb	v_{hel}	v_{mod}	t	b/a	w_{mx}	$\log w^{i}_{mx}$	I	I^{*}	[3.6]	$[3.6]^{*}$	$C_{[3.6]}$	M_C	$M_{[3.6]}$	μ_C	d_C	$\mu_{[3.6]}$	$d_{[3.6]}$
3020	UGC00525	122.9675	-33.1553	325.0605	8.4396	4941	4685	3.5	0.42	199	2.331	13.25	13.25	14.11	14.21	14.08	-18.78	-18.66	32.88	37.6	32.89	37.9
3062	PG0003062	123.4703	-66.8380	292.4467	-0.4180	1409	1082	6.8	0.33	144	2.175	/	/	15.19	15.27	/	/	-17.13	/	/	32.41	30.4
3081	UGC00536	123.2326	-33.6638	324.6116	8.1076	4862	4604	3.0	0.51	219	2.398	13.94	13.98	15.10	15.20	14.94	-19.38	-19.31	34.38	75.2	34.62	84.0
3089	NGC000289	299.1260	-85.9130	266.0845	-7.5839	1628	1371	4.0	0.68	271	2.556	10.26	10.40	10.42	10.51	10.83	-20.82	-20.86	31.65	21.4	31.37	18.8
3133	UGC00542	123.4573	-33.5994	324.7178	7.9401	4516	4250	3.4	0.23	366	2.567	12.33	11.94	12.65	12.70	12.68	-20.92	-20.96	33.63	53.3	33.72	55.5
3183	P0003183	123.1261	10.2141	8.9127	15.0819	4775	4692	1.0	0.58	311	2.573	/	/	12.06	12.04	/	/	-21.02	/	/	33.09	41.6
3184	P0003184	123.6086	-32.5226	325.8063	8.0579	6783	6584	4.4	0.41	281	2.479	13.71	13.60	14.47	14.57	14.44	-20.12	-20.10	34.63	84.3	34.79	90.7
3218	UGC00549	123.6591	-26.1022	332.1612	9.3882	6061	5856	5.9	0.23	220	2.346	14.69	14.52	15.31	15.40	15.32	-18.91	-18.80	34.29	72.0	34.29	72.2
3222	UGC00557	123.7695	-31.5005	326.8437	8.1498	4513	4253	3.5	0.46	258	2.454	13.64	13.59	14.63	14.72	14.51	-19.89	-19.86	34.46	78.1	34.69	86.6
3235	UGC00556	123.8226	-33.6193	324.7672	7.6391	4633	4371	1.5	0.53	366	2.626	12.96	12.90	12.35	12.44	13.05	-21.46	-21.54	34.58	82.5	34.05	64.6
3250	NGC000298	125.5672	-70.1866	289.3897	-1.9859	1753	1435	5.9	0.33	193	2.302	/	/	13.74	13.80	/	/	-18.37	/	/	32.18	27.3
3260	NGC00296	123.8518	-31.3229	327.0342	8.1199	5464	5228	3.1	0.36	455	2.679	11.35	11.05	11.53	11.60	11.69	-21.94	-22.06	33.67	54.1	33.72	55.5
3274	UGC00565	123.9073	-31.1875	327.1782	8.1028	5645	5415	5.8	0.31	222	2.360	13.82	13.71	14.35	14.44	14.44	-19.03	-18.94	33.50	50.2	33.43	48.5
3285	P0003285	123.9815	-32.4652	325.9327	7.7637	6678	6477	3.0	0.52	218	2.400	14.39	14.42	15.28	15.39	15.26	-19.40	-19.33	34.73	88.5	34.84	93.0
3332	UGC00575	124.1204	-31.7869	326.6268	7.7961	4658	4401	4.0	0.23	276	2.444	13.90	13.62	14.16	14.22	14.28	-19.80	-19.76	34.13	67.1	34.06	64.8
3466	P0003466	124.6031	-32.1453	326.3619	7.3194	4722	4467	3.4	0.64	179	2.361	13.98	14.09	14.81	14.92	14.86	-19.04	-18.95	33.95	61.6	33.93	61.2
3526	AGC020704	134.9897	-81.4377	278.6006	-5.8952	2000	1711	4.2	0.44	271	2.471	11.47	11.46	12.32	12.40	12.28	-20.04	-20.03	32.34	29.3	32.43	30.7
3543	ES541-005	138.6985	-83.2087	276.8327	-6.4326	1955	1671	8.0	0.46	152	2.225	/	/	15.36	15.46	/	/	-17.62	/	/	33.11	41.8
3572	AGC400534	129.1303	-70.3488	289.4716	-3.1969	1649	1334	6.7	0.62	225	2.449	10.78	10.78	11.44	11.46	11.49	-19.84	-19.81	31.33	18.4	31.27	18.0
3603	UGC00622	124.4947	-14.8491	343.5389	10.7117	2717	2480	5.8	0.60	247	2.482	12.24	12.16	12.52	12.58	12.74	-20.15	-20.13	32.90	38.0	32.74	35.3
3606	IC000066	125.2381	-32.0339	326.5847	6.8165	4827	4577	1.0	0.40	359	2.584	12.96	12.79	13.24	13.32	13.42	-21.08	-21.13	34.56	81.8	34.56	81.5
3611	UGC00624	125.2612	-32.1615	326.4630	6.7711	4797	4546	2.0	0.39	529	2.750	11.44	11.15	11.60	11.66	11.77	-22.59	-22.76	34.42	76.6	34.52	80.2
3635	UGC00625	124.5858	-15.1592	343.2426	10.5735	2619	2380	4.0	0.32	332	2.536	11.44	11.07	11.77	11.80	11.80	-20.64	-20.66	32.44	30.8	32.48	31.3
3639	UGC00628	125.9881	-43.3399	315.6107	3.8478	5471	5217	8.7	0.54	219	2.406	/	/	15.05	15.16	/	/	-19.40	/	/	34.66	85.7
3664	UGC00633	125.4057	-31.3165	327.3214	6.8233	5596	5368	3.0	0.27	392	2.601	13.06	12.69	13.40	13.46	13.43	-21.23	-21.30	34.74	88.9	34.88	94.8
3667	UGC00634	127.2641	-55.1618	304.2234	0.5316	2214	1893	8.8	0.49	133	2.175	13.75	13.89	14.91	15.00	14.80	-17.35	-17.13	32.15	27.0	32.14	26.8
3743	NGC000360	301.0396	-51.4762	231.7545	-15.0811	2310	2230	4.4	0.20	361	2.558	11.27	10.87	11.60	11.64	11.61	-20.83	-20.87	32.46	31.0	32.52	32.0
3773	UGC00646	125.8793	-30.5657	328.1438	6.5752	5298	5065	2.5	0.37	367	2.588	12.36	12.13	12.90	12.98	12.91	-21.11	-21.17	34.08	65.3	34.23	70.3
3853	P0003853	132.3600	-68.8341	291.1376	-4.0895	1095	779	7.0	0.69	164	2.346	10.55	10.58	11.46	11.53	11.41	-18.91	-18.81	30.32	11.6	30.34	11.7
3855	PG0003855	132.4295	-68.8980	291.0770	-4.1221	2417	2111	8.8	0.25	148	2.175	/	/	15.34	15.41	/	/	-17.14	/	/	32.56	32.5
3866	UGC00669	126.3799	-31.0968	327.7041	6.0500	5859	5641	5.8	0.25	264	2.426	13.47	13.21	13.32	13.39	13.67	-19.64	-19.59	33.34	46.6	33.01	40.1
3903	UGC00673	126.6109	-31.3607	327.4819	5.8053	6272	6067	5.3	0.35	279	2.466	14.07	13.92	14.89	14.98	14.81	-20.00	-19.98	34.89	95.2	35.10	104.9
3950	UGC00679	126.7540	-30.3663	328.4867	5.8737	5125	4890	7.8	0.23	174	2.243	14.93	14.86	15.72	15.82	15.69	-17.98	-17.80	33.71	55.1	33.68	54.4
3980	NGC000406	300.9117	-47.1880	227.3663	-15.7908	1508	1445	4.9	0.42	228	2.392	11.58	11.61	12.36	12.44	12.38	-19.33	-19.25	31.71	22.0	31.70	21.9
4063	UGC00711	131.7944	-60.9341	298.9539	-2.8260	1964	1648	6.5	0.20	164	2.215	13.04	13.02	14.23	14.31	14.02	-17.72	-17.52	31.73	22.2	31.84	23.3
4110	UGC00714	127.3065	-30.5692	328.3756	5.3681	4638	4392	5.2	0.70	216	2.475	12.77	12.88	13.32	13.43	13.52	-20.08	-20.06	33.64	53.4	33.54	51.2

PGC	Name	l	b	sgl	sgb	v_{hel}	v_{mod}	t	b/a	w_{mx}	$logw^{i}_{mx}$	I	I^{*}	[3.6]	$[3.6]^{*}$	$C_{[3.6]}$	M_C	$M_{[3.6]}$	μ_C	d_C	$\mu_{[3.6]}$	$d_{[3.6]}$
4143	PG0004143	133.6758	-64.7570	295.2575	-4.1438	1863	1551	9.8	0.48	142	2.200	/	/	14.94	15.03	/	/	-17.38	/	/	32.43	30.6
4210	UGC00732	127.5350	-29.1407	329.8227	5.4329	5461	5240	6.4	0.55	260	2.485	12.79	12.81	13.44	13.54	13.54	-20.18	-20.17	33.75	56.3	33.77	56.7
4286	UGC00748	127.5954	-27.4118	331.5416	5.6882	4855	4624	3.3	0.46	298	2.517	/	/	13.80	13.89	/	/	-20.48	/	/	34.46	78.0
4367	UGC00763	134.2162	-61.4184	298.6121	-4.0430	1155	838	8.6	0.67	148	2.290	10.74	10.94	11.71	11.76	11.70	-18.40	-18.26	30.10	10.5	30.01	10.1
4387	UGC00764	127.9680	-27.6928	331.3216	5.3138	4739	4505	6.0	0.20	199	2.299	15.41	15.27	16.17	16.25	16.12	-18.48	-18.35	34.68	86.1	34.72	87.8
4540	UGC00806	136.3298	-63.1049	297.0089	-5.1643	1762	1452	5.8	0.64	166	2.324	11.43	11.59	12.41	12.50	12.40	-18.71	-18.59	31.11	16.7	31.10	16.6
4561	UGC00810	129.0567	-31.5013	327.7210	3.7274	4851	4612	6.4	0.24	253	2.407	13.34	13.10	13.99	14.06	13.94	-19.46	-19.40	33.43	48.5	33.51	50.3
4563	UGC00809	128.7201	-28.7863	330.3543	4.4736	4210	3963	5.9	0.21	300	2.478	13.62	13.26	13.91	13.96	13.97	-20.11	-20.09	34.13	67.1	34.13	67.1
4596	NGC00452	129.1678	-31.5374	327.7014	3.6280	4964	4728	2.0	0.27	457	2.667	11.64	11.20	11.94	11.99	11.95	-21.83	-21.95	33.83	58.3	34.01	63.3
4650	UGC000825	127.3451	-13.6375	345.1930	8.1744	5337	5165	7.6	0.20	290	2.462	/	/	14.44	14.49	/	/	-19.94	/	/	34.53	80.6
4735	UGC00841	129.6072	-29.4815	329.7957	3.5943	5600	5388	4.0	0.23	282	2.453	13.65	13.35	13.98	14.06	14.06	-19.88	-19.85	34.00	63.0	33.98	62.5
4777	UGC00858	136.6290	-58.7070	301.4240	-5.0135	2375	2072	3.1	0.55	364	2.629	10.85	10.84	11.28	11.31	11.44	-21.48	-21.57	32.94	38.8	32.91	38.1
4805	UGC00866	138.4573	-62.2097	297.9566	-6.0950	1739	1432	7.8	0.29	125	2.107	14.14	14.28	15.24	15.34	15.16	-16.73	-16.47	31.90	24.0	31.81	23.0
4921	UGC00895	136.0246	-55.0884	305.0194	-4.4113	2290	1986	6.0	0.33	235	2.388	12.53	12.43	13.13	13.20	13.17	-19.29	-19.21	32.47	31.2	32.43	30.6
4948	UGC00903	133.1302	-44.6773	315.1826	-1.4411	2551	2254	4.0	0.25	363	2.565	12.19	11.76	11.60	11.63	12.07	-20.90	-20.94	32.99	39.6	32.59	33.0
4957	NGC00489	135.4633	-52.9225	307.1537	-3.8926	2514	2213	5.0	0.25	382	2.587	11.59	11.23	12.15	12.19	12.06	-21.10	-21.16	33.19	43.5	33.40	47.8
4971	UGC00909	129.6341	-25.0719	334.1629	4.2745	5096	4883	6.4	0.73	238	2.533	13.06	13.18	13.81	13.92	13.91	-20.61	-20.63	34.59	82.9	34.66	85.7
4979	UGC00914	138.9115	-60.9695	299.2104	-6.2707	2342	2042	5.9	0.24	257	2.414	11.60	11.41	12.28	12.34	12.23	-19.53	-19.47	31.76	22.5	31.81	23.1
4992	UGC00915	140.0142	-62.7157	297.4637	-6.8259	8142	7994	4.0	0.43	541	2.768	11.78	11.54	12.23	12.33	12.29	-22.75	-22.93	35.14	106.7	35.42	121.6
5061	NGC00496	130.4870	-28.8766	330.5157	2.9316	6015	5819	4.0	0.49	285	2.506	12.60	12.54	13.10	13.20	13.23	-20.36	-20.36	33.63	53.2	33.62	52.9
5132	UGC00944	130.6143	-28.4778	330.9274	2.8823	4859	4633	2.0	0.28	521	2.726	12.10	11.62	12.26	12.30	12.32	-22.36	-22.52	34.77	89.9	34.95	97.8
5139	UGC00947	135.1454	-49.1791	310.8672	-3.3299	2472	2173	5.2	0.68	242	2.507	10.77	10.90	11.67	11.72	11.67	-20.37	-20.38	32.04	25.6	32.10	26.3
5147	UGC00949	136.1146	-52.1021	308.0082	-4.2145	2422	2122	3.0	0.50	183	2.316	13.27	13.32	14.07	14.16	14.09	-18.64	-18.51	32.74	35.4	32.69	34.5
5194	UGC00958	134.3164	-45.6011	314.3678	-2.3847	2446	2150	5.7	0.21	152	2.183	14.35	14.28	15.43	15.50	15.24	-17.42	-17.21	32.68	34.3	32.74	35.3
5198	UGC00964	137.0769	-54.2377	305.9166	-4.9539	2740	2444	3.0	0.27	204	2.317	14.10	14.02	14.40	14.47	14.61	-18.65	-18.52	33.28	45.4	33.03	40.3
5218	NGC00522	136.3365	-52.0081	308.1136	-4.3425	2720	2424	4.1	0.20	379	2.579	11.61	11.09	11.88	11.90	11.85	-21.03	-21.08	32.90	38.0	33.01	39.9
5264	NGC00532	136.7979	-52.6939	307.4499	-4.6774	2370	2070	1.9	0.34	384	2.603	11.01	10.70	11.37	11.41	11.42	-21.24	-21.31	32.67	34.3	32.74	35.4
5284	UGC00987	131.2785	-30.1826	329.3277	2.0533	4669	4435	1.0	0.30	383	2.595	12.13	11.82	12.45	12.51	12.53	-21.18	-21.24	33.74	56.0	33.81	57.9
5329	AGC410199	144.0363	-65.4290	294.6840	-8.5163	1997	1701	8.0	0.35	135	2.150	/	/	15.02	15.11	/	/	-16.89	/	/	32.01	25.2
5341	AGC410203	145.9709	-67.3957	292.6390	-9.1348	1959	1666	5.6	0.20	236	2.373	12.16	11.93	12.90	12.90	12.77	-19.15	-19.07	31.93	24.3	31.97	24.8
5344	UGC01013	131.0287	-27.6190	331.8325	2.6501	5183	4969	3.1	0.36	513	2.731	11.15	10.83	11.65	11.72	11.63	-22.42	-22.57	34.10	66.1	34.38	75.2
5375	ES476-010	201.9959	-81.8875	273.5676	-13.6334	1604	1351	8.8	0.33	117	2.084	13.98	14.18	15.37	15.47	15.17	-16.53	-16.25	31.70	21.9	31.72	22.1
5382	UGC01020	134.8436	-44.7894	315.2169	-2.6629	2592	2300	2.1	0.37	231	2.387	/	/	13.71	13.76	/	/	-19.20	/	/	32.99	39.7
5440	UGC01033	131.8850	-30.6879	328.9038	1.4622	4058	3812	5.8	0.20	337	2.528	12.77	12.35	13.26	13.30	13.18	-20.56	-20.58	33.78	57.1	33.95	61.7
5450	NGC00551	130.8970	-25.1277	334.2820	3.1357	5188	4981	4.0	0.42	372	2.603	12.10	11.94	12.65	12.73	12.69	-21.25	-21.32	33.99	62.8	34.12	66.8
5518	UGC01054	131.6553	-27.8922	331.6432	2.0617	2668	2406	6.2	0.20	167	2.223	/	/	16.51	16.59	/	/	-17.60	/	/	34.27	71.5

PGC	Name	l	b	sgl	sgb	v_{hel}	v_{mod}	t	b/a	w_{mx}	$logw^{i}_{mx}$	I	I^{*}	[3.6]	$[3.6]^{*}$	$C_{[3.6]}$	M_{C}	$M_{[3.6]}$	μ_{C}	d_{C}	$\mu_{[3.6]}$	$d_{[3.6]}$
5563	UGC01066	132.2157	-30.1230	329.5036	1.2600	5073	4852	6.0	0.33	158	2.214	15.28	15.33	16.79	16.89	16.46	-17.71	-17.52	34.22	69.9	34.51	79.9
5619	AGC021148	188.3085	-80.0921	276.4149	-13.9592	1628	1371	5.0	0.56	256	2.481	10.40	10.49	11.08	11.17	11.19	-20.14	-20.13	31.33	18.4	31.29	18.1
5643	UGC01082	136.2435	-44.6603	315.4457	-3.6394	2809	2523	3.0	0.28	385	2.594	11.90	11.49	11.89	11.93	12.07	-21.16	-21.23	33.26	45.0	33.19	43.5
5702	UGC001094	132.5565	-28.6366	331.0171	1.1714	4363	4131	3.1	0.26	438	2.647	11.98	11.55	12.25	12.29	12.28	-21.65	-21.75	33.98	62.6	34.12	66.8
5792	UGC01110	138.3333	-48.2838	311.9330	-5.3528	2768	2481	5.9	0.21	204	2.311	13.49	13.33	14.28	14.35	14.19	-18.59	-18.46	32.80	36.2	32.83	36.9
5794	UGC01112	143.0448	-58.1566	302.0494	-8.3585	1705	1408	5.8	0.39	147	2.195	13.45	13.59	14.51	14.60	14.45	-17.53	-17.33	31.98	24.9	31.93	24.4
5897	AGC410271	152.5473	-67.6663	291.9850	-11.5782	1842	1558	3.0	0.38	369	2.593	10.62	10.47	11.10	11.16	11.17	-21.15	-21.21	32.33	29.3	32.39	30.0
6045	UGC01160	134.2055	-29.3550	330.4919	-0.3519	5469	5266	6.1	0.20	319	2.504	13.67	13.29	13.73	13.79	13.91	-20.34	-20.35	34.31	72.8	34.23	70.0
6189	UGC01178	134.2559	-27.1659	332.6699	-0.1273	5525	5331	5.9	0.21	366	2.564	12.88	12.45	12.62	12.68	12.94	-20.89	-20.94	33.87	59.5	33.67	54.2
6190	AGC410313	153.4888	-65.4413	294.1314	-12.4045	2125	1846	6.8	0.25	170	2.236	13.61	13.60	14.68	14.76	14.53	-17.91	-17.73	32.45	30.9	32.51	31.8
6228	AGC410316	153.8899	-65.4092	294.1271	-12.5743	1493	1210	8.7	0.40	163	2.241	12.50	12.59	13.59	13.67	13.48	-17.95	-17.78	31.44	19.4	31.46	19.5
6249	NGC002573	302.7687	-27.7776	207.1277	-15.8422	2416	2474	5.8	0.39	217	2.363	/	/	12.98	13.04	/	/	-18.98	/	/	32.02	25.4
6275	NGC00658	141.7591	-48.4069	311.8980	-7.6327	2992	2716	3.0	0.62	298	2.571	11.56	11.62	12.12	12.21	12.28	-20.95	-21.00	33.26	44.8	33.25	44.7
6294	UGC01197	139.5913	-42.9065	317.3784	-5.9212	2795	2521	9.8	0.26	175	2.249	13.82	13.75	14.88	14.96	14.71	-18.03	-17.86	32.75	35.5	32.84	37.1
6309	UGC01200	141.7395	-47.8312	312.4785	-7.6097	824	531	9.9	0.56	117	2.139	12.60	12.79	13.78	13.87	13.68	-17.03	-16.79	30.71	13.9	30.66	13.5
6473	UGC01234	135.3436	-26.4456	333.5001	-1.0060	5654	5469	5.3	0.56	265	2.497	13.65	13.68	14.41	14.52	14.46	-20.28	-20.28	34.83	92.4	34.93	97.0
6500	UGC01240	147.9122	-55.9217	304.1548	-11.1321	1815	1531	7.9	0.32	123	2.104	/	/	15.31	15.41	/	/	-16.45	/	/	31.86	23.5
6502	UGC01238	135.1064	-25.1094	334.8029	-0.6397	4499	4288	3.1	0.68	279	2.572	12.03	12.12	12.57	12.67	12.76	-20.96	-21.01	33.76	56.5	33.74	56.0
6607	UGC01257	135.4834	-25.0333	334.9178	-0.9703	4661	4455	2.0	0.42	324	2.544	13.16	13.05	13.74	13.82	13.80	-20.71	-20.74	34.58	82.6	34.68	86.3
6624	UGC01259	144.4573	-48.9559	311.3392	-9.4129	5181	4955	5.3	0.71	315	2.640	11.59	11.63	11.99	12.09	12.23	-21.58	-21.68	33.85	59.0	33.83	58.4
6671	AGC410359	164.8344	-68.4628	289.7771	-15.7044	1756	1490	2.0	0.68	372	2.696	10.56	10.64	11.02	11.10	11.24	-22.10	-22.23	33.36	47.1	33.38	47.3
6675	UGC01276	140.7178	-40.1556	320.1853	-6.6238	2748	2482	7.8	0.45	212	2.367	12.15	12.12	12.82	12.90	12.87	-19.10	-19.01	31.97	24.8	31.91	24.1
6703	PG0006703	170.8881	-70.8033	286.6153	-16.5246	1439	1177	3.1	0.28	164	2.224	/	/	14.46	14.54	/	/	-17.61	/	/	32.16	27.0
6793	UGC01305	140.7382	-39.0542	321.2935	-6.5866	2669	2404	4.0	0.69	317	2.631	10.59	10.63	11.30	11.39	11.37	-21.50	-21.59	32.89	37.8	33.00	39.9
6799	NGC00688	136.3732	-26.0348	334.0105	-1.8785	4148	3931	3.1	0.60	337	2.614	11.74	11.75	12.34	12.44	12.45	-21.35	-21.43	33.85	58.8	33.93	61.1
6826	AGC410368	164.6580	-67.6051	290.6224	-15.9850	1830	1565	5.0	0.48	247	2.440	11.09	11.13	11.47	11.55	11.71	-19.76	-19.72	31.47	19.7	31.28	18.0
6833	UGC01313	140.8080	-38.8775	321.4738	-6.6322	2938	2677	5.0	0.56	148	2.243	12.73	12.84	13.45	13.55	13.55	-17.97	-17.80	31.53	20.2	31.35	18.6
6851	UGC01316	136.6195	-26.4271	333.6435	-2.1396	4688	4482	3.1	0.44	205	2.351	14.48	14.50	15.60	15.70	15.45	-18.95	-18.85	34.47	78.5	34.67	85.8
6864	AGC410377	160.3276	-64.9344	293.8563	-15.3050	2130	1863	6.9	0.26	175	2.250	14.05	14.06	15.35	15.43	15.09	-18.03	-17.87	33.15	42.6	33.34	46.5
6865	UGC01319	136.3163	-25.2403	334.7954	-1.7425	5312	5125	3.6	0.68	241	2.510	12.80	12.87	13.11	13.22	13.41	-20.40	-20.40	33.85	59.0	33.68	54.5
6898	PG0006898	159.2347	-64.0262	294.9014	-15.1338	1643	1371	7.9	0.35	146	2.184	/	/	15.46	15.55	/	/	-17.22	/	/	32.79	36.1
6966	PGC006966	157.3565	-62.1438	297.0171	-14.8365	5008	4789	5.0	0.20	517	2.713	11.98	11.39	11.60	11.64	11.88	-22.25	-22.40	34.19	68.9	34.11	66.3
6972	NGC00710	136.6248	-25.1793	334.8858	-2.0136	6112	5949	5.9	0.65	210	2.433	/	/	12.98	13.09	/	/	-19.65	/	/	32.76	35.7
7066	UGC01366	136.7641	-24.5469	335.5283	-2.0729	5107	4918	5.8	0.28	412	2.624	12.43	12.03	12.85	12.90	12.82	-21.44	-21.52	34.32	73.1	34.52	80.3
7097	NGC00721	136.0634	-21.8682	338.1232	-1.1442	5597	5428	3.8	0.59	275	2.523	12.39	12.43	13.06	13.16	13.16	-20.52	-20.54	33.72	55.4	33.76	56.5
7247	UGC01378	127.6272	11.0054	10.0498	10.7264	2933	2831	1.2	0.47	496	2.741	/	/	10.68	10.66	/	/	-22.66	/	/	33.36	47.0

PGC	Name	l	b	sgl	sgb	v_{hel}	v_{mod}	t	b/a	w_{mx}	$logw^{i}_{mx}$	I	I^{*}	[3.6]	$[3.6]^{*}$	$C_{[3.6]}$	M_{C}	$M_{[3.6]}$	μ_{C}	d_{C}	$\mu_{[3.6]}$	$d_{[3.6]}$
7262	AGC410401	166.3108	-66.2983	291.5958	-17.1055	1639	1377	3.4	0.33	221	2.361	11.77	11.74	12.48	12.56	12.51	-19.04	-18.95	31.55	20.4	31.51	20.0
7300	UGC01416	137.2041	-24.1681	335.9468	-2.4325	5471	5294	3.1	0.52	368	2.626	13.16	13.06	13.68	13.76	13.77	-21.46	-21.54	35.34	117.1	35.48	124.9
7324	PG0007324	171.1763	-68.2714	288.8580	-17.8778	1856	1601	8.0	0.20	152	2.182	13.96	13.99	15.10	15.19	14.94	-17.41	-17.20	32.36	29.7	32.40	30.2
7504	UGC01459	137.9543	-24.8267	335.3581	-3.1769	5466	5289	5.8	0.20	362	2.559	13.26	12.74	13.10	13.15	13.31	-20.84	-20.88	34.21	69.4	34.11	66.3
7537	NGC00769	139.7614	-29.7245	330.6038	-5.1979	4427	4215	5.5	0.54	300	2.543	12.25	12.25	12.59	12.68	12.83	-20.70	-20.73	33.57	51.7	33.46	49.2
7544	NGC000779	163.4911	-63.3247	294.9503	-17.1465	1393	1129	3.0	0.37	351	2.568	10.01	9.86	10.60	10.66	10.62	-20.93	-20.97	31.55	20.4	31.64	21.2
7545	UGC01470	139.3867	-28.5992	331.7043	-4.7842	5186	4994	7.7	0.20	232	2.365	/	/	15.16	15.23	/	/	-19.00	/	/	34.32	73.1
7646	UGC01493	137.6587	-22.6661	337.4846	-2.6964	4147	3945	2.0	0.36	346	2.561	12.16	11.97	12.38	12.45	12.57	-20.86	-20.90	33.47	49.4	33.40	47.8
7663	UGC01500	144.6302	-40.2388	320.1767	-9.6131	2433	2174	5.9	0.24	154	2.192	14.35	14.27	14.90	14.97	14.98	-17.50	-17.30	32.49	31.5	32.28	28.5
7847	UGC01550	138.2191	-22.4567	337.7441	-3.1908	5772	5613	5.3	0.24	459	2.666	11.52	11.04	11.85	11.90	11.83	-21.82	-21.93	33.68	54.4	33.89	60.1
7849	UGC01554	147.1705	-43.4117	316.9179	-11.4523	2099	1836	5.3	0.37	247	2.416	11.40	11.32	12.20	12.22	12.13	-19.55	-19.49	31.68	21.7	31.72	22.1
7933	UGC001567	136.8995	-17.7147	342.3387	-1.4739	9015	8992	6.3	0.20	543	2.735	13.69	13.00	13.21	13.26	13.50	-22.45	-22.60	36.10	166.2	36.09	165.1
7957	AGC120016	139.7027	-25.6666	334.6605	-4.8267	4416	4216	3.0	0.25	341	2.538	13.63	13.25	13.71	13.77	13.87	-20.66	-20.69	34.60	83.3	34.56	81.5
7972	UGC01581	139.7304	-25.5612	334.7680	-4.8430	4421	4222	7.2	0.48	330	2.567	12.62	12.49	12.69	12.77	13.00	-20.92	-20.96	33.96	62.1	33.79	57.4
8066	UGC01598	136.8078	-16.2584	343.7774	-1.2295	5161	5004	5.9	0.24	435	2.643	11.76	11.27	12.02	12.06	12.02	-21.61	-21.70	33.67	54.1	33.83	58.2
8165	UGC01629	149.5327	-44.5098	315.7026	-13.0914	4418	4196	2.9	0.64	342	2.640	11.80	11.82	12.20	12.30	12.42	-21.58	-21.67	34.05	64.6	34.04	64.4
8173	UGC01636	154.8946	-51.6986	307.8914	-15.7764	3415	3174	1.1	0.47	459	2.707	11.88	11.72	12.28	12.35	12.39	-22.20	-22.33	34.67	85.7	34.80	91.2
8185	UGC01633	139.0493	-21.6629	338.6083	-3.8822	4265	4074	4.4	0.38	448	2.677	11.40	11.16	11.71	11.78	11.83	-21.92	-22.04	33.79	57.3	33.88	59.7
8232	AGC420030	173.1555	-64.6386	291.7582	-20.3904	1938	1694	4.1	0.23	268	2.431	11.65	11.43	11.66	11.71	11.94	-19.68	-19.63	31.62	21.1	31.35	18.6
8237	UGC01650	139.7161	-23.0580	337.2698	-4.6203	4594	4407	6.2	0.20	221	2.344	/	/	15.45	15.53	/	/	-18.79	/	/	34.41	76.3
8295	AGC420037	173.5220	-64.5231	291.7780	-20.5847	2017	1774	5.0	0.23	152	2.185	13.08	13.12	14.07	14.15	13.99	-17.44	-17.23	31.44	19.4	31.39	18.9
8372	NGC00841	140.0078	-22.7125	337.6382	-4.8587	4545	4359	2.0	0.50	394	2.648	11.39	11.30	11.90	11.99	12.00	-21.65	-21.75	33.70	54.8	33.80	57.7
8396	UGC01685	141.3489	-25.9428	334.4964	-6.3254	6181	6033	2.0	0.29	427	2.641	12.94	12.51	12.94	12.99	13.12	-21.59	-21.68	34.79	90.7	34.80	91.1
8480	E544-027	194.5725	-69.7525	281.7597	-23.1051	2463	2246	3.5	0.24	250	2.402	13.38	13.20	13.56	13.63	13.78	-19.41	-19.35	33.22	44.1	33.00	39.9
8599	UGC01726	143.0661	-28.1197	332.3995	-7.9835	5295	5120	4.0	0.26	339	2.537	13.16	12.82	13.38	13.44	13.49	-20.65	-20.67	34.19	68.9	34.19	69.0
8673	IC000217	179.6527	-64.9809	289.7948	-22.4923	1890	1656	5.7	0.20	208	2.318	12.30	12.17	12.96	13.02	12.95	-18.65	-18.53	31.61	21.0	31.55	20.5
8678	UGC01747	144.5999	-30.6787	329.8687	-9.4244	3002	2776	4.0	0.29	271	2.444	12.28	12.04	12.55	12.61	12.69	-19.80	-19.76	32.49	31.5	32.38	29.9
8691	UGC01753	144.8395	-31.0215	329.5274	-9.6401	3006	2780	9.9	0.39	142	2.179	/	/	15.00	15.09	/	/	-17.18	/	/	32.27	28.5
8778	AGC120150	143.6047	-27.4914	333.0574	-8.4281	6063	5914	3.3	0.53	290	2.525	13.76	13.72	13.81	13.91	14.18	-20.54	-20.56	34.80	91.4	34.57	82.0
8851	ES545-002	195.4614	-68.2407	282.4370	-24.5204	1607	1388	8.9	0.40	135	2.160	13.28	13.42	14.50	14.59	14.35	-17.22	-16.99	31.57	20.6	31.58	20.7
8862	ES545-003	201.8624	-69.1763	279.7204	-24.9473	1597	1384	4.0	0.22	129	2.112	14.05	14.16	15.17	15.26	15.07	-16.78	-16.52	31.85	23.5	31.79	22.8
8896	AGC021790	197.7003	-68.4062	281.5810	-24.8463	2337	2128	7.6	0.25	251	2.404	12.35	12.18	12.85	12.91	12.91	-19.44	-19.37	32.35	29.6	32.30	28.8
8974	NGC00895	171.7744	-59.5474	296.8710	-22.3044	2290	2057	6.0	0.65	254	2.515	10.96	11.08	11.63	11.67	11.74	-20.45	-20.46	32.20	27.5	32.14	26.8
8984	UGC01820	143.9513	-26.1371	334.4405	-8.6710	3980	3784	5.9	0.22	227	2.358	13.59	13.35	14.05	14.12	14.09	-19.02	-18.92	33.13	42.3	33.07	41.2
9028	UGC01839	166.2158	-55.6410	302.0195	-21.1926	1541	1298	7.1	0.23	142	2.155	/	/	15.14	15.23	/	/	-16.94	/	/	32.18	27.3
9054	AGC021830	200.8171	-68.1433	280.6403	-25.6684	1655	1445	7.6	0.36	262	2.440	11.66	11.59	12.24	12.31	12.31	-19.77	-19.72	32.08	26.1	32.04	25.6

PGC	Name	l	b	sgl	sgb	v_{hel}	v_{mod}	t	b/a	w_{mx}	$logw^{i}_{mx}$	I	I*	[3.6]	[3.6]*	$C_{[3.6]}$	M_C	$M_{[3.6]}$	μ_C	d_C	$\mu_{[3.6]}$	$d_{[3.6]}$
9057	AGC021831	202.1393	-68.3224	280.0677	-25.7477	1508	1298	5.1	0.43	377	2.612	9.31	9.20	9.68	9.75	9.84	-21.33	-21.40	31.17	17.1	31.15	17.0
9115	UGC01845	138.5622	-12.0690	348.1254	-2.4782	4642	4496	2.0	0.32	235	2.386	/	/	12.04	12.09	/	/	-19.19	/	/	31.28	18.1
9186	UGC01867	139.6823	-14.3469	345.9651	-3.7916	5193	5055	5.9	0.20	279	2.446	13.57	13.19	13.99	14.05	13.98	-19.81	-19.78	33.84	58.5	33.90	60.2
9236	UGC01888	152.1608	-38.9581	321.2656	-15.4574	1509	1267	5.2	0.55	241	2.451	10.93	10.52	11.22	11.24	11.24	-19.87	-19.83	31.11	16.6	31.07	16.4
9253	UGC01887	141.0989	-17.3646	343.0756	-5.4253	5535	5399	5.3	0.61	339	2.620	12.32	12.32	12.64	12.74	12.89	-21.40	-21.49	34.36	74.5	34.31	72.9
9272	P0009272	179.7598	-61.7257	292.6072	-24.4788	2106	1883	8.0	0.32	180	2.271	13.43	13.46	14.44	14.52	14.35	-18.22	-18.07	32.58	32.8	32.61	33.3
9273	ES479-004	210.6892	-68.4633	276.7837	-26.8662	1510	1311	8.5	0.47	182	2.305	11.63	11.75	12.63	12.71	12.58	-18.54	-18.41	31.12	16.8	31.12	16.8
9332	NGC00925	144.8853	-25.1743	335.4545	-9.4668	553	326	7.0	0.51	194	2.346	9.27	9.31	10.20	10.27	10.14	-18.91	-18.80	29.05	6.5	29.07	6.5
9354	AGC420105	180.6853	-61.7130	292.3301	-24.8380	2099	1878	5.1	0.33	144	2.174	13.07	13.19	14.09	14.18	14.04	-17.34	-17.13	31.38	18.9	31.30	18.2
9399	UGC01935	146.1145	-27.1661	333.4748	-10.6434	4999	4830	3.6	0.27	422	2.633	11.51	11.06	10.94	10.99	11.40	-21.52	-21.61	32.94	38.8	32.62	33.4
9510	UGC01970	149.4600	-32.4938	328.0429	-13.5752	1924	1696	5.8	0.20	218	2.338	13.15	12.86	13.60	13.64	13.61	-18.84	-18.73	32.46	31.0	32.38	30.0
9549	UGC01986	169.5002	-54.7581	302.1332	-23.2617	1485	1252	2.0	0.30	328	2.527	10.82	10.60	11.32	11.37	11.34	-20.56	-20.58	31.90	24.0	31.95	24.5
9550	UGC01980	146.2173	-26.1749	334.4859	-10.7048	4777	4606	2.9	0.44	418	2.659	12.13	11.92	12.08	12.15	12.41	-21.76	-21.86	34.22	69.9	34.09	65.8
9560	NGC0958	171.6769	-56.1096	300.2291	-23.8128	5739	5583	4.9	0.34	570	2.774	11.08	10.73	11.13	11.19	11.33	-22.80	-22.98	34.18	68.6	34.26	71.2
9590	UGC01988	142.7485	-18.6099	341.9544	-7.0897	5779	5651	2.0	0.36	324	2.532	12.91	12.73	13.11	13.19	13.33	-20.60	-20.62	33.98	62.4	33.88	59.7
9617	UGC01998	168.3519	-53.4934	303.6854	-23.1328	6345	6206	6.0	0.56	183	2.334	14.39	14.52	15.23	15.35	15.29	-18.80	-18.69	34.15	67.6	34.12	66.7
9618	UGC01993	143.2545	-19.5054	341.0890	-7.6319	8025	7974	3.2	0.22	483	2.686	12.77	12.22	13.07	13.13	13.03	-22.00	-22.13	35.13	106.2	35.43	121.7
9638	UGC01999	153.3749	-37.7108	322.4792	-16.5070	975	738	5.7	0.25	143	2.161	13.52	13.48	14.71	14.78	14.48	-17.22	-17.00	31.70	21.9	31.78	22.7
9665	UGC02002	145.0888	-22.9959	337.6697	-9.5490	596	378	7.9	0.60	134	2.213	11.58	11.71	12.37	12.45	12.44	-17.70	-17.51	30.14	10.7	29.96	9.8
9773	UGC02035	141.5935	-14.7801	345.7040	-5.6736	5078	4942	3.2	0.61	301	2.571	12.55	12.53	12.84	12.94	13.10	-20.95	-21.00	34.11	66.3	34.01	63.4
9788	UGC02045	148.3956	-28.4293	332.2225	-12.6837	1541	1319	2.1	0.47	300	2.522	9.89	9.76	10.04	10.09	10.29	-20.51	-20.53	30.81	14.5	30.62	13.3
9795	UGC02048	146.8659	-25.5398	335.1507	-11.2688	4865	4701	3.3	0.20	583	2.766	11.43	10.67	11.01	11.02	11.22	-22.73	-22.91	33.99	62.8	34.00	63.1
9800	P0009800	183.9828	-60.8244	292.0001	-26.6304	4766	4600	3.9	0.42	371	2.603	12.27	12.16	12.44	12.53	12.71	-21.25	-21.32	34.01	63.5	33.92	60.8
9816	AGC120356	145.8200	-23.3754	337.3169	-10.2382	3762	3578	4.2	0.35	222	2.366	13.25	13.17	13.10	13.18	13.55	-19.09	-19.00	32.65	34.0	32.19	27.4
9869	UGC02081	169.5892	-52.7085	304.1669	-24.1194	2622	2405	5.8	0.60	181	2.344	13.06	13.21	14.16	14.26	14.09	-18.89	-18.78	33.00	39.7	33.07	41.1
9888	UGC02082	150.8871	-31.6959	328.8352	-14.8034	707	479	5.8	0.22	191	2.283	11.85	11.56	12.61	12.64	12.45	-18.33	-18.19	30.79	14.4	30.82	14.6
9938	NGC00992	153.6278	-35.3758	324.8925	-16.8948	4136	3946	5.1	0.66	295	2.585	12.17	12.09	11.79	11.87	12.36	-21.08	-21.14	33.48	49.6	33.04	40.6
10029	UGC02134	150.1867	-29.2784	331.3448	-14.2501	4585	4413	3.1	0.40	321	2.536	12.07	11.76	12.31	12.37	12.43	-20.64	-20.66	33.09	41.4	33.06	40.9
10052	NGC01003	144.0041	-17.5449	343.1141	-8.2023	624	423	6.0	0.27	204	2.317	10.82	10.70	11.70	11.76	11.58	-18.64	-18.52	30.23	11.1	30.28	11.4
10065	NGC01035	181.3687	-58.1509	295.2754	-27.2472	1242	1026	5.2	0.28	241	2.390	11.01	10.90	11.44	11.50	11.56	-19.31	-19.24	30.87	14.9	30.74	14.0
10126	UGC02159	149.3736	-27.1344	333.5565	-13.5424	5191	5038	6.6	0.20	164	2.215	15.23	15.01	15.78	15.85	15.79	-17.72	-17.52	33.54	50.9	33.42	48.3
10172	NGC001051	180.1341	-57.0790	296.6892	-27.3340	1295	1080	8.8	0.58	175	2.323	/	/	12.97	13.06	/	/	-18.58	/	/	31.65	21.4
10208	NGC01055	171.3298	-51.7502	304.6675	-25.4789	992	769	3.1	0.47	386	2.631	9.38	9.30	9.39	9.45	9.74	-21.50	-21.59	31.24	17.7	31.03	16.1
10218	UGC02171	148.6610	-25.2057	335.5307	-12.8825	4571	4407	6.5	0.20	211	2.325	14.73	14.37	15.18	15.23	15.16	-18.72	-18.60	33.92	60.8	33.89	60.1
10272	UGC02183	150.6761	-28.2305	332.4218	-14.6916	1557	1344	1.0	0.70	266	2.565	10.89	10.84	11.38	11.45	11.51	-20.90	-20.95	32.42	30.5	32.41	30.3
10312	UGC02194	144.5054	-16.7256	343.9746	-8.6221	5482	5359	3.0	0.38	302	2.505	/	/	13.26	13.34	/	/	-20.36	/	/	33.76	56.5

PGC	Name	l	b	sgl	sgb	v_{hel}	v_{mod}	t	b/a	w_{mx}	$logw^{i}_{mx}$	I	I*	[3.6]	[3.6]*	$C_{[3.6]}$	M_C	$M_{[3.6]}$	μ_C	d_C	$\mu_{[3.6]}$	$d_{[3.6]}$
10331	UGC02201	148.8314	-24.6673	336.0858	-13.0276	4148	3978	6.4	0.25	321	2.511	13.56	13.05	13.35	13.38	13.58	-20.41	-20.42	34.05	64.5	33.87	59.3
10448	AGC120493	169.6596	-48.9801	307.9549	-25.5647	6806	6699	4.0	0.36	294	2.490	13.35	13.23	13.57	13.67	13.82	-20.22	-20.21	34.08	65.6	33.95	61.7
10464	AGC420244	182.4810	-56.5545	296.3188	-28.6822	1406	1199	4.9	0.65	296	2.583	9.69	9.80	10.12	10.21	10.37	-21.07	-21.12	31.43	19.4	31.33	18.4
10488	NGC001097	226.9150	-64.6804	270.2285	-31.6387	1271	1108	3.3	0.64	384	2.692	8.19	8.25	8.70	8.73	8.85	-22.06	-22.19	30.91	15.2	30.91	15.2
10496	NGC001087	173.7451	-51.6513	304.0589	-26.8760	1518	1304	5.2	0.61	209	2.412	10.27	10.39	10.75	10.83	10.98	-19.51	-19.45	30.49	12.5	30.29	11.4
10507	NGC001090	173.5090	-51.4438	304.3402	-26.8353	2757	2556	3.8	0.43	310	2.527	11.07	11.01	11.60	11.68	11.70	-20.55	-20.57	32.27	28.4	32.26	28.4
10673	NGC001110	183.7298	-56.1064	296.2441	-29.5043	1332	1129	8.9	0.20	159	2.201	13.09	13.06	14.05	14.13	13.95	-17.59	-17.39	31.54	20.3	31.52	20.1
10913	UGC02364	168.6322	-45.2409	312.1253	-26.1904	5429	5288	3.0	0.36	323	2.531	13.59	13.16	13.89	13.94	13.91	-20.59	-20.61	34.57	82.1	34.67	85.7
10943	UGC02375	169.0791	-45.3447	311.9017	-26.4540	7610	7542	2.0	0.29	440	2.654	13.17	12.58	13.28	13.33	13.31	-21.71	-21.82	35.12	105.9	35.30	114.9
10965	AGC022202	202.7802	-60.4866	284.1077	-32.7535	2064	1891	5.2	0.20	320	2.506	11.48	11.13	11.75	11.79	11.82	-20.36	-20.36	32.18	27.3	32.16	27.0
10966	AGC420295	188.3252	-56.3400	294.1172	-31.2973	1500	1308	9.2	0.50	177	2.302	11.85	11.95	12.68	12.71	12.69	-18.50	-18.37	31.20	17.3	31.09	16.5
11004	P0011004	134.8772	6.4415	6.1374	3.1705	3485	3391	4.8	0.50	371	2.623	12.82	11.27	11.81	11.69	11.85	-21.43	-21.51	33.30	45.8	33.24	44.5
11016	ES356-018	239.9914	-62.2675	263.0136	-33.2831	1438	1302	5.0	0.22	117	2.070	13.78	13.95	14.93	15.02	14.84	-16.40	-16.11	31.24	17.7	31.13	16.9
11067	UGC02404	174.6762	-48.8857	306.5732	-28.6231	5032	4887	6.1	0.20	276	2.441	14.43	14.05	14.47	14.52	14.65	-19.77	-19.73	34.49	79.2	34.35	74.0
11074	UGC02405	169.3718	-44.8582	312.3397	-26.8090	7696	7634	5.7	0.36	400	2.624	13.14	12.72	13.43	13.50	13.47	-21.44	-21.52	35.00	99.9	35.16	107.9
11102	UGC02415	169.7958	-45.0483	312.0267	-27.0288	7773	7715	4.0	0.33	323	2.525	14.09	13.71	14.07	14.15	14.30	-20.54	-20.55	34.92	96.4	34.82	92.1
11153	UGC02429	174.7747	-48.4748	306.9634	-28.8599	1772	1573	9.0	0.28	144	2.167	/	/	15.28	15.35	/	/	-17.06	/	/	32.42	30.5
11202	IC0001870	179.0608	-50.8918	303.0100	-30.1597	1542	1345	9.0	0.47	181	2.304	11.81	11.85	12.88	12.96	12.76	-18.53	-18.40	31.29	18.1	31.36	18.7
11245	UGC02443	178.8314	-50.6000	303.3860	-30.1837	2515	2328	5.8	0.50	204	2.365	12.79	12.78	13.44	13.52	13.51	-19.08	-18.99	32.60	33.2	32.53	32.0
11248	AGC420325	181.5474	-52.0827	300.8808	-30.8298	2374	2188	6.4	0.42	193	2.319	/	/	13.31	13.39	/	/	-18.54	/	/	31.93	24.4
11255	UGC02444	170.2165	-44.5892	312.3998	-27.4645	6714	6619	3.5	0.61	361	2.651	13.06	12.86	12.97	13.05	13.33	-21.68	-21.78	35.11	105.2	34.97	98.6
11282	UGC02411	130.6540	14.8188	14.1337	8.0783	2538	2460	8.2	0.20	306	2.486	13.02	11.93	12.65	12.60	12.62	-20.18	-20.17	32.82	36.6	32.79	36.1
11306	UGC02454	169.5079	-43.7079	313.5255	-27.2753	7623	7562	6.3	0.23	359	2.558	13.93	13.31	14.02	14.06	14.04	-20.84	-20.88	34.97	98.7	35.08	103.7
11350	AGC120852	171.2062	-44.7602	311.9436	-28.0659	8406	8379	4.1	0.70	188	2.412	14.20	14.25	14.67	14.79	14.89	-19.50	-19.45	34.46	77.9	34.33	73.4
11359	AGC420340	201.1734	-58.6301	286.0800	-33.9344	2286	2120	4.1	0.21	293	2.468	12.51	12.21	12.68	12.73	12.83	-20.01	-19.99	32.86	37.4	32.75	35.4
11365	PG0011365	191.8464	-55.8838	292.8698	-33.0140	8972	8988	1.3	0.62	416	2.716	/	/	12.80	12.93	/	/	-22.42	/	/	35.52	127.1
11368	UGC02459	143.6729	-8.5556	352.1271	-7.1391	2469	2318	7.9	0.20	318	2.502	13.03	12.06	12.33	12.29	12.55	-20.33	-20.33	32.90	38.0	32.65	33.8
11403	UGC02475	145.7781	-12.0822	348.7565	-9.5064	2529	2371	5.9	0.45	252	2.442	11.80	11.51	12.18	12.22	12.22	-19.78	-19.74	32.01	25.2	31.97	24.8
11479	NGC001187	212.0911	-60.0562	279.2434	-35.0275	1389	1229	5.0	0.71	263	2.567	9.90	10.06	10.44	10.53	10.66	-20.92	-20.96	31.57	20.7	31.49	19.9
11521	UGC02503	145.4277	-10.6334	350.1915	-9.0467	2386	2231	2.6	0.62	450	2.751	9.87	9.61	10.28	10.33	10.33	-22.59	-22.76	32.94	38.8	33.12	42.1
11538	AGC022291	216.9322	-60.3273	276.3183	-35.4182	1723	1572	8.8	0.58	104	2.097	/	/	14.96	15.07	/	/	-16.37	/	/	31.44	19.4
11574	UGC002511	144.5979	-8.9313	351.8343	-8.0840	3860	3733	2.2	0.29	381	2.591	/	/	12.48	12.46	/	/	-21.20	/	/	33.71	55.3
11606	E300-009	245.6969	-59.6393	258.8290	-34.8810	6075	6048	3.7	0.34	307	2.506	13.99	13.86	14.68	14.77	14.68	-20.36	-20.37	35.14	106.5	35.30	114.7
11617	NGC1186	147.5468	-13.5375	347.4084	-11.3324	2742	2587	4.5	0.40	421	2.653	10.60	10.27	11.03	11.08	11.03	-21.70	-21.81	32.75	35.5	32.91	38.2
11679	UGC02540	151.3839	-19.1049	341.8737	-15.2754	3926	3782	2.1	0.55	411	2.683	/	/	12.81	12.86	/	/	-22.10	/	/	35.10	104.7
11744	PG0011744	197.3573	-55.4794	290.3340	-35.3404	1573	1405	1.0	0.47	107	2.075	/	/	13.73	13.83	/	/	-16.16	/	/	29.98	9.9

PGC	Name	l	b	sgl	sgb	v_{hel}	v_{mod}	t	b/a	w_{mx}	$logw^i_{mx}$	I	I^*	[3.6]	$[3.6]^*$	$C_{[3.6]}$	M_C	$M_{[3.6]}$	μ_C	d_C	$\mu_{[3.6]}$	$d_{[3.6]}$
11750	IC0001892	213.1263	-58.8086	279.1064	-36.3769	2883	2746	7.7	0.67	173	2.360	12.85	13.03	13.81	13.91	13.83	-19.04	-18.94	32.88	37.7	32.88	37.7
11767	PGC011767	187.6387	-51.7392	298.5327	-34.0399	8712	8722	1.1	0.30	412	2.627	/	/	13.26	13.35	/	/	-21.55	/	/	35.03	101.3
11782	AGC430066	192.1568	-53.4905	294.7149	-34.8627	3119	2965	1.1	0.40	291	2.493	/	/	13.40	13.46	/	/	-20.24	/	/	33.76	56.6
11793	UGC02519	128.8162	18.8736	18.1103	10.1075	2344	2281	5.9	0.61	228	2.448	11.93	11.69	12.19	12.24	12.33	-19.84	-19.80	32.17	27.2	32.05	25.7
11809	AGC022360	203.9821	-56.8758	285.5948	-36.2068	2015	1859	7.9	0.20	123	2.090	/	/	16.69	16.78	/	/	-16.30	/	/	33.12	42.0
11812	ES300-014	248.0576	-58.4621	256.8871	-35.4634	956	846	8.9	0.48	124	2.142	11.83	12.04	12.93	13.02	12.88	-17.05	-16.81	29.94	9.7	29.83	9.3
11836	NGC001249	268.2131	-53.4145	242.4896	-32.4487	1072	999	6.0	0.40	217	2.365	10.97	11.00	11.90	11.97	11.84	-19.09	-19.00	30.93	15.3	30.97	15.6
11846	UGC02567	149.4207	-14.8608	346.1701	-13.2265	2992	2842	7.4	0.45	276	2.481	12.35	12.14	12.54	12.60	12.73	-20.14	-20.13	32.89	37.8	32.75	35.4
11851	AGC022377	212.1415	-58.2222	279.9442	-36.7716	1324	1172	5.7	0.20	246	2.391	11.66	11.45	12.22	12.27	12.22	-19.32	-19.24	31.54	20.3	31.52	20.1
11856	ES357-007	232.8664	-59.5019	266.5262	-36.6523	1117	988	9.0	0.30	125	2.109	13.35	13.52	14.75	14.79	14.50	-16.75	-16.49	31.25	17.8	31.28	18.0
11941	NGC001233	150.6084	-15.8521	345.2094	-14.4198	4389	4266	3.0	0.41	419	2.652	12.05	11.70	12.11	12.16	12.30	-21.70	-21.80	34.04	64.3	34.03	64.0
12007	NGC001255	218.6023	-58.2626	275.8095	-37.6142	1685	1547	4.0	0.61	221	2.438	9.99	10.14	11.06	11.15	11.00	-19.74	-19.70	30.74	14.1	30.86	14.8
12011	ES481-014	217.6176	-58.1286	276.4854	-37.6406	1733	1594	8.9	0.20	158	2.199	12.83	12.85	14.17	14.25	13.90	-17.57	-17.37	31.46	19.6	31.62	21.1
12041	NGC01253	183.6907	-48.1171	303.8730	-34.1838	1709	1536	5.9	0.37	293	2.491	10.77	10.58	11.53	11.53	11.41	-20.22	-20.22	31.64	21.3	31.75	22.4
12080	UGC02609	151.8399	-16.8011	344.2766	-15.6387	4951	4842	3.1	0.65	337	2.638	12.56	12.24	12.55	12.60	12.79	-21.57	-21.66	34.42	76.6	34.35	74.1
12130	P0012130	187.3351	-49.3849	300.9017	-35.3770	2314	2153	2.3	0.28	273	2.444	12.18	11.95	12.79	12.84	12.75	-19.80	-19.77	32.57	32.6	32.63	33.6
12132	UGC02617	150.3132	-14.1749	346.9230	-14.0520	4698	4588	6.3	0.40	278	2.473	12.48	12.22	13.02	13.09	13.01	-20.06	-20.05	33.10	41.6	33.17	43.1
12181	AGC022447	237.3039	-58.0192	263.3664	-37.7268	1568	1456	7.0	0.71	123	2.231	12.65	12.88	13.63	13.68	13.64	-17.87	-17.69	31.51	20.0	31.36	18.7
12227	UGC02637	152.1862	-16.4105	344.6944	-15.9567	5146	5045	6.1	0.20	274	2.438	13.99	13.18	13.49	13.50	13.71	-19.74	-19.70	33.48	49.7	33.23	44.3
12285	AGC022455	222.4210	-57.5238	273.4004	-38.6501	1367	1237	5.0	0.41	227	2.388	11.28	11.31	12.02	12.10	12.06	-19.29	-19.22	31.36	18.7	31.32	18.3
12333	UGC02655	149.4392	-11.9223	349.1833	-13.0664	6190	6128	6.3	0.38	295	2.495	12.81	12.48	13.18	13.25	13.22	-20.26	-20.26	33.52	50.5	33.56	51.4
12390	IC0001914	261.4893	-53.8953	246.1978	-35.0162	1028	952	6.9	0.58	192	2.362	11.89	12.03	13.10	13.19	12.96	-19.06	-18.97	32.02	25.4	32.16	27.0
12404	AGC022474	231.4916	-57.5849	267.1729	-38.6340	1449	1331	3.4	0.21	157	2.197	13.21	13.24	14.10	14.13	14.04	-17.55	-17.35	31.60	20.9	31.48	19.8
12466	NGC001299	189.2036	-48.9898	300.3253	-36.5728	2335	2181	3.0	0.51	218	2.395	12.01	12.06	12.52	12.61	12.70	-19.35	-19.28	32.06	25.8	31.90	24.0
12484	AGC022479	220.4563	-56.8997	274.8611	-39.1281	1749	1622	6.9	0.33	115	2.076	14.31	14.52	15.30	15.40	15.32	-16.46	-16.17	31.77	22.6	31.58	20.7
12608	PG0012608	202.6316	-53.3409	288.7123	-38.8491	2003	1860	9.0	0.50	123	2.144	/	/	15.28	15.37	/	/	-16.83	/	/	32.21	27.7
12737	AGC022540	212.3081	-54.8415	281.2632	-39.9917	1588	1455	4.0	0.33	334	2.540	10.51	10.34	11.27	11.32	11.19	-20.68	-20.70	31.87	23.6	32.04	25.5
12798	AGC430249	204.0059	-52.7750	288.1856	-39.7636	1874	1736	7.6	0.20	215	2.332	12.73	12.55	13.39	13.45	13.36	-18.79	-18.67	32.15	26.9	32.13	26.7
12807	IC0001933	265.5352	-51.6332	242.1384	-34.8446	1061	1000	6.2	0.51	172	2.291	11.76	11.90	12.70	12.79	12.70	-18.41	-18.27	31.11	16.7	31.06	16.3
12816	UGC002730	151.9878	-13.2516	347.9655	-15.6280	3767	3647	3.1	0.20	451	2.654	12.78	11.99	12.46	12.46	12.59	-21.71	-21.82	34.37	74.7	34.37	74.8
12889	AGC022597	212.1621	-54.0443	281.7242	-40.7123	1683	1555	7.7	0.20	167	2.223	13.19	13.16	14.05	14.13	14.00	-17.79	-17.60	31.79	22.8	31.73	22.2
12916	AGC430266	193.5410	-48.5182	298.3286	-39.0035	1239	1089	6.0	0.25	244	2.393	10.81	10.60	11.68	11.73	11.52	-19.33	-19.26	30.85	14.8	30.99	15.8
12952	NGC1351A	236.3571	-55.6165	263.3691	-40.1847	1352	1251	4.2	0.23	200	2.304	12.31	12.24	12.82	12.89	12.93	-18.52	-18.39	31.45	19.5	31.28	18.0
13059	NGC1350	233.6122	-55.1679	265.2873	-40.8965	1903	1806	1.9	0.47	390	2.636	9.11	9.06	9.84	9.86	9.82	-21.55	-21.64	31.37	18.8	31.50	20.0
13089	ES418-008	227.6614	-54.9310	269.7768	-41.3884	1191	1082	7.7	0.71	121	2.226	12.79	13.04	13.76	13.81	13.78	-17.82	-17.64	31.60	20.9	31.44	19.4
13090	IC0001954	263.6451	-51.2013	242.7240	-36.0058	1063	1005	3.2	0.53	213	2.392	10.52	10.64	11.18	11.26	11.31	-19.33	-19.26	30.64	13.4	30.52	12.7

PGC	Name	l	b	sgl	sgb	v_{hel}	v_{mod}	t	b/a	w_{mx}	$logw^{i}_{mx}$	I	I^{*}	[3.6]	$[3.6]^{*}$	$C_{[3.6]}$	M_{C}	$M_{[3.6]}$	μ_{C}	d_{C}	$\mu_{[3.6]}$	$d_{[3.6]}$
13108	NGC01353	212.0339	-52.9290	282.3354	-41.7313	1535	1411	3.2	0.41	378	2.609	10.16	10.03	10.66	10.72	10.74	-21.30	-21.38	32.04	25.6	32.10	26.4
13154	ES482-005	217.4728	-53.6064	277.8917	-42.0330	1916	1802	7.7	0.20	155	2.190	/	/	15.11	15.19	/	/	-17.28	/	/	32.49	31.5
13163	IC0001959	261.2809	-51.5385	244.3128	-36.8163	639	577	8.5	0.26	119	2.082	12.10	12.29	13.33	13.37	13.18	-16.50	-16.22	29.68	8.6	29.59	8.3
13171	IC0001952	216.8244	-53.4151	278.4576	-42.1272	1814	1699	4.0	0.37	239	2.402	11.68	11.65	12.34	12.41	12.39	-19.41	-19.35	31.81	23.0	31.76	22.5
13255	NGC001367	218.9543	-53.3471	276.8028	-42.4746	1462	1349	1.1	0.64	382	2.688	9.49	9.55	10.25	10.33	10.30	-22.02	-22.14	32.33	29.2	32.49	31.5
13283	AGC022735	213.1896	-52.2760	281.7463	-42.5848	1809	1693	7.8	0.22	149	2.175	13.40	13.45	14.62	14.70	14.42	-17.35	-17.14	31.78	22.7	31.84	23.4
13304	ES482-011	220.1531	-53.2082	275.8801	-42.7428	1593	1484	4.6	0.31	124	2.106	/	/	14.24	14.33	/	/	-16.47	/	/	30.80	14.4
13368	NGC001385	218.4606	-52.7084	277.3761	-43.0394	1501	1390	5.9	0.63	173	2.339	10.05	10.23	10.65	10.75	10.85	-18.84	-18.74	29.70	8.7	29.48	7.9
13400	UGC02798	153.7726	-11.6961	349.6803	-17.2869	4942	4863	3.8	0.37	411	2.638	12.11	11.61	12.34	12.38	12.35	-21.56	-21.65	33.96	62.0	34.11	66.3
13410	UGC02801	153.6067	-11.4309	349.9483	-17.1102	6012	5963	5.7	0.21	390	2.592	13.65	12.86	13.14	13.15	13.38	-21.15	-21.21	34.59	82.9	34.46	77.8
13458	NGC001406	229.7850	-53.3358	268.0303	-42.9429	1067	969	4.4	0.22	322	2.510	10.67	10.38	10.81	10.80	10.95	-20.40	-20.41	31.35	18.7	31.20	17.4
13561	ES482-035	217.7425	-51.7159	278.2693	-43.9103	1880	1777	2.2	0.63	185	2.370	11.97	12.14	12.91	13.00	12.93	-19.13	-19.04	32.06	25.9	32.05	25.8
13569	AGC022861	214.4370	-51.0788	281.2658	-43.9664	1639	1530	2.3	0.25	143	2.160	12.44	12.52	13.08	13.16	13.20	-17.22	-16.99	30.42	12.2	30.16	10.7
13602	AGC022873	227.5201	-52.5993	269.8739	-43.7205	1512	1418	3.2	0.46	354	2.592	9.87	9.83	10.71	10.73	10.64	-21.15	-21.21	31.79	22.8	31.95	24.5
13620	NGC001421	202.8026	-47.8797	292.5941	-43.4656	2078	1962	4.1	0.27	344	2.544	10.42	10.09	10.74	10.78	10.80	-20.71	-20.74	31.51	20.0	31.52	20.1
13631	AGC022880	208.4120	-49.4385	287.0836	-44.0179	1722	1609	4.2	0.51	143	2.212	/	/	15.44	15.52	/	/	-17.50	/	/	33.04	40.6
13646	AGC430438	202.1100	-47.5314	293.3955	-43.4811	2163	2048	4.8	0.20	358	2.554	11.85	11.38	11.78	11.80	11.96	-20.80	-20.84	32.77	35.9	32.66	34.0
13684	PG0013684	206.4259	-48.6805	289.1776	-44.0720	1214	1096	8.1	0.50	175	2.297	/	/	13.80	13.88	/	/	-18.32	/	/	32.22	27.8
13687	NGC01436	237.3503	-52.5847	261.7197	-43.0149	1393	1312	2.0	0.66	201	2.419	10.61	10.79	11.32	11.37	11.44	-19.57	-19.51	31.01	15.9	30.88	15.0
13695	ES015-001	294.7818	-34.1184	214.3548	-22.1978	1648	1676	9.8	0.37	120	2.102	13.35	13.45	14.66	14.75	14.45	-16.69	-16.42	31.14	16.9	31.17	17.2
13716	AGC430459	204.2133	-47.9153	291.4794	-43.9621	1580	1463	4.0	0.31	289	2.474	11.72	11.52	12.22	12.27	12.25	-20.07	-20.05	32.33	29.3	32.33	29.3
13727	NGC1448	251.5220	-51.3942	250.3258	-40.6853	1169	1106	6.0	0.20	388	2.589	9.76	9.33	10.03	10.00	10.03	-21.12	-21.18	31.15	17.0	31.18	17.2
13794	NGC1437B	238.1588	-52.1100	260.9031	-43.3538	1506	1429	8.9	0.32	111	2.060	12.24	12.46	12.97	13.07	13.13	-16.31	-16.01	29.43	7.7	29.08	6.5
13809	AGC022940	235.8582	-52.0392	262.7796	-43.7472	1927	1852	7.7	0.26	285	2.461	10.72	10.54	11.21	11.27	11.27	-19.95	-19.93	31.22	17.5	31.20	17.4
13821	P0013821	207.5967	-48.2141	288.5422	-44.8562	1253	1141	8.9	0.44	140	2.184	11.65	11.76	12.09	12.17	12.33	-17.43	-17.22	29.77	9.0	29.40	7.6
13871	ES549-018	214.8391	-49.5248	281.5966	-45.5239	1587	1487	4.8	0.57	223	2.424	11.69	11.74	12.49	12.57	12.51	-19.62	-19.56	32.13	26.7	32.14	26.8
13884	UGC02868	159.1528	-14.9806	346.3732	-22.6285	5426	5367	4.0	0.22	386	2.588	13.57	12.85	13.34	13.36	13.47	-21.12	-21.17	34.66	85.4	34.64	84.8
13912	IC0002000	257.6482	-49.6042	244.8306	-39.7989	980	931	6.2	0.20	255	2.407	11.30	11.09	12.08	12.13	11.96	-19.46	-19.40	31.42	19.2	31.52	20.2
13926	AGC022986	223.3077	-50.5292	273.6943	-45.6605	1526	1437	5.1	0.20	215	2.332	12.34	12.21	13.03	13.09	13.00	-18.79	-18.67	31.79	22.8	31.77	22.5
13931	ES054-021	286.3376	-39.2291	221.3728	-27.8091	1430	1438	7.9	0.52	193	2.344	11.14	11.21	12.34	12.42	12.17	-18.89	-18.79	31.06	16.3	31.21	17.5
13998	E359-003	233.5517	-50.8150	264.4584	-45.2073	1577	1503	1.4	0.38	112	2.074	12.73	12.95	14.31	14.42	14.03	-16.43	-16.14	30.46	12.4	30.56	13.0
13999	IC0002051	297.8127	-31.3858	211.1477	-19.9599	1716	1755	4.1	0.56	341	2.607	10.35	10.24	10.65	10.72	10.84	-21.28	-21.35	32.13	26.7	32.07	26.0
14071	NGC001484	239.0863	-50.4155	259.4875	-44.8284	1041	973	3.2	0.25	162	2.214	12.24	12.28	13.13	13.21	13.10	-17.71	-17.52	30.81	14.5	30.73	14.0
14099	AGC023045	214.0012	-47.6735	283.2209	-47.0974	1821	1731	6.0	0.71	115	2.204	/	/	15.41	15.51	/	/	-17.42	/	/	32.95	39.0
14169	NGC001494	257.1704	-48.2279	243.9611	-41.0458	1130	1090	7.0	0.57	156	2.268	11.20	11.40	12.08	12.17	12.15	-18.20	-18.05	30.35	11.7	30.22	11.1
14236	NGC001511	281.3718	-40.7246	224.3524	-30.9673	1327	1330	1.8	0.34	273	2.455	10.45	10.31	10.55	10.60	10.83	-19.90	-19.87	30.73	14.0	30.47	12.4

PGC	Name	l	b	sgl	sgb	v_{hel}	v_{mod}	t	b/a	w_{mx}	$logw^{i}_{mx}$	I	I^{*}	[3.6]	$[3.6]^{*}$	$C_{[3.6]}$	M_{C}	$M_{[3.6]}$	μ_{C}	d_{C}	$\mu_{[3.6]}$	$d_{[3.6]}$
14246	UGC02915	162.7252	-15.3291	346.0000	-26.0774	5304	5255	6.1	0.21	287	2.459	14.52	13.91	14.38	14.41	14.52	-19.93	-19.90	34.52	80.3	34.41	76.0
14276	UGC02920	161.1948	-13.4309	348.0934	-24.5870	4184	4110	6.0	0.20	364	2.561	13.12	12.43	13.22	13.23	13.19	-20.87	-20.91	34.11	66.3	34.22	69.9
14286	UGC02906	135.0444	15.8601	15.5434	3.9497	2492	2433	3.0	0.59	445	2.732	11.25	10.92	11.47	11.51	11.58	-22.42	-22.58	34.05	64.6	34.17	68.2
14370	AGC130364	136.8383	14.2434	14.1059	2.0645	4512	4487	5.0	0.28	311	2.502	/	/	13.90	13.93	/	/	-20.33	/	/	34.35	74.0
14391	NGC001512	248.6680	-48.1658	250.1794	-44.4003	900	854	1.1	0.67	234	2.487	9.26	9.42	9.98	10.02	10.08	-20.19	-20.18	30.28	11.4	30.21	11.0
14397	NGC001515	264.0947	-45.8511	237.4179	-39.3364	1182	1159	4.0	0.25	368	2.571	9.79	9.49	10.32	10.36	10.28	-20.96	-21.00	31.24	17.7	31.36	18.7
14409	UGC02947	193.0645	-37.5576	309.9312	-45.8863	865	761	8.5	0.24	172	2.240	11.52	11.31	12.15	12.20	12.11	-17.94	-17.77	30.05	10.2	29.96	9.8
14468	UGC02956	164.7201	-15.3449	345.9567	-28.0009	4542	4482	5.9	0.32	329	2.532	13.26	12.56	13.06	13.06	13.17	-20.60	-20.62	33.81	57.9	33.74	56.0
14475	AGC023188	216.3313	-45.3069	282.0549	-49.8497	923	845	8.2	0.34	157	2.213	10.98	11.04	11.80	11.88	11.82	-17.70	-17.50	29.51	8.0	29.38	7.5
14514	AGC023201	211.2105	-43.6814	288.2610	-50.0339	1833	1758	3.0	0.33	186	2.286	12.04	12.07	12.81	12.89	12.84	-18.36	-18.22	31.20	17.4	31.11	16.7
14600	AGC440044	199.4885	-38.8377	303.6357	-48.8818	2930	2860	6.8	0.20	200	2.301	/	/	14.06	14.12	/	/	-18.37	/	/	32.50	31.6
14626	AGC440053	210.3742	-42.6127	289.8634	-50.7197	1877	1806	8.8	0.24	178	2.254	/	/	14.95	15.02	/	/	-17.91	/	/	32.96	39.1
14638	NGC001532	233.1684	-46.5841	263.8717	-49.4270	1201	1149	3.1	0.31	518	2.728	8.75	8.42	8.98	9.01	9.08	-22.39	-22.54	31.47	19.6	31.55	20.5
14651	UGC02982	186.7401	-31.5021	321.0918	-44.4808	5318	5291	2.0	0.51	368	2.622	/	/	11.78	11.81	/	/	-21.51	/	/	33.35	46.8
14693	UGC02988	170.1788	-18.3173	342.2281	-33.0830	3822	3755	3.0	0.20	446	2.649	/	/	11.95	11.89	/	/	-21.77	/	/	33.71	55.2
14768	AGC440077	211.6162	-41.7213	289.1860	-51.9291	1953	1890	7.6	0.35	168	2.245	/	/	14.28	14.36	/	/	-17.82	/	/	32.19	27.4
14780	PG0014780	206.3935	-39.8955	296.1810	-51.5012	8914	9043	3.1	0.37	414	2.640	/	/	13.31	13.41	/	/	-21.68	/	/	35.24	111.9
14814	NGC001559	274.5105	-41.1983	227.3292	-35.5354	1302	1307	5.9	0.51	242	2.442	9.78	9.84	10.18	10.21	10.39	-19.78	-19.74	30.17	10.8	29.95	9.8
14853	UGC03009	170.5286	-16.9461	343.8363	-33.5122	3750	3690	5.7	0.22	248	2.396	13.52	12.88	13.85	13.86	13.73	-19.37	-19.30	33.12	42.0	33.20	43.6
14897	NGC001566	264.3102	-43.3932	234.7922	-40.7595	1504	1499	4.0	0.65	196	2.403	8.67	8.85	9.30	9.35	9.46	-19.42	-19.36	28.89	6.0	28.70	5.5
14936	ES550-024	218.6140	-42.3113	280.8271	-53.1817	898	841	6.7	0.38	168	2.250	11.23	11.32	12.56	12.64	12.33	-18.03	-17.86	30.36	11.8	30.51	12.6
15018	UGC03013	135.2231	17.7646	17.4601	3.9592	2459	2411	3.0	0.55	316	2.568	10.15	9.99	10.46	10.52	10.62	-20.93	-20.97	31.55	20.4	31.49	19.9
15047	UGC03028	165.5878	-10.8111	351.1148	-28.8329	5482	5471	4.4	0.40	417	2.649	/	/	11.81	11.82	/	/	-21.77	/	/	33.64	53.6
15263	UGC03048	139.3218	14.8583	14.9810	-0.2574	3050	3008	4.0	0.68	257	2.536	/	/	12.24	12.29	/	/	-20.66	/	/	32.98	39.5
15355	UGC03066	189.8455	-27.7449	324.4350	-48.4944	4642	4628	6.5	0.67	314	2.617	12.43	12.10	12.45	12.50	12.67	-21.38	-21.46	34.10	66.0	34.03	64.0
15356	UGC003070	197.1546	-31.8377	313.9503	-51.9743	2518	2470	3.1	0.51	156	2.251	13.14	13.25	14.36	14.45	14.20	-18.05	-17.88	32.25	28.2	32.34	29.4
15455	ES202-035	256.7618	-42.5516	238.9908	-45.4297	1877	1880	3.5	0.20	275	2.439	11.84	11.58	12.51	12.56	12.43	-19.76	-19.72	32.19	27.4	32.29	28.7
15461	UGC03078	167.1959	-10.0659	352.0157	-30.3961	5419	5417	4.0	0.30	417	2.631	13.05	11.96	12.38	12.35	12.52	-21.51	-21.59	34.08	65.4	34.01	63.4
15481	UGC03084	185.7442	-24.5550	330.7620	-46.1794	4062	4034	5.8	0.20	322	2.508	13.05	12.22	12.91	12.90	12.92	-20.38	-20.39	33.33	46.3	33.33	46.3
15533	UGC03089	180.3154	-20.3791	338.1026	-42.3075	4603	4586	3.9	0.60	308	2.577	/	/	12.66	12.70	/	/	-21.06	/	/	33.82	57.9
15638	UGC03103	196.1557	-29.6695	317.6689	-52.4746	3514	3489	4.5	0.30	427	2.642	10.95	10.60	11.39	11.43	11.37	-21.60	-21.69	32.99	39.7	33.16	42.9
15693	UGC003092	138.3285	16.6023	16.6060	0.8893	4784	4784	6.4	0.20	307	2.487	14.10	13.57	13.86	13.89	14.10	-20.19	-20.18	34.36	74.3	34.16	67.9
15793	UGC03114	142.9674	13.1636	13.7317	-3.9754	3723	3697	5.8	0.39	361	2.584	12.47	11.92	12.54	12.56	12.60	-21.08	-21.14	33.72	55.5	33.75	56.3
15810	UGC03110	137.3263	17.6309	17.5260	1.9522	4487	4482	5.9	0.40	409	2.641	11.72	11.36	11.99	12.04	12.06	-21.59	-21.68	33.69	54.6	33.79	57.2
15869	P0015869	205.1376	-32.1864	305.8485	-56.8538	2524	2501	8.0	0.62	188	2.371	/	/	13.99	14.08	/	/	-19.05	/	/	33.16	42.8
15924	UGC03148	180.6151	-17.2412	342.2598	-43.0774	4733	4735	3.5	0.51	347	2.597	/	/	12.87	12.87	/	/	-21.26	/	/	34.21	69.4

PGC	Name	l	b	sgl	sgb	v_{hel}	v_{mod}	t	b/a	w_{mx}	$logw^{i}_{mx}$	I	I^{*}	[3.6]	$[3.6]^{*}$	$C_{[3.6]}$	M_{C}	$M_{[3.6]}$	μ_{C}	d_{C}	$\mu_{[3.6]}$	$d_{[3.6]}$
15967	UGC03137	135.2257	19.5512	19.2437	4.1222	993	942	4.4	0.22	225	2.354	12.33	12.01	12.93	12.96	12.84	-18.98	-18.88	31.82	23.1	31.84	23.4
15982	UGC03161	196.8935	-27.1371	320.7385	-54.3422	8786	8946	5.9	0.20	499	2.698	/	/	13.91	13.96	/	/	-22.25	/	/	36.47	196.7
15986	UGC03143	140.5232	15.7830	16.0359	-1.2989	4560	4557	6.0	0.20	329	2.517	13.77	13.19	13.52	13.55	13.73	-20.47	-20.48	34.26	71.0	34.10	66.1
16027	UGC03147	138.3092	17.5194	17.5157	1.0086	2884	2851	4.0	0.49	247	2.443	/	/	13.07	13.12	/	/	-19.76	/	/	32.91	38.1
16033	UGC03172	189.6003	-22.4681	332.1194	-50.1841	4732	4745	6.7	0.20	343	2.535	/	/	13.41	13.44	/	/	-20.65	/	/	34.17	68.4
16084	ES421-019	230.0780	-38.1368	265.9689	-58.0884	1477	1473	9.0	0.72	131	2.267	/	/	13.12	13.22	/	/	-18.03	/	/	31.25	17.8
16092	UGC03167	145.7298	12.1850	13.1215	-6.7775	4736	4737	4.0	0.35	437	2.660	13.27	12.35	12.05	12.03	12.57	-21.77	-21.87	34.40	75.9	33.97	62.4
16118	AGC440373	208.8478	-31.8257	301.7928	-59.1819	4479	4505	4.0	0.51	218	2.394	13.57	13.58	14.27	14.36	14.33	-19.35	-19.28	33.72	55.4	33.69	54.8
16120	AGC023772	233.5623	-38.5519	261.0207	-57.2841	1052	1049	9.4	0.68	129	2.236	10.94	11.17	11.77	11.82	11.85	-17.91	-17.74	29.77	9.0	29.56	8.1
16144	IC002098	203.4248	-29.2359	311.6897	-57.8257	2820	2811	5.8	0.20	323	2.509	12.70	12.31	12.50	12.54	12.80	-20.39	-20.40	33.22	44.0	32.97	39.3
16191	UGC03186	194.7613	-24.4437	326.3258	-53.8775	4578	4597	6.1	0.20	240	2.380	14.40	14.14	14.79	14.86	14.86	-19.22	-19.14	34.13	67.1	34.08	65.3
16199	ES361-015	235.1864	-38.3533	258.6478	-57.1928	1169	1170	6.7	0.24	181	2.261	12.01	11.98	13.05	13.12	12.90	-18.14	-17.98	31.04	16.1	31.10	16.6
16299	ES085-014	272.8853	-37.1483	223.4515	-38.4335	1407	1440	9.0	0.38	173	2.263	/	/	13.24	13.32	/	/	-17.99	/	/	31.31	18.3
16317	AGC023849	240.5241	-38.3956	251.5081	-55.7826	2317	2337	1.1	0.35	111	2.065	/	/	14.07	14.18	/	/	-16.06	/	/	30.24	11.2
16322	P0016322	202.6879	-27.6629	314.7681	-58.3198	3850	3865	3.6	0.20	374	2.573	12.29	11.84	12.37	12.41	12.49	-20.97	-21.02	33.50	50.0	33.48	49.7
16359	UGC03207	196.8060	-24.3019	325.1537	-55.6186	4563	4590	3.1	0.36	497	2.718	11.71	11.37	12.09	12.15	12.11	-22.30	-22.44	34.48	78.6	34.70	87.1
16360	UGC03205	172.9608	-8.2063	354.4323	-36.0326	3588	3577	2.0	0.41	417	2.651	/	/	12.02	11.99	/	/	-21.79	/	/	33.85	58.8
16420	UGC03214	199.2164	-25.0833	322.0349	-57.1772	4910	4951	3.0	0.28	547	2.746	11.45	10.91	11.47	11.51	11.57	-22.55	-22.72	34.18	68.6	34.31	72.9
16423	UGC03203	142.6457	15.5197	16.0318	-3.3596	882	834	5.0	0.59	216	2.418	10.57	10.49	11.03	11.09	11.15	-19.57	-19.51	30.72	13.9	30.60	13.2
16502	AGC023914	223.1000	-34.1251	277.5231	-61.9157	1764	1771	8.9	0.42	142	2.186	/	/	15.45	15.55	/	/	-17.24	/	/	32.81	36.4
16517	AGC023923	226.9930	-35.0221	270.6428	-61.2957	741	745	6.7	0.41	187	2.302	10.53	10.58	11.67	11.74	11.51	-18.51	-18.38	30.02	10.1	30.12	10.6
16537	UGC03218	147.8877	12.1810	13.4227	-8.8657	5228	5251	3.1	0.59	495	2.779	/	/	11.47	11.49	/	/	-23.03	/	/	34.63	84.4
16600	NGC01752	207.7621	-28.0084	308.2969	-61.4405	3577	3601	4.9	0.30	437	2.652	11.25	10.76	11.48	11.51	11.50	-21.69	-21.80	33.22	44.0	33.35	46.8
16646	UGC03237	199.2310	-23.4962	324.6111	-57.9587	4194	4226	5.8	0.23	290	2.465	13.44	13.06	13.48	13.54	13.67	-19.99	-19.97	33.69	54.8	33.55	51.4
16654	NGC01762	198.3946	-23.0014	326.0921	-57.5004	4753	4798	5.1	0.70	420	2.764	11.60	11.60	11.98	12.08	12.21	-22.71	-22.89	35.01	100.3	35.11	105.1
16709	AGC024019	241.6956	-36.4527	248.4812	-57.1408	1208	1231	4.0	0.48	296	2.519	9.05	9.05	9.34	9.41	9.60	-20.49	-20.50	30.08	10.4	29.91	9.6
16716	AGC450011	211.8854	-28.8405	301.1765	-63.1435	2316	2329	4.8	0.59	324	2.593	10.40	10.29	10.72	10.78	10.90	-21.16	-21.22	32.07	25.9	32.01	25.2
16761	NGC001824	268.7876	-36.2523	224.3315	-41.7715	1248	1287	8.9	0.29	146	2.175	11.97	12.05	13.04	13.12	12.94	-17.35	-17.13	30.29	11.4	30.25	11.2
16779	NGC1808	241.2119	-35.9016	248.6686	-57.8086	996	1021	1.2	0.51	271	2.490	8.80	8.83	8.88	8.95	9.26	-20.21	-20.21	29.47	7.8	29.16	6.8
16790	ES305-009	242.2024	-35.9414	247.3729	-57.4047	1021	1047	8.0	0.64	105	2.129	12.76	12.99	13.72	13.81	13.76	-16.94	-16.69	30.70	13.8	30.50	12.6
16858	UGC03250	147.7788	13.6298	14.8560	-8.5443	4529	4541	3.1	0.66	431	2.750	/	/	11.94	11.99	/	/	-22.75	/	/	34.87	94.0
16878	AGC024102	220.7268	-30.5405	283.6307	-64.9889	1968	1992	5.0	0.26	146	2.171	14.26	14.32	15.83	15.92	15.46	-17.32	-17.10	32.79	36.2	33.05	40.7
16911	NGC001853	265.8320	-35.8171	225.4160	-44.0674	1411	1455	7.1	0.54	192	2.348	12.21	12.34	12.82	12.91	12.99	-18.93	-18.83	31.92	24.2	31.74	22.3
16957	AGC150027	148.5212	13.6572	14.9948	-9.2531	112	74	9.9	0.42	114	2.090	/	/	11.67	11.70	/	/	-16.31	/	/	28.01	4.0
16976	ES305-017	246.1697	-35.0449	241.4746	-56.4626	1071	1108	9.9	0.42	146	2.198	/	/	14.56	14.64	/	/	-17.36	/	/	32.00	25.2
16983	ES423-002	233.2987	-32.9519	259.0682	-62.8035	1468	1501	6.5	0.27	223	2.356	11.83	11.75	12.63	12.69	12.58	-19.00	-18.91	31.58	20.7	31.60	20.9

PGC	Name	l	b	sgl	sgb	v_{hel}	v_{mod}	t	b/a	w_{mx}	$logw^{i}_{mx}$	I	I*	[3.6]	[3.6]*	$C_{[3.6]}$	M_C	$M_{[3.6]}$	μ_C	d_C	$\mu_{[3.6]}$	$d_{[3.6]}$
17027	ES362-011	241.0785	-34.0774	247.2601	-59.4828	1344	1382	4.3	0.21	269	2.431	11.02	10.74	11.57	11.62	11.54	-19.68	-19.64	31.22	17.5	31.25	17.8
17031	UGC03275	195.5694	-17.5949	337.1888	-56.9799	7965	8135	4.0	0.22	498	2.699	13.26	12.51	13.36	13.39	13.31	-22.12	-22.25	35.55	128.7	35.85	148.0
17042	NGC001892	274.9174	-34.3164	219.3098	-38.0364	1359	1409	5.6	0.34	203	2.326	11.42	11.35	12.11	12.18	12.12	-18.73	-18.61	30.85	14.8	30.79	14.4
17056	AGC450046	217.0388	-27.5833	293.5767	-66.5837	2823	2865	5.0	0.25	349	2.548	12.11	11.73	12.38	12.41	12.43	-20.75	-20.78	33.20	43.7	33.23	44.2
17058	UGC03283	202.8723	-21.2899	325.2982	-61.9689	4494	4558	5.9	0.20	338	2.529	13.82	13.22	13.39	13.41	13.68	-20.57	-20.59	34.32	73.0	34.08	65.5
17104	UGC03253	128.9602	24.6827	24.0121	10.2562	4121	4121	3.0	0.54	335	2.589	12.16	12.11	12.69	12.77	12.80	-21.12	-21.18	33.97	62.3	34.03	64.0
17157	E362-019	241.1012	-33.1857	246.3925	-60.2611	1287	1330	8.9	0.24	132	2.125	13.12	13.21	14.55	14.63	14.27	-16.90	-16.65	31.16	17.1	31.28	18.0
17170	UGC03257	128.5560	24.9122	24.2310	10.6317	2193	2162	1.1	0.45	158	2.239	/	/	13.16	13.24	/	/	-17.76	/	/	31.00	15.9
17174	NGC01886	226.2527	-29.6357	272.4519	-66.6606	1754	1795	3.7	0.20	335	2.525	11.57	11.21	11.68	11.72	11.83	-20.54	-20.55	32.37	29.8	32.28	28.6
17229	AGC450056	219.4871	-26.8687	289.1691	-68.1245	3187	3246	4.8	0.47	269	2.475	12.70	12.67	13.30	13.38	13.39	-20.08	-20.07	33.50	50.1	33.50	50.1
17395	P0017395	213.4005	-22.3857	308.5865	-69.0295	2719	2778	2.1	0.29	266	2.435	12.47	12.07	12.51	12.54	12.67	-19.72	-19.68	32.40	30.1	32.22	27.8
17402	IC0002130	226.4029	-27.2417	272.4063	-69.0581	1827	1883	7.6	0.48	154	2.236	12.34	12.46	13.15	13.24	13.21	-17.90	-17.73	31.11	16.7	30.97	15.6
17433	AGC024358	241.0485	-30.6880	243.9095	-62.4580	1322	1381	5.9	0.20	226	2.354	11.34	11.15	11.77	11.83	11.85	-18.98	-18.88	30.83	14.7	30.71	13.9
17436	AGC024354	225.2750	-26.5018	275.4160	-69.7197	1660	1716	3.3	0.41	409	2.642	9.70	9.54	10.12	10.17	10.22	-21.60	-21.70	31.82	23.1	31.87	23.7
17456	UGC03319	142.7316	19.2279	19.7236	-2.9485	4216	4232	5.8	0.20	332	2.521	14.11	13.63	13.30	13.34	13.86	-20.50	-20.52	34.43	76.9	33.92	60.8
17475	AGC450071	213.4101	-21.4986	310.2808	-69.6855	7039	7215	5.1	0.20	305	2.484	14.59	13.94	14.77	14.81	14.73	-20.17	-20.16	34.99	99.6	35.11	105.1
17509	UGC03329	189.4015	-8.2302	354.7087	-52.3022	5265	5364	4.1	0.42	484	2.718	12.08	11.09	12.23	12.20	12.00	-22.29	-22.44	34.35	74.2	34.76	89.4
17513	AGC024404	222.1464	-24.5441	284.8134	-71.1000	2861	2935	5.4	0.20	195	2.290	14.16	14.00	15.04	15.10	14.90	-18.40	-18.26	33.33	46.3	33.40	48.0
17554	UGC03332	190.6391	-8.2703	354.6271	-53.5265	5821	5941	3.8	0.22	440	2.645	/	/	12.54	12.50	/	/	-21.73	/	/	34.32	73.2
17561	UGC03326	136.0141	22.6185	22.3729	3.6721	4089	4098	5.9	0.20	543	2.735	12.36	11.60	11.86	11.87	12.10	-22.45	-22.60	34.62	84.1	34.58	82.3
17657	NGC02049	234.7006	-27.0190	252.2106	-68.1579	2988	3079	1.0	0.49	418	2.671	11.44	11.36	12.15	12.23	12.15	-21.86	-21.98	34.06	65.0	34.29	72.2
17776	UGC03351	153.9928	15.0111	17.2765	-14.2478	4471	4513	2.0	0.20	451	2.654	/	/	11.60	11.58	/	/	-21.82	/	/	33.44	48.8
17810	IC2143	223.2536	-22.3771	283.4824	-73.4588	3051	3144	3.5	0.45	324	2.551	11.62	11.48	12.06	12.12	12.16	-20.77	-20.81	32.96	39.0	32.96	39.0
17819	AGC024538	239.4557	-27.4295	242.8462	-65.9712	921	995	4.6	0.45	277	2.483	9.75	9.73	10.42	10.48	10.46	-20.16	-20.15	30.62	13.3	30.63	13.4
17831	UGC03354	156.4512	13.9734	16.6877	-16.7817	3088	3107	2.0	0.33	396	2.614	12.07	11.57	11.64	11.66	11.99	-21.35	-21.42	33.36	47.1	33.12	42.1
17969	AGC024602	224.5973	-21.9770	279.4332	-74.1155	2369	2458	4.3	0.20	320	2.505	12.54	12.14	12.47	12.50	12.69	-20.36	-20.36	33.07	41.1	32.89	37.8
18000	IC002150	244.1417	-27.6348	235.1869	-63.3984	3117	3221	4.9	0.27	352	2.554	11.73	11.42	12.31	12.36	12.25	-20.80	-20.84	33.07	41.1	33.24	44.4
18047	AGC450098	223.0130	-20.7080	285.9415	-75.0050	3123	3226	5.0	0.64	298	2.581	11.19	11.22	11.75	11.84	11.89	-21.05	-21.10	32.96	39.1	32.97	39.2
18089	UGC03375	160.8445	13.0631	16.6589	-21.1489	5791	5887	5.2	0.44	490	2.728	11.52	11.07	11.81	11.86	11.82	-22.39	-22.54	34.27	71.4	34.49	79.2
18109	AGC150194	163.9581	11.6121	15.8276	-24.4306	5798	5900	5.0	0.65	295	2.580	/	/	13.02	13.09	/	/	-21.09	/	/	34.27	71.4
18147	AGC024702	225.6643	-20.4985	276.4926	-75.7253	2963	3072	3.1	0.29	424	2.638	11.34	10.97	11.84	11.88	11.78	-21.57	-21.66	33.38	47.3	33.59	52.2
18148	IC0002152	228.7453	-21.6483	265.1770	-74.6141	1866	1961	1.1	0.71	194	2.431	11.64	11.80	12.37	12.46	12.49	-19.68	-19.64	32.18	27.3	32.11	26.4
18161	UGC03379	145.3504	20.4404	21.2804	-5.2129	4114	4144	3.1	0.46	369	2.610	/	/	12.15	12.22	/	/	-21.38	/	/	33.66	53.9
18181	UGC03373	135.1949	23.9997	23.6849	4.5447	4758	4788	5.2	0.62	267	2.523	12.77	12.75	13.17	13.26	13.37	-20.52	-20.53	33.94	61.3	33.86	59.2
18369	AGC024782	226.5589	-19.1747	273.4389	-77.1211	2893	3011	6.6	0.20	270	2.431	13.25	12.92	13.76	13.81	13.72	-19.69	-19.64	33.44	48.7	33.50	50.1
18373	PG0018373	219.1517	-16.0231	309.0060	-77.3914	2216	2322	3.0	0.20	240	2.380	/	/	12.69	12.69	/	/	-19.14	/	/	31.84	23.3

PGC	Name	l	b	sgl	sgb	v_{hel}	v_{mod}	t	b/a	w_{mx}	$logw^i_{mx}$	I	I*	[3.6]	[3.6]*	$C_{[3.6]}$	M_C	$M_{[3.6]}$	μ_C	d_C	$\mu_{[3.6]}$	$d_{[3.6]}$
18394	ES005-004	299.2013	-27.7466	207.2105	-18.9980	1870	1930	2.8	0.20	413	2.616	10.92	10.29	10.47	10.47	10.75	-21.37	-21.45	32.12	26.6	31.92	24.2
18437	ES121-006	270.9720	-28.8167	214.1086	-43.1318	1211	1297	5.2	0.20	281	2.449	11.42	11.10	11.12	11.16	11.50	-19.84	-19.81	31.35	18.6	30.97	15.6
18445	ES489-006	229.9393	-19.6576	259.6346	-76.4307	2223	2337	7.2	0.57	192	2.359	12.07	12.19	12.80	12.89	12.90	-19.02	-18.93	31.93	24.3	31.82	23.2
18487	ES425-011	235.6975	-21.4350	242.7573	-72.8721	3202	3332	5.9	0.20	220	2.342	/	/	14.91	14.98	/	/	-18.77	/	/	33.82	58.0
18556	UGC003406	147.0045	21.0828	22.1635	-6.6389	5200	5266	6.7	0.20	237	2.375	/	/	14.97	15.02	/	/	-19.09	/	/	34.19	68.8
18557	UGC03403	142.8045	22.4412	22.9200	-2.5781	1264	1255	5.8	0.28	226	2.362	11.77	11.38	12.18	12.20	12.15	-19.06	-18.96	31.21	17.4	31.17	17.1
18581	P0018581	222.5529	-15.7797	296.1313	-79.4274	2064	2179	3.9	0.60	209	2.408	12.15	11.98	12.58	12.63	12.67	-19.47	-19.41	32.15	26.9	32.05	25.7
18747	UGC03432	157.3379	17.9731	20.9592	-16.7913	4998	5082	5.9	0.29	285	2.466	13.65	13.37	14.01	14.08	14.09	-20.00	-19.98	34.14	67.3	34.13	67.1
18764	UGC03413	132.6454	25.4691	24.9825	6.9641	4213	4231	4.7	0.71	264	2.563	11.70	11.74	12.15	12.24	12.35	-20.89	-20.93	33.27	45.0	33.20	43.7
18765	AGC024981	234.6077	-19.1343	241.8687	-75.3779	1702	1823	4.1	0.25	315	2.504	11.49	11.22	11.72	11.76	11.86	-20.34	-20.35	32.21	27.6	32.12	26.5
18778	UGC03423	135.1437	24.9631	24.6439	4.6726	4272	4296	7.9	0.29	211	2.334	/	/	15.15	15.23	/	/	-18.69	/	/	33.99	62.8
18813	P0018813	192.9611	1.5220	11.7197	-54.7656	5477	5646	7.8	0.60	387	2.676	/	/	12.30	12.24	/	/	-22.03	/	/	34.36	74.5
18855	P0018855	217.1108	-10.6141	336.3651	-78.9840	732	848	5.9	0.41	274	2.469	10.90	9.65	10.22	10.12	10.25	-20.03	-20.01	30.28	11.4	30.13	10.6
18989	P0018989	149.0407	21.9200	23.3227	-8.3620	4300	4355	3.7	0.69	143	2.287	/	/	14.08	14.18	/	/	-18.23	/	/	32.42	30.4
19024	AGC025099	235.9490	-17.5471	234.0149	-75.9915	7056	7316	4.2	0.20	370	2.568	13.77	13.32	13.97	14.04	14.04	-20.93	-20.98	35.07	103.1	35.16	107.6
19064	IC002166	155.8723	20.0212	22.7217	-14.9908	2685	2726	4.7	0.49	310	2.542	11.17	11.05	11.69	11.75	11.76	-20.69	-20.72	32.47	31.1	32.49	31.5
19121	ES490-005	235.5905	-16.6403	232.7620	-76.9154	7110	7377	4.5	0.20	400	2.602	/	/	13.85	13.91	/	/	-21.31	/	/	35.38	119.0
19222	UGC03474	143.1462	24.1731	24.6806	-2.6470	3634	3666	5.9	0.20	357	2.553	/	/	12.45	12.46	/	/	-20.82	/	/	33.32	46.2
19249	UGC03489	192.1760	5.6786	18.1370	-52.8788	5458	5643	4.0	0.20	467	2.669	/	/	12.51	12.50	/	/	-21.96	/	/	34.56	81.8
19255	E490-014	233.7712	-14.7697	233.8569	-79.4681	2709	2866	3.9	0.51	225	2.410	12.34	12.35	13.03	13.11	13.09	-19.49	-19.43	32.59	32.9	32.56	32.4
19261	UGC003484	156.4107	20.8165	23.6413	-15.3058	7422	7597	4.1	0.20	406	2.609	/	/	13.51	13.57	/	/	-21.37	/	/	35.08	103.7
19281	ES557-005	228.7150	-12.2349	257.4540	-83.9381	11126	11597	4.8	0.20	592	2.772	/	/	13.22	13.25	/	/	-22.97	/	/	36.49	198.3
19292	UGC03498	197.7802	3.2970	17.2137	-58.9299	3797	3952	3.8	0.20	341	2.533	/	/	12.74	12.69	/	/	-20.63	/	/	33.36	47.0
19343	PG0019343	224.9290	-9.7039	305.3764	-85.8417	749	893	8.1	0.36	188	2.295	/	/	12.23	12.24	/	/	-18.31	/	/	30.55	12.9
19355	NGC02263	234.0883	-13.7243	228.7530	-80.0741	2741	2905	2.2	0.39	316	2.527	11.08	10.90	11.53	11.59	11.60	-20.55	-20.57	32.16	27.1	32.17	27.1
19413	ES122-001	268.0416	-24.2435	209.1910	-47.1019	2615	2746	3.0	0.49	293	2.518	11.46	11.35	11.59	11.66	11.87	-20.47	-20.48	32.35	29.5	32.15	26.9
19512	UGC03524	201.0396	4.0005	20.7644	-61.7577	3923	4097	1.6	0.31	404	2.619	/	/	11.65	11.63	/	/	-21.48	/	/	33.14	42.5
19531	AGC025325	237.3052	-13.5501	217.2312	-77.8387	1897	2058	5.9	0.46	384	2.626	10.19	9.99	10.51	10.56	10.64	-21.46	-21.54	32.10	26.3	32.11	26.4
19627	UGC03500	129.4798	26.8867	26.2671	9.8735	4385	4406	4.9	0.28	236	2.382	/	/	14.05	14.13	/	/	-19.15	/	/	33.32	46.2
19652	UGC03539	149.1696	24.4210	25.8289	-8.0218	3307	3356	4.3	0.21	310	2.492	13.22	12.81	12.95	12.99	13.27	-20.24	-20.23	33.54	51.1	33.26	44.9
19732	UGC03561	166.3564	20.3932	25.7992	-24.4003	5688	5841	3.1	0.57	349	2.619	12.70	12.61	12.97	13.06	13.20	-21.40	-21.48	34.67	86.0	34.65	85.0
19788	UGC03576	166.3008	20.7116	26.1156	-24.2556	5962	6124	3.0	0.50	356	2.607	12.54	12.42	13.00	13.09	13.12	-21.28	-21.35	34.47	78.2	34.55	81.2
19792	UGC03584	188.6303	12.3372	25.8545	-47.2087	4439	4613	4.1	0.20	284	2.453	/	/	13.85	13.91	/	/	-19.85	/	/	33.82	58.2
19838	UGC03575	144.4078	25.7768	26.4374	-3.5427	3890	3940	6.1	0.20	266	2.425	/	/	14.20	14.24	/	/	-19.58	/	/	33.88	59.8
19861	ES491-009	237.3407	-10.9760	205.9734	-79.1013	2056	2233	7.7	0.28	268	2.437	/	/	12.93	12.95	/	/	-19.69	/	/	32.67	34.1
19877	UGC03605	200.9853	7.2539	26.8662	-60.3844	7967	8286	6.0	0.20	456	2.659	/	/	13.67	13.71	/	/	-21.86	/	/	35.77	142.6

PGC	Name	l	b	sgl	sgb	v_{hel}	v_{mod}	t	b/a	w_{mx}	$logw^{i}_{mx}$	I	I^{*}	[3.6]	$[3.6]^{*}$	$C_{[3.6]}$	M_{C}	$M_{[3.6]}$	μ_{C}	d_{C}	$\mu_{[3.6]}$	$d_{[3.6]}$
19920	E491-012	235.8059	-9.7685	202.9855	-80.9646	2578	2765	5.0	0.20	343	2.535	/	/	12.45	12.45	/	/	-20.65	/	/	33.14	42.4
19975	P0019975	156.6790	24.1410	27.0478	-14.7669	3296	3371	3.9	0.58	193	2.366	/	/	13.86	13.95	/	/	-19.00	/	/	32.98	39.5
19996	E491-015	238.5516	-10.2331	200.2231	-78.2658	2678	2870	5.1	0.20	356	2.551	11.81	11.19	12.02	12.03	11.96	-20.78	-20.81	32.76	35.6	32.87	37.4
20007	UGC03627	165.4279	22.2805	27.4813	-23.0083	6284	6461	6.4	0.66	255	2.522	13.16	13.22	13.60	13.71	13.83	-20.51	-20.52	34.40	75.9	34.33	73.3
20027	UGC03637	209.7273	4.5473	31.2553	-69.3033	3548	3750	8.0	0.37	222	2.369	/	/	13.60	13.63	/	/	-19.03	/	/	32.68	34.4
20214	UGC03691	201.1257	10.4563	32.5415	-58.9463	2205	2380	6.1	0.52	229	2.421	11.88	11.86	12.52	12.60	12.59	-19.59	-19.54	32.18	27.3	32.14	26.8
20222	UGC03693	197.8349	12.0576	32.0043	-55.3553	2254	2424	4.0	0.68	316	2.624	10.60	10.62	10.85	10.93	11.14	-21.44	-21.52	32.59	33.0	32.46	31.1
20274	PG0020274	219.8332	1.5421	46.0134	-79.1176	1717	1911	9.8	0.55	266	2.494	12.20	11.61	12.11	12.10	12.22	-20.26	-20.25	32.49	31.5	32.37	29.8
20293	UGC003675	139.9367	27.3482	27.4524	0.6323	3781	3823	5.7	0.20	334	2.524	13.23	12.82	13.25	13.30	13.43	-20.53	-20.54	34.00	63.1	33.91	60.5
20361	UGC03731	188.3036	16.8965	31.5779	-44.9419	4901	5106	7.9	0.29	405	2.618	/	/	12.55	12.61	/	/	-21.46	/	/	34.15	67.6
20418	UGC03717	141.1268	27.4839	27.7170	-0.3994	4187	4242	4.0	0.38	366	2.589	11.93	11.77	12.32	12.40	12.44	-21.12	-21.18	33.60	52.5	33.63	53.3
20458	UGC03653	129.2391	27.5465	26.9290	10.1106	2230	2216	4.0	0.51	365	2.619	10.38	10.30	10.85	10.91	10.97	-21.40	-21.48	32.37	29.8	32.40	30.2
20486	UGC003757	168.7182	23.7892	30.1179	-25.3876	5529	5703	5.9	0.20	365	2.562	14.28	13.77	14.01	14.06	14.28	-20.88	-20.92	35.26	112.9	35.12	105.6
20487	UGC03763	183.0264	19.5888	31.7439	-39.2546	7150	7419	6.1	0.20	322	2.508	14.65	14.25	14.95	15.02	14.99	-20.38	-20.39	35.49	125.5	35.59	131.4
20504	E428-009	241.7135	-8.1912	188.3635	-75.6501	2251	2453	5.2	0.29	260	2.425	12.95	12.58	13.12	13.15	13.23	-19.63	-19.58	32.87	37.6	32.75	35.5
20513	UGC03770	194.1676	15.4759	33.8514	-50.5455	6378	6646	9.8	0.44	314	2.536	12.94	12.83	13.51	13.61	13.58	-20.64	-20.66	34.28	71.6	34.36	74.6
20526	UGC03749	147.7263	27.2756	28.4165	-6.2210	1154	1187	5.8	0.20	172	2.236	13.55	13.48	14.35	14.42	14.30	-17.90	-17.73	32.21	27.7	32.15	26.9
20539	UGC03759	151.3841	26.9402	28.7269	-9.4796	4425	4518	3.1	0.65	431	2.747	11.51	11.48	11.83	11.92	12.07	-22.56	-22.73	34.70	87.2	34.77	89.8
20556	NGC002369	273.3130	-21.0122	203.0121	-43.2090	3237	3395	1.2	0.25	442	2.651	10.87	10.34	10.77	10.80	10.93	-21.68	-21.78	32.62	33.5	32.60	33.0
20559	UGC03776	183.9755	19.6281	32.3086	-40.0369	3881	4056	3.0	0.23	294	2.471	12.68	12.39	13.09	13.15	13.13	-20.05	-20.03	33.20	43.7	33.22	44.0
20562	UGC03777	188.0661	18.1769	33.0105	-44.1369	3211	3384	5.9	0.20	268	2.428	12.68	12.37	13.16	13.21	13.15	-19.66	-19.61	32.82	36.6	32.84	37.0
20577	E428-017	241.5801	-7.6434	186.2010	-75.8342	2388	2595	5.0	0.28	245	2.398	/	/	13.33	13.36	/	/	-19.31	/	/	32.69	34.5
20592	UGC03782	194.4409	15.9107	34.6513	-50.5434	2277	2451	5.8	0.20	315	2.498	11.94	11.54	11.96	11.99	12.13	-20.29	-20.29	32.43	30.7	32.30	28.8
20603	UGC03783	193.1183	16.4999	34.4016	-49.1525	6183	6445	6.1	0.20	360	2.556	13.99	13.53	14.04	14.10	14.18	-20.82	-20.86	35.10	104.5	35.10	104.6
20608	UGC03784	191.3003	17.2425	34.0219	-47.2780	2591	2763	5.9	0.24	192	2.287	/	/	15.70	15.76	/	/	-18.23	/	/	34.07	65.2
20766	NGC002397	280.2981	-22.5951	203.5207	-36.5454	1357	1475	3.0	0.46	307	2.529	10.61	10.31	10.73	10.77	10.91	-20.58	-20.59	31.48	19.8	31.36	18.7
20830	P0020830	199.1243	15.0863	37.6338	-54.7603	5135	5382	2.3	0.34	356	2.569	13.74	13.49	13.44	13.51	13.88	-20.94	-20.99	34.90	95.7	34.61	83.5
20835	UGC03820	200.6522	14.4606	38.2665	-56.3242	2530	2725	5.7	0.21	299	2.477	12.85	12.49	12.74	12.78	13.01	-20.10	-20.08	33.12	42.2	32.89	37.9
20844	UGC03804	143.6939	28.0814	28.6229	-2.5662	2869	2911	5.8	0.58	294	2.550	11.52	11.59	12.21	12.30	12.31	-20.77	-20.80	33.10	41.6	33.14	42.4
20865	ES123-009	273.2518	-20.2245	201.9651	-43.4172	3212	3375	4.9	0.37	274	2.461	12.61	12.31	12.67	12.72	12.88	-19.96	-19.93	32.86	37.3	32.67	34.2
20903	AGC025665	243.2391	-6.9178	183.0783	-74.2261	2242	2453	5.5	0.20	369	2.567	11.87	11.15	11.32	11.31	11.60	-20.92	-20.96	32.53	32.1	32.29	28.7
21020	UGC03845	171.0001	25.2699	32.4858	-26.7948	3030	3162	3.7	0.67	195	2.408	12.58	12.69	13.32	13.41	13.41	-19.47	-19.41	32.90	38.0	32.85	37.1
21033	NGC2336	133.9581	28.2168	27.8204	5.9793	2201	2204	4.0	0.57	439	2.719	9.60	9.57	10.26	10.33	10.31	-22.30	-22.45	32.63	33.5	32.81	36.4
21136	UGC003879	185.2416	22.0920	35.8717	-39.9124	4794	5007	7.6	0.24	248	2.398	13.71	13.50	14.46	14.54	14.37	-19.39	-19.32	33.80	57.5	33.92	60.9
21154	NGC02393	184.9207	22.2676	35.8796	-39.5673	4884	5099	5.3	0.58	265	2.505	12.84	12.88	13.48	13.58	13.59	-20.36	-20.36	34.00	63.1	34.01	63.5
21164	UGC03834	134.2929	28.3785	28.0035	5.6967	2033	2036	5.2	0.42	286	2.490	11.62	11.58	12.33	12.41	12.35	-20.22	-20.21	32.58	32.8	32.63	33.6

PGC	Name	l	b	sgl	sgb	v_{hel}	v_{mod}	t	b/a	w_{mx}	$logw^{i}_{mx}$	I	I^{*}	[3.6]	$[3.6]^{*}$	$C_{[3.6]}$	M_{C}	$M_{[3.6]}$	μ_{C}	d_{C}	$\mu_{[3.6]}$	$d_{[3.6]}$
21167	ES123-016	273.3508	-19.3078	200.6997	-43.4900	3254	3423	7.6	0.22	257	2.412	13.23	12.79	12.86	12.89	13.21	-19.51	-19.45	32.74	35.3	32.35	29.6
21328	IC002199	188.0918	22.3468	37.9538	-42.0471	4674	4896	3.9	0.59	307	2.571	12.36	12.38	12.62	12.72	12.92	-20.96	-21.01	33.92	61.0	33.79	57.3
21338	ES257-019	259.5336	-12.5881	193.5977	-57.6883	2871	3076	6.1	0.20	321	2.507	12.38	11.74	12.40	12.41	12.43	-20.37	-20.38	32.82	36.7	32.81	36.4
21375	NGC002427	260.2869	-12.6993	193.6100	-56.9450	973	1156	7.8	0.41	236	2.403	10.23	9.95	10.55	10.58	10.63	-19.43	-19.36	30.06	10.3	29.94	9.7
21380	UGC03922	162.5765	28.2911	32.7447	-18.6967	8790	9085	5.8	0.28	465	2.676	13.60	13.16	13.37	13.45	13.67	-21.91	-22.03	35.72	139.1	35.66	135.7
21397	UGC03919	151.7715	29.1699	31.0086	-9.3346	4866	4983	5.9	0.20	287	2.458	14.16	13.84	13.11	13.17	13.89	-19.93	-19.90	33.86	59.2	33.10	41.7
21425	UGC03937	183.7982	24.2175	37.3908	-37.7038	3994	4191	3.7	0.38	319	2.530	12.18	12.05	12.43	12.51	12.64	-20.58	-20.60	33.25	44.6	33.14	42.5
21451	UGC003921	144.5518	29.3345	29.9780	-3.1182	2486	2532	6.1	0.35	177	2.267	/	/	15.66	15.75	/	/	-18.04	/	/	33.85	58.9
21488	E560-004	237.8397	-0.0664	149.4866	-77.8233	2177	2413	4.1	0.22	406	2.610	/	/	11.58	11.46	/	/	-21.39	/	/	32.87	37.6
21503	UGC003955	210.3235	14.6727	51.2680	-63.0477	5108	5394	6.9	0.20	325	2.512	/	/	13.08	13.14	/	/	-20.43	/	/	33.62	52.9
21549	AGC170347	193.7645	21.7701	41.4391	-46.7139	8388	8761	5.4	0.22	382	2.584	/	/	14.59	14.67	/	/	-21.13	/	/	36.02	159.7
21558	UGC03959	180.1364	25.8048	37.1056	-34.0328	3355	3531	3.3	0.23	431	2.637	11.49	11.02	11.81	11.84	11.79	-21.56	-21.65	33.38	47.3	33.54	51.0
21660	ES163-014	269.2490	-15.7290	196.5175	-47.9160	2861	3047	2.3	0.29	318	2.512	12.27	11.83	12.38	12.41	12.48	-20.42	-20.43	32.92	38.4	32.86	37.4
21684	UGC03979	148.6564	29.9672	31.2306	-6.5190	4063	4154	4.0	0.20	373	2.572	12.88	12.41	12.91	12.95	13.04	-20.96	-21.01	34.05	64.7	34.03	64.0
21697	PG0021697	158.2229	29.7761	33.0427	-14.6211	5174	5326	7.9	0.27	176	2.253	/	/	16.48	16.58	/	/	-17.90	/	/	34.58	82.5
21759	ES560-012	235.6632	3.1791	131.3083	-77.3985	3305	3570	6.2	0.25	364	2.566	/	/	12.33	12.30	/	/	-20.96	/	/	33.29	45.5
21822	E560-013	236.0096	3.3738	131.8991	-77.0237	3239	3505	4.0	0.20	503	2.702	/	/	11.28	11.23	/	/	-22.28	/	/	33.56	51.6
21831	AGC170349	192.0543	24.0986	42.7514	-44.0581	4723	4969	6.7	0.20	190	2.279	/	/	15.58	15.67	/	/	-18.15	/	/	33.88	59.7
21854	UGC04024	154.5187	30.3802	32.7713	-11.3702	1716	1793	5.8	0.29	204	2.319	13.22	13.13	14.00	14.07	13.95	-18.67	-18.55	32.63	33.6	32.63	33.6
21857	UGC04032	190.2754	24.7689	42.1749	-42.3564	8126	8486	5.9	0.20	357	2.553	14.37	13.93	14.36	14.43	14.54	-20.79	-20.82	35.45	123.0	35.43	121.7
21918	UGC04040	186.3366	26.1571	41.0248	-38.6405	4798	5032	5.8	0.20	451	2.654	12.94	12.38	12.36	12.40	12.76	-21.71	-21.82	34.55	81.2	34.30	72.5
22002	UGC04060	206.7735	19.5086	52.3014	-57.1632	4677	4958	2.0	0.35	399	2.621	12.12	11.90	12.62	12.70	12.66	-21.41	-21.50	34.12	66.8	34.28	71.7
22174	ES035-018	288.7558	-22.7003	202.4683	-28.7905	1765	1875	5.0	0.25	296	2.476	11.76	11.30	12.24	12.26	12.13	-20.10	-20.08	32.24	28.0	32.35	29.5
22188	IC0000480	194.3672	25.0931	45.6798	-45.0880	4626	4882	4.0	0.21	318	2.503	13.09	12.73	12.89	12.95	13.21	-20.34	-20.34	33.59	52.1	33.33	46.4
22297	UGC04113	189.5059	26.9484	43.9747	-40.5100	5271	5533	6.1	0.20	197	2.294	/	/	16.44	16.53	/	/	-18.30	/	/	34.96	98.1
22306	E561-003	237.5929	5.0724	132.0800	-74.7050	3515	3797	6.1	0.20	331	2.520	/	/	12.59	12.60	/	/	-20.50	/	/	33.14	42.4
22338	ES209-009	264.0140	-10.5807	189.2625	-53.5270	1117	1314	6.2	0.20	303	2.481	10.68	10.01	10.28	10.27	10.51	-20.14	-20.13	30.65	13.5	30.40	12.0
22381	UGC04132	188.0734	27.7444	43.8305	-39.0132	5215	5473	4.0	0.31	515	2.725	12.01	11.59	11.91	11.97	12.14	-22.35	-22.50	34.57	82.0	34.58	82.3
22401	AGC170378	194.9108	25.9329	47.0334	-44.9152	7403	7755	5.9	0.20	375	2.574	13.90	13.45	13.98	14.05	14.11	-20.98	-21.03	35.20	109.5	35.23	111.4
22446	UGC04148	177.8142	30.1110	40.4056	-30.1677	731	886	7.2	0.21	127	2.105	14.25	14.34	15.82	15.90	15.47	-16.71	-16.45	32.18	27.3	32.36	29.7
22561	UGC04169	155.4741	32.0348	34.6170	-11.7379	1585	1672	5.8	0.49	206	2.365	12.55	12.58	13.39	13.46	13.38	-19.08	-18.99	32.46	31.1	32.46	31.1
22565	UGC04180	194.2084	26.8382	47.4092	-43.8459	5226	5504	5.2	0.50	332	2.575	12.49	12.45	12.89	12.98	13.08	-20.99	-21.04	34.13	66.9	34.10	66.1
22596	UGC04191	198.5116	25.6207	49.8950	-47.5021	4714	4990	3.0	0.61	337	2.620	11.93	11.95	12.18	12.28	12.48	-21.40	-21.48	33.93	61.0	33.82	58.0
22640	UGC04078	128.7347	28.6863	28.0739	10.5886	1862	1850	4.0	0.20	208	2.318	13.16	12.98	13.42	13.47	13.59	-18.65	-18.53	32.25	28.2	32.01	25.3
22695	UGC04195	149.1019	31.9996	33.3119	-6.4915	4880	5003	3.0	0.57	361	2.636	12.32	12.30	12.89	12.99	13.00	-21.55	-21.64	34.62	84.1	34.74	88.7
22712	ES494-021	241.7260	4.7404	142.6737	-71.8962	1584	1843	6.7	0.21	149	2.174	/	/	15.63	15.67	/	/	-17.13	/	/	32.82	36.6

PGC	Name	l	b	sgl	sgb	v_{hel}	v_{mod}	t	b/a	w_{mx}	$logw^{i}_{mx}$	I	I^{*}	[3.6]	$[3.6]^{*}$	$C_{[3.6]}$	M_{C}	$M_{[3.6]}$	μ_{C}	d_{C}	$\mu_{[3.6]}$	$d_{[3.6]}$
22873	UGC004247	205.9739	24.4629	56.6668	-52.8219	2839	3097	6.8	0.20	188	2.274	15.20	15.09	16.39	16.46	16.12	-18.25	-18.10	34.44	77.3	34.67	86.1
22921	UGC04257	197.5306	27.6393	51.0691	-45.4551	4160	4426	6.0	0.20	240	2.380	13.97	13.73	14.65	14.72	14.58	-19.22	-19.14	33.84	58.6	33.93	61.0
22969	UGC04238	137.8402	30.9877	30.8727	2.8478	1544	1568	6.6	0.41	169	2.259	12.05	12.12	13.47	13.56	13.19	-18.12	-17.96	31.30	18.2	31.51	20.1
23028	NGC02543	185.1493	31.3061	45.5904	-34.8684	2475	2678	3.0	0.51	299	2.534	11.35	11.31	11.85	11.87	11.95	-20.62	-20.64	32.58	32.8	32.53	32.0
23071	UGC04278	174.1234	33.0572	41.6555	-26.0029	557	709	6.5	0.20	169	2.228	12.01	11.94	13.16	13.17	12.90	-17.83	-17.65	30.74	14.0	30.82	14.6
23110	UGC04284	170.1834	33.4780	40.4670	-22.8632	559	699	6.0	0.51	188	2.330	11.07	11.15	12.09	12.17	12.01	-18.76	-18.64	30.77	14.3	30.81	14.5
23146	AGC180141	201.5263	27.6394	54.8697	-47.8484	4263	4545	5.2	0.20	267	2.427	14.02	13.74	14.29	14.36	14.41	-19.64	-19.59	34.11	66.2	34.02	63.7
23147	UGC04296	214.9532	22.4522	67.4657	-58.7657	9014	9495	6.1	0.20	299	2.476	14.73	14.42	15.17	15.27	15.20	-20.09	-20.07	35.41	120.5	35.52	126.9
23169	UGC04299	199.8340	28.3335	53.8808	-46.3445	4284	4563	4.1	0.20	389	2.590	12.56	12.07	12.45	12.49	12.65	-21.13	-21.19	33.82	58.0	33.74	55.9
23239	UGC04306	186.3149	32.0520	47.0415	-35.2278	2415	2624	1.3	0.50	207	2.370	12.54	12.56	12.45	12.53	12.92	-19.13	-19.04	32.06	25.8	31.57	20.7
23289	UGC004324	202.6592	28.0469	56.4137	-48.1689	4816	5118	2.2	0.39	308	2.515	12.88	12.76	13.14	13.22	13.36	-20.45	-20.46	33.85	58.9	33.74	56.0
23338	AGC180197	202.7306	28.2044	56.6342	-48.0847	5029	5337	3.0	0.68	185	2.393	14.04	14.18	15.04	15.15	15.02	-19.34	-19.27	34.42	76.6	34.52	80.2
23340	NGC002552	169.0971	34.2908	40.8569	-21.7040	521	660	9.0	0.57	126	2.177	11.64	11.82	12.73	12.76	12.64	-17.37	-17.15	30.01	10.1	29.91	9.6
23347	AGC180199	202.4205	28.3343	56.4357	-47.8131	4856	5159	5.0	0.71	162	2.353	14.03	14.19	14.58	14.69	14.81	-18.97	-18.87	33.82	58.2	33.62	53.0
23355	UGC04332	202.3889	28.4192	56.4822	-47.7293	5484	5805	2.5	0.59	471	2.757	12.36	12.31	12.56	12.66	12.85	-22.65	-22.82	35.63	133.6	35.67	135.8
23362	UGC04334	201.4237	28.7719	55.8398	-46.9213	3581	3852	3.7	0.47	403	2.650	11.40	11.28	11.94	12.02	12.01	-21.68	-21.78	33.72	55.6	33.86	59.1
23374	P0023374	202.4726	28.4791	56.6233	-47.7284	4235	4523	5.1	0.35	232	2.385	14.74	14.67	15.54	15.63	15.50	-19.26	-19.18	34.85	93.2	34.94	97.2
23420	AGC180218	200.8395	29.2037	55.6698	-46.2626	4143	4426	3.2	0.66	215	2.448	13.05	13.16	13.76	13.87	13.87	-19.83	-19.80	33.75	56.2	33.72	55.5
23447	IC002327	220.6540	21.4306	76.8215	-61.4780	2677	2968	1.1	0.37	286	2.479	12.74	12.66	13.36	13.43	13.40	-20.12	-20.11	33.56	51.5	33.59	52.2
23465	UGC04361	200.9524	29.4338	55.9919	-46.1488	3742	4017	5.8	0.32	174	2.255	14.27	14.27	15.18	15.27	15.12	-18.08	-17.91	33.23	44.2	33.22	44.1
23519	UGC04381	224.6617	19.8797	84.2512	-63.6652	4617	4954	4.3	0.26	335	2.531	12.71	12.42	12.88	12.94	13.04	-20.60	-20.62	33.68	54.3	33.61	52.8
23522	UGC04375	201.0401	29.7208	56.3399	-45.9759	2061	2309	5.3	0.68	277	2.566	11.29	11.39	12.10	12.19	12.15	-20.91	-20.95	33.08	41.2	33.17	43.1
23567	UGC04386	202.8871	29.3516	57.8405	-47.2630	4642	4944	3.0	0.23	480	2.684	11.84	11.33	12.08	12.12	12.08	-21.98	-22.11	34.12	66.7	34.31	72.9
23574	PG0023574	236.9677	13.0248	116.2255	-68.4329	4722	5065	7.4	0.20	204	2.310	/	/	15.32	15.40	/	/	-18.45	/	/	33.92	60.8
23589	AGC180254	203.4473	29.2486	58.3253	-47.6396	5969	6312	2.0	0.52	293	2.526	13.78	13.79	14.41	14.52	14.51	-20.54	-20.56	35.15	107.4	35.23	111.2
23604	NGC02550	140.3606	32.3597	32.4723	0.8661	2262	2308	3.1	0.43	221	2.380	12.26	12.29	12.78	12.87	12.94	-19.22	-19.14	32.17	27.1	32.01	25.2
23616	UGC04392	224.6446	20.4087	84.3400	-63.1373	4995	5344	3.6	0.27	472	2.682	11.76	11.33	11.87	11.92	11.99	-21.96	-22.08	34.00	63.0	34.08	65.3
23660	UGC04393	174.0886	35.1743	43.7103	-24.9817	2125	2298	3.5	0.57	108	2.111	12.45	12.66	13.29	13.40	13.39	-16.77	-16.51	30.16	10.7	29.90	9.6
23661	UGC04400	202.3828	30.0220	57.9283	-46.4644	4390	4686	5.9	0.20	214	2.330	14.85	14.67	15.72	15.80	15.59	-18.77	-18.65	34.42	76.5	34.56	81.5
23662	UGC04399	202.6148	29.9575	58.1033	-46.6378	4476	4775	7.7	0.35	232	2.386	13.77	13.71	14.49	14.58	14.50	-19.27	-19.19	33.81	57.8	33.83	58.4
23709	AGC180284	200.8424	30.8057	57.1280	-45.0267	5289	5607	3.8	0.26	305	2.490	14.12	13.88	14.53	14.60	14.60	-20.22	-20.21	34.91	95.8	34.95	97.7
23748	UGC04424	204.0952	29.9862	59.6425	-47.3753	4438	4741	3.0	0.26	203	2.314	14.73	14.66	15.77	15.86	15.61	-18.62	-18.49	34.28	71.9	34.45	77.6
23757	AGC180599	202.1779	30.6213	58.2523	-45.8812	6450	6809	4.0	0.22	194	2.290	15.25	15.14	16.01	16.11	15.98	-18.40	-18.26	34.45	77.6	34.47	78.4
23840	UGC004413	140.4252	32.7536	32.8700	0.8597	2292	2341	6.0	0.21	144	2.159	/	/	15.48	15.57	/	/	-16.98	/	/	32.57	32.7
23878	UGC04446	203.9676	30.6634	60.0852	-46.7591	6012	6362	5.9	0.20	328	2.516	14.06	13.69	13.92	13.99	14.21	-20.45	-20.47	34.74	88.7	34.56	81.5
23997	NGC002613	245.3603	10.0554	137.7094	-65.7257	1675	1964	3.1	0.27	599	2.785	9.22	8.64	9.38	9.38	9.37	-22.90	-23.09	32.28	28.6	32.49	31.5

PGC	Name	l	b	sgl	sgb	v_{hel}	v_{mod}	t	b/a	w_{mx}	$logw^{i}_{mx}$	I	I^{*}	[3.6]	$[3.6]^{*}$	$C_{[3.6]}$	M_{C}	$M_{[3.6]}$	μ_{C}	d_{C}	$\mu_{[3.6]}$	$d_{[3.6]}$
24034	ES562-018	244.1069	11.0699	133.8406	-65.9192	4729	5076	6.4	0.20	214	2.330	/	/	15.98	16.05	/	/	-18.65	/	/	34.83	92.3
24111	NGC02608	195.4559	34.0479	55.3560	-39.5995	2156	2400	3.3	0.54	207	2.383	11.26	11.34	11.81	11.85	11.96	-19.25	-19.17	31.21	17.5	31.02	16.0
24189	AGC480047	236.3402	16.9767	110.7215	-65.0727	5915	6306	6.8	0.20	317	2.501	/	/	13.97	14.03	/	/	-20.32	/	/	34.44	77.4
24219	AGC026102	245.2795	11.1901	135.5780	-65.0149	1653	1946	5.2	0.20	160	2.204	/	/	14.38	14.44	/	/	-17.42	/	/	31.86	23.6
24231	UGC04472	135.5645	31.9001	31.6124	4.8620	1333	1353	5.9	0.21	258	2.413	11.48	11.27	11.82	11.87	11.93	-19.52	-19.46	31.45	19.5	31.33	18.4
24242	UGC004499	167.0911	37.1956	42.9662	-19.0248	691	836	8.0	0.44	110	2.079	/	/	13.81	13.91	/	/	-16.20	/	/	30.11	10.5
24351	UGC04514	164.8069	37.3956	42.4034	-17.2767	694	832	5.9	0.33	149	2.189	12.71	12.80	13.76	13.84	13.67	-17.48	-17.28	31.16	17.0	31.11	16.7
24374	UGC04524	220.6558	26.7191	79.1434	-56.3265	1940	2238	6.7	0.24	146	2.169	14.44	14.49	15.40	15.48	15.34	-17.29	-17.07	32.65	33.8	32.57	32.6
24479	E563-014	244.2604	13.5677	130.0864	-63.9854	1709	2010	6.6	0.22	306	2.488	11.85	11.38	11.70	11.72	11.92	-20.20	-20.19	32.13	26.7	31.92	24.3
24490	UGC004550	213.3793	30.6398	70.8332	-50.6864	2068	2358	3.4	0.25	268	2.433	12.73	12.50	13.13	13.19	13.20	-19.70	-19.65	32.92	38.3	32.86	37.4
24530	UGC04559	194.0782	36.3179	56.2857	-37.1726	2084	2330	2.1	0.26	341	2.539	12.19	11.86	12.44	12.48	12.54	-20.67	-20.69	33.23	44.2	33.21	43.9
24548	UGC04565	217.2268	29.3885	75.2339	-52.9835	4066	4399	6.0	0.20	224	2.350	15.23	15.00	15.67	15.74	15.73	-18.95	-18.85	34.75	89.2	34.70	87.0
24558	E563-017	244.7318	13.6881	130.6826	-63.5916	3460	3789	1.4	0.63	389	2.690	11.38	11.25	11.68	11.75	11.86	-22.03	-22.16	33.94	61.5	33.98	62.6
24602	IC000499	127.2179	29.0932	28.4639	11.9238	1958	1945	1.0	0.48	384	2.632	/	/	11.90	11.97	/	/	-21.60	/	/	33.62	53.0
24685	ES563-021	244.8672	14.3975	129.8566	-62.9731	4582	4940	4.3	0.20	664	2.823	11.53	10.57	11.30	11.28	11.28	-23.25	-23.46	34.60	83.3	34.87	94.2
24711	UGC04576	140.3156	34.0600	34.1561	1.1081	2383	2440	3.0	0.28	179	2.261	12.98	12.99	13.61	13.69	13.70	-18.14	-17.98	31.84	23.4	31.68	21.6
24723	UGC04574	139.6800	33.8725	33.9082	1.6098	2170	2221	3.0	0.65	256	2.521	10.99	11.12	11.26	11.30	11.58	-20.50	-20.52	32.09	26.2	31.82	23.1
24778	P0024778	234.6008	21.7527	103.9741	-61.0461	2907	3236	4.0	0.61	228	2.450	12.30	12.39	12.92	13.01	13.06	-19.86	-19.82	32.94	38.7	32.86	37.3
24784	UGC04605	156.1243	37.8086	40.4251	-10.6604	1358	1473	2.0	0.28	422	2.634	10.66	10.27	11.03	11.06	11.03	-21.53	-21.62	32.56	32.6	32.70	34.6
24829	UGC04621	188.2576	38.5206	54.2594	-32.3312	2299	2535	1.0	0.50	239	2.431	12.37	12.41	12.81	12.90	13.02	-19.68	-19.63	32.71	34.8	32.54	32.3
24830	UGC04625	224.1102	27.9139	84.8945	-55.6216	8476	8975	6.1	0.20	422	2.625	13.90	13.38	13.88	13.95	14.03	-21.45	-21.53	35.61	132.3	35.68	136.5
24840	AGC026184	244.9032	15.2928	128.6476	-62.2705	3404	3738	6.4	0.20	170	2.230	/	/	15.26	15.32	/	/	-17.68	/	/	33.02	40.3
24854	ES563-028	246.9590	13.8885	133.8122	-61.9573	2578	2895	1.5	0.26	402	2.611	11.79	11.22	11.50	11.51	11.73	-21.32	-21.39	33.07	41.1	32.93	38.5
24870	P0024870	243.3633	16.5960	124.4232	-62.1543	2001	2315	6.5	0.29	306	2.497	12.08	11.70	12.69	12.72	12.56	-20.28	-20.28	32.86	37.3	33.03	40.3
24893	UGC04640	229.7552	25.3844	94.0929	-58.2109	3307	3644	5.3	0.34	324	2.528	12.06	11.91	12.79	12.86	12.74	-20.56	-20.58	33.33	46.4	33.49	49.9
24930	UGC04641	190.4556	38.7603	55.8670	-33.4183	411	639	3.0	0.27	426	2.637	8.43	8.07	8.84	8.82	8.80	-21.55	-21.64	30.36	11.8	30.46	12.4
24947	UGC04623	136.8775	33.2791	33.0820	3.8730	2885	2934	5.8	0.29	365	2.573	11.48	11.23	12.25	12.31	12.12	-20.97	-21.02	33.11	42.0	33.37	47.1
24960	UGC04655	223.2717	29.2423	83.8773	-54.2198	6188	6597	6.1	0.20	265	2.423	14.82	14.54	15.06	15.13	15.20	-19.61	-19.56	34.90	95.4	34.82	91.9
25012	UGC04659	172.7888	40.1148	47.8775	-21.6904	1749	1933	8.0	0.31	174	2.254	13.70	13.74	14.89	14.97	14.70	-18.07	-17.90	32.79	36.1	32.90	38.1
25102	NGC02706	230.8139	26.1086	95.7460	-57.3996	1629	1946	3.8	0.27	304	2.490	11.94	11.74	11.69	11.74	12.12	-20.22	-20.22	32.35	29.5	31.96	24.7
25161	UGC04691	225.6620	29.1655	87.4327	-54.4764	3916	4267	2.5	0.43	629	2.835	10.36	10.11	10.79	10.85	10.84	-23.36	-23.58	34.26	71.0	34.54	80.8
25166	UGC04601	128.0340	29.7421	29.1361	11.2219	1789	1780	2.5	0.31	271	2.446	12.34	12.16	12.45	12.51	12.70	-19.82	-19.78	32.53	32.1	32.30	28.9
25221	AGC480085	232.2737	26.0358	98.1726	-57.2960	2761	3096	4.2	0.52	250	2.458	12.09	12.16	12.58	12.67	12.78	-19.92	-19.90	32.72	35.0	32.58	32.8
25237	UGC04695	164.0128	40.2326	44.8858	-15.6144	2328	2490	5.2	0.68	239	2.504	11.43	11.59	12.13	12.23	12.27	-20.35	-20.35	32.63	33.6	32.60	33.1
25248	UGC04708	175.6469	41.0028	49.9009	-23.1058	1821	2018	3.1	0.54	303	2.546	11.06	11.10	11.63	11.66	11.74	-20.73	-20.76	32.48	31.3	32.43	30.6
25258	NGC02710	161.4935	40.0254	43.9477	-13.9025	2523	2678	3.1	0.50	265	2.477	12.18	12.22	12.91	12.99	12.97	-20.10	-20.08	33.09	41.4	33.11	41.9

PGC	Name	l	b	sgl	sgb	v_{hel}	v_{mod}	t	b/a	w_{mx}	$logw^{i}_{mx}$	I	I^{*}	[3.6]	$[3.6]^{*}$	$C_{[3.6]}$	M_{C}	$M_{[3.6]}$	μ_{C}	d_{C}	$\mu_{[3.6]}$	$d_{[3.6]}$
25318	UGC04725	192.6666	40.2190	58.5531	-33.5630	1998	2250	6.1	0.20	131	2.117	15.31	15.40	16.42	16.52	16.31	-16.83	-16.57	33.16	42.8	33.12	42.0
25371	UGC04701	134.6963	32.9573	32.6180	5.6694	1406	1430	7.0	0.52	175	2.303	/	/	14.55	14.64	/	/	-18.38	/	/	33.05	40.7
25373	ES090-015	281.5159	-12.0762	190.3598	-36.3212	1678	1860	3.2	0.35	264	2.441	12.34	12.03	12.37	12.41	12.58	-19.77	-19.73	32.37	29.7	32.15	26.9
25376	NGC02731	220.7996	32.7712	81.3164	-50.4126	2585	2908	4.2	0.61	174	2.333	12.38	12.48	12.76	12.80	13.01	-18.79	-18.68	31.80	22.9	31.48	19.8
25412	ES564-012	245.5412	18.5625	125.4288	-59.3372	3542	3891	6.2	0.21	179	2.254	/	/	16.46	16.52	/	/	-17.90	/	/	34.53	80.5
25450	UGC004754	229.5995	29.0710	93.3604	-54.5440	5679	6086	4.0	0.22	318	2.504	/	/	13.87	13.94	/	/	-20.35	/	/	34.39	75.4
25472	UGC004753	175.1135	41.8854	50.4840	-22.2998	1836	2035	6.7	0.20	156	2.193	/	/	14.88	14.96	/	/	-17.31	/	/	32.28	28.6
25498	NGC02726	155.9198	39.7864	42.3022	-9.9351	1517	1642	1.0	0.43	374	2.608	11.80	11.68	12.34	12.40	12.40	-21.29	-21.36	33.73	55.7	33.83	58.3
25525	UGC04769	201.3295	39.8292	64.6796	-37.9735	2674	2961	5.3	0.66	134	2.242	11.48	11.68	11.84	11.94	12.18	-17.97	-17.79	30.14	10.7	29.74	8.9
25562	UGC04777	189.4672	41.8045	57.8037	-30.7455	2052	2299	9.2	0.22	171	2.235	13.73	13.71	14.62	14.70	14.56	-17.90	-17.72	32.47	31.1	32.43	30.7
25563	PG0025563	236.1279	26.0799	104.3474	-56.5036	3758	4120	6.9	0.20	302	2.480	/	/	13.93	13.98	/	/	-20.11	/	/	34.18	68.5
25640	UGC04779	155.1216	39.9563	42.2890	-9.2994	1294	1415	5.3	0.51	285	2.511	10.50	10.51	11.18	11.20	11.21	-20.41	-20.42	31.63	21.2	31.62	21.1
25676	UGC04759	134.7283	33.3225	32.9860	5.6673	1323	1349	5.2	0.35	277	2.461	10.53	10.44	11.08	11.15	11.15	-19.96	-19.93	31.11	16.7	31.08	16.4
25694	ES564-023	250.0125	16.7483	133.8536	-57.8525	7741	8221	5.5	0.22	311	2.494	14.68	14.16	14.76	14.82	14.85	-20.26	-20.26	35.21	110.3	35.23	111.0
25732	ES314-005	262.4599	6.1828	161.0173	-52.8153	4867	5212	3.3	0.30	460	2.674	/	/	12.03	12.03	/	/	-22.01	/	/	34.12	66.7
25761	NGC002788	284.3412	-13.5124	192.0418	-33.5369	1640	1809	2.2	0.28	218	2.348	12.39	12.21	12.03	12.08	12.52	-18.93	-18.82	31.45	19.5	30.91	15.2
25781	UGC04800	162.1887	41.5056	45.5652	-13.8561	2433	2596	5.9	0.31	231	2.376	13.22	13.16	14.03	14.10	13.99	-19.18	-19.10	33.19	43.5	33.24	44.5
25806	UGC04806	191.5700	42.1967	59.4331	-31.5525	1952	2205	5.3	0.25	318	2.508	11.12	10.86	11.82	11.87	11.72	-20.38	-20.38	32.11	26.4	32.27	28.4
25867	ES497-018	251.1365	16.4665	135.6094	-57.2588	5116	5503	1.2	0.21	442	2.646	13.17	12.46	13.09	13.11	13.14	-21.64	-21.74	34.87	94.2	34.98	99.0
25886	PG0025886	238.9033	25.5894	108.9039	-56.1794	1839	2172	3.3	0.20	518	2.714	10.06	9.44	10.11	10.11	10.14	-22.26	-22.40	32.41	30.3	32.53	32.1
25910	UGC04824	166.9523	42.4830	47.9623	-16.7092	2182	2361	6.4	0.23	244	2.391	12.63	12.47	13.59	13.65	13.41	-19.31	-19.24	32.74	35.3	32.92	38.4
25926	AGC026338	248.6566	18.9000	129.3426	-57.1957	2177	2508	6.3	0.20	328	2.516	12.21	11.66	12.22	12.24	12.31	-20.45	-20.47	32.78	36.0	32.72	35.0
25932	E497-022	254.0016	14.5580	141.5027	-56.3335	2423	2748	2.9	0.50	212	2.380	12.74	12.65	13.04	13.11	13.24	-19.22	-19.14	32.47	31.2	32.25	28.2
25956	UGC04845	220.3923	35.7837	81.6301	-47.3885	2120	2442	6.9	0.35	207	2.336	13.13	13.05	14.07	14.14	13.95	-18.82	-18.71	32.78	36.0	32.88	37.6
26003	ES091-003	281.3722	-10.3006	188.1550	-36.4735	1901	2095	2.3	0.66	333	2.638	/	/	11.14	11.19	/	/	-21.66	/	/	32.87	37.5
26018	NGC02748	136.2549	34.3615	34.1199	4.4793	1473	1510	4.0	0.36	279	2.467	10.81	10.72	11.06	11.12	11.29	-20.01	-19.99	31.30	18.2	31.11	16.7
26057	E564-031	248.6268	19.7502	128.2767	-56.5755	5150	5547	4.4	0.32	345	2.552	12.76	12.44	13.01	13.07	13.12	-20.79	-20.82	33.95	61.7	33.96	62.0
26068	UGC04867	181.0932	43.8081	54.9317	-24.8068	2493	2726	7.0	0.63	191	2.382	13.03	13.19	14.40	14.50	14.19	-19.24	-19.16	33.46	49.2	33.71	55.3
26093	AGC026360	255.5757	14.1138	143.7211	-55.3476	2122	2442	4.9	0.65	244	2.499	11.85	11.77	12.36	12.43	12.46	-20.30	-20.30	32.78	35.9	32.75	35.5
26135	ES564-033	248.3372	20.3999	127.1416	-56.2563	5168	5567	7.9	0.20	240	2.380	/	/	15.49	15.56	/	/	-19.14	/	/	34.82	92.1
26157	AGC026375	252.1723	17.3983	135.5597	-55.8989	2543	2878	2.9	0.31	545	2.749	10.51	9.97	10.77	10.79	10.74	-22.57	-22.74	33.34	46.5	33.58	51.9
26192	AGC026380	254.7273	15.3651	141.0931	-55.2895	2436	2764	4.0	0.33	385	2.602	11.89	11.52	11.86	11.89	12.07	-21.23	-21.30	33.34	46.5	33.23	44.3
26295	UGC04888	138.9917	35.9307	35.8931	2.3968	2255	2316	5.2	0.44	289	2.499	11.28	11.26	11.99	12.06	12.02	-20.30	-20.30	32.33	29.2	32.37	29.9
26304	UGC004922	171.3351	44.0859	51.0003	-18.8007	1992	2188	8.9	0.41	226	2.385	12.56	12.58	13.63	13.71	13.50	-19.27	-19.19	32.78	36.0	32.92	38.4
26383	ES061-008	285.7751	-13.4240	191.9037	-32.1445	3372	3564	5.0	0.30	306	2.498	12.51	12.19	12.85	12.90	12.91	-20.29	-20.29	33.22	44.1	33.23	44.2
26390	IC002461	186.2841	44.7179	58.3738	-27.0567	2261	2509	3.3	0.27	367	2.572	12.45	12.18	12.36	12.41	12.66	-20.97	-21.02	33.67	54.2	33.47	49.5

PGC	Name	l	b	sgl	sgb	v_{hel}	v_{mod}	t	b/a	w_{mx}	$logw^i_{mx}$	I	I^*	[3.6]	$[3.6]^*$	$C_{[3.6]}$	M_C	$M_{[3.6]}$	μ_C	d_C	$\mu_{[3.6]}$	$d_{[3.6]}$
26411	PG0026411	239.5536	28.0911	108.3008	-53.6348	3437	3803	3.0	0.51	359	2.612	/	/	12.46	12.54	/	/	-21.40	/	/	34.01	63.5
26455	AGC026407	260.1700	11.6930	151.1652	-52.7319	2427	2744	3.1	0.21	375	2.575	12.18	11.47	11.53	11.52	11.87	-20.99	-21.04	32.87	37.6	32.58	32.8
26495	UGC04970	183.0050	45.1429	57.0212	-25.0337	2409	2650	5.7	0.20	227	2.356	13.98	13.81	14.40	14.47	14.50	-19.00	-18.90	33.53	50.9	33.41	48.2
26501	UGC04971	182.1172	45.1525	56.5907	-24.5444	1480	1708	1.0	0.55	314	2.566	11.54	11.59	12.35	12.37	12.34	-20.91	-20.96	33.28	45.2	33.37	47.3
26512	UGC04966	166.9418	44.1508	49.5245	-15.9782	633	805	3.0	0.44	592	2.809	8.05	7.86	8.65	8.65	8.61	-23.13	-23.33	31.74	22.3	31.99	25.0
26561	IC002469	259.9222	12.5112	149.7861	-52.5645	1666	1977	2.1	0.21	495	2.696	9.71	9.00	9.90	9.89	9.80	-22.09	-22.22	31.89	23.9	32.12	26.6
26563	UGC04982	175.8602	45.1956	53.7949	-20.9661	2659	2882	7.9	0.32	269	2.445	12.69	12.59	13.23	13.30	13.31	-19.81	-19.77	33.14	42.5	33.11	41.8
26608	E498-003	255.8444	16.4402	140.7128	-53.7858	2368	2700	3.2	0.31	296	2.485	12.15	11.89	12.18	12.23	12.43	-20.17	-20.16	32.61	33.3	32.41	30.3
26752	UGC05020	190.0005	45.7656	61.2937	-28.1749	1623	1878	5.8	0.24	194	2.292	13.34	13.29	14.33	14.40	14.20	-18.42	-18.28	32.63	33.5	32.70	34.6
26932	UGC05056	225.3261	38.4920	87.7316	-45.1478	2136	2475	1.0	0.61	395	2.687	11.05	11.03	11.69	11.76	11.75	-22.01	-22.13	33.81	57.7	33.96	62.0
27045	ES434-011	259.6745	15.3218	145.6415	-51.3647	2559	2891	6.8	0.46	192	2.326	12.58	12.54	13.05	13.12	13.19	-18.73	-18.61	31.92	24.2	31.73	22.2
27054	PG0027054	248.6046	25.1192	122.4963	-52.3816	4366	4757	6.1	0.20	323	2.509	/	/	13.58	13.63	/	/	-20.40	/	/	34.10	66.2
27074	UGC05081	224.9035	39.4032	87.3405	-44.2199	2144	2484	5.9	0.55	348	2.611	11.20	11.19	11.69	11.71	11.81	-21.32	-21.39	33.16	42.8	33.14	42.5
27077	UGC05079	208.7108	44.5403	73.5331	-36.4398	554	850	4.0	0.49	368	2.617	7.82	7.77	8.37	8.38	8.43	-21.37	-21.45	29.81	9.1	29.83	9.2
27130	PG0027130	249.4789	24.9205	123.7260	-52.0660	2117	2466	3.0	0.68	231	2.490	11.43	11.53	12.06	12.14	12.20	-20.21	-20.21	32.42	30.5	32.36	29.7
27158	AGC490097	244.9380	28.5586	115.0466	-51.2284	2666	3027	4.0	0.28	309	2.499	12.10	11.86	12.51	12.56	12.57	-20.30	-20.30	32.89	37.8	32.89	37.8
27214	NGC002921	253.0443	22.3385	130.4802	-51.8809	2967	3325	1.1	0.32	430	2.648	/	/	11.63	11.68	/	/	-21.76	/	/	33.48	49.7
27232	UGC05102	223.1747	40.8472	85.6832	-42.6756	2431	2773	3.7	0.35	314	2.516	12.02	11.88	12.48	12.55	12.57	-20.46	-20.47	33.05	40.7	33.05	40.7
27248	UGC05107	229.0911	38.4134	91.9152	-45.2380	2010	2355	6.4	0.23	166	2.223	13.93	13.91	15.09	15.16	14.89	-17.79	-17.61	32.69	34.6	32.79	36.2
27458	ES091-016	283.2489	-8.2646	185.6993	-34.5808	1999	2203	3.0	0.31	218	2.352	12.01	11.66	11.93	11.96	12.18	-18.96	-18.86	31.14	16.9	30.82	14.6
27473	UGC05115	135.4790	35.6745	35.3858	5.2119	2286	2336	5.8	0.56	198	2.370	13.03	13.15	13.93	14.02	13.94	-19.12	-19.04	33.09	41.4	33.09	41.4
27606	E373-019	262.9033	14.8055	148.7772	-48.9249	2808	3143	1.1	0.31	361	2.571	/	/	11.80	11.83	/	/	-21.00	/	/	32.86	37.3
27690	E434-023	259.7780	18.3750	141.7115	-49.6087	2527	2869	6.8	0.57	245	2.467	12.30	12.26	12.84	12.91	12.95	-20.01	-19.98	32.97	39.3	32.92	38.4
27747	AGC490130	241.9207	33.4170	108.2400	-47.9344	1851	2207	6.1	0.21	198	2.298	13.48	13.38	14.21	14.27	14.18	-18.47	-18.34	32.67	34.1	32.63	33.5
27810	PG0027810	245.4679	31.2454	113.7003	-48.6439	2701	3069	6.8	0.37	304	2.505	12.40	12.24	13.14	13.20	13.08	-20.36	-20.36	33.46	49.3	33.61	52.8
28087	UGC05238	236.0706	38.3695	99.5857	-44.5845	1792	2147	7.0	0.35	181	2.278	13.37	13.19	14.20	14.25	14.07	-18.29	-18.14	32.37	29.8	32.40	30.2
28098	UGC05203	131.7712	33.9114	33.4483	8.1572	1540	1563	6.4	0.20	166	2.220	13.70	13.69	14.87	14.94	14.66	-17.76	-17.58	32.43	30.7	32.53	32.1
28117	AGC026634	258.2653	21.6507	136.3982	-48.7732	4299	4686	5.0	0.24	365	2.566	12.06	11.65	12.53	12.58	12.47	-20.91	-20.95	33.41	48.1	33.59	52.2
28136	UGC05245	238.7928	37.0161	103.0076	-45.3670	1420	1773	8.0	0.20	145	2.161	13.77	13.79	15.02	15.10	14.79	-17.23	-17.00	32.02	25.4	32.11	26.4
28147	IC002510	264.0697	15.8345	148.2264	-47.4451	2805	3144	2.8	0.54	250	2.462	12.02	11.93	12.36	12.43	12.54	-19.97	-19.94	32.52	31.9	32.38	30.0
28148	UGC05249	233.9745	39.7453	97.0065	-43.5325	1878	2232	6.7	0.22	201	2.306	12.90	12.76	13.95	14.02	13.74	-18.54	-18.41	32.29	28.7	32.44	30.8
28186	UGC05251	192.3425	50.3406	65.9984	-25.7664	1481	1751	4.3	0.24	270	2.435	11.12	10.94	11.77	11.83	11.74	-19.72	-19.68	31.46	19.6	31.50	20.0
28196	UGC05250	175.7182	49.8103	57.7896	-18.2918	4772	5054	5.2	0.48	374	2.622	11.74	11.70	12.21	12.31	12.37	-21.42	-21.50	33.83	58.3	33.87	59.4
28224	AGC026650	255.2264	25.1800	129.6104	-48.4528	4701	5107	4.0	0.25	268	2.434	13.65	13.45	13.81	13.89	14.03	-19.71	-19.66	33.78	57.1	33.60	52.6
28246	IC002511	264.3443	16.0681	148.1101	-47.1015	2888	3229	1.7	0.20	414	2.617	11.30	10.68	11.48	11.49	11.44	-21.37	-21.45	32.83	36.9	32.97	39.3
28283	IC002513	264.4737	16.1189	148.1319	-46.9681	2868	3209	2.1	0.20	438	2.641	/	/	10.98	10.98	/	/	-21.69	/	/	32.70	34.6

PGC	Name	l	b	sgl	sgb	v_{hel}	v_{mod}	t	b/a	w_{mx}	$logw^{i}_{mx}$	I	I^{*}	[3.6]	$[3.6]^{*}$	$C_{[3.6]}$	M_{C}	$M_{[3.6]}$	μ_{C}	d_{C}	$\mu_{[3.6]}$	$d_{[3.6]}$
28296	UGC05271	222.3635	45.3333	85.5255	-38.1522	1442	1777	5.9	0.43	202	2.340	11.96	12.00	12.82	12.90	12.81	-18.85	-18.74	31.66	21.5	31.65	21.3
28313	E499-009	257.4631	23.4501	133.6079	-48.1694	2086	2437	2.6	0.43	290	2.498	/	/	12.39	12.46	/	/	-20.29	/	/	32.77	35.8
28357	UGC05280	192.1783	50.8387	66.2587	-25.3149	1537	1809	4.0	0.56	254	2.476	11.15	11.24	11.63	11.67	11.82	-20.09	-20.07	31.91	24.1	31.75	22.3
28376	AGC026671	264.5895	16.3890	147.8629	-46.7411	2790	3131	2.8	0.60	397	2.687	10.44	10.31	10.85	10.92	10.98	-22.01	-22.14	33.01	39.9	33.08	41.3
28380	PG0028380	249.3412	30.9492	118.1888	-47.2135	2526	2895	5.7	0.62	178	2.347	/	/	14.17	14.27	/	/	-18.81	/	/	33.11	42.0
28416	AGC026676	264.9242	16.2426	148.2734	-46.5286	2928	3270	5.6	0.34	249	2.414	12.09	11.91	12.98	13.04	12.82	-19.53	-19.47	32.36	29.6	32.52	32.0
28485	UGC05303	217.6683	47.5708	81.9789	-35.4319	1411	1738	5.4	0.64	265	2.530	10.57	10.67	11.27	11.35	11.37	-20.59	-20.61	31.96	24.7	31.96	24.7
28492	NGC03045	254.6520	27.0856	127.0972	-47.4220	2256	2617	2.9	0.45	237	2.415	12.39	12.39	12.79	12.87	13.00	-19.54	-19.48	32.54	32.3	32.36	29.7
28517	UGC05311	236.1971	40.3741	99.1389	-42.6038	1289	1642	5.6	0.20	317	2.501	10.99	10.65	11.26	11.29	11.33	-20.32	-20.32	31.65	21.4	31.62	21.1
28590	NGC003049	227.5655	44.7228	90.1786	-38.9569	1495	1840	2.5	0.47	199	2.343	11.68	11.74	12.38	12.41	12.44	-18.88	-18.78	31.32	18.3	31.18	17.2
28607	IC0002523	265.5477	16.5744	148.2595	-45.8448	2615	2953	4.0	0.51	179	2.311	12.05	12.07	12.47	12.56	12.68	-18.59	-18.46	31.27	17.9	31.02	16.0
28617	NGC03055	233.5392	42.2223	96.0653	-41.1326	1821	2177	5.3	0.53	255	2.469	11.34	11.36	11.87	11.90	11.99	-20.02	-20.00	32.02	25.4	31.90	24.0
28636	NGC03027	138.7809	39.0524	38.9841	2.8860	1059	1126	6.4	0.37	206	2.336	11.44	11.45	12.48	12.55	12.35	-18.82	-18.71	31.18	17.2	31.27	17.9
28741	UGC05347	233.6153	42.7746	96.0350	-40.5780	2154	2515	6.5	0.20	207	2.316	13.76	13.58	14.40	14.46	14.37	-18.64	-18.51	33.03	40.4	33.00	39.8
28778	AGC026733	262.7822	20.5211	141.4499	-46.0594	2662	3014	5.0	0.20	286	2.456	12.65	12.25	12.93	12.97	12.97	-19.91	-19.88	32.90	38.0	32.87	37.6
28795	UGC05349	186.1655	52.3051	64.3044	-21.7240	1376	1633	7.8	0.27	182	2.268	/	/	14.05	14.12	/	/	-18.04	/	/	32.17	27.1
28801	E499-025	260.4019	23.1918	136.4541	-46.2684	2403	2758	5.0	0.20	200	2.301	/	/	13.64	13.70	/	/	-18.37	/	/	32.07	26.0
28821	UGC05358	225.5657	46.5872	88.4460	-37.0684	2914	3276	3.1	0.32	194	2.302	/	/	14.63	14.72	/	/	-18.38	/	/	33.13	42.2
28830	UGC05354	169.5310	50.7355	56.4062	-14.4549	1169	1376	4.3	0.60	161	2.295	12.80	12.99	14.31	14.40	14.04	-18.44	-18.31	32.49	31.5	32.73	35.1
28840	AGC026748	264.2141	19.3758	143.8767	-45.5480	2810	3161	5.2	0.22	264	2.423	12.15	11.85	12.37	12.42	12.50	-19.61	-19.56	32.12	26.5	31.99	25.0
28909	AGC026767	263.9258	19.9758	142.9456	-45.4596	2472	2819	5.0	0.20	469	2.671	10.93	10.31	10.89	10.90	10.96	-21.87	-21.98	32.85	37.1	32.90	38.1
28939	UGC05376	235.5206	42.7874	97.8452	-40.3364	2050	2412	7.8	0.32	363	2.575	/	/	11.94	12.00	/	/	-21.04	/	/	33.06	41.0
29022	ES567-006	257.5796	27.1628	129.7438	-45.5576	3725	4114	6.5	0.20	227	2.356	14.64	14.43	15.46	15.53	15.33	-19.00	-18.90	34.39	75.7	34.53	80.6
29036	UGC005393	193.0179	53.0624	68.2288	-23.8993	1458	1735	8.0	0.52	145	2.221	/	/	14.46	14.55	/	/	-17.58	/	/	32.15	26.9
29086	PG0029086	245.6432	37.4316	109.9182	-43.0428	662	1019	7.2	0.20	117	2.068	/	/	14.73	14.77	/	/	-16.09	/	/	30.86	14.9
29157	IC0002536	267.4413	17.1054	148.7839	-43.9930	2732	3074	4.9	0.25	250	2.403	12.58	12.30	12.79	12.84	12.93	-19.43	-19.36	32.37	29.8	32.21	27.7
29203	IC0002539	265.8710	19.2249	145.1947	-44.2841	2833	3184	4.0	0.37	275	2.462	12.10	11.96	12.40	12.47	12.58	-19.96	-19.93	32.55	32.4	32.42	30.4
29278	NGC003120	267.9365	17.1349	149.0454	-43.5581	2791	3134	4.2	0.62	205	2.410	11.62	11.64	12.04	12.12	12.24	-19.50	-19.44	31.74	22.3	31.56	20.5
29296	NGC003057	130.6924	34.1952	33.7061	9.0597	1524	1545	7.9	0.63	133	2.225	/	/	13.44	13.54	/	/	-17.62	/	/	31.16	17.0
29427	UGC005451	170.0032	52.3109	57.9646	-13.9205	635	845	9.9	0.41	114	2.088	12.49	12.72	13.54	13.63	13.53	-16.56	-16.28	30.09	10.4	29.92	9.6
29466	PG0029466	224.6404	49.4175	87.8530	-34.2117	2756	3116	6.2	0.20	156	2.193	15.30	15.29	16.45	16.53	16.26	-17.52	-17.31	33.82	58.1	33.91	60.6
29472	UGC005459	160.8352	50.2756	53.5070	-9.6872	1109	1290	5.2	0.20	261	2.417	/	/	12.12	12.12	/	/	-19.50	/	/	31.61	21.0
29487	ES435-044	266.3669	20.0667	144.5144	-43.4557	2200	2544	6.4	0.20	130	2.114	/	/	16.64	16.72	/	/	-16.54	/	/	33.29	45.6
29530	NGC003137	265.2097	21.6742	141.8458	-43.5336	1104	1441	5.9	0.45	244	2.427	10.73	10.69	11.42	11.48	11.44	-19.65	-19.60	31.09	16.5	31.08	16.4
29641	ES435-050	266.4260	20.8360	143.6461	-43.0143	2716	3070	5.4	0.20	182	2.260	14.55	14.40	15.25	15.32	15.22	-18.13	-17.97	33.37	47.2	33.33	46.3
29691	NGC003157	267.3776	19.9847	145.2628	-42.6750	2840	3193	5.0	0.25	302	2.486	11.95	11.60	12.16	12.21	12.27	-20.18	-20.17	32.46	31.0	32.39	30.1

PGC	Name	l	b	sgl	sgb	v_{hel}	v_{mod}	t	b/a	w_{mx}	$logw^{i}_{mx}$	I	I^{*}	[3.6]	$[3.6]^{*}$	$C_{[3.6]}$	M_{C}	$M_{[3.6]}$	μ_{C}	d_{C}	$\mu_{[3.6]}$	$d_{[3.6]}$
29727	IC2556	269.5032	17.6367	149.3442	-41.9963	2503	2842	6.9	0.52	214	2.390	12.72	12.67	13.53	13.60	13.49	-19.31	-19.24	32.82	36.6	32.86	37.4
29743	ES436-001	265.0721	23.1348	140.0772	-42.8360	2614	2973	4.5	0.23	346	2.542	12.03	11.64	12.05	12.09	12.23	-20.69	-20.72	32.94	38.7	32.83	36.9
29835	UGC05522	233.8863	47.6186	95.4089	-35.7552	1220	1575	6.4	0.50	209	2.374	13.03	13.11	14.02	14.10	13.96	-19.16	-19.08	33.15	42.6	33.22	44.0
29892	AGC026974	266.1194	22.5773	141.4303	-42.3364	1090	1430	1.9	0.31	324	2.523	9.98	9.72	10.15	10.19	10.32	-20.52	-20.54	30.84	14.7	30.73	14.0
29898	IC0002559	269.4558	18.4367	148.3566	-41.6791	2990	3340	3.1	0.39	256	2.435	12.46	12.32	12.82	12.89	12.97	-19.71	-19.67	32.70	34.6	32.58	32.8
29993	IC002560	269.4218	19.0267	147.6352	-41.4387	2924	3275	3.4	0.46	376	2.617	10.63	10.45	11.07	11.14	11.15	-21.38	-21.45	32.54	32.2	32.61	33.2
30022	ES213-011	278.5252	6.5295	166.7910	-37.3613	2745	3038	5.0	0.51	360	2.613	10.58	10.28	10.81	10.85	10.92	-21.34	-21.41	32.27	28.4	32.27	28.5
30041	AGC500062	246.3249	41.8189	108.1073	-38.8410	1308	1675	7.8	0.54	168	2.291	/	/	13.55	13.63	/	/	-18.27	/	/	31.91	24.1
30059	UGC05554	213.2224	54.7039	80.8097	-27.8414	1248	1570	1.2	0.56	263	2.491	11.09	11.16	11.68	11.76	11.82	-20.23	-20.22	32.06	25.8	31.99	25.0
30064	NGC03155	135.3688	38.8398	38.5518	5.5130	2945	3022	3.5	0.54	248	2.460	12.72	12.78	13.35	13.44	13.47	-19.95	-19.92	33.45	49.1	33.41	48.0
30182	UGC05574	212.1751	55.3780	80.3767	-27.0249	1468	1791	5.9	0.28	128	2.115	13.88	14.01	15.00	15.09	14.90	-16.81	-16.55	31.72	22.0	31.65	21.4
30197	NGC03198	171.2186	54.8288	60.5646	-13.2329	660	881	5.2	0.34	296	2.490	9.57	9.47	10.33	10.33	10.26	-20.22	-20.21	30.48	12.5	30.54	12.9
30308	AGC027067	270.7960	19.0907	148.3370	-40.2516	2896	3246	3.4	0.70	415	2.754	9.73	9.70	9.85	9.92	10.18	-22.62	-22.79	32.82	36.6	32.73	35.2
30322	UGC05589	154.0945	50.1613	51.9360	-5.6647	1162	1325	6.0	0.59	164	2.300	11.76	11.94	12.79	12.88	12.77	-18.49	-18.35	31.26	17.8	31.23	17.7
30492	E436-014	267.9710	23.7697	141.3029	-40.2604	3887	4271	4.4	0.51	176	2.302	/	/	14.78	14.88	/	/	-18.38	/	/	33.29	45.5
30534	E317-023	274.3014	15.2733	154.6194	-38.7375	2751	3083	1.0	0.44	363	2.597	11.63	11.43	11.65	11.70	11.93	-21.19	-21.25	33.14	42.6	32.98	39.5
30569	UGC05631	152.1236	49.8645	51.2959	-4.5310	2121	2287	5.8	0.54	254	2.471	12.41	12.50	13.08	13.17	13.20	-20.04	-20.03	33.27	45.0	33.23	44.4
30604	UGC05642	229.9612	52.5435	91.8400	-31.0951	2359	2722	4.1	0.20	242	2.384	13.36	13.14	13.80	13.86	13.86	-19.25	-19.17	33.13	42.4	33.07	41.0
30670	IC000610	216.7851	56.2218	83.4268	-26.8527	1165	1494	3.8	0.20	303	2.481	/	/	12.15	12.19	/	/	-20.13	/	/	32.33	29.2
30688	ES568-012	263.7881	29.7971	132.0692	-39.7448	5699	6148	5.5	0.20	300	2.477	14.39	13.98	14.11	14.17	14.45	-20.10	-20.09	34.62	84.0	34.34	73.9
30714	NGC3245A	201.6435	58.1720	75.6799	-22.2519	1326	1628	3.4	0.20	179	2.253	13.32	13.26	14.11	14.17	14.07	-18.06	-17.90	32.14	26.8	32.08	26.0
30716	E375-026	272.9316	18.0953	150.6288	-38.8496	3128	3477	4.3	0.20	332	2.521	12.35	11.91	12.31	12.35	12.50	-20.50	-20.52	33.02	40.1	32.89	37.8
30774	NGC3250C	275.1965	15.0046	155.3359	-38.0280	2593	2921	1.9	0.37	348	2.565	/	/	12.09	12.14	/	/	-20.94	/	/	33.12	42.0
30867	NGC03256B	277.8233	11.4154	160.6510	-36.7648	2714	3028	3.9	0.31	326	2.526	11.79	11.45	11.85	11.89	12.04	-20.55	-20.57	32.60	33.1	32.47	31.3
30895	NGC03254	200.1086	58.7545	75.2197	-21.3568	1359	1659	4.0	0.32	393	2.610	10.69	10.46	11.42	11.47	11.32	-21.31	-21.38	32.64	33.7	32.87	37.6
30915	AGC027187	265.9322	28.3868	135.0079	-39.1532	3805	4199	6.7	0.52	245	2.449	13.01	13.00	13.89	13.97	13.84	-19.84	-19.81	33.72	55.5	33.85	58.8
31011	UGC005689	134.9406	39.7920	39.4866	5.9018	2827	2906	6.4	0.32	254	2.419	/	/	13.72	13.79	/	/	-19.52	/	/	33.35	46.8
31037	UGC05708	240.7977	49.6307	100.3128	-32.8408	1177	1541	6.6	0.20	167	2.223	12.92	12.87	14.22	14.29	13.93	-17.79	-17.60	31.72	22.1	31.90	24.0
31053	NGC3258C	273.1328	19.4229	149.1903	-38.1210	2561	2905	1.2	0.66	194	2.403	/	/	13.12	13.20	/	/	-19.36	/	/	32.58	32.9
31059	UGC05711	209.0458	58.5747	79.7070	-23.4536	6258	6682	3.1	0.30	512	2.721	11.81	11.45	12.07	12.14	12.16	-22.32	-22.47	34.54	81.0	34.72	87.8
31075	UGC005713	206.9519	58.8192	78.6978	-22.8354	6294	6715	4.0	0.26	477	2.685	12.61	12.21	12.80	12.86	12.90	-22.00	-22.12	34.99	99.4	35.13	106.1
31094	NGC3258D	273.3369	19.3215	149.4105	-37.9894	2480	2822	3.1	0.43	219	2.376	/	/	12.28	12.35	/	/	-19.10	/	/	31.45	19.5
31125	NGC003264	153.9364	51.8400	53.5196	-5.0797	935	1103	7.9	0.30	132	2.132	/	/	13.76	13.85	/	/	-16.72	/	/	30.57	13.0
31126	IC002589	266.4586	28.8109	134.9283	-38.5289	3703	4096	3.2	0.48	212	2.374	/	/	12.88	12.97	/	/	-19.08	/	/	32.06	25.8
31145	UGC05717	143.2583	46.2282	46.5150	0.5129	1675	1796	3.7	0.60	233	2.454	11.91	12.04	12.51	12.60	12.69	-19.89	-19.86	32.59	33.0	32.48	31.3
31154	ES436-034	269.4599	25.1006	140.7687	-38.4062	3611	3992	3.1	0.22	533	2.729	11.98	11.38	11.72	11.74	11.93	-22.39	-22.55	34.39	75.4	34.38	75.2

PGC	Name	l	b	sgl	sgb	v_{hel}	v_{mod}	t	b/a	w_{mx}	$logw^{i}_{mx}$	I	I^{*}	[3.6]	$[3.6]^{*}$	$C_{[3.6]}$	M_{C}	$M_{[3.6]}$	μ_{C}	d_{C}	$\mu_{[3.6]}$	$d_{[3.6]}$
31186	ES501-011	266.9654	28.5063	135.5784	-38.3522	3769	4163	6.0	0.20	293	2.467	13.55	13.19	13.69	13.74	13.83	-20.01	-19.99	33.88	59.7	33.78	57.1
31217	NGC03285	268.9156	26.1640	139.2887	-38.2518	3394	3774	1.2	0.50	545	2.791	10.71	10.52	11.10	11.17	11.20	-22.96	-23.15	34.22	69.7	34.41	76.3
31238	E436-038	269.2104	25.8902	139.7642	-38.1769	2748	3116	4.2	0.58	190	2.359	/	/	15.04	15.13	/	/	-18.93	/	/	34.14	67.3
31242	E436-039	270.6575	23.9547	142.7328	-38.0600	3493	3868	3.9	0.20	412	2.615	12.79	12.27	12.48	12.51	12.76	-21.36	-21.43	34.17	68.2	34.02	63.6
31265	IC0002596	293.3305	-12.9807	191.4074	-24.7885	3380	3561	2.2	0.62	121	2.179	/	/	12.18	12.26	/	/	-17.18	/	/	29.44	7.7
31273	NGC3281D	273.2013	20.4334	148.0698	-37.6280	2643	2992	6.5	0.22	255	2.408	12.55	12.26	12.90	12.95	12.96	-19.48	-19.42	32.45	30.9	32.38	29.9
31276	E436-040	271.9263	22.3077	145.2771	-37.8387	4435	4827	2.1	0.31	281	2.462	/	/	13.19	13.25	/	/	-19.94	/	/	33.23	44.2
31293	NGC3285B	269.2476	26.1255	139.5349	-38.0220	3027	3400	3.2	0.63	241	2.483	/	/	12.82	12.90	/	/	-20.14	/	/	33.08	41.3
31302	UGC05741	232.6218	54.1729	93.5239	-29.3465	1392	1748	6.4	0.20	347	2.540	11.69	11.29	11.75	11.78	11.90	-20.68	-20.70	32.59	32.9	32.50	31.6
31307	UGC005740	161.1693	54.9767	57.9721	-8.0500	656	853	8.8	0.59	127	2.188	/	/	14.69	14.78	/	/	-17.26	/	/	32.05	25.7
31311	NGC03287	215.3858	58.5059	83.1558	-24.4598	1305	1633	7.6	0.41	188	2.305	11.42	11.49	12.18	12.26	12.24	-18.54	-18.41	30.77	14.3	30.67	13.6
31355	E501-022	269.4271	26.1818	139.5848	-37.8560	2900	3271	4.2	0.23	170	2.233	/	/	15.91	15.99	/	/	-17.71	/	/	33.75	56.3
31360	E437-004	269.8131	25.6701	140.3674	-37.8348	3298	3675	4.0	0.47	317	2.546	12.18	12.07	12.53	12.61	12.71	-20.73	-20.76	33.46	49.2	33.41	48.0
31428	UGC05753	184.6183	59.8424	69.2473	-15.7521	1573	1844	5.1	0.47	386	2.631	10.23	10.17	10.78	10.80	10.84	-21.51	-21.59	32.36	29.6	32.40	30.3
31482	E501-037	268.1889	28.3739	136.5081	-37.5537	3669	4060	2.7	0.72	127	2.254	/	/	14.98	15.09	/	/	-17.90	/	/	33.02	40.3
31487	E437-012	271.4937	23.9027	143.2692	-37.4220	3566	3942	3.8	0.46	122	2.129	/	/	16.20	16.30	/	/	-16.69	/	/	33.02	40.2
31493	ES437-014	272.5083	22.4567	145.4278	-37.2933	2859	3218	2.2	0.39	364	2.588	11.44	11.24	11.62	11.68	11.83	-21.11	-21.17	32.96	39.0	32.88	37.6
31494	E501-041	269.3441	26.9046	138.7660	-37.5271	3551	3936	3.8	0.60	188	2.362	/	/	14.76	14.86	/	/	-18.96	/	/	33.89	59.8
31528	UGC05774	230.9791	55.4311	92.3222	-28.1762	2890	3263	7.8	0.49	259	2.463	12.48	12.52	12.65	12.73	13.00	-19.98	-19.95	32.99	39.7	32.71	34.8
31533	NGC03318	277.6690	14.5693	156.8701	-35.9297	2773	3100	3.6	0.54	330	2.585	11.02	10.95	11.37	11.44	11.56	-21.08	-21.14	32.65	34.0	32.59	33.0
31560	UGC005765	138.9931	43.8966	43.8268	3.2125	1826	1925	4.0	0.23	200	2.304	/	/	14.47	14.54	/	/	-18.39	/	/	32.96	39.1
31590	ES437-018	271.7240	23.9883	143.3049	-37.1966	3369	3742	3.5	0.29	300	2.488	13.34	13.11	13.54	13.60	13.72	-20.20	-20.19	33.97	62.1	33.86	59.1
31593	E437-019	270.6922	25.4799	141.0939	-37.2576	4382	4782	1.7	0.68	288	2.584	12.27	12.34	12.77	12.87	12.97	-21.07	-21.13	34.09	65.8	34.07	65.2
31600	ES019-003	297.7498	-19.5998	198.5975	-20.5688	2004	2117	5.2	0.56	200	2.376	12.23	12.24	12.77	12.84	12.90	-19.18	-19.10	32.09	26.1	31.94	24.5
31626	AGC027386	270.7527	25.5408	141.0637	-37.1793	4387	4787	4.0	0.26	284	2.459	13.53	13.27	14.12	14.18	14.09	-19.94	-19.91	34.08	65.3	34.18	68.4
31638	AGC027392	270.1115	26.5358	139.6214	-37.1485	4413	4816	6.5	0.57	148	2.248	12.60	12.72	13.18	13.29	13.37	-18.02	-17.85	31.39	18.9	31.14	16.9
31642	E437-025	270.6385	25.8514	140.6635	-37.1067	3463	3843	3.4	0.37	245	2.412	12.76	12.66	13.15	13.22	13.31	-19.51	-19.45	32.83	36.9	32.70	34.6
31653	AGC500163	258.8818	39.6227	119.6890	-35.6251	2487	2875	5.1	0.48	265	2.472	12.12	12.10	12.91	12.99	12.90	-20.06	-20.04	32.98	39.4	33.06	40.9
31671	UGC05789	175.9803	59.3417	65.8825	-12.8012	739	984	6.0	0.49	195	2.342	10.76	10.87	11.74	11.82	11.70	-18.87	-18.76	30.57	13.0	30.59	13.1
31677	ES437-030	271.7820	24.4610	142.8216	-36.9184	3762	4144	4.2	0.22	428	2.634	11.63	11.13	11.74	11.77	11.81	-21.53	-21.62	33.37	47.2	33.43	48.6
31683	AGC027404	269.7188	27.3787	138.4952	-36.9890	3080	3457	4.0	0.34	323	2.528	12.50	12.29	13.02	13.08	13.04	-20.56	-20.58	33.64	53.5	33.72	55.4
31690	E437-031	271.3867	25.0775	141.9292	-36.9224	3881	4267	7.2	0.62	203	2.403	13.40	13.50	14.32	14.43	14.32	-19.43	-19.36	33.79	57.3	33.85	58.9
31697	UGC05791	164.9637	56.9874	60.7228	-9.1210	852	1066	3.0	0.34	143	2.173	13.53	13.67	15.09	15.18	14.77	-17.34	-17.12	32.11	26.4	32.31	28.9
31708	UGC05794	165.8441	57.2593	61.1895	-9.4212	2315	2545	5.8	0.44	277	2.481	11.84	11.83	12.41	12.49	12.52	-20.14	-20.12	32.67	34.2	32.63	33.6
31720	UGC05798	164.9406	57.0442	60.7683	-9.0841	1529	1748	6.4	0.34	169	2.247	13.46	13.54	14.73	14.82	14.53	-18.00	-17.83	32.54	32.3	32.67	34.2
31732	E437-034	271.4134	25.2959	141.7087	-36.7913	3767	4151	3.8	0.38	170	2.255	14.50	14.54	16.07	16.17	15.70	-18.08	-17.92	33.82	58.0	34.16	68.0

PGC	Name	l	b	sgl	sgb	v_{hel}	v_{mod}	t	b/a	w_{mx}	$logw^{i}_{mx}$	I	I^{*}	[3.6]	$[3.6]^{*}$	$C_{[3.6]}$	M_{C}	$M_{[3.6]}$	μ_{C}	d_{C}	$\mu_{[3.6]}$	$d_{[3.6]}$
31738	E437-035	271.9301	24.5815	142.7734	-36.7417	3392	3767	3.9	0.37	236	2.396	12.76	12.67	13.20	13.28	13.34	-19.36	-19.29	32.71	34.9	32.59	32.9
31761	NGC3347A	275.4308	19.3642	150.3814	-36.1713	2785	3131	5.6	0.28	322	2.516	11.62	11.32	11.95	12.00	12.02	-20.46	-20.47	32.49	31.4	32.48	31.3
31797	NGC03347C	275.4655	19.5267	150.2134	-36.0760	2656	3000	6.9	0.69	113	2.185	/	/	14.50	14.60	/	/	-17.23	/	/	31.83	23.3
31805	AGC027441	270.2220	27.3772	138.7994	-36.6144	4743	5157	5.0	0.50	322	2.562	11.76	11.69	12.27	12.36	12.39	-20.87	-20.92	33.29	45.5	33.32	46.1
31809	E437-039	271.2232	25.9825	140.8632	-36.5887	3744	4130	2.9	0.56	152	2.255	/	/	14.94	15.04	/	/	-17.91	/	/	32.99	39.6
31829	E501-078	269.7246	28.1857	137.6568	-36.5417	4440	4848	3.0	0.21	253	2.404	/	/	14.04	14.10	/	/	-19.37	/	/	33.53	50.7
31875	NGC03347B	276.0162	19.0813	150.9734	-35.7764	3187	3538	7.2	0.24	327	2.519	11.90	11.54	12.55	12.59	12.42	-20.48	-20.49	32.92	38.3	33.12	42.0
31883	NGC03338	230.3314	57.0195	91.8026	-26.6142	1298	1649	5.1	0.52	331	2.578	10.10	10.09	10.75	10.77	10.79	-21.02	-21.08	31.82	23.1	31.86	23.5
31919	ES501-080	268.6224	30.2208	134.8984	-36.1768	1043	1400	4.9	0.25	132	2.126	12.70	12.76	13.67	13.75	13.61	-16.91	-16.66	30.52	12.7	30.41	12.1
31951	ES501-082	270.1841	28.3456	137.7675	-36.1158	4520	4930	4.0	0.43	383	2.619	12.40	12.23	12.75	12.83	12.89	-21.39	-21.47	34.34	73.8	34.39	75.5
31987	AGC027491	269.1495	30.0021	135.4457	-35.9320	3728	4124	4.2	0.46	335	2.567	12.17	12.06	12.74	12.82	12.80	-20.92	-20.97	33.76	56.6	33.85	59.0
31995	E318-004	277.0489	18.1126	152.5331	-35.2431	2935	3278	5.1	0.21	382	2.583	11.47	11.00	11.69	11.72	11.72	-21.07	-21.12	32.80	36.3	32.87	37.5
31996	UGC05844	203.3727	61.8234	78.2546	-19.3731	1465	1774	6.6	0.22	129	2.112	/	/	15.59	15.68	/	/	-16.52	/	/	32.21	27.7
32039	E437-056	273.9027	23.4053	145.1189	-35.7162	2929	3291	3.9	0.64	239	2.485	12.17	12.22	12.84	12.92	12.93	-20.17	-20.16	33.13	42.2	33.12	42.1
32044	AGC500190	259.9342	40.8317	119.4917	-34.1825	1915	2296	5.0	0.35	249	2.416	11.90	11.84	12.56	12.63	12.59	-19.55	-19.49	32.14	26.8	32.13	26.6
32059	NGC003329	131.6928	38.0794	37.6557	8.3539	1890	1939	2.9	0.62	322	2.604	11.08	11.16	11.81	11.90	11.89	-21.26	-21.33	33.17	43.1	33.27	45.0
32153	NGC03365	247.7518	50.7552	104.7812	-30.2763	988	1357	5.9	0.20	217	2.336	11.76	11.58	12.55	12.60	12.44	-18.82	-18.71	31.26	17.9	31.31	18.3
32183	NGC03359	143.5967	48.5922	48.8864	0.6452	1014	1142	5.2	0.72	237	2.527	10.08	10.27	10.86	10.96	10.97	-20.55	-20.57	31.53	20.2	31.53	20.2
32192	UGC05882	234.4355	57.0102	94.2884	-26.4066	892	1245	2.2	0.64	328	2.621	8.12	8.21	8.77	8.80	8.87	-21.42	-21.50	30.28	11.4	30.30	11.5
32207	UGC05887	225.3509	59.6722	88.8842	-23.9883	1283	1626	5.1	0.55	264	2.492	11.15	11.21	11.70	11.73	11.83	-20.24	-20.23	32.08	26.0	31.97	24.8
32251	UGC05897	235.8052	56.7996	95.1495	-26.5029	2716	3092	5.2	0.32	283	2.466	12.09	11.96	12.83	12.90	12.78	-20.00	-19.98	32.80	36.3	32.90	38.1
32287	UGC05906	202.5714	62.7982	78.3470	-18.3333	1603	1913	1.0	0.56	111	2.118	11.68	11.91	12.33	12.43	12.53	-16.84	-16.58	29.37	7.5	29.01	6.3
32306	UGC05914	233.7198	57.7405	93.7573	-25.7323	1306	1661	5.3	0.44	247	2.430	11.12	11.13	11.77	11.84	11.85	-19.67	-19.63	31.52	20.1	31.47	19.7
32532	UGC05958	204.3580	63.4053	79.3887	-18.1263	1182	1491	4.0	0.24	166	2.224	13.44	13.45	14.04	14.11	14.14	-17.80	-17.61	31.94	24.5	31.73	22.2
32550	AGC027566	268.0294	34.7199	130.1552	-33.8512	2054	2430	6.4	0.20	253	2.403	12.16	11.91	12.89	12.94	12.78	-19.43	-19.36	32.21	27.7	32.31	29.0
32565	ES376-023	277.0431	21.2993	148.9633	-34.0070	4756	5149	4.9	0.21	337	2.528	13.62	13.18	13.59	13.64	13.77	-20.57	-20.59	34.40	76.0	34.31	72.9
32614	UGC05982	192.9020	63.6382	74.8923	-15.3803	1585	1878	5.1	0.50	337	2.580	10.68	10.67	11.23	11.31	11.35	-21.04	-21.10	32.40	30.2	32.41	30.4
32625	ES437-067	275.7238	23.8293	145.5754	-34.0359	3186	3552	2.0	0.52	121	2.142	/	/	12.08	12.18	/	/	-16.82	/	/	29.00	6.3
32648	UGC05995	215.1816	62.8195	84.1004	-20.2343	1276	1603	5.3	0.36	300	2.499	10.99	10.90	11.22	11.23	11.43	-20.30	-20.30	31.74	22.2	31.54	20.3
32666	AGC027580	275.9842	23.6679	145.8770	-33.8932	3277	3644	2.1	0.38	503	2.727	10.72	10.40	11.10	11.15	11.13	-22.37	-22.52	33.54	51.0	33.73	55.7
32671	UGC06000	225.9867	61.0847	89.2757	-22.5866	1133	1475	6.6	0.49	169	2.277	12.80	12.91	13.92	14.01	13.81	-18.28	-18.13	32.10	26.3	32.15	26.9
32714	UGC06009	149.5546	53.5012	54.4235	-2.0795	1908	2081	3.0	0.35	222	2.366	12.99	12.99	13.94	14.02	13.86	-19.09	-19.00	32.97	39.3	33.05	40.8
32719	NGC03403	133.4429	40.9516	40.5967	7.0977	1261	1325	4.0	0.34	282	2.467	11.60	11.38	12.06	12.10	12.10	-20.01	-19.99	32.12	26.5	32.10	26.3
32754	UGC06023	205.8873	64.0213	80.2988	-17.8286	1333	1646	6.6	0.47	227	2.400	11.99	12.05	12.80	12.88	12.82	-19.40	-19.33	32.23	27.9	32.22	27.8
32813	NGC003463	272.7617	29.8362	137.7192	-33.4152	3948	4346	3.0	0.45	390	2.631	12.05	11.88	12.42	12.50	12.55	-21.51	-21.59	34.11	66.3	34.17	68.2
32869	AGC027604	276.1459	24.8730	144.6596	-33.2261	3334	3705	6.0	0.21	359	2.556	12.72	12.21	12.88	12.91	12.92	-20.82	-20.86	33.78	57.0	33.83	58.2

PGC	Name	l	b	sgl	sgb	v_{hel}	v_{mod}	t	b/a	w_{mx}	$logw^{i}_{mx}$	I	I^{*}	[3.6]	$[3.6]^{*}$	$C_{[3.6]}$	M_{C}	$M_{[3.6]}$	μ_{C}	d_{C}	$\mu_{[3.6]}$	$d_{[3.6]}$
33163	UGC06083	229.2797	62.2933	90.9533	-21.3709	946	1290	4.1	0.20	167	2.223	13.89	13.87	14.82	14.89	14.73	-17.79	-17.60	32.53	32.0	32.50	31.6
33188	UGC06080	143.7345	51.0985	51.3767	0.9441	2180	2331	6.5	0.20	169	2.228	13.99	13.98	15.07	15.15	14.92	-17.83	-17.65	32.77	35.7	32.83	36.8
33234	UGC06098	249.8872	54.7261	104.2600	-26.1261	1126	1496	6.4	0.23	297	2.475	10.79	10.50	11.28	11.27	11.24	-20.09	-20.07	31.33	18.4	31.34	18.5
33242	UGC06096	147.6777	53.8409	54.5085	-0.9201	2994	3179	5.2	0.60	232	2.452	12.13	12.26	12.94	13.04	13.01	-19.87	-19.84	32.89	37.9	32.90	38.0
33276	UGC06104	229.7863	62.5643	91.1930	-21.0907	2946	3314	4.0	0.29	229	2.371	13.49	13.42	14.40	14.48	14.31	-19.13	-19.05	33.47	49.4	33.58	52.0
33343	UGC06116	227.2718	63.3743	89.9531	-20.3057	1129	1471	5.9	0.20	291	2.464	11.51	11.21	11.67	11.71	11.82	-19.98	-19.96	31.81	23.0	31.67	21.5
33385	NGC003511	272.9003	33.4089	134.2440	-31.3733	1105	1467	5.1	0.31	279	2.459	10.01	9.82	10.45	10.50	10.52	-19.93	-19.91	30.45	12.3	30.41	12.1
33408	UGC06126	202.3635	66.2108	79.8214	-15.2250	706	1009	8.6	0.26	177	2.254	12.21	12.20	13.24	13.26	13.08	-18.07	-17.91	31.16	17.0	31.17	17.1
33474	ES377-004	280.6291	20.5574	151.3071	-31.2013	3155	3506	5.9	0.20	165	2.217	/	/	15.51	15.58	/	/	-17.55	/	/	33.16	42.9
33550	UGC06150	255.5318	52.8293	108.5325	-26.2132	802	1174	4.0	0.58	441	2.725	7.73	7.68	8.19	8.20	8.30	-22.35	-22.50	30.66	13.5	30.70	13.8
33601	E377-010	280.9668	20.7036	151.2823	-30.8537	2875	3221	3.1	0.31	394	2.609	11.24	10.85	11.59	11.63	11.60	-21.30	-21.38	32.92	38.3	33.04	40.5
33633	UGC06162	155.1956	58.8719	60.4544	-3.6153	2207	2418	6.4	0.49	215	2.383	12.25	12.33	13.33	13.42	13.23	-19.25	-19.17	32.49	31.4	32.60	33.2
33635	UGC06167	246.9673	58.1859	101.1237	-23.5823	1420	1788	5.2	0.21	190	2.280	12.36	12.27	13.15	13.22	13.10	-18.31	-18.16	31.41	19.1	31.38	18.9
33647	NGC03533	280.8657	21.1893	150.7157	-30.7640	3122	3474	2.8	0.27	392	2.601	11.48	11.04	11.76	11.79	11.77	-21.23	-21.30	33.02	40.2	33.12	42.0
33705	ES265-007	284.9839	12.7032	161.4720	-29.6783	1068	1359	6.1	0.29	232	2.376	10.15	9.90	10.63	10.67	10.65	-19.19	-19.10	29.83	9.2	29.77	9.0
33813	ES502-020	274.2361	34.2463	134.1436	-29.9858	1380	1745	5.0	0.71	115	2.204	/	/	13.80	13.89	/	/	-17.42	/	/	31.31	18.3
33866	NGC03547	242.5353	61.0332	97.8323	-21.6099	1589	1952	3.1	0.49	185	2.317	12.05	12.15	12.77	12.86	12.87	-18.64	-18.52	31.51	20.0	31.38	18.9
33952	NGC003568	281.7033	21.2411	150.9898	-30.0181	2442	2782	5.0	0.32	264	2.436	11.38	11.15	11.49	11.54	11.71	-19.73	-19.69	31.44	19.4	31.23	17.6
33962	ES377-021	281.0862	22.5891	149.2986	-30.0517	2762	3112	3.1	0.40	272	2.463	12.29	12.15	12.86	12.92	12.90	-19.97	-19.94	32.88	37.7	32.89	37.9
33964	UGC06215	151.3384	57.8426	58.8811	-1.9772	2851	3059	5.1	0.34	406	2.627	11.08	10.88	11.61	11.67	11.63	-21.46	-21.55	33.11	42.0	33.25	44.7
34030	UGC06225	148.3145	56.2518	56.9420	-0.7622	699	871	6.0	0.35	300	2.498	9.03	8.93	9.38	9.44	9.55	-20.29	-20.29	29.84	9.3	29.72	8.8
34248	UGC06267	231.6630	65.5381	91.8685	-18.0722	1297	1642	5.3	0.23	188	2.278	12.64	12.61	13.22	13.29	13.31	-18.29	-18.14	31.60	20.9	31.43	19.3
34260	UGC006271	198.6375	68.5774	79.6408	-12.4654	1996	2305	1.0	0.38	217	2.361	/	/	13.44	13.52	/	/	-18.96	/	/	32.50	31.6
34292	E438-015	278.4675	29.8605	140.5773	-29.1112	3369	3751	4.2	0.40	306	2.514	11.97	11.81	12.48	12.55	12.54	-20.44	-20.45	33.00	39.8	33.03	40.3
34308	UGC06275	142.1439	52.6901	52.8110	2.1444	1969	2122	7.0	0.51	147	2.224	12.97	13.15	14.31	14.41	14.13	-17.80	-17.61	31.93	24.3	32.03	25.4
34362	ES377-031	281.2380	24.8524	146.9617	-29.0469	3017	3377	4.0	0.49	273	2.487	12.20	12.15	12.96	13.04	12.95	-20.19	-20.18	33.16	42.9	33.26	44.8
34508	UGC06309	152.5338	59.9290	61.0581	-2.0063	2873	3092	4.5	0.70	211	2.460	12.10	12.27	12.63	12.74	12.87	-19.94	-19.92	32.83	36.8	32.67	34.2
34519	ES319-011	284.3566	18.8799	154.5046	-28.4746	3096	3436	5.8	0.68	273	2.562	11.73	11.70	12.65	12.72	12.56	-20.87	-20.92	33.47	49.4	33.70	54.9
34554	NGC003621	281.2141	26.0988	145.6488	-28.5667	731	1068	6.9	0.44	266	2.462	8.46	8.37	8.93	8.98	9.04	-19.96	-19.93	29.00	6.3	28.92	6.1
34561	UGC06318	161.5459	63.7840	66.1502	-4.6495	2328	2570	5.2	0.61	285	2.548	11.12	11.23	12.10	12.19	12.06	-20.75	-20.78	32.83	36.8	33.00	39.8
34612	UGC06328	241.3297	64.2218	96.3585	-18.6843	807	1159	1.0	0.29	483	2.695	8.11	7.75	8.63	8.61	8.54	-22.08	-22.21	30.62	13.3	30.82	14.6
34691	ES570-019	276.2199	36.6241	132.8674	-27.3378	1339	1706	4.5	0.54	154	2.254	/	/	14.01	14.10	/	/	-17.90	/	/	32.01	25.2
34692	UGC06339	135.7685	47.5488	47.3050	5.7376	1316	1422	6.0	0.68	149	2.299	12.24	12.46	13.09	13.13	13.16	-18.48	-18.35	31.64	21.3	31.48	19.8
34695	UGC06346	241.9619	64.4182	96.5841	-18.4237	728	1079	3.1	0.55	333	2.593	7.75	7.77	8.27	8.29	8.39	-21.15	-21.22	29.55	8.1	29.51	8.0
34697	NGC03628	240.8527	64.7802	96.0025	-18.1944	845	1196	3.1	0.22	451	2.656	8.09	7.62	8.46	8.42	8.38	-21.73	-21.83	30.11	10.5	30.26	11.3
34718	UGC06348	144.2185	55.4288	55.6993	1.3404	1946	2116	3.1	0.32	238	2.392	12.70	12.65	13.45	13.52	13.45	-19.32	-19.25	32.78	36.1	32.80	36.3

PGC	Name	l	b	sgl	sgb	v_{hel}	v_{mod}	t	b/a	w_{mx}	$logw^{i}_{mx}$	I	I^{*}	[3.6]	$[3.6]^{*}$	$C_{[3.6]}$	M_C	$M_{[3.6]}$	μ_C	d_C	$\mu_{[3.6]}$	$d_{[3.6]}$
34719	NGC03629	208.1715	69.7855	83.3094	-12.7698	1507	1823	5.9	0.71	190	2.422	11.93	12.13	13.02	13.12	12.98	-19.60	-19.55	32.59	33.0	32.69	34.5
34733	UGC06355	195.8197	69.8056	79.4003	-10.8989	2182	2490	6.4	0.20	178	2.250	13.62	13.57	14.65	14.73	14.50	-18.04	-17.87	32.55	32.4	32.62	33.4
34836	UGC06376	226.8524	68.3466	89.8020	-15.3325	4246	4631	4.6	0.50	508	2.759	10.38	10.27	10.90	10.98	10.99	-22.67	-22.85	33.70	54.9	33.89	59.9
34869	UGC06378	133.8169	45.5629	45.2500	6.9917	1308	1399	6.5	0.20	146	2.164	13.48	13.53	14.41	14.49	14.37	-17.26	-17.03	31.62	21.1	31.52	20.2
34874	ES319-016	284.1764	21.5319	151.6025	-27.7598	2884	3229	5.3	0.45	360	2.596	13.04	12.84	13.58	13.64	13.60	-21.18	-21.25	34.87	94.0	35.02	101.2
34917	NGC03652	177.6527	68.5406	73.6458	-7.6228	1995	2272	5.7	0.40	225	2.381	11.86	11.88	12.67	12.70	12.65	-19.22	-19.14	31.87	23.7	31.85	23.5
34929	UGC06390	137.9454	50.3962	50.2519	4.4996	1013	1137	6.4	0.20	150	2.177	13.86	13.92	15.00	15.08	14.85	-17.37	-17.15	32.22	27.9	32.24	28.1
34935	UGC06396	235.5865	66.9685	93.3426	-16.4729	1501	1850	5.0	0.73	285	2.611	10.78	10.94	11.11	11.15	11.41	-21.32	-21.40	32.75	35.5	32.56	32.5
34971	UGC06399	152.0791	60.9605	61.9874	-1.5048	792	992	8.8	0.28	167	2.231	12.87	12.92	14.07	14.09	13.86	-17.86	-17.68	31.72	22.1	31.78	22.7
34995	NGC03659	233.0786	67.7547	92.2430	-15.8142	1285	1628	7.7	0.51	206	2.370	11.90	12.00	12.48	12.51	12.62	-19.12	-19.04	31.75	22.3	31.55	20.4
35006	AGC510055	271.8302	45.2298	122.9527	-24.9265	5016	5462	3.9	0.72	314	2.647	/	/	12.42	12.53	/	/	-21.74	/	/	34.36	74.5
35025	NGC03654	133.7425	45.8403	45.5276	7.0527	1574	1668	4.0	0.55	195	2.358	12.26	12.40	13.02	13.11	13.11	-19.02	-18.92	32.13	26.7	32.04	25.5
35043	UGC06420	246.4031	64.1789	98.5928	-18.0688	1059	1416	5.2	0.33	257	2.427	11.04	10.95	11.55	11.56	11.62	-19.64	-19.59	31.26	17.9	31.16	17.0
35088	AGC510059	270.4229	47.5490	120.3273	-24.1412	1866	2249	5.0	0.44	377	2.615	10.20	10.09	10.62	10.63	10.72	-21.36	-21.44	32.09	26.2	32.08	26.0
35097	AGC027880	280.0942	32.2830	138.8824	-26.7517	1939	2302	3.2	0.42	312	2.527	10.20	10.09	10.98	11.04	10.92	-20.56	-20.58	31.48	19.8	31.62	21.1
35113	NGC003669	143.3449	55.8673	56.0569	1.8949	1846	2015	6.8	0.20	224	2.350	12.07	11.91	13.00	13.06	12.84	-18.95	-18.85	31.79	22.8	31.91	24.1
35164	UGC06439	163.6604	66.1897	68.7137	-4.4169	768	1006	3.0	0.57	405	2.684	8.75	8.77	9.24	9.31	9.40	-21.98	-22.11	31.39	18.9	31.42	19.2
35249	UGC06458	143.8159	56.7179	56.9377	1.7646	1709	1881	5.0	0.41	354	2.581	11.05	10.96	10.86	10.87	11.29	-21.04	-21.10	32.34	29.4	31.98	24.8
35288	ES378-003	284.7874	23.3743	149.8790	-26.5926	3019	3371	5.4	0.51	257	2.466	12.12	12.03	12.94	13.01	12.87	-20.00	-19.97	32.89	37.8	33.01	40.0
35294	UGC06467	212.7145	71.3200	85.2523	-11.7532	2738	3074	5.3	0.61	327	2.607	11.24	11.31	11.63	11.72	11.88	-21.28	-21.35	33.19	43.4	33.11	41.8
35314	NGC03692	251.1340	63.5797	100.8564	-17.8285	1718	2084	3.1	0.22	404	2.608	11.29	10.85	11.71	11.74	11.65	-21.29	-21.37	32.96	39.1	33.13	42.4
35347	NGC3697	227.0504	70.1264	89.8882	-13.5533	6265	6707	3.4	0.30	504	2.715	12.02	11.66	12.52	12.59	12.48	-22.26	-22.41	34.83	92.4	35.14	106.7
35405	UGC06493	217.6929	71.2985	86.8399	-12.1156	2804	3147	4.0	0.50	249	2.451	12.19	12.25	12.97	13.06	13.01	-19.86	-19.83	32.89	37.9	32.91	38.2
35440	UGC06498	252.0215	63.7858	101.1371	-17.4738	1018	1378	2.4	0.45	345	2.577	9.81	9.72	10.46	10.47	10.45	-21.01	-21.07	31.46	19.6	31.53	20.3
35521	UGC06509	221.0056	71.4608	87.9342	-12.1051	2914	3261	6.6	0.20	177	2.248	14.26	14.22	15.43	15.51	15.21	-18.02	-17.85	33.26	44.8	33.40	47.9
35539	NGC003717	283.1292	29.4730	142.9687	-25.6401	1733	2084	3.1	0.28	406	2.617	9.72	9.34	9.89	9.92	9.99	-21.37	-21.45	31.37	18.8	31.37	18.8
35540	AGC510082	275.3620	44.3214	125.4324	-23.5138	2120	2503	3.8	0.65	262	2.529	11.63	11.74	11.94	12.03	12.25	-20.57	-20.59	32.84	37.0	32.64	33.7
35608	NGC03752	129.7859	41.4339	41.0361	9.8573	1918	1982	2.0	0.44	212	2.363	12.42	12.44	12.85	12.93	13.05	-19.07	-18.98	32.12	26.5	31.91	24.1
35622	AGC210432	230.2292	70.6642	90.9712	-12.9917	6130	6569	5.3	0.56	243	2.458	13.95	14.04	14.56	14.68	14.72	-19.93	-19.90	34.73	88.4	34.70	87.0
35675	UGC06534	136.9535	51.6699	51.4828	5.2116	1271	1401	6.4	0.23	162	2.213	12.51	12.52	13.50	13.58	13.41	-17.70	-17.50	31.10	16.6	31.08	16.5
35676	UGC06537	155.3789	64.8789	66.1762	-1.7641	865	1085	5.1	0.57	263	2.497	9.48	9.57	10.25	10.28	10.29	-20.28	-20.28	30.57	13.0	30.56	13.0
35705	PG0035705	268.4146	54.1452	114.2404	-20.4784	1610	1989	7.9	0.62	129	2.207	/	/	14.85	14.95	/	/	-17.45	/	/	32.41	30.4
35797	UGC06554	144.3775	58.9812	59.2209	1.8253	1185	1364	5.6	0.32	227	2.371	/	/	12.61	12.68	/	/	-19.05	/	/	31.73	22.2
35869	UGC06567	131.7423	45.2795	44.9334	8.4416	2694	2794	5.3	0.24	486	2.691	10.72	10.27	10.85	10.84	10.92	-22.04	-22.17	32.98	39.4	33.04	40.6
35900	UGC06575	140.6991	56.2751	56.2718	3.4117	1216	1376	5.8	0.30	206	2.325	13.11	13.09	14.02	14.09	13.95	-18.72	-18.60	32.68	34.4	32.72	34.9
35913	UGC06577	177.9547	71.6251	76.0784	-5.7027	1571	1848	5.2	0.40	262	2.446	11.98	11.94	12.88	12.95	12.80	-19.82	-19.79	32.63	33.6	32.75	35.5

PGC	Name	l	b	sgl	sgb	v_{hel}	v_{mod}	t	b/a	w_{mx}	$logw^{i}_{mx}$	I	I*	[3.6]	[3.6]*	$C_{[3.6]}$	M_C	$M_{[3.6]}$	μ_C	d_C	$\mu_{[3.6]}$	$d_{[3.6]}$
35931	UGC06579	144.5763	59.5866	59.8350	1.8232	1290	1473	4.0	0.52	284	2.514	10.41	10.47	11.17	11.24	11.21	-20.43	-20.44	31.65	21.4	31.69	21.8
35942	UGC06583	231.7145	71.5073	91.4082	-12.1196	6209	6651	8.4	0.58	319	2.586	13.10	13.15	13.30	13.42	13.65	-21.09	-21.15	34.83	92.3	34.68	86.2
35952	UGC06586	242.9320	69.2180	95.6227	-13.6983	3959	4348	4.0	0.66	252	2.516	12.89	12.99	13.55	13.65	13.68	-20.45	-20.46	34.19	68.9	34.20	69.1
35978	P0035978	224.6306	72.5835	89.1648	-11.0767	6861	7318	4.0	0.50	261	2.469	13.85	13.88	14.56	14.67	14.64	-20.03	-20.01	34.74	88.8	34.80	91.2
35991	UGC06594	240.8811	69.9097	94.7286	-13.2135	1040	1383	6.4	0.20	155	2.190	13.25	13.26	14.30	14.37	14.17	-17.49	-17.28	31.66	21.5	31.66	21.5
36029	UGC06603	181.1447	72.3836	77.3085	-5.9226	1628	1911	5.9	0.21	169	2.229	13.26	13.25	14.26	14.34	14.15	-17.84	-17.66	31.99	25.0	32.00	25.2
36079	UGC06610	185.3909	73.0025	78.6538	-6.3569	1852	2143	5.9	0.22	197	2.297	13.28	13.21	14.19	14.26	14.09	-18.46	-18.33	32.56	32.5	32.61	33.2
36132	AGC210570	233.8045	71.8316	92.0453	-11.7341	6777	7240	3.0	0.61	247	2.485	13.59	13.70	14.19	14.32	14.37	-20.17	-20.16	34.62	83.8	34.59	82.7
36174	AGC006626	256.7705	65.1163	102.3681	-15.3370	1987	2356	9.8	0.50	148	2.224	/	/	14.02	14.11	/	/	-17.61	/	/	31.72	22.1
36192	UGC06629	139.5696	56.1514	56.0848	4.0241	1213	1370	3.7	0.25	218	2.344	12.35	12.27	13.06	13.13	13.06	-18.89	-18.79	31.95	24.6	31.92	24.2
36238	UGC06640	141.6319	58.2912	58.3359	3.1429	1383	1555	6.3	0.57	168	2.301	12.21	12.38	13.25	13.34	13.22	-18.50	-18.36	31.71	22.0	31.70	21.9
36243	UGC06644	252.9407	67.2202	99.9276	-14.2202	994	1348	5.2	0.69	242	2.516	9.74	9.86	10.23	10.31	10.45	-20.46	-20.47	30.91	15.2	30.78	14.3
36266	UGC06651	176.1902	72.4223	76.3429	-4.7739	1466	1741	3.3	0.49	278	2.496	10.72	10.75	11.12	11.20	11.34	-20.27	-20.27	31.61	21.0	31.47	19.7
36330	AGC210622	233.5460	72.6274	91.8750	-10.9521	7806	8308	8.7	0.47	226	2.400	14.27	14.33	14.81	14.94	15.00	-19.40	-19.34	34.47	78.2	34.37	74.7
36343	UGC06667	146.2692	62.2902	62.6419	1.4876	974	1169	5.9	0.21	173	2.239	12.54	12.52	13.54	13.56	13.39	-17.93	-17.76	31.33	18.4	31.32	18.3
36349	AGC210629	233.1791	72.7280	91.7535	-10.8636	5971	6403	4.5	0.54	327	2.581	13.00	13.02	13.10	13.21	13.49	-21.05	-21.10	34.61	83.5	34.41	76.1
36371	AGC210634	233.5649	72.7599	91.8659	-10.8198	6330	6774	2.8	0.46	292	2.509	13.10	13.09	13.62	13.73	13.77	-20.39	-20.39	34.22	69.7	34.21	69.4
36381	UGC006679	164.3613	70.3546	72.5470	-2.7504	5163	5487	6.6	0.20	307	2.487	/	/	14.02	14.09	/	/	-20.18	/	/	34.36	74.6
36386	UGC06675	127.6987	39.1133	38.6952	11.4786	1709	1753	6.0	0.49	191	2.332	/	/	13.80	13.88	/	/	-18.67	/	/	32.57	32.6
36431	UGC06686	243.4729	70.9867	95.2995	-11.9482	6543	7005	3.3	0.20	398	2.600	12.76	12.29	13.09	13.14	13.08	-21.22	-21.29	34.36	74.4	34.53	80.6
36475	NGC03839	255.5048	67.2069	100.8412	-13.7725	5913	6366	7.4	0.52	310	2.551	12.52	12.50	12.75	12.85	13.04	-20.77	-20.81	33.86	59.2	33.72	55.4
36493	UGC06703	137.5267	55.0588	54.9005	5.0878	2456	2616	2.0	0.31	400	2.615	11.57	11.32	12.10	12.16	12.10	-21.36	-21.44	33.49	49.9	33.65	53.7
36604	UGC06724	234.6125	73.2121	92.1212	-10.3345	5087	5492	3.1	0.56	459	2.735	11.61	11.57	12.26	12.35	12.32	-22.45	-22.60	34.85	93.5	35.10	104.7
36643	PG0036643	277.4439	49.4747	121.8727	-19.3187	1715	2093	6.3	0.34	185	2.284	12.66	12.68	13.47	13.55	13.47	-18.35	-18.20	31.82	23.1	31.76	22.5
36660	NGC003850	140.8461	58.8923	58.8870	3.6187	1154	1326	5.3	0.44	167	2.262	12.30	12.43	13.54	13.63	13.38	-18.14	-17.98	31.52	20.1	31.61	21.0
36664	AGC028071	285.8011	32.3089	141.1533	-22.3923	1843	2198	7.9	0.55	166	2.289	13.40	13.46	14.26	14.34	14.26	-18.39	-18.25	32.67	34.1	32.61	33.3
36683	P0036683	232.8581	73.6702	91.5644	-9.9352	7068	7537	9.5	0.38	265	2.449	13.64	13.60	14.01	14.12	14.22	-19.85	-19.81	34.12	66.7	34.00	63.1
36699	UGC06745	150.7194	65.9565	66.6448	0.4029	889	1105	5.1	0.23	347	2.543	9.86	9.53	10.20	10.19	10.22	-20.70	-20.73	30.92	15.3	30.92	15.2
36743	NGC003879	131.1442	46.7009	46.3701	8.8609	1430	1522	8.0	0.25	196	2.297	/	/	13.84	13.91	/	/	-18.33	/	/	32.25	28.1
36779	AGC210791	235.7485	73.7291	92.3743	-9.7781	6167	6605	3.5	0.37	379	2.602	13.36	13.18	13.91	14.00	13.94	-21.24	-21.30	35.29	114.1	35.47	124.2
36836	UGC06774	141.0678	59.8534	59.8566	3.6120	2419	2608	5.9	0.24	230	2.365	13.86	13.74	14.77	14.84	14.64	-19.09	-19.00	33.77	56.8	33.90	60.3
36856	AGC210803	232.1232	74.4574	91.2887	-9.1694	6821	7279	3.0	0.26	366	2.570	13.58	13.27	13.69	13.77	13.88	-20.95	-21.00	34.92	96.5	34.89	95.1
36882	ES440-011	286.5396	32.5755	141.1573	-21.7144	1939	2294	6.9	0.62	92	2.060	/	/	12.33	12.42	/	/	-16.01	/	/	28.44	4.9
36887	UGC06780	273.1136	57.1704	113.8857	-16.4720	1729	2105	6.4	0.41	210	2.354	13.00	13.04	14.18	14.26	14.00	-18.98	-18.88	33.00	39.9	33.18	43.3
36930	UGC06792	164.5166	71.9587	73.9926	-2.0504	851	1105	5.9	0.20	163	2.212	13.05	13.05	14.11	14.14	13.94	-17.69	-17.50	31.64	21.3	31.64	21.3
36932	UGC06791	210.9953	76.1749	86.1086	-6.9488	1855	2172	6.5	0.21	208	2.319	13.16	13.04	13.86	13.93	13.84	-18.66	-18.54	32.51	31.8	32.48	31.4

PGC	Name	l	b	sgl	sgb	v_{hel}	v_{mod}	t	b/a	w_{mx}	$logw^{i}_{mx}$	I	I^{*}	[3.6]	$[3.6]^{*}$	$C_{[3.6]}$	M_{C}	$M_{[3.6]}$	μ_{C}	d_{C}	$\mu_{[3.6]}$	$d_{[3.6]}$
37036	NGC03917	143.6499	62.7941	62.9366	2.7625	962	1154	5.9	0.23	273	2.439	10.81	10.60	11.51	11.51	11.41	-19.76	-19.72	31.17	17.1	31.23	17.6
37040	AGC210829	233.0171	74.9700	91.4790	-8.6375	7681	8172	3.7	0.54	252	2.468	13.53	13.57	13.98	14.10	14.20	-20.02	-20.00	34.28	71.9	34.18	68.7
37132	UGC06833	168.1942	73.4093	75.7948	-2.2879	918	1180	5.2	0.64	145	2.268	11.23	11.43	12.49	12.58	12.36	-18.20	-18.05	30.56	13.0	30.63	13.4
37143	UGC06837	241.8715	73.8357	94.0511	-9.3321	5974	6408	6.1	0.20	331	2.520	14.60	14.23	14.51	14.57	14.77	-20.49	-20.50	35.37	118.5	35.23	111.1
37153	P0037153	233.6818	75.1761	91.6294	-8.4146	6639	7089	4.9	0.70	193	2.421	13.08	13.22	13.64	13.77	13.86	-19.59	-19.54	33.48	49.7	33.35	46.8
37178	AGC028144	286.9872	34.1297	139.7863	-20.7541	2021	2380	4.4	0.20	292	2.466	11.03	10.66	11.44	11.48	11.43	-20.00	-19.98	31.43	19.3	31.46	19.6
37243	AGC028152	290.0645	24.7699	150.1888	-21.5848	2952	3298	5.1	0.20	350	2.544	11.99	11.52	12.08	12.11	12.18	-20.71	-20.74	32.91	38.1	32.88	37.6
37259	UGC06862	258.7178	69.3445	100.7869	-11.3277	2737	3108	6.7	0.20	181	2.258	14.88	14.81	16.17	16.25	15.88	-18.10	-17.94	34.03	64.0	34.28	71.8
37264	NGC03947	235.4931	75.2878	92.0780	-8.2455	6199	6634	3.0	0.56	386	2.661	12.10	12.08	12.54	12.65	12.72	-21.77	-21.88	34.57	82.0	34.64	84.6
37271	ES440-027	287.7884	32.6063	141.5653	-20.7329	1707	2058	6.6	0.23	263	2.423	11.51	11.22	11.81	11.85	11.90	-19.61	-19.55	31.50	20.0	31.40	19.1
37280	ES504-024	287.3512	34.1212	139.9225	-20.4809	1893	2249	9.0	0.72	90	2.104	/	/	15.30	15.39	/	/	-16.44	/	/	31.84	23.3
37288	UGC06867	225.7614	76.4254	89.6194	-7.2493	6457	6893	2.0	0.48	371	2.618	12.54	12.48	12.85	12.96	13.08	-21.39	-21.46	34.54	80.9	34.52	80.2
37290	UGC06869	147.6336	66.4057	66.7945	1.7189	803	1015	4.0	0.63	252	2.501	10.19	10.32	10.90	10.93	10.99	-20.32	-20.32	31.31	18.3	31.26	17.8
37306	UGC06870	142.2177	62.5906	62.6451	3.3857	1050	1240	4.0	0.50	404	2.659	9.01	8.95	9.53	9.54	9.61	-21.75	-21.86	31.36	18.7	31.40	19.0
37325	NGC003956	285.2049	40.3195	133.1796	-19.4025	1657	2023	5.1	0.30	254	2.416	11.49	11.36	12.23	12.29	12.18	-19.55	-19.49	31.73	22.2	31.78	22.7
37352	UGC06879	275.6767	57.5033	114.5655	-15.2085	2388	2772	7.1	0.30	229	2.371	/	/	13.44	13.46	/	/	-19.05	/	/	32.53	32.1
37409	UGC06891	246.6603	73.8467	95.3383	-8.9317	6783	7248	2.0	0.26	344	2.543	13.41	13.07	13.76	13.83	13.81	-20.70	-20.73	34.58	82.6	34.67	86.0
37418	UGC06894	139.5226	60.6289	60.5541	4.4518	850	1025	5.9	0.20	121	2.083	14.00	14.15	14.93	14.97	14.92	-16.51	-16.23	31.43	19.3	31.20	17.4
37463	P0037463	245.7762	74.1837	94.9945	-8.6922	6350	6798	6.7	0.36	293	2.489	13.92	13.80	14.53	14.63	14.57	-20.21	-20.20	34.86	93.9	34.96	98.3
37466	NGC3972	138.8481	60.0535	59.9513	4.7373	846	1017	4.0	0.28	258	2.420	11.29	11.17	11.96	11.97	11.93	-19.58	-19.53	31.51	20.1	31.50	20.0
37483	UGC06906	267.5344	65.7333	105.7376	-12.2284	2496	2871	3.2	0.31	424	2.640	10.67	10.40	11.14	11.14	11.13	-21.58	-21.67	32.73	35.1	32.84	37.0
37496	AGC028198	285.5782	41.1043	132.5739	-18.7956	1720	2087	4.1	0.40	284	2.481	10.64	10.56	10.81	10.87	11.08	-20.14	-20.13	31.22	17.6	31.00	15.9
37525	UGC06917	143.4703	64.4518	64.5674	3.0820	911	1110	8.8	0.59	178	2.334	11.62	11.77	12.92	13.01	12.74	-18.80	-18.69	31.55	20.4	31.71	21.9
37542	UGC06921	145.9417	66.2760	66.5359	2.3599	938	1148	8.8	0.64	150	2.284	11.75	11.94	12.56	12.61	12.64	-18.34	-18.20	30.98	15.7	30.81	14.5
37549	AGC028206	291.2557	23.4368	151.9061	-20.9536	2997	3338	5.0	0.67	209	2.439	12.16	12.12	12.73	12.80	12.82	-19.76	-19.71	32.59	33.0	32.53	32.1
37553	UGC06923	140.5150	62.0639	62.0313	4.1120	1067	1252	9.8	0.53	139	2.205	12.45	12.63	13.56	13.66	13.50	-17.62	-17.43	31.12	16.8	31.08	16.5
37566	ES572-024	285.8721	41.0745	132.7071	-18.6112	1847	2215	7.0	0.23	146	2.167	/	/	15.02	15.10	/	/	-17.06	/	/	32.17	27.1
37598	UGC06931	136.3730	57.7665	57.5812	5.8740	1192	1350	9.0	0.65	105	2.132	/	/	14.39	14.49	/	/	-16.71	/	/	31.20	17.3
37617	NGC3992	140.0920	61.9234	61.8719	4.2962	1048	1231	4.0	0.60	459	2.749	8.88	8.88	9.54	9.56	9.58	-22.57	-22.74	32.16	27.0	32.31	29.0
37681	ES572-030	287.1540	38.8021	135.3181	-18.7134	1795	2158	9.1	0.41	133	2.154	12.88	13.00	14.01	14.10	13.90	-17.16	-16.93	31.06	16.3	31.03	16.1
37689	UGC06955	165.0320	74.4068	76.2244	-1.0317	904	1164	9.8	0.38	144	2.183	12.93	13.08	13.65	13.74	13.77	-17.43	-17.22	31.20	17.4	30.96	15.5
37691	UGC06963	151.8655	70.0890	70.7448	1.0758	832	1063	3.1	0.26	388	2.595	10.04	9.73	10.03	10.02	10.24	-21.18	-21.24	31.42	19.2	31.26	17.8
37697	UGC06964	146.6732	67.3589	67.6543	2.2778	903	1118	6.8	0.20	248	2.394	11.51	11.29	11.80	11.79	11.90	-19.35	-19.28	31.25	17.8	31.07	16.4
37723	UGC06971	193.8957	78.0456	83.4262	-3.6713	761	1052	6.9	0.45	152	2.222	11.78	11.93	12.72	12.76	12.70	-17.78	-17.60	30.49	12.5	30.35	11.8
37832	UGC06992	141.9766	64.5432	64.5735	3.7316	755	951	7.9	0.46	128	2.149	12.93	13.12	13.88	13.97	13.90	-17.11	-16.88	31.02	16.0	30.85	14.8
37906	ES505-003	288.5910	36.8982	137.6404	-18.4557	1790	2148	7.7	0.21	196	2.293	12.52	12.37	13.29	13.35	13.22	-18.43	-18.29	31.65	21.4	31.65	21.4

PGC	Name	l	b	sgl	sgb	v_{hel}	v_{mod}	t	b/a	w_{mx}	$logw^{i}_{mx}$	I	I^{*}	[3.6]	$[3.6]^{*}$	$C_{[3.6]}$	M_C	$M_{[3.6]}$	μ_C	d_C	$\mu_{[3.6]}$	$d_{[3.6]}$
37935	NGC004034	129.3797	47.1742	46.8681	10.0585	2370	2471	6.0	0.61	201	2.393	12.89	13.04	13.70	13.80	13.78	-19.34	-19.27	33.14	42.4	33.10	41.6
38012	AGC007016	257.5760	73.2326	98.4320	-8.1868	7276	7765	2.1	0.26	535	2.735	/	/	12.46	12.52	/	/	-22.60	/	/	35.28	113.7
38014	UGC07019	132.4956	53.7924	53.5357	7.9733	1517	1651	9.9	0.40	112	2.078	/	/	14.93	15.03	/	/	-16.19	/	/	31.22	17.6
38031	NGC4045	275.9771	62.2705	110.9097	-12.0260	1976	2348	1.3	0.65	308	2.601	10.60	10.71	11.14	11.23	11.33	-21.23	-21.30	32.57	32.7	32.54	32.2
38049	NGC004050	286.3799	44.9325	129.2759	-16.5318	1761	2130	2.2	0.54	340	2.597	10.29	10.26	11.14	11.21	11.09	-21.20	-21.26	32.29	28.8	32.49	31.5
38068	NGC4051	148.8827	70.0854	70.4894	2.0591	704	931	4.0	0.59	233	2.451	9.43	9.56	9.86	9.89	10.09	-19.87	-19.84	29.96	9.8	29.73	8.8
38087	AGC028292	287.6531	41.9196	132.5243	-17.0417	1660	2024	5.8	0.22	170	2.232	13.43	13.37	14.58	14.65	14.36	-17.87	-17.69	32.24	28.1	32.36	29.6
38126	ES505-009	290.1859	34.0885	140.8991	-18.3219	2140	2495	5.0	0.34	149	2.191	/	/	15.28	15.36	/	/	-17.29	/	/	32.67	34.2
38150	UGC07045	185.2649	78.6533	82.4144	-2.1291	766	1050	5.3	0.37	291	2.488	9.95	9.87	10.57	10.63	10.61	-20.20	-20.19	30.81	14.5	30.82	14.6
38167	UGC07054	249.0753	76.0849	95.1368	-6.6165	933	1263	1.4	0.40	185	2.296	10.34	10.42	11.10	11.13	11.13	-18.45	-18.31	29.59	8.3	29.45	7.7
38168	UGC07048	266.3384	70.2924	102.4000	-9.0304	2414	2778	3.1	0.71	243	2.529	11.74	11.90	12.39	12.49	12.56	-20.57	-20.59	33.15	42.8	33.12	42.0
38212	NGC04081	131.1055	51.9406	51.6729	8.8319	1455	1576	1.1	0.38	206	2.340	11.94	11.97	12.37	12.45	12.57	-18.85	-18.75	31.43	19.3	31.19	17.3
38222	ES440-046	290.5408	33.6280	141.4634	-18.2133	1751	2100	8.7	0.63	97	2.088	12.43	12.61	13.42	13.52	13.42	-16.56	-16.28	29.98	9.9	29.80	9.1
38244	NGC004080	211.0236	79.6339	87.0913	-3.6309	571	872	9.5	0.48	155	2.238	/	/	13.27	13.30	/	/	-17.75	/	/	31.06	16.3
38283	UGC07075	140.5868	65.1672	65.1312	4.3862	744	940	5.2	0.25	268	2.434	11.27	11.10	11.49	11.49	11.66	-19.71	-19.66	31.37	18.8	31.15	17.0
38302	UGC07081	140.3368	65.0104	64.9646	4.4761	746	941	4.7	0.38	331	2.544	9.44	9.33	9.79	9.79	9.93	-20.71	-20.74	30.64	13.4	30.53	12.8
38346	AGC520004	286.6908	46.9043	127.5585	-15.4322	1440	1807	5.4	0.35	247	2.412	/	/	11.62	11.68	/	/	-19.45	/	/	31.14	16.9
38347	UGC07086	126.0950	39.3424	38.9671	12.7134	2013	2058	3.1	0.25	271	2.438	12.18	11.90	12.52	12.57	12.60	-19.74	-19.70	32.34	29.4	32.28	28.6
38356	UGC07089	149.9189	71.5220	71.9668	2.0609	772	1005	7.9	0.22	137	2.139	12.34	12.44	13.42	13.45	13.30	-17.02	-16.78	30.32	11.6	30.23	11.1
38361	UGC07090	143.5441	67.7911	67.8826	3.5264	571	781	5.3	0.25	301	2.483	9.75	9.52	10.27	10.27	10.25	-20.16	-20.15	30.41	12.1	30.41	12.1
38370	NGC04100	141.1097	65.9164	65.9006	4.2463	1074	1276	4.1	0.29	374	2.583	9.98	9.73	10.44	10.44	10.44	-21.07	-21.13	31.51	20.1	31.56	20.5
38392	NGC04102	138.0768	63.0727	62.9493	5.3129	837	1021	3.1	0.58	298	2.554	9.96	10.03	10.20	10.23	10.50	-20.81	-20.84	31.30	18.2	31.07	16.4
38464	AGC028345	291.6621	31.8781	143.5341	-17.9378	1723	2066	5.6	0.23	262	2.422	12.14	11.88	12.21	12.26	12.43	-19.60	-19.54	32.03	25.5	31.80	23.0
38536	AGC028356	292.3679	29.9756	145.6322	-17.9925	2220	2564	4.1	0.21	157	2.197	13.48	13.43	14.32	14.39	14.26	-17.55	-17.35	31.82	23.1	31.74	22.3
38550	UGC07122	126.1209	40.0569	39.6981	12.6648	1815	1862	5.1	0.56	248	2.466	11.84	11.82	12.35	12.42	12.48	-20.00	-19.98	32.49	31.5	32.41	30.4
38553	NGC004120	128.4194	47.1235	46.8385	10.7130	2246	2343	5.5	0.24	208	2.322	/	/	13.66	13.74	/	/	-18.57	/	/	32.32	29.1
38567	UGC007125	163.3362	76.7619	78.1186	0.4298	1071	1335	8.8	0.42	139	2.176	/	/	13.98	14.07	/	/	-17.15	/	/	31.22	17.5
38580	AGC520011	285.5494	52.3934	122.2179	-13.4496	1175	1541	2.3	0.30	247	2.404	11.59	11.42	11.75	11.80	11.98	-19.44	-19.38	31.42	19.2	31.18	17.2
38582	UGC07129	151.0006	72.9908	73.4723	2.1060	936	1176	2.0	0.68	97	2.113	12.19	12.46	12.93	13.03	13.11	-16.79	-16.53	29.89	9.5	29.56	8.1
38628	ES441-011	291.9287	33.1710	142.3382	-17.2874	2144	2495	5.7	0.24	140	2.150	14.15	14.19	15.34	15.43	15.16	-17.13	-16.89	32.29	28.7	32.33	29.3
38645	NGC004142	136.8009	62.8801	62.7262	5.8819	1165	1348	6.5	0.52	168	2.286	12.77	12.91	13.85	13.94	13.78	-18.37	-18.22	32.15	27.0	32.17	27.2
38652	AGC028378	290.6492	38.4600	136.7936	-16.3487	1676	2032	9.0	0.32	128	2.122	/	/	15.57	15.66	/	/	-16.62	/	/	32.28	28.6
38669	UGC07147	132.9420	57.4624	57.2391	7.7052	1900	2057	6.0	0.65	155	2.301	/	/	14.39	14.49	/	/	-18.36	/	/	32.87	37.5
38680	UGC07153	131.1965	54.1863	53.9437	8.7319	2608	2754	5.9	0.20	229	2.360	13.60	13.43	14.33	14.40	14.27	-19.03	-18.94	33.33	46.3	33.38	47.4
38688	UGC07151	143.1747	69.0075	69.0714	3.8281	265	478	5.9	0.22	150	2.178	10.78	10.84	11.76	11.83	11.69	-17.38	-17.16	29.07	6.5	28.99	6.3
38711	AGC028383	292.3490	32.2873	143.3343	-17.2523	2135	2483	5.0	0.27	274	2.445	11.33	11.11	12.12	12.18	11.99	-19.81	-19.78	31.81	23.0	31.96	24.6

PGC	Name	l	b	sgl	sgb	v_{hel}	v_{mod}	t	b/a	w_{mx}	$logw^{i}_{mx}$	I	I^{*}	[3.6]	$[3.6]^{*}$	$C_{[3.6]}$	M_C	$M_{[3.6]}$	μ_C	d_C	$\mu_{[3.6]}$	$d_{[3.6]}$
38712	AGC028382	292.4243	31.9513	143.6884	-17.3034	2164	2512	4.2	0.29	225	2.362	13.50	13.37	14.38	14.45	14.26	-19.06	-18.97	33.35	46.7	33.46	49.2
38777	NGC004159	126.1253	40.7501	40.4076	12.6318	1755	1805	6.5	0.41	164	2.246	/	/	13.35	13.43	/	/	-17.83	/	/	31.26	17.8
38795	UGC07183	138.4712	65.4081	65.3009	5.2871	764	958	3.3	0.20	387	2.588	9.88	9.44	9.70	9.72	9.95	-21.11	-21.17	31.06	16.3	30.89	15.1
38803	AGC007181	266.1524	73.5126	100.3080	-6.5653	266	602	7.6	0.40	111	2.073	13.38	13.58	15.11	15.19	14.73	-16.43	-16.14	31.16	17.0	31.34	18.5
38815	UGC07184	280.6944	62.6197	112.0026	-10.0943	2112	2483	6.4	0.43	175	2.279	13.31	13.40	14.37	14.46	14.29	-18.29	-18.15	32.59	33.0	32.63	33.5
38841	ES321-010	294.4607	23.6689	152.5488	-18.0694	3140	3478	1.0	0.20	315	2.498	12.55	12.12	12.49	12.53	12.69	-20.29	-20.29	33.00	39.9	32.84	37.0
38851	UGC07193	229.3622	80.5932	90.3260	-3.0812	2573	2901	4.0	0.64	310	2.599	11.23	11.30	11.72	11.81	11.92	-21.21	-21.28	33.16	42.8	33.12	42.1
38897	NGC04173	197.0748	81.1405	85.5428	-1.3411	1120	1414	7.2	0.21	141	2.150	12.41	12.48	13.73	13.81	13.50	-17.13	-16.89	30.62	13.3	30.71	13.8
38916	UGC07209	269.7444	72.4399	101.8141	-6.6948	2209	2564	4.0	0.61	240	2.472	11.77	11.88	12.91	13.00	12.79	-20.06	-20.04	32.86	37.4	33.07	41.1
38943	UGC07215	271.8619	71.3662	103.0389	-7.0209	374	716	7.0	0.28	244	2.396	10.57	10.45	11.29	11.29	11.23	-19.37	-19.30	30.60	13.2	30.59	13.1
38988	UGC07222	145.3974	71.7271	71.8774	3.4978	929	1158	5.8	0.20	227	2.356	11.48	11.32	12.33	12.34	12.18	-19.00	-18.90	31.18	17.3	31.24	17.7
39025	AGC007235	268.3712	73.7152	100.6604	-6.0084	2110	2461	6.0	0.60	248	2.482	10.85	10.95	11.40	11.49	11.58	-20.15	-20.14	31.73	22.2	31.63	21.2
39040	UGC07234	268.9091	73.5125	100.9095	-6.0608	2472	2828	4.1	0.46	336	2.568	11.30	11.24	11.88	11.95	11.95	-20.93	-20.97	32.90	38.0	32.95	38.9
39113	UGC07249	270.0804	73.2903	101.3089	-6.0014	622	960	9.5	0.30	122	2.098	14.38	14.53	15.62	15.70	15.47	-16.65	-16.38	32.13	26.6	32.09	26.2
39114	NGC004197	278.9660	66.9492	108.0537	-8.0744	2062	2426	6.7	0.23	258	2.414	12.02	11.83	12.48	12.54	12.54	-19.53	-19.47	32.08	26.1	32.02	25.3
39143	NGC004205	129.5993	52.8703	52.6419	9.7229	1439	1562	4.0	0.40	176	2.275	12.03	12.12	12.61	12.70	12.77	-18.26	-18.11	31.03	16.1	30.81	14.5
39152	UGC07255	268.1971	74.3936	100.1780	-5.5267	2316	2667	5.2	0.20	289	2.461	12.62	12.31	13.14	13.19	13.11	-19.96	-19.93	33.08	41.4	33.15	42.7
39183	UGC07260	270.2035	73.5535	101.1553	-5.7842	706	1044	4.0	0.20	268	2.428	11.24	10.97	11.90	11.94	11.81	-19.66	-19.61	31.47	19.7	31.55	20.4
39201	E321-016	295.1826	24.1856	152.2118	-17.2953	3180	3519	5.6	0.29	229	2.370	12.45	12.27	12.90	12.96	12.98	-19.13	-19.04	32.11	26.4	32.01	25.2
39206	AGC007268	275.4459	70.5146	104.4729	-6.7617	600	944	9.3	0.49	182	2.309	11.61	11.73	11.83	11.86	12.17	-18.58	-18.45	30.74	14.1	30.31	11.5
39212	E380-006	294.7815	26.6737	149.6040	-16.9615	2944	3286	3.1	0.45	435	2.679	10.19	9.99	10.76	10.82	10.76	-21.94	-22.06	32.71	34.9	32.90	38.0
39224	UGC07275	268.8899	74.3576	100.3430	-5.4312	-85	248	4.9	0.63	245	2.491	10.09	10.20	10.67	10.74	10.83	-20.23	-20.22	31.06	16.3	30.96	15.6
39237	NGC4218	138.8760	67.8782	67.7867	5.2868	722	927	1.0	0.62	116	2.160	12.43	12.67	13.33	13.42	13.41	-17.21	-16.98	30.62	13.3	30.41	12.1
39241	UGC07282	139.8975	68.8468	68.7844	4.9822	1031	1243	3.1	0.28	383	2.592	9.89	9.62	9.91	9.95	10.15	-21.15	-21.21	31.30	18.2	31.16	17.1
39308	UGC07291	270.5353	73.9315	100.9650	-5.4442	231	566	6.6	0.20	216	2.334	12.14	11.98	12.46	12.51	12.61	-18.80	-18.69	31.41	19.2	31.20	17.4
39315	NGC004219	296.2099	19.0904	157.6343	-17.6407	1989	2291	4.0	0.34	358	2.573	10.45	10.11	10.47	10.50	10.67	-20.97	-21.02	31.65	21.3	31.52	20.2
39328	UGC07292	278.5306	68.6655	106.5940	-7.1367	2593	2961	1.0	0.40	519	2.744	10.51	10.29	11.16	11.22	11.11	-22.53	-22.70	33.68	54.4	33.99	62.7
39344	UGC07301	140.6210	69.8380	69.7975	4.8132	706	921	6.6	0.20	139	2.143	14.01	14.09	15.17	15.20	15.00	-17.06	-16.82	32.07	25.9	32.03	25.5
39366	UGC07308	129.3801	53.2843	53.0674	9.8365	2765	2905	6.5	0.31	230	2.376	12.86	12.80	13.71	13.78	13.65	-19.18	-19.09	32.84	37.0	32.90	38.1
39390	AGC007313	272.5630	73.2707	101.8399	-5.5204	2132	2484	6.1	0.20	206	2.314	13.28	13.14	14.15	14.22	14.03	-18.62	-18.49	32.66	34.1	32.73	35.2
39393	UGC07315	267.2113	75.7628	99.0956	-4.6454	864	1197	4.0	0.62	235	2.468	10.57	10.69	11.14	11.17	11.29	-20.01	-19.99	31.31	18.3	31.16	17.1
39422	NGC04244	154.5696	77.1568	77.7293	2.4070	245	497	6.0	0.42	192	2.317	9.39	9.46	10.25	10.27	10.22	-18.65	-18.52	28.87	5.9	28.79	5.7
39423	UGC07323	140.7708	70.3158	70.2796	4.8064	514	730	7.9	0.63	116	2.166	10.25	10.50	11.48	11.53	11.37	-17.27	-17.05	28.64	5.3	28.58	5.2
39432	UGC07321	241.9342	81.0535	92.2430	-2.3416	408	718	6.5	0.20	216	2.334	12.41	12.26	13.12	13.12	13.05	-18.80	-18.69	31.85	23.5	31.82	23.1
39483	UGC07333	280.2165	68.0386	107.4774	-7.0307	735	1084	5.5	0.69	115	2.195	12.32	12.56	13.51	13.61	13.44	-17.54	-17.33	30.97	15.7	30.94	15.4
39600	NGC004258	138.3199	68.8423	68.7409	5.5499	456	663	4.0	0.41	372	2.602	7.32	7.22	7.93	7.99	7.96	-21.23	-21.30	29.19	6.9	29.29	7.2

PGC	Name	l	b	sgl	sgb	v_{hel}	v_{mod}	t	b/a	w_{mx}	$logw^{i}_{mx}$	I	I^{*}	[3.6]	$[3.6]^{*}$	$C_{[3.6]}$	M_{C}	$M_{[3.6]}$	μ_{C}	d_{C}	$\mu_{[3.6]}$	$d_{[3.6]}$
39613	UGC07352	278.6909	70.1882	105.4333	-6.1404	2467	2829	7.9	0.56	154	2.259	13.39	13.56	14.36	14.46	14.37	-18.11	-17.95	32.49	31.5	32.42	30.5
39738	UGC07380	282.5303	66.9594	108.8810	-6.9459	2374	2740	5.2	0.70	261	2.552	10.89	11.05	11.28	11.33	11.56	-20.79	-20.82	32.35	29.5	32.16	27.0
39775	UGC07393	130.8417	58.5532	58.3662	8.7931	4204	4402	4.0	0.43	350	2.580	12.34	12.27	13.02	13.10	13.04	-21.04	-21.09	34.14	67.3	34.28	71.9
39794	UGC07387	283.6083	65.8979	110.0100	-7.1854	4969	5392	6.7	0.20	252	2.401	13.09	12.86	13.43	13.51	13.54	-19.41	-19.35	32.98	39.4	32.88	37.6
39819	UGC07394	285.4936	63.2879	112.6675	-7.9092	1593	1954	6.6	0.20	171	2.233	13.68	13.65	14.68	14.75	14.55	-17.88	-17.70	32.44	30.8	32.47	31.2
39860	NGC004287	282.8270	67.3082	108.6579	-6.6529	2149	2511	3.4	0.32	193	2.300	/	/	13.83	13.91	/	/	-18.36	/	/	32.28	28.5
39886	UGC07403	284.3796	65.4929	110.5267	-7.1417	2539	2909	5.7	0.20	353	2.548	12.35	11.96	12.29	12.33	12.51	-20.74	-20.78	33.28	45.3	33.14	42.4
39925	UGC07407	277.0941	72.8524	103.0466	-4.8332	347	684	5.8	0.39	210	2.349	11.33	11.34	12.13	12.19	12.13	-18.94	-18.84	31.06	16.3	31.03	16.1
40023	E380-019	296.2617	26.6979	149.9595	-15.6836	2935	3274	5.8	0.20	455	2.658	10.99	10.39	11.21	11.23	11.16	-21.75	-21.85	32.93	38.6	33.11	41.9
40033	NGC04307	280.5837	70.6313	105.4725	-5.3674	1054	1399	3.2	0.25	311	2.497	10.74	10.49	11.13	11.17	11.19	-20.29	-20.28	31.48	19.8	31.46	19.6
40085	NGC004331	125.2041	40.8286	40.5237	13.3244	1564	1611	9.9	0.23	158	2.202	/	/	14.12	14.19	/	/	-17.39	/	/	31.59	20.8
40095	AGC007442	271.3783	76.6043	99.2786	-3.3555	144	471	2.0	0.27	217	2.344	10.65	10.57	11.31	11.32	11.30	-18.89	-18.79	30.20	10.9	30.10	10.5
40105	NGC04313	277.7436	73.2484	102.8654	-4.4331	1445	1788	2.1	0.24	257	2.414	10.53	10.33	11.04	11.04	11.05	-19.53	-19.47	30.57	13.0	30.51	12.7
40119	UGC07447	280.7138	70.9543	105.2388	-5.1394	1252	1598	5.6	0.24	303	2.485	11.60	11.35	11.66	11.71	11.90	-20.18	-20.17	32.08	26.1	31.88	23.8
40201	AGC007456	278.8069	72.9069	103.3270	-4.4100	1563	1907	6.1	0.20	251	2.400	11.43	11.20	11.99	11.99	11.96	-19.40	-19.33	31.35	18.7	31.32	18.4
40205	UGC07459	195.4608	83.5305	86.5853	0.8201	569	856	6.5	0.20	149	2.173	13.64	13.67	14.36	14.43	14.41	-17.34	-17.12	31.75	22.4	31.55	20.4
40208	ES380-023	296.7670	25.1525	151.6322	-15.6524	2748	3079	5.9	0.20	286	2.457	13.25	12.86	13.73	13.77	13.67	-19.92	-19.89	33.62	53.0	33.71	55.3
40273	UGC07469	283.4767	69.0079	107.3820	-5.4964	1422	1772	7.9	0.47	154	2.232	12.43	12.57	13.32	13.41	13.35	-17.87	-17.69	31.22	17.5	31.10	16.6
40284	AGC520051	289.6105	58.7148	117.6800	-8.4140	2017	2384	4.1	0.25	382	2.587	11.20	10.84	11.33	11.37	11.47	-21.10	-21.16	32.58	32.8	32.54	32.3
40342	NGC004356	282.5830	70.3258	106.1146	-5.0059	1133	1478	5.8	0.24	218	2.342	11.54	11.43	12.13	12.19	12.17	-18.88	-18.77	31.04	16.2	30.96	15.5
40475	NGC04384	131.1093	62.2036	62.0496	8.5067	2528	2714	1.0	0.66	142	2.268	12.33	12.54	12.90	13.01	13.14	-18.20	-18.04	31.34	18.5	31.05	16.2
40507	AGC007503	281.9420	71.8180	104.7726	-4.3126	963	1304	2.3	0.51	265	2.481	10.10	10.15	11.08	11.11	10.98	-20.14	-20.13	31.12	16.8	31.23	17.6
40530	UGC07510	279.4687	73.9411	102.6335	-3.6185	-139	193	7.4	0.21	160	2.205	13.14	13.15	13.89	13.95	13.91	-17.63	-17.43	31.54	20.3	31.38	18.9
40537	NGC04389	136.7308	70.7441	70.6285	6.1758	716	930	4.1	0.51	154	2.243	10.87	11.04	11.54	11.58	11.67	-17.97	-17.80	29.65	8.5	29.38	7.5
40566	UGC07513	284.7173	69.1735	107.4882	-5.0356	991	1337	6.0	0.20	281	2.449	11.80	11.52	12.01	12.05	12.15	-19.84	-19.81	32.00	25.1	31.86	23.6
40581	AGC007520	279.1221	74.3354	102.2648	-3.4480	2513	2865	2.8	0.25	364	2.566	9.97	9.64	10.32	10.32	10.34	-20.91	-20.95	31.25	17.8	31.27	18.0
40607	UGC07518	284.5764	69.5112	107.1765	-4.8938	1194	1541	6.3	0.25	195	2.296	12.40	12.35	12.98	13.05	13.06	-18.45	-18.31	31.51	20.1	31.37	18.8
40621	UGC07522	287.4337	65.5321	111.1572	-6.0411	1427	1781	5.8	0.20	308	2.489	12.23	11.90	12.38	12.42	12.53	-20.21	-20.20	32.75	35.4	32.64	33.7
40644	UGC07528	278.7876	74.7856	101.8572	-3.2358	239	570	3.3	0.29	267	2.436	10.65	10.51	10.80	10.80	11.02	-19.73	-19.69	30.75	14.2	30.49	12.5
40649	ES322-009	297.5904	23.4857	153.5019	-15.3440	3571	3910	3.2	0.40	202	2.333	12.38	12.32	13.03	13.11	13.08	-18.79	-18.68	31.87	23.7	31.80	22.9
40692	NGC04414	174.5410	83.1818	84.5678	2.1783	714	992	5.2	0.58	378	2.658	9.00	9.04	9.36	9.38	9.58	-21.75	-21.86	31.33	18.4	31.24	17.7
40775	UGC07549	288.5211	64.6796	112.1300	-6.0615	1693	2050	4.7	0.50	177	2.301	11.37	11.50	12.01	12.05	12.14	-18.50	-18.36	30.63	13.4	30.41	12.1
40811	AGC007563	275.0949	77.4389	99.2670	-2.1756	2340	2682	9.9	0.53	122	2.149	13.22	13.41	14.31	14.41	14.27	-17.12	-16.88	31.38	18.9	31.29	18.1
40839	UGC07565	282.5832	72.7806	104.0994	-3.5959	925	1263	6.0	0.20	148	2.170	14.07	14.10	15.38	15.46	15.12	-17.31	-17.09	32.44	30.8	32.56	32.5
40860	NGC004428	292.7510	54.2295	122.5280	-8.7842	2976	3357	5.0	0.43	332	2.557	11.68	11.60	11.87	11.95	12.14	-20.83	-20.87	32.99	39.7	32.84	37.0
40987	NGC04445	284.6621	71.4813	105.5357	-3.7958	363	700	2.1	0.20	234	2.369	/	/	12.26	12.30	/	/	-19.03	/	/	31.34	18.5

PGC	Name	l	b	sgl	sgb	v_{hel}	v_{mod}	t	b/a	w_{mx}	$logw^i_{mx}$	I	I^*	[3.6]	$[3.6]^*$	$C_{[3.6]}$	M_C	$M_{[3.6]}$	μ_C	d_C	$\mu_{[3.6]}$	$d_{[3.6]}$
40988	NGC04448	195.3514	84.6652	87.1730	1.7909	663	949	1.8	0.45	382	2.622	9.78	9.70	10.43	10.43	10.43	-21.42	-21.51	31.85	23.5	31.94	24.5
40993	UGC07590	285.3044	70.8054	106.2181	-3.9866	1119	1462	4.1	0.48	162	2.258	13.20	13.34	14.12	14.21	14.13	-18.10	-17.94	32.24	28.1	32.15	27.0
41010	E322-017	297.9973	24.1637	152.9148	-14.8178	3405	3742	5.0	0.48	147	2.215	13.90	13.97	14.95	15.05	14.86	-17.71	-17.52	32.59	33.0	32.59	32.9
41024	NGC004450	273.9121	78.6422	98.2216	-1.5304	1954	2287	2.4	0.67	304	2.601	8.86	8.97	9.63	9.67	9.68	-21.23	-21.29	30.90	15.2	30.96	15.6
41050	UGC07600	285.1224	71.3392	105.7351	-3.7495	862	1202	2.4	0.63	204	2.411	11.58	11.74	12.29	12.37	12.42	-19.50	-19.44	31.92	24.2	31.81	23.0
41061	UGC07602	278.2452	76.7696	100.2339	-2.0849	1680	2015	2.4	0.41	178	2.282	11.19	11.25	11.77	11.80	11.89	-18.32	-18.18	30.21	11.0	29.98	9.9
41150	NGC004462	296.3564	39.4231	137.4610	-11.8537	1792	2141	2.1	0.37	378	2.601	/	/	11.08	11.12	/	/	-21.29	/	/	32.43	30.6
41189	UGC07627	286.9447	70.0158	107.1811	-3.9317	2341	2698	1.4	0.69	131	2.247	11.68	11.90	12.37	12.48	12.55	-18.01	-17.84	30.56	12.9	30.32	11.6
41399	NGC004487	294.2353	54.4737	122.6468	-7.8931	1036	1391	6.0	0.55	189	2.346	/	/	11.36	11.44	/	/	-18.80	/	/	30.25	11.2
41472	UGC07669	277.9024	78.7520	98.6615	-0.8747	1508	1835	6.4	0.49	182	2.310	11.25	11.35	12.17	12.21	12.14	-18.58	-18.45	30.72	13.9	30.66	13.6
41504	AGC007676	281.2301	77.1653	100.3372	-1.3111	2097	2435	6.0	0.69	118	2.203	12.12	12.34	12.96	13.07	13.06	-17.61	-17.41	30.68	13.6	30.48	12.5
41517	NGC4501	282.3310	76.5077	101.0167	-1.4954	2280	2622	3.3	0.48	508	2.754	8.34	8.20	8.80	8.81	8.87	-22.62	-22.79	31.49	19.9	31.61	20.9
41555	AGC520071	294.6400	54.9999	122.2468	-7.4756	997	1351	6.0	0.58	223	2.430	10.56	10.68	11.56	11.64	11.51	-19.68	-19.63	31.19	17.3	31.27	18.0
41599	IC0003474	291.6961	65.1210	112.3603	-4.6631	1734	2089	6.8	0.20	136	2.134	13.37	13.45	14.47	14.56	14.36	-16.98	-16.73	31.34	18.5	31.29	18.1
41608	UGC07695	283.5155	76.2110	101.4200	-1.4362	-168	156	9.6	0.65	126	2.211	12.10	12.31	12.87	12.91	12.97	-17.68	-17.48	30.65	13.5	30.39	12.0
41618	UGC07694	292.7362	62.6160	114.8285	-5.3250	1125	1476	6.0	0.22	298	2.476	9.45	9.17	9.81	9.85	9.87	-20.09	-20.07	29.96	9.8	29.92	9.6
41620	UGC007699	142.2705	78.7971	78.7909	5.2492	498	746	6.1	0.28	186	2.278	/	/	13.16	13.18	/	/	-18.14	/	/	31.32	18.4
41639	UGC07697	270.4787	81.8582	95.5541	0.3556	2534	2864	5.9	0.21	217	2.338	13.84	13.69	14.67	14.73	14.56	-18.83	-18.72	33.43	48.5	33.50	50.2
41725	AGC520073	294.6036	57.6984	119.7284	-6.4587	1289	1644	8.8	0.20	123	2.090	/	/	15.00	15.09	/	/	-16.30	/	/	31.39	19.0
41729	UGC07711	288.9356	71.5620	106.1652	-2.5935	2326	2678	6.0	0.25	209	2.326	11.35	11.28	12.00	12.02	12.01	-18.73	-18.61	30.73	14.0	30.63	13.4
41755	UGC07714	172.6553	85.0221	85.9310	3.4311	1175	1456	5.9	0.50	140	2.201	11.70	11.88	12.59	12.68	12.64	-17.59	-17.39	30.23	11.1	30.07	10.3
41763	UGC07716	282.9990	77.5442	100.2559	-0.7756	2344	2684	5.2	0.68	115	2.187	12.19	12.40	13.07	13.17	13.15	-17.46	-17.25	30.61	13.2	30.42	12.1
41789	NGC4527	292.5933	65.1772	112.4727	-4.2987	1737	2091	4.0	0.29	352	2.557	9.27	9.03	9.36	9.36	9.56	-20.83	-20.86	30.39	12.0	30.22	11.1
41811	UGC07726	291.0253	68.9427	108.8133	-3.1958	2005	2357	9.7	0.41	181	2.290	11.05	11.13	11.80	11.89	11.87	-18.40	-18.26	30.27	11.3	30.15	10.7
41823	NGC4536	292.9499	64.7299	112.9433	-4.3509	1806	2161	4.3	0.37	322	2.531	9.46	9.35	9.84	9.85	9.97	-20.59	-20.61	30.56	12.9	30.46	12.4
41838	UGC07747	126.0913	53.4997	53.4242	11.7779	2738	2873	5.6	0.58	248	2.474	11.73	11.84	12.48	12.58	12.57	-20.07	-20.05	32.65	33.9	32.65	33.8
41955	UGC07758	231.8529	86.2280	90.2949	2.5595	1352	1649	7.1	0.32	118	2.086	12.51	12.71	13.57	13.67	13.54	-16.55	-16.27	30.09	10.4	29.94	9.7
41958	UGC07756	293.3257	65.6106	112.2070	-3.8398	1151	1498	1.5	0.36	184	2.286	11.96	12.02	12.50	12.58	12.66	-18.36	-18.21	31.02	16.0	30.79	14.4
41965	PG0041965	296.1325	54.7863	122.7672	-6.7575	986	1338	8.0	0.40	156	2.222	/	/	13.21	13.29	/	/	-17.60	/	/	30.88	15.0
41978	AGC220825	286.0865	76.7670	101.2822	-0.6295	9172	9731	3.0	0.43	340	2.567	14.09	13.98	9.61	9.73	12.31	-20.92	-20.96	33.26	44.8	30.69	13.7
42002	NGC04559	198.4192	86.4704	88.2896	3.2291	814	1100	6.0	0.38	231	2.389	9.22	9.23	10.08	10.10	10.02	-19.30	-19.23	29.32	7.3	29.32	7.3
42038	UGC07772	230.7637	86.4377	90.2110	2.7640	1226	1521	3.3	0.20	500	2.699	8.25	7.70	8.42	8.43	8.42	-22.12	-22.25	30.54	12.8	30.68	13.7
42045	UGC07774	135.6087	76.7501	76.6677	6.5547	523	759	6.3	0.20	186	2.270	13.22	13.16	14.14	14.15	14.01	-18.21	-18.06	32.23	27.9	32.22	27.8
42081	AGC007784	288.2785	75.7108	102.4564	-0.7219	1120	1449	9.6	0.56	100	2.073	12.11	12.33	13.38	13.42	13.23	-16.42	-16.14	29.65	8.5	29.56	8.2
42123	ES442-013	299.1525	34.2747	143.1543	-11.2315	1521	1853	5.9	0.38	192	2.308	12.51	12.49	13.66	13.73	13.46	-18.57	-18.44	32.03	25.5	32.18	27.3
42166	AGC028657	299.7928	27.2705	150.2167	-12.4950	2954	3287	4.8	0.61	239	2.471	12.02	12.06	12.65	12.73	12.76	-20.04	-20.02	32.82	36.6	32.78	35.9

PGC	Name	l	b	sgl	sgb	v_{hel}	v_{mod}	t	b/a	w_{mx}	$logw^{i}_{mx}$	I	I^{*}	[3.6]	$[3.6]^{*}$	$C_{[3.6]}$	M_{C}	$M_{[3.6]}$	μ_{C}	d_{C}	$\mu_{[3.6]}$	$d_{[3.6]}$
42230	UGC07802	293.1725	70.5149	107.7228	-1.8403	1786	2131	6.1	0.20	150	2.176	13.39	13.41	14.28	14.36	14.24	-17.36	-17.15	31.60	20.9	31.50	20.0
42245	E322-040	300.2599	22.4367	155.1416	-13.1953	3348	3673	3.8	0.68	248	2.520	/	/	12.74	12.82	/	/	-20.51	/	/	33.37	47.3
42336	UGC07819	296.4247	62.1865	115.8991	-3.9232	1070	1418	8.0	0.29	191	2.292	11.06	11.06	12.03	12.05	11.91	-18.42	-18.28	30.33	11.6	30.33	11.6
42348	AGC007822	293.9222	70.6255	107.7258	-1.5675	2072	2420	9.9	0.47	103	2.059	13.47	13.70	14.72	14.83	14.61	-16.30	-16.01	30.92	15.2	30.83	14.7
42369	NGC4603A	300.5155	22.0765	155.5554	-13.0427	3672	4002	5.1	0.40	270	2.460	12.23	12.01	12.43	12.49	12.62	-19.95	-19.92	32.58	32.8	32.43	30.6
42396	UGC07826	289.5386	77.8674	100.7120	0.5784	631	951	3.8	0.68	131	2.242	11.55	11.75	12.46	12.50	12.49	-17.96	-17.78	30.45	12.3	30.29	11.4
42407	NGC004594	298.4607	51.1493	126.6907	-6.6799	1095	1444	1.1	0.44	733	2.903	6.61	6.31	7.44	7.43	7.22	-23.98	-24.25	31.20	17.4	31.68	21.7
42475	UGC007844	123.9542	43.3883	43.2170	14.0757	1825	1887	6.1	0.20	125	2.097	/	/	15.43	15.53	/	/	-16.37	/	/	31.90	24.0
42476	NGC004602	297.8936	57.6333	120.4318	-4.8431	2536	2902	4.2	0.43	404	2.643	10.72	10.60	10.97	11.04	11.19	-21.61	-21.70	32.81	36.4	32.76	35.7
42510	NGC04603	300.7932	21.8518	155.8373	-12.8394	2594	2903	5.0	0.65	353	2.658	10.31	10.18	10.62	10.68	10.79	-21.75	-21.85	32.55	32.4	32.56	32.4
42520	UGC07848	124.8992	53.5686	53.5678	12.4758	2499	2629	5.9	0.41	264	2.453	12.77	12.76	13.70	13.78	13.63	-19.88	-19.85	33.54	51.0	33.69	54.6
42544	AGC007843	293.4839	74.5700	104.0798	-0.0553	2270	2612	4.0	0.20	170	2.230	11.82	11.78	11.91	11.93	12.23	-17.86	-17.68	30.08	10.4	29.61	8.4
42640	NGC4603D	301.0337	22.0167	155.7207	-12.5864	2712	3023	6.9	0.62	235	2.469	12.05	11.96	12.50	12.57	12.63	-20.03	-20.01	32.67	34.1	32.59	33.0
42689	NGC04632	298.0748	62.7052	115.6844	-3.0256	1724	2075	5.1	0.39	216	2.361	10.90	10.92	11.43	11.51	11.58	-19.05	-18.96	30.62	13.3	30.46	12.4
42692	NGC004629	298.2786	61.4409	116.9075	-3.3667	1110	1456	9.2	0.69	149	2.305	/	/	14.08	14.17	/	/	-18.40	/	/	32.59	32.9
42726	UGC07877	208.1721	88.0711	89.3639	4.4980	5913	6296	3.0	0.28	321	2.515	13.99	13.78	14.40	14.48	14.49	-20.45	-20.46	35.03	101.4	35.08	103.8
42765	UGC07890	194.9128	88.0570	88.9539	4.6796	7523	7963	4.0	0.71	233	2.513	13.65	13.82	14.30	14.43	14.49	-20.43	-20.43	35.01	100.3	35.00	100.1
42791	UGC07893	298.5717	62.1589	116.2772	-2.9944	2644	3008	3.9	0.31	295	2.482	12.30	12.14	12.90	12.97	12.91	-20.15	-20.14	33.08	41.4	33.14	42.4
42818	UGC07908	123.6905	43.5036	43.3518	14.2570	1667	1727	5.9	0.24	131	2.121	/	/	14.44	14.53	/	/	-16.61	/	/	31.14	16.9
42833	UGC07901	293.0690	79.1168	99.9134	1.7692	801	1117	5.2	0.64	364	2.668	9.69	9.77	10.35	10.37	10.43	-21.84	-21.95	32.28	28.5	32.33	29.3
42857	UGC07902	295.4274	75.8890	103.0717	0.9288	1042	1367	5.9	0.54	282	2.515	9.55	9.60	10.10	10.12	10.22	-20.45	-20.46	30.67	13.6	30.58	13.1
42863	NGC004656	140.3366	84.7033	84.6810	6.0192	648	913	9.0	0.20	135	2.130	10.48	10.58	11.75	11.83	11.56	-16.95	-16.70	28.50	5.0	28.53	5.1
42880	E381-014	301.3000	26.3377	151.4644	-11.4043	3303	3637	4.2	0.22	213	2.330	13.83	13.63	14.47	14.54	14.44	-18.76	-18.65	33.23	44.2	33.22	44.1
42929	AGC520135	300.1626	52.7521	125.4891	-5.1832	2396	2757	4.0	0.50	254	2.460	11.58	11.60	12.08	12.16	12.24	-19.95	-19.92	32.19	27.5	32.08	26.1
42975	UGC07926	299.5378	62.3684	116.2267	-2.5009	1517	1865	5.1	0.30	379	2.590	9.46	9.21	9.30	9.35	9.65	-21.13	-21.19	30.78	14.3	30.54	12.8
42999	UGC07931	299.7549	62.3002	116.3236	-2.4272	1616	1965	7.4	0.55	147	2.236	12.28	12.46	13.21	13.30	13.24	-17.90	-17.73	31.14	16.9	31.03	16.1
43001	UGC07932	296.9244	76.1345	102.9800	1.3563	965	1288	5.0	0.38	161	2.231	12.84	12.93	13.96	13.99	13.81	-17.86	-17.68	31.68	21.7	31.68	21.6
43020	PG0043020	300.3234	56.7701	121.6767	-3.8755	1476	1826	8.9	0.71	143	2.299	/	/	12.69	12.78	/	/	-18.34	/	/	31.13	16.8
43052	UGC07941	123.8893	52.5489	52.6005	13.1961	2300	2420	7.0	0.24	224	2.354	13.43	13.31	14.85	14.92	14.46	-18.98	-18.89	33.47	49.5	33.87	59.4
43073	NGC04672	301.8959	21.1553	156.7532	-11.9806	3254	3569	1.1	0.56	353	2.621	11.94	11.78	12.02	12.08	12.30	-21.41	-21.49	33.75	56.2	33.62	53.0
43118	NGC04680	301.1626	51.2195	127.1416	-5.0454	2429	2789	1.0	0.63	186	2.370	11.57	11.70	12.12	12.17	12.30	-19.13	-19.04	31.43	19.3	31.21	17.5
43142	UGC07955	236.3811	88.9671	90.1625	5.2998	6759	7171	5.8	0.20	361	2.558	13.60	13.20	13.76	13.83	13.88	-20.83	-20.87	34.79	90.8	34.82	92.0
43164	AGC221022	192.2078	89.0593	89.4557	5.5507	6615	7018	1.8	0.54	224	2.417	13.06	13.17	13.15	13.28	13.60	-19.56	-19.50	33.18	43.2	32.80	36.3
43170	NGC04679	302.1066	23.2947	154.6565	-11.3496	4646	4999	4.8	0.40	398	2.630	11.49	11.24	11.78	11.85	11.91	-21.49	-21.58	33.43	48.5	33.47	49.5
43254	UGC07970	300.5688	71.3452	107.8325	0.7106	1010	1341	1.7	0.58	419	2.702	9.37	9.38	10.10	10.12	10.11	-22.15	-22.29	32.27	28.4	32.42	30.5
43278	AGC221033	262.1075	89.0628	90.5366	5.5496	6889	7306	5.0	0.28	311	2.502	13.62	13.43	13.60	13.70	13.93	-20.32	-20.33	34.32	73.0	34.10	66.1

PGC	Name	l	b	sgl	sgb	v_{hel}	v_{mod}	t	b/a	w_{mx}	$logw^{i}_{mx}$	I	I*	[3.6]	[3.6]*	$C_{[3.6]}$	M_C	$M_{[3.6]}$	μ_C	d_C	$\mu_{[3.6]}$	$d_{[3.6]}$
43330	NGC004700	302.0221	51.4560	127.0650	-4.4636	1410	1756	4.9	0.20	124	2.093	11.35	11.44	12.18	12.26	12.21	-16.61	-16.34	28.82	5.8	28.60	5.3
43341	PG0043341	301.9036	58.8511	119.9333	-2.4583	1507	1854	/	0.49	127	2.155	/	/	14.46	14.56	/	/	-16.94	/	/	31.49	19.9
43345	PG0043345	302.1003	52.7486	125.8323	-4.0614	1310	1655	9.0	0.47	124	2.139	/	/	12.51	12.61	/	/	-16.78	/	/	29.39	7.5
43359	UGC07978	128.9457	86.2615	86.2753	6.8541	8078	8526	5.9	0.63	295	2.571	13.24	13.34	13.85	13.98	14.02	-20.95	-21.00	35.07	103.5	35.13	106.2
43397	UGC007982	301.9600	65.7208	113.3542	-0.4728	1157	1495	4.7	0.20	217	2.336	12.02	11.85	12.57	12.63	12.60	-18.82	-18.71	31.42	19.2	31.34	18.5
43413	UGC07985	301.9451	68.1802	110.9960	0.2255	652	984	6.8	0.72	159	2.351	11.05	11.25	11.79	11.83	11.90	-18.96	-18.86	30.86	14.8	30.68	13.7
43451	UGC07989	295.0800	88.3574	91.5273	5.6948	1206	1495	2.2	0.54	397	2.665	8.19	8.20	8.83	8.85	8.89	-21.81	-21.92	30.70	13.8	30.77	14.3
43458	PG0043458	302.5536	52.0166	126.6138	-3.9943	2391	2748	9.0	0.34	253	2.420	12.16	12.06	13.03	13.10	12.93	-19.59	-19.53	32.53	32.0	32.65	33.8
43470	UGC07991	302.4770	64.3356	114.7448	-0.6541	1270	1610	6.6	0.20	177	2.248	12.85	12.80	13.57	13.64	13.57	-18.02	-17.85	31.59	20.8	31.48	19.8
43507	AGC520188	302.7447	56.4779	122.3406	-2.6838	1492	1838	5.9	0.40	211	2.352	10.76	10.78	11.53	11.61	11.55	-18.97	-18.87	30.52	12.7	30.47	12.4
43527	UGC08006	122.9586	45.4916	45.4459	14.5908	1746	1817	3.0	0.25	333	2.528	11.99	11.73	11.73	11.77	12.12	-20.56	-20.58	32.70	34.6	32.36	29.7
43575	UGC08004	122.3685	85.7753	85.8852	7.3965	6187	6559	6.4	0.40	285	2.483	13.63	13.58	14.38	14.48	14.39	-20.16	-20.14	34.62	83.9	34.74	88.9
43601	UGC08007	303.3862	74.9543	104.6041	2.5195	1780	2109	3.1	0.28	323	2.518	11.63	11.39	11.68	11.73	11.93	-20.47	-20.49	32.41	30.4	32.23	27.9
43686	UGC08013	337.4762	89.5410	90.4338	6.4776	7884	8337	3.0	0.28	365	2.571	13.75	13.49	14.44	14.54	14.37	-20.96	-21.00	35.44	122.4	35.74	140.4
43707	UGC08014	304.5304	78.7142	101.0234	3.7112	1243	1558	9.1	0.20	178	2.250	11.75	11.69	12.43	12.50	12.46	-18.04	-17.87	30.49	12.6	30.37	11.9
43717	E323-027	303.2208	22.4194	155.7418	-10.5222	3846	4174	5.0	0.52	322	2.569	11.70	11.59	12.10	12.17	12.24	-20.94	-20.98	33.20	43.7	33.19	43.5
43726	UGC08017	108.4940	88.7162	88.8676	6.9387	7065	7479	2.2	0.36	521	2.738	12.61	12.35	12.55	12.63	12.86	-22.48	-22.64	35.46	123.3	35.44	122.4
43744	NGC4767A	303.2629	23.0354	155.1357	-10.3618	2913	3225	6.0	0.46	224	2.393	/	/	13.91	13.98	/	/	-19.26	/	/	33.28	45.3
43840	P0043840	106.9820	88.0735	88.3247	7.2917	7938	8385	6.0	0.43	286	2.491	14.15	14.13	14.56	14.68	14.76	-20.23	-20.22	35.09	104.3	35.04	101.8
43863	UGC08025	110.0590	87.4592	87.7232	7.4805	6317	6698	3.2	0.20	505	2.703	12.56	11.99	12.68	12.72	12.72	-22.16	-22.30	34.97	98.5	35.17	108.0
43902	NGC004781	304.1218	52.3279	126.5615	-2.9849	1260	1602	7.0	0.45	226	2.395	10.46	10.47	10.96	11.03	11.11	-19.36	-19.29	30.47	12.4	30.32	11.6
43931	NGC04800	121.2803	70.5870	70.9961	11.2668	889	1088	3.0	0.71	291	2.607	/	/	10.85	10.94	/	/	-21.36	/	/	32.31	29.0
43939	NGC004793	101.5728	88.0546	88.4087	7.4554	2484	2773	5.1	0.52	315	2.557	10.85	10.88	11.08	11.16	11.39	-20.83	-20.87	32.22	27.8	32.03	25.5
43961	UGC08036	308.6706	82.0116	97.9269	5.0555	920	1223	5.8	0.37	203	2.331	12.70	12.73	13.65	13.72	13.58	-18.77	-18.65	32.36	29.6	32.39	30.1
43970	PG0043970	304.2574	50.9704	127.8999	-3.2378	2469	2824	7.9	0.20	172	2.236	/	/	14.58	14.65	/	/	-17.73	/	/	32.39	30.0
43975	UGC08052	122.5857	43.9477	43.8851	15.0110	1543	1603	4.7	0.24	221	2.348	/	/	13.41	13.48	/	/	-18.83	/	/	32.32	29.0
43994	AGC28979	303.6608	21.8960	156.3445	-10.2248	4202	4535	4.2	0.33	279	2.461	12.23	11.99	12.57	12.64	12.67	-19.96	-19.93	32.64	33.8	32.59	32.9
44014	UGC08041	305.0081	62.9732	116.3512	0.0784	1324	1663	6.9	0.47	179	2.299	11.30	11.42	12.52	12.56	12.34	-18.48	-18.35	30.82	14.6	30.91	15.2
44025	UGC08051	121.9379	58.7766	59.0957	13.3699	2507	2661	3.1	0.62	338	2.628	10.84	10.93	11.50	11.59	11.62	-21.47	-21.56	33.12	42.0	33.18	43.3
44086	UGC08054	305.7439	67.1520	112.3602	1.3563	760	1090	5.9	0.38	251	2.425	10.97	10.92	11.34	11.40	11.52	-19.62	-19.57	31.15	17.0	30.97	15.6
44147	AGC221130	41.5015	88.8682	90.1167	7.4459	7526	7960	6.6	0.69	181	2.387	13.97	14.17	14.67	14.81	14.85	-19.29	-19.21	34.19	68.9	34.10	65.9
44182	UGC08062	315.6839	84.4222	95.6076	6.1261	410	702	2.3	0.53	305	2.547	7.31	7.31	7.91	7.93	7.98	-20.74	-20.77	28.72	5.6	28.70	5.5
44191	NGC04818	305.2119	54.3227	124.7811	-1.8719	1064	1403	2.0	0.35	253	2.423	10.05	9.98	10.47	10.54	10.62	-19.61	-19.56	30.23	11.1	30.10	10.4
44254	UGC08067	305.9166	61.1316	118.2413	0.0638	2843	3201	3.7	0.27	293	2.475	12.54	12.36	12.92	12.98	13.03	-20.08	-20.06	33.13	42.3	33.08	41.2
44278	PG0044278	305.6306	57.4951	121.7489	-0.9072	1257	1597	7.9	0.66	136	2.249	/	/	13.89	13.99	/	/	-17.86	/	/	31.85	23.4
44358	PG0044358	305.5424	53.2059	125.9134	-1.9407	1482	1823	6.7	0.20	240	2.380	/	/	12.50	12.55	/	/	-19.14	/	/	31.69	21.8

PGC	Name	l	b	sgl	sgb	v_{hel}	v_{mod}	t	b/a	w_{mx}	$logw^{i}_{mx}$	I	I^{*}	[3.6]	$[3.6]^{*}$	$C_{[3.6]}$	M_{C}	$M_{[3.6]}$	μ_{C}	d_{C}	$\mu_{[3.6]}$	$d_{[3.6]}$
44392	UGC08078	306.7409	64.3989	115.1364	1.1493	1098	1432	2.3	0.25	375	2.579	9.83	9.51	10.27	10.31	10.27	-21.03	-21.08	31.30	18.2	31.39	19.0
44416	AGC221206	80.1192	87.8320	88.8155	8.1419	7619	8050	4.2	0.31	260	2.428	13.62	13.53	13.95	14.06	14.16	-19.66	-19.61	33.86	59.1	33.73	55.6
44432	UGC08085	310.5090	77.3277	102.6226	4.6663	2041	2363	5.8	0.20	220	2.342	12.81	12.64	13.57	13.63	13.49	-18.88	-18.77	32.37	29.8	32.41	30.3
44506	PG0044506	306.2724	56.7117	122.5907	-0.7438	1600	1942	7.9	0.21	138	2.141	/	/	14.45	14.54	/	/	-16.80	/	/	31.34	18.5
44663	AGC029082	305.0960	33.2366	145.3750	-6.6841	2813	3147	5.7	0.28	327	2.523	12.76	12.43	12.53	12.58	12.87	-20.52	-20.53	33.42	48.4	33.14	42.5
44795	UGC08118	76.3778	87.2226	88.6377	8.7470	7289	7704	4.2	0.47	368	2.611	12.89	12.84	13.41	13.53	13.55	-21.32	-21.39	34.95	97.8	35.06	102.7
44846	UGC08121	308.1459	62.7476	116.8804	1.4272	1173	1506	5.8	0.66	179	2.367	11.06	11.24	11.78	11.88	11.92	-19.10	-19.01	31.02	16.0	30.88	15.0
44921	UGC08140	73.7197	87.0307	88.6662	8.9789	7091	7498	2.0	0.29	467	2.680	12.88	12.54	13.23	13.31	13.28	-21.95	-22.07	35.34	116.9	35.56	129.2
44961	UGC08146	120.2832	58.3731	58.8520	14.2924	666	799	6.4	0.20	158	2.199	13.07	13.10	14.25	14.32	14.06	-17.57	-17.37	31.63	21.2	31.69	21.8
44966	ES381-051	305.5078	29.6977	148.9368	-7.0616	5021	5394	3.7	0.22	430	2.635	12.43	11.90	12.13	12.17	12.40	-21.54	-21.63	33.99	62.9	33.86	59.3
44982	PG0044982	306.6163	45.5567	133.5362	-2.9385	750	1078	9.7	0.62	104	2.114	/	/	14.91	14.94	/	/	-16.53	/	/	31.47	19.7
44992	ES219-021	304.7155	12.5000	165.9342	-10.8800	1375	1625	6.8	0.27	233	2.375	11.34	10.98	11.83	11.86	11.77	-19.17	-19.09	30.95	15.5	30.95	15.5
45097	UGC08161	21.4753	87.2513	91.2143	8.7911	6675	7073	2.3	0.43	355	2.586	13.19	13.11	13.48	13.59	13.72	-21.09	-21.15	34.89	95.2	34.86	93.7
45098	ES443-042	306.0491	32.9700	145.8018	-5.9571	2909	3241	3.0	0.20	365	2.562	11.81	11.30	12.04	12.07	12.05	-20.88	-20.92	32.94	38.7	33.02	40.2
45137	UGC08166	313.7901	73.5813	106.4515	5.0514	2942	3281	6.0	0.20	159	2.201	15.12	15.13	16.22	16.30	16.06	-17.59	-17.39	33.70	54.8	33.75	56.3
45170	AGC530010	308.0967	52.4039	127.0241	-0.6013	3110	3469	4.0	0.54	444	2.713	10.21	10.15	10.70	10.78	10.82	-22.25	-22.39	33.10	41.6	33.21	43.8
45190	AGC230051	37.1607	87.1034	90.5198	9.1705	5499	5855	4.3	0.60	156	2.281	14.43	14.63	15.28	15.40	15.37	-18.32	-18.17	33.73	55.8	33.63	53.2
45224	NGC004948	308.7311	54.7720	124.7705	0.2180	1353	1688	7.3	0.34	139	2.162	12.05	12.14	12.80	12.88	12.87	-17.23	-17.00	30.10	10.5	29.88	9.5
45241	AGC029208	307.0734	40.3781	138.6822	-3.6708	2542	2881	3.3	0.33	214	2.346	13.10	12.94	13.53	13.59	13.63	-18.91	-18.81	32.55	32.3	32.41	30.3
45311	UGC08185	44.5195	86.7578	90.1634	9.5582	2533	2819	5.6	0.66	209	2.437	12.36	12.54	13.13	13.23	13.25	-19.74	-19.69	33.00	39.8	32.96	39.0
45484	UGC08209	1.4776	85.6699	93.1494	9.3229	6343	6732	3.0	0.64	227	2.460	12.84	12.98	13.33	13.46	13.58	-19.95	-19.92	33.56	51.6	33.42	48.3
45487	ES508-011	307.8284	39.8588	139.3051	-3.2057	2610	2947	6.6	0.20	230	2.362	12.61	12.28	13.26	13.31	13.15	-19.05	-18.96	32.21	27.6	32.28	28.5
45524	ES575-061	308.1916	41.6984	137.5486	-2.5877	1649	1976	7.0	0.20	153	2.185	14.56	14.45	14.41	14.47	14.84	-17.44	-17.23	32.29	28.7	31.71	21.9
45549	UGC08220	1.5964	85.4555	93.3000	9.4777	7131	7549	4.1	0.20	524	2.719	12.78	12.19	12.90	12.95	12.93	-22.31	-22.45	35.35	117.3	35.58	130.7
45552	UGC08219	336.5859	82.7741	96.9002	8.6474	2618	2924	3.8	0.41	235	2.403	13.01	13.01	13.73	13.82	13.77	-19.43	-19.36	33.22	44.1	33.22	44.0
45563	AGC029277	306.3902	21.2947	157.4132	-7.8398	3126	3427	4.9	0.55	114	2.126	12.85	12.93	13.52	13.61	13.63	-16.91	-16.66	30.54	12.8	30.27	11.3
45574	NGC4981	310.6281	55.8344	123.9097	1.4644	1678	2013	4.0	0.69	244	2.521	10.40	10.53	11.04	11.13	11.19	-20.50	-20.51	31.69	21.8	31.64	21.3
45580	UGC08229	49.2052	85.9914	89.8696	10.3266	5989	6354	3.1	0.52	342	2.595	12.65	12.67	13.09	13.20	13.30	-21.18	-21.24	34.54	81.0	34.54	81.0
45596	NGC004980	307.6288	34.0684	144.9747	-4.4530	1428	1739	1.1	0.47	158	2.243	12.26	12.33	13.27	13.35	13.19	-17.97	-17.80	31.16	17.1	31.15	17.0
45643	NGC04995	310.7774	54.7604	124.9840	1.3791	1743	2078	3.1	0.71	284	2.595	10.17	10.28	10.70	10.79	10.90	-21.17	-21.24	32.08	26.0	32.03	25.5
45666	ES508-019	308.2950	38.4399	140.7689	-3.1158	2929	3268	8.8	0.33	235	2.387	12.95	12.74	13.84	13.89	13.67	-19.28	-19.21	32.97	39.3	33.14	42.4
45668	UGC08244	51.0924	85.7342	89.7185	10.5768	7101	7505	6.4	0.37	238	2.400	14.23	14.23	15.13	15.25	15.09	-19.40	-19.33	34.57	81.9	34.70	86.9
45683	ES269-057	306.2755	16.3137	162.3579	-8.7798	3107	3390	1.7	0.58	322	2.588	/	/	10.98	11.06	/	/	-21.17	/	/	32.24	28.0
45684	UGC08246	94.4777	81.8903	83.9393	11.7951	808	1051	5.9	0.20	128	2.107	13.12	13.25	14.28	14.37	14.16	-16.74	-16.47	30.90	15.1	30.84	14.7
45721	AGC029327	308.8209	40.9044	138.4167	-2.2690	2959	3301	6.7	0.37	218	2.362	12.68	12.56	13.47	13.54	13.40	-19.05	-18.96	32.46	31.1	32.51	31.7
45728	NGC05002	100.9613	79.6612	81.4966	12.3668	1081	1315	9.0	0.51	104	2.074	/	/	14.18	14.28	/	/	-16.14	/	/	30.42	12.2

PGC	Name	l	b	sgl	sgb	v_{hel}	v_{mod}	t	b/a	w_{mx}	$logw^{i}_{mx}$	I	I*	[3.6]	[3.6]*	$C_{[3.6]}$	M_C	$M_{[3.6]}$	μ_C	d_C	$\mu_{[3.6]}$	$d_{[3.6]}$
45742	AGC230139	65.3082	85.0233	88.4400	11.0519	6367	6738	3.3	0.65	227	2.466	13.60	13.76	14.25	14.38	14.43	-20.00	-19.98	34.50	79.6	34.46	77.9
45749	NGC5005	101.6137	79.2490	81.0799	12.5029	940	1172	4.0	0.43	535	2.764	8.52	8.35	9.03	9.02	9.05	-22.71	-22.89	31.76	22.5	31.92	24.2
45757	NGC5004A	63.6929	85.0430	88.5820	11.0748	7267	7672	2.3	0.42	336	2.560	12.78	12.72	13.09	13.20	13.32	-20.85	-20.89	34.23	70.2	34.17	68.4
45772	ES576-005	309.3080	42.7953	136.6195	-1.5757	2733	3073	8.0	0.23	270	2.434	/	/	14.33	14.38	/	/	-19.67	/	/	34.12	66.8
45787	UGC08271	99.2032	79.9030	81.8844	12.4774	1142	1378	1.4	0.31	116	2.077	11.97	12.18	12.51	12.60	12.75	-16.46	-16.18	29.21	7.0	28.78	5.7
45795	UGC08270	351.3629	83.7849	95.2257	9.7642	2609	2908	5.1	0.53	393	2.657	10.72	10.71	11.26	11.30	11.37	-21.74	-21.85	33.13	42.2	33.18	43.2
45807	UGC08282	118.3175	56.6977	57.3830	15.6730	2064	2196	5.9	0.36	191	2.302	14.07	14.13	15.02	15.11	14.98	-18.51	-18.38	33.52	50.6	33.53	50.9
45847	NGC5011A	306.9268	19.4032	159.3805	-7.6636	3177	3471	4.8	0.53	237	2.437	12.30	12.21	12.63	12.71	12.82	-19.74	-19.70	32.57	32.7	32.42	30.5
45848	UGC08280	96.8515	80.3831	82.5258	12.4984	813	1049	5.8	0.20	180	2.255	12.59	12.55	13.59	13.65	13.45	-18.08	-17.92	31.54	20.3	31.58	20.7
45849	UGC08286	110.3867	72.5811	74.0498	13.8886	408	607	5.9	0.20	170	2.230	11.41	11.39	12.43	12.45	12.27	-17.86	-17.68	30.13	10.6	30.12	10.6
45877	P0045877	310.0752	45.0357	134.5065	-0.6472	2760	3102	4.9	0.28	363	2.569	11.16	10.82	11.23	11.27	11.41	-20.94	-20.99	32.36	29.6	32.27	28.4
45901	ES443-083	308.1518	29.9600	149.1089	-4.7594	2376	2687	6.9	0.23	231	2.366	11.83	11.61	12.53	12.59	12.45	-19.09	-19.00	31.55	20.4	31.59	20.8
45905	UGC08294	75.5314	83.7453	86.9887	11.8233	6073	6427	5.8	0.66	195	2.404	13.97	14.15	14.91	15.04	14.95	-19.44	-19.38	34.46	77.9	34.52	80.2
45911	ES576-011	309.8485	42.6041	136.8764	-1.2174	2757	3096	5.8	0.20	294	2.468	12.23	11.83	12.60	12.64	12.59	-20.02	-20.00	32.62	33.5	32.66	34.0
45947	NGC05032	42.0547	85.0715	90.4649	11.2270	6413	6791	3.0	0.58	524	2.800	11.66	11.64	12.24	12.34	12.35	-23.04	-23.24	35.52	126.8	35.79	143.7
45948	UGC08307	98.0588	79.4480	81.6415	12.9165	873	1104	5.1	0.48	422	2.674	8.92	8.86	9.40	9.41	9.50	-21.89	-22.01	31.40	19.0	31.43	19.3
45952	NGC005022	310.0525	43.0197	136.4917	-0.9999	3004	3348	3.7	0.21	372	2.572	11.69	11.18	11.99	11.97	11.93	-20.96	-21.01	32.92	38.3	33.01	40.0
46028	UGC08317	68.0063	83.9560	87.8261	11.9704	6039	6394	4.2	0.43	276	2.477	13.45	13.44	14.14	14.25	14.20	-20.10	-20.09	34.37	74.7	34.43	76.8
46124	UGC08328	36.1838	84.6646	91.0550	11.5527	6482	6862	5.9	0.28	248	2.403	14.86	14.76	15.75	15.85	15.66	-19.43	-19.37	35.19	109.2	35.38	119.3
46126	AGC029403	309.9705	38.5590	140.8812	-1.8039	1390	1705	5.0	0.54	222	2.411	10.56	10.42	11.35	11.41	11.27	-19.50	-19.44	30.76	14.2	30.84	14.7
46153	UGC08334	105.9971	74.2878	76.1990	14.2465	500	706	4.0	0.52	375	2.634	7.55	7.55	7.95	7.96	8.12	-21.53	-21.62	29.65	8.5	29.58	8.2
46159	UGC08333	17.1492	84.2624	92.9411	11.2676	941	1211	9.7	0.25	119	2.081	14.13	14.31	15.29	15.38	15.20	-16.50	-16.22	31.70	21.9	31.60	20.9
46246	ES508-034	310.1730	37.1752	142.2732	-1.8739	1909	2226	8.1	0.44	147	2.205	13.50	13.54	14.39	14.47	14.36	-17.63	-17.43	31.99	25.0	31.90	24.0
46247	NGC5054	311.7225	45.8007	133.9326	0.6148	1740	2066	4.2	0.58	319	2.586	9.55	9.52	10.01	10.08	10.16	-21.09	-21.15	31.25	17.8	31.23	17.6
46252	IC0004216	313.0829	51.5966	128.3128	2.2989	2839	3183	5.8	0.38	240	2.405	/	/	13.27	13.35	/	/	-19.38	/	/	32.75	35.5
46261	AGC530085	311.8446	46.1750	133.5748	0.7535	2631	2969	5.2	0.20	274	2.438	12.75	12.39	13.20	13.25	13.17	-19.74	-19.70	32.93	38.6	32.98	39.4
46304	IC004214	309.3850	30.4407	148.8159	-3.6273	2314	2622	1.4	0.63	370	2.669	10.08	10.09	10.64	10.72	10.77	-21.85	-21.96	32.63	33.6	32.71	34.8
46373	AGC029453	311.3352	41.1290	138.5099	-0.3610	1949	2271	6.8	0.20	145	2.161	13.78	13.65	14.48	14.54	14.45	-17.23	-17.00	31.68	21.7	31.55	20.4
46386	UGC08365	104.0291	74.1611	76.3607	14.7736	1265	1474	6.4	0.30	127	2.115	13.40	13.57	14.42	14.51	14.40	-16.81	-16.55	31.20	17.4	31.06	16.3
46409	NGC005064	307.7010	14.7076	164.1769	-7.6728	2984	3255	2.7	0.53	493	2.756	10.31	10.04	10.40	10.45	10.61	-22.64	-22.81	33.27	45.1	33.29	45.6
46427	UGC08366	47.2193	83.7233	90.0169	12.5966	6658	7038	2.9	0.39	530	2.751	12.07	11.83	12.64	12.72	12.63	-22.59	-22.76	35.33	116.5	35.67	136.3
46441	AGC530097	312.9370	47.4843	132.3810	1.6746	2745	3084	5.1	0.20	367	2.565	11.31	10.84	11.49	11.53	11.55	-20.90	-20.94	32.45	30.9	32.48	31.4
46452	ES382-041	309.3907	27.4183	151.8054	-4.1163	1749	2042	5.7	0.20	147	2.167	14.05	14.03	14.90	14.97	14.86	-17.28	-17.06	32.14	26.8	32.04	25.6
46491	ES576-032	311.5422	40.1172	139.5339	-0.3579	1628	1944	5.8	0.71	135	2.272	11.48	11.58	12.10	12.18	12.24	-18.23	-18.08	30.48	12.5	30.27	11.3
46502	ES269-085	307.9444	15.3120	163.6099	-7.3497	2845	3115	5.0	0.54	308	2.555	10.90	10.76	11.28	11.35	11.42	-20.81	-20.84	32.23	27.9	32.20	27.5
46535	AGC530112	313.8689	49.6853	130.2724	2.5601	1431	1753	4.2	0.30	224	2.362	11.64	11.54	12.45	12.51	12.38	-19.05	-18.96	31.43	19.3	31.47	19.7

PGC	Name	l	b	sgl	sgb	v_{hel}	v_{mod}	t	b/a	w_{mx}	$logw^{i}_{mx}$	I	I^{*}	[3.6]	$[3.6]^{*}$	$C_{[3.6]}$	M_{C}	$M_{[3.6]}$	μ_{C}	d_{C}	$\mu_{[3.6]}$	$d_{[3.6]}$
46574	AGC029511	311.8447	40.3133	139.3741	-0.1005	2085	2406	6.7	0.22	169	2.230	12.95	12.81	13.81	13.83	13.67	-17.86	-17.68	31.53	20.2	31.50	20.0
46633	NGC05104	319.1905	62.2651	117.9109	6.4380	5561	5963	1.2	0.43	436	2.674	12.08	11.94	12.05	12.13	12.41	-21.90	-22.01	34.36	74.6	34.23	70.2
46664	AGC530120	314.2422	48.9967	130.9853	2.7222	2903	3243	5.0	0.62	205	2.408	12.15	12.26	12.97	13.07	13.02	-19.47	-19.41	32.51	31.7	32.50	31.6
46671	UGC08403	96.0655	76.7585	79.7426	14.9174	969	1187	5.8	0.60	187	2.360	10.96	11.13	12.01	12.05	11.95	-19.03	-18.94	30.98	15.7	30.99	15.8
46710	PGC046710	313.5144	45.5280	134.3731	1.8184	6855	7301	3.0	0.30	390	2.603	/	/	11.86	11.94	/	/	-21.31	/	/	33.29	45.5
46744	UGC08410	33.5212	82.9888	91.7192	13.1236	2889	3171	4.9	0.37	328	2.538	11.87	11.74	12.38	12.45	12.46	-20.66	-20.68	33.14	42.4	33.17	43.1
46746	UGC08411	44.4227	82.9292	90.3728	13.3813	2392	2662	5.7	0.43	214	2.365	12.95	13.00	13.41	13.50	13.62	-19.09	-19.00	32.72	34.9	32.51	31.8
46768	AGC029560	311.7481	36.0279	143.6025	-0.8020	2263	2578	4.1	0.23	236	2.376	12.47	12.25	13.06	13.12	13.04	-19.18	-19.10	32.23	27.9	32.22	27.9
46878	AGC029585	313.1919	41.0745	138.7614	1.0163	2667	2994	3.5	0.67	311	2.613	11.30	11.32	11.88	11.96	12.00	-21.34	-21.42	33.37	47.2	33.42	48.3
46889	ES576-050	313.5714	42.4878	137.3957	1.4782	1969	2288	5.1	0.42	172	2.269	11.76	11.77	12.65	12.72	12.60	-18.21	-18.05	30.81	14.5	30.77	14.3
47102	ES444-037	312.0258	32.1664	147.4573	-1.1321	1897	2197	7.5	0.60	133	2.212	13.84	13.99	15.05	15.14	14.92	-17.69	-17.50	32.62	33.4	32.65	34.0
47270	UGC08470	105.1227	68.8969	71.4245	17.0762	2704	2901	6.6	0.23	211	2.328	13.40	13.30	14.48	14.55	14.27	-18.74	-18.63	33.04	40.5	33.22	44.0
47321	AGC029708	311.9737	29.0336	150.5528	-1.6218	2389	2687	5.4	0.32	333	2.537	10.45	10.22	11.10	11.15	11.04	-20.65	-20.67	31.69	21.8	31.83	23.2
47345	ES383-005	311.8031	27.9458	151.6088	-1.9247	3609	3926	3.8	0.22	428	2.633	12.17	11.67	11.71	11.75	12.08	-21.52	-21.61	33.64	53.5	33.40	47.9
47368	UGC08490	113.5013	58.0047	59.4010	17.8457	200	321	8.9	0.62	110	2.138	10.54	10.79	11.88	11.93	11.71	-17.01	-16.77	28.73	5.6	28.70	5.5
47394	AGC029724	315.6540	43.9553	136.1081	3.1517	1502	1813	4.9	0.20	509	2.707	9.90	9.24	10.13	10.13	10.04	-22.19	-22.33	32.24	28.0	32.47	31.2
47425	UGC08501	115.3553	54.0450	55.1013	17.9304	1765	1874	3.5	0.61	252	2.492	11.73	11.84	12.53	12.62	12.59	-20.24	-20.23	32.84	37.0	32.87	37.5
47514	AGC530277	316.9465	46.6892	133.4623	4.3047	4232	4590	4.9	0.22	284	2.456	13.33	13.02	14.01	14.07	13.90	-19.91	-19.88	33.84	58.7	34.02	63.6
47549	NGC005188	312.1788	27.3576	152.2383	-1.6781	2429	2722	3.0	0.48	317	2.549	10.71	10.65	10.80	10.87	11.13	-20.76	-20.79	31.89	23.9	31.67	21.5
47788	UGC08550	103.9490	67.6120	70.4638	18.0767	359	527	6.8	0.28	121	2.092	/	/	13.78	13.82	/	/	-16.32	/	/	30.14	10.7
47847	ES270-017	310.8305	16.6587	162.6733	-4.4097	828	1073	8.8	0.22	129	2.112	10.44	10.42	11.12	11.19	11.17	-16.78	-16.52	27.94	3.9	27.71	3.5
47903	ES040-012	305.3457	-14.9752	193.9486	-13.2072	2657	2785	3.9	0.22	412	2.617	11.65	10.97	11.39	11.39	11.55	-21.38	-21.45	32.94	38.8	32.87	37.5
47948	AGC029872	315.7240	37.6964	142.3473	2.5632	2589	2902	4.7	0.27	334	2.532	11.78	11.43	12.02	12.06	12.11	-20.60	-20.62	32.72	34.9	32.70	34.7
47971	UGC08587	77.4220	77.2987	83.3795	17.2500	2233	2465	5.8	0.67	240	2.498	11.92	12.07	12.75	12.84	12.82	-20.29	-20.29	33.13	42.3	33.17	43.0
47985	UGC08593	105.3973	65.6224	68.3313	18.5115	1611	1776	3.0	0.23	253	2.406	12.31	12.15	12.67	12.73	12.80	-19.46	-19.39	32.27	28.4	32.13	26.7
48093	NGC005219	311.4726	16.2307	163.1826	-3.8581	2517	2775	3.5	0.67	203	2.428	11.76	11.80	12.25	12.33	12.43	-19.65	-19.61	32.09	26.2	31.95	24.5
48130	UGC08616	335.9299	68.7502	110.6092	12.5480	1151	1442	4.0	0.60	267	2.515	9.27	9.36	9.69	9.72	9.91	-20.44	-20.45	30.35	11.8	30.17	10.8
48161	ES444-086	314.5561	30.8881	149.0069	0.8387	4079	4406	3.5	0.23	433	2.639	12.22	11.74	12.18	12.22	12.34	-21.58	-21.67	33.97	62.2	33.96	61.9
48175	ES324-044	312.5828	22.1555	157.4445	-2.0235	2530	2807	5.9	0.54	206	2.379	12.48	12.51	13.06	13.15	13.19	-19.21	-19.13	32.41	30.3	32.28	28.6
48206	UGC08630	66.3163	78.2197	86.0159	17.4388	2427	2669	5.7	0.25	212	2.331	/	/	13.56	13.64	/	/	-18.66	/	/	32.31	29.0
48291	UGC08642	99.3224	68.8482	72.5224	18.8871	2428	2618	6.8	0.20	131	2.117	14.73	14.84	15.90	16.00	15.77	-16.83	-16.57	32.61	33.2	32.59	32.9
48307	AGC530342	321.3477	49.6469	130.6426	7.3848	2312	2628	5.0	0.43	332	2.556	10.97	10.82	11.52	11.58	11.56	-20.82	-20.86	32.39	30.0	32.45	30.9
48392	UGC08658	107.9154	61.3369	63.7292	19.3308	2022	2169	5.0	0.54	228	2.424	12.19	12.30	13.06	13.15	13.08	-19.62	-19.57	32.71	34.9	32.74	35.3
48441	UGC08662	67.7236	77.3830	85.4151	18.1179	2033	2265	5.9	0.20	165	2.217	/	/	15.09	15.17	/	/	-17.55	/	/	32.75	35.4
48533	ES445-015	315.5725	30.5846	149.4090	1.6716	4379	4710	3.9	0.35	377	2.596	12.48	12.25	13.06	13.12	13.04	-21.19	-21.25	34.29	72.0	34.47	78.4
48534	UGC08684	112.0676	55.2663	56.8948	19.4206	2193	2310	5.9	0.30	207	2.327	12.48	12.46	13.19	13.26	13.22	-18.74	-18.62	31.96	24.7	31.89	23.9

PGC	Name	l	b	sgl	sgb	v_{hel}	v_{mod}	t	b/a	w_{mx}	$logw^{i}_{mx}$	I	I^{*}	[3.6]	$[3.6]^{*}$	$C_{[3.6]}$	M_{C}	$M_{[3.6]}$	μ_{C}	d_{C}	$\mu_{[3.6]}$	$d_{[3.6]}$
48629	ES383-067	315.4115	28.6857	151.2809	1.3203	4096	4415	5.4	0.20	226	2.354	13.90	13.68	14.15	14.22	14.31	-18.98	-18.88	33.32	46.1	33.13	42.3
48690	UGC08693	71.6437	76.1020	84.0079	18.9345	2439	2668	4.2	0.45	235	2.411	12.91	12.96	13.44	13.53	13.61	-19.50	-19.44	33.13	42.3	33.00	39.8
48749	NGC005289	88.9097	71.8923	77.3605	19.6243	2526	2732	2.0	0.31	376	2.588	11.66	11.44	12.24	12.29	12.23	-21.11	-21.17	33.37	47.2	33.52	50.5
48767	UGC08700	89.2755	71.7142	77.1413	19.6709	2583	2789	4.0	0.20	456	2.659	10.73	10.24	10.88	10.91	10.93	-21.76	-21.86	32.70	34.7	32.79	36.2
48816	UGC08711	96.7005	68.1210	72.4846	20.0920	1507	1681	4.7	0.24	299	2.480	10.95	10.72	11.35	11.39	11.42	-20.13	-20.11	31.55	20.4	31.51	20.0
48925	UGC08726	85.4342	72.2812	78.4769	20.0610	2330	2535	6.4	0.20	169	2.228	13.59	13.59	14.74	14.82	14.56	-17.84	-17.66	32.40	30.3	32.49	31.5
48953	UGC08737	115.0370	48.1627	49.1138	19.5077	1784	1858	4.0	0.20	338	2.529	12.06	11.70	12.03	12.07	12.25	-20.57	-20.59	32.84	37.0	32.68	34.4
48959	UGC08727	335.7500	63.1426	116.2066	13.8743	1170	1458	5.2	0.66	200	2.415	10.81	10.97	11.64	11.73	11.71	-19.54	-19.48	31.25	17.8	31.21	17.5
48989	UGC08733	91.2397	70.0253	75.3717	20.3792	2333	2526	5.9	0.52	180	2.314	12.86	13.00	13.79	13.89	13.80	-18.61	-18.49	32.42	30.5	32.39	30.1
49063	ES383-088	316.7389	28.2397	151.8502	2.4325	4237	4554	3.9	0.34	329	2.536	12.31	12.10	12.93	13.00	12.90	-20.63	-20.66	33.57	51.8	33.71	55.2
49069	NGC05313	83.4129	72.3611	79.0348	20.3913	2562	2771	3.1	0.53	404	2.669	10.94	10.94	11.25	11.33	11.50	-21.85	-21.96	33.38	47.4	33.33	46.4
49112	UGC08749	86.3660	71.3241	77.5700	20.5877	2609	2813	5.2	0.50	299	2.529	11.39	11.43	12.14	12.23	12.19	-20.57	-20.59	32.77	35.8	32.84	37.0
49138	UGC008756	88.7462	70.4430	76.3183	20.6949	1342	1527	1.2	0.26	253	2.409	/	/	12.92	12.98	/	/	-19.43	/	/	32.42	30.5
49301	UGC08795	75.4909	73.4403	81.7370	20.8154	2301	2513	6.0	0.33	192	2.300	13.52	13.54	14.46	14.54	14.40	-18.49	-18.36	32.90	38.1	32.92	38.4
49322	UGC08804	81.0518	72.1482	79.5078	20.9974	2507	2714	5.8	0.46	215	2.376	12.69	12.77	13.70	13.80	13.64	-19.18	-19.10	32.83	36.8	32.92	38.3
49347	UGC08810	82.8376	71.5926	78.6737	21.1041	2326	2527	3.6	0.65	292	2.574	10.23	10.35	11.22	11.31	11.19	-20.99	-21.04	32.18	27.3	32.36	29.7
49411	NGC005348	340.0273	63.4849	115.3281	15.6304	1452	1735	3.8	0.20	180	2.255	12.24	12.17	13.02	13.09	12.99	-18.08	-17.92	31.07	16.4	31.01	15.9
49464	UGC08835	84.4319	70.7438	77.6705	21.4380	2169	2363	3.4	0.40	253	2.431	11.78	11.79	12.45	12.53	12.52	-19.68	-19.64	32.21	27.6	32.17	27.2
49489	NGC05376	108.5593	55.8049	58.1370	21.1155	2076	2191	2.3	0.61	291	2.556	11.13	11.23	11.67	11.76	11.86	-20.82	-20.86	32.69	34.6	32.63	33.6
49563	UGC08863	94.9057	66.2096	71.3064	21.8029	1798	1964	1.0	0.41	375	2.606	10.10	9.99	10.80	10.81	10.76	-21.27	-21.34	32.03	25.5	32.16	27.1
49573	ES384-015	318.3183	27.8526	152.3701	3.7828	3545	3840	7.6	0.20	187	2.272	/	/	14.67	14.74	/	/	-18.08	/	/	32.85	37.1
49580	AGC030236	318.4857	28.2670	151.9696	3.9668	4372	4687	4.1	0.43	464	2.701	12.19	11.97	12.35	12.42	12.56	-22.14	-22.28	34.78	90.5	34.82	92.0
49656	AGC030254	321.1048	34.7352	145.6510	6.6571	2363	2650	9.0	0.59	121	2.167	/	/	14.60	14.69	/	/	-17.05	/	/	31.75	22.4
49676	IC0004351	319.9088	31.3557	148.9793	5.4443	2672	2958	3.3	0.20	481	2.682	10.59	10.00	10.51	10.53	10.63	-21.97	-22.09	32.61	33.2	32.64	33.7
49728	ES445-085	319.2009	28.9693	151.3211	4.6518	4286	4599	5.7	0.20	250	2.398	14.67	14.37	14.84	14.90	15.00	-19.38	-19.31	34.45	77.5	34.30	72.6
49763	UGC08899	18.0753	73.8340	98.3524	20.3081	2854	3117	4.0	0.30	177	2.260	14.40	14.43	15.36	15.45	15.29	-18.12	-17.96	33.45	48.9	33.46	49.2
49881	NGC05430	107.3095	55.6474	58.2573	21.8280	2961	3086	3.1	0.67	321	2.629	10.96	11.08	11.32	11.42	11.62	-21.48	-21.57	33.12	42.0	33.01	40.0
49889	NGC05425	95.2751	64.7915	69.9897	22.5430	2072	2232	6.5	0.27	228	2.366	12.69	12.61	13.48	13.55	13.44	-19.09	-19.00	32.54	32.2	32.57	32.7
49993	NGC05443	103.7985	58.6077	62.0138	22.3498	1803	1928	3.0	0.33	355	2.566	10.88	10.71	11.57	11.62	11.52	-20.91	-20.96	32.44	30.8	32.60	33.1
50031	UGC08969	95.7173	64.0122	69.1884	22.8550	2020	2175	1.4	0.38	388	2.615	10.61	10.47	11.22	11.23	11.21	-21.35	-21.43	32.58	32.8	32.68	34.4
50069	UGC008988	108.1705	54.0293	56.4386	21.9563	2077	2181	5.9	0.22	189	2.278	13.61	13.56	14.37	14.44	14.36	-18.29	-18.14	32.66	34.1	32.60	33.1
50166	ES384-043	319.9659	26.9277	153.4177	5.1629	4407	4713	6.8	0.20	232	2.365	/	/	15.32	15.39	/	/	-19.00	/	/	34.48	78.8
50194	UGC08995	349.7711	64.7710	112.3806	19.0619	1234	1498	7.4	0.37	150	2.199	13.12	13.24	14.03	14.11	14.03	-17.57	-17.37	31.61	21.0	31.49	19.8
50317	NGC005470	346.5493	62.3595	115.3335	18.8037	1023	1288	3.1	0.20	242	2.384	/	/	12.31	12.36	/	/	-19.17	/	/	31.54	20.3
50334	UGC09024	20.5490	72.1870	98.5672	22.0952	2322	2569	3.0	0.62	108	2.130	13.53	13.76	15.43	15.54	14.99	-16.94	-16.69	31.93	24.4	32.24	28.1
50404	ES325-055	319.0483	22.3072	157.9652	3.9402	4030	4315	4.4	0.20	244	2.387	/	/	14.70	14.76	/	/	-19.21	/	/	34.05	64.5

PGC	Name	l	b	sgl	sgb	v_{hel}	v_{mod}	t	b/a	w_{mx}	$logw^{i}_{mx}$	I	I^{*}	[3.6]	$[3.6]^{*}$	$C_{[3.6]}$	M_{C}	$M_{[3.6]}$	μ_{C}	d_{C}	$\mu_{[3.6]}$	$d_{[3.6]}$
50509	UGC09056	93.6748	63.4282	69.2780	23.9283	2015	2166	3.1	0.37	170	2.253	13.22	13.28	13.99	14.08	14.04	-18.06	-17.89	32.10	26.3	31.97	24.8
50581	UGC09071	100.2673	59.3141	63.6259	23.6189	1827	1954	5.9	0.23	190	2.281	13.39	13.34	14.16	14.23	14.14	-18.32	-18.18	32.47	31.2	32.42	30.5
50587	UGC09057	338.6108	54.7446	124.3029	17.3220	1563	1836	7.0	0.25	212	2.331	12.80	12.66	13.69	13.75	13.56	-18.77	-18.66	32.34	29.4	32.42	30.5
50620	AGC240147	0.6200	67.0533	107.7738	21.5235	4900	5214	1.3	0.58	165	2.298	13.27	13.43	13.34	13.46	13.82	-18.47	-18.33	32.29	28.8	31.79	22.8
50675	AGC030464	322.7568	29.3653	151.1296	7.7760	6925	7309	4.5	0.20	466	2.668	13.23	12.62	13.30	13.35	13.35	-21.84	-21.96	35.30	114.6	35.48	124.5
50676	UGC09079	340.4566	55.7559	122.9929	18.0781	1541	1811	6.5	0.20	239	2.378	11.84	11.59	12.80	12.84	12.57	-19.20	-19.12	31.77	22.6	31.97	24.8
50728	NGC005520	94.7666	62.1219	67.8084	24.3245	1876	2018	3.1	0.56	276	2.514	11.84	11.91	12.26	12.29	12.47	-20.44	-20.44	32.92	38.4	32.76	35.6
50798	ES271-022	317.6944	15.0929	165.0277	1.9540	2995	3236	5.9	0.20	364	2.561	11.95	11.39	12.16	12.18	12.15	-20.87	-20.91	33.03	40.4	33.12	42.1
50832	UGC09115	103.2617	56.0957	59.7040	23.7195	2046	2158	4.1	0.22	249	2.398	12.53	12.36	12.62	12.63	12.86	-19.39	-19.32	32.26	28.3	31.95	24.6
50895	UGC09119	32.1154	71.2225	95.3356	24.3864	1045	1262	5.8	0.28	261	2.426	11.34	11.22	12.17	12.23	12.08	-19.63	-19.58	31.71	22.0	31.82	23.1
50973	UGC09133	62.6258	70.1750	84.3311	25.3892	3848	4073	2.4	0.56	418	2.695	10.51	10.52	11.11	11.21	11.22	-22.08	-22.21	33.33	46.4	33.46	49.3
51015	IC004390	318.4441	15.3023	164.8940	2.6952	2113	2339	4.2	0.32	246	2.406	/	/	12.08	12.13	/	/	-19.39	/	/	31.52	20.1
51061	AGC030549	323.7852	28.0011	152.5502	8.6116	2757	3021	5.8	0.20	315	2.498	12.76	12.35	12.63	12.66	12.88	-20.29	-20.29	33.19	43.5	32.99	39.5
51106	NGC005530	319.2639	16.7057	163.5733	3.6181	1193	1413	4.2	0.45	251	2.440	10.06	9.94	10.38	10.44	10.56	-19.76	-19.72	30.32	11.6	30.16	10.8
51143	AGC030573	322.6199	24.6476	155.8743	7.3868	3749	4024	6.1	0.20	271	2.433	13.75	13.42	13.96	14.01	14.08	-19.70	-19.66	33.82	58.1	33.73	55.6
51210	NGC05585	100.9968	56.4747	60.7022	24.6654	305	406	6.9	0.62	141	2.244	10.42	10.63	11.61	11.65	11.49	-17.98	-17.80	29.47	7.8	29.46	7.8
51265	AGC030592	325.5013	29.8996	150.6815	10.1802	7231	7619	5.4	0.20	313	2.496	14.31	13.89	14.71	14.78	14.69	-20.27	-20.27	35.06	102.6	35.20	109.6
51291	PG0051291	341.4880	52.2491	126.3850	19.6143	2733	3009	2.0	0.45	160	2.244	/	/	14.75	14.85	/	/	-17.81	/	/	32.68	34.3
51344	NGC005584	345.1143	54.8559	123.0419	20.8767	1637	1895	6.0	0.71	186	2.416	10.81	10.98	11.75	11.79	11.74	-19.55	-19.49	31.29	18.1	31.28	18.0
51351	UGC09206	7.9019	65.6591	106.7493	24.6167	2283	2528	3.8	0.48	128	2.155	/	/	13.97	14.07	/	/	-16.94	/	/	31.01	16.0
51400	UGC09215	347.7775	56.3647	120.9489	21.7344	1391	1644	6.3	0.49	209	2.372	11.99	12.06	12.87	12.95	12.86	-19.14	-19.06	32.01	25.2	32.01	25.3
51404	IC0004407	340.2832	50.0841	128.8103	19.4349	2722	2996	8.8	0.47	194	2.333	/	/	14.56	14.65	/	/	-18.68	/	/	33.37	47.2
51445	AGC540081	332.7749	40.7109	139.4108	15.7793	2702	2974	4.9	0.53	298	2.536	11.26	11.20	11.43	11.51	11.72	-20.64	-20.66	32.37	29.8	32.18	27.2
51471	AGC540084	343.1160	52.2281	126.1081	20.5769	2746	3018	1.3	0.59	311	2.577	11.74	11.73	12.03	12.11	12.29	-21.01	-21.06	33.32	46.2	33.21	43.8
51503	UGC09242	71.3915	66.8982	79.6523	27.2234	1441	1608	6.6	0.20	187	2.272	13.14	13.08	13.99	14.06	13.93	-18.23	-18.08	32.17	27.1	32.15	26.9
51509	UGC09245	99.4362	56.3098	61.0053	25.5008	1894	2003	6.4	0.36	125	2.118	13.41	13.59	14.37	14.47	14.39	-16.83	-16.57	31.22	17.5	31.04	16.2
51523	PG0051523	341.4781	50.2757	128.4108	20.1284	1697	1955	9.0	0.50	121	2.136	/	/	13.94	14.03	/	/	-16.76	/	/	30.79	14.4
51549	IC4423	35.9687	68.8250	94.5982	27.0383	9078	9503	4.2	0.49	413	2.667	13.35	13.28	13.75	13.88	13.94	-21.83	-21.94	35.91	152.4	36.04	161.4
51613	ES001-006	303.9313	-25.0891	204.3302	-14.8255	2254	2323	5.6	0.25	305	2.489	11.85	11.46	12.17	12.20	12.19	-20.21	-20.21	32.41	30.4	32.42	30.5
51635	NGC005630	74.7326	65.7414	77.6987	27.5829	2653	2826	7.9	0.36	228	2.379	12.38	12.38	13.14	13.23	13.16	-19.21	-19.13	32.38	29.9	32.37	29.8
51641	NGC005671	111.3449	45.2068	46.6775	22.6668	8981	9237	3.1	0.72	358	2.704	/	/	12.62	12.76	/	/	-22.30	/	/	35.21	110.3
51665	UGC09279	56.6880	68.1862	86.0993	27.8176	4090	4314	6.0	0.37	165	2.241	/	/	16.04	16.15	/	/	-17.78	/	/	33.99	62.9
51713	UGC09291	69.4888	66.5436	80.2386	27.8721	2888	3071	6.4	0.47	250	2.444	12.06	12.10	13.15	13.24	13.02	-19.80	-19.76	32.84	37.0	33.04	40.5
51745	UGC09303	54.1834	68.1334	87.1311	28.0168	4274	4504	3.4	0.43	209	2.356	14.71	14.78	15.52	15.62	15.56	-19.00	-18.90	34.63	84.3	34.63	84.3
51776	ES385-031	324.8917	24.0301	156.6134	9.4192	3113	3365	6.2	0.20	128	2.107	/	/	16.25	16.34	/	/	-16.47	/	/	32.84	37.0
51780	UGC09299	347.9424	54.0458	123.2279	22.7014	1543	1791	6.4	0.41	173	2.269	13.19	13.25	14.24	14.27	14.12	-18.21	-18.05	32.33	29.3	32.34	29.3

PGC	Name	l	b	sgl	sgb	v_{hel}	v_{mod}	t	b/a	w_{mx}	$logw^i_{mx}$	I	I^*	[3.6]	$[3.6]^*$	$C_{[3.6]}$	M_C	$M_{[3.6]}$	μ_C	d_C	$\mu_{[3.6]}$	$d_{[3.6]}$
51820	AGC030669	324.0044	21.8333	158.7891	8.4840	2840	3083	4.6	0.67	264	2.541	11.55	11.61	12.14	12.23	12.28	-20.68	-20.71	32.98	39.5	32.96	39.1
51831	NGC05656	60.2821	67.3849	84.3993	28.3043	3159	3357	2.0	0.69	357	2.681	11.33	11.45	11.64	11.73	11.96	-21.96	-22.08	33.97	62.1	33.88	59.7
51846	UGC09328	357.3365	59.2178	115.6259	24.9173	1366	1604	6.6	0.55	179	2.322	11.25	11.39	12.20	12.29	12.19	-18.69	-18.57	30.88	15.0	30.85	14.8
51854	AGC240420	9.3396	63.6417	107.7971	26.5020	12158	12779	1.5	0.58	360	2.638	13.73	13.75	16.23	16.39	15.39	-21.57	-21.66	37.21	276.1	38.58	521.2
51901	UGC09347	89.7159	60.2190	67.8587	27.4135	2080	2211	5.2	0.22	256	2.411	12.60	12.40	13.48	13.53	13.32	-19.50	-19.44	32.83	36.8	33.00	39.8
51909	UGC09345	356.1366	58.2527	116.8922	24.9023	2340	2588	6.4	0.20	211	2.324	/	/	15.37	15.43	/	/	-18.59	/	/	34.10	66.2
51932	UGC09358	100.0446	54.5048	59.0665	26.0750	1906	2004	3.4	0.58	383	2.662	10.26	10.30	10.64	10.72	10.88	-21.79	-21.90	32.68	34.3	32.64	33.7
51948	E447-019	328.4452	29.4447	151.1818	12.7314	3863	4137	2.2	0.24	333	2.526	12.35	11.94	12.55	12.59	12.63	-20.55	-20.57	33.20	43.7	33.20	43.6
51953	UGC09352	359.0798	59.4358	114.8791	25.5353	2237	2481	5.0	0.59	194	2.373	11.20	11.34	11.70	11.80	11.93	-19.15	-19.07	31.09	16.5	30.87	14.9
51955	IC0001029	89.4360	60.1392	67.8943	27.5708	2378	2512	3.1	0.38	444	2.672	11.15	10.95	11.51	11.57	11.62	-21.87	-21.99	33.53	50.7	33.61	52.6
51973	UGC09353	1.9339	60.5564	112.9378	26.0210	1368	1599	6.0	0.60	182	2.348	11.00	11.15	11.94	11.97	11.92	-18.93	-18.83	30.85	14.8	30.80	14.5
51978	UGC09366	88.6767	60.3857	68.3849	27.6876	2106	2238	4.7	0.47	443	2.693	10.03	9.93	10.33	10.40	10.53	-22.07	-22.20	32.61	33.3	32.61	33.3
52090	AGC030724	329.1422	29.5742	151.0481	13.3378	3776	4046	5.8	0.51	302	2.537	12.28	12.19	12.77	12.84	12.88	-20.64	-20.67	33.55	51.4	33.56	51.6
52159	UGC09389	7.8096	61.8081	109.7960	27.3244	1830	2058	3.2	0.28	222	2.355	12.61	12.53	13.89	13.96	13.59	-18.99	-18.89	32.59	32.9	32.88	37.6
52167	UGC09394	8.3025	61.9322	109.5124	27.4016	1801	2028	5.9	0.24	169	2.232	13.48	13.49	14.44	14.52	14.36	-17.87	-17.69	32.24	28.0	32.22	27.8
52251	NGC05698	66.7605	65.1705	80.7755	29.5774	3676	3867	3.1	0.43	295	2.505	/	/	12.49	12.58	/	/	-20.36	/	/	32.97	39.2
52266	NGC05707	90.8888	58.4551	65.8985	28.0916	2215	2337	2.0	0.25	405	2.613	11.24	10.89	11.93	11.97	11.78	-21.33	-21.41	33.14	42.5	33.42	48.4
52273	UGC09416	353.1551	54.4535	121.4444	25.3059	1749	1987	5.4	0.30	293	2.478	10.81	10.63	11.17	11.23	11.29	-20.11	-20.10	31.41	19.1	31.33	18.5
52307	UGC09431	82.9175	61.3401	71.4136	28.9764	2240	2379	5.8	0.20	333	2.522	12.01	11.66	12.31	12.35	12.36	-20.51	-20.53	32.89	37.9	32.90	38.1
52315	NGC05708	70.9697	64.2652	78.4622	29.6458	2723	2890	7.8	0.38	236	2.399	12.33	12.34	12.94	13.03	13.04	-19.39	-19.32	32.44	30.8	32.36	29.7
52324	IC004468	333.1314	34.1535	146.1952	16.5720	2455	2703	4.7	0.32	269	2.444	11.91	11.70	12.30	12.36	12.39	-19.80	-19.77	32.20	27.5	32.13	26.7
52328	UGC09439	89.5876	58.8089	66.6995	28.3847	7784	8058	3.0	0.60	409	2.700	12.38	12.42	12.94	13.07	13.10	-22.13	-22.26	35.34	117.0	35.50	126.1
52361	UGC09437	19.8750	63.8697	103.4630	29.1519	14401	15161	3.3	0.47	404	2.652	/	/	14.65	14.81	/	/	-21.79	/	/	36.92	241.9
52381	NGC005688	322.2500	13.7579	166.7839	6.2177	2798	3014	5.0	0.46	438	2.684	10.59	10.29	10.59	10.64	10.83	-21.99	-22.11	32.83	36.9	32.77	35.8
52455	UGC09462	351.2195	51.9783	124.4676	25.3237	1741	1977	2.4	0.40	375	2.604	10.48	10.34	10.63	10.69	10.88	-21.25	-21.32	32.14	26.8	32.01	25.3
52460	PG0052460	343.1914	45.2523	133.3137	22.5166	1877	2118	1.4	0.66	173	2.353	/	/	13.46	13.55	/	/	-18.88	/	/	32.44	30.7
52521	AGC540121	337.3245	38.0986	141.7229	19.5637	2784	3035	1.2	0.47	393	2.640	10.18	9.99	10.54	10.55	10.63	-21.58	-21.68	32.22	27.8	32.23	27.9
52558	UGC009482	352.8509	52.3932	123.5830	26.0565	1803	2037	6.6	0.20	164	2.215	/	/	15.35	15.42	/	/	-17.52	/	/	32.97	39.3
52620	ES386-016	327.0872	21.3994	159.3776	11.3241	7285	7639	4.1	0.20	363	2.560	/	/	14.41	14.47	/	/	-20.90	/	/	35.54	128.2
52665	NGC5746	354.9659	52.9555	122.3756	26.9472	1723	1952	3.0	0.22	634	2.804	9.33	8.68	9.40	9.40	9.40	-23.08	-23.28	32.49	31.5	32.70	34.7
52730	AGC030834	337.7491	36.9814	142.8542	20.0419	2224	2462	7.7	0.69	145	2.293	/	/	13.32	13.41	/	/	-18.29	/	/	31.69	21.8
52809	AGC540131	338.4701	37.2971	142.4391	20.5695	2200	2436	5.8	0.20	224	2.350	11.90	11.62	11.93	11.97	12.17	-18.95	-18.85	31.11	16.7	30.82	14.6
52811	AGC540133	341.1316	40.3987	138.7902	22.1068	2909	3157	3.1	0.34	382	2.599	11.37	11.07	11.90	11.95	11.87	-21.21	-21.28	33.10	41.7	33.27	45.0
52824	AGC030851	336.9681	35.3196	144.6877	19.6128	2591	2832	5.0	0.20	328	2.516	12.10	11.64	12.09	12.12	12.24	-20.45	-20.47	32.71	34.8	32.60	33.1
52825	AGC540134	340.3317	39.4402	139.9260	21.6775	2148	2384	3.9	0.40	291	2.493	11.24	11.08	11.55	11.61	11.71	-20.25	-20.24	31.96	24.6	31.86	23.5
52832	UGC09530	5.9764	57.4982	114.1107	29.5699	8603	9014	4.1	0.68	234	2.495	/	/	14.10	14.25	/	/	-20.26	/	/	34.62	83.9

PGC	Name	l	b	sgl	sgb	v_{hel}	v_{mod}	t	b/a	w_{mx}	$logw^{i}_{mx}$	I	I^{*}	[3.6]	$[3.6]^{*}$	$C_{[3.6]}$	M_{C}	$M_{[3.6]}$	μ_{C}	d_{C}	$\mu_{[3.6]}$	$d_{[3.6]}$
52853	AGC540136	340.8435	39.8610	139.4044	21.9904	2045	2280	6.0	0.69	198	2.431	12.05	12.13	13.19	13.27	13.06	-19.68	-19.64	32.75	35.5	32.94	38.6
52991	ES580-041	338.7881	36.2902	143.4687	20.9593	2945	3188	4.1	0.20	229	2.360	12.78	12.49	13.32	13.37	13.29	-19.03	-18.94	32.33	29.2	32.32	29.1
53043	UGC09568	98.2108	52.0106	57.1991	28.2344	2141	2225	3.2	0.20	413	2.616	11.53	11.08	11.68	11.71	11.75	-21.37	-21.44	33.14	42.5	33.19	43.4
53093	P0053093	344.6989	42.1341	136.3117	24.3454	2583	2820	2.9	0.52	292	2.525	/	/	12.52	12.60	/	/	-20.55	/	/	33.19	43.4
53134	AGC540146	351.2431	47.6220	128.9272	27.0458	1952	2177	8.0	0.35	149	2.193	/	/	13.52	13.59	/	/	-17.31	/	/	30.90	15.1
53183	AGC030906	338.3335	34.6369	145.2742	20.8023	3978	4237	4.2	0.24	259	2.418	13.54	13.26	13.98	14.04	14.01	-19.56	-19.51	33.60	52.5	33.59	52.3
53217	UGC09586	88.8193	56.1987	64.7275	30.3925	2337	2446	5.2	0.63	242	2.483	11.94	12.04	12.84	12.94	12.84	-20.16	-20.15	33.02	40.2	33.12	42.0
53247	UGC09579	359.4314	52.4229	121.3652	29.5578	1681	1896	5.2	0.20	392	2.593	10.10	9.63	9.95	9.98	10.17	-21.16	-21.22	31.33	18.4	31.20	17.4
53469	UGC09649	110.1038	42.1571	43.7002	24.2948	447	469	3.3	0.42	153	2.218	/	/	12.31	12.34	/	/	-17.55	/	/	29.90	9.5
53499	UGC09631	355.3529	48.4268	126.8211	29.2258	1922	2138	3.0	0.39	422	2.652	9.92	9.70	10.24	10.29	10.35	-21.70	-21.80	32.05	25.8	32.09	26.2
53578	UGC09645	359.0910	50.1942	123.6937	30.5323	1360	1565	3.2	0.54	340	2.598	10.33	10.30	10.83	10.90	10.96	-21.20	-21.27	32.17	27.2	32.18	27.3
53634	AGC540178	343.5080	37.3400	141.6694	24.5122	2928	3158	7.0	0.23	199	2.302	13.70	13.51	14.61	14.67	14.44	-18.51	-18.37	32.96	39.1	33.07	41.2
53657	UGC09665	81.7757	57.0928	68.6443	32.5430	2558	2675	4.0	0.23	291	2.467	12.49	12.25	12.56	12.62	12.80	-20.01	-19.99	32.82	36.7	32.62	33.5
53764	PG0053764	347.7391	40.3240	137.5950	27.0222	2438	2657	5.5	0.20	190	2.279	/	/	14.76	14.82	/	/	-18.15	/	/	32.99	39.7
53779	PG0053779	350.8528	42.9607	133.9616	28.4441	1874	2084	3.0	0.71	145	2.305	/	/	13.09	13.18	/	/	-18.40	/	/	31.59	20.8
53796	AGC550006	344.8625	37.3759	141.3885	25.5590	2932	3158	6.2	0.20	216	2.334	/	/	14.59	14.64	/	/	-18.69	/	/	33.38	47.3
53802	UGC09682	357.2093	47.5010	127.1293	30.7525	1821	2027	8.6	0.25	190	2.284	/	/	14.65	14.72	/	/	-18.20	/	/	32.94	38.8
53861	UGC09703	78.3349	57.2845	70.4992	33.5899	2498	2616	3.0	0.30	214	2.342	/	/	13.43	13.51	/	/	-18.77	/	/	32.29	28.6
54097	NGC5861	348.5268	39.0531	138.7895	27.9495	1852	2056	5.0	0.51	321	2.562	10.54	10.42	10.89	10.95	11.05	-20.88	-20.92	31.93	24.3	31.87	23.7
54117	UGC09753	93.2294	51.3966	58.4384	31.1916	770	836	3.6	0.39	269	2.457	10.52	10.49	11.15	11.16	11.19	-19.92	-19.89	31.11	16.6	31.05	16.2
54134	UGC09746	1.7370	48.2945	124.5460	32.9953	1739	1934	4.0	0.29	195	2.300	13.12	13.07	13.73	13.80	13.79	-18.49	-18.36	32.29	28.7	32.16	27.1
54234	NGC5894	96.5168	49.5064	55.2909	30.3909	2476	2547	7.8	0.20	440	2.643	11.21	10.73	11.46	11.49	11.46	-21.62	-21.71	33.10	41.7	33.23	44.3
54250	NGC005833	312.9424	-12.7776	192.2738	-5.6918	3031	3154	4.2	0.37	407	2.633	10.72	10.36	10.74	10.78	10.93	-21.52	-21.61	32.46	31.1	32.40	30.2
54262	UGC09760	1.8951	47.8067	124.9730	33.3437	2023	2219	6.6	0.20	135	2.130	14.19	14.23	15.42	15.50	15.22	-16.95	-16.70	32.17	27.1	32.21	27.7
54324	IC0004536	344.1234	33.1573	146.1108	25.7707	2282	2486	7.4	0.68	165	2.343	/	/	12.83	12.92	/	/	-18.78	/	/	31.70	21.9
54348	ES581-025	342.3440	31.1134	148.5962	24.5921	2269	2471	6.9	0.21	333	2.523	11.53	11.00	11.47	11.48	11.61	-20.52	-20.54	32.13	26.7	32.03	25.4
54364	AGC550029	347.1860	36.0927	142.3300	27.6578	1992	2192	3.2	0.35	444	2.667	10.38	9.96	10.79	10.81	10.74	-21.83	-21.94	32.58	32.8	32.78	35.9
54392	ES274-001	326.8056	9.3372	171.6166	10.2908	522	680	6.7	0.20	156	2.193	10.20	9.87	10.61	10.63	10.61	-17.52	-17.31	28.13	4.2	27.94	3.9
54428	UGC09789	69.3982	57.2155	75.4121	36.2598	2589	2712	5.3	0.37	472	2.697	10.69	10.44	10.96	11.02	11.09	-22.10	-22.23	33.22	44.0	33.29	45.5
54431	UGC09790	69.6795	57.1671	75.2169	36.2318	2463	2583	3.0	0.34	412	2.633	12.06	11.83	11.63	11.68	12.13	-21.52	-21.61	33.69	54.7	33.33	46.3
54470	UGC09801	91.5844	51.0871	58.8190	32.2170	667	730	5.3	0.20	469	2.671	9.10	8.59	9.15	9.12	9.22	-21.87	-21.98	31.08	16.5	31.10	16.6
54754	AGC031140	345.6075	31.8797	147.2768	27.2231	2215	2408	5.0	0.35	202	2.325	13.10	12.93	14.28	14.33	13.98	-18.72	-18.60	32.71	34.8	32.96	39.1
54755	ES387-026	333.3838	16.9557	164.1629	17.1202	4374	4593	4.7	0.40	455	2.687	11.25	10.92	11.61	11.67	11.65	-22.01	-22.14	33.70	55.0	33.87	59.4
54761	NGC05913	359.3860	43.3194	130.7062	34.0236	2008	2194	1.0	0.44	345	2.576	11.57	11.21	11.59	11.62	11.78	-21.00	-21.05	32.80	36.3	32.69	34.6
54944	PG0054944	358.3587	41.8138	132.7390	34.0061	1999	2183	1.8	0.63	174	2.341	12.05	12.09	12.54	12.62	12.72	-18.87	-18.76	31.59	20.8	31.38	18.9
54969	AGC031164	341.1593	25.8829	154.4285	24.1269	3694	3904	5.4	0.20	189	2.276	15.54	15.23	15.96	16.01	15.98	-18.28	-18.13	34.32	73.0	34.22	69.8

PGC	Name	l	b	sgl	sgb	v_{hel}	v_{mod}	t	b/a	w_{mx}	$logw^{i}_{mx}$	I	I^{*}	[3.6]	$[3.6]^{*}$	$C_{[3.6]}$	M_{C}	$M_{[3.6]}$	μ_{C}	d_{C}	$\mu_{[3.6]}$	$d_{[3.6]}$
55078	UGC09845	14.2016	49.3689	117.1636	38.7054	1892	2058	5.8	0.20	163	2.212	14.01	13.99	15.83	15.91	15.28	-17.69	-17.50	33.00	39.8	33.46	49.1
55081	AGC031181	343.8596	28.0372	151.7849	26.2980	2318	2503	5.0	0.55	274	2.506	11.02	10.91	11.44	11.51	11.57	-20.37	-20.37	31.94	24.4	31.88	23.8
55097	UGC09856	67.1648	55.3149	75.7416	38.5140	2491	2602	6.3	0.20	197	2.294	13.71	13.60	14.67	14.75	14.53	-18.44	-18.30	32.99	39.5	33.08	41.3
55104	UGC09858	65.9010	55.4207	76.6333	38.7178	2618	2732	4.0	0.24	356	2.556	11.69	11.38	12.29	12.34	12.22	-20.82	-20.86	33.05	40.8	33.23	44.2
55165	UGC09866	100.5709	44.9717	49.1797	29.9338	425	454	4.0	0.46	177	2.291	11.07	11.19	11.79	11.82	11.86	-18.41	-18.27	30.28	11.4	30.09	10.4
55256	ES329-007	333.9285	14.4874	166.7650	17.5654	4654	4867	3.0	0.43	472	2.709	11.58	11.17	11.52	11.57	11.74	-22.22	-22.36	34.00	63.1	34.00	63.0
55281	NGC005937	1.3269	41.3073	132.0889	36.2211	2809	2992	3.2	0.61	333	2.615	11.24	11.07	11.24	11.30	11.56	-21.35	-21.43	32.93	38.5	32.75	35.6
55305	NGC005950	65.3923	54.5412	76.5220	39.6403	2599	2708	3.1	0.50	208	2.372	/	/	13.27	13.37	/	/	-19.06	/	/	32.44	30.7
55328	AGC031212	343.2559	25.2639	154.9227	26.0658	4435	4651	5.2	0.20	278	2.444	14.14	13.60	14.25	14.28	14.30	-19.80	-19.76	34.16	67.8	34.12	66.8
55388	UGC09888	3.0523	41.6346	130.9623	37.2023	2797	2975	7.3	0.58	197	2.376	12.58	12.52	13.08	13.15	13.20	-19.18	-19.10	32.39	30.0	32.26	28.3
55435	UGC09895	23.5230	50.4494	110.1321	41.5856	1778	1924	5.2	0.23	261	2.419	11.88	11.63	12.58	12.63	12.49	-19.58	-19.52	32.07	25.9	32.16	27.1
55588	UGC09926	26.2516	50.4729	108.1070	42.4540	1957	2099	5.1	0.67	338	2.647	10.38	10.44	10.77	10.85	11.01	-21.65	-21.74	32.67	34.2	32.61	33.3
55620	UGC09940	69.8233	52.9624	72.5557	39.8787	5712	5877	5.7	0.70	304	2.620	11.95	12.07	12.27	12.39	12.60	-21.40	-21.48	34.05	64.6	33.94	61.4
55647	NGC05981	93.2156	46.9911	54.0367	33.5568	2594	2648	4.2	0.20	449	2.652	11.63	11.11	11.80	11.78	11.81	-21.70	-21.80	33.53	50.9	33.63	53.2
55665	UGC09943	20.4118	48.1692	114.1240	42.2893	1956	2101	5.0	0.60	306	2.574	10.50	10.55	11.16	11.24	11.25	-20.98	-21.03	32.24	28.1	32.28	28.6
55725	UGC09969	92.9788	46.8301	53.9721	33.7787	2520	2572	3.0	0.52	534	2.788	10.22	10.15	10.66	10.74	10.80	-22.93	-23.12	33.78	56.9	33.93	61.1
55739	UGC09963	33.9474	51.3629	101.5455	43.6004	4389	4560	3.5	0.46	358	2.597	12.24	12.12	12.28	12.36	12.61	-21.19	-21.25	33.84	58.6	33.67	54.1
55800	NGC05980	25.8081	49.0518	109.4086	43.5474	4088	4259	4.4	0.32	416	2.634	/	/	11.78	11.84	/	/	-21.62	/	/	33.50	50.2
55821	UGC09977	7.3441	41.3253	129.1607	40.1099	1913	2065	5.3	0.20	246	2.391	12.47	12.12	12.92	12.96	12.90	-19.32	-19.24	32.22	27.8	32.21	27.7
55853	UGC09987	23.8676	48.1099	111.6008	43.6729	1107	1235	6.4	0.27	222	2.354	11.74	11.63	12.42	12.48	12.41	-18.98	-18.88	31.39	19.0	31.37	18.8
55867	UGC09991	24.2237	48.0837	111.3445	43.8244	1951	2086	5.9	0.23	199	2.302	13.49	13.40	14.72	14.79	14.44	-18.51	-18.38	32.97	39.3	33.21	43.8
56077	IC0004555	311.5891	-18.3975	197.8034	-7.4545	2662	2753	5.8	0.22	238	2.379	12.37	12.09	12.86	12.91	12.86	-19.21	-19.13	32.07	25.9	32.04	25.6
56078	NGC005967	313.2985	-16.4948	196.0253	-5.6770	2905	3005	5.7	0.63	301	2.581	11.06	11.04	11.40	11.47	11.62	-21.05	-21.10	32.68	34.4	32.59	33.0
56094	UGC10043	35.4684	49.5387	101.0340	45.6334	2175	2294	4.2	0.20	319	2.504	13.05	12.66	12.59	12.63	13.02	-20.34	-20.35	33.39	47.7	33.00	39.9
56111	UGC10041	13.6324	42.4191	124.2193	43.1908	2167	2307	7.9	0.54	192	2.349	12.51	12.56	13.56	13.65	13.46	-18.94	-18.84	32.41	30.3	32.50	31.6
56157	ES515-010	347.4886	23.3955	156.5741	30.0959	5736	5963	2.5	0.40	377	2.605	/	/	12.92	12.96	/	/	-21.34	/	/	34.39	75.6
56219	UGC10075	95.6924	44.1246	50.0219	33.4392	833	854	5.9	0.48	295	2.518	10.16	10.18	10.83	10.90	10.90	-20.47	-20.48	31.37	18.8	31.39	18.9
56500	AGC031339	349.7512	22.9873	156.7584	32.2095	7403	7678	5.0	0.20	500	2.699	/	/	13.19	13.21	/	/	-22.25	/	/	35.65	135.1
56537	UGC10113	30.3645	45.9035	107.6261	47.7703	2170	2281	5.1	0.40	226	2.383	12.10	12.09	12.86	12.89	12.85	-19.24	-19.16	32.10	26.3	32.06	25.8
56723	UGC10133	12.0558	37.8952	130.2105	45.0425	1926	2047	5.1	0.51	235	2.427	11.93	11.86	12.58	12.64	12.61	-19.64	-19.59	32.26	28.3	32.25	28.1
56917	UGC010194	96.4842	42.2036	47.6465	33.7707	871	880	6.8	0.20	127	2.104	/	/	15.88	15.96	/	/	-16.44	/	/	32.42	30.4
57140	E451-008	346.1372	16.8122	164.2430	29.3223	4718	4893	3.0	0.20	471	2.673	/	/	12.47	12.47	/	/	-22.00	/	/	34.58	82.3
57173	UGC10205	48.9182	47.3726	88.4042	48.9260	6562	6745	1.0	0.59	541	2.817	/	/	12.15	12.26	/	/	-23.41	/	/	35.87	149.6
57205	UGC10210	19.8851	39.9538	122.1259	48.2968	2848	2966	5.9	0.55	265	2.493	12.23	12.27	13.02	13.06	13.02	-20.24	-20.24	33.29	45.5	33.34	46.5
57261	UGC10219	19.5517	39.5082	122.8694	48.4394	1369	1469	6.0	0.20	199	2.299	12.65	12.51	13.19	13.25	13.24	-18.48	-18.35	31.72	22.1	31.60	20.9
57271	ES516-008	349.6882	19.4659	160.9115	32.5260	7124	7373	4.0	0.25	337	2.532	14.23	13.74	14.14	14.20	14.33	-20.60	-20.62	35.03	101.3	34.95	97.8

PGC	Name	l	b	sgl	sgb	v_{hel}	v_{mod}	t	b/a	w_{mx}	$logw^{i}_{mx}$	I	I*	[3.6]	[3.6]*	$C_{[3.6]}$	M_C	$M_{[3.6]}$	μ_C	d_C	$\mu_{[3.6]}$	$d_{[3.6]}$
57345	NGC06070	12.4700	35.5919	132.6515	46.6312	2005	2115	6.0	0.52	373	2.631	/	/	10.84	10.89	/	/	-21.59	/	/	32.49	31.5
57582	UGC10288	12.2858	34.1609	134.5246	47.2918	2044	2148	5.3	0.20	359	2.555	11.85	11.28	11.83	11.84	11.92	-20.81	-20.85	32.75	35.5	32.71	34.8
57627	UGC10297	34.2512	42.6480	105.6850	51.8651	2312	2398	5.1	0.21	223	2.349	13.35	13.15	13.95	14.01	13.94	-18.94	-18.84	32.89	37.9	32.87	37.5
57665	IC0004596	352.7858	19.8666	160.0793	35.3883	7623	7880	2.1	0.23	577	2.764	/	/	12.72	12.74	/	/	-22.89	/	/	35.83	146.7
57799	UGC10328	21.0100	37.1671	124.1368	50.9125	1447	1531	5.3	0.58	227	2.437	11.35	11.40	12.02	12.10	12.11	-19.74	-19.70	31.85	23.4	31.80	22.9
57876	IC0004595	319.0275	-14.1288	194.2236	0.0578	3391	3493	5.1	0.20	434	2.637	11.60	10.98	11.04	11.05	11.39	-21.56	-21.65	32.97	39.3	32.73	35.1
57924	NGC006118	11.4579	31.4696	138.4855	48.0786	1570	1659	6.0	0.39	338	2.555	10.38	10.07	10.70	10.74	10.76	-20.81	-20.85	31.58	20.7	31.59	20.8
58115	NGC006155	75.1553	43.7138	61.3403	45.3692	2419	2450	5.2	0.68	193	2.410	11.73	11.92	12.31	12.42	12.53	-19.49	-19.43	32.03	25.4	31.85	23.4
58336	UGC10413	38.7444	40.3357	101.5307	55.1163	2996	3068	5.7	0.37	240	2.404	13.12	13.07	13.98	14.06	13.92	-19.44	-19.37	33.38	47.5	33.48	49.6
58423	UGC10434	37.5054	39.5486	103.5239	55.6047	2529	2592	8.0	0.24	257	2.414	12.52	12.28	12.84	12.90	12.95	-19.53	-19.47	32.49	31.5	32.38	29.9
58470	UGC10439	37.1664	39.2081	104.1526	55.8481	2373	2433	5.2	0.50	362	2.613	10.69	10.60	10.96	11.03	11.18	-21.34	-21.42	32.53	32.1	32.46	31.1
58596	UGC10469	62.3114	42.1427	71.9903	51.8054	9021	9252	3.1	0.54	517	2.779	12.09	12.03	12.58	12.70	12.72	-22.85	-23.04	35.71	138.7	35.96	155.3
58792	ES517-013	354.9984	13.8799	167.3062	37.9893	8286	8533	6.2	0.20	302	2.480	/	/	15.44	15.45	/	/	-20.11	/	/	35.76	141.7
58798	AGC560012	12.0476	25.7437	146.0357	51.1030	1566	1625	4.0	0.43	278	2.480	11.61	10.93	11.48	11.46	11.56	-20.13	-20.12	31.69	21.8	31.58	20.7
58827	UGC10521	59.5360	40.6793	74.2386	53.9580	852	864	5.0	0.51	215	2.390	10.80	10.91	11.46	11.49	11.56	-19.31	-19.23	30.87	14.9	30.73	14.0
58864	UGC10564	102.1899	35.7836	38.6217	31.9323	1130	1105	6.4	0.58	148	2.250	12.80	12.96	13.84	13.93	13.80	-18.04	-17.87	31.84	23.4	31.81	23.0
58891	UGC10546	102.7407	35.7736	38.4602	31.5069	1277	1253	5.9	0.62	178	2.346	11.99	12.14	13.06	13.15	13.00	-18.90	-18.80	31.91	24.0	31.95	24.6
59083	UGC10577	67.3831	39.7641	64.6882	52.0259	938	936	3.3	0.46	237	2.418	11.58	11.63	12.32	12.40	12.37	-19.56	-19.50	31.94	24.4	31.91	24.1
59175	NGC006221	329.7378	-9.5727	191.0752	11.0470	1489	1550	4.9	0.59	279	2.530	9.31	9.18	9.35	9.40	9.66	-20.58	-20.60	30.24	11.2	30.00	10.0
59244	UGC10606	59.4852	38.3040	72.7863	56.1835	920	918	5.9	0.34	174	2.259	12.14	12.22	13.46	13.54	13.23	-18.12	-17.95	31.34	18.6	31.49	19.9
59551	UGC10713	104.0294	33.7405	35.8386	31.0245	1071	1034	3.0	0.50	228	2.412	12.73	12.77	12.82	12.89	13.20	-19.51	-19.45	32.72	35.0	32.35	29.5
59635	ES138-014	328.4569	-12.6830	194.0095	9.3403	1509	1559	6.7	0.20	223	2.348	12.91	12.56	12.68	12.71	13.01	-18.93	-18.83	31.94	24.5	31.54	20.3
59676	UGC10721	47.0604	33.0522	90.5769	63.2662	2919	2927	5.8	0.58	264	2.502	/	/	12.83	12.92	/	/	-20.33	/	/	33.29	45.4
59735	UGC10757	103.8439	33.3411	35.4308	31.2727	1168	1129	6.0	0.56	208	2.392	13.19	13.27	14.17	14.25	14.11	-19.33	-19.25	33.47	49.5	33.56	51.4
59769	UGC10738	26.4998	24.9516	134.7327	62.6813	6712	6828	4.1	0.22	585	2.769	12.88	12.08	12.56	12.58	12.70	-22.76	-22.94	35.58	130.7	35.71	139.0
59782	UGC10743	28.6680	25.8255	130.3999	63.5561	2571	2583	1.0	0.37	215	2.356	12.50	12.30	12.69	12.74	12.89	-19.00	-18.90	31.89	23.8	31.64	21.3
59884	IC0004633	315.1226	-21.4595	201.1407	-4.3901	2945	3012	6.0	0.61	318	2.593	10.86	10.63	10.92	10.97	11.17	-21.16	-21.22	32.34	29.3	32.20	27.6
59908	UGC10791	103.7266	33.0213	35.0957	31.4461	1327	1287	8.8	0.67	152	2.302	13.13	13.29	14.27	14.36	14.18	-18.51	-18.38	32.71	34.8	32.76	35.7
59995	UGC10780	28.6232	24.4053	132.8274	64.4990	6743	6850	5.9	0.20	353	2.548	14.36	13.74	13.95	13.99	14.23	-20.74	-20.78	35.07	103.5	34.90	95.4
60001	NGC006300	328.4916	-14.0515	195.3850	9.1637	1109	1149	3.1	0.62	291	2.560	9.03	9.01	9.27	9.34	9.54	-20.86	-20.90	30.40	12.0	30.24	11.2
60003	UGC10790	65.5716	34.5812	61.7201	57.1245	2108	2084	6.3	0.60	211	2.412	11.68	11.80	12.45	12.54	12.53	-19.50	-19.45	32.04	25.6	31.99	25.0
60124	IC004660	107.5313	31.6775	32.7779	28.5984	1250	1206	3.3	0.26	116	2.071	/	/	13.84	13.93	/	/	-16.12	/	/	30.04	10.2
60241	UGC10854	86.6798	34.1030	42.8584	44.3069	2817	2788	6.0	0.43	167	2.258	14.32	14.41	15.40	15.49	15.31	-18.11	-17.95	33.45	48.9	33.49	49.8
60271	UGC10858	88.1677	33.9255	41.8486	43.2962	5432	5459	5.8	0.22	201	2.305	15.34	15.23	16.17	16.27	16.10	-18.53	-18.40	34.71	87.7	34.79	90.7
60277	UGC10887	109.5556	30.9617	31.6382	27.0215	1838	1798	5.9	0.21	145	2.162	/	/	15.71	15.79	/	/	-17.01	/	/	32.82	36.7
60286	UGC10852	33.7045	23.9746	125.1903	68.0015	2778	2767	7.6	0.20	140	2.146	/	/	15.62	15.69	/	/	-16.85	/	/	32.56	32.5

PGC	Name	l	b	sgl	sgb	v_{hel}	v_{mod}	t	b/a	w_{mx}	$logw^{i}_{mx}$	I	I*	[3.6]	[3.6]*	$C_{[3.6]}$	M_C	$M_{[3.6]}$	μ_C	d_C	$\mu_{[3.6]}$	$d_{[3.6]}$
60291	UGC10876	101.9750	32.3980	34.8185	33.0290	1162	1115	5.8	0.30	199	2.310	12.07	12.03	13.09	13.16	12.95	-18.58	-18.45	31.53	20.2	31.61	21.0
60315	UGC10856	34.0312	23.8672	124.7429	68.2715	2765	2752	3.1	0.25	408	2.616	11.08	10.52	11.42	11.44	11.34	-21.36	-21.44	32.71	34.9	32.90	38.1
60330	NGC06372	49.6253	29.2405	84.9624	66.9809	4753	4769	3.8	0.62	259	2.508	12.02	12.09	12.49	12.59	12.71	-20.38	-20.38	33.11	41.8	33.01	39.9
60370	UGC10874	52.8424	29.7699	78.2615	65.9902	6799	6874	5.9	0.20	238	2.377	15.39	15.15	16.30	16.39	16.12	-19.19	-19.10	35.42	121.6	35.69	137.2
60376	AGC270324	31.5737	22.3069	132.0449	67.9107	8759	8926	4.8	0.26	374	2.579	/	/	14.10	14.17	/	/	-21.08	/	/	35.42	121.5
60459	UGC10891	30.2599	20.7710	137.2703	68.0072	1665	1634	3.6	0.54	362	2.625	10.36	10.21	9.99	10.05	10.51	-21.44	-21.53	31.96	24.6	31.58	20.7
60568	UGC10917	67.7044	31.1538	55.0729	58.7070	2161	2113	2.0	0.38	253	2.428	12.65	12.60	13.27	13.34	13.33	-19.66	-19.61	33.01	39.9	32.98	39.4
60573	UGC10934	102.9648	31.4290	33.4558	32.4534	2488	2449	4.0	0.43	315	2.533	11.76	11.69	12.42	12.49	12.45	-20.61	-20.63	33.08	41.3	33.15	42.7
60925	UGC10997	45.5483	22.5698	95.9875	73.6555	3364	3321	5.8	0.56	278	2.515	12.15	12.12	12.65	12.73	12.79	-20.45	-20.46	33.26	44.8	33.23	44.2
60957	UGC11001	39.2206	19.8844	119.5032	74.2950	4216	4191	8.1	0.46	298	2.517	/	/	13.17	13.25	/	/	-20.48	/	/	33.78	57.1
60972	UGC11004	42.4475	21.0874	107.4129	74.4824	3039	2990	2.3	0.54	269	2.496	/	/	12.88	12.96	/	/	-20.27	/	/	33.26	44.9
60975	UGC11003	39.7895	19.9999	117.5722	74.4656	4064	4035	5.7	0.23	277	2.445	/	/	13.28	13.34	/	/	-19.78	/	/	33.15	42.7
61008	UGC11010	49.5238	23.4175	83.3113	72.7774	3112	3060	3.0	0.52	360	2.616	/	/	11.91	11.99	/	/	-21.44	/	/	33.48	49.6
61036	UGC11021	54.3206	24.7604	70.8841	70.3937	5186	5176	3.1	0.23	380	2.582	13.51	13.08	13.23	13.28	13.55	-21.06	-21.12	34.69	86.7	34.50	79.4
61092	UGC11041	60.5155	26.0216	58.9691	66.6435	4876	4855	2.0	0.60	364	2.649	12.23	12.25	12.12	12.22	12.61	-21.67	-21.77	34.34	73.8	34.06	64.8
61120	UGC11050	60.3680	25.7996	58.9247	66.9016	4861	4838	4.1	0.22	285	2.457	13.76	13.47	14.27	14.34	14.26	-19.92	-19.89	34.24	70.4	34.32	73.0
61161	UGC11055	37.9837	17.5198	128.4833	75.5270	2948	2890	3.3	0.71	216	2.478	/	/	12.73	12.81	/	/	-20.09	/	/	32.93	38.5
61164	UGC11060	53.5374	23.4645	71.5487	71.8579	4662	4633	1.0	0.28	440	2.653	12.21	11.83	12.15	12.20	12.38	-21.70	-21.80	34.14	67.3	34.08	65.6
61300	UGC11093	33.5717	14.1779	148.8449	74.3230	1963	1888	6.0	0.21	306	2.486	11.45	10.89	11.51	11.51	11.56	-20.19	-20.18	31.75	22.4	31.69	21.8
61353	P0061353	33.9102	13.6765	149.9232	74.8496	1798	1718	2.0	0.49	194	2.339	/	/	13.41	13.45	/	/	-18.73	/	/	32.19	27.5
61469	UGC11132	65.6767	24.3370	47.6869	64.8410	2836	2756	3.1	0.22	318	2.504	13.00	12.68	12.98	13.02	13.22	-20.35	-20.35	33.60	52.5	33.42	48.3
61526	UGC11142	52.4288	19.6355	70.2026	75.8058	4508	4454	5.8	0.23	355	2.553	13.27	12.71	13.17	13.20	13.32	-20.79	-20.83	34.17	68.3	34.11	66.4
61553	UGC11159	66.7327	24.0263	45.6548	64.3270	2827	2744	4.0	0.22	285	2.457	12.20	11.94	12.45	12.51	12.59	-19.92	-19.89	32.52	31.9	32.42	30.4
61600	NGC06586	48.1522	17.4820	86.1519	78.8118	3138	3055	2.0	0.51	257	2.466	/	/	12.75	12.83	/	/	-19.98	/	/	32.84	36.9
61637	UGC011182	85.1137	27.2901	34.8186	48.4990	4266	4220	4.1	0.31	248	2.408	/	/	14.44	14.53	/	/	-19.41	/	/	34.00	63.2
61658	P0061658	41.4553	13.9976	126.6953	80.3675	2998	2911	5.0	0.45	131	2.158	/	/	13.51	13.59	/	/	-16.96	/	/	30.55	12.9
61690	UGC11188	46.4338	15.7819	95.4631	80.4937	5284	5242	6.6	0.25	293	2.472	/	/	13.56	13.61	/	/	-20.04	/	/	33.70	55.0
61698	UGC11194	54.0612	18.7242	62.8860	75.9879	4742	4685	4.0	0.53	357	2.615	12.05	11.89	12.47	12.55	12.58	-21.36	-21.44	33.99	62.7	34.06	64.9
61712	ES182-010	339.7518	-17.3658	200.8808	19.1690	3546	3555	5.1	0.56	182	2.333	/	/	12.92	13.00	/	/	-18.68	/	/	31.68	21.7
61742	UGC11218	105.5357	28.1747	29.1741	30.9384	1483	1416	5.2	0.51	326	2.570	10.02	9.97	10.40	10.47	10.59	-20.94	-20.99	31.53	20.2	31.46	19.6
61836	UGC11236	102.1882	27.7638	29.3610	33.9191	5761	5767	4.4	0.51	360	2.613	12.30	12.22	12.56	12.65	12.80	-21.34	-21.41	34.19	69.0	34.14	67.4
61936	UGC11255	80.2797	24.3105	33.2768	53.6831	9724	9857	5.9	0.20	432	2.635	13.57	13.05	13.53	13.61	13.69	-21.54	-21.63	35.35	117.4	35.41	121.0
61942	UGC11254	58.6627	17.6778	46.8408	74.1715	4987	4921	5.9	0.20	237	2.375	14.32	13.98	14.50	14.56	14.63	-19.17	-19.09	33.85	58.8	33.71	55.1
61972	UGC11269	98.1801	26.9325	29.3255	37.5746	2572	2500	2.0	0.52	360	2.617	11.20	11.14	11.60	11.68	11.77	-21.38	-21.46	33.17	43.1	33.17	43.0
62017	UGC011295	106.5032	27.3325	28.0437	30.2346	2366	2304	7.9	0.20	173	2.238	/	/	15.24	15.30	/	/	-17.75	/	/	33.08	41.4
62037	UGC11275	60.6489	17.5163	41.9643	72.8675	5453	5395	5.9	0.20	389	2.590	13.73	13.19	13.93	13.97	13.94	-21.13	-21.19	35.17	108.2	35.32	115.9

PGC	Name	l	b	sgl	sgb	v_{hel}	v_{mod}	t	b/a	w_{mx}	$logw^{i}_{mx}$	I	I*	[3.6]	[3.6]*	$C_{[3.6]}$	M_C	$M_{[3.6]}$	μ_C	d_C	$\mu_{[3.6]}$	$d_{[3.6]}$
62059	UGC11280	60.6186	17.3850	41.6790	72.9726	5480	5422	2.0	0.31	468	2.683	/	/	12.50	12.55	/	/	-22.10	/	/	34.77	90.0
62066	IC0004721	336.7975	-20.7476	203.6569	15.6736	2234	2218	5.9	0.28	310	2.501	10.69	10.41	11.12	11.17	11.15	-20.32	-20.32	31.47	19.7	31.49	19.9
62077	UGC11300	101.0521	26.8315	28.5040	35.0979	489	403	6.4	0.29	204	2.319	11.23	11.13	12.06	12.11	11.97	-18.67	-18.55	30.64	13.4	30.66	13.5
62097	UGC11289	51.5965	13.3197	59.5834	81.8565	3991	3891	4.5	0.62	283	2.548	/	/	12.65	12.73	/	/	-20.78	/	/	33.56	51.4
62149	UGC11305	68.7550	19.5743	34.5331	65.3519	2495	2378	4.0	0.72	255	2.554	11.34	11.42	11.94	12.03	12.09	-20.81	-20.84	32.91	38.2	32.90	38.0
62164	UGC11301	47.2230	10.8038	91.8460	85.5138	4502	4410	5.4	0.20	485	2.686	/	/	12.10	12.08	/	/	-22.12	/	/	34.30	72.3
62178	UGC11308	54.5923	13.9192	47.4831	79.5973	3429	3316	3.0	0.58	431	2.715	10.81	10.69	11.23	11.30	11.35	-22.26	-22.41	33.65	53.8	33.76	56.6
62204	UGC011334	104.7731	26.7980	27.7217	31.8417	4562	4534	5.6	0.33	264	2.438	/	/	15.10	15.17	/	/	-19.70	/	/	35.01	100.5
62231	UGC11320	53.2175	12.7667	48.6333	81.3528	4813	4725	4.1	0.20	456	2.659	12.60	11.92	12.41	12.43	12.54	-21.76	-21.86	34.36	74.4	34.38	75.3
62248	UGC011328	66.9542	18.2525	33.7635	67.4860	5660	5603	5.9	0.20	291	2.464	14.38	13.99	14.69	14.76	14.73	-19.98	-19.96	34.80	91.0	34.84	92.7
62296	NGC06695	69.4235	18.7322	32.0438	65.1972	5496	5435	3.1	0.56	421	2.697	/	/	12.79	12.88	/	/	-22.24	/	/	35.28	113.5
62338	UGC11344	53.9788	12.2362	42.6999	81.1965	3834	3720	2.0	0.41	394	2.627	11.64	11.36	12.32	12.37	12.22	-21.46	-21.55	33.72	55.5	33.99	62.8
62380	UGC11350	52.7598	11.1764	42.7345	82.7927	4702	4604	5.9	0.63	319	2.605	/	/	12.66	12.72	/	/	-21.33	/	/	34.13	67.0
62509	UGC11371	56.8968	11.6334	30.1314	79.1968	3750	3625	4.4	0.33	358	2.570	12.35	11.85	12.35	12.37	12.47	-20.95	-20.99	33.45	49.0	33.41	48.1
62518	UGC11377	104.1962	25.8123	26.6745	32.5153	7458	7513	6.0	0.20	362	2.559	/	/	13.87	13.93	/	/	-20.88	/	/	34.95	97.6
62550	ES396-007	1.6139	-15.5674	206.2774	39.6795	5867	5850	4.8	0.34	448	2.670	11.84	11.45	12.03	12.09	12.13	-21.86	-21.97	34.04	64.2	34.14	67.3
62585	E281-038	353.4223	-19.0110	206.7345	31.1435	4958	4934	1.8	0.32	381	2.596	12.40	12.09	12.33	12.39	12.61	-21.19	-21.25	33.84	58.6	33.70	54.9
62595	UGC11380	66.8526	14.7827	25.4194	69.0810	2878	2740	2.0	0.25	285	2.460	/	/	12.21	12.26	/	/	-19.92	/	/	32.19	27.4
62651	UGC011385	51.2131	6.9932	10.2214	86.1239	3118	2969	8.1	0.68	256	2.534	/	/	12.47	12.47	/	/	-20.64	/	/	33.15	42.6
62671	NGC06750	89.4248	21.9195	25.4103	46.5300	3696	3605	5.0	0.65	243	2.496	/	/	12.62	12.72	/	/	-20.27	/	/	33.02	40.1
62706	IC0004810	340.3709	-23.8107	207.6187	18.1118	3182	3150	6.6	0.20	283	2.452	12.44	12.03	12.83	12.87	12.80	-19.87	-19.84	32.69	34.5	32.73	35.1
62717	UGC11394	59.0505	9.7556	17.3075	77.9369	4227	4097	6.0	0.20	377	2.576	/	/	12.93	12.93	/	/	-21.06	/	/	34.06	64.8
62781	UGC11404	60.6648	9.6764	15.1680	76.4159	3916	3776	3.6	0.55	405	2.677	/	/	11.12	11.17	/	/	-22.04	/	/	33.24	44.5
62806	UGC11407	81.4985	18.2322	22.8378	54.6751	2414	2280	3.6	0.52	261	2.478	11.01	11.00	11.52	11.60	11.67	-20.11	-20.09	31.78	22.6	31.70	21.9
62836	NGC006744	332.2237	-26.1460	208.1009	10.3822	841	804	4.0	0.58	315	2.578	7.62	7.65	8.30	8.37	8.37	-21.02	-21.08	29.40	7.6	29.45	7.8
62861	E282-018	353.2539	-21.7950	209.6909	30.0044	5603	5584	5.9	0.36	352	2.568	12.59	12.31	12.88	12.95	12.99	-20.93	-20.97	33.96	62.0	33.99	62.8
62882	ES593-003	15.9507	-13.7816	212.9380	52.8964	8226	8243	5.9	0.20	401	2.603	13.89	13.26	13.58	13.63	13.81	-21.25	-21.32	35.16	107.7	35.09	104.4
62889	E459-006	5.4649	-18.0893	211.3312	41.9889	5750	5701	4.2	0.32	453	2.671	12.15	11.72	12.44	12.49	12.47	-21.86	-21.98	34.39	75.6	34.58	82.2
62982	UGC11422	74.7981	14.1855	18.4328	61.9176	4655	4540	5.9	0.20	295	2.470	/	/	12.49	12.55	/	/	-20.02	/	/	32.58	32.8
63040	UGC11426	67.0507	10.0707	12.2090	70.1681	4453	4317	2.0	0.68	277	2.568	/	/	12.20	12.29	/	/	-20.98	/	/	33.30	45.8
63096	UGC11429	74.9129	13.1986	16.3312	62.0225	4638	4517	3.1	0.51	518	2.771	11.04	10.83	11.49	11.56	11.55	-22.77	-22.96	34.39	75.6	34.62	84.1
63121	NGC006796	92.3106	20.0703	21.9879	44.3140	2191	2068	4.0	0.24	391	2.596	11.43	11.00	11.56	11.59	11.66	-21.19	-21.25	32.86	37.3	32.86	37.4
63165	UGC11433	67.5205	9.0466	9.0563	69.8489	4437	4295	6.7	0.20	283	2.452	/	/	13.65	13.69	/	/	-19.84	/	/	33.58	51.9
63166	UGC11435	87.3373	17.9270	20.2659	49.3457	3748	3633	5.8	0.20	299	2.476	12.52	12.10	12.66	12.70	12.76	-20.09	-20.07	32.87	37.4	32.79	36.2
63173	ES397-018	3.3248	-21.4870	214.0819	38.6418	5410	5345	5.0	0.20	353	2.548	13.36	12.77	13.14	13.17	13.34	-20.75	-20.78	34.14	67.3	34.03	63.9
63229	UGC11443	85.9940	16.8090	18.9442	50.8202	4364	4255	5.8	0.51	288	2.515	12.23	12.09	12.65	12.72	12.77	-20.45	-20.46	33.24	44.4	33.21	43.9

PGC	Name	l	b	sgl	sgb	v_{hel}	v_{mod}	t	b/a	w_{mx}	$logw^{i}_{mx}$	I	I^{*}	[3.6]	$[3.6]^{*}$	$C_{[3.6]}$	M_{C}	$M_{[3.6]}$	μ_{C}	d_{C}	$\mu_{[3.6]}$	$d_{[3.6]}$
63286	UGC11455	103.7484	22.8450	23.2507	33.3607	5392	5359	5.8	0.20	608	2.784	12.05	11.12	11.59	11.59	11.72	-22.89	-23.08	34.69	86.5	34.79	90.7
63395	IC0004871	339.7605	-28.4500	212.1205	16.2863	1925	1856	6.6	0.20	249	2.396	12.28	11.98	13.01	13.05	12.87	-19.37	-19.30	32.24	28.1	32.36	29.7
63424	UGC11459	74.0834	9.3839	8.3431	63.3681	3119	2947	6.3	0.56	359	2.627	11.48	11.24	11.84	11.89	11.93	-21.46	-21.55	33.42	48.3	33.49	49.8
63540	AGC590024	24.0528	-18.2660	227.3132	56.3308	5996	5881	5.0	0.20	462	2.665	12.56	11.82	12.52	12.54	12.54	-21.81	-21.92	34.41	76.2	34.56	81.8
63552	UGC11466	78.6905	10.6319	10.0942	58.7392	821	631	5.0	0.56	185	2.342	11.42	11.34	11.63	11.69	11.88	-18.87	-18.76	30.75	14.1	30.45	12.3
63592	AGC032742	12.7868	-22.9989	222.0797	45.2548	5802	5705	4.8	0.20	480	2.682	12.56	11.74	12.50	12.51	12.48	-21.96	-22.08	34.51	79.9	34.71	87.3
63622	E398-029	5.2020	-25.4737	219.5876	38.1493	5758	5679	4.4	0.20	361	2.558	/	/	13.45	13.47	/	/	-20.87	/	/	34.44	77.2
63664	UGC11477	89.5853	15.3917	15.9541	47.6411	3715	3585	6.5	0.27	265	2.431	/	/	13.15	13.21	/	/	-19.63	/	/	32.87	37.4
63751	ES461-006	8.5922	-26.0040	222.3390	40.4013	5953	5864	4.9	0.20	366	2.563	/	/	13.39	13.42	/	/	-20.93	/	/	34.44	77.4
63766	UGC11492	90.4527	14.9530	15.1583	46.8656	3563	3428	4.1	0.50	294	2.522	11.91	11.80	12.44	12.52	12.52	-20.51	-20.52	33.05	40.7	33.07	41.2
63776	AGC032834	15.8142	-24.0398	225.7469	46.7730	5854	5743	6.2	0.20	283	2.452	14.38	13.96	14.65	14.71	14.69	-19.87	-19.84	34.64	84.7	34.66	85.5
63840	E339-008	2.2294	-28.5379	221.0906	34.2851	5679	5597	1.0	0.35	381	2.600	12.64	12.34	12.70	12.77	12.92	-21.22	-21.29	34.20	69.2	34.14	67.4
64060	AGC033027	23.0763	-24.3266	233.1856	51.2724	2231	2019	7.5	0.38	221	2.370	12.77	12.58	13.22	13.27	13.29	-19.13	-19.04	32.42	30.5	32.33	29.2
64070	UGC11515	96.0902	16.0988	15.9116	41.3409	3255	3125	6.6	0.66	118	2.187	/	/	13.02	13.10	/	/	-17.25	/	/	30.35	11.8
64318	UGC11527	41.5935	-18.8160	257.3434	64.2271	5487	5298	2.2	0.26	451	2.661	12.31	11.69	12.40	12.43	12.42	-21.77	-21.88	34.24	70.6	34.40	75.8
64373	PG0064373	29.7524	-24.7185	241.7151	54.5355	5681	5513	8.0	0.35	451	2.674	/	/	12.69	12.75	/	/	-22.01	/	/	34.89	94.9
64429	ES340-009	2.5576	-32.6376	225.3982	32.3032	2587	2423	7.1	0.20	168	2.225	13.60	13.53	14.53	14.60	14.42	-17.81	-17.63	32.23	28.0	32.24	28.0
64458	UGC11537	43.1279	-19.3719	260.8499	63.9707	5418	5221	5.3	0.28	499	2.707	11.73	11.17	12.02	12.06	11.97	-22.20	-22.34	34.22	70.0	34.49	79.2
64485	UGC11540	100.4582	16.6713	16.1498	37.1155	2485	2352	3.0	0.53	349	2.606	11.53	10.75	11.21	11.19	11.34	-21.27	-21.34	32.62	33.4	32.55	32.3
64488	ES340-017	1.9316	-33.1951	225.5979	31.5560	2614	2450	8.0	0.58	209	2.400	/	/	13.53	13.62	/	/	-19.34	/	/	32.98	39.5
64506	E527-019	19.2381	-29.6703	234.5938	44.9990	3118	2912	4.2	0.62	234	2.466	12.27	12.31	12.86	12.95	12.99	-20.00	-19.97	33.01	39.9	32.95	38.9
64534	AGC600053	33.5750	-24.7824	247.1474	56.1209	5660	5479	7.0	0.20	426	2.629	/	/	12.69	12.73	/	/	-21.57	/	/	34.40	75.8
64540	UGC011545	88.1963	8.7749	6.1221	49.4718	2951	2770	5.4	0.22	187	2.274	/	/	13.06	13.10	/	/	-18.10	/	/	31.20	17.4
64552	NGC06901	49.6190	-16.8973	275.4420	66.6764	4791	4570	2.4	0.40	371	2.598	/	/	12.90	12.96	/	/	-21.27	/	/	34.32	73.1
64601	NGC06906	49.7926	-17.1472	275.7928	66.4109	4859	4638	3.8	0.43	436	2.675	/	/	11.97	12.03	/	/	-22.02	/	/	34.13	66.9
64637	UGC11552	55.2298	-14.2029	290.7679	68.0454	4527	4297	2.0	0.37	466	2.691	12.29	11.89	12.03	12.08	12.36	-22.05	-22.18	34.47	78.3	34.35	74.0
64638	UGC11551	50.3514	-17.1270	277.1229	66.3685	4881	4659	4.0	0.22	397	2.601	12.35	11.79	12.33	12.36	12.44	-21.23	-21.29	33.70	55.0	33.71	55.3
64724	ES400-025	9.7421	-33.5305	230.6957	36.5397	2175	1977	7.8	0.47	158	2.245	13.39	13.46	14.65	14.74	14.45	-17.99	-17.82	32.45	30.9	32.58	32.8
64759	UGC11568	54.2614	-15.8771	287.0197	66.7779	4225	3984	5.8	0.31	435	2.652	11.84	11.38	11.82	11.86	11.99	-21.69	-21.79	33.71	55.3	33.71	55.1
64812	P0064812	42.8051	-22.7263	261.3964	60.6124	5648	5446	2.5	0.35	297	2.492	/	/	13.49	13.55	/	/	-20.23	/	/	33.85	59.0
64862	UGC11579	44.2560	-22.2993	264.0080	61.2187	5901	5704	5.8	0.20	407	2.610	13.40	12.67	13.44	13.46	13.43	-21.31	-21.38	34.82	91.9	34.98	98.9
64891	UGC11584	46.4321	-21.4119	268.1243	62.2528	5348	5133	5.8	0.20	437	2.641	13.47	12.71	12.84	12.85	13.15	-21.59	-21.69	34.83	92.3	34.64	84.9
64909	ES234-043	350.9954	-36.3410	223.5718	22.2168	2444	2305	8.9	0.52	122	2.146	13.22	13.40	14.39	14.50	14.30	-17.09	-16.85	31.39	19.0	31.35	18.6
64980	AGC033592	11.2713	-34.6938	232.8284	36.7018	2789	2589	4.0	0.29	506	2.714	9.69	9.26	10.51	10.55	10.25	-22.26	-22.40	32.52	31.9	32.97	39.4
65003	ES340-042	0.8291	-36.2752	227.9649	29.0794	2656	2485	7.8	0.54	132	2.187	/	/	14.28	14.38	/	/	-17.25	/	/	31.63	21.2
65007	UGC11595	47.2381	-21.9151	269.7413	61.7646	4013	3763	4.1	0.20	328	2.516	13.10	12.64	13.00	13.04	13.20	-20.45	-20.47	33.70	54.9	33.55	51.4

PGC	Name	l	b	sgl	sgb	v_{hel}	v_{mod}	t	b/a	w_{mx}	$logw^{i}_{mx}$	I	I^{*}	[3.6]	$[3.6]^{*}$	$C_{[3.6]}$	M_{C}	$M_{[3.6]}$	μ_{C}	d_{C}	$\mu_{[3.6]}$	$d_{[3.6]}$
65022	AGC600084	39.4332	-25.9308	256.8774	56.8412	5797	5599	5.2	0.20	515	2.712	12.73	12.11	12.48	12.51	12.68	-22.24	-22.38	35.01	100.3	35.03	101.2
65052	UGC11603	98.8248	13.5966	12.3887	38.8929	5189	5089	5.0	0.20	351	2.545	/	/	13.10	13.07	/	/	-20.75	/	/	33.89	60.0
65060	UGC11599	56.0555	-17.1753	289.9503	64.9857	4452	4208	3.1	0.68	377	2.702	/	/	11.53	11.62	/	/	-22.29	/	/	33.97	62.4
65086	UGC11604	100.8958	14.8531	13.8430	36.8215	1426	1273	4.0	0.66	309	2.605	/	/	9.70	9.71	/	/	-21.34	/	/	31.05	16.2
65131	PG0065131	40.4787	-26.4282	258.7513	56.5769	3900	3651	1.2	0.26	380	2.586	/	/	11.96	12.01	/	/	-21.15	/	/	33.20	43.6
65150	UGC11613	98.9359	13.1972	11.8700	38.8035	2670	2517	6.1	0.20	211	2.324	14.06	13.40	14.10	14.10	14.11	-18.71	-18.59	32.84	37.0	32.72	34.9
65211	P0065211	92.6084	8.3127	5.4472	45.1083	2856	2673	5.0	0.46	284	2.496	/	/	12.62	12.58	/	/	-20.27	/	/	32.87	37.6
65249	AGC033738	14.3435	-36.0695	236.2687	37.5003	2713	2497	4.0	0.30	241	2.394	11.88	11.71	12.26	12.32	12.38	-19.34	-19.27	31.72	22.1	31.60	20.8
65255	UGC11635	113.5500	22.1975	21.5405	24.4091	4801	4765	3.6	0.44	488	2.725	11.51	11.15	11.69	11.74	11.81	-22.36	-22.51	34.22	69.9	34.34	73.9
65258	AGC033741	14.5442	-36.1050	236.4488	37.5849	2716	2500	6.7	0.61	241	2.475	11.75	11.79	12.34	12.43	12.47	-20.09	-20.07	32.57	32.7	32.52	31.9
65295	NGC006943	325.9551	-35.2971	216.0641	3.2957	3113	3073	5.9	0.50	400	2.654	10.42	10.33	10.92	11.00	11.02	-21.71	-21.82	32.75	35.5	32.84	37.0
65375	NGC6962	47.4062	-25.3728	270.0623	58.3072	4222	3965	1.7	0.66	475	2.794	10.62	10.55	11.09	11.18	11.23	-22.98	-23.18	34.27	71.4	34.45	77.7
65506	AGC600138	40.5098	-29.4824	259.9096	53.5952	6015	5810	5.0	0.20	473	2.675	12.97	12.37	12.76	12.79	12.95	-21.90	-22.02	34.94	97.1	34.94	97.4
65642	UGC11648	102.7488	14.2070	12.9405	35.0605	3364	3232	9.7	0.28	283	2.461	/	/	12.94	12.91	/	/	-19.93	/	/	32.86	37.3
65683	UGC11647	64.0017	-17.0565	304.8911	61.4218	8000	7853	5.9	0.20	466	2.668	13.58	12.93	13.06	13.11	13.39	-21.84	-21.96	35.34	117.1	35.21	110.4
65834	UGC11656	59.1805	-21.8501	292.0114	59.5441	4584	4322	5.9	0.20	267	2.427	14.11	13.77	14.24	14.30	14.40	-19.64	-19.59	34.09	65.8	33.96	61.9
65887	UGC11662	65.0060	-18.2748	304.9722	59.8732	5320	5078	3.7	0.70	263	2.557	12.41	12.48	12.92	13.03	13.12	-20.83	-20.87	34.00	63.0	33.97	62.2
65960	AGC600179	31.4197	-36.3741	251.8429	44.7629	1474	1193	5.0	0.26	254	2.412	11.40	11.17	12.16	12.21	12.04	-19.50	-19.45	31.55	20.4	31.65	21.4
66094	UGC11677	64.3021	-20.4123	301.5037	58.5107	4960	4703	6.2	0.50	338	2.583	/	/	13.11	13.20	/	/	-21.12	/	/	34.41	76.2
66239	ES342-013	5.6778	-42.7625	236.4073	28.0445	2635	2426	1.0	0.30	184	2.276	12.35	12.32	13.09	13.18	13.11	-18.28	-18.13	31.38	18.9	31.30	18.2
66242	AGC610018	46.7137	-32.3131	269.1116	51.3619	2233	1929	4.1	0.46	187	2.315	13.12	13.15	14.01	14.09	13.98	-18.63	-18.51	32.62	33.4	32.61	33.3
66366	UGC11701	59.2756	-26.0953	289.1365	55.5869	6116	5882	3.9	0.71	195	2.433	/	/	13.25	13.36	/	/	-19.66	/	/	33.05	40.8
66396	UGC11706	65.0136	-22.4320	300.4677	56.4594	4724	4454	3.3	0.22	369	2.569	13.55	13.02	13.46	13.49	13.62	-20.93	-20.98	34.63	84.3	34.58	82.4
66407	NGC07046	53.9457	-29.8906	279.5500	53.2432	4165	3881	5.9	0.71	271	2.576	/	/	12.49	12.59	/	/	-21.06	/	/	33.70	55.0
66434	UGC11711	67.0090	-21.3570	304.3197	56.2772	8971	8848	6.0	0.20	400	2.602	/	/	14.49	14.55	/	/	-21.31	/	/	36.09	164.9
66461	UGC11712	50.5980	-32.1982	274.3763	51.3592	5801	5559	3.1	0.50	419	2.677	12.15	12.03	12.63	12.72	12.73	-21.92	-22.04	34.73	88.5	34.89	94.9
66478	UGC11738	117.5157	23.3605	22.6204	20.7041	4229	4195	4.0	0.50	281	2.504	13.34	13.21	13.70	13.78	13.86	-20.34	-20.35	34.26	71.2	34.21	69.4
66546	UGC11719	66.1237	-23.0037	301.4239	55.4160	8566	8421	2.1	0.30	485	2.697	/	/	13.44	13.51	/	/	-22.24	/	/	35.97	156.2
66548	AGC310060	73.9969	-16.6557	318.5541	55.0529	936	625	1.0	0.42	149	2.206	/	/	13.46	13.52	/	/	-17.44	/	/	30.96	15.6
66622	UGC11731	71.1057	-19.8715	311.1868	54.9105	4955	4691	2.1	0.28	369	2.576	12.68	12.26	12.93	12.98	12.98	-21.00	-21.05	34.03	64.0	34.11	66.2
66738	PG0066738	49.0326	-35.7887	272.0103	47.8623	2937	2629	7.4	0.20	199	2.299	/	/	14.91	14.98	/	/	-18.34	/	/	33.37	47.1
66784	NGC007059	334.6949	-42.4348	224.6022	8.2892	1734	1615	5.6	0.32	260	2.429	12.37	12.26	11.89	11.95	12.49	-19.66	-19.62	32.16	27.0	31.57	20.6
66812	AGC034475	5.4164	-46.3843	239.2796	25.4799	2661	2443	5.0	0.65	236	2.482	11.35	11.41	11.97	12.05	12.09	-20.14	-20.13	32.24	28.1	32.19	27.5
66836	NGC007064	344.1623	-44.8185	229.2855	13.8987	855	692	5.1	0.20	153	2.185	11.89	11.93	13.07	13.09	12.86	-17.44	-17.23	30.30	11.5	30.32	11.6
66880	UGC11758	66.7487	-26.3291	299.1181	52.3280	8635	8483	4.2	0.20	612	2.787	/	/	12.81	12.84	/	/	-23.11	/	/	36.19	173.3
66969	UGC11766	73.6616	-21.6080	311.9745	51.9936	5323	5061	1.1	0.35	438	2.661	12.53	12.22	12.82	12.88	12.91	-21.77	-21.88	34.77	89.8	34.89	95.1

PGC	Name	l	b	sgl	sgb	v_{hel}	v_{mod}	t	b/a	w_{mx}	$logw^{i}_{mx}$	I	I^{*}	[3.6]	$[3.6]^{*}$	$C_{[3.6]}$	M_{C}	$M_{[3.6]}$	μ_{C}	d_{C}	$\mu_{[3.6]}$	$d_{[3.6]}$
66972	NGC007091	7.2280	-47.5239	241.1393	25.5875	2565	2337	7.9	0.71	121	2.226	/	/	13.45	13.56	/	/	-17.64	/	/	31.19	17.3
66986	UGC11768	71.4845	-23.6867	307.2903	51.8629	6610	6382	4.0	0.20	426	2.629	13.72	13.12	13.55	13.59	13.72	-21.49	-21.57	35.32	115.9	35.33	116.2
67045	NGC007090	341.2957	-45.3852	229.0135	11.8144	846	689	5.0	0.20	198	2.297	9.84	9.74	10.59	10.65	10.55	-18.46	-18.32	29.01	6.3	28.97	6.2
67078	ES287-043	356.3500	-47.9590	236.4336	19.6904	2489	2291	5.9	0.22	178	2.252	13.32	13.28	14.08	14.16	14.08	-18.05	-17.89	32.13	26.7	32.05	25.7
67205	UGC11794	67.5332	-29.4044	297.4530	49.3558	5850	5588	2.0	0.34	340	2.549	13.07	12.78	13.32	13.39	13.45	-20.76	-20.79	34.26	71.2	34.27	71.3
67246	UGC11799	90.7506	-7.1326	343.4287	44.6788	5342	5132	4.5	0.69	332	2.653	/	/	12.52	12.55	/	/	-21.80	/	/	34.45	77.6
67258	ES403-017	8.0069	-49.5221	243.0928	24.5259	2708	2475	5.1	0.47	124	2.139	13.73	13.93	14.92	15.02	14.83	-17.02	-16.78	31.85	23.5	31.81	23.0
67335	ES403-024	7.9755	-50.0361	243.4671	24.1409	2609	2374	6.0	0.36	143	2.177	/	/	14.61	14.71	/	/	-17.15	/	/	31.86	23.5
67347	UGC11818	109.9976	14.4043	12.9781	28.0341	2404	2271	5.0	0.62	283	2.546	12.01	10.93	11.66	11.60	11.62	-20.73	-20.76	32.36	29.6	32.37	29.8
67373	ES403-031	7.0883	-50.3176	243.2354	23.5432	2529	2294	4.0	0.41	136	2.164	14.39	14.54	15.39	15.49	15.37	-17.25	-17.03	32.63	33.6	32.53	32.1
67495	UGC011833	85.5579	-15.3702	329.8060	46.3934	5232	4985	5.9	0.20	354	2.549	/	/	14.12	14.15	/	/	-20.79	/	/	35.08	103.8
67532	NGC007140	338.7925	-47.1540	230.0610	9.5644	2981	2844	3.8	0.54	291	2.530	10.98	11.03	11.36	11.45	11.61	-20.58	-20.60	32.19	27.5	32.06	25.8
67550	UGC11838	81.7237	-19.9160	321.3682	47.2211	3496	3196	6.5	0.20	246	2.391	13.68	13.37	14.29	14.35	14.21	-19.32	-19.24	33.56	51.6	33.64	53.5
67556	UGC11839	87.3167	-13.7617	332.9528	45.5549	5942	5721	4.0	0.23	453	2.660	13.28	12.59	12.89	12.92	13.12	-21.76	-21.87	34.97	98.7	34.91	96.1
67605	ES145-025	335.9156	-46.5531	228.8357	7.9017	1837	1697	9.0	0.39	118	2.099	/	/	14.61	14.71	/	/	-16.39	/	/	31.10	16.6
67619	UGC11844	72.0523	-29.7331	302.0219	46.8545	7377	7160	2.0	0.49	507	2.756	/	/	12.29	12.38	/	/	-22.81	/	/	35.35	117.5
67727	UGC11862	89.7224	-12.4854	335.8945	43.8963	5843	5624	7.5	0.26	349	2.549	/	/	13.54	13.57	/	/	-20.79	/	/	34.46	78.1
67823	NGC07177	75.3669	-28.9582	305.9543	45.6092	1149	803	2.5	0.69	288	2.591	10.20	10.26	10.71	10.78	10.89	-21.14	-21.20	32.03	25.4	31.99	25.0
67835	ES404-017	9.4406	-52.9331	246.3347	22.6252	2515	2268	7.6	0.33	187	2.288	13.85	13.88	14.99	15.08	14.83	-18.38	-18.23	33.23	44.3	33.35	46.8
67839	NGC007171	43.4565	-47.9258	266.7738	35.6446	2724	2408	3.1	0.51	345	2.595	11.24	11.21	11.84	11.92	11.92	-21.18	-21.24	33.12	42.1	33.20	43.6
67842	ES404-018	13.9353	-52.9257	248.6185	24.3432	2271	2010	6.8	0.20	163	2.212	13.86	13.83	15.09	15.17	14.85	-17.69	-17.50	32.55	32.3	32.69	34.5
67846	ES466-036	15.6748	-52.8951	249.5318	24.9854	2379	2115	1.5	0.55	266	2.493	12.71	12.77	13.37	13.46	13.48	-20.24	-20.24	33.76	56.4	33.75	56.4
67893	AGC034977	32.5105	-51.1134	259.1560	31.1588	1789	1483	8.2	0.26	131	2.124	13.91	14.02	14.80	14.89	14.81	-16.89	-16.64	31.70	21.9	31.52	20.2
67904	AGC034988	32.8912	-51.1112	259.4222	31.2313	2623	2325	4.5	0.25	524	2.724	10.15	9.66	10.36	10.39	10.38	-22.35	-22.50	32.74	35.3	32.91	38.2
67920	AGC034989	30.3768	-51.6560	257.8875	30.2221	1716	1414	5.9	0.46	110	2.084	13.93	14.14	15.43	15.53	15.18	-16.53	-16.25	31.71	22.0	31.78	22.7
67932	IC005156	11.8604	-53.4043	247.8679	23.2010	2496	2242	2.2	0.40	365	2.590	11.12	10.99	11.58	11.65	11.68	-21.13	-21.19	32.83	36.8	32.87	37.4
67943	NGC007188	33.7358	-51.1400	260.0269	31.3534	1760	1451	3.5	0.43	152	2.217	/	/	13.19	13.28	/	/	-17.55	/	/	30.83	14.7
67954	AGC035005	14.4740	-53.4637	249.2544	24.1037	2535	2275	5.0	0.39	266	2.452	12.12	12.07	12.88	12.95	12.87	-19.88	-19.85	32.76	35.6	32.82	36.6
67966	UGC11893	88.8275	-15.6218	331.4369	43.4509	5589	5351	6.3	0.21	606	2.784	12.59	11.70	12.29	12.29	12.36	-22.89	-23.08	35.36	118.0	35.55	128.7
67977	UGC011895	91.2708	-12.6432	336.4466	42.4310	4727	4479	3.1	0.64	334	2.629	11.99	11.76	12.35	12.42	12.45	-21.49	-21.57	33.99	62.7	34.06	65.0
68044	UGC011918	112.7770	15.5267	14.2142	25.3415	4097	4004	5.2	0.32	322	2.522	/	/	13.39	13.35	/	/	-20.53	/	/	33.95	61.6
68128	NGC007205	334.8242	-48.3603	230.3464	6.6507	1686	1540	4.0	0.47	317	2.546	9.98	9.96	10.31	10.38	10.54	-20.73	-20.76	31.27	18.0	31.15	17.0
68163	UGC11921	74.3943	-32.8252	301.5774	43.1848	1674	1324	9.9	0.37	141	2.172	/	/	14.32	14.40	/	/	-17.11	/	/	31.51	20.1
68199	AGC620014	40.0996	-51.3433	264.6515	31.9988	1657	1335	5.6	0.44	263	2.458	11.23	11.22	11.67	11.74	11.84	-19.93	-19.90	31.77	22.6	31.64	21.3
68246	UGC11941	86.1876	-21.3780	322.8556	42.9219	6850	6632	4.0	0.26	277	2.448	14.85	14.59	15.27	15.36	15.33	-19.84	-19.81	35.28	113.9	35.32	116.1
68248	UGC11946	96.3140	-8.1398	344.1239	39.0975	5529	5324	5.2	0.64	354	2.655	12.54	12.27	12.81	12.88	12.94	-21.72	-21.82	34.73	88.4	34.82	92.2

PGC	Name	l	b	sgl	sgb	v_{hel}	v_{mod}	t	b/a	w_{mx}	$logw^{i}_{mx}$	I	I*	[3.6]	[3.6]*	$C_{[3.6]}$	M_C	$M_{[3.6]}$	μ_C	d_C	$\mu_{[3.6]}$	$d_{[3.6]}$
68305	ES146-014	328.5879	-46.3885	227.3465	3.0765	1694	1574	6.5	0.20	120	2.079	13.98	14.10	14.98	15.02	14.92	-16.48	-16.20	31.40	19.0	31.22	17.5
68345	AGC035176	24.0012	-55.0989	255.4274	25.5789	2597	2314	5.2	0.20	318	2.502	12.28	11.93	12.40	12.44	12.55	-20.33	-20.33	32.90	38.0	32.80	36.3
68381	UGC011961	94.3649	-11.8376	338.8167	39.8604	4203	3949	3.2	0.26	426	2.636	12.82	12.18	12.50	12.52	12.72	-21.55	-21.64	34.32	73.2	34.24	70.5
68389	IC0005176	322.9963	-43.6854	223.9727	-0.3190	1749	1657	4.5	0.20	360	2.556	11.23	10.82	11.15	11.18	11.37	-20.82	-20.86	32.19	27.5	32.05	25.7
68413	IC001441	91.5464	-15.8795	332.5696	40.9588	5133	4883	2.7	0.55	325	2.581	/	/	13.23	13.31	/	/	-21.10	/	/	34.51	79.9
68429	UGC11967	89.3318	-18.8828	327.7536	41.5804	5036	4772	7.5	0.20	279	2.446	/	/	14.13	14.19	/	/	-19.78	/	/	34.04	64.2
68442	UGC11968	79.5867	-30.2488	308.3954	42.1404	1461	1112	4.0	0.70	379	2.716	11.09	11.15	11.14	11.22	11.56	-22.28	-22.42	33.88	59.6	33.69	54.8
68455	IC5179	6.5024	-55.9274	247.1503	19.2634	3413	3180	4.0	0.48	396	2.646	10.78	10.72	10.78	10.86	11.16	-21.64	-21.73	32.82	36.6	32.61	33.3
68482	UGC11973	94.2916	-12.6145	337.8311	39.6742	4216	3959	3.9	0.28	494	2.703	11.17	10.51	11.33	11.35	11.28	-22.15	-22.29	33.47	49.4	33.69	54.7
68511	NGC007247	29.7947	-55.2533	258.8912	26.7174	2475	2178	3.1	0.56	251	2.473	11.68	11.75	12.08	12.17	12.32	-20.06	-20.04	32.39	30.1	32.22	27.7
68617	UGC11994	90.0771	-19.8016	327.1014	40.5331	4876	4606	4.1	0.20	425	2.628	12.47	11.90	12.51	12.54	12.58	-21.48	-21.56	34.11	66.4	34.18	68.7
68618	IC0005201	350.3262	-54.8463	240.3034	12.7861	915	699	6.1	0.45	182	2.301	10.80	10.92	11.64	11.72	11.68	-18.50	-18.37	30.18	10.8	30.09	10.4
68658	NGC07264	92.1803	-17.4220	331.0413	39.7788	4278	4003	3.1	0.22	527	2.724	12.37	11.71	12.07	12.09	12.27	-22.35	-22.50	34.70	87.0	34.71	87.4
68704	AGC035331	36.0919	-55.4536	262.8161	27.5210	2674	2367	6.7	0.28	158	2.208	14.51	14.55	15.76	15.85	15.55	-17.65	-17.45	33.22	44.1	33.34	46.5
68727	UGC12010	69.7135	-41.5443	291.1523	37.9547	2815	2468	2.0	0.22	201	2.305	/	/	13.80	13.86	/	/	-18.41	/	/	32.27	28.5
68843	UGC12034	95.0715	-14.5547	335.8174	38.2995	4544	4287	3.2	0.35	339	2.551	12.08	11.71	12.57	12.62	12.52	-20.77	-20.80	33.32	46.2	33.47	49.5
68872	PGC068872	57.3275	-49.8360	277.6577	33.1804	7630	7416	5.0	0.20	415	2.618	13.43	12.89	13.46	13.52	13.57	-21.38	-21.46	35.04	102.1	35.13	106.1
68875	E533-028	28.6127	-57.5003	259.0652	24.3825	2578	2283	4.6	0.52	219	2.400	12.47	12.56	13.13	13.22	13.25	-19.40	-19.33	32.67	34.1	32.57	32.6
68942	UGC12045	80.7471	-33.7626	306.0307	38.9642	2899	2557	4.0	0.54	244	2.453	12.46	12.47	13.09	13.18	13.18	-19.89	-19.85	33.09	41.5	33.06	41.0
68977	UGC12054	73.2274	-41.0642	294.3202	37.0170	2081	1724	3.0	0.25	199	2.303	13.60	13.41	14.38	14.43	14.27	-18.52	-18.39	32.81	36.5	32.85	37.1
69161	NGC007307	357.9289	-58.6043	245.9218	14.0466	2089	1853	6.0	0.23	228	2.361	11.89	11.76	12.61	12.68	12.58	-19.04	-18.95	31.62	21.1	31.63	21.2
69253	NGC007314	27.1344	-59.7421	259.1643	22.0140	1427	1123	4.0	0.39	300	2.504	10.10	10.02	10.51	10.58	10.67	-20.35	-20.35	31.01	15.9	30.93	15.3
69284	AGC320265	80.2001	-37.4039	302.4539	36.6249	7101	6857	3.7	0.25	289	2.465	14.73	14.45	14.88	14.96	15.07	-20.00	-19.97	35.17	108.0	35.07	103.4
69327	NGC07331	93.7221	-20.7242	328.0068	37.0625	816	491	3.9	0.44	501	2.739	8.16	7.90	8.37	8.41	8.52	-22.48	-22.64	31.00	15.9	31.05	16.2
69349	NGC07328	77.6185	-40.2713	298.2597	35.7286	2824	2474	2.1	0.47	309	2.534	11.87	11.76	12.23	12.30	12.39	-20.62	-20.64	33.03	40.4	32.97	39.3
69364	UGC12122	87.4629	-29.7271	314.6582	37.2794	1353	1004	4.0	0.28	329	2.525	10.94	10.68	10.92	10.97	11.19	-20.54	-20.56	31.74	22.2	31.53	20.2
69367	UGC12123	88.3884	-28.5766	316.4254	37.2938	4079	3767	6.1	0.21	187	2.273	14.58	14.48	15.53	15.62	15.40	-18.24	-18.09	33.68	54.4	33.77	56.7
69383	UGC12135	113.2684	12.2123	10.5596	24.8330	4063	3951	5.8	0.29	281	2.459	13.69	12.86	13.34	13.33	13.46	-19.93	-19.90	33.42	48.3	33.27	45.0
69404	AGC620157	60.9412	-51.9983	279.6565	30.5382	2915	2574	8.0	0.32	231	2.378	/	/	12.01	12.09	/	/	-19.12	/	/	31.21	17.5
69428	UGC12133	76.4770	-42.0598	296.0991	34.8199	7427	7191	5.8	0.20	443	2.647	13.46	12.81	13.33	13.37	13.46	-21.64	-21.74	35.20	109.8	35.27	113.1
69443	NGC07347	78.6401	-40.2734	299.0059	35.2404	2246	1889	4.4	0.22	253	2.406	12.66	12.42	12.88	12.93	13.04	-19.45	-19.39	32.50	31.6	32.33	29.2
69448	AGC620162	65.4731	-50.0621	283.5254	31.4710	2968	2624	4.0	0.61	208	2.412	12.09	12.19	12.77	12.86	12.89	-19.50	-19.45	32.40	30.2	32.32	29.1
69453	NGC007329	320.9726	-45.7899	225.8652	-2.0262	3252	3174	3.6	0.66	369	2.684	10.72	10.80	11.17	11.26	11.40	-21.98	-22.11	33.41	48.0	33.41	48.2
69472	UGC12160	114.7362	14.4114	12.9974	23.4446	1555	1423	5.8	0.64	235	2.477	12.15	11.42	11.89	11.86	12.01	-20.10	-20.08	32.11	26.4	31.95	24.5
69539	NGC007361	19.3044	-61.5963	256.3346	18.6850	1249	958	4.6	0.24	211	2.328	11.47	11.39	12.39	12.45	12.27	-18.74	-18.63	31.02	16.0	31.08	16.5
69561	UGC12165	94.0288	-22.5621	326.1107	35.9956	6525	6295	4.1	0.20	325	2.512	13.84	13.39	13.69	13.75	13.94	-20.42	-20.43	34.42	76.6	34.27	71.3

PGC	Name	l	b	sgl	sgb	v_{hel}	v_{mod}	t	b/a	w_{mx}	$logw^{i}_{mx}$	I	I^{*}	[3.6]	$[3.6]^{*}$	$C_{[3.6]}$	M_{C}	$M_{[3.6]}$	μ_{C}	d_{C}	$\mu_{[3.6]}$	$d_{[3.6]}$
69605	UGC12173	97.1125	-18.0161	332.6703	35.2229	4774	4512	5.4	0.51	354	2.606	11.84	11.67	12.33	12.40	12.39	-21.28	-21.35	33.71	55.3	33.82	58.0
69650	UGC12178	75.9630	-44.6199	293.9494	32.9464	1930	1568	8.0	0.50	214	2.384	/	/	12.68	12.75	/	/	-19.18	/	/	31.93	24.3
69661	NGC007368	359.8121	-61.1730	248.5706	13.1188	2351	2108	3.1	0.22	358	2.555	11.48	11.13	11.44	11.49	11.67	-20.81	-20.85	32.50	31.6	32.35	29.5
69691	AGC620175	50.5654	-58.1345	271.8683	25.4937	2599	2269	7.1	0.20	179	2.253	/	/	14.92	14.99	/	/	-17.90	/	/	32.92	38.3
69707	IC0005249	321.8832	-47.4628	227.6047	-1.6180	2366	2265	6.9	0.20	217	2.336	13.11	12.94	13.91	13.98	13.81	-18.82	-18.71	32.65	33.8	32.71	34.8
69734	NGC07378	54.6892	-57.2223	274.4077	26.1774	2558	2222	2.2	0.56	223	2.419	11.99	12.05	12.34	12.43	12.61	-19.58	-19.52	32.19	27.4	31.96	24.6
69759	E346-001	358.8559	-61.6504	248.6355	12.4606	2334	2092	5.1	0.20	253	2.403	13.09	12.86	13.28	13.34	13.46	-19.43	-19.36	32.91	38.2	32.72	35.0
69797	UGC12204	99.0332	-16.9080	334.7218	33.9071	6725	6525	4.0	0.22	371	2.572	14.06	13.50	13.91	13.96	14.09	-20.96	-21.01	35.16	107.5	35.11	105.1
69934	UGC12234	96.5484	-23.0596	326.8067	33.6901	6306	6070	4.0	0.54	410	2.679	/	/	11.49	11.59	/	/	-22.06	/	/	33.70	55.0
69994	NGC07410	358.0216	-62.8297	249.3033	11.4047	1740	1492	1.0	0.29	577	2.772	10.50	10.10	9.80	9.83	10.35	-22.79	-22.97	33.15	42.7	32.82	36.7
69998	ES346-014	0.2723	-63.1738	250.2510	11.9531	2693	2450	6.6	0.20	204	2.310	13.90	13.79	14.81	14.88	14.69	-18.58	-18.45	33.29	45.5	33.38	47.3
70009	UGC12249	94.0291	-27.9301	320.3619	33.4457	7551	7343	5.9	0.20	296	2.471	14.73	14.36	15.02	15.10	15.09	-20.05	-20.03	35.24	111.9	35.29	114.0
70025	AGC620200	65.8681	-54.9822	281.7682	26.7900	2859	2514	3.1	0.25	361	2.563	11.22	10.88	11.64	11.69	11.64	-20.88	-20.93	32.53	32.1	32.63	33.6
70026	UGC12252	95.9543	-24.9688	324.4637	33.3381	7136	6922	6.4	0.24	290	2.466	14.66	14.37	15.15	15.23	15.16	-20.00	-19.98	35.26	112.9	35.38	118.9
70027	NGC007412	351.9249	-61.8760	246.8048	9.7097	1710	1476	3.2	0.65	132	2.233	10.60	10.83	11.14	11.24	11.40	-17.88	-17.71	29.29	7.2	28.95	6.2
70070	IC005269B	5.1900	-64.0451	252.4527	12.9074	1666	1402	5.5	0.22	218	2.340	11.89	11.76	12.82	12.88	12.68	-18.85	-18.75	31.53	20.2	31.63	21.2
70075	NGC07418A	4.0200	-63.9430	252.0006	12.6262	2107	1849	6.5	0.50	182	2.314	/	/	14.11	14.20	/	/	-18.49	/	/	32.71	34.8
70102	ES603-031	46.3140	-62.1756	269.4702	21.4996	2267	1941	1.0	0.54	168	2.291	/	/	14.37	14.46	/	/	-18.27	/	/	32.75	35.6
70107	UGC12265	89.4737	-35.5799	310.2240	32.3914	5755	5471	2.3	0.38	198	2.322	/	/	13.93	14.03	/	/	-18.57	/	/	32.62	33.4
70128	IC0005271	10.7928	-64.7656	254.8265	13.9280	1710	1435	3.0	0.39	343	2.562	10.39	10.29	10.87	10.93	10.97	-20.88	-20.92	31.85	23.4	31.85	23.5
70175	UGC12281	85.6434	-41.0049	303.0892	31.1061	2568	2213	7.5	0.20	248	2.394	12.79	12.49	13.40	13.44	13.32	-19.35	-19.28	32.68	34.4	32.74	35.4
70184	IC0005273	1.6417	-64.2376	251.4702	11.6786	1293	1033	5.7	0.67	192	2.404	10.54	10.73	11.23	11.32	11.39	-19.43	-19.37	30.82	14.6	30.69	13.7
70213	NGC7448	87.5659	-39.1242	305.8716	31.2994	2195	1838	5.0	0.45	276	2.481	10.81	10.76	11.36	11.39	11.43	-20.14	-20.13	31.57	20.6	31.51	20.1
70266	UGC12307	85.5336	-42.0055	302.1886	30.4661	2825	2472	9.8	0.25	209	2.325	/	/	14.86	14.89	/	/	-18.60	/	/	33.54	51.0
70271	UGC12308	86.7443	-40.6685	304.0413	30.7323	2237	1879	5.8	0.22	218	2.340	13.30	13.10	14.25	14.31	14.05	-18.85	-18.75	32.93	38.5	33.09	41.4
70291	UGC12316	88.0411	-39.3540	305.9525	30.8711	2371	2016	3.1	0.33	232	2.382	11.91	11.79	12.56	12.63	12.56	-19.23	-19.15	31.80	22.9	31.78	22.7
70301	UGC12320	96.7653	-26.4915	323.2462	31.9957	6624	6389	5.9	0.20	312	2.494	14.37	13.96	14.18	14.25	14.47	-20.26	-20.25	34.81	91.6	34.61	83.4
70304	NGC007456	357.1847	-64.1598	250.1081	10.2716	1198	946	6.0	0.35	221	2.365	10.99	11.01	11.83	11.90	11.81	-19.08	-18.99	30.89	15.1	30.89	15.1
70324	NGC007462	354.4072	-63.7977	249.0599	9.5303	1064	817	3.6	0.22	179	2.255	10.90	10.88	11.92	11.99	11.79	-18.08	-17.92	29.87	9.4	29.91	9.6
70371	AGC035868	22.7213	-66.2293	259.9645	15.2708	1760	1465	9.0	0.43	147	2.203	/	/	15.59	15.68	/	/	-17.41	/	/	33.12	42.0
70433	UGC12350	89.5516	-39.0315	307.1161	30.1856	2135	1778	8.6	0.29	186	2.280	12.69	12.56	13.96	14.02	13.64	-18.31	-18.16	31.95	24.5	32.19	27.4
70460	UGC12355	94.3611	-32.3918	316.0206	30.8977	7720	7510	5.9	0.28	277	2.452	14.52	14.04	14.86	14.92	14.84	-19.87	-19.84	34.79	90.8	34.89	94.9
70558	UGC12388	87.6424	-42.8789	302.6997	28.7379	4594	4272	7.0	0.30	245	2.401	/	/	14.58	14.65	/	/	-19.34	/	/	34.07	65.0
70565	ES469-015	17.3477	-67.3271	258.5692	13.3058	1634	1346	3.5	0.22	207	2.318	12.94	12.84	13.45	13.52	13.54	-18.66	-18.54	32.20	27.5	32.06	25.8
70569	NGC07497	91.3766	-38.3415	308.7607	29.4996	1704	1345	6.2	0.26	264	2.428	11.09	10.69	11.53	11.56	11.48	-19.65	-19.61	31.13	16.9	31.16	17.1
70582	ES407-007	3.2504	-66.5499	253.6327	10.5421	1631	1366	3.1	0.36	260	2.436	12.05	12.00	12.22	12.30	12.52	-19.72	-19.68	32.25	28.2	31.98	24.9

PGC	Name	l	b	sgl	sgb	v_{hel}	v_{mod}	t	b/a	w_{mx}	$logw^{i}_{mx}$	I	I^{*}	[3.6]	$[3.6]^{*}$	$C_{[3.6]}$	M_{C}	$M_{[3.6]}$	μ_{C}	d_{C}	$\mu_{[3.6]}$	$d_{[3.6]}$
70588	NGC007496	347.8353	-63.8011	247.4505	7.1062	1650	1419	3.2	0.63	152	2.283	/	/	11.05	11.15	/	/	-18.19	/	/	29.34	7.4
70664	UGC12410	99.0024	-27.1814	323.5679	29.9018	7095	6877	5.8	0.20	435	2.638	13.90	13.32	13.30	13.35	13.71	-21.57	-21.66	35.39	119.8	35.16	107.4
70697	AGC035947	0.8791	-66.9051	253.2289	9.6225	1569	1308	6.7	0.38	192	2.308	12.66	12.72	13.69	13.77	13.60	-18.57	-18.44	32.17	27.2	32.22	27.7
70702	IC001474	83.3802	-49.3441	295.2536	26.1233	3490	3145	5.8	0.50	255	2.459	12.98	12.90	12.98	13.06	13.35	-19.93	-19.91	33.31	45.9	32.99	39.7
70714	NGC07513	23.9595	-68.2735	261.2961	13.6139	1566	1268	3.2	0.59	223	2.434	10.58	10.68	11.20	11.29	11.34	-19.71	-19.66	31.05	16.2	30.95	15.5
70734	UGC12430	98.4606	-29.1772	321.2687	29.4325	3700	3386	6.5	0.20	226	2.354	13.51	13.20	14.20	14.26	14.08	-18.98	-18.88	33.08	41.4	33.17	43.1
70786	UGC12442	82.7612	-50.6616	293.9737	25.3715	2674	2317	3.6	0.31	308	2.501	12.18	11.94	12.43	12.49	12.58	-20.32	-20.32	32.91	38.2	32.83	36.8
70795	NGC7541	82.8436	-50.6545	294.0232	25.3437	2679	2323	4.7	0.32	422	2.640	10.58	10.25	10.52	10.57	10.78	-21.58	-21.68	32.37	29.7	32.26	28.3
70800	NGC007531	346.4176	-64.4907	247.7454	6.2277	1598	1367	4.0	0.52	324	2.570	10.34	10.37	10.96	11.04	11.06	-20.95	-21.00	32.02	25.3	32.04	25.6
70803	UGC12451	83.6360	-49.9360	294.9649	25.5663	3640	3298	9.8	0.22	172	2.237	14.00	13.88	14.98	15.06	14.82	-17.92	-17.74	32.76	35.6	32.82	36.7
70823	UGC12458	99.6940	-27.5438	323.5006	29.1910	6857	6630	4.1	0.23	396	2.601	14.22	13.75	13.91	13.98	14.23	-21.23	-21.30	35.58	130.9	35.44	122.5
70880	UGC12467	85.1041	-49.0832	296.3828	25.5724	3513	3168	8.0	0.25	198	2.302	13.70	13.53	14.61	14.68	14.45	-18.51	-18.38	32.98	39.5	33.08	41.4
70927	P0070927	85.8334	-48.8335	296.9600	25.4302	3592	3249	5.0	0.64	180	2.359	13.57	13.62	14.41	14.50	14.42	-19.03	-18.94	33.48	49.7	33.48	49.7
70966	AGC035993	6.2431	-68.5490	255.8687	9.8657	2745	2485	5.1	0.56	225	2.427	12.36	12.47	13.06	13.15	13.17	-19.64	-19.59	32.83	36.9	32.77	35.8
70981	UGC12483	89.3371	-45.3372	301.5864	26.1791	4128	3796	3.5	0.64	239	2.484	12.78	12.89	13.26	13.37	13.49	-20.16	-20.15	33.70	54.9	33.57	51.8
70996	NGC07591	85.7656	-49.4436	296.4636	25.0148	4954	4639	3.6	0.50	382	2.637	11.85	11.69	11.85	11.93	12.18	-21.56	-21.65	33.78	56.9	33.63	53.2
71034	UGC12494	86.2011	-49.2790	296.8161	24.9407	4206	3874	6.7	0.30	208	2.330	13.81	13.65	14.60	14.68	14.52	-18.76	-18.65	33.31	45.8	33.36	47.1
71047	NGC7606	69.0994	-61.2842	280.9335	20.3082	2232	1884	3.0	0.41	505	2.734	9.97	9.75	10.30	10.36	10.42	-22.44	-22.59	32.87	37.5	32.98	39.4
71049	UGC12501	89.3188	-45.9620	301.0631	25.7678	3824	3486	3.0	0.27	258	2.419	13.74	13.55	14.09	14.16	14.22	-19.57	-19.52	33.84	58.6	33.74	56.0
71051	IC005309	87.2932	-48.2758	298.1572	25.1601	4182	3850	3.1	0.48	270	2.479	12.59	12.53	13.06	13.15	13.20	-20.12	-20.11	33.35	46.8	33.29	45.6
71052	UGC12497	86.9672	-48.6189	297.7211	25.0676	3779	3439	9.9	0.29	160	2.214	14.06	13.97	14.81	14.89	14.79	-17.71	-17.52	32.51	31.7	32.42	30.5
71055	UGC12500	87.5014	-48.0785	298.4198	25.2017	3531	3187	3.7	0.28	279	2.455	12.86	12.63	13.16	13.22	13.29	-19.90	-19.87	33.21	43.9	33.12	42.1
71066	NGC07599	348.0900	-65.9064	249.3315	6.1298	1688	1452	5.2	0.35	283	2.471	10.39	10.31	10.83	10.90	10.96	-20.05	-20.03	31.01	15.9	30.93	15.3
71087	UGC12511	89.0256	-46.5585	300.4243	25.5122	3557	3214	5.9	0.55	241	2.450	12.52	12.58	13.24	13.34	13.32	-19.86	-19.83	33.20	43.7	33.20	43.6
71102	UGC12519	93.0082	-41.5481	306.7390	26.5564	4382	4058	4.5	0.26	307	2.494	12.69	12.44	13.02	13.09	13.13	-20.25	-20.25	33.41	48.1	33.38	47.5
71155	UGC12535	87.9316	-48.4516	298.3502	24.7356	4217	3886	4.0	0.23	187	2.274	13.98	13.84	14.19	14.27	14.42	-18.26	-18.11	32.70	34.6	32.39	30.1
71159	AGC330260	87.8934	-48.5266	298.2719	24.7009	3889	3551	4.0	0.40	148	2.200	13.79	13.82	14.51	14.61	14.57	-17.58	-17.38	32.16	27.0	31.99	25.0
71171	P0071171	87.4648	-49.0821	297.6203	24.5078	3998	3662	3.0	0.39	204	2.336	13.57	13.44	13.78	13.86	14.01	-18.82	-18.71	32.85	37.1	32.58	32.8
71181	UGC12539	88.0946	-48.4721	298.4175	24.6441	3768	3428	3.1	0.40	366	2.593	11.91	11.71	12.41	12.48	12.45	-21.16	-21.22	33.65	53.6	33.75	56.3
71197	AGC330277	88.7610	-47.8377	299.2597	24.7658	3599	3256	2.9	0.44	169	2.266	/	/	14.77	14.87	/	/	-18.02	/	/	32.92	38.4
71201	AGC330282	89.0527	-47.5449	299.6426	24.8247	3523	3179	4.2	0.72	118	2.222	/	/	14.53	14.64	/	/	-17.59	/	/	32.24	28.0
71220	NGC07640	105.2405	-18.9374	334.7408	27.6627	370	62	5.3	0.23	233	2.370	10.76	10.48	10.93	10.96	11.09	-19.13	-19.04	30.22	11.1	30.01	10.0
71260	UGC12562	91.1053	-45.5502	302.3199	25.1080	3861	3524	7.9	0.27	153	2.193	14.62	14.64	15.63	15.73	15.53	-17.51	-17.31	33.07	41.1	33.06	41.0
71262	UGC12561	89.1748	-47.9949	299.3440	24.4564	3741	3401	7.8	0.32	184	2.279	14.24	14.23	15.20	15.29	15.11	-18.30	-18.15	33.45	48.9	33.49	50.0
71430	IC0005321	53.5442	-68.3584	272.3556	15.1953	2872	2553	1.8	0.59	197	2.379	13.02	13.14	13.59	13.69	13.78	-19.20	-19.12	33.00	39.8	32.84	37.0
71529	AGC330473	89.8910	-49.8401	298.2288	22.8493	3524	3180	4.8	0.67	157	2.316	13.75	13.82	14.28	14.37	14.46	-18.64	-18.52	33.12	42.1	32.92	38.3

PGC	Name	l	b	sgl	sgb	v_{hel}	v_{mod}	t	b/a	w_{mx}	$logw^{i}_{mx}$	I	I^{*}	[3.6]	$[3.6]^{*}$	$C_{[3.6]}$	M_C	$M_{[3.6]}$	μ_C	d_C	$\mu_{[3.6]}$	$d_{[3.6]}$
71597	UGC12631	101.4244	-32.3623	319.3766	25.7157	9183	9041	3.0	0.34	451	2.672	13.19	12.86	13.38	13.47	13.53	-21.88	-21.99	35.52	127.2	35.65	135.0
71619	UGC12639	102.8429	-29.4712	322.8563	25.8678	4548	4255	3.2	0.65	132	2.231	/	/	13.44	13.53	/	/	-17.68	/	/	31.21	17.5
71636	UGC12641	98.4670	-38.7652	311.9019	24.6936	2696	2351	4.0	0.28	173	2.247	14.01	13.91	14.77	14.84	14.73	-18.01	-17.84	32.75	35.5	32.70	34.6
71688	UGC12650	104.0752	-27.5254	325.3177	25.6567	5099	4825	5.8	0.23	309	2.493	13.48	13.08	13.58	13.63	13.72	-20.25	-20.24	34.02	63.6	33.94	61.5
71728	NGC007694	82.1431	-59.2365	287.9534	18.8449	2280	1926	/	0.53	138	2.203	12.18	12.33	13.20	13.30	13.17	-17.60	-17.40	30.77	14.3	30.71	13.8
71729	NGC007689	325.6333	-59.4532	239.7954	-1.2722	1971	1801	5.9	0.64	239	2.486	10.82	10.97	11.49	11.58	11.64	-20.19	-20.18	31.83	23.2	31.76	22.5
71753	UGC12667	103.5651	-29.8760	322.7342	25.1293	3812	3504	5.8	0.64	225	2.456	12.30	12.34	12.82	12.92	12.99	-19.91	-19.88	32.92	38.4	32.82	36.7
71754	P0071754	108.8653	-15.5674	339.4502	25.3018	4809	4573	3.6	0.41	240	2.411	13.61	13.42	13.74	13.81	13.98	-19.50	-19.44	33.52	50.5	33.29	45.6
71784	AGC630216	80.5103	-60.9102	286.2251	17.9644	2214	1861	3.7	0.37	329	2.540	11.82	11.67	12.60	12.66	12.52	-20.68	-20.70	33.22	44.1	33.40	48.0
71795	UGC12678	102.2860	-33.4705	318.6409	24.5720	8963	8810	3.0	0.24	505	2.707	13.39	12.84	13.61	13.68	13.62	-22.19	-22.33	35.96	155.6	36.26	178.4
71804	UGC12681	98.4927	-41.1405	309.7094	23.4151	1479	1120	4.2	0.50	129	2.164	13.91	14.02	14.97	15.06	14.89	-17.25	-17.03	32.15	27.0	32.10	26.2
71838	UGC12692	99.8254	-39.1612	312.1297	23.5849	2194	1844	5.9	0.26	225	2.359	13.39	13.22	13.65	13.71	13.83	-19.03	-18.93	32.88	37.6	32.66	34.0
71839	UGC12693	104.8891	-27.8201	325.3238	24.8780	4971	4694	5.9	0.20	220	2.342	14.51	14.26	15.39	15.46	15.21	-18.88	-18.77	34.14	67.3	34.32	73.3
71866	NGC007713	353.8020	-70.8770	254.6550	5.1268	692	431	6.7	0.46	178	2.293	10.48	10.59	11.44	11.47	11.39	-18.43	-18.29	29.82	9.2	29.76	8.9
71880	UGC12701	103.3497	-32.0680	320.4564	24.3804	8858	8704	5.9	0.26	358	2.561	14.42	14.01	14.21	14.30	14.52	-20.86	-20.90	35.50	126.0	35.36	118.0
71881	ES347-029	351.5310	-70.4872	253.8987	4.7414	1568	1315	7.9	0.41	199	2.331	12.61	12.68	13.85	13.93	13.65	-18.77	-18.65	32.43	30.6	32.60	33.2
71895	UGC12707	98.7285	-41.8162	309.1933	22.9027	2610	2261	3.9	0.54	178	2.315	13.10	13.17	14.12	14.21	14.04	-18.62	-18.50	32.68	34.3	32.73	35.2
71948	ES240-011	332.9523	-64.8836	245.8645	0.7823	2839	2645	4.9	0.20	551	2.741	10.97	10.37	11.01	11.03	11.06	-22.50	-22.67	33.60	52.4	33.75	56.3
72001	AGC630233	79.7095	-63.1211	284.5981	16.3481	2016	1665	4.9	0.31	302	2.494	10.65	10.49	11.15	11.16	11.19	-20.25	-20.25	31.44	19.4	31.41	19.2
72006	PG0072006	80.7361	-62.5091	285.3614	16.5904	2048	1696	9.0	0.46	140	2.189	/	/	15.06	15.16	/	/	-17.27	/	/	32.44	30.8
72009	NGC07723	69.2380	-67.9058	278.3083	14.1787	1860	1520	3.1	0.68	314	2.624	10.17	10.28	10.73	10.82	10.91	-21.44	-21.53	32.36	29.7	32.36	29.6
72024	UGC12721	103.7122	-33.0460	319.6315	23.6859	7611	7404	3.0	0.44	394	2.634	12.93	12.73	13.30	13.39	13.42	-21.53	-21.62	35.04	102.0	35.16	107.5
72115	AGC330768	103.6225	-34.6751	317.9977	23.0455	9409	9276	4.5	0.49	425	2.680	13.06	12.96	12.64	12.76	13.24	-21.95	-22.07	35.29	114.5	34.96	98.3
72169	AGC330778	104.5956	-33.0694	319.9503	23.0054	7409	7196	3.0	0.29	377	2.587	13.78	13.43	13.60	13.67	13.92	-21.10	-21.16	35.13	105.9	34.97	98.5
72233	UGC12755	105.3271	-32.2108	321.0753	22.7985	8794	8640	3.1	0.54	503	2.767	12.45	12.24	12.92	13.02	12.99	-22.74	-22.91	35.87	149.1	36.17	171.7
72237	UGC12754	104.5092	-34.3688	318.6408	22.5201	750	403	5.9	0.68	183	2.388	10.48	10.58	11.50	11.53	11.41	-19.29	-19.22	30.70	13.8	30.75	14.1
72252	AGC630257	82.5618	-63.6377	285.3774	15.1916	2114	1765	5.0	0.51	155	2.248	12.69	12.85	13.67	13.77	13.66	-18.01	-17.85	31.68	21.7	31.62	21.1
72325	UGC12769	88.6497	-59.6700	290.3201	16.3898	2083	1728	8.0	0.42	126	2.134	/	/	15.97	16.07	/	/	-16.73	/	/	32.82	36.7
72367	UGC12777	93.6208	-55.3404	295.5117	17.4769	2927	2578	5.5	0.49	218	2.388	11.94	11.97	12.48	12.57	12.63	-19.29	-19.21	31.92	24.3	31.79	22.8
72411	AGC330918	106.2357	-32.3938	321.2277	22.0217	9034	8892	4.2	0.45	367	2.605	13.23	13.08	13.59	13.71	13.75	-21.26	-21.34	35.12	105.5	35.19	109.2
72438	P0072438	105.9789	-33.3383	320.2017	21.8402	9295	9162	5.0	0.31	398	2.613	13.66	13.34	13.60	13.69	13.89	-21.33	-21.41	35.33	116.3	35.26	112.6
72443	ES149-001	319.2566	-57.9933	237.9088	-4.3589	1905	1753	8.0	0.23	187	2.275	/	/	13.41	13.48	/	/	-18.11	/	/	31.60	20.8
72491	NGC007757	94.7422	-55.2328	296.0327	17.0623	2952	2604	5.3	0.69	139	2.272	12.10	12.28	12.66	12.76	12.89	-18.23	-18.08	31.12	16.7	30.84	14.7
72506	UGC12792	106.0898	-34.0341	319.5583	21.4727	11531	11515	3.1	0.47	421	2.670	13.05	12.88	13.37	13.50	13.55	-21.85	-21.97	35.53	127.5	35.65	135.1
72599	UGC12807	109.3835	-25.4947	329.2377	21.9386	12343	12402	7.6	0.20	379	2.579	15.11	14.59	15.07	15.16	15.24	-21.03	-21.08	36.45	195.0	36.51	200.8
72632	UGC12814	112.9122	-12.6208	343.5875	22.1796	5794	5603	6.0	0.20	347	2.540	13.97	13.37	13.90	13.93	14.02	-20.68	-20.70	34.77	90.1	34.76	89.4

PGC	Name	l	b	sgl	sgb	v_{hel}	v_{mod}	t	b/a	w_{mx}	$\log w^i_{mx}$	I	I*	[3.6]	[3.6]*	$C_{[3.6]}$	M_C	$M_{[3.6]}$	μ_C	d_C	$\mu_{[3.6]}$	$d_{[3.6]}$
72633	AGC330965	105.9524	-36.2244	317.3730	20.6652	9959	9854	4.2	0.71	229	2.506	14.29	14.39	14.76	14.91	15.02	-20.37	-20.37	35.50	126.1	35.45	123.2
72734	PG0072734	121.8483	23.2789	22.4519	16.7280	5818	5835	6.2	0.21	300	2.478	/	/	14.86	14.90	/	/	-20.10	/	/	35.14	106.7
72784	AGC330996	107.5301	-33.7236	320.3750	20.5006	7967	7778	3.0	0.48	344	2.584	13.81	13.74	14.19	14.30	14.38	-21.07	-21.13	35.58	130.7	35.62	132.9
72957	ES012-010	305.3777	-35.2980	214.8380	-13.4242	1941	1943	7.7	0.64	211	2.432	13.17	13.15	13.78	13.85	13.86	-19.69	-19.65	33.59	52.3	33.55	51.2
72968	AGC331021	108.1786	-34.0942	320.2338	19.8608	7906	7715	4.0	0.27	321	2.514	14.30	14.04	14.76	14.86	14.81	-20.44	-20.45	35.36	117.9	35.48	124.8
72983	UGC12857	95.9604	-58.6262	293.7712	14.3756	2456	2105	4.0	0.22	233	2.370	12.58	12.42	12.99	13.05	13.09	-19.12	-19.04	32.23	27.9	32.10	26.2
73049	NGC007793	4.5157	-77.1712	261.3011	3.1214	227	0	7.4	0.65	162	2.320	8.40	8.60	9.23	9.27	9.29	-18.67	-18.55	27.96	3.9	27.82	3.7
75289	AGC150063	195.2978	-17.7214	337.0971	-56.6963	8198	8376	4.8	0.21	352	2.547	14.69	14.06	14.42	14.47	14.63	-20.74	-20.77	35.49	125.6	35.42	121.1
79913	PG0079913	235.1633	9.5107	116.1994	-72.3673	6560	6942	5.4	0.20	426	2.629	/	/	13.05	13.10	/	/	-21.57	/	/	34.79	91.0
85512	P0085512	102.7082	-33.5380	318.7466	24.2267	8036	7844	4.7	0.55	234	2.439	/	/	15.76	15.88	/	/	-19.71	/	/	35.79	144.2
85551	P0085551	103.2945	-33.2898	319.2262	23.8960	8743	8582	1.9	0.47	338	2.574	14.48	14.37	14.35	14.47	14.79	-20.99	-21.04	35.93	153.2	35.70	137.9
85610	P0085610	103.6305	-33.3087	319.3405	23.6347	8004	7812	2.3	0.71	171	2.376	15.33	15.45	15.79	15.93	16.06	-19.19	-19.10	35.35	117.6	35.18	108.7
86266	P0086266	166.8226	-15.4697	345.7623	-30.0246	4662	4613	4.2	0.66	233	2.483	/	/	13.68	13.65	/	/	-20.14	/	/	33.85	59.0
86269	P0086269	172.7348	-11.4149	350.4657	-35.8503	3389	3358	3.2	0.66	333	2.638	/	/	11.68	11.61	/	/	-21.66	/	/	33.31	45.8
86285	P0086285	206.3955	-5.7400	0.4608	-69.1349	2902	3029	3.2	0.46	538	2.774	11.20	9.99	10.34	10.26	10.49	-22.80	-22.98	33.32	46.1	33.28	45.3
86290	P0086290	40.4707	7.9917	165.8634	82.9536	3385	3275	5.0	0.32	274	2.452	/	/	13.56	13.58	/	/	-19.84	/	/	33.47	49.5
86633	PG0086633	232.4206	70.6041	91.7194	-13.0005	3759	4134	4.8	0.40	284	2.482	/	/	14.63	14.72	/	/	-20.14	/	/	34.99	99.4
89942	PG0089942	137.5050	6.3526	6.3290	0.5646	3168	3077	5.0	0.26	325	2.518	/	/	11.73	11.60	/	/	-20.49	/	/	32.10	26.2
90023	P0090023	204.3876	-14.8652	337.4070	-65.8737	4317	4417	2.0	0.66	301	2.594	/	/	12.58	12.63	/	/	-21.23	/	/	33.93	61.0
90392	P0090392	88.7312	-6.6350	343.3010	46.7425	4078	3840	5.0	0.31	265	2.436	/	/	12.56	12.51	/	/	-19.69	/	/	32.21	27.7
90402	P0090402	110.4855	13.3220	11.7536	27.5625	2526	2389	5.0	0.51	269	2.486	/	/	11.62	11.50	/	/	-20.18	/	/	31.68	21.7
90453	AGC101097	112.6246	-28.9805	326.6992	18.0961	4954	4687	5.9	0.20	170	2.230	15.68	15.61	16.49	16.58	16.45	-17.86	-17.68	34.37	74.9	34.35	74.0
90540	PG0090540	140.0527	-63.7343	296.4380	-6.8519	2224	1924	7.9	0.20	116	2.064	/	/	16.84	16.94	/	/	-16.05	/	/	33.03	40.3
90548	PG0090548	128.7055	-11.3176	347.7022	7.1933	6039	5901	6.2	0.34	233	2.385	/	/	15.79	15.84	/	/	-19.19	/	/	35.18	108.4
90553	PG0090553	144.6848	-58.9656	301.1978	-9.1817	2607	2321	7.6	0.20	151	2.179	/	/	16.31	16.39	/	/	-17.17	/	/	33.62	52.9
90564	AGC110840	136.2487	-27.5502	332.4910	-1.9295	5778	5596	6.3	0.20	197	2.294	15.43	15.29	16.12	16.22	16.11	-18.44	-18.30	34.62	84.1	34.63	84.2
90591	AGC121120	141.0323	-26.4331	333.9844	-6.0764	11721	11823	6.2	0.20	352	2.547	/	/	14.98	15.07	/	/	-20.76	/	/	36.06	163.0
90592	AGC121109	140.1581	-23.6986	336.6632	-5.0781	7667	7575	6.2	0.20	226	2.354	/	/	15.91	16.01	/	/	-18.88	/	/	35.03	101.4
90595	PG0090595	138.8962	-19.6194	340.6339	-3.5487	5828	5684	6.2	0.28	321	2.515	/	/	15.23	15.31	/	/	-20.46	/	/	35.98	157.3
90653	AGC121048	156.4742	-28.4394	332.0075	-19.7834	6786	6703	6.2	0.20	242	2.384	/	/	15.08	15.13	/	/	-19.17	/	/	34.40	75.9
90694	PG0090694	205.1601	-47.3320	291.1634	-44.7966	1686	1575	7.9	0.20	131	2.117	/	/	15.21	15.30	/	/	-16.57	/	/	31.87	23.7
90695	AGC130398	173.1980	-28.9533	329.0894	-34.2199	6379	6344	6.2	0.20	269	2.430	15.38	14.47	14.84	14.83	15.02	-19.67	-19.62	34.77	90.1	34.56	81.8
90717	AGC140146	194.2565	-29.3804	319.4508	-51.2086	10072	10274	6.7	0.20	316	2.500	/	/	15.31	15.40	/	/	-20.31	/	/	35.92	153.0
90726	AGC140148	197.4670	-26.5592	321.1597	-55.0748	8486	8638	6.7	0.20	356	2.551	/	/	14.41	14.48	/	/	-20.81	/	/	35.46	123.5
90737	PG0090737	200.5778	-19.5049	330.6182	-60.8164	4351	4413	6.2	0.20	235	2.371	/	/	15.58	15.63	/	/	-19.05	/	/	34.80	91.1
90751	PG0090751	147.0954	22.0668	23.1545	-6.5600	4296	4345	7.9	0.20	188	2.274	/	/	16.66	16.73	/	/	-18.10	/	/	34.96	98.3

PGC	Name	l	b	sgl	sgb	v_{hel}	v_{mod}	t	b/a	w_{mx}	$logw^i_{mx}$	I	I^*	[3.6]	$[3.6]^*$	$C_{[3.6]}$	M_C	$M_{[3.6]}$	μ_C	d_C	$\mu_{[3.6]}$	$d_{[3.6]}$
90766	PG0090766	147.3165	25.2443	26.3400	-6.2194	5315	5407	5.6	0.20	208	2.318	/	/	16.29	16.38	/	/	-18.53	/	/	35.05	102.3
90771	AGC170342	193.3573	14.4005	31.7723	-50.4090	6599	6867	5.6	0.38	161	2.232	/	/	16.62	16.74	/	/	-17.69	/	/	34.53	80.6
90775	AGC170343	184.9992	19.2657	32.4630	-41.0613	7313	7595	6.2	0.20	239	2.378	15.38	15.12	15.86	15.95	15.89	-19.20	-19.12	35.20	109.7	35.23	110.9
90776	AGC170355	187.6639	18.3219	32.9334	-43.7321	3287	3460	6.7	0.20	170	2.230	/	/	16.39	16.47	/	/	-17.68	/	/	34.23	70.2
90778	AGC170344	195.2194	15.5180	34.7509	-51.3871	9642	10055	4.8	0.33	431	2.651	/	/	13.94	14.04	/	/	-21.78	/	/	36.05	162.0
90783	AGC170345	190.5213	20.1206	37.0188	-45.1496	6475	6752	5.6	0.24	204	2.314	/	/	16.18	16.28	/	/	-18.49	/	/	34.90	95.4
90784	AGC170357	198.7274	18.1338	41.3680	-52.6275	8662	9052	6.7	0.56	310	2.564	/	/	15.16	15.28	/	/	-20.94	/	/	36.49	198.6
90789	AGC170346	187.3435	23.2287	38.4619	-40.9941	8134	8476	5.6	0.24	355	2.554	14.57	14.20	14.22	14.30	14.63	-20.80	-20.84	35.55	128.8	35.30	114.8
90795	AGC170358	191.7501	24.2458	42.6840	-43.7477	6853	7165	6.2	0.23	205	2.314	15.77	15.66	17.06	17.16	16.76	-18.62	-18.50	35.50	125.8	35.87	149.0
90796	AGC170376	183.6671	26.6260	39.9081	-36.3705	8544	8904	5.6	0.21	348	2.543	14.55	14.13	14.68	14.76	14.81	-20.70	-20.73	35.63	133.6	35.68	136.6
90800	AGC170377	196.8507	23.6400	46.2180	-47.7510	13676	14379	5.6	0.20	509	2.707	14.43	13.79	14.08	14.18	14.35	-22.19	-22.33	36.74	223.3	36.81	230.2
90801	PG0090801	180.2240	28.3892	39.8577	-32.8447	3877	4075	6.7	0.20	157	2.196	/	/	16.47	16.56	/	/	-17.34	/	/	33.97	62.3
90803	AGC170350	187.9046	26.7216	42.6425	-39.4845	5311	5568	5.6	0.20	215	2.332	14.97	14.75	15.72	15.80	15.63	-18.79	-18.67	34.48	78.8	34.58	82.3
90806	AGC170359	183.9461	27.8399	41.3462	-35.9383	6065	6334	5.6	0.21	204	2.310	15.62	15.47	16.54	16.64	16.40	-18.58	-18.46	35.08	103.9	35.25	112.0
90811	PG0090811	184.9012	28.1325	42.2190	-36.4871	4153	4374	6.7	0.25	190	2.284	/	/	16.17	16.26	/	/	-18.20	/	/	34.56	81.7
90815	PG0090815	212.9715	19.3105	61.3370	-60.7082	2549	2807	6.7	0.26	159	2.208	/	/	16.50	16.59	/	/	-17.45	/	/	34.12	66.7
90817	AGC180619	184.9967	29.5995	43.7839	-35.7382	5587	5852	6.7	0.21	191	2.282	/	/	16.73	16.82	/	/	-18.18	/	/	35.14	106.9
90831	AGC180597	201.9617	26.9811	54.6758	-48.6009	11291	11868	6.6	0.20	386	2.587	15.31	14.82	15.02	15.11	15.34	-21.10	-21.16	36.63	211.8	36.54	203.1
90844	AGC180602	201.8658	29.8145	57.2307	-46.3526	4703	5005	5.4	0.20	227	2.356	14.12	13.90	14.60	14.67	14.65	-19.00	-18.90	33.68	54.6	33.63	53.2
90927	PG0090927	248.8651	25.3578	122.5764	-52.0499	4625	5024	5.6	0.20	224	2.350	/	/	15.74	15.81	/	/	-18.85	/	/	34.78	90.2
90941	PG0090941	249.1564	29.1122	119.5110	-48.8317	2352	2714	6.7	0.22	163	2.214	/	/	15.35	15.43	/	/	-17.52	/	/	32.97	39.3
91580	AGC270321	29.0679	27.2113	127.6838	62.8161	10625	10923	5.6	0.20	507	2.705	/	/	13.97	14.03	/	/	-22.31	/	/	36.62	211.2
91586	AGC270322	28.1236	24.5659	133.2499	64.0529	6320	6415	5.6	0.32	231	2.378	/	/	15.57	15.65	/	/	-19.12	/	/	34.90	95.5
91594	AGC270323	36.1728	24.6941	119.0889	68.7218	9057	9237	6.2	0.21	230	2.363	/	/	16.25	16.34	/	/	-18.97	/	/	35.48	124.8
91621	AGC280104	43.2744	16.8856	110.4137	78.7007	6547	6559	6.2	0.20	329	2.517	/	/	13.84	13.89	/	/	-20.48	/	/	34.46	78.1
91630	AGC280105	53.4177	16.4543	60.2160	78.2633	5302	5248	6.2	0.23	175	2.246	/	/	16.02	16.10	/	/	-17.83	/	/	34.00	63.2
91643	PG0091643	72.3212	16.7092	25.2057	63.4773	4889	4796	5.6	0.23	235	2.374	/	/	15.56	15.63	/	/	-19.08	/	/	34.83	92.6
91656	PG0091656	85.7269	16.1884	18.0493	51.1857	3750	3624	5.6	0.23	206	2.317	/	/	14.07	14.13	/	/	-18.52	/	/	32.67	34.1
91661	PG0091661	95.8447	19.5746	20.5357	41.1263	5579	5522	6.2	0.23	292	2.468	/	/	14.83	14.90	/	/	-20.00	/	/	35.04	101.7
91705	AGC310299	69.7711	-21.6539	307.5148	54.4346	5376	5119	6.7	0.25	212	2.331	/	/	15.86	15.94	/	/	-18.66	/	/	34.72	88.0
91731	AGC320524	81.2011	-26.8104	313.1585	43.4112	7209	6988	5.6	0.20	241	2.382	/	/	15.42	15.50	/	/	-19.16	/	/	34.78	90.4
91742	PG0091742	112.8577	12.3702	10.7238	25.2377	2600	2464	8.0	0.31	277	2.456	/	/	13.86	13.81	/	/	-19.88	/	/	33.74	56.0
91747	AGC320540	93.7370	-21.7141	326.9027	36.6160	6583	6358	6.5	0.20	230	2.362	15.20	14.94	15.70	15.78	15.72	-19.05	-18.96	34.85	93.5	34.87	94.0
91755	PG0091755	115.3911	14.7352	13.3581	22.8149	1554	1426	7.9	0.22	115	2.063	/	/	15.10	15.14	/	/	-16.04	/	/	31.17	17.2
91777	PG0091777	101.2703	-19.7397	332.4499	30.9319	5075	4819	5.6	0.51	211	2.381	/	/	15.02	15.10	/	/	-19.15	/	/	34.33	73.5
91787	AGC331184	101.0005	-24.3943	327.3461	29.4263	5215	4949	6.7	0.42	186	2.303	/	/	15.95	16.05	/	/	-18.38	/	/	34.53	80.7

PGC	Name	l	b	sgl	sgb	v_{hel}	v_{mod}	t	b/a	w_{mx}	$logw^{i}_{mx}$	I	I^{*}	[3.6]	$[3.6]^{*}$	$C_{[3.6]}$	M_{C}	$M_{[3.6]}$	μ_{C}	d_{C}	$\mu_{[3.6]}$	$d_{[3.6]}$
91814	AGC331095	104.8941	-32.4017	320.7237	23.0545	7166	6946	5.8	0.20	239	2.379	14.48	14.16	14.83	14.91	14.89	-19.21	-19.12	34.15	67.6	34.11	66.4
92378	PG0092378	305.4105	26.3650	152.2162	-7.7963	5917	6308	5.6	0.20	179	2.253	/	/	16.25	16.35	/	/	-17.90	/	/	34.34	73.7
93031	AGC331412	88.1675	-49.1344	297.9364	24.1453	3476	3131	5.0	0.20	139	2.143	15.54	15.48	16.39	16.47	16.33	-17.07	-16.83	33.43	48.5	33.34	46.5
93038	AGC111414	127.1261	-29.2062	329.6929	5.7722	11281	11306	5.9	0.20	266	2.425	16.24	15.94	17.21	17.32	16.98	-19.63	-19.58	36.82	231.5	37.26	283.2
97023	PG0097023	156.5597	-10.6228	350.9615	-19.9618	5596	5551	4.6	0.45	226	2.394	/	/	13.00	12.99	/	/	-19.28	/	/	32.27	28.5
97032	PG0097032	154.8363	-4.5206	357.2666	-17.8225	4471	4418	3.8	0.41	286	2.487	/	/	12.93	12.86	/	/	-20.19	/	/	33.08	41.3
97067	AGC140130	153.7948	8.3948	10.5016	-15.1862	4378	4383	3.8	0.36	266	2.446	/	/	13.19	13.13	/	/	-19.78	/	/	32.94	38.8
97081	P0097081	183.0480	-10.6915	351.1414	-45.9847	5584	5652	4.6	0.66	209	2.435	/	/	13.40	13.39	/	/	-19.68	/	/	33.11	41.8
97109	P0097109	160.6087	10.7270	14.1538	-21.3966	5991	6080	4.6	0.69	118	2.203	/	/	13.15	13.23	/	/	-17.41	/	/	30.64	13.4
97136	P0097136	196.1165	-6.4126	358.0570	-58.9440	3496	3590	3.8	0.43	286	2.492	/	/	13.45	13.48	/	/	-20.23	/	/	33.77	56.7
97187	P0097187	185.7905	13.2472	25.4846	-44.3052	5208	5395	3.8	0.39	344	2.564	/	/	13.77	13.85	/	/	-20.93	/	/	34.90	95.6
100768	P0100768	184.6150	-23.4928	332.6465	-45.4951	4369	4349	5.0	0.34	295	2.488	/	/	13.24	13.22	/	/	-20.19	/	/	33.45	49.0
142820	P0142820	202.4506	29.4515	57.4875	-46.9519	5092	5405	5.0	0.29	190	2.289	14.90	14.85	15.80	15.90	15.73	-18.39	-18.25	34.17	68.2	34.23	70.1
155511	P0155511	268.7063	28.3644	136.8443	-37.1849	3876	4271	3.4	0.38	209	2.345	/	/	15.50	15.59	/	/	-18.80	/	/	34.49	79.1
165356	PG0165356	135.8526	8.1351	7.9253	2.3860	3164	3076	5.0	0.52	264	2.481	/	/	12.51	12.41	/	/	-20.13	/	/	32.55	32.3
165788	P0165788	51.0923	7.0218	10.9604	86.2370	5101	4994	5.0	0.56	348	2.614	/	/	12.78	12.79	/	/	-21.43	/	/	34.30	72.6
166472	P0166472	134.9564	13.1972	12.8786	3.7776	4302	4260	5.0	0.65	234	2.480	/	/	13.83	13.84	/	/	-20.11	/	/	34.03	63.8
166559	P0166559	51.8668	11.1056	47.4319	83.4695	4428	4325	5.0	0.38	282	2.475	/	/	14.16	14.21	/	/	-20.07	/	/	34.37	74.8
166628	P0166628	40.3702	-10.1956	247.0658	72.0733	5893	5753	3.8	0.71	83	2.063	/	/	13.59	13.65	/	/	-16.04	/	/	29.68	8.6
166755	PG0166755	114.1865	14.9675	13.5995	23.9814	2453	2332	5.0	0.48	275	2.487	/	/	12.34	12.29	/	/	-20.19	/	/	32.49	31.5
166758	P0166758	110.8214	8.8628	6.7439	27.1226	4354	4225	5.0	0.45	396	2.638	/	/	12.19	12.14	/	/	-21.66	/	/	33.86	59.2
166785	P0166785	118.5547	7.5976	5.8553	19.4084	4645	4533	5.0	0.24	316	2.504	/	/	13.72	13.67	/	/	-20.35	/	/	34.09	65.8
169662	AGC330925	106.1253	-33.1704	320.4205	21.7960	8307	8131	3.3	0.26	355	2.557	14.46	14.12	14.76	14.85	14.84	-20.82	-20.86	35.81	145.0	35.92	152.7
906205	P0906205	246.1023	22.7733	121.6248	-55.6174	4810	5203	2.3	0.30	297	2.484	/	/	13.89	13.96	/	/	-20.16	/	/	34.20	69.2
1059326	PG1059326	338.8609	52.5643	126.4886	17.9840	2740	3023	3.6	0.44	199	2.337	/	/	15.28	15.37	/	/	-18.71	/	/	34.16	68.0
1210567	AGC121506	168.7141	-51.1898	305.9313	-24.1931	6022	5880	1.6	0.35	193	2.305	/	/	14.98	15.09	/	/	-18.41	/	/	33.55	51.2
1809186	AGC331322	105.3831	-33.1355	320.1819	22.3778	9200	9063	3.0	0.35	281	2.469	14.42	14.25	14.80	14.91	14.94	-20.03	-20.01	35.07	103.2	35.06	102.7

TABLE C.1: Distance measurements for 1935 galaxies observed with Spitzer for which we have all the parameters requested (in particular W_{mx}, b/a, [3.6] and, for 1511 galaxies, I) to compute an estimate (Complete table online): (1) Principal Galaxy Catalog number, (2) Common name, (3) galactic longitude, degrees, (4) galactic latitude, degrees, (5) supergalactic longitude, degrees, (6) supergalactic latitude, degrees, (7) heliocentric velocities, km s^{-1}, (8) velocity with respect to the cosmic microwave background modified for the cosmology, km s^{-1}, (9) numerical morphological type, (10) axial ratio, (11) HI linewidth, km s^{-1}, (12) logarithm of the de-projected HI linewidth, km s^{-1}, (13) I band magnitude, mag (Vega system), (14) $I^{b,i,k}$, I band magnitude corrected for extinctions and k-corrected, mag (AB system), (15) [3.6] band magnitude, mag (AB system), (16) $[3.6]^{b,i,k,a}$, extinctions, aperture and k-corrected [3.6] band magnitude, mag (AB system), (17) pseudo apparent magnitude at [3.6], mag, (18) pseudo absolute magnitude at [3.6], mag, (19) apparent magnitude at [3.6], mag, (20) absolute magnitude at [3.6], mag, (21) distance modulus corrected for the selection bias obtained with the color adjusted TF relation, mag, (22) selection bias corrected distance estimates obtained with the color adjusted TFR, Mpc, (23) distance modulus corrected for the selection bias obtained with the TFR, mag, (24) selection bias corrected distance estimates obtained with the TFR, Mpc .

Appendix D

Abbreviations and Acronyms

2LPT	**Second** Order **L**agrangian **P**erturbation **T**heory
2MASS	**Two** **M**icron **A**ll **S**ky **S**urvey
ΛCDM	**Lambda** **C**old **D**ark **M**atter
A1	**A**bell **1**367
A2	**A**bell **2**634/66
A4	**A**bell **4**00
ART	**A**daptive **R**efinement **T**ree
An	**An**tlia
BC	**B**olometric **C**orrection
BFJR	**B**aryonic **F**aber-**J**ackson **R**elation
BTFR	**B**aryonic **T**ully-**F**isher **R**elation
Ca	**Ca**ncer
Calib	**Calib**rator subsample
Co	**Co**ma
Ce	**Ce**ntaurus
CDM	**C**old **D**ark **M**atter
CHP	**C**arnegie **H**ubble **P**rogram
CIC	**C**loud **I**n **C**ell
CLUES	**C**onstrained **L**ocal **U**niversE **S**imulations
CFS	**C**osmic**f**lows with **S**pitzer
CF2	**C**osmic**f**lows-**2**
CMB	**C**osmic **M**icrowave **B**ackground
CR	**C**onstrained **R**ealization
DTFR	**D**irect **T**ully-**F**isher **R**elation
EDD	**E**xtragalactic **D**istance **D**atabase
F	**F**ornax
FG	**F**lat **G**alaxies
FJR	**F**aber-**J**ackson **R**elation
FP	**F**undamental **P**lane
FWHM	**F**ull **W**idth at **H**alf **M**aximum
GADGET	**GA**laxies with **D**ark matter and **G**as int**E**rac**T**
HDM	**H**ot **D**ark **M**atter

H	**H**ydra
HSB	**H**igh **S**urface **B**rightness
ICeCoRe	**I**nitial **C**onditions & **C**onstrained **R**ealizations
IRAC	**I**nfra**R**ed **A**rray **C**amera
ITFR	**I**nverse **T**ully-**F**isher **R**elation
ISB	**I**ntermediate **S**urface **B**rightness
LMC	**L**arge **M**agellanic **C**loud
LPT	**L**agrangian **P**erturbation **T**heory
LSB	**L**ow **S**urface **B**rightness
LVL	**L**ocal **V**olume **L**arge galaxy survey
M	**M**iscellaneous
mag	**mag**nitude
Mpc	**M**ega**p**arse**c**
NGP	**N**earest **G**rid **P**oint
pc	**p**arse**c**
Pe	**Pe**gasus
Pi	**Pi**sces
PL, P	cepheid **P**eriod **L**uminosity
PSCz	**P**oint **S**ource **C**olor **redshift** survey
RC3	**Third R**eference **C**atalog
RR	**R**andom **R**ealization
RZA	**R**everse **Z**el'dovich **A**pproximation
SBF, S	**S**urface **B**rightness **F**luctuation
SDSS	**S**loan **D**igital **S**ky **S**urvey
SINGS	**S**pitzer **I**nfrared **N**earby **G**alaxies **S**urvey
SNIa, SN	**S**uper**N**ovae of type **Ia**
SNIa-H	**S**uper**N**ovae of type **Ia** **H**ost subsample
SPH	**S**mooth **P**article **H**ydrodynamics
S^4G	**S**pitzer **S**urvey of **S**tellar **S**tructures in **G**alaxies
SB	**S**urface **B**rigthness
SEE	**S**tandard **E**rror of the **E**stimate
SGL,B,X,Y,Z	**S**uper**g**alactic **L**ongitude, Latitude (**B**), **X**, **Y**, **Z** coordinates
sr	**s**te**r**adian
TC12	**T**ully & **C**ourtois 20**12**
TF	**T**ully-**F**isher
TFR	**T**ully-**F**isher **R**elation
TRGB, T	**T**ip of the **R**ed **G**iant **B**ranch
TSC	**T**riangular **S**hape **C**loud
U	**U**rsa **M**ajor
V	**V**irgo
WDM	**W**arm **D**ark **M**atter
WF	**W**iener-**F**ilter
WISE	**W**ide-**F**ield **I**nfrared **S**urvey **E**xplorer
WIMP	**W**eakly **I**nteracting **M**assive **P**article
WMAP	**W**ilkinson **M**icrowave **A**nisotropy **P**robe
ZoA	**Z**one **o**f **A**voidance
ZP	**Z**ero **P**oint calibrator

Appendix E

Physical Constants and Units

Physical Constants:

- Constant of Boltzmann: $\mathbf{k_B} = 1.380\ 65\ \times\ 10^{-23}$ J K^{-1}
- Constant of Rydberg associated with the hydrogen: $\mathbf{R_H} = 1.097\ \times\ 10^{7}$ m^{-1}
- Gravitational constant: $\mathbf{G} = 6.673\ 84\ \pm\ 0.000\ 80\ \times\ 10^{-11}$ m^3 kg^{-1} s^{-2}
- Vacuum speed of Light: $\mathbf{c} = 2.997\ 924\ 58 \times 10^{8}$ m s$^{-\mathrm{S}}$

Units:

- Megaparsec, kiloparsec, parsec: **Mpc**, **kpc**, **pc**,
  1 Mpc $= 10^3$ kpc $= 10^6$ pc $= 3.085\ 68\ \times\ 10^{19}$ m
- Solar Luminosity: $\mathbf{L}_\odot$, 1 $L_\odot\ =\ 3.839\ \times\ 10^{26}$ W
- Solar Mass: $\mathbf{M}_\odot$, 1 $M_\odot\ =\ 1.988\ 4\ \pm 0.000\ 2\ \times\ 10^{30}$ kg
- arcminutes: **arcmin** / $'$, $1' = 4.629\ 63\ \times\ 10^{-5}$ rad
- arcseconds: **arcsec** / $''$, $1'' = \frac{1'}{60} = 7.716\ 05\ \times\ 10^{-7}$ rad
- jansky: **Jy**, 1 $Jy\ =\ 10^{-26}$ W m^{-2} Hz^{-1}

Other:

- Number Pi: π, $\mathbf{\Pi} = 3.141\ 592\ 653\ 59...$

Appendix F

Symbols and Mathematical Functions

Symbols:

[3.6]	apparent magnitude in the [3.6] band
$[3.6]_0$	apparent magnitude in the [3.6] band obtained with the "sky" value
$[3.6]_+$	apparent magnitude in the [3.6] band obtained with the "sky" value plus its uncertainty
$[3.6]_-$	apparent magnitude in the [3.6] band obtained with the "sky" value minus its uncertainty
$[3.6]^{b,k,i,a}$	corrected apparent magnitude in the [3.6] band
$[3.6]_{26.5}$	apparent magnitude at the 26.5 mag arcsec^{-2} isophote at [3.6]
$[3.6]_{ext}$	extrapolated apparent magnitude in the [3.6] band
$[3.6]_{tot}$	total (asymptotic) apparent magnitude in the [3.6] band
α	disk scale length / slope of the Schechter luminosity function
α, β, i, j	indices
$\gamma_{[3.6]}$	correction factor for internal extinction at 3.6
γ_λ	correction factor for internal extinction at λ
δ	overdensity or perturbation density field
$\tilde{\delta}$	spatial dependent part of the overdensity
δ_0	overdensity today
δ^{CR}	constrained realization of the density field
δ^{RR}	random realization of the density field
δ^{WF}	wiener-filter estimate of the mean density field
Δ	radial peculiar velocity uncertainty
$\Delta\nu$	spectral resolution after smoothing

$\Delta[3.6]^{color},\ \Delta M^{color}_{[3.6]}$	color correction term
Δvar	uncertainty on the variable var
ϵ	constraint error/uncertainty
$\zeta,\ \Psi,\ \Psi_T,\ \Psi_R$	correlation function
η	correlation vector
λ	wavelength / HI linewidth adjustment parameter
λ_e	emitted wavelength
λ_r	received wavelength
λ_{r_h}	hypothetical received wavelength in the case of sole expansion
Λ	cosmological constant
μ	distance modulus / surface brightness
$\langle\mu\rangle$	average surface brightness
$\mu_{[3.6]}$	distance modulus obtained with the Tully-Fisher relation
μ_0, L_0	disk central surface brightness in magnitude / in intensity units
$\mu_0^{[3.6],a}$	disk central surface brightness corrected for aperture at 3.6 μm
$\mu_0^{[3.6],a,i}$	disk central surface brightness totally corrected at 3.6 μm
μ_{20}	surface brightness at the isophote encompassing 20% of the total light
$\langle\mu_{20}\rangle$	average surface brightness within the radius enclosing 20% of the total light
μ_{80}	surface brightness at the isophote encompassing 80% of the total light
μ^c	bias corrected distance modulus
μ_C	distance modulus obtained with the color corrected Tully-Fisher relation
μ_e	effective surface brightness
$\langle\mu_e\rangle$	average effective surface brightness
$\langle\mu_{SN}\rangle$	distance modulus obtained with Type Ia Supernovae
$\langle\mu_{TF}\rangle$	distance modulus obtained with the Tully-Fisher relation
ξ	autocorrelation function of the perturbation density field
ρ	density
$\bar{\rho}$	mean density
ρ_m	matter density
ρ_{m_0}	matter density today
n_s	spectral index
ρ_r	radiation density
ρ_{r_0}	radiation density today
σ	variance / standard deviation
σ_0	velocity dispersion

σ_8	normalization parameter
$\sigma_{b/a}$	uncertainty of the axial ratio
σ_m	root mean square deviations from the rational function fit
σ_{NL}	sigma non-linear
σ_{sky}	uncertainty on the "sky"
$\sigma_x,\ \sigma_y$	variances of x and y variables
Φ	gravitational potential
Φ^*	normalization of the Schechter luminosity function
ϕ	gravitational potential due to fluctuations
ψ	displacement field
ψ_0	displacement field today
Ω_Λ	dark energy density parameter
Ω_K	scalar curvature density parameter
Ω_m	matter density parameter
Ω_r	radiation density parameter
ω	constant linking pressure and mass / white noise field
a	scale factor
$a,\ b,\ c$	trio of constants
$a_1,\ a_2,\ a_3,\ a_4$	quatuor of constants
a_0	scale factor today
$\dot{a},\ \ddot{a},\ \dddot{a}$	first, second and third derivatives of the scale factor with respect to time
a_{20}	radius of the isophotal level encompassing 20% of the total light
$a_{26.5}$	radius of the isophotal level 26.5 magnitudes per square arcsecond at [3.6]
a_{80}	radius of the isophotal level encompassing 80% of the total light
$a_e,\ r_e$	effective radius
$A_a^{[3.6]}$	aperture correction in the [3.6] band
$A_b^{[3.6]}$	galactic extinction correction in the [3.6] band
A_b^{λ}	galactic extinction correction for the wavelength λ
$A_i^{[3.6]}$	internal extinction correction in the [3.6] band
$A_k^{[3.6]}$	k-correction in the [3.6] band
A_b^I	galactic extinction correction in the I band
A_i^I	internal extinction correction in the I band
A_k^I	k-correction in the I band
b	galactic latitude / bias
$\frac{b}{a},\ b/a$	axial ratio
c	vacuum speed of light / constraint
$corr$	correlation coefficient

cov	covariance
cst	constant
C	conversion factor / constraint plus its uncertainty
$C^{[3.6]}$	intrinsic extinction factor
$C_{[3.6]}$	color adjusted magnitude or pseudo-apparent magnitude
C_{82}	concentration index
C_ℓ	cutoff factor
$d_{[3.6]}$	distance obtained with the Tully-Fisher relation
d_C	distance obtained with the color corrected Tully-Fisher relation
d_{25}	diameter at the B-isophote of 25 magnitudes per square arcsecond
D	distance
D_0	distance today
D_+	increasing solution of the second-order differential equation on the time dependent part of the overdensity
D_{+0}	increasing solution of the second-order differential equation on the time dependent part of the overdensity, value today
$D_\pm$	general solution of the second-order differential equation on the time dependent part of the overdensity
D_L	luminosity distance
D_n	diameter of the isophote encompassing 20.75 magnitudes per square arcsecond
err_{var}	errors on the variable var
E, U	energy
E_k	kinetic energy
E_p	potential energy
$E(B-V)$	reddening
f	growth rate / probability distribution function / underlying field / probability of the estimate to be wrong
f^{CR}	constrained realization of the underlying field
f^{WF}	wiener-filter estimate of the underlying field
$\tilde{f}^{RR}$	random underlying field
$\tilde{f}^{WF}$	wiener-filter estimate of the random underlying field
F	gravitational force / flux / decomposition factor of underlying fields or of their models
F_0	instrumental zero point
F_{HI}	flux integrated within the HI profile
$F_{[3.6]}$, $F_{[4.5]}$	flux in [3.6] and [4.5] Spitzer bands
G	universal gravitational constant
h	Hubble constant divided by one hundred

H	(generalized) Hubble constant / Hamiltonian
$H_\alpha,\ H_\beta,\ H_\gamma,\ H_\delta,\ H_\epsilon$	hydrogen lines of the Balmer series
H_0	Hubble constant (today)
i	inclination
I	apparent magnitude in the I-band
$I^{b,i,k}$	corrected apparent magnitude in the I-band
j_0	jerk parameter
$j_0,\ j_1$	Bessel functions
k	curvature of space / Fourier mode or wavevector
k_B	constant of Boltzmann
$k_r,\ k_L,\ k_v,\ k_s$	parameters reflecting density, luminosity and kinematic structures of galaxies ; k_s is inversely proportional to the product of the first three parameters
K	scalar curvature
l, b	galactic coordinates
L	length / luminosity
L^*	characteristic luminosity of the Schechter function
$L_\odot$	solar luminosity
L_{lim}	luminosity of the limiting isophote
m	mass / apparent magnitude
m_r	apparent magnitude at the galactocentric radius r
m_T	total apparent magnitude
$\bar{m}$	fluctuation magnitude
M	absolute magnitude
M^*	characteristic magnitude of the Schechter function
M_*	stellar mass
$M_\odot$	solar mass
$M^{b,i,k,a}_{[3.6]}$	corrected absolute magnitude at 3.6 μm
$M_{C_{[3.6]}}$	color adjusted magnitude or pseudo-apparent magnitude
$M_{baryonic}$	baryonic mass
M_{gas}	gas mass
n	number of particles, bodies, constraints, points, galaxies
N	noise
$\bar{N}$	fluctuation star counts
p	probability (not to belong to the theoretical gaussian)
P	pressure / power spectrum / period
PA	position angle
q_0	deceleration parameter / statistical axial ratio for a galaxy viewed edge-on

$\langle r \rangle$	true distance
r	proper coordinate / galactocentric radius / distance estimate
$\hat{\mathbf{r}}$	normalized directional vector
r_{lim}	radius of the limiting isophote
$R,\ \tilde{R}$	residual
$R_{[3.6]}$	factor accounting for the shift to Spitzer passband centroid
R_λ	factor accounting for the shift to a photometric passband (wavelength λ) centroid
R_H	constant of Rydberg associated with the hydrogen
$SGL,\ SGB$	spherical supergalactic coordinates
$SGX,\ SGY,\ SGZ$	cartesian supergalactic coordinates
s	path, geodesic
S	signal / "sky"
$stddev$	standard deviation (scatter)
t	time, morphological type
T	period / temperature
u	peculiar velocity
$U,\ B,\ V,\ G,\ R,\ R_C$	
$I,\ I_C,\ Z,\ Y,\ J,\ H$	
$K,\ K_s,\ K'$	photometric band
v	velocity
v_{hel}	heliocentric velocity
v_{mod}	velocity with respect to the cosmic microwave background corrected for cosmological effects
v_{pec}	(radial) peculiar velocity
$v_{pec\ c}$	"corrected" radial peculiar velocity
v_{CMB}	velocity with respect to the cosmic microwave background
v^{CR}	constrained realization of the velocity field
v^{RR}	random realization of the velocity field
v^{WF}	wiener-filter estimate of the velocity field
V	volume
w	phase space
W	linewidth of the 21-cm line
W_{m50}	HI profile width at 50% of the mean flux within the velocity range encompassing 90% of the total HI flux
$W^c_{m50},\ W_{mx}$	partially corrected HI linewidth
$W_{t,m50},\ W_{c,m50}$	HI linewidth adjustment parameter
W_{mx}	non de-projected corrected HI linewidth
W^i_{mx}	fully corrected HI linewidth, corresponds to twice the rotational

	velocity of a galaxy
x	comoving coordinate
$x,\ y$	set of variables to model data
$\bar{x},\ \bar{y}$	means of x and y variables
x_E	eulerian coordinate
x_L	lagrangian coordinate
z	redshift
z_{cos}	cosmological redshift
z_{extra}	extra term in the observational redshift not due to the sole expansion
z_{obs}	observational redshift
z_{pec}	peculiar redshift
zpt	zeropoint
$\bar{zpt}$	mean zeropoint

Mathematical Functions:

$\wedge$	vectorial product
$[function, H]$	Poisson bracket
$\int var(var')dvar'$	integral of the variable var with respect to the variable var'
$\sum_n$	summation over n
δ_{ij}^K	Kronecker symbol
$\langle var\ var' \rangle$	average over the volume / correlation function of the variables var and var'
$\dot{var},\ \ddot{var},\ \dddot{var}$	first, second and third derivatives with respect to time of the variable var
$\frac{d}{d\ var}$	total derivative with respect to the variable var
$\frac{\partial}{\partial var}$	partial derivative with respect to the variable var
$(\frac{\partial}{\partial var})_{var'}$	partial derivative with respect to the variable var with the prime variable var' fixed
∇	divergence
∇^2	laplacian
cos, sin	trigonometric cosinus and sinus functions
$\mathrm{e}^{function}$, exp()	exponential function
ln()	Neperian logarithm
log()	decimal logarithm

Bibliography

Aaronson, M.; Huchra, J.; and Mould, J. *The infrared luminosity/H I velocity-width relation and its application to the distance scale.* ApJ, 229:1–13, 1979.

Abazajian, K.; Adelman-McCarthy, J. K.; Agüeros, M. A.; Allam, S. S.; Anderson, S. F.; Annis, J.; Bahcall, N. A.; Baldry, I. K.; Bastian, S.; Berlind, A.; et al. *The First Data Release of the Sloan Digital Sky Survey.* AJ, 126:2081–2086, 2003.

Adler, R. J., The Geometry of Random Fields, 1981.

Alimi, J.-M.; Bouillot, V.; Rasera, Y.; Reverdy, V.; Corasaniti, P.-S.; Balmes, I.; Requena, S.; Delaruelle, X.; and Richet, J.-N. *DEUS Full Observable {\Lambda}CDM Universe Simulation: the numerical challenge.* ArXiv e-prints 1206.2838, 2012.

Amanullah, R.; Lidman, C.; Rubin, D.; Aldering, G.; Astier, P.; Barbary, K.; Burns, M. S.; Conley, A.; Dawson, K. S.; Deustua, S. E.; et al. *Spectra and Hubble Space Telescope Light Curves of Six Type Ia Supernovae at 0.511 < z < 1.12 and the Union2 Compilation.* ApJ, 716:712–738, 2010.

Angulo, R. E.; Springel, V.; White, S. D. M.; Jenkins, A.; Baugh, C. M.; and Frenk, C. S. *Scaling relations for galaxy clusters in the Millennium-XXL simulation.* MNRAS, 426:2046–2062, 2012a.

Angulo, R. E.; Springel, V.; White, S. D. M.; Jenkins, A.; Baugh, C. M.; and Frenk, C. S. *Scaling relations for galaxy clusters in the Millennium-XXL simulation.* MNRAS, 426:2046–2062, 2012b.

Appel, A. W. *An Efficient Program for Many-Body Simulation.* SIAM Journal on Scientific and Statistical Computing, vol. 6, no. 1, January 1985, p. 85-103., 6:85–103, 1985.

Bahcall, N. A. *Superclustering and the large-scale structure of the Universe.* Advances in Space Research, 3:367–377, 1984.

Bailin, J. and Harris, W. E. *Galaxy concentrations are trimodal.* MNRAS, 385:1835–1845, 2008.

Baldry, I. K.; Glazebrook, K.; Brinkmann, J.; Ivezić, Ž.; Lupton, R. H.; Nichol, R. C.; and Szalay, A. S. *Quantifying the Bimodal Color-Magnitude Distribution of Galaxies.* ApJ, 600:681–694, 2004.

Bardeen, J. M.; Bond, J. R.; Kaiser, N.; and Szalay, A. S. *The statistics of peaks of Gaussian random fields.* ApJ, 304:15–61, 1986.

Barnes, J. and Hut, P. *A hierarchical O(N log N) force-calculation algorithm.* Nature, 324:446–449, 1986.

Baugh, C. M. *Luminosity Bias: From Haloes to Galaxies.* PASA, 30:e030, 2013.

Bedregal, A. G.; Aragón-Salamanca, A.; and Merrifield, M. R. *The Tully-Fisher relation for S0 galaxies.* MNRAS, 373:1125–1140, 2006.

Behroozi, P. S.; Conroy, C.; and Wechsler, R. H. *A Comprehensive Analysis of Uncertainties Affecting the Stellar Mass-Halo Mass Relation for $0 < z < 4$.* ApJ, 717:379–403, 2010.

Bell, E. F. and de Blok, W. J. G. *The bimodal spiral galaxy surface brightness distribution.* MNRAS, 311:668–672, 2000.

Bertone, G. *The moment of truth for WIMP dark matter.* Nature, 468:389–393, 2010.

Bertschinger, E. *Multiscale Gaussian Random Fields and Their Application to Cosmological Simulations.* ApJS, 137:1–20, 2001.

Bhattacharya, S., Cosmology using galaxy cluster peculiar velocities, 2008.

Binney, J. and Tremaine, S., Galactic dynamics, 1987.

Birrell, J. and Rafelski, J. *Boltzmann Equation Solver Adapted to Emergent Chemical Non-equilibrium.* ArXiv e-prints, 2014.

Bistolas, V. and Hoffman, Y. *Nonlinear Constrained Realizations of the Large-Scale Structure.* ApJ, 492:439, 1998.

Blakeslee, J. P.; Cantiello, M.; Mei, S.; Côté, P.; Barber DeGraaff, R.; Ferrarese, L.; Jordán, A.; Peng, E. W.; Tonry, J. L.; and Worthey, G. *Surface Brightness Fluctuations in the Hubble Space Telescope ACS/WFC F814W Bandpass and an Update on Galaxy Distances.* ApJ, 724:657–668, 2010.

Blanton, M. R. and Roweis, S. *K-Corrections and Filter Transformations in the Ultraviolet, Optical, and Near-Infrared.* AJ, 133:734–754, 2007.

Bothun, G. D. and Mould, J. R. *Sources of error in the Tully-Fisher relation - Reducing the scatter with CCD I-band surface photometry of spiral galaxies.* ApJ, 313:629–643, 1987.

Bottinelli, L.; Gouguenheim, L.; Paturel, G.; and Teerikorpi, P. *The Malmquist bias and the value of H0 from the Tully-Fisher relation.* A&A, 156:157–171, 1986.

Brammer, G. B.; Whitaker, K. E.; van Dokkum, P. G.; Marchesini, D.; Labbé, I.; Franx, M.; Kriek, M.; Quadri, R. F.; Illingworth, G.; Lee, K.-S.; et al. *The Dead Sequence: A Clear Bimodality in Galaxy Colors from $z = 0$ to $z = 2.5$.* ApJL, 706:L173–L177, 2009.

Brook, C. B.; Di Cintio, A.; Knebe, A.; Gottlöber, S.; Hoffman, Y.; and Yepes, G. *The stellar-to-halo mass relation for Local Group galaxies.* ArXiv e-prints, 2013.

Burstein, D.; Faber, S. M.; and Dressler, A. *Evidence from the motions of galaxies for a large-scale, large-amplitude flow toward the great attractor.* ApJ, 354:18–32, 1990.

Caputi, K. I.; McLure, R. J.; Dunlop, J. S.; Cirasuolo, M.; and Schael, A. M. *Further constraints on the evolution of K_s-selected galaxies in the GOODS/CDFS field.* MNRAS, 366:609–623, 2006.

Cardelli, J. A.; Clayton, G. C.; and Mathis, J. S. *The relationship between infrared, optical, and ultraviolet extinction.* ApJ, 345:245–256, 1989.

Carroll, S. M.; Press, W. H.; and Turner, E. L. *The cosmological constant.* ARA&A, 30:499–542, 1992.

Catinella, B.; Kauffmann, G.; Schiminovich, D.; Lemonias, J.; Scannapieco, C.; Wang, J.; Fabello, S.; Hummels, C.; Moran, S. M.; Wu, R.; et al. *The GALEX Arecibo SDSS Survey - IV. Baryonic mass-velocity-size relations of massive galaxies.* MNRAS, 420:1959–1976, 2012.

Chamaraux, P.; Cayatte, V.; Balkowski, C.; and Fontanelli, P. *A connection between the Perseus-Pisces supercluster and the A 569 cloud?* A&A, 229:340–350, 1990.

Chiba, T. and Nakamura, T. *The Luminosity Distance, the Equation of State, and the Geometry of the Universe.* Progress of Theoretical Physics, 100:1077–1082, 1998.

Chilingarian, I. V.; Melchior, A.-L.; and Zolotukhin, I. Y. *Analytical approximations of K-corrections in optical and near-infrared bands.* MNRAS, 405:1409–1420, 2010.

Chincarini, G. *Large-scale structure of the universe.* The Messenger, 26:14–15, 1981.

Cole, S.; Lacey, C. G.; Baugh, C. M.; and Frenk, C. S. *Hierarchical galaxy formation.* MNRAS, 319:168–204, 2000.

Colless, M.; Saglia, R. P.; Burstein, D.; Davies, R. L.; McMahan, R. K.; and Wegner, G. *The peculiar motions of early-type galaxies in two distant regions - VII. Peculiar velocities and bulk motions.* MNRAS, 321:277–305, 2001.

Courteau, S. *Optical Rotation Curves and Linewidths for Tully-Fisher Applications.* AJ, 114:2402, 1997.

Courteau, S.; Dutton, A. A.; van den Bosch, F. C.; MacArthur, L. A.; Dekel, A.; McIntosh, D. H.; and Dale, D. A. *Scaling Relations of Spiral Galaxies.* ApJ, 671:203–225, 2007.

Courtois, H. M.; Hoffman, Y.; Tully, R. B.; and Gottlöber, S. *Three-dimensional Velocity and Density Reconstructions of the Local Universe with Cosmicflows-1.* ApJ, 744:43, 2012.

Courtois, H. M.; Pomarède, D.; Tully, R. B.; Hoffman, Y.; and Courtois, D. *Cosmography of the Local Universe.* AJ, 146:69, 2013.

Courtois, H. M. and Tully, R. B. *Cosmic Flows surveys and CLUES simulations.* Astronomische Nachrichten, 333:436, 2012a.

Courtois, H. M. and Tully, R. B. *Cosmicflows-2: Type Ia Supernova Calibration and* H_0. ApJ, 749:174, 2012b.

Courtois, H. M.; Tully, R. B.; Fisher, J. R.; Bonhomme, N.; Zavodny, M.; and Barnes, A. *The Extragalactic Distance Database: All Digital H I Profile Catalog.* AJ, 138:1938–1956, 2009.

Courtois, H. M.; Tully, R. B.; and Héraudeau, P. *Cosmic flows: University of Hawaii 2.2-m I-band photometry.* MNRAS, 415:1935–1942, 2011a.

Courtois, H. M.; Tully, R. B.; Makarov, D. I.; Mitronova, S.; Koribalski, B.; Karachentsev, I. D.; and Fisher, J. R. *Cosmic Flows: Green Bank Telescope and Parkes H I observations.* MNRAS, 414:2005–2016, 2011b.

Cowie, L. L.; Gardner, J. P.; Hu, E. M.; Songaila, A.; Hodapp, K.-W.; and Wainscoat, R. J. *The Hawaii K-band galaxy survey. 1: Deep K-band imaging.* ApJ, 434:114–127, 1994.

Cox, T. J. and Loeb, A. *The collision between the Milky Way and Andromeda.* MNRAS, 386:461–474, 2008.

da Costa, L. N.; Freudling, W.; Wegner, G.; Giovanelli, R.; Haynes, M. P.; and Salzer, J. J. *The Mass Distribution in the Nearby Universe.* ApJL, 468:L5, 1996.

da Costa, L. N.; Nusser, A.; Freudling, W.; Giovanelli, R.; Haynes, M. P.; Salzer, J. J.; and Wegner, G. *Comparison of the SFI peculiar velocities with the IRAS 1.2-Jy gravity field.* MNRAS, 299:425–432, 1998.

Dale, D. A.; Bendo, G. J.; Engelbracht, C. W.; Gordon, K. D.; Regan, M. W.; Armus, L.; Cannon, J. M.; Calzetti, D.; Draine, B. T.; Helou, G.; et al. *Infrared Spectral Energy Distributions of Nearby Galaxies.* ApJ, 633:857–870, 2005.

Dale, D. A.; Cohen, S. A.; Johnson, L. C.; Schuster, M. D.; Calzetti, D.; Engelbracht, C. W.; Gil de Paz, A.; Kennicutt, R. C.; Lee, J. C.; Begum, A.; et al. *The Spitzer Local Volume Legacy: Survey Description and Infrared Photometry.* ApJ, 703:517–556, 2009.

Dale, D. A.; Gil de Paz, A.; Gordon, K. D.; Hanson, H. M.; Armus, L.; Bendo, G. J.; Bianchi, L.; Block, M.; Boissier, S.; Boselli, A.; et al. *An Ultraviolet-to-Radio Broadband Spectral Atlas of Nearby Galaxies.* ApJ, 655:863–884, 2007.

Davis, M.; Efstathiou, G.; Frenk, C. S.; and White, S. D. M. *The evolution of large-scale structure in a universe dominated by cold dark matter.* ApJ, 292:371–394, 1985.

de Jong, R. S. *Near-infrared and optical broadband surface photometry of 86 face-on disk dominated galaxies. II. A two-dimensional method to determine bulge and disk parameters.* A&A Supplement Series, 118:557–573, 1996a.

de Jong, R. S. *Near-infrared and optical broadband surface photometry of 86 face-on disk dominated galaxies. III. The statistics of the disk and bulge parameters.* A&A, 313:45–64, 1996b.

de Vaucouleurs, G. *Evidence for a local super,galaxy.* AJ, 58:30, 1953.

de Vaucouleurs, G. *Contributions to the galaxy photometry. I - Standard total magnitudes, luminosity curves, and photometric parameters of 115 bright galaxies in the B system from detailed surface photometry.* ApJS, 33:211–218, 1977.

Dehnen, W. *A Very Fast and Momentum-conserving Tree Code.* ApJL, 536:L39–L42, 2000.

Dekel, A. *Dynamics of Cosmic Flows.* ARA&A, 32:371–418, 1994.

Dekel, A.; Eldar, A.; Kolatt, T.; Yahil, A.; Willick, J. A.; Faber, S. M.; Courteau, S.; and Burstein, D. *POTENT Reconstruction from Mark III Velocities.* ApJ, 522:1–38, 1999.

Desmond, H. *The baryonic Tully-Fisher Relation predicted by cold dark matter cosmogony.* ArXiv e-prints, 2012.

Doumler, T.; Courtois, H.; Gottlöber, S.; and Hoffman, Y. *Reconstructing cosmological initial conditions from galaxy peculiar velocities - II. The effect of observational errors.* MNRAS, 430:902–911, 2013a.

Doumler, T.; Gottlöber, S.; Hoffman, Y.; and Courtois, H. *Reconstructing cosmological initial conditions from galaxy peculiar velocities - III. Constrained simulations.* MNRAS, 430:912–923, 2013b.

Doumler, T.; Hoffman, Y.; Courtois, H.; and Gottlöber, S. *Reconstructing cosmological initial conditions from galaxy peculiar velocities - I. Reverse Zeldovich Approximation.* MNRAS, 430:888–901, 2013c.

Draine, B. T. and Lee, H. M. *Optical properties of interstellar graphite and silicate grains.* ApJ, 285:89–108, 1984.

Dressler, A. *The Dn-sigma relation for bulges of disk galaxies - A new, independent measure of the Hubble constant.* ApJ, 317:1–10, 1987.

Dutton, A. A. *The baryonic Tully-Fisher relation and galactic outflows.* MNRAS, 424:3123–3128, 2012.

Eddington, A. S. *On a formula for correcting statistics for the effects of a known error of observation.* MNRAS, 73:359–360, 1913.

Efstathiou, G. *Fred Hoyle: Contributions to the Theory of Galaxy Formation.* ArXiv Astrophysics e-prints, 2003.

Efstathiou, G.; Davis, M.; White, S. D. M.; and Frenk, C. S. *Numerical techniques for large cosmological N-body simulations.* ApJS, 57:241–260, 1985.

Einasto, J.; Suhhonenko, I.; Hütsi, G.; Saar, E.; Einasto, M.; Liivamägi, L. J.; Müller, V.; Starobinsky, A. A.; Tago, E.; and Tempel, E. *Towards understanding the structure of voids in the cosmic web.* A&A, 534:A128, 2011.

Ekholm, T.; Lanoix, P.; Teerikorpi, P.; Fouqué, P.; and Paturel, G. *Investigations of the Local Supercluster velocity field. III. Tracing the backside infall with distance moduli from the direct Tully-Fisher relation.* A&A, 355:835–847, 2000.

Erdoğdu, P.; Lahav, O.; Huchra, J. P.; Colless, M.; Cutri, R. M.; Falco, E.; George, T.; Jarrett, T.; Jones, D. H.; Macri, L. M.; et al. *Reconstructed density and velocity fields from the 2MASS Redshift Survey.* MNRAS, 373:45–64, 2006.

Erwin, P.; Pohlen, M.; and Beckman, J. E. *The Outer Disks of Early-Type Galaxies. I. Surface-Brightness Profiles of Barred Galaxies.* AJ, 135:20–54, 2008.

Eskew, M.; Zaritsky, D.; and Meidt, S. *Converting from 3.6 and 4.5 μm Fluxes to Stellar Mass.* AJ, 143:139, 2012.

Faber, S. M. and Jackson, R. E. *Velocity dispersions and mass-to-light ratios for elliptical galaxies.* ApJ, 204:668–683, 1976.

Fazio, G. G.; Hora, J. L.; Allen, L. E.; Ashby, M. L. N.; Barmby, P.; Deutsch, L. K.; Huang, J.-S.; Kleiner, S.; Marengo, M.; Megeath, S. T.; et al. *The Infrared Array Camera (IRAC) for the Spitzer Space Telescope.* ApJS, 154:10–17, 2004.

Feindt, U.; Kerschhaggl, M.; Kowalski, M.; Aldering, G.; Antilogus, P.; Aragon, C.; Bailey, S.; Baltay, C.; Bongard, S.; Buton, C.; et al. *Measuring cosmic bulk flows with Type Ia supernovae from the Nearby Supernova Factory.* A&A, 560:A90, 2013.

Fisher, K. B.; Lahav, O.; Hoffman, Y.; Lynden-Bell, D.; and Zaroubi, S. *Wiener reconstruction of density, velocity and potential fields from all-sky galaxy redshift surveys.* MNRAS, 272:885–908, 1995.

Fixsen, D. J.; Cheng, E. S.; Gales, J. M.; Mather, J. C.; Shafer, R. A.; and Wright, E. L. *The Cosmic Microwave Background Spectrum from the Full COBE FIRAS Data Set.* ApJ, 473:576, 1996.

Focardi, P.; Marano, B.; and Vettolani, G. *The north extension of the Perseus supercluster.* A&A, 136:178–180, 1984.

Folatelli, G.; Phillips, M. M.; Burns, C. R.; Contreras, C.; Hamuy, M.; Freedman, W. L.; Persson, S. E.; Stritzinger, M.; Suntzeff, N. B.; Krisciunas, K.; et al. *The Carnegie Supernova Project: Analysis of the First Sample of Low-Redshift Type-Ia Supernovae.* AJ, 139:120–144, 2010.

Forero-Romero, J. E.; Hoffman, Y.; Yepes, G.; Gottlöber, S.; Piontek, R.; Klypin, A.; and Steinmetz, M. *The dark matter assembly of the Local Group in constrained cosmological simulations of a Λ cold dark matter universe.* MNRAS, 417:1434–1443, 2011.

Fosalba, P.; Crocce, M.; Gaztanaga, E.; and Castander, F. J. *The MICE Grand Challenge Lightcone Simulation I: Dark matter clustering.* ArXiv e-prints, 2013.

Freedman, W. L. and Madore, B. F. *The Hubble Constant.* ARA&A, 48:673–710, 2010.

Freedman, W. L.; Madore, B. F.; Gibson, B. K.; Ferrarese, L.; Kelson, D. D.; Sakai, S.; Mould, J. R.; Kennicutt, R. C., Jr.; Ford, H. C.; Graham, J. A.; et al. *Final Results from the Hubble Space Telescope Key Project to Measure the Hubble Constant.* ApJ, 553:47–72, 2001.

Freedman, W. L.; Madore, B. F.; Scowcroft, V.; Burns, C.; Monson, A.; Persson, S. E.; Seibert, M.; and Rigby, J. *Carnegie Hubble Program: A Mid-infrared Calibration of the Hubble Constant.* ApJ, 758:24, 2012.

Freedman, W. L.; Madore, B. F.; Scowcroft, V.; Monson, A.; Persson, S. E.; Seibert, M.; Rigby, J. R.; Sturch, L.; and Stetson, P. *The Carnegie Hubble Program.* AJ, 142:192, 2011.

Freeman, K. C. *On the Disks of Spiral and so Galaxies.* ApJ, 160:811, 1970.

Frei, Z. and Gunn, J. E. *Generating colors and K corrections from existing catalog data.* AJ, 108:1476–1485, 1994.

Friedmann, A. *Über die Krümmung des Raumes.* Zeitschrift fur Physik, 10:377–386, 1922.

Ganon, G. and Hoffman, Y. *Constrained realizations of Gaussian fields - Reconstruction of the large-scale structure.* ApJL, 415:L5–L8, 1993.

Garrison-Kimmel, S.; Boylan-Kolchin, M.; Bullock, J.; and Lee, K. *ELVIS: Exploring the Local Volume in Simulations.* ArXiv e-prints, 2013.

Garrison-Kimmel, S.; Boylan-Kolchin, M.; Bullock, J. S.; and Lee, K. *ELVIS: Exploring the Local Volume in Simulations.* MNRAS, 438:2578–2596, 2014.

Giovanelli, R.; Haynes, M. P.; Herter, T.; Vogt, N. P.; da Costa, L. N.; Freudling, W.; Salzer, J. J.; and Wegner, G. *The I Band Tully-Fisher Relation for Cluster Galaxies: a Template Relation, its Scatter and Bias Corrections.* AJ, 113:53–79, 1997a.

Giovanelli, R.; Haynes, M. P.; Herter, T.; Vogt, N. P.; Wegner, G.; Salzer, J. J.; da Costa, L. N.; and Freudling, W. *The I band Tully-Fisher relation for cluster galaxies: data presentation.* AJ, 113:22–52, 1997b.

Giovanelli, R.; Haynes, M. P.; Salzer, J. J.; Wegner, G.; da Costa, L. N.; and Freudling, W. *Dependence on Luminosity of Photometric Properties of Disk Galaxies: Surface Brightness, Size, and Internal Extinction.* AJ, 110:1059, 1995.

Gottlöber, S.; Hoffman, Y.; and Yepes, G. *Constrained Local UniversE Simulations (CLUES).* ArXiv e-prints, 2010.

Gould, A. *Selection, covariance, and Malmquist bias.* ApJL, 412:L55–L58, 1993.

Gunn, J. E. *The Friedmann models and optical observations in cosmology.* page 1, 1978.

Gunn, J. E. and Gott, J. R., III. *On the Infall of Matter Into Clusters of Galaxies and Some Effects on Their Evolution.* ApJ, 176:1, 1972.

Hahn, O. and Abel, T. *Multi-scale initial conditions for cosmological simulations.* MNRAS, 415:2101–2121, 2011.

Hall, M.; Courteau, S.; Dutton, A. A.; McDonald, M.; and Zhu, Y. *An investigation of Sloan Digital Sky Survey imaging data and multiband scaling relations of spiral galaxies.* MNRAS, 425:2741–2765, 2012.

Hamann, J. and Hasenkamp, J. *A new life for sterile neutrinos: resolving inconsistencies using hot dark matter.* JCAP, 10:044, 2013.

Hamuy, M.; Phillips, M. M.; Maza, J.; Suntzeff, N. B.; Schommer, R. A.; and Aviles, R. *A Hubble diagram of distant type IA supernovae.* AJ, 109:1–13, 1995.

Han, M. *I-band CCD surface photometry of spiral galaxies in 16 nearby clusters.* ApJS, 81:35–47, 1992a.

Han, M. *The large-scale velocity field beyond the local supercluster.* ApJ, 395:75–90, 1992b.

Hattori, M. *Is the universe gravitationally dominated by non-baryonic dark matter?* pages 447–448, 1994.

Heath, D. J. *The growth of density perturbations in zero pressure Friedmann-Lemaitre universes.* MNRAS, 179:351–358, 1977.

Heitmann, K.; Lukić, Z.; Fasel, P.; Habib, S.; Warren, M. S.; White, M.; Ahrens, J.; Ankeny, L.; Armstrong, R.; O'Shea, B.; et al. *The cosmic code comparison project.* Computational Science and Discovery, 1(1):015003, 2008.

Heitmann, K.; Ricker, P. M.; Warren, M. S.; and Habib, S. *Robustness of Cosmological Simulations. I. Large-Scale Structure.* ApJS, 160:28–58, 2005.

Hendry, M. A. and Simmons, J. F. L. *Optimal galaxy distance estimators.* ApJ, 435:515–527, 1994.

Heß, S.; Kitaura, F.-S.; and Gottlöber, S. *Simulating structure formation of the Local Universe.* MNRAS, 435:2065–2076, 2013.

Hicken, M.; Wood-Vasey, W. M.; Blondin, S.; Challis, P.; Jha, S.; Kelly, P. L.; Rest, A.; and Kirshner, R. P. *Improved Dark Energy Constraints from ˜100 New CfA Supernova Type Ia Light Curves.* ApJ, 700:1097–1140, 2009.

Hinshaw, G.; Larson, D.; Komatsu, E.; Spergel, D. N.; Bennett, C. L.; Dunkley, J.; Nolta, M. R.; Halpern, M.; Hill, R. S.; Odegard, N.; et al. *Nine-year Wilkinson Microwave Anisotropy Probe (WMAP) Observations: Cosmological Parameter Results.* ApJS, 208:19, 2013.

Hoffman, Y. *Gaussian Fields and Constrained Simulations of the Large-Scale Structure.* In Martínez, V. J.; Saar, E.; Martínez-González, E.; and Pons-Bordería, M.-J., editors, Data Analysis in Cosmology, volume 665 of Lecture Notes in Physics, Berlin Springer Verlag, pages 565–583. 2009.

Hoffman, Y.; Lahav, O.; Yepes, G.; and Dover, Y. *The future of the local large scale structure: the roles of dark matter and dark energy.* JCAP, 10:016, 2007.

Hoffman, Y. and Ribak, E. *Constrained realizations of Gaussian fields - A simple algorithm.* ApJL, 380:L5–L8, 1991.

Hoffman, Y. and Ribak, E. *Primordial Gaussian perturbation fields - Constrained realizations.* ApJ, 384:448–452, 1992.

Holmberg, E. *A photographic photometry of extragalactic nebulae.* Meddelanden fran Lunds Astronomiska Observatorium Serie II, 136:1, 1958.

Huang, J.-S.; Ashby, M. L. N.; Barmby, P.; Brodwin, M.; Brown, M. J. I.; Caldwell, N.; Cool, R. J.; Eisenhardt, P.; Eisenstein, D.; Fazio, G. G.; et al. *The Local Galaxy 8 μm Luminosity Function.* ApJ, 664:840–849, 2007.

Hubble, E. *A Relation between Distance and Radial Velocity among Extra-Galactic Nebulae.* Contributions from the Mount Wilson Observatory, vol. 3, pp.23-28, 3:23–28, 1929.

Huchra, J. P.; Macri, L. M.; Masters, K. L.; Jarrett, T. H.; Berlind, P.; Calkins, M.; Crook, A. C.; Cutri, R.; Erdoğdu, P.; Falco, E.; et al. *The 2MASS Redshift Survey: Description and Data Release.* ApJS, 199:26, 2012.

Hudson, M. J. *Optical galaxies within 8000 km s^{-1}. III. Inhomogeneous Malmquist bias corrections and the Great Attractor.* MNRAS, 266:468–474, 1994.

Huizinga, J. E., Extinction studies of spiral galaxies, 1994.

Iocco, F. *WIMP Dark Matter and the First Stars.* 1294:66–69, 2010.

Jacobs, B. A.; Rizzi, L.; Tully, R. B.; Shaya, E. J.; Makarov, D. I.; and Makarova, L. *The Extragalactic Distance Database: Color-Magnitude Diagrams.* AJ, 138:332–337, 2009.

Jacoby, G. H.; Branch, D.; Ciardullo, R.; Davies, R. L.; Harris, W. E.; Pierce, M. J.; Pritchet, C. J.; Tonry, J. L.; and Welch, D. L. *A critical review of selected techniques for measuring extragalactic distances.* PASP, 104:599–662, 1992.

Jeong, K. S.; Kawasaki, M.; and Takahashi, F. *Axions as hot and cold dark matter.* JCAP, 2:046, 2014.

Jha, S.; Riess, A. G.; and Kirshner, R. P. *Improved Distances to Type Ia Supernovae with Multicolor Light-Curve Shapes: MLCS2k2.* ApJ, 659:122–148, 2007.

Johnston, S. and Deboer, D. *Testing of focal plane array technologies for ASKAP.* ATNF Proposal, page 1450, 2008.

Kaiser, N. *Clustering in real space and in redshift space.* MNRAS, 227:1–21, 1987.

Kaiser, N.; Aussel, H.; Burke, B. E.; Boesgaard, H.; Chambers, K.; Chun, M. R.; Heasley, J. N.; Hodapp, K.-W.; Hunt, B.; Jedicke, R.; et al. *Pan-STARRS: A Large Synoptic Survey Telescope Array.* 4836:154–164, 2002.

Karachentsev, I. D.; Karachentseva, V. E.; Kudrya, Y. N.; Sharina, M. E.; and Parnovskij, S. L. *The revised Flat Galaxy Catalogue.* Bulletin of the Special Astrophysics Observatory, 47:5, 1999.

Karachentsev, I. D.; Kashibadze, O. G.; Makarov, D. I.; and Tully, R. B. *The Hubble flow around the Local Group.* MNRAS, 393:1265–1274, 2009.

Karachentsev, I. D.; Mitronova, S. N.; Karachentseva, V. E.; Kudrya, Y. N.; and Jarrett, T. H. *The 2MASS Tully-Fisher relation for flat edge-on galaxies.* A&A, 396:431–438, 2002.

Karachentsev, I. D. and Nasonova, O. G. *The observed infall of galaxies towards the Virgo cluster.* MNRAS, 405:1075–1083, 2010.

Karachentsev, I. D.; Nasonova, O. G.; and Courtois, H. M. *Fast Motions of Galaxies in the Coma I Cloud: A Case of Dark Attractor?* ApJ, 743:123, 2011.

Karachentsev, I. D.; Nasonova, O. G.; and Courtois, H. M. *Anatomy of Ursa Majoris.* MNRAS, 429:2264–2273, 2013.

Kashlinsky, A.; Atrio-Barandela, F.; and Ebeling, H. *Measuring bulk motion of X-ray clusters via the kinematic Sunyaev-Zeldovich effect: summarizing the "dark flow" evidence and its implications.* ArXiv e-prints, 2012.

Kashlinsky, A.; Atrio-Barandela, F.; Ebeling, H.; Edge, A.; and Kocevski, D. *A New Measurement of the Bulk Flow of X-Ray Luminous Clusters of Galaxies.* ApJL, 712:L81–L85, 2010.

Kent, S. M. *CCD surface photometry of field Galaxies. II - Bulge/disk decompositions.* ApJS, 59:115–159, 1985.

Kitaura, F.-S. *The initial conditions of the Universe from constrained simulations.* MNRAS, 429:L84–L88, 2013.

Kitaura, F.-S.; Erdoğdu, P.; Nuza, S. E.; Khalatyan, A.; Angulo, R. E.; Hoffman, Y.; and Gottlöber, S. *Cosmic structure and dynamics of the local Universe.* MNRAS, 427:L35–L39, 2012.

Kitaura, F.-S. and Heß, S. *Cosmological structure formation with augmented Lagrangian perturbation theory.* MNRAS, 435:L78–L82, 2013.

Kitaura, F. S.; Jasche, J.; Li, C.; Enßlin, T. A.; Metcalf, R. B.; Wandelt, B. D.; Lemson, G.; and White, S. D. M. *Cosmic cartography of the large-scale structure with Sloan Digital Sky Survey data release 6.* MNRAS, 400:183–203, 2009.

Klypin, A.; Hoffman, Y.; Kravtsov, A. V.; and Gottlöber, S. *Constrained Simulations of the Real Universe: The Local Supercluster.* ApJ, 596:19–33, 2003.

Klypin, A.; Kravtsov, A. V.; Valenzuela, O.; and Prada, F. *Where Are the Missing Galactic Satellites?* ApJ, 522:82–92, 1999.

Klypin, A.; Prada, F.; Yepes, G.; Hess, S.; and Gottlober, S. *Halo Abundance Matching: accuracy and conditions for numerical convergence.* ArXiv e-prints, 2013.

Klypin, A. A. and Shandarin, S. F. *Three-dimensional numerical model of the formation of large-scale structure in the Universe.* MNRAS, 204:891–907, 1983.

Klypin, A. A.; Trujillo-Gomez, S.; and Primack, J. *Dark Matter Halos in the Standard Cosmological Model: Results from the Bolshoi Simulation.* ApJ, 740:102, 2011.

Knebe, A.; Libeskind, N. I.; Pearce, F.; Behroozi, P.; Casado, J.; Dolag, K.; Dominguez-Tenreiro, R.; Elahi, P.; Lux, H.; Muldrew, S. I.; et al. *Galaxies going MAD: the Galaxy-Finder Comparison Project.* MNRAS, 428:2039–2052, 2013.

Knebe, A.; Wagner, C.; Knollmann, S.; Diekershoff, T.; and Krause, F. *On the Starting Redshift Cosmological Simulations: Focusing on Halo Properties.* ApJ, 698:266–274, 2009.

Knollmann, S. R. and Knebe, A. *AHF: Amiga's Halo Finder.* ApJS, 182:608–624, 2009.

Kolatt, T.; Dekel, A.; Ganon, G.; and Willick, J. A. *Simulating Our Cosmological Neighborhood: Mock Catalogs for Velocity Analysis.* ApJ, 458:419, 1996.

Kolb, E. W.; Salopek, D. S.; and Turner, M. S. *Origin of density fluctuations in extended inflation.* PRD, 42:3925–3935, 1990.

Komatsu, E.; Dunkley, J.; Nolta, M. R.; Bennett, C. L.; Gold, B.; Hinshaw, G.; Jarosik, N.; Larson, D.; Limon, M.; Page, L.; et al. *Five-Year Wilkinson Microwave Anisotropy Probe Observations: Cosmological Interpretation.* ApJS, 180:330–376, 2009.

Komatsu, E.; Smith, K. M.; Dunkley, J.; Bennett, C. L.; Gold, B.; Hinshaw, G.; Jarosik, N.; Larson, D.; Nolta, M. R.; Page, L.; et al. *Seven-year Wilkinson Microwave Anisotropy Probe (WMAP) Observations: Cosmological Interpretation.* ApJS, 192:18, 2011.

Kowal, C. T. *Absolute magnitudes of supernovae.* AJ, 73:1021–1024, 1968.

Kraan-Korteweg, R. C.; Cayette, V.; Balkowski, C.; Fairall, A. P.; and Henning, P. A. *The 3-Dimensional Galaxy Distribution in the ZOA from Hydra/Antlia to the Great Attractor Region.* 67:99, 1994.

Krauss, L. M. *Big Bang Nucleosynthesis and Dark Matter: Baryons and Neutrinos.* page 65, 1995.

Kravtsov, A. V.; Klypin, A. A.; and Khokhlov, A. M. *Adaptive Refinement Tree: A New High-Resolution N-Body Code for Cosmological Simulations.* ApJS, 111:73, 1997.

Lahav, O.; Santiago, B. X.; Webster, A. M.; Strauss, M. A.; Davis, M.; Dressler, A.; and Huchra, J. P. *The supergalactic plane revisited with the Optical Redshift Survey.* MNRAS, 312:166–176, 2000.

Landy, S. D. and Szalay, A. S. *A general analytical solution to the problem of Malmquist bias due to lognormal distance errors.* ApJ, 391:494–501, 1992.

Larson, D.; Dunkley, J.; Hinshaw, G.; Komatsu, E.; Nolta, M. R.; Bennett, C. L.; Gold, B.; Halpern, M.; Hill, R. S.; Jarosik, N.; et al. *Seven-year Wilkinson Microwave Anisotropy Probe (WMAP) Observations: Power Spectra and WMAP-derived Parameters.* ApJS, 192:16, 2011.

Lavaux, G. *Precision constrained simulation of the local Universe.* MNRAS, 406:1007–1013, 2010.

Lavaux, G.; Afshordi, N.; and Hudson, M. J. *First measurement of the bulk flow of nearby galaxies using the cosmic microwave background.* MNRAS, 430:1617–1635, 2013.

Lavaux, G.; Mohayaee, R.; Colombi, S.; Tully, R. B.; Bernardeau, F.; and Silk, J. *Observational biases in Lagrangian reconstructions of cosmic velocity fields.* MNRAS, 383:1292–1318, 2008.

Lavaux, G.; Tully, R. B.; Mohayaee, R.; and Colombi, S. *Cosmic Flow From Two Micron All-Sky Redshift Survey: the Origin of Cosmic Microwave Background Dipole and Implications for ΛCDM Cosmology.* ApJ, 709:483–498, 2010.

Lee, M. G.; Freedman, W. L.; and Madore, B. F. *The Tip of the Red Giant Branch as a Distance Indicator for Resolved Galaxies.* ApJ, 417:553, 1993.

Leeuwin, F.; Combes, F.; and Binney, J. *N-body simulations with perturbation particles. I - Method and tests.* MNRAS, 262:1013–1022, 1993.

Lemaître, G. *Expansion of the universe, A homogeneous universe of constant mass and increasing radius accounting for the radial velocity of extra-galactic nebulae.* MNRAS, 91:483–490, 1931a.

Lemaître, G. *Expansion of the universe, The expanding universe.* MNRAS, 91:490–501, 1931b.

Libeskind, N. I.; Di Cintio, A.; Knebe, A.; Yepes, G.; Gottlöber, S.; Steinmetz, M.; Hoffman, Y.; and Martinez-Vaquero, L. A. *Cold versus Warm Dark Matter Simulations of a Galaxy Group.* PASA, 30:e039, 2013.

Longair, M. S. and Einasto, J. *The large scale structure of the universe; Proceedings of the Symposium, Tallin, Estonian SSR, September 12-16, 1977.* 79, 1978.

Lynden-Bell, D.; Burstein, D.; Davies, R. L.; Dressler, A.; and Faber, S. M. *On best distance estimators and galaxy streaming.* 4:307–316, 1988a.

Lynden-Bell, D.; Faber, S. M.; Burstein, D.; Davies, R. L.; Dressler, A.; Terlevich, R. J.; and Wegner, G. *Spectroscopy and photometry of elliptical galaxies. V - Galaxy streaming toward the new supergalactic center.* ApJ, 326:19–49, 1988b.

MacArthur, L. A.; Courteau, S.; and Holtzman, J. A. *Structure of Disk-dominated Galaxies. I. Bulge/Disk Parameters, Simulations, and Secular Evolution.* ApJ, 582:689–722, 2003.

Makarov, D.; Makarova, L.; Rizzi, L.; Tully, R. B.; Dolphin, A. E.; Sakai, S.; and Shaya, E. J. *Tip of the Red Giant Branch Distances. I. Optimization of a Maximum Likelihood Algorithm.* AJ, 132:2729–2742, 2006.

Martínez, H. J.; O'Mill, A. L.; and Lambas, D. G. *The evolution of the bimodal colour distribution of galaxies in Sloan Digital Sky Survey groups.* MNRAS, 372:253–258, 2006.

Marzke, R. O.; Huchra, J. P.; and Geller, M. J. *Large-Scale Structure at Low Galactic Latitude.* AJ, 112:1803, 1996.

Masters, K. L.; Springob, C. M.; Haynes, M. P.; and Giovanelli, R. *SFI++ I: A New I-Band Tully-Fisher Template, the Cluster Peculiar Velocity Dispersion, and H_0.* ApJ, 653:861–880, 2006.

Mathewson, D. S.; Ford, V. L.; and Buchhorn, M. *A southern sky survey of the peculiar velocities of 1355 spiral galaxies.* ApJS, 81:413–659, 1992.

Mathis, H.; Lemson, G.; Springel, V.; Kauffmann, G.; White, S. D. M.; Eldar, A.; and Dekel, A. *Simulating the formation of the local galaxy population.* MNRAS, 333:739–762, 2002.

McDonald, M.; Courteau, S.; and Tully, R. B. *Bulge-disc decompositions and structural bimodality of Ursa Major cluster spiral galaxies.* MNRAS, 393:628–640, 2009a.

McDonald, M.; Courteau, S.; and Tully, R. B. *The near-IR luminosity function and bimodal surface brightness distributions of Virgo cluster galaxies.* MNRAS, 394:2022–2042, 2009b.

McGaugh, S. S. *The number, luminosity and mass density of spiral galaxies as a function of surface brightness.* MNRAS, 280:337–354, 1996.

McGaugh, S. S. *The Baryonic Tully-Fisher Relation of Gas-rich Galaxies as a Test of ΛCDM and MOND.* AJ, 143:40, 2012.

McGaugh, S. S.; Bothun, G. D.; and Schombert, J. M. *Galaxy Selection and the Surface Brightness Distribution.* AJ, 110:573, 1995.

McGaugh, S. S. and de Blok, W. J. G. *Gas Mass Fractions and the Evolution of Spiral Galaxies.* ApJ, 481:689, 1997.

McGaugh, S. S.; Schombert, J. M.; Bothun, G. D.; and de Blok, W. J. G. *The Baryonic Tully-Fisher Relation.* ApJL, 533:L99–L102, 2000.

Meidt, S. E.; Schinnerer, E.; Knapen, J. H.; Bosma, A.; Athanassoula, E.; Sheth, K.; Buta, R. J.; Zaritsky, D.; Laurikainen, E.; Elmegreen, D.; et al. *Reconstructing the Stellar Mass Distributions of Galaxies Using S^4G IRAC 3.6 and 4.5 μm Images. I. Correcting for Contamination by Polycyclic Aromatic Hydrocarbons, Hot Dust, and Intermediate-age Stars.* ApJ, 744:17, 2012.

Mestel, L. *On the galactic law of rotation.* MNRAS, 126:553, 1963.

Meyerdierks, H. *A cloud-Galaxy collision - Observation and theory.* A&A, 251:269–275, 1991.

Milgrom, M. *A modification of the Newtonian dynamics - Implications for galaxies.* ApJ, 270:371–389, 1983a.

Milgrom, M. *A Modification of the Newtonian Dynamics - Implications for Galaxy Systems.* ApJ, 270:384, 1983b.

Milgrom, M. *A modification of the Newtonian dynamics as a possible alternative to the hidden mass hypothesis.* ApJ, 270:365–370, 1983c.

Milvang-Jensen, B. and Jørgensen, I. *Galaxy Surface Photometry.* Baltic Astronomy, 8:535–574, 1999.

Mitronova, S. N.; Karachentsev, I. D.; Karachentseva, V. E.; Jarrett, T. H.; and Kudrya, Y. N. *The 2MASS-selected Flat Galaxy Catalog.* Bulletin of the Special Astrophysics Observatory, 57:5–163, 2004.

Mocz, P.; Green, A.; Malacari, M.; and Glazebrook, K. *The Tully-Fisher relation for 25 000 Sloan Digital Sky Survey galaxies as a function of environment.* MNRAS, 425:296–310, 2012.

Monson, A. J.; Freedman, W. L.; Madore, B. F.; Persson, S. E.; Scowcroft, V.; Seibert, M.; and Rigby, J. R. *The Carnegie Hubble Program: The Leavitt Law at 3.6 and 4.5 μm in the Milky Way.* ApJ, 759:146, 2012.

Moore, B.; Ghigna, S.; Governato, F.; Lake, G.; Quinn, T.; Stadel, J.; and Tozzi, P. *Dark Matter Substructure within Galactic Halos.* ApJL, 524:L19–L22, 1999.

Mosenkov, A. V.; Sotnikova, N. Y.; and Reshetnikov, V. P. *2MASS photometry of edge-on spiral galaxies - I. Sample and general results.* MNRAS, 401:559–576, 2010.

Moster, B. P.; Somerville, R. S.; Maulbetsch, C.; van den Bosch, F. C.; Macciò, A. V.; Naab, T.; and Oser, L. *Constraints on the Relationship between Stellar Mass and Halo Mass at Low and High Redshift.* ApJ, 710:903–923, 2010.

Muñoz-Mateos, J. C.; Gil de Paz, A.; Zamorano, J.; Boissier, S.; Dale, D. A.; Pérez-González, P. G.; Gallego, J.; Madore, B. F.; Bendo, G.; Boselli, A.; et al. *Radial Distribution of Stars, Gas, and Dust in SINGS Galaxies. I. Surface Photometry and Morphology.* ApJ, 703:1569, 2009.

Noordermeer, E. and Verheijen, M. A. W. *The high-mass end of the Tully-Fisher relation.* MNRAS, 381:1463–1472, 2007.

Nusser, A. *Boundary-value problems in cosmological dynamics.* Physica D Nonlinear Phenomena, 237:2158–2161, 2008.

Nusser, A. and Davis, M. *The Cosmological Bulk Flow: Consistency with ΛCDM and z 0 Constraints on σ_8 and γ.* ApJ, 736:93, 2011.

Nuza, S. E.; Hoeft, M.; van Weeren, R. J.; Gottlöber, S.; and Yepes, G. *How many radio relics await discovery?* MNRAS, 420:2006–2019, 2012.

Obreschkow, D. and Meyer, M. *Precise Tully-Fisher Relations without Galaxy Inclinations.* ApJ, 777:140, 2013.

Oke, J. B. and Sandage, A. *Energy Distributions, K Corrections, and the Stebbins-Whitford Effect for Giant Elliptical Galaxies.* ApJ, 154:21, 1968.

Oort, J. H. *The evolution of large-scale structures in the universe. I.* Sterne und Weltraum, 21:456–461, 1982.

Ootsubo, T.; Onaka, T.; Yamamura, I.; Tanabé, T.; Roellig, T. L.; Chan, K.-W.; and Matsumoto, T. *IRTS observation of the mid-infrared spectrum of the zodiacal emission.* Earth, Planets, and Space, 50:507–511, 1998.

Pantoja, C. A.; Altschuler, D. R.; Giovanardi, C.; and Giovanelli, R. *21-cm Line Observations of Galaxies in the Zone of Avoidance.* AJ, 113:905–936, 1997.

Paturel, G.; Petit, C.; Prugniel, P.; Theureau, G.; Rousseau, J.; Brouty, M.; Dubois, P.; and Cambrésy, L. *HYPERLEDA. I. Identification and designation of galaxies.* A&A, 412:45–55, 2003.

Peacock, J. A., Cosmological Physics, 1999.

Peebles, P. J. E., The large-scale structure of the universe, 1980.

Peebles, P. J. E., Principles of Physical Cosmology, 1993.

Peebles, P. J. E.; Phelps, S. D.; Shaya, E. J.; and Tully, R. B. *Radial and Transverse Velocities of Nearby Galaxies.* ApJ, 554:104–113, 2001.

Peebles, P. J. E. and Tully, R. B. *The Variety of Solutions for Dynamics in the Local Group.* ArXiv e-prints, 2013.

Perlmutter, S.; Aldering, G.; Boyle, B. J.; Castro, P. G.; Couch, W. J.; Deustua, S.; Fabbro, S.; Ellis, R. S.; Filippenko, A. V.; Fruchter, A.; et al. *Measurements of Omega and Lambda from 42 High-Redshift Supernovae.* 1998.

Perlmutter, S.; Aldering, G.; Goldhaber, G.; Knop, R. A.; Nugent, P.; Castro, P. G.; Deustua, S.; Fabbro, S.; Goobar, A.; Groom, D. E.; et al. *Measurements of Omega and Lambda from 42 High-Redshift Supernovae.* ApJ, 517:565–586, 1999.

Petry, C. E.; Impey, C. D.; and Foltz, C. B. *Small-Scale Structure in the Ly alpha Forest at High Redshift.* ApJ, 494:60, 1998.

Phillips, M. M. *The absolute magnitudes of Type IA supernovae.* ApJL, 413:L105–L108, 1993.

Pierce, M. J. and Tully, R. B. *Distances to the Virgo and Ursa Major clusters and a determination of H0.* ApJ, 330:579–581, 1988.

Pizagno, J.; Prada, F.; Weinberg, D. H.; Rix, H.-W.; Pogge, R. W.; Grebel, E. K.; Harbeck, D.; Blanton, M.; Brinkmann, J.; and Gunn, J. E. *The Tully-Fisher Relation and its Residuals for a Broadly Selected Sample of Galaxies.* AJ, 134:945–972, 2007.

Planck Collaboration. *Planck 2013 results. XVI. Cosmological parameters.* ArXiv e-prints, 2013.

Pomarède, D.; Courtois, H.; and Tully, R. B. *Visualization of structures and cosmic flows in the local Universe.* 289:323–326, 2013.

Power, C. and Knebe, A. *The impact of box size on the properties of dark matter haloes in cosmological simulations.* MNRAS, 370:691–701, 2006.

Prada, F.; Klypin, A. A.; Cuesta, A. J.; Betancort-Rijo, J. E.; and Primack, J. *Halo concentrations in the standard Λ cold dark matter cosmology.* MNRAS, 423:3018–3030, 2012.

Press, W. H. and Schechter, P. *Formation of Galaxies and Clusters of Galaxies by Self-Similar Gravitational Condensation.* ApJ, 187:425–438, 1974.

Prieto, J. L.; Rest, A.; and Suntzeff, N. B. *A New Method to Calibrate the Magnitudes of Type Ia Supernovae at Maximum Light.* ApJ, 647:501–512, 2006.

Prunet, S.; Pichon, C.; Aubert, D.; Pogosyan, D.; Teyssier, R.; and Gottloeber, S. *Initial Conditions For Large Cosmological Simulations.* ApJS, 178:179–188, 2008.

Rauch, M.; Sargent, W. L. W.; and Barlow, T. A. *Small-Scale Structure at High Redshift. I. Glimpses of the Interstellar Medium at Redshift ~3.5.* ApJ, 515:500–505, 1999.

Rauch, M.; Sargent, W. L. W.; Barlow, T. A.; and Carswell, R. F. *Small-Scale Structure at High Redshift. III. The Clumpiness of the Intergalactic Medium on Subkiloparsec Scales.* ApJ, 562:76–87, 2001.

Rawle, T. D.; Lucey, J. R.; Smith, R. J.; and Head, J. T. C. G. *S0 galaxies in the Coma cluster: environmental dependence of the S0 offset from the Tully-Fisher relation.* MNRAS, 433:2667–2692, 2013.

Reach, W. T.; Megeath, S. T.; Cohen, M.; Hora, J.; Carey, S.; Surace, J.; Willner, S. P.; Barmby, P.; Wilson, G.; Glaccum, W.; et al. *Absolute Calibration of the Infrared Array Camera on the Spitzer Space Telescope.* PASP, 117:978–990, 2005.

Reisenegger, A.; Quintana, H.; Proust, D.; and Slezak, E. *Dynamics and mass of the Shapley Supercluster, the largest bound structure in the local Universe.* The Messenger, 107:18–23, 2002.

Riess, A. G.; Filippenko, A. V.; Challis, P.; Clocchiatti, A.; Diercks, A.; Garnavich, P. M.; Gilliland, R. L.; Hogan, C. J.; Jha, S.; Kirshner, R. P.; et al. *Observational Evidence from Supernovae for an Accelerating Universe and a Cosmological Constant.* AJ, 116:1009–1038, 1998.

Riess, A. G.; Macri, L.; Casertano, S.; Lampeitl, H.; Ferguson, H. C.; Filippenko, A. V.; Jha, S. W.; Li, W.; and Chornock, R. *A 3% Solution: Determination of the Hubble Constant with the Hubble Space Telescope and Wide Field Camera 3.* ApJ, 730:119, 2011.

Riess, A. G.; Macri, L.; Casertano, S.; Sosey, M.; Lampeitl, H.; Ferguson, H. C.; Filippenko, A. V.; Jha, S. W.; Li, W.; Chornock, R.; et al. *A Redetermination of the Hubble Constant with the Hubble Space Telescope from a Differential Distance Ladder.* ApJ, 699:539–563, 2009.

Riess, A. G.; Press, W. H.; and Kirshner, R. P. *Using Type IA supernova light curve shapes to measure the Hubble constant.* ApJL, 438:L17–L20, 1995.

Rizzi, L.; Tully, R. B.; Makarov, D.; Makarova, L.; Dolphin, A. E.; Sakai, S.; and Shaya, E. J. *Tip of the Red Giant Branch Distances. II. Zero-Point Calibration.* ApJ, 661:815–829, 2007.

Robertson, H. P. *Relativistic Cosmology.* Reviews of Modern Physics, 5:62–90, 1933.

Robertson, H. P. *Kinematics and World-Structure.* ApJ, 82:284, 1935.

Robertson, H. P. *Kinematics and World-Structure II.* ApJ, 83:187, 1936a.

Robertson, H. P. *Kinematics and World-Structure III.* ApJ, 83:257, 1936b.

Rowan-Robinson, M., The cosmological distance ladder: Distance and time in the universe, 1985.

Rubin, V. C.; Burstein, D.; Ford, W. K., Jr.; and Thonnard, N. *Rotation velocities of 16 SA galaxies and a comparison of Sa, Sb, and SC rotation properties.* ApJ, 289:81–98, 1985.

Rybicki, G. B. and Press, W. H. *Interpolation, realization, and reconstruction of noisy, irregularly sampled data.* ApJ, 398:169–176.

Sandage, A. *Bias properties of extragalactic distance indicators. 1: The Hubble constant does not increase outward.* ApJ, 430:1–12, 1994.

Saunders, W.; Sutherland, W. J.; Maddox, S. J.; Keeble, O.; Oliver, S. J.; Rowan-Robinson, M.; McMahon, R. G.; Efstathiou, G. P.; Tadros, H.; White, S. D. M.; et al. *The PSCz catalogue.* MNRAS, 317:55–63, 2000.

Scannapieco, C.; Tissera, P. B.; White, S. D. M.; and Springel, V. *Feedback and metal enrichment in cosmological smoothed particle hydrodynamics simulations - I. A model for chemical enrichment.* MNRAS, 364:552–564, 2005.

Schechter, P. *An analytic expression for the luminosity function for galaxies.* ApJ, 203:297–306, 1976.

Schlafly, E. F. and Finkbeiner, D. P. *Measuring Reddening with Sloan Digital Sky Survey Stellar Spectra and Recalibrating SFD.* ApJ, 737:103, 2011.

Schlegel, D. J.; Finkbeiner, D. P.; and Davis, M. *Maps of Dust Infrared Emission for Use in Estimation of Reddening and Cosmic Microwave Background Radiation Foregrounds.* ApJ, 500:525, 1998.

Schombert, J. *ARCHANGEL Galaxy Photometry System.* ArXiv Astrophysics e-prints, 2007.

Schombert, J. and Smith, A. *The Structure of Galaxies I: Surface Photometry Techniques.* PASA, 29:174–192, 2012.

Schweizer, F. *Colliding and Merging Galaxies. III. The Dynamically Young Merger Remnant NGC 3921.* AJ, 111:109, 1996.

Sersic, J. L. *The H II regions as distance indicators.* The Observatory, 79:54–56, 1959.

Shaya, E. J.; Peebles, P. J. E.; and Tully, R. B. *Action Principle Solutions for Galaxy Motions within 3000 Kilometers per Second.* ApJ, 454:15, 1995.

Sheth, K.; Regan, M.; Hinz, J. L.; Gil de Paz, A.; Menéndez-Delmestre, K.; Muñoz-Mateos, J.-C.; Seibert, M.; Kim, T.; Laurikainen, E.; Salo, H.; et al. *The Spitzer Survey of Stellar Structure in Galaxies (S^4G).* PASP, 122:1397–1414, 2010.

Sheth, R. K. and Diaferio, A. *Peculiar velocities of galaxies and clusters.* MNRAS, 322:901–917, 2001.

Silk, J.; Szalay, A. S.; and Zel'dovich, Y. B. *The large-scale structure of the universe.* Scientific American, 249:56–64, 1983.

Silva, L.; Granato, G. L.; Bressan, A.; and Danese, L. *Modeling the Effects of Dust on Galactic Spectral Energy Distributions from the Ultraviolet to the Millimeter Band.* ApJ, 509:103–117, 1998.

Smith, J. A.; Tucker, D. L.; Kent, S.; Richmond, M. W.; Fukugita, M.; Ichikawa, T.; Ichikawa, S.-i.; Jorgensen, A. M.; Uomoto, A.; Gunn, J. E.; et al. *The u'g'r'i'z' Standard-Star System.* AJ, 123:2121–2144, 2002.

Sorce, J. G.; Courtois, H. M.; Gottlöber, S.; Hoffman, Y.; and Tully, R. B. *Simulations of the Local Universe constrained by observational peculiar velocities.* MNRAS, 437:3586–3595, 2014.

Sorce, J. G.; Courtois, H. M.; Sheth, K.; and Tully, R. B. *Bimodality of galaxy disc central surface brightness distribution in the Spitzer 3.6 μm band.* MNRAS, 433:751–758, 2013a.

Sorce, J. G.; Courtois, H. M.; and Tully, R. B. *The Mid-infrared Tully-Fisher Relation: Spitzer Surface Photometry.* AJ, 144:133, 2012a.

Sorce, J. G.; Courtois, H. M.; Tully, R. B.; Seibert, M.; Scowcroft, V.; Freedman, W. L.; Madore, B. F.; Persson, S. E.; Monson, A.; and Rigby, J. *Calibration of the Mid-infrared Tully-Fisher Relation.* ApJ, 765:94, 2013b.

Sorce, J. G.; Tully, R. B.; and Courtois, H. M. *The Mid-infrared Tully-Fisher Relation: Calibration of the Type Ia Supernova Scale and H* $_0$. ApJL, 758:L12, 2012b.

Spergel, D. N.; Bean, R.; Doré, O.; Nolta, M. R.; Bennett, C. L.; Dunkley, J.; Hinshaw, G.; Jarosik, N.; Komatsu, E.; Page, L.; et al. *Three-Year Wilkinson Microwave Anisotropy Probe (WMAP) Observations: Implications for Cosmology.* ApJS, 170:377–408, 2007.

Springel, V. *The cosmological simulation code GADGET-2.* MNRAS, 364:1105–1134, 2005.

Springel, V.; White, S. D. M.; Jenkins, A.; Frenk, C. S.; Yoshida, N.; Gao, L.; Navarro, J.; Thacker, R.; Croton, D.; Helly, J.; et al. *Simulations of the formation, evolution and clustering of galaxies and quasars.* Nature, 435:629–636, 2005.

Springob, C. M.; Masters, K. L.; Haynes, M. P.; Giovanelli, R.; and Marinoni, C. *SFI++. II. A New I-Band Tully-Fisher Catalog, Derivation of Peculiar Velocities, and Data Set Properties.* ApJS, 172:599–614, 2007.

Stoughton, C.; Lupton, R. H.; Bernardi, M.; Blanton, M. R.; Burles, S.; Castander, F. J.; Connolly, A. J.; Eisenstein, D. J.; Frieman, J. A.; Hennessy, G. S.; et al. *Sloan Digital Sky Survey: Early Data Release.* AJ, 123:485–548, 2002.

Strauss, M. A. and Willick, J. A. *The density and peculiar velocity fields of nearby galaxies.* Physics Reports, 261:271–431, 1995.

Sunyaev, R. A. and Zeldovich, I. B. *Microwave background radiation as a probe of the contemporary structure and history of the universe.* ARA&A, 18:537–560, 1980.

Sunyaev, R. A. and Zeldovich, Y. B. *Small-Scale Fluctuations of Relic Radiation.* APSS, 7:3–19, 1970.

Swaters, R. A.; Sanders, R. H.; and McGaugh, S. S. *Testing Modified Newtonian Dynamics with Rotation Curves of Dwarf and Low Surface Brightness Galaxies.* ApJ, 718:380–391, 2010.

Teerikorpi, P. *Theoretical aspects in the use of the inverse Tully-Fisher relation for distance determination.* A&A, 234:1–4, 1990.

Teerikorpi, P. *On general Malmquist corrections to direct and inverse Tully-Fisher distance moduli.* A&A, 280:443–450, 1993.

Teerikorpi, P. *The inverse Tully-Fisher relation.* Astrophysical Letters and Communications, 31:263, 1995.

Teerikorpi, P. *Observational Selection Bias Affecting the Determination of the Extragalactic Distance Scale.* ARA&A, 35:101–136, 1997.

Teyssier, R. *Cosmological hydrodynamics with adaptive mesh refinement. A new high resolution code called RAMSES.* A&A, 385:337–364, 2002.

Thompson, R. I. *Tests and constraints on theories of galaxy formation and evolution.* APSS, 284:353–356, 2003.

Tielens, A. G. G. M. *Interstellar Polycyclic Aromatic Hydrocarbon Molecules.* ARA&A, 46:289–337, 2008.

Tikhonov, A. V. and Klypin, A. *The emptiness of voids: yet another overabundance problem for the* Λ *cold dark matter model.* MNRAS, 395:1915–1924, 2009.

Tonry, J. L.; Dressler, A.; Blakeslee, J. P.; Ajhar, E. A.; Fletcher, A. B.; Luppino, G. A.; Metzger, M. R.; and Moore, C. B. *The SBF Survey of Galaxy Distances. IV. SBF Magnitudes, Colors, and Distances.* ApJ, 546:681–693, 2001.

Torres-Flores, S.; Mendes de Oliveira, C.; Plana, H.; Amram, P.; and Epinat, B. *The Tully-Fisher relations for Hickson compact group galaxies.* MNRAS, 432:3085–3096, 2013.

Tully, R. *Galaxies: Lighthouses in the Shoals of Dark Halos.* ArXiv e-prints, 2010.

Tully, R. B. *Our CMB Motion: The Role of the Local Void.* In Metcalfe, N. and Shanks, T., editors, Cosmic Frontiers, volume 379 of ASPCS, page 24. 2007.

Tully, R. B., The Local Velocity Anomaly, 2008a. page 3.

Tully, R. B. *The Local Void is Really Empty.* In J. Davies & M. Disney, editor, IAU Symposium, volume 244 of IAU Symposium, pages 146–151. 2008b.

Tully, R. B. and Courtois, H. M. *Cosmicflows-2: I-band Luminosity-H I Linewidth Calibration.* ApJ, 749:78, 2012.

Tully, R. B.; Courtois, H. M.; Dolphin, A. E.; Fisher, J. R.; Héraudeau, P.; Jacobs, B. A.; Karachentsev, I. D.; Makarov, D.; Makarova, L.; Mitronova, S.; et al. *Cosmicflows-2: The Data.* AJ, 146:86, 2013.

Tully, R. B. and Fisher, J. R. *A new method of determining distances to galaxies.* A&A, 54:661–673, 1977.

Tully, R. B. and Fouque, P. *The extragalactic distance scale. I - Corrections to fundamental observables.* ApJS, 58:67–80, 1985.

Tully, R. B.; Mould, J. R.; and Aaronson, M. *A color-magnitude relation for spiral galaxies.* ApJ, 257:527–537, 1982.

Tully, R. B. and Pierce, M. J. *Distances to Galaxies from the Correlation between Luminosities and Line Widths. III. Cluster Template and Global Measurement of* H_0. ApJ, 533:744–780, 2000.

Tully, R. B.; Pierce, M. J.; Huang, J.-S.; Saunders, W.; Verheijen, M. A. W.; and Witchalls, P. L. *Global Extinction in Spiral Galaxies.* AJ, 115:2264–2272, 1998.

Tully, R. B.; Rizzi, L.; Shaya, E. J.; Courtois, H. M.; Makarov, D. I.; and Jacobs, B. A. *The Extragalactic Distance Database.* AJ, 138:323–331, 2009.

Tully, R. B.; Shaya, E. J.; Karachentsev, I. D.; Courtois, H. M.; Kocevski, D. D.; Rizzi, L.; and Peel, A. *Our Peculiar Motion Away from the Local Void.* ApJ, 676:184–205, 2008.

Tully, R. B. and Verheijen, M. A. W. *The Ursa Major Cluster of Galaxies. II. Bimodality of the Distribution of Central Surface Brightnesses.* ApJ, 484:145, 1997.

Tully, R. B.; Verheijen, M. A. W.; Pierce, M. J.; Huang, J.-S.; and Wainscoat, R. J. *The Ursa Major Cluster of Galaxies.I.Cluster Definition and Photometric Data.* AJ, 112:2471, 1996.

Turnbull, S. J.; Hudson, M. J.; Feldman, H. A.; Hicken, M.; Kirshner, R. P.; and Watkins, R. *Cosmic flows in the nearby universe from Type Ia supernovae.* MNRAS, 420:447–454, 2012.

Verheijen, M. A. W.; Oosterloo, T. A.; van Cappellen, W. A.; Bakker, L.; Ivashina, M. V.; and van der Hulst, J. M. *Apertif, a focal plane array for the WSRT.* 1035:265–271, 2008.

Watson, W. A.; Iliev, I. T.; Diego, J. M.; Gottlöber, S.; Knebe, A.; Martínez-González, E.; and Yepes, G. *Statistics of extreme objects in the Juropa Hubble Volume simulation.* ArXiv e-prints, 2013.

Werner, M. W.; Roellig, T. L.; Low, F. J.; Rieke, G. H.; Rieke, M.; Hoffmann, W. F.; Young, E.; Houck, J. R.; Brandl, B.; Fazio, G. G.; et al. *The Spitzer Space Telescope Mission.* ApJS, 154:1–9, 2004.

Wetzel, A. R.; Tinker, J. L.; and Conroy, C. *Galaxy evolution in groups and clusters: star formation rates, red sequence fractions and the persistent bimodality.* MNRAS, 424:232–243, 2012.

Whitaker, K. E.; Labbé, I.; van Dokkum, P. G.; Brammer, G.; Kriek, M.; Marchesini, D.; Quadri, R. F.; Franx, M.; Muzzin, A.; Williams, R. J.; et al. *The NEWFIRM Medium-band Survey: Photometric Catalogs, Redshifts, and the Bimodal Color Distribution of Galaxies out to z ˜ 3.* ApJ, 735:86, 2011.

White, S. D. M.; Frenk, C. S.; and Davis, M. *Clustering in a neutrino-dominated universe.* ApJL, 274:L1–L5, 1983.

Williams, M. J.; Bureau, M.; and Cappellari, M. *The Tully-Fisher relations of early-type spiral and S0 galaxies.* MNRAS, 409:1330–1346, 2010.

Willick, J. A. *Statistical bias in distance and peculiar velocity estimation. 1: The 'calibration' problem.* ApJS, 92:1–31, 1994.

Willick, J. A.; Courteau, S.; Faber, S. M.; Burstein, D.; and Dekel, A. *Homogeneous Velocity-Distance Data for Peculiar Velocity Analysis. I. Calibration of Cluster Samples.* ApJ, 446:12, 1995.

Willick, J. A.; Courteau, S.; Faber, S. M.; Burstein, D.; Dekel, A.; and Kolatt, T. *Mark III Catalog of Galaxy Peculiar Velocities (Willick+ 1997).* VizieR Online Data Catalog, 7198:0, 1996.

Wright, E. L. *WISE the Wide-field Infrared Survey Explorer.* In Zinnecker, H.; Epchtein, N.; and Rauer, H., editors, EAS Publications Series, volume 33 of EAS Publications Series, pages 57–62. 2008.

Xia, J.-Q.; Vitagliano, V.; Liberati, S.; and Viel, M. *Cosmography beyond standard candles and rulers.* PRD, 85(4):043520, 2012.

Xu, G. *A New Parallel N-Body Gravity Solver: TPM.* ApJS, 98:355, 1995.

Zaritsky, D.; Courtois, H.; Muñoz-Mateos, J.-C.; Sorce, J.; Erroz-Ferrer, S.; Comerón, S.; Gadotti, D. A.; Gil de Paz, A.; Hinz, J. L.; Laurikainen, E.; et al. *The Baryonic Tully-Fisher Relationship for S$ˆ4$G Galaxies and the "Condensed" Baryon Fraction of Galaxies.* ArXiv e-prints, 2014.

Zaroubi, S. *Reconstructing the ZOA from Galaxy Peculiar Velocities.* In R. C. Kraan-Korteweg, P. A. Henning, & H. Andernach, editor, Mapping the Hidden Universe: The Universe behind the Mily Way - The Universe in HI, volume 218 of ASPCS, page 173. 2000.

Zaroubi, S. *Unbiased reconstruction of the large-scale structure.* MNRAS, 331:901–908, 2002.

Zaroubi, S.; Hoffman, Y.; and Dekel, A. *Wiener Reconstruction of Large-Scale Structure from Peculiar Velocities.* ApJ, 520:413–425, 1999.

Zaroubi, S.; Hoffman, Y.; Fisher, K. B.; and Lahav, O. *Wiener Reconstruction of the Large-Scale Structure.* ApJ, 449:446, 1995.

Zavala, J.; Jing, Y. P.; Faltenbacher, A.; Yepes, G.; Hoffman, Y.; Gottlöber, S.; and Catinella, B. *The Velocity Function in the Local Environment from ΛCDM and ΛWDM Constrained Simulations.* ApJ, 700:1779–1793, 2009.

Zel'dovich, Y. B. *Gravitational instability: An approximate theory for large density perturbations.* A&A, 5:84–89, 1970.

Zemp, M.; Stadel, J.; Moore, B.; and Carollo, C. M. *An optimum time-stepping scheme for N-body simulations.* MNRAS, 376:273–286, 2007.

Zhong, G. H.; Liang, Y. C.; Liu, F. S.; Hammer, F.; Hu, J. Y.; Chen, X. Y.; Deng, L. C.; and Zhang, B. *A large sample of low surface brightness disc galaxies from the SDSS - I. The sample and the stellar populations.* MNRAS, 391:986–999, 2008.

Zwicky, F. *Die Rotverschiebung von extragalaktischen Nebeln.* Helvetica Physica Acta, 6:110–127, 1933.

Acknowledgements

Completing a PhD is a road ahead with its challenges but this long road has been worthwhile. I would like to thank every single person who walked alongside me on this tortuous path. First of all, I would like to acknowledge the persons who supervised my scientific work. In that sense thanks go to Hélène Courtois, Stefan Gottlöber, Brent Tully and Yehuda Hoffman who answered every single question I had, helped me develop my critiscism and my research abilities and welcomed me in their collaborations to accomplish this work. I would like to add Matthias Steinmetz, Gustavo Yepes and Christophe Dujardin who also contributed to the successful proceedings of my PhD. Special thanks go to my referee. The members I have not mentioned yet are Corinne Augier and Cristiano Porciani.

This thesis required lots of codes implying developers. I am thus particularly in debt to James Schombert for Archangel, Timur Doumler for ICeCoRe (but also for the german language), Steffen Knollmann for Ginnungagap, Volker Springel for Gadget, Alexander Knebe for Amiga halo finder and Daniel Pomarède for SDvision. Because this thesis work is the result of two international collaborations, Cosmicflows and CLUES, I am grateful to the different universities and institutes who welcomed me for several months at a time. I want to mention the Universities of Hawaii, Potsdam and Lyon and the Institutes for Astronomy and of Nuclear Physics as well as the Leibniz-Institute for Astrophysics. With these different locations over the world comes a multitude of persons to thank. Also I thank Noam Libeskind, Steffen Hess, Francisco-Shu Kitaura, Jabran Zahid, Kirsten Larson and Alain Khayat. I would like to add to this list Don Neil, Mark Seibert, Barry Madore, Wendy Freedman, Victoria Scowcroft, Igor Karachentsev, Kartik Sheth, Dennis Zaritsky and Tom Jarrett and all the others that I may have forgotten and to whom I present my deepest apologizes. I would like to give a special thank to Sylvie Flores who assumed the role of my PhD godmother during these three years and was always able to discern when I was in my most distressing times, hence needed support.

This thesis used lots of computer facilities and thanks go to people in charge of the maintenance of such computing systems in Potsdam, in Lyon, in Hawaii and in Munich. This work also made use of powerful databases (NED, EDD and HyperLeda), thanks go to their founders. I think that it is worthwhile mentioning the numerous wonderful persons that I met at conferences and that I will never forget. Unfortunately this page will not be enough to mention all of them but I want to express how much I enjoyed meeting every single one of them.

Then there are lots of persons upstream this thesis to thank beginning with the teacher I had the year before the last in grammar school, and continuing with all the physics teachers I had after that subsequently in (junior) high schools, preparatory school and at the Ecole Normale Supérieure de Lyon. I would like to thank Roy Gal and Lisa Kewley for being my supervisors for my first long term internship in astrophysics.

Last but not least, come the persons who have continuously followed the flows with me, to whom I owe everything: my parents. A very special thank goes to Pierre who always supported me during these three years and never doubted of me even when I would. He helped me go through the most difficult times bringing light, joy and love into my life.

Declaration of independent work

I hereby declare that this thesis is the product of my own independent work and that I have listed all the literature and resources that have been used.

Déclaration sur l'honneur

Je certifie que cette thèse est le fruit de mon propre travail et qu'elle a été rédigée sans autre aide que les sources et références dûment citées.

Selbständigkeitserklärung

Hiermit versichere ich, dass ich die vorliegende Arbeit selbständig verfasst und keine anderen als die angegebenen Quellen und Hilfsmittel benutzt habe.

Jenny Sorce
Lyon, 12 06 2014

The scientific results presented in this thesis have been or will be published in ApJ, ApJL, AJ and MNRAS journals as an ensemble of papers. (Sorce et al., 2014, 2013a, 2012a, 2013b, 2012b, and others are in preparation)